




on-line
28º CONGRESSO DA SOCIEDADE BRASILEIRA
DE MICROSCOPIA E MICROANÁLISE
12 a 15 JUL 2021

50 anos
SOCIEDADE BRASILEIRA DE
MICROSCOPIA E MICROANÁLISE

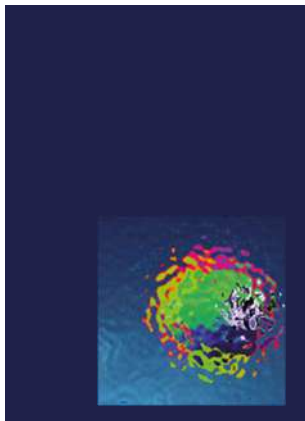
CADERNO DE ANAIS



RESUMOS APRESENTADOS NO
28º CONGRESSO BRASILEIRO DE
MICROSCOPIA E MICROANÁLISE
DA SBMM. ON-LINE, 2021



CADERNO DE ANAIS



**RESUMOS APRESENTADOS NO
28º CONGRESSO BRASILEIRO DE
MICROSCOPIA E MICROANÁLISE
DA SBMM. ON-LINE, 2021**



DIRETORIA DA SBMM (2020-2022)

Presidente

Marco Cesar Cunegundes Guimarães (UFES)

Vice-Presidente (Ciências de Materiais)

Prof. Rodrigo Prioli Menezes (PUC-Rio)

Vice-Presidente (Ciências Biológicas)

Rodrigo Villares Portugal (LNNANO-CNPEM)

Tesoureiro

Eduardo José Lopes Torres (UERJ)

Secretário-Geral

Paula Mendes Jardim (UFRJ)

COMISSÃO DE MÍDIAS SOCIAIS

Beatriz Rodrigues Canabarro (UFRJ)

Dayane Alvarinho de Oliveira (UERJ)

Flávio Cunha Monteiro (UFES)

EDIÇÃO DOS ANAIS

Emerson Campos Gonçalves (UFES)



COMISSÃO CIENTÍFICA NACIONAL

Adriana Lanfredi (Fiocruz)	José Brant de Campos (UERJ)
Alberto Moreira (UFSCAR)	Karla Balzuweit (UFMG)
Alexandre Bruni-Cardoso (USP)	Kildare Miranda (UFRJ)
André Galembeck (UFPE)	Leonardo Salgado (Jardim Botânico)
André Linhares Rossi (CBPF)	Jefferson Bettini (LNNANO)
Andre LB Ambrosio (USP)	Jesiel Freitas Carvalho (UFG)
Antonio Gomes Souza Filho (UFC)	Lia Carolina Soares Medeiros (Fiocruz)
Benjamin Fagneaud (UFJF)	Luciano Paulino Silva (EMBRAPA)
Bernardo Ruegger de Almeida Neves (UFMG)	Lucio Ayres Caldas (UFRJ)
Bráulio S. Archanjo (INMETRO)	Luiz Henrique de Almeida (UFRJ)
Carlos Alberto Ospina Ramirez (LNNANO)	Marcia Attias (UFRJ)
Carlos Lenz (UNICAMP)	Marcos Farina (UFRJ)
Clara Muniz Almeida (INMETRO)	Marin Gerard Van Heel (LNNANO)
Cristiani Campos (UFSC)	Marlene Benchimol (Unigranrio e UFRJ)
Daniel Lorscheitter Baptista (UFFRGS)	Marcia Rizzutto (USP)
Daniel Mario Ugarte (UNICAMP)	Maura da Cunha (UENF)
Daniela Zanchet (UNICAMP)	Paola Barbosa (UNB)
Diego Ferreira Regalado (UEA)	Paulo Fichtner (UFRGS)
Edilene Oliveira da Silva (UFPA)	Richard Charles Garratt (USP)
Elane Giese (UFRA)	Rita Sinigaglia (UNIFESP)
Emilio de Castro Miguel (UFC)	Rossana Melo (UFJF)
Fabio Mendonca Gomes (UFRJ)	Sidnei Paciornik (PUC-Rio)
Francisco Gil Coury (UFSCAR)	Sônia Nair Baó (UNB)
Gilberto Weissmuller (BIOF-UFRJ)	Suzana Peripolli (UERJ)
Giovanna Machado (CETENE)	Wandereley de Souza (UFRJ)
Greg Kitten (UFMG)	Wendell Girard Dias (Fiocruz)
Hernandes Carvalho (UNICAMP)	Witor Wolf (UFMG)
Henrique Duarte Fonseca Filho (UFAM)	Yaro Parizek (CENPES Petrobras)

TODOS OS DIREITOS RESERVADOS.

SOCIEDADE BRASILEIRA DE MICROSCOPIA E MICROANÁLISE – SBMM

Instituto de Biofísica Carlos Chagas Filho – UFRJ. Av. Carlos Chagas Filho, 373 edifício
do CCS Bloco G. CEP 21941-902 - Rio de Janeiro - RJ Brasil

Congresso Brasileiro de Microscopia e Microanálise da SBMM (28.
: 2021 : on-line)

Anais do 28º Congresso Brasileiro de Microscopia e
Microanálise da SBMM, 12 a 15 de julho de 2021, online [recurso
eletrônico, PDF] – Rio de Janeiro, UFRJ, SBMM, 2021.

Edição digital

Disponível em:

ISSN –

1. Microscopia. 2. Microanálise. I. Título.



PATROCÍNIO MASTER



PATROCÍNIO OURO

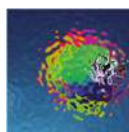


PATROCÍNIO PRATA



APOIO








APRESENTAÇÃO

Prezados colegas,

Temos o prazer de apresentar os anais do **28º Congresso Brasileiro de Microscopia e Microanálise**, realizado exclusivamente on-line pela Sociedade Brasileira de Microscopia e Microanálise (SBMM) no período de 12 a 15 de julho de 2021.

Esta foi, seguramente, a atividade científica mais importante da Microscopia e Microanálise no Brasil, promovida pela maior sociedade científica de Microscopia e Microanálise da América Latina.

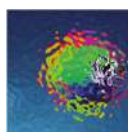
Em sua edição de número 28, o Congresso buscou um triplo objetivo:

-  Atualizar os participantes sobre os temas de maior importância em microscopia e microanálise;
-  Informar sobre as novidades e avanços tecnológicos apresentados pelos patrocinadores;
-  E possibilitar a atualização e o esclarecimento de dúvidas dos participantes com eminentes professores nacionais e internacionais da área.

Nestes anais, estão reunidos os resumos das exposições orais e dos pôsteres apresentados no 28º CSBMM. A publicação desses trabalhos tem como objetivo compartilhar os debates científicos realizados na ocasião, fomentando o estabelecimento de vínculos colaborativos entre diferentes núcleos de pesquisa e fortalecendo o compromisso da SBMM com a consolidação de uma atmosfera de constante formação de recursos humanos de alto nível no Brasil.

Prof. Marco Cesar Cunegundes Guimarães (UFES)

Presidente da Sociedade Brasileira de Microscopia e Microanálise



SUMÁRIO

APRESENTAÇÕES ORAIS

- Characterization of *Giardia intestinalis* cytoskeleton using high-resolution microscopy techniques** 26
Raphael Verdan, Ana Paula Gadelha, Kildare Miranda, Marlene Benchimol
- Characterization of bacteria adhered on the cuticle of nematodes isolated from ear canal of Gir cattle** 28
Makoto Enoki Caracciolo, Ander Castello Branco Santos and Eduardo José Lopes Torres
- Morphological and Morphometric Aspect Of Embryos And Larvae Of *Heros severus*: An Ornamental Fish.** 30
Alex S. Paiva, Ivana K.S. Viana, Yuri W.M. Favacho, Andrews H. F. Leão, João M.S. Rodrigues, Breno R.M. Silva, Yanne A.Mendes and Maria A.P. Ferreira.
- Structural mechanism and polymerization of Glutaminase *in vitro* and *in situ*.** 32
Marília M Dias, Jose Edwin N Quesñay, Camila T Rodrigues, Flávia MO Abreu, Alliny CS Bastos, Zhengyi Yang, Anna Steyer, Ievgeniia Zagoriy, Simone Mattei, Zeyaul Islam, Alexandre Cassago, Marin van Heel, Silvio R Consonni, Julia Mahamid, Rodrigo V Portugal, Andre LB Ambrosio, Sandra MG Dias.
- The involvement of the Nucleolar Protein 16 (Nop16) in the Physiology of *Cryptococcus gattii*, a fungal pathogen.** 34
Rafael F. Castelli, Flavia C. G. Reis, Haroldo C. de Oliveira, Ane W. A. Garcia, Anny W. Robert, Tabata Klimeck, Charley C. Staats, Marcio L. Rodrigues
- Cryo-EM To Visualize Viruses And Protein Filaments At Near-Atomic Resolution** 37
Guilherme A. P. de Oliveira
- Unravelling The Structure Of A Type IV Pilus Dependent Bacteriophage** 39
Germán Gustavo Sgro, Alexandre Cassago, Rodrigo Villares Portugal, Shaker Chuck Farah



Exploring the Structure and Filament Assembly of Septin Complexes with Cryo-EM. 41

Deborah Cezar Mendonça, Rodrigo Villares Portugal and Richard Charles Garratt

Cryo-EM Structure Of The Mature And Infective Mayaro Virus At 4.4 Å Resolution Reveals Features Of Arthritogenic Alphaviruses 43

Helder V. Ribeiro-Filho, Lais D. Coimbra, Alexandre Cassago, Rebeca P. F. Rocha, João Victor da Silva Guerra, Rafael de Felicio, Carolina Moretto Carnieli, Luiza Leme, Antonio Cláudio Padilha, Adriana F. Paes Leme, Daniela B. B. Trivella, Rodrigo Villares Portugal, Paulo Sérgio Lopes-de-Oliveira, Rafael Elias Marques.

Structural basis of N-glycan demannosylation by the probiotic *Bifidobacterium longum* 45

Rosa L. Cordeiro, Camila R. Santos, Mariane N. Domingues, Tatiani B. Lima, Renan A. S. Pirolla, Mariana A. B. Morais, Felipe M. Colombari, Renan Y. Miyamoto, Rafael S. Bezerra, Gabriela F. Persinoti, Antonio C. Borges, Fabiane Stoffel, Marin van Heel, Rodrigo V. Portugal, Priscila O. Giuseppe and Mario T. Murakami

Impact of androgenic stimulation on mitochondrial oxygen consumption and organelle distribution in prostatic epithelial cells. 47

Francisco Breno S. Teófilo, Estela N. B. Busanello, Claudia D. C. Navarro, Anibal E. Vercesi, Hernandes F. Carvalho.

Super-Resolution Structured Illumination Microscopy for Analysis of New Chemotherapeutics Against *Toxoplasma gondii* 50

Carlla Assis Araujo-Silva, Jennifer Mendonça Guimarães, Franz Bracher, Wanderley de Souza, Erica dos Santos Martins-Duarte and Rossiane Claudia Vommaro

Ultrastructural Characterization of *Mabuya nigropunctata* Leukocytes 52

Brenda Fachetti, Maíra Turiel-Silva, Edilene O. Silva, Ana Paula Drummond, José Diniz

Morphology and Morphogenesis of SARS-CoV-2 in Vero-E6 Cells 54

Debora Ferreira Barreto-Vieira, Marcos Alexandre Nunes da Silva, Cristiana Couto Garcia, Milene Dias Miranda, Aline da Rocha Matos, Braulia Costa Caetano, Paola Cristina Resende, Fernando Couto Motta, Marilda Mendonça Siqueira, Wendell Girard-Dias, Bráulio Soares Archanjo, Ortrud Monika Barth

Eosinophil cytolytic cell death during human inflammatory diseases: a mechanism underlying release of extracellular traps, granules and vesicles 57

Vitor H. Neves, Cinthia Palazzi, Kennedy Bonjour, Peter F. Weller, Rossana C. N. Melo



- The Exomembrane System of *Cyrtia lignieresi*-Infected Erythrocytes** 59
Maíra Turiel-Silva, Camila Wendt, Brenda Fachetti, Edilene da Silva, Ana Paula Drummond, Wanderley de Souza, Kildare Miranda, José Diniz
- Three-dimensional Characterization of Membrane Fusion Events During Osmoregulation in *Trypanosoma cruzi*** 61
Ingrid Augusto, Wendell Girard Dias, Wanderley de Souza, Veronica Jimenez and Kildare Miranda
- Deciphering the Mayaro virus structure using single-particle Cryo-EM analysis** 63
Helder V. Ribeiro-Filho, Lais D. Coimbra, Alexandre Cassago, Rebeca P. F. Rocha, João Victor da Silva Guerra, Rafael de Felicio, Carolina Moretto Carnieli, Luiza Leme, Antonio Cláudio Padilha, Adriana F. Paes Leme, Daniela B. B. Trivella, Rodrigo Villares Portugal, Paulo Sérgio Lopes-de-Oliveira and Rafael Elias Marques
- A Simple and Straightforward Method for Making Holey Carbon Grids** 66
Ingrid Augusto e Kildare Miranda
- How to Prepare Pathogenic Protists for SEM Using a Simple Low-Cost Chemical Method Without Critical Point Drying** 68
Tuanne Santos Melo and Antonio Pereira-Neves
- High content image-based assays as a tool for experimental chemotherapy** 70
Ana Paula R. Gadelha & Wanderley de Souza
- The use of thiocarbohydrazide to increase membrane contrast and peroxidase labeling of cellular structures in electron microscopy.** 72
Carolina L Alcantara, Narcisa L Cunha e Silva, Wanderley de Souza
- Immunolabeling In Epoxy Resin Embedded Samples** 74
Noêmia Rodrigues, Wanderley de Souza, Marlene Benchimol
- Freeze-Fracture Preparation Without Special Equipment** 76
Luis Otavio da Silva Pacheco, Márcia Attias, Kildare Miranda, Wanderley de Souza
- Cryo-TEM specimen preparation of concentrated polymeric micelle** 79
Laura C. E. da Silva, Antonio C. Borges, Marcelo G. de Oliveira, Marcelo A. de Farias
- Protocol for Cellulose Nanomaterials Size and Morphology Characterization by TEM.** 81
Laura C. E. da Silva, Alexandre Cassago Liliâne C. Battirola, Maria do Carmo Gonçalves and Rodrigo V. Portugal
- Using free software to produce 3D models of helminth eggs** 83
Dias Y; Freitas, EO; Machado, LP; Lopes-Torres EJ



- 1nm Resolution With 0.1m Wavelength: Using Twisted Bilayer Graphene Moiré Patterns To Evaluated The Limits Of Near Field Immersion Microscopy.** 86
Douglas A. A. Ohlberg, Diego Tami, Andreij C. Gadelha, Eliel G. S. Neto, Fabiano C. Santana, Daniel Miranda, Wellington Avelino, Kenji Watanabe, Takashi Taniguchi, Leonardo C. Campos, Jhonattan C. Ramirez, Cássio Gonçalves do Rego, Ado Jorio, Gilberto Medeiros-Ribeiro
- Using atomic force microscopy and self-assembled monolayers to reveal crystal orientation and grain boundaries in 2D materials.** 88
Mariana C. Prado, Regiane Nascimento, Luciano Moura, Camilla K. B. Q. Oliveira, Barbara E. N. Faria, Matheus J. S. Matos, Mario C. Mazzoni, Luiz G. Caçado, Helio Chacham and Bernardo R. A. Neves
- Gypsum: An Environment-Friendly, Inexpensive And Robust Height Calibration Standard At Nanometer-Scale For Atomic Force Microscopy** 90
Ana P. M. Barboza, Joyce C. C. Santos, Elisângela Silva-Pinto and Bernardo R. A. Neves
- Atomic Resolution From Friction Force Microscopy Using The Jarzynski Equality** 92
Yasmin Watanabe, Rodrigo Capaz and Renata Simão
- Electrostatic Force Microscopy Measurements Of The Local Dielectric Constant Of A Biological Nanostructured System** 94
Wesley Walison Valeriano, Rodrigo Ribeiro Andrade, Juan Pablo Vasco, Angelo Malachias, Bernardo Ruegger Almeida Neves, Paulo Sergio Soares Guimarães, and Wagner Nunes Rodrigues
- Microfabrication of Pyramidal Nanoantennae for TERS (Tip Enhanced Raman Spectroscopy)** 96
Fabiano C. Santana, Vitor P. Monken, Bruno S. Oliveira, Thiago L. Vasconcelos, Wagner N. Rodrigues, Luiz Gustavo Caçado, Ado Jório
- Engineering New 2D Functional Materials at Surfaces: from Doped Graphene to Metal-Organic Frameworks** 98
Abner de Siervo
- Local (Cross) Information Density: Powerful Practical Tools for Interpreting 3D Structures, Especially in Cryo-EM.** 100
Sayan Bhakta, Rodrigo V Portugal, Michael Schatz and Marin van Heel
- Use of Deep Convolutional Neural Networks in Automatic Recognition and Classification of Coal Macerals** 102
Magalhães Santos, R. B.; Paciornik, S.; Augusto K.S.; Alvarez Iglesias, J.C.; Rodrigues, S.; Esterle, J.S.; Domingues, A.L.A.



Elemental and structural analysis of granular deposits in the bone growth zone of fin bony rays of zebrafish (*Danio rerio*) 104

Marcos Farina, Jacques Werckmann, Andréa P.C. Campos Mair M.M. de Oliveira and Ovidiu Ersen.

Insight by In Situ-TEM Into the Nucleation and Crystallization Processes of Calcium Phosphate Nanoparticles 106

Gisele Dalmônico, Dris Ihiawakrim, Nathaly Ortiz, Marcos Farina, Ovidiu Ersen and André L. Rossi

Intrinsic Antitumor Properties of Gum Arabic-Gold Nanocomposites 107

Jenifer P Gonçalves, Anderson F da Cruz, Ábner M Nunes, Mario R Meneghetti, Heloíse R de Barros, Beatriz S Borges, Lia CAS de Medeiros, Maurílio J Soares, Gustavo R Rossi, Daniel L Bellan, Stelée MP Biscaia, Aline M Cristal, Edvaldo da S Trindade, Fernanda F Simas, Izabel C Riegel-Vidotti, Carolina C de Oliveira

Conjugation of Spike and Nucleocapsid Proteins of SARS-CoV-2 with Gold Nanoparticles 109

Luis Alberto Contreras, Wanderson Juvencio Keijok, Jairo Pinto de Oliveira and Marco Cesar Cunegundes Guimarães

High Quality Quantitative Structural Analysis of Nanosystems using Pair Distribution Function (PDF) based on Precession Electron Diffraction (PED) 111

Leonardo Corrêa, Murilo Moreira, Varlei Rodrigues and Daniel Ugarte

Finding Hidden Correlations in EDS Hyperspectral images: Elemental Distribution Inside of small Bimetallic Nanoparticles. 113

Murilo Moreira, Matthias Hillenkamp, Varlei Rodrigues, Daniel Ugarte

Phase Identification in NaNbO₃ Perovskite Nanoribbons by STEM - DPC 115

Beatriz Canabarro, Sebastian Calderon, Paulo Ferreira and Paula Jardim

Experimental Evaluation of the Stacking Fault Energy of a Fe-Mn Alloy Through the Measurement of the Partial Dislocations Distance 117

Lucas B. Otani, André L. Vidilli, Claudio S. Kiminami, Walter J. Botta, Francisco G. Coury, Guilherme Zepon and Claudemiro Bolfarini

Production and Characterization of Nb-Ni-WC-Cu Alloys via Spark Plasma Sintering 119

Yara Daniel Ribeiro, Alexandre Candido Soares, José Izabel Liberato Júnior and Gilberto Henrique Tavares Álvares da Silva

Production and Characterization of Nb-10W-15(Ti6Al4V) -1Cu Alloy Via Spark Plasma Sintering 121

Alexandre Candido Soares, Yara Daniel Ribeiro, José Izabel Liberato Júnior and Gilberto Henrique Tavares Álvares da Silva



- Nanomechanical characterization of organic matter and clay mineral using AFAM in shale** 123
D. L.P. de Lacerda, R. Prioli, Y. M. Parizek-Silva and G. F. Vasquez
- Characterization of Sandstones Through Image Analysis and Simulations** 125
Rafael da Silva Vianna, André Maués Brabo Pereira, Ricardo Leiderman, Janine Domingos Vieira
- Digital Volume Correlation (DVC) applied to in-situ microCT Images of Strain-Hardening Cement-Based Composites (SHCC)** 127
Renata Lorenzoni, Iurie Curosu, Sidnei Paciornik, Viktor Mechtcherine, Flavio A. Silva and Giovanni Bruno
- Microstructural characterization of maraging steels Fe-13Ni-15Co-(7.5-15)Mo-(0.06-0.88)Ti (wt.%) after aging** 129
Daniela Passarelo Moura da Fonseca and Angelo Fernando Padilha
- Effect of Heat Treatment on the Microstructure of Polycrystalline Superconducting Ceramic $\text{SmBa}_2\text{Cu}_3\text{O}_{7-d}$.** 131
Carlos A. C. Passos, Raoni C. Barbieri, João V. S. Chagas
- Oxidation Assisted Intergranular Cracking of Alloy 718 associated to γ'' grain boundary dynamic precipitation** 134
Amanda Varela, Luiz Henrique de Almeida
- Application of Electron Pair Distribution Function (ePDF) for Characterization of Beam-sensitive NaREF_4 Nanoparticles** 136
Leonardo Corrêa, Flávia S. Ferreira, Fernando Sigoli and Daniel Ugarte
- Microstructural characterization of the $\text{Cr}_{29.7}\text{Co}_{29.7}\text{Ni}_{35.4}\text{Al}_{4.0}\text{Ti}_{1.2}$ precipitation-hardened multi-principal element alloy** 138
Diego de Araujo Santana, Claudio Shyinti Kiminami and Francisco Gil Coury
- Image and Diffraction Artifacts in TEM Analysis of a Cr-Co-Ni Multi-Principal Element Alloy** 140
Gustavo BERTOLI, Claudio S. KIMINAMI and Francisco G. COURY
- Pair Distribution Function Obtained from Electron Diffraction – ePDF: An Advanced Structural Characterization Tool.** 142
João Batista Souza Junior, Gabriel Ravanhani Schleder, Adalberto Fazzio, Edson Roberto Leite and Jefferson Bettini
- Pitting Corrosion Initiation in Super Duplex Stainless Steel Investigated by EBSD** 145
Ribeiro, T.G.M., Spadotto, J.C., Labre, C. and Bott, I.S.
- Eta phase characterization in HP40 steels after long-term exposure in service conditions** 147
M.C. Mendes, M. Nascimento, L.S. Araújo, L. Mallet, J. Dille, L.H. de Almeida



Assessment of Crystallographic Orientation Relationships Between δ -phase and γ -matrix in Alloy 718 by Electron Backscattered Diffraction 149
Flávia da Cruz Gallo, Luiz Maurício Barreto de Azevedo, Cilene Labre, Loic Mallet, Leonardo Sales Araújo, Luiz Henrique de Almeida

Evaluation of the Twinning Induced Plasticity Effect on a FeMnAlC Steel during Cyclic Deformation 151
André L. Vidilli, Lucas B. Otani, Witor Wolf, Claudio S. Kiminami, Walter J. Botta, Francisco G. Coury and Claudemiro Bolfarini

PÔSTERES

Ultrastructural Analysis of Flagellar Ectosomes-Like Structures in *Tritrichomonas foetus* 154
Abigail Miranda-Magalhães and Antonio Pereira-Neves

Scanning Electron Microscopy of Testicular Maturation of *Baryancistrus xanthellus* 156
Ivana K.S.Viana, Alex S. Paiva, Leocyvan Nunes, Yanne A. Mendes, Renata S. Oliveira, Yuri W.M. Favacho, João M. S. Rodrigues, Liziane A. B. Gonçalves, Rossineide M.Rocha

Activity of the Synthetic Compound 4-(((4-fluorophenyl)amino)methyl)-5-(4-nitrophenyl)-3-[N'-(pyridin-2-ylmethylene)hydrazinecarbonyl]-isoxazole on *Leishmania amazonensis* 158
Amanda Beatriz Kawano Bakoshi, Rayanne Regina Beltrame Machado, Hélio Volpato, Samara Mendes de Souza Melo, Fernanda Andreia Rosa, Tania Ueda-Nakamura, Sueli de Oliveira Silva, Celso Vataru Nakamura and Danielle Lazzarin-Bidóia

The KAP7 importance to cell proliferation, mitochondrial DNA arrangement and repair in the trypanosomatid *Angomonas deanei* 161
Camila Silva Gonçalves, Carolina Moura Costa Catta Preta, Bruno Repolês, Jeremy Mottram, Wanderley de Souza, Carlos Renato Machado and Maria Cristina Machado Motta

Interactions of TiO₂ Microparticles in Sunscreens with Lettuce Plants (*Lactuca Sativa* L.) 163
Ana Kamila Medeiros Lima, Thaiz B. A. R. Miguel and Emilio de Castro Miguel

Characteristic of Human Milk Powder Obtained by Lyophilization. 165
Otávio Augusto Silva Ribeiro, Karla Veloso Gonçalves Ribeiro, Cristiane do Carmo Cesário and Jane Sélia dos Reis Coimbra

Effect of Buparvaquone as Antifungal Agent 167
Luana Pereira Borba-Santos, Thayná Lopes Barreto, Kelly Ishida, Sonia Rozental.



Investigation of Silver Nanoparticles Penetration Into Dentinal Tubules By FIB-SEM 169

Maria Clara Müller de Andrade, Aronita Rosenblatt and André Galembeck

Toxicity of Poly Lactic-co-Glycolic Acid (PLGA) Nanoparticles in *Artemia salina* (Crustacea, Brachiopoda). 171

Marlos de Medeiros Chaves, Vanessa Pinheiro Gonçalves Ferreira, Sergimar Kennedy de Paiva Pinheiro, Thaiz Batista Azevedo Rangel Miguel, Roberto Nicolete, Wilson Savino and Emilio de Castro Miguel

Ultrastructural and Morphological Alterations Induced by a New Synergic Ternary Combination on Promastigotes of *Leishmania amazonensis* 173

Rodolfo Bento Balbinot, Danielle Lazarin-Bidóia, Tania Ueda-Nakamura, Sueli de Oliveira Silva Lautenschlager and Celso Vataru Nakamura

Tubulization Technique Using Polycaprolactone And Fibrin Biopolymer Promotes Axonal Growth And Functional Recovery After Peripheral Nerve Injury 175

Muller, S. K., Leite, A. P. S., Tibúrcio, F. C, R. S., Pinto, C. G., Matsumura, Y. C. and Matheus, S. M. M.

Mayaro virus sample preparation to cryo-EM data collection. 177

Lais Durço Coimbra, Helder Veras Ribeiro-Filho, Alexandre Cassago, Rebeca de Paiva Froes Rocha, João Victor da Silva Guerra, Rafael de Felício, Carolina Moretto Carnieli, Luiza Leme, Antonio Claudio Padilha, Adriana Paes Leme, Daniela Baretto Barbosa Trivella, Rodrigo Villares Portugal, Paulo Sérgio Lopes-de-Oliviera, Rafael Elias Marques

Bovine coronavirus. Detection by transmission electron microscopy techniques. 179

Catroxo, M.H.B., Martins, A.M.C.R.P.F., and Santos, E.M.

Cellular and Metabolic Reprogramming by TGF- β Increases V-ATPase Expression and Tumor Malignancy. 181

Brunna Xavier Martins, Enrico Cossi Arantes, Anna Lvovna Okorokova Façanha Milton Masahiko Kanashiro and Arnaldo Rocha Façanha.

Melanoma Three-Dimensional Model: Refining *in vitro* Models Aiming Treatment Efficacy Prediction. 183

Gabriel Henrique Barbosa da Costa Salkovski, Anderson Fraga da Cruz, Fernanda Fogagnoli Simas, Edvaldo da Silva Trindade and Carolina Camargo de Oliveira

Localization of Beta-NGF Receptors (P75 and Trk) In Cumulus Cells and Bovine Immature Oocytes. 185

Natália Cristina Sossai Arle, Muller Carrara Martins, Lucas Melo Gonçalves and Marcelo Emilio Beletti



- Effect of lead, cadmium, and perfluorooctanoic acid, in single and combined exposures, on the development of the cephalic region of *Gallus gallus*.** 187
Mariliza Cristine Vieira da Costa, Melyssa Kmecick and Claudia Feijó Ortolani-Machado
- Super-resolution microscopy and 3D modeling of the embryonated egg of *Trichuris muris*** 193
Belém LF; Durães CG; Lopes-Torres EJ
- FMRamide-related Peptides in *Aedes aegypti* Midgut: Neuromuscular Connections and Enteric Nervous System** 195
Raquel Soares Maia Godoy, Renata Cristina Barbosa, Breno dos Anjos Costa, Marcelo Jacobs-Lorena, Gustavo Ferreira Martins
- Microanatomical and Secretory Characterization of The Salivary Gland of The *Rhodnius prolixus* (Hemiptera, Reduviidae, Triatominae), a Main Vector of Chagas Disease** 197
Raquel Soares Maia Godoy, Ana Carolina Borella Marfil Anhê, Nágila Francinete Costa Secundino, Paulo Filemon Paolucci Pimenta
- Action of *Caryocar villosum* oil on the ultrastructure of promastigotes of *Leishmania (Leishmania) amazonensis*.** 199
Adan Jesús Galué Parra, Amanda Anastácia Pinto Hage, Lienne Silveira de Moraes and Edilene Oliveira da Silva
- High Resolution Electron Microscopy Analysis of Hemozoin Crystals** 201
Wendt, C., de Souza, W. and Miranda, K.
- Ultrastructural characterization of the freshwater microalgae *Tetrademus obliquus* BR003 (Chlorophyta: Chlorophyceae)** 203
Cristiane do Carmo Cesário, Karla Gonçalves Ribeiro, Jamile Fernanda Silva Cossolin, José Eduardo Serrão and Jane Sélia dos Reis Coimbra
- More than Fixative Solution, Sample Processing is a Differential Step in Cell Ultrastructure Preservation of Porifera** 205
Daniele Stillitani, Guilherme Muricy, Márcia Attias
- Case study of cobalamin F deficiency and hyperchromia: TEM as a key investigation method on the discovery of a novel genetic mutation** 207
Guilherme S. S. S. Tonelli, Shelida V. Braz, Patricia N. S. Moretti, Rosenelle A. Benicio, Juliana F. M. Araújo, Sônia N. Bão
- Characterization of Hypofractionated Radiation Surviving Cells in Two Colorectal Cancer Cell Lines.** 209
Josiane Weber Tessmann, Murilo Ramos Rocha, Renata Ivo Vasconcellos, Danielle Lazarin-Bidoia, Celso Vataru Nakamura and Jose Andres Morgado Diaz



Effect of Sperm Chromatin Defects Identified by Transmission Electron Microscopy on Bovine *In Vitro* Embryo Production. 211

Lays Oliveira Rocha, Paulo Henrique Mazzutti Alves, Sara Hissae Hiraiwa and Marcelo Emílio Beletti

Ultrastructural Studies of Vero-E6 Cells Infected with SARS-CoV-2 and Treated with Antiviral Molecules 213

Marcos Alexandre Nunes da Silva, Maria Eduarda Monteiro, Milene Dias Miranda, and Debora Ferreira Barreto- Vieira

The Effect of Amiodarone on *Trichomonas vaginalis* 215

Tatiana Guinancio de Souza, Wanderley de Souza and Marlene Benchimol

***Trichomonas vaginalis*: secretion of microvesicles and projection of tunneling nanotubes** 217

Júlio César Santana de Andrade, Wanderley de Souza and Marlene Benchimol

EXTRACELLULAR VESICLES IN *Tritrichomonas foetus* AFTER PHOTODYNAMIC THERAPY 219

Amanda Lira G. Albuquerque; Mariela Ines Batista dos Santos, Lais Silva; Bruno H. Godoi; Cristina Pacheco Soares; Newton Soares da Silva

Ultrastructural and Biochemical Alterations Induced by ACET-1 on Amastigote Forms of *Leishmania amazonensis* 222

Rayanne Regina Beltrame Machado, Deysiane Lima Salvador, Aline Rufino de Oliveira, Maria Helena Sarragiotto, Tânia Ueda-Nakamura, Sueli de Oliveira Silva, Danielle Lazarin-Bidóia and Celso Vataru Nakamura

Ultrastructural aspects of the aflagellarepimastigote form of *Trypanosoma caninum* 224

Kátia C. S. Nascimento, Roger M. M. Silva, Francisco O. R. de Oliveira Jr., Sandra M. O. Souza, Suzana Côrte-Real and Juliana H. S. Barros

Mitochondrial dynamics during human eosinophil development: an ultrastructural analysis 226

Cinthia Palazzi, Vitor H. Neves, Kennedy Bonjour, Kássia K. Malta, Thiago P. Silva, Rossana C. N. Melo

ArtScience applied in microscopy: integration for production a new perspective in parasitology results 228

Vitória Meirelles; Eduardo José Lopes-Torres

Caveolin-1 induces mitochondrial plasticity and chances in inter-organelle communication of hepatic stellate cell. 230

Mariana Ilha, Leo Anderson Meira Martins, Francieli Rohden, Radovan Borojevic, Vera Maria Treis Trindade, Guido Lenz, Fátima C. R. Guma



- The Intravacuolar Network of *Cyrtia Lignieresii*-Infected Erythrocytes** 233
Maíra Turiel-Silva, Brenda Fachetti, Camila Wendt, Edilene da Silva, Ana Paula Drummond, Wanderley de Souza, Kildare Miranda, José Diniz
- Microbiome Analysis Of The Midgut From Female Adult *Toxorhynchites theobaldi* (Culicidae: Diptera)** 235
Renata C. Barbosa, Raquel S. M. Godoy, Juliana S. Silva, Gustavo F. Martins
- Histopathology and ultrastructural analyses reveal neurodegeneration and inflammatory process during optic nerve lesion induced by Zika virus infection** 237
Felipe E. O. Rocha; Jenniffer R. Martins; Matheus R. Gonçalves; Vivian V. Costa; Felipe F. Dias
- Cell infection by the Ilheus virus: unraveling the morphogenesis of a neglected arbovirus** 240
Gabriela Cardoso Caldas, Helver Gonçalves Dias, Marcos Alexandre Nunes da Silva, Vinícius Tadeu Martins Guerra Campos, Flavia Barreto dos Santos, Alex Pauvolid-Corrêa, Ana Maria Bispo de Filippis and Debora Ferreira Barreto-Vieira
- Study of SARS-CoV-2 morphogenesis and interaction with the cell by transmission and high resolution scanning electron microscopy** 242
Lucio Ayres Caldas, Fabiana Avila Carneiro, Luiza Mendonça Higa, Fábio Luis Monteiro, Gustavo Peixoto da Silva, Luciana Jesus da Costa, Ingrid Augusto, Edison Luiz Durigon, Kildare Miranda, Amilcar Tanuri, Wandelely de Souza
- The Use of 2-hydroxyethyl methacrylate Resin for Histopathology Analysis in the Ocular Toxoplasmosis Model** 244
Carlla Assis Araujo-Silva, Milena Ribeiro Peclat de Araujo, Wanderley de Souza
- Optimization of Lipase Production Using Fungal Isolates from Oily Residues** 246
Letícia Miranda Cesário, Rafael Freitas Santos Pereira, Jairo Pinto de Oliveira
- Proposal Of a Rapid And Low-Cost Method To Assess Sublethal Effects Of Pesticides On Bees' Hypopharyngeal Glands.** 248
Murion Monteiro De Godoi and Pedro Brito
- Detection Of Autophagy In Secretory Canals Of *Anacardium humile* St. Hill By Immunofluorescence** 250
Shelly Favorito de Carvalho, Elton Luiz Scudeler, Daniela Carvalho dos Santos e Silvia Rodrigues Machado
- Antitumoral Activity of a Dibenzylideneacetone Derivative (A3K2A3) Against Hela Cells** 252
Aline Pinto Zani, Zia Ud Din, Edson Rodrigues-Filho, Sueli de Oliveira Silva, Francielle Pelegrin Garcia, Tania Ueda-Nakamura and Celso Vataru Nakamura



Testicular Morphohistology of the Crab *Sesarma rectum* on the East Coast of Marajó Island, Pará, Brazil. 254

Álvaro Aragão de Lima, Joelly Corrêa dos Santos, Fernanda Simas Corrêa Biancalana and Adriano Biancalana

Investigation On The Occurrence of Microplastics In Mussels Of The Bragantine Estuary (Pará/Brazil) 256

João M.S. Rodrigues, Juliana C.D. Pantoja, Andrews H.F. Leão, Alex S. Paiva, Yuri W.M. Favacho, Renata S. Oliveira, Liziane A.B. Gonçalves and Rossineide M. Rocha.

Apoptosis In The Hepatopancreas Of *M. amazonicum* From Estuarine Environment 258

Yuri W.M. Favacho, Juliana C.D. Pantoja, João M.S. Rodrigues, Andrews H.F. Leão, Alex S. Paiva, Gicelle M. F. Silva, Breno R.M. Silva, Maria A. P. Ferreira.

On The Tribological Properties Of 2D Materials: A Brief Comparison Between Graphene And MoS₂ 260

Felipe Ptak, Clara M. Almeida and Rodrigo Prioli

Investigation of Topographical Patterns of Spin Coated GdMnO₃ Thin Films 262

Cíndel Cavalcante de Souza, Heloísa David Yasumura, Yonny Romaguera-Barcelay and Henrique Duarte da Fonseca Filho

Scanning Microwave Impedance Microscopy And Raman Spectroscopy As Complementary Tools In The Analysis Of The Structural And Electronic Properties Of Twisted Bilayer Graphene 264

Douglas A. A. Ohlberg, Andrej C. Gadelha, Fabiano C. Santana, Gomes S. N. Eliel, Jessica S. Lemos, Vinícius Ornelas, Daniel Miranda, Rafael Battistella Nadas, Cassiano Rabelo, Pedro Paulo de Mello Venezuela, Gilberto Medeiros-Ribeiro, Ado Jorio, Luiz Gustavo Cançado, and Leonardo C. Campos

Partially Ordered Porous Structure on Layer-by-Layer PANI/PVS Ultrathin Films: Easy Fabrication of Robust Submicroscopic Patterning 266

Adriana M. A. Faria, Gislayne E. Gonçalves, Rodrigo F. Bianchi, Andréa G. C. Bianchi, Carolina Cuba, Bernardo R. A. Neves, Elisângela Silva-Pinto

Two-Dimensional Talc from Waste of Soapstone Industry 268

Cláudio C. Nascimento, Samuel M. de Sousa, Helane L. O. de Moraes, Ariana C. S. Almeida, Bernardo R. A. Neves, Mariana de C. Prado and Elisângela Silva-Pinto

EXFOLIATED LEAD SULFIDE CHARACTERIZATION BY SCANNING PROBE MICROSCOPY 270

Felipe R. G. Beato, Elisângela S. Pinto, Fernando G. Araújo, Bernardo R. A. Neves Mariana C. Prado and Ana Paula M. Barboza



Topographical Investigation at the Nanoscale of DyMnO₃ Thin Films Produced by Sol-Gel Method. 272

Heloísa David Yasumura, Cíndel Cavalcante de Souza, Yonny Romaguera-Barcelay and Henrique Duarte da Fonseca Filho

Stereometric Analysis of Amazon Rainforest *Anacardium occidentale* L. Leaves 274

Glenda Quaresma Ramos, Heloísa David Yasumura, Cíndel Cavalcante de Souza, Henrique Duarte da Fonseca Filho

Hexamethyldisiloxane Plasma Coating On Fabric Surfaces To Be Used In The Manufacture Of Mask Against COVID-19 276

Leonardo Pereira Pacheco, Sílvia Renata de Souza Marski, Audrey Wallace da Costa Barros, Carlos Alberto Achete, Maíra do Prado, Renata Antoun Simão

2D talc nanosheets obtained via liquid phase exfoliation. 278

Mariana C. Prado, Helane O. Morais, Samuel M. Sousa, Joyce C. Santos, Ana Paula M. Barboza, Elisângela S. Pinto, Bernardo R. A. Neves

Mechanical Properties Characterization of Human Hair Fibers Cortex Region by Multi-parametric Atomic Force Microscopy Mapping 280

Raissa L. Oblitas, Flávio B. Camargo Jr, Wagner V. Magalhães, Maria Cecília Salvadori

Analysis of Surface Nanostructures Induced by Slow Highly-Charged Ions in Thin Polymer Films by SFM 282

R. Thomaz, F. V. Filho, J. P. M. May, M. Schleberger and R. M. Papaléo

Instance Segmentation of Quartz in Iron Ore Optical Microscopy Images by Deep Learning 284

Bernardo Amaral Pascarelli Ferreira, Thalita Dias Pinheiro Caldas, Karen Soares Augusto, Sidnei Paciornik and Julio Cesar Alvarez Iglesias

Automatic Iron Ore Characterization by Digital Microscopy and Machine Learning Tools. 287

Thalita Dias Pinheiro Caldas, Bernardo Amaral Pascarelli Ferreira, Karen Soares Augusto, Sidnei Paciornik, Julio Cesar Alvarez Iglesias and Alei Leite Alcântara Domingues

Methylene Blue Associated with Maghemite Nanoparticles has Antitumor Activity in Breast and Ovarian Carcinoma Cell Lines 289

Ana Luísa G. Silva, Natália V. Carvalho, Leonardo G. Paterno, Ludmilla D. Moura, Cleber L. Filomeno, Eneida de Paula and Sônia N. Bão

Polyaniline-Gum Arabic Nanocomposite Compatibility with Physiological-Like Environment and Murine Cells 291

Jenifer P. Gonçalves, Anderson F. da Cruz, Carolina C. de Oliveira, Edvaldo da S. Trindade, Izabel C. Riegel-Vidotti, Marcio Vidotti, Fernanda F. Simas



Post-Mortem Changes in Cenozoic Stromatolites from Hypersaline Lagoa Vermelha, Brazil 293

Carolina N. Keim

Evaluation of the Antitumor Potential of Copper Oxide Nanorods in MCF-7 Tumor Cells 295

Giovanna de Carvalho Nardeli Basílio Lôbo, Matheus Pereira Sales, Leonardo Giordano Paterno and Sônia Nair Bão

Internalization of Emerging Metallic Contaminants from Atmospheric Particulate Matter (PM10) in Human Lung Cells. 297

Iara da C. Souza, Mariana Morozesk, Priscila Siqueira, Enzo Zini, Iasmini N. Galter, Silvia T. Matsumoto, Marisa N. Fernandes

AFM characterization of spirulina coated magnetite nanoparticles for magnetic hyperthermia 298

Lima, I.R.; Sampaio, F. A., Pereira, V.G, da Silva. H. S. Simão. R. A., Campos, M. F

High-Resolution *In Situ* Electron Microscopy technique to study biomaterials: Magnetosome thermal stability 300

Jefferson Cypriano, Mounib Bahri, Walid Baazis, Kassioyé Dembelé, Pedro Leão, Dennis A. Bazylnski, Fernanda Abreu, Marcos Farina, Ovidiu Ersen, and Jacques Werckmann

Nanostructure of calcium phosphate films synthesized by pulsed laser deposition under 1 Torr: effect of wavelength and laser energy 302

N.R. Checca, F.F. Borghi, A.M. Rossi, A. Mello, A.L. Rossi

Less is more: Impact of the conjugation method on enzymatic activity in magnetic nanoconjugates 304

Thais de Andrade Silva and Jairo P. de Oliveira

Iron oxide and gold nanoparticles functionalized with Jacalin for IgA purification system 306

Wanderson Juvencio Keijok, Luis Alberto Contreras, Jairo Pinto de Oliveira and Marco Cesar Cunegundes Guimarães

Characterization of the Resonance and Morphological Frequency of Hybrid Cantilever Sensors Functionalized With M13 Bacteriophages. 308

Wellington Silva Ferreira, Luís Fernando Hill, Gustavo Miranda Rocha, Paulo Mascarello Bisch and Gilberto Weissmüller

Electron microscopy characterization of nanostructured Mg/Nb₂O₅ composite processed by High Pressure Torsion (HPT) Technique 310

Caires, A.J, Castro, M. M, Montoro, L. A., Figueiredo, R. B, Isaac, A. N



Observation of Chiral Spin Textures in Pd/Co/Pd Multilayers by Lorentz Transmission Electron Microscopy 312

C. Labre, R. Dutra, R. P. Loreto, B. G. Silva, D. E. Gonzalez-Chavez and R. L. Sommer

Solvent Effect in the Crystalline Phase of ZrO₂ Nanocrystals Obtained by Solvothermal Syntheses 314

Mayara da Silva Santos, Walter Sperandio Sampaio and Cleocir José Dalmaschio

Optimizing PCA Denoising of EDS Hyperspectral images: Avoiding Random Noise Bias and Improving Precision and Accuracy of Quantitative Chemical Analysis. 316

Murilo Moreira, Matthias Hillenkamp, Giorgio Divitini, Luiz H.G. Tizei, Caterina Ducati, Monica A. Cotta, Varlei Rodrigues, Daniel Ugarte

Cross-sectional studies in hydroxyapatite crystalline films produced at room temperature by RF magnetron sputtering. 318

Elvis O. López, Alexandre Mello, Alexandre M. Rossi, André L. Rossi

Transmission Electron Microscopy Characterization Of Indoor Particulate Matter 320

H. Coelho-Júnior, P. E. Santiago Brito and R. L. Sommer

Design of Experiments Approach to nanocellulose production: transforming food waste in nanoproduct 322

Laryssa Pinheiro Costa Silva, Pedro Henrique Cassaro Lirio and Marco Cesar Cunegundes Guimarães

Influence of Particle Size and Inversion Degree on the Raman Spectra of MnFe₂O₄ Synthesized by the Sol-Gel and Combustion Methods 324

Matheus Torquato, Eliel Gomes da Silva Neto, Emilson Ribeiro Viana Junior and Ronaldo Sergio de Biasi

Characterization of Precipitates in an CuAlNi Shape-Memory Alloy After Aging Thermal Treatments. 327

Micaela Panizo, Fran Bubani, Rosana Gastien, Eugenia Zelaya

TEM CHARACTERIZATION OF Ti-12Mo-xNb (0 ≤ x ≤ 20) ALLOYS 329

Caio Marcello Felbinger Azevedo Cossú, Carlos Angelo Nunes, Loic Charles Malet, Luiz Henrique de Almeida e Sinara Borborema

In vitro* culture and characterization of life cycle of *Metarhizobium blumi 331

Santos ACB; Caracciolo ME; Lopes-Torres EJ

Non-paraxial Theory for the microscope image of Spherical Dielectric Objects and Colloidal Particles 333

Fran Gómez, Rafael. S. Dutra, Luis. B. Pires, Glauber R. de S. Araújo, Bruno Pontes, Paulo A. Maia Neto, Herch M. Nussenzveig and Nathan B. Viana



- Sintering of Al-Si Hypereutectic alloy for the production of metal matrix composite via powder metallurgy – a preliminary study** 335
Anderson F. Pereira, Paulo Henrique Barreto de Souza de Faria, Luciano Monteiro Rodrigues, Bojan Marinkovic and Paula Mendes Jardim
- Characterization of Polyurethane Foams Synthesized from Biopolyols** 337
Camila Gomes Peçanha de Souza, Sidnei Paciornik, José Roberto Moraes d’Almeida, Lorenleyn De la Hoz Alford, Brenno Santos Leite
- Morphologic Study of Polymeric Nanofibers Obtained by Electrospinning: Influence of Technique Variables for Producing Antimicrobial Tissues** 339
Giovanna Picoli Libel, Bárbara Stephani Caldas and Eduardo Radovanovic
- Microscopy Techniques to the Characterization of Biocompatible Materials and Tissues** 342
Bárbara S. Caldas, Giovanna Picoli Libel, Cátia S. Nunes, Manuela R. Panice, Marília Cestari, Débora B. Scariot, Danielle Lazarin-Bidóia, Celso Vataru Nakamura, Sami Halila, Redouane Borsali, Edvani Curti Muniz, Eduardo Radovanovic.
- Characterization of graphene-based materials deposited on interdigitated electrodes for ammonia gas sensor applications** 345
Eric Schwartz, Suzana Bottega Peripolli, José Brant de Campos, Fernando Massa Fernandes, Hirschel Valiente Rouco
- In-Situ X-Ray MicroCT Imaging of The Microstructural Changes in Carbonate Coquina Under Oedometric Loading Conditions** 348
SILVA JUNIOR, Francisco José Rodrigues da, VELLOSO, Raquel Q. and PACIORNIK, S., ZHEMCHUZHNIKOV, Alexandr, DE PINHO MAURÍCIO, Marcos Henrique
- Controlling the Morphology Of ZnO Microstructured Films Grown On Copper.** 351
Ígor Silveira, Jonder Morais and Maria do Carmo M. Alves
- Analysis of the Formation of Concrete Porosity with Addition of Recycled Aggregate Through the Study by X-Ray Microtomography** 353
Isabel Christina de Almeida Ferreira, Sidnei Paciornik and Flávio A. Silva
- Synthesis and Crystal Growth of Dolomite under Hydrothermal Conditions** 355
Hannah Larissa Siqueira Matos Pimentel, Flávia Gomes de Souza, Cecília Maria Alves de Oliveira, Jesiel Freitas Carvalho.
- Microwave Irradiation Treatment for Recycling Titanium Alloys to be Applied to Reinforcement of Weld Metal** 357
Alicia Ramos Modesto, Leonardo Shigueo Moreira Wagatuma, Rafael Borgheri dos Santos and Juno Gallego



Microstructure of Nd:YAG Laser Welding TiC Reinforced Formed by Addition of Recycled Titanium 359

Rafael Borgheri dos Santos, João Gustavo Souza Lago, Alícia Ramos Modesto and Juno Gallego

Comparing quantitative EDS and WDS using microanalytical standards 361

Karla Balzuweit, Márcio de Almeida Flores Luis A.R. Garcia, Breno Barbosa Moreira, Ramon Aranda

Effects Of Aluminum Intake On Trabecular Bone – A Preliminar Study In Neonatal Rats. 363

Mara Rubia Marques, Anderson Camargo Moreira, Iara Frangiotti Mantovani, Celso Peres Fernandes, Fernanda Cristina Alcântara dos Santos.

Aging Stability Of The Structure Of Mn-based M41S Family Silicas. 365

Marcus Andrei Ullmann, Daniela Bianchini

Advancing Life Science SEM-EDS analysis with the XFlash® FlatQUAD 367

Patzschke, M. and Menzies, A.H.

Study of Morphological and Chemical Changes on FCC Equilibrium Catalysts by Scanning Electron Microscopy 370

Paulo Sergio S. Carvalho, Beatriz R. Canabarro, Anderson F. Pereira, Manoel Jorge R. Marim, Marco Antonio S. de Abreu, Edisson Morgado Junior, Paula Mendes Jardim

Heat Treatment post SLM from the Mixed Ni and Ti Powders 372

Eduardo Hoisler Sallet, Rodolfo da Silva Teixeira, Rebeca Vieira de Oliveira, Patrícia Freitas Rodrigues, Talita Gama de Sousa, Naiara Vieira Le Sénéchal, Ygor Pereira de Lima, Danilo Abílio Correa Gonçalves, Edilainea Alves Oliveira Melo, Paulo Inforçatti Neto, Jorge Vicente Lopes da Silva, Luiz Paulo Mendonça Brandão, Andersan dos Santos Paula

Yttrium Effect on δ Precipitation In The Hot Forged Nickel-Alloy 718 374

Rosa Maria Sales da Silveira, Alessandra Vieira Guimarães, Leonardo Sales Araujo, Loïc Malet and Luiz Henrique de Almeida

HMDSO thin films and their potential application as flame retardant coatings for fabrics 377

Soraya Nassar Sakalem and Renata Antoun Simão

Effect of Cold Rolling on the Microstructure and Young's Modulus of a New β -metastable Ti-24Nb-4Mo-6Zr alloy 379

Aline Raquel Vieira Nunes, Sinara Borborema, Leonardo Sales Araújo, Luiz Henrique de Almeida



Nanostructured $\text{Pr}_{1-x}\text{Sr}_x\text{MnO}_3$ films synthesized by pulsed laser deposition under 1 torr: impact of thermal treatment on morphology, crystallinity and magnetization 381

N. R. Checca, W. S. Torres, F. Garcia, A. Mello, A. L. Rossi and D. Rocco

DOI:
ISSN:



28º CONGRESSO DA SOCIEDADE BRASILEIRA
DE MICROSCÓPIA E MICROANÁLISE
12 a 15 JUL 2021

on-line

50anos
SOCIEDADE BRASILEIRA DE
MICROSCÓPIA E MICROANÁLISE





Characterization of *Giardia intestinalis* cytoskeleton using high-resolution microscopy techniques

Raphael Verdan¹, Ana Paula Gadelha^{2,3}, Kildare Miranda^{1,3}, Marlene Benchimol^{3,4}

* Corresponding Author: marlenebenchimol@gmail.com ¹Lab. de Ultraestrutura Celular Hertha Meyer, IBCCF, UFRJ, RJ, Brazil; ²Lab. de Microscopia Aplicada às Ciências da Vida, Dimav - Inmetro, RJ, Brazil; ³Instituto Nacional de Ciência e Tecnologia em Biologia Estrutural e Bioimagens, and Centro Nacional de Biologia Estrutural e Bioimagens, UFRJ, RJ, Brazil; ⁴Universidade do Grande Rio (UNIGRANRIO), RJ, Brazil.

Giardia intestinalis is the causative agent of giardiasis [1], and it can survive the great variations in physicochemical conditions in the host [1]. The parasite has a set of complex cytoskeletal structures involved in a wide range of functions. This protozoan adheres to host cells and moves around in this environment. This exceptional adaptive capacity can be partly attributed to its cytoskeleton, whose organization and properties have not been fully clarified. *G. intestinalis* cytoskeleton is composed primarily of microtubules and is organized in unique structures such as the ventral disc, the median body, funis, in addition to four pairs of flagella. Trophozoites still have actin filaments distributed in the cytoplasm [2]. Advances in scanning microscopy technology become interesting tools for studying cell structures and reveal the organization of cytoskeleton elements not previously known [3]. This study analyzes the organization of the *G. intestinalis* trophozoites cytoskeleton during interphase, cell division, and differentiation. For this, the samples are treated with 2% NP-40 detergent for 10 min to remove the plasma membrane and expose the cytoskeleton. Then, the cells are observed with high-resolution Zeiss Auriga 40 scanning electron microscopy. Our observations demonstrate that the externalizing region of the flagellum, i.e., the flagellar channel, also known as the flagellar pore, is a differentiated region (Figs. 1a-b). Analysis of membrane extracted-cells reveal an extra-axonemal structure that may be associated with this region (Figs. 1c-d). Morphometric data are in course to confirm these findings. The extra-axonemal structure appears collar-shaped around the axoneme and measures about 50 nm in thickness (Figs. 1c-d). As observed by negative stain, this structure remains attached to the axoneme even when the connections between the axoneme microtubules are disrupted after detergent treatment. In addition, we are also interested in the biogenesis and dynamic of the cytoskeleton elements during cell division and differentiation. Our data will contribute to a better understanding of the organization and functional role of the *G. intestinalis* cytoskeleton.

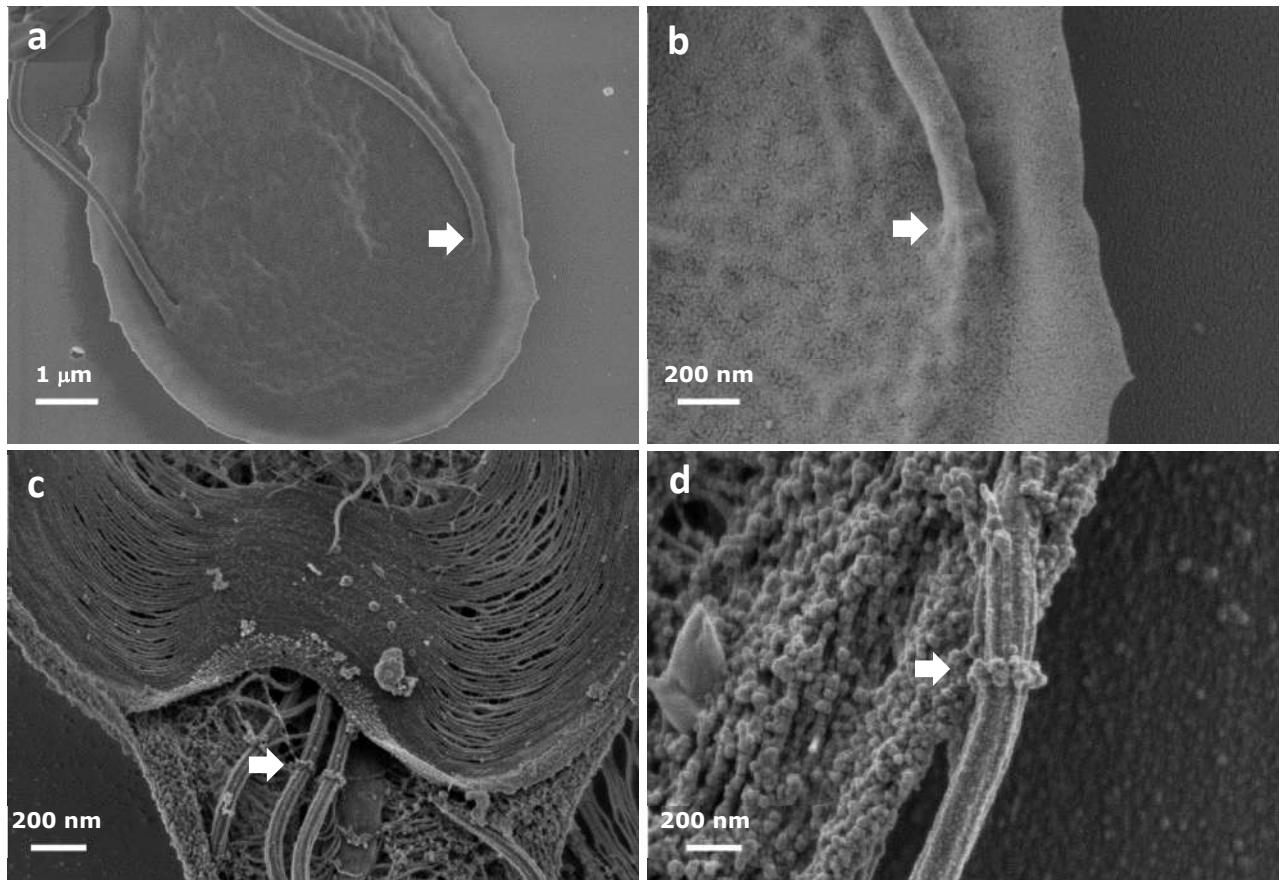


Figure 1. High-resolution scanning electron microscopy of *G. intestinalis* trophozoites. **(a).** Note the region of the axoneme exit of the cell body (arrow). **(b).** High magnification image of **a**. **(c).** Extra axonemal structure (arrow) is observed in the axoneme of ventral flagella in membrane extracted cells. **(d)** The extra-axonemal structure is also observed in the axoneme of posterior flagella (arrow) in membrane extracted cells.

1. Adam, R.D., *Biology of Giardia lamblia*. Clin Microbiol Rev, 2001. **14**(3): p. 447-75.
2. Castillo-Romero, A., et al., *Participation of actin on Giardia lamblia growth and encystation*. PLoS One, 2009. **4**(9): p. e7156.
3. Gadelha, A.P.R., M. Benchimol, and W. de Souza, *The structural organization of Giardia intestinalis cytoskeleton*. Adv Parasitol, 2020. **107**: p. 1-23.



Characterization of bacteria adhered on the cuticle of nematodes isolated from ear canal of Gir cattle

Makoto Enoki Caracciolo¹, Ander Castello Branco Santos² and Eduardo José Lopes Torres^{2*}

¹ Centro Multiusuário para Análise de Fenômenos Biomédicos (CMABio) ESA/UEA Manaus, Brasil. ² Laboratório de Helminologia Romero Lascasas Porto (LHRLP), FCM/UERJ, Rio de Janeiro, Brasil. *lopestorresej@gmail.com

The Parasitic otitis is an infection associated with nematodes and secondary infection caused by different species of bacteria. This infection results in an intense inflammatory process, which can affect external and internal ears, and serious cases have been reported in countries with hot and humid climates [1]. Clinical signs of otitis caused by rhabditiform nematodes initially include apathy and repetitive movement of the head. The aggravation of infection can lead to damages in the central nervous system, causing dysfunction or facial paralysis, as well as vestibulocochlear nerve damage and meningitis. [2]. In Brazil, two species of nematodes *Metarhabditis costai* and *Metarhabditis freitasi* have been reported, causing parasitic otitis on Gir Cattle (*Bos taurus indicus*) [3]. The main objective of this study is to identify pathogenic bacteria and show them adhered on the cuticle surface of nematodes collected from infected animals from farms located in the Rio de Janeiro and Pará states. Nematodes recovered were washed using PBS (Phosphate Buffer Saline), fixed with Karnovsky's solution, adhered on glass coverslips, post-fixed in osmium tetroxide, dehydrated in ethanol series, critical point dried, mounted in metal stubs, sputtered with gold and analyzed using conventional and field emission scanning electron microscopes FEI-Quanta 250, ZEISS Auriga 600 Compact and Jeol JSM-7100F. The isolated bacteria were submitted to the MALDI-TOF technique for species identification. Our results identified two species *M. freitasi* (Figs. 1-3) and *M. costai* (Figs. 4-6) and bacteria adhered on the cuticle surface (Figs 3 and 6). We identified five bacterial species of veterinary interest, which have already been described as biofilm-forming. The biofilm is associated with the pathological and antibiotic resistance increase of the bacteria and presence of nematodes would likely contribute to increase the difficult to control of this infection.

[1] Leite P. V. B. et al. *Pesq. Veterinária Brasileira*. 32 (2012) 855.

[2] Duarte E. R., Hamdan J. S. *J. J. Vet. Med. B Infect. Dis. Vet. Public. Health*. 51 (2004) 1.

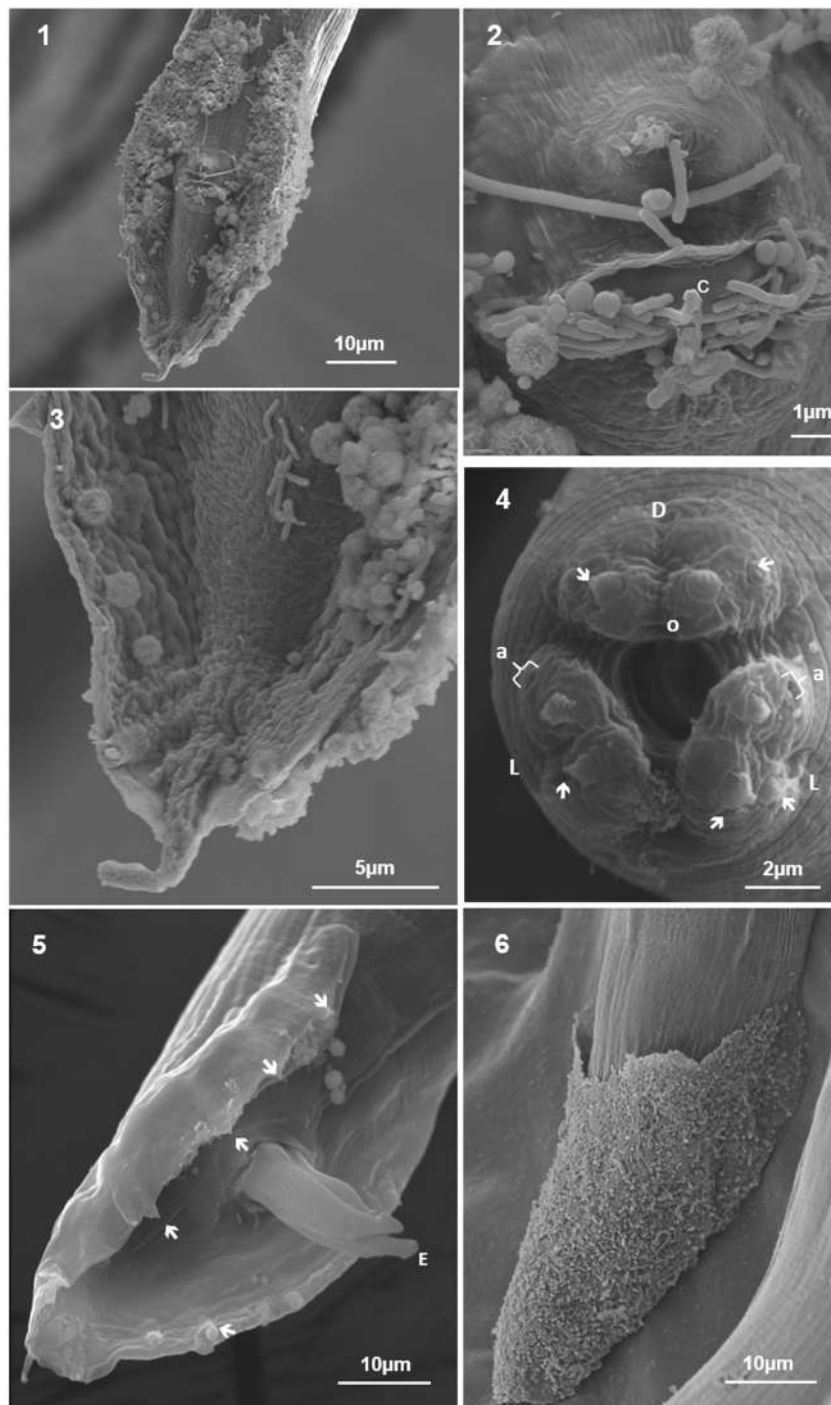
[3] Martins W. Jr. *Mem. do Inst. Oswaldo Cruz*. 80 (1985) 11.

[4] This research was supported by CNPq (Brazil), FAPERJ (Brazil) and CAPES (Brazil).

[5] Financial support by FAPERJ, CNPq (Brazil) and Capes

Thanks

CENABIO, NANOFAB, Unidade de Pesquisa Urogenital (UERJ) and IQ (UERJ).



Legends: Conventional SEM of nematodes adult male. Measure in micrometers (μm) **Fig. 1** - Posterior region of *M. freitasi*, showing adhered bacteria; ; **Fig. 2** - Adhered bacteria at cloacal opening of *M. freitasi* (C); **Fig. 3** - Posterior end of male *M. freitasi*, showing adhered bacteria; **Fig. 4** - Anterior end of *M. costai*, showing triangular oral opening (O) cephalic papillae (\rightarrow), two latero-ventral lips (L) and dorsal lip (D) and amphids (a); **Fig. 5** - Posterior end of *M. freitasi* showing genital papillae (\rightarrow) and spicules (E); **Fig. 6** - Posterior region of *M. costai*, showing adhered bacteria;



Morphological and Morphometric Aspect Of Embryos And Larvae Of *Heros severus*: An Ornamental Fish.

Allex S. Paiva^{1*}, Ivana K.S. Viana², Yuri W.M. Favacho¹, Andrews H. F. Leão², João M.S. Rodrigues², Breno R.M. Silva¹, Yanne A.Mendes¹ and Maria A.P Ferreira¹.

¹ Laboratory of Immunohistochemistry and Developmental Biology, Federal University of Pará (UFPA), Belém/PA, Brazil. ² Laboratory of Cell Ultrastructure, Federal University of Pará (UFPA), Belém/PA, Brazil. *allex.paiva@icb.ufpa.br

Heros severus is an ornamental fish of the Cichlidae family native from the Amazon region with continuous reproduction throughout the year [1]. Information regarding this species embryonic development is absent and could be an important way of understanding its ontogeny, spawning and growth in natural environments [2]. This study aimed to describe the embryonic development and larvae of *H. severus* using histological and morphometrical analysis. For this, fertilized eggs and larvae of *H. severus* were collected from culture sites and submitted to histological procedure for light and scanning electronic microscopy (SEM) and morphometry of the larvae. We analyzed the embryonic and larval stages of *H. severus* from the 1^o to the 15^o day post fertilization (DPF). The samples were submitted to standard histological procedure for light microscopy with paraffin inclusion and hematoxylin-eosin staining. For SEM, the samples were fixed in Karnovsky's solution for 24 h at 4°C and post-fixed in a 1% osmium tetroxide solution buffered with sodium cacodylate (0.1 M, pH 7.3) for 2 h at room temperature and dehydrated in a graded ethanol series. The samples were subsequently mounted on conductive tabs and vacuum-dried in a CPD 030 BAL TEC Critical PointDryer, followed by sputter-coating with gold for 2 min. Images were obtained using a LEO 1430 scanning electron microscope (LEOZEISS, Cambridge, England). On the 1^o DPF blastomeres were observed in the animal pole of the egg. From the 4^o to 7^o DPF the larvae ecloded and the optical primordium was originated with later pigmentation and adhesive gland formation. From the 8^o to 15^o DPF occurred the formation of the mouth opening and lateral and caudal fin. Throughout the embryo's development there was an increase on both head and trunk size, with an average daily growth of 1,4 mm and 9,7 mm respectively (Fig.1,2). Morphometry of the larvae from the 4^o to 15^o DPF shows a linear increase on head, trunk and standard length through time (Fig. 3). Our data suggest that the embryogenesis of *H. severus* follows the same pattern of most neotropical fish and contributes for development of biotechnological techniques for aquaculture production and conservation of this specie.

References

- [1] S. O. Kullander, et al. Family Cichlidae. Porto Alegre, 2003.
- [2] H.D.B. dos Anjos, C.R. dos Anjos, Bol. Inst. Pesca. 32 (2006) 151.

Acknowledgement: To UFPA by support.

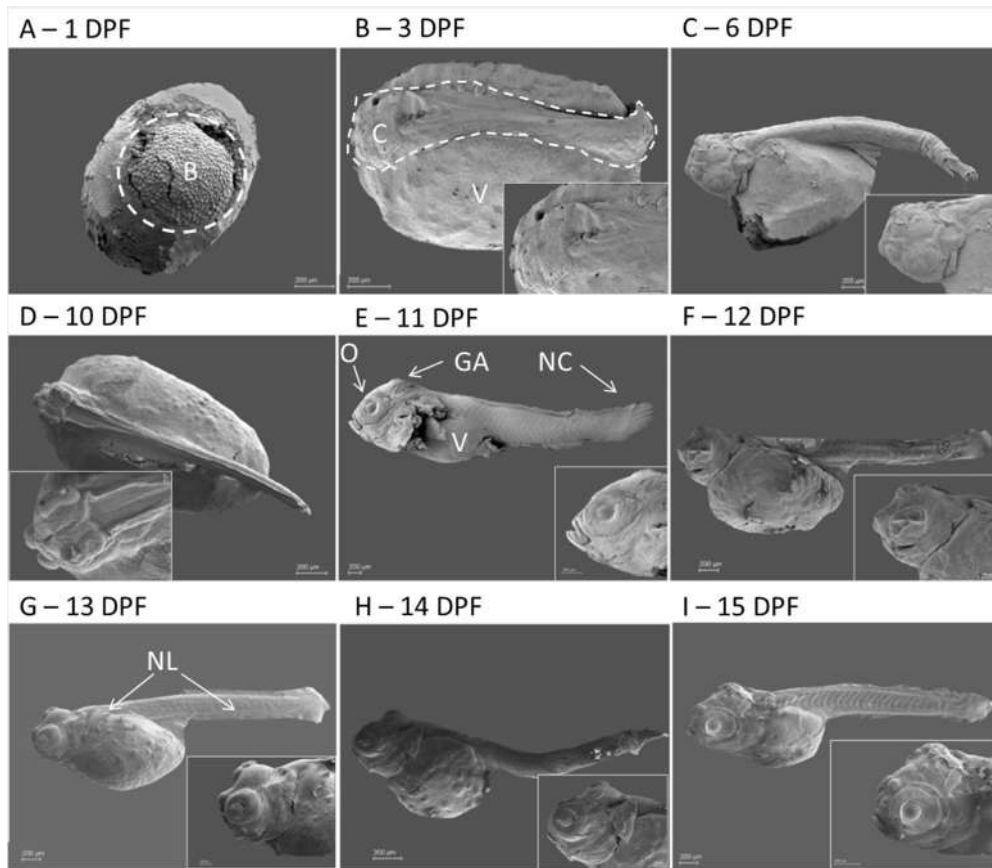


Fig. 1: SEM of the embryo and larvae of the *H. severus*. A-B: Embryonic stages; C-I: Larvae stages. Abbreviation: B - blastomeres; C - head; GA - adhesive gland; NC - tail fin; NL - side fin; O - eye; V - yolk.



Fig. 2: Photomicrography of larvae of the *H. severus* 10° DPF. Abbreviation: B - mouth; E - stomach; I - midgut; O - Eye; RC - tail region; V - yolk.

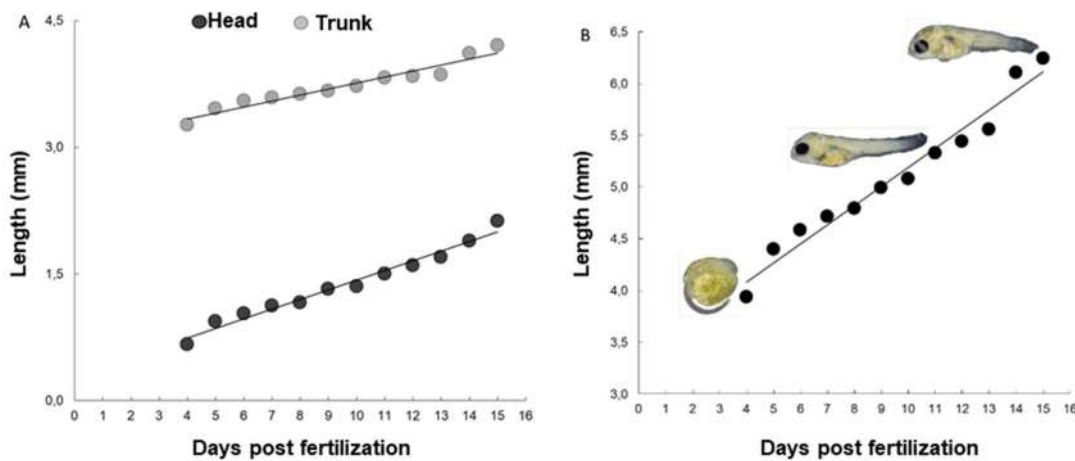


Fig. 3: Morphometry of larvae of the *H. severus* (4° - 15° DPF). A: Head and Trunk. B: Standard length



Structural mechanism and polymerization of Glutaminase *in vitro* and *in situ*.

Marília M Dias¹, Jose Edwin N Quesñay^{1,2}, Camila T Rodrigues², Flávia MO Abreu², Alliny CS Bastos¹, Zhengyi Yang³, Anna Steyer³, Ievgeniia Zagoriy³, Simone Mattei³, Zeyaul Islam¹, Alexandre Cassago⁴, Marin van Heel⁴, Silvio R Consonni⁵, Julia Mahamid³, Rodrigo V Portugal⁴, Andre LB Ambrosio^{2*}, Sandra MG Dias^{1*}.

¹ LNBio, CNPEM, Campinas, Brazil.

² IFSC, USP, São Carlos, Brazil.

³ EMBL, Heidelberg, Germany.

⁴ LNNano, CNPEM, Campinas, Brazil.

⁵ IB, UNICAMP, Campinas, Brazil.

*andre@ifsc.usp.br, sandra.dias@lnbio.cnpem.br

Glutaminases deaminate glutamine to glutamate in the first step of glutaminolysis. As such, they are key for the highly proliferative behavior and aggressiveness of cancer cells and a promising pharmacological target for different types of tumors. Four glutaminase isozymes have been confirmed in humans as products of two different genes, GLS1 and GLS2, and display concerted tissue- and context-specific expression profiles. In addition to being mitochondrial enzymes, as multidomain proteins, glutaminases have additional regulatory functions in the cell and can even localize outside the mitochondria. Earlier *in vitro* biochemistry and biophysical studies, supported by X-ray methods, such as crystallography and SAXS, proposed GLS' minimum functional unit as a homotetramer composed of a dimer of dimers. More precisely, a transition between inactive dimers into active tetramers, promoted by inorganic phosphate, has long been the accepted mechanism for GLS activation even though phosphate-induced polymerization was the critical feature that allowed its first purification to homogeneity from pig renal cells nearly fifty years ago. The tetramer-dependent activation model remained unchallenged primarily due to a complete lack of evidence of GLS polymerization in cells. However, recent data suggested that GLS polymerization, promoted by inorganic phosphate (Pi), is required for its cellular function. Filaments make GLS remarkably more efficient by facilitating substrate accessibility to the active site and increasing turnover numbers. We introduce a cryo-EM structure (Figure 1) of the GLS filament which uncovers at an atomic level how a phosphate anion promotes polymerization and activates the nucleophile serine residue via stabilizing the activation loop and bonding the active site tetrad. We also observe that a dynamically and reversible GLS association into these polymers in cells positively correlates with known morphological changes in the mitochondria in response to glutamine starvation. Finally, at the preliminary stages, we provide the unprecedented direct observation of GLS polymerization *in situ*, organized as a meshwork in thin mitochondria lamellae.

Acknowledgements: FAPESP, CIBFar/CEPID

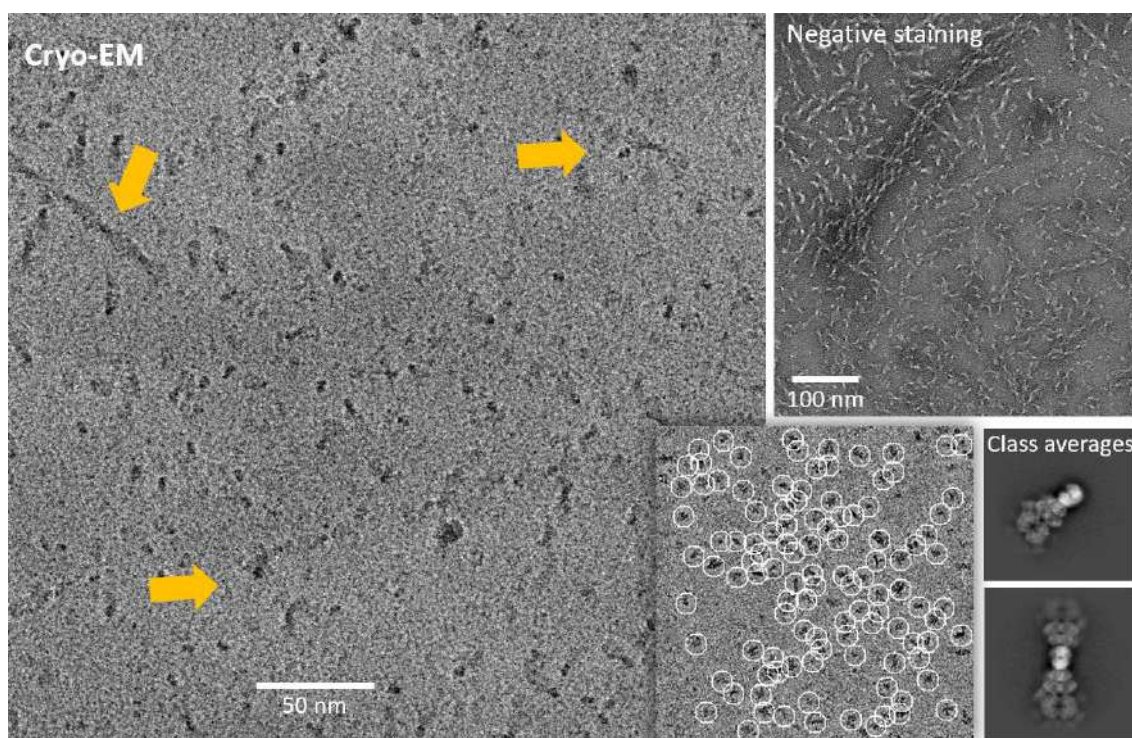


FIGURE 1. Negative staining (right top panel) and cryo-EM (large left panel) analysis of the GLS filament, with yellow arrows indicating longer stretches, followed by a single particle picking strategy (inset) and 2D class averaging (lower right panel).



The involvement of the Nucleolar Protein 16 (Nop16) in the Physiology of *Cryptococcus gattii*, a fungal pathogen.

Rafael F. Castelli^{1*}, Flavia C. G. Reis^{1,3}, Haroldo C. de Oliveira¹, Ane W. A. Garcia⁴, Anny W. Robert¹, Tabata Klimeck¹, Charley C. Staats⁴, Marcio L. Rodrigues^{1,2}

¹ Instituto Carlos Chagas, Fundação Oswaldo Cruz (Fiocruz), Curitiba, Brazil.

² Instituto de Microbiologia Paulo de Góes (IMPG), Universidade Federal do Rio de Janeiro, Cidade Universitária, Rio de Janeiro, Brazil.

³ Centro de Desenvolvimento Tecnológico em Saúde (CDTS), Fundação Oswaldo Cruz, Rio de Janeiro, Brazil.

⁴ Centro de Biotecnologia and Departamento de Biologia Molecular e Biotecnologia, Universidade Federal do Rio Grande do Sul, Porto Alegre, Brazil.

* rafaelf.castelli@gmail.com

The *Cryptococcus* genus comprises two pathogenic species, *C. neoformans* and *C. gattii*. Both species correspond to yeast-like cells surrounded by a polysaccharide capsule mainly composed of glucuronoxylomannan (GXM), which is essential for virulence [1]. Our previous studies suggested that the Nop16 protein, which is possibly involved in ribosomal biogenesis, was important for the activity of antifungals, but its role in fungal physiology and pathogenesis remained unknown [2]. In order to study the role of Nop16 in *C. gattii* (R265 strain), two knockout strains, namely *nop16Δ1* and 2, were constructed and compared with the parental strain by a combination of fluorescence, scanning, and transmission electron microscopy. To visualize the capsule, the cells were centrifuged at 3,000 xg, washed with PBS and fixed in 4% paraformaldehyde, for further counterstaining with India Ink and observation using a Leica DMi8 inverted microscope. Immunofluorescence was used to observe the capsule and cell wall structures. The cells were blocked with 1% BSA in PBS, and had their cell walls stained with 25 μM calcofluor white (CFW). The capsule was stained after incubation of the cells with a monoclonal anti-GXM antibody, namely 18B7, followed by a secondary antibody conjugated with Alexa 546. The cells were finally stained with 5 μg/ml of FITC-labeled wheat germ agglutinin (WGA), for detection of chitin oligomers. The cells were observed in a Leica DMi8 inverted microscope. For SEM, the cells were adhered to circular slides previous treated with 0.01% poly-L-lysine type I. The systems were dehydrated with ethanol (30, 50, 70, 90 and 100%) and dried using the critical point (Leica EM CPD300). The samples were covered with gold (Leica EM ACE200) and visualized with a JEOL JSM-6010 Plus/LA at 5 Kv. Fungal cells were also prepared for TEM. They were fixed as described above, and treated with 1% osmium tetroxide, 1.6% 5 mM potassium ferrocyanide in 0.1 M cacodylate buffer. The cells were washed with cacodylate buffer and dehydrated with acetone (30, 50, 70, 90, 100 and 100%). The cells were mounted on EMbed 812 (EMS) resin pads, ultra-sliced, fitted in grids and observed with a JEOL 1400Plus at 90 Kv. Fungal extracellular vesicles (EVs) were recovered according to Reis et al.[3], and prepared for TEM. The EVs were placed in Formvar-covered grids, fixed with the Karnowski solution for 10 minutes, and counterstained with 5% uranyl acetate for 2 minutes. The EVs were observed with a JEOL 1400Plus at a 90 Kv acceleration. Microscopic analyses of all parameters described here revealed similar properties for wild type and mutant cells. However, additional experiments in our laboratory revealed that the mutants were less efficient producers of EVs and had reduced virulence in an

invertebrate model of infection. These results indicate that Nop16 participates in the physiology and virulence of *C. gattii* by still unknown mechanisms.

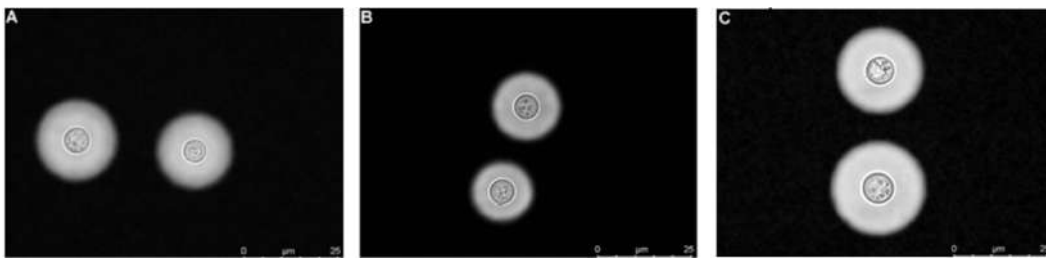


Figure 1: *C. gattii* strains counterstained with India Ink. (A) R265, (B) *nop16Δ.1* and (C) *nop16Δ.2*. Bars 25 μ m.

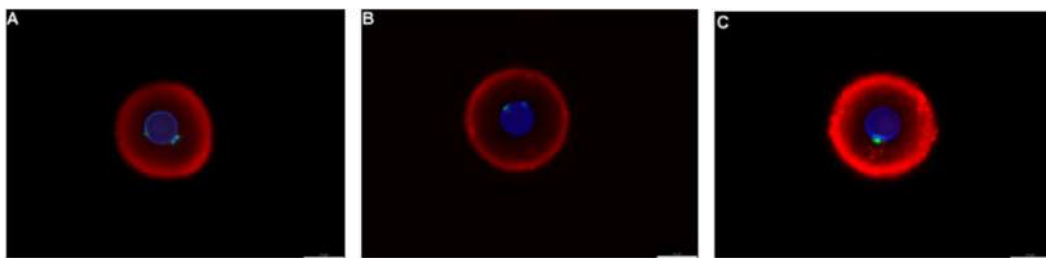


Figure 2: *C. gattii* cells observed by immunofluorescence. The cell wall was stained in blue, while chitooligomers appear as green structures. The capsule was stained in red. (A) R265, (B) *nop16Δ.1* and (C) *nop16Δ.2*. Bars 10 μ m.

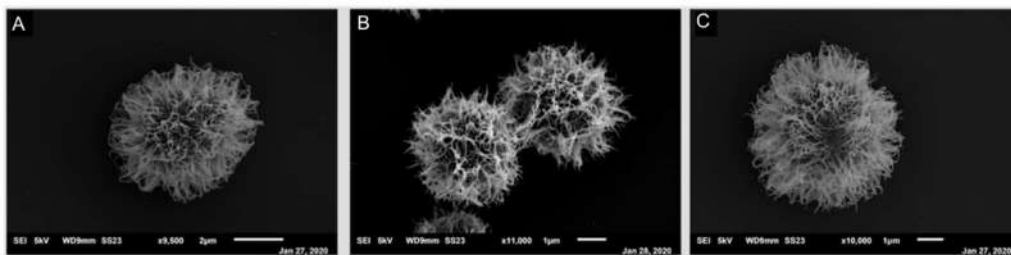


Figure 3: *C. gattii* strains observed by SEM. (A) R265, (B) *nop16Δ.1* and (C) *nop16Δ.2*.

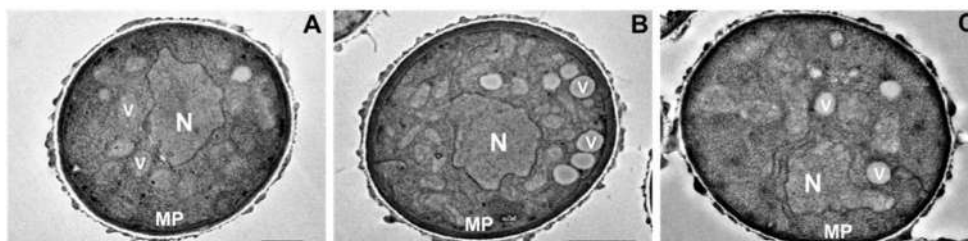


Figure 4: Ultrastructure of *C. gattii* strains observed by TEM. (A) R265, (B) *nop16Δ.1* and (C) *nop16Δ.2*. N: nucleus, MP: plasma membrane and V: vacuoles. Bars 500 nm.

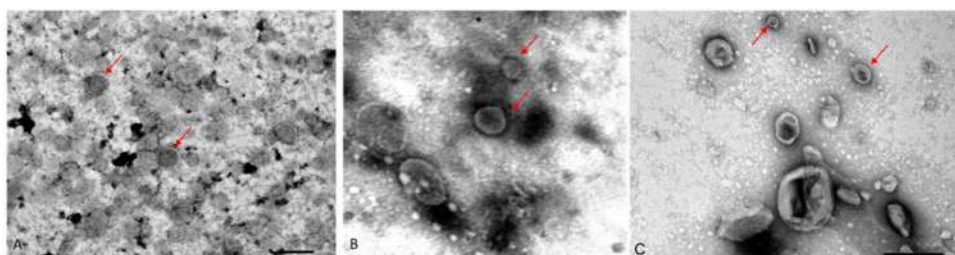


Figure 5: Extracellular vesicles produced by *C. gattii* and analyzed by TEM. Vesicles were highlighted by the red arrows. The vesicles were produced by strains (A) R265, (B) *nop16Δ.1* and (C) *nop16Δ.2*. Bars 200 nm.

References:

1. de Oliveira, H.C. et al. Elsevier, 2020, doi:10.1016/B978-0-12-809633-8.21019-4



2. Joffe, L.S. et al. *Front. Microbiol.* **2017**, 8, 535, doi:10.3389/fmicb.2017.00535.
3. Reis, F.C.G. et al. *mSphere* **2019**, 4, doi:10.1128/mSphere.00080-19.



Cryo-EM To Visualize Viruses And Protein Filaments At Near-Atomic Resolution

Guilherme A. P. de Oliveira^{1*}

¹ Institute of Medical Biochemistry Leopoldo de Meis, National Institute of Science and Technology for Structural Biology and Bioimaging, National Center of Nuclear Magnetic Resonance Jiri Jonas, Federal University of Rio de Janeiro, Rio de Janeiro RJ 21941-901, Brazil.

*gaugusto@bioqmed.ufrj.br / mrguioli@gmail.com

A quick search to the Electron Microscopy Database (www.emdataresource.org) shows that cryo-EM has become tremendously popular. There are several aspects that jointly contributed to what is today recognized as a resolution revolution in the field [1]. The vitrification process of EM samples [2] and technological developments such as the field emission gun [3], the automated electron microscope [4], and the direct electron detector [5] are turning points to the progress of cryo-EM. Software development for processing frozen hydrated images and 3D reconstruction is moving very rapidly [6, 7] and pipelines for automated pre-processing and on-the-fly monitoring of data collection are routinely used. Here we provide two examples on how electron cryo-microscopy is a powerful technique to obtain models at near-atomic resolution of filaments and icosahedral viruses. The first example is a pili on the surface of *Sulfolobus islandicus*, a polyextremophilic archaeon growing optimally at $\sim 80^{\circ}\text{C}$ and pH 3. By means of electron cryo-microscopy we determined the structure of these filaments at 4.1 Å resolution [8]. An atomic model was built by combining the electron density map with bioinformatics without previous knowledge of the pili sequence. The atomic structure of the pilus was unusual, with almost one-third of the residues being either threonine or serine, and with many hydrophobic surface residues. While the map showed extra density consistent with glycosylation for only three residues, mass measurements suggested extensive glycosylation [8]. We propose that this extensive glycosylation renders these filaments soluble and provides the remarkable structural stability. The second example is a 3.7 Å resolution structure of the *Sulfolobus* polyhedral virus 1 (SPV1), originally isolated from a hot acid spring in Beppu, Japan [9]. The circular dsDNA in SPV1 is fully covered with a viral protein forming a nucleoprotein filament with attractive interactions between layers. Most strikingly, we have been able to show that the DNA is in an A-form, as it is in the filamentous viruses infecting hyperthermophilic acidophiles [9]. Previous studies have suggested that DNA is in the B-form in bacteriophages, and our study is a direct visualization of the structure of DNA in an icosahedral virus.

References

- [1] Kuhlbrandt W. *Science* 343:1443-1444 (2014).
- [2] Dubochet J. *Biophys J.* 110:756-757 (2016).
- [3] Crewe AV. *Rev Sci Instrum* 39:576-583 (1968).
- [4] Suloway C et al., *J Struct Biol*, 151:41-60 (2005).



- [5] Faruqi AR et al., *Adv Imaging Electron Phys*, 190:103-141 (2015).
[6] Zivanov J et al., *eLife*, 7 (2018).
[7] Punjani A et al., *Nat Methods*, 14:290-296 (2017).
[8] Wang F et al., *Nat Microbiol*, 4(8):1401-1410 (2019).
[9] Wang F et al., *Proc Natl Acad Sci USA*, 116(45):22591-22597 (2019).

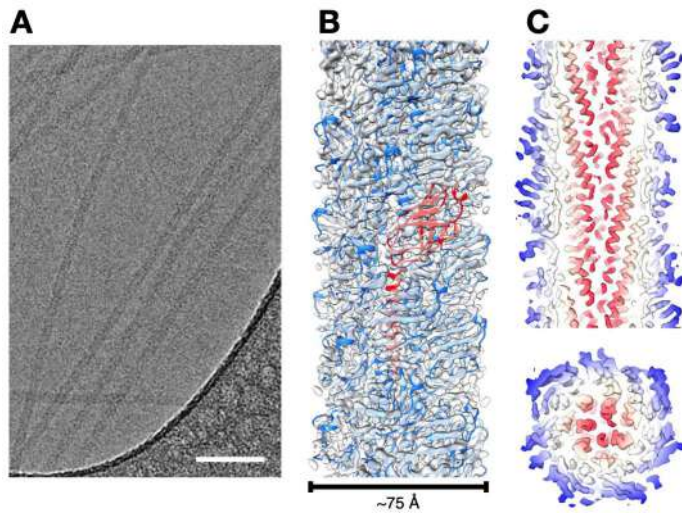


Figure 1. **A**, Representative cryo-EM micrograph of the pili. Scale bar, 50 nm. **B**, Cryo-EM reconstruction of the pilus at 4.1 Å with the fitted atomic model. **C**, Thin slices parallel (top) and perpendicular (bottom) to the helical axis of the pilus are shown. The tight packing of the all- α -helical core can be seen.

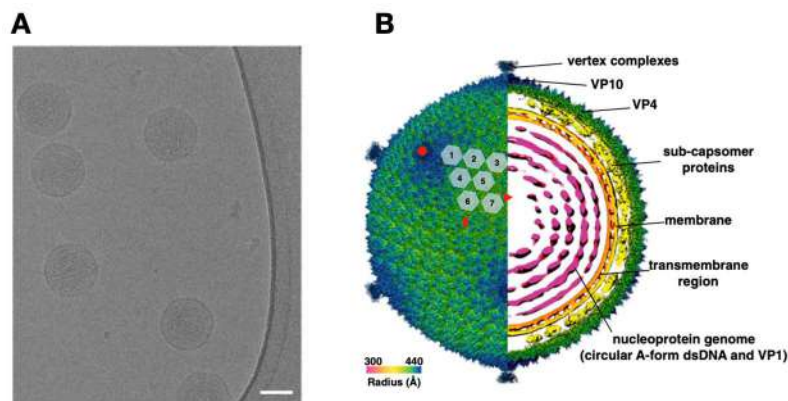


Figure 2. **A**, Cryo-EM image of the SPV1, scale bar 50 nm. **B**, Overall cryo-EM density map of SPV1, rendered to display the outer capsid (left half) and a central slice showing the interior of the virus (right half).



Unravelling The Structure Of A Type IV Pilus Dependent Bacteriophage

Germán Gustavo Sgro^{1,2,*}, Alexandre Cassago³, Rodrigo Villares Portugal³, Shaker Chuck Farah¹

¹Instituto de Química, Universidade de São Paulo, São Paulo, Brazil.

²Faculdade de Ciências Farmacêuticas de Ribeirão Preto, Universidade de São Paulo, Ribeirão Preto, Brazil.

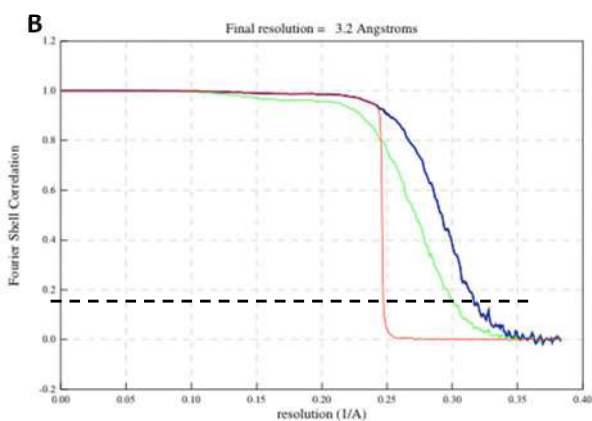
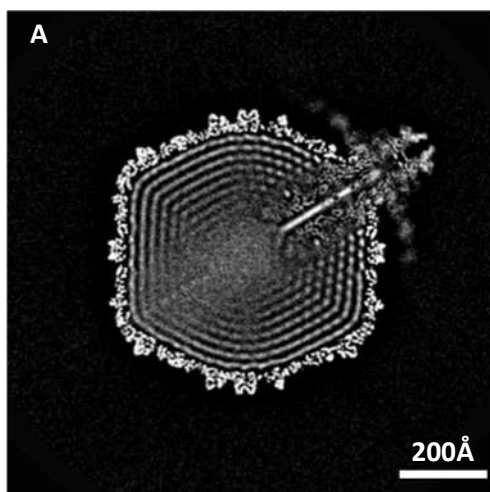
³Laboratório Nacional de Nanotecnologia, Centro Nacional de Pesquisa em Energia e Materiais, Campinas, Brazil.

*ggsgro@usp.br

The bacterium *Xanthomonas citri* is the causative agent of Citrus canker, a major disease that affects a variety of citrus plants, and makes great losses in the production of fruits and derivatives. We have previously shown that the infection of *X. citri* cells by the bacteriophage Φ Xacm4-11 is dependent on its Type 4 Pilus (T4P) [1]. After establishing a purification protocol, we have also obtained negative stained electron microscopy images, allowing us to classify this phage as a podovirus. This allowed us to have access and to collect an initial cryo-electron microscopy (cryo-EM) dataset on the Titan Krios microscope at the LNNano, from which we initially obtained a preliminary icosahedral 3D map of the capsid particle with resolution of approximately 5 Å. With improved phage samples, we subsequently prepared new grids and collected two more datasets, one in linear charge-integration mode and another in electron-counting mode, and have been able to improve the map to approximately 3.2 Å in resolution, where the features and the level of details were enhanced. This allowed us to build an initial model of the capsid asymmetric unit containing 7 copies each of the major capsid protein (MCP) and the decorating cement protein (CP). Overall, Φ Xacm4-11 is an icosahedral T7-like phage with a capsid made of 60 asymmetric units and a total of 840 protein subunits. The same datasets were pooled and used for the asymmetric reconstruction of Φ Xacm4-11, showing a defined density for its tail structure, as well as internal novel features. This processing strategy is still being improved using different approaches, but the results are very promising. Here, we present a summary of the results obtained so far in the structure determination of this T4P dependent bacteriophage.

[1] Dunger et al., Molecular Plant-Microbe Interactions (2014) 1132.

This project was supported by FAPESP (Brazil).



(A) Slice cut of the asymmetrically reconstructed (C1) map of Φ Xacm4-11 by cryo-EM. (B) Fourier Shell Correlation (FSC) curves for the symmetric reconstruction of the same phage. The curves represent the phase-randomised (red line), unmasked (green line) and mask-corrected (blue line) FSCs between two independently refined half-maps after post-processing, and indicate the resolution achieved at 3.2Å.



Exploring the Structure and Filament Assembly of Septin Complexes with Cryo-EM.

Deborah Cezar Mendonça^{1*}, Rodrigo Villares Portugal² and Richard Charles Garratt¹

¹ Universidade de São Paulo, Instituto de Física de São Carlos, São Carlos, Brasil.

² Centro Nacional de Pesquisa em Energia e Materiais, Laboratório Nacional de Nanotecnologia, Campinas, Brasil

*deborah.mendonca@usp.br

Septins are GTP binding proteins considered as a novel component of the cytoskeleton. These proteins interact with each other to form filamentous heterocomplexes and high order structures which are important for cytokinesis and a variety of other cellular processes [1]. In order to form functional filaments, human septins must assemble into hetero-oligomeric rod-like particles which polymerize end-to-end. The oligomers themselves can vary in size and composition from species to species but always present a specific subunit arrangement. In humans, these can be either hexamers, composed of three distinct septins, or octamers, composed of four [2,3]. The rules governing the assembly of these particles and the subsequent filaments are incompletely understood. Although crystallographic approaches have been successful in studying the separate components of the system, there has been difficulty in obtaining high resolution structures of the full particle. We used single particle cryo-EM to obtain the structure of a hexameric rod composed of human septins 2, 6 and 7 with a global resolution of $\sim 3.6\text{\AA}$. By fitting the high-resolution crystal structures of the component subunits into the cryo-EM map, we were able to provide an essentially complete model for this hexameric complex. This exposes SEPT2 NC-interfaces at the termini of the hexamer and leaves internal cavities between the SEPT6-SEPT7 pairs. The floor of the cavity is formed by the two $\alpha 0$ helices including their polybasic regions. These are locked into place between the two subunits by interactions made with the $\alpha 5$ and $\alpha 6$ helices of the neighbouring monomer together with its polyacidic region. The cavity may serve to provide space allowing the subunits to move with respect to one another. Additionally, the elongated particle shows a tendency to bend at its centre where two copies of SEPT7 form a homodimeric G-interface. Such bending is almost certainly related to the ability of septin filaments to recognize and even induce membrane curvature.

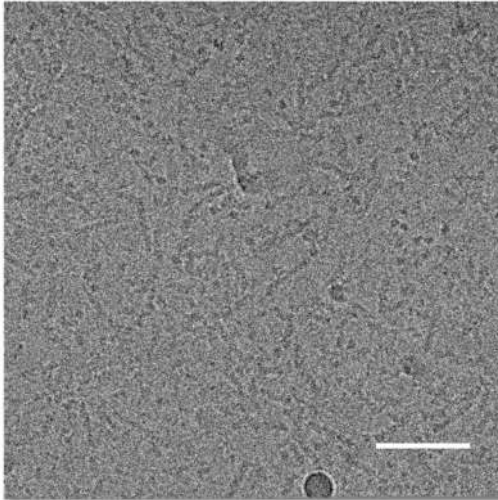
[1] S. Mostowy et al., *Nat. Rev. Mol. Cell Biol.* 13 (2012) 183–94.

[2] M. Sirajuddin et al., *Nat.* 449 (2007) 311-117.

[3] D.C. Mendonça et al., *Cytoskeleton.* 76 (2019) 457–466.

We gratefully acknowledge the support of the São Paulo Research Foundation (FAPESP) via grants 2014/15546-1 and 2017/15340-2. D.C.M (2018/20209-5) and S.L.G (2018/20816-9 and 2017/05665-1) received scholarships from FAPESP.

(a)



(b)

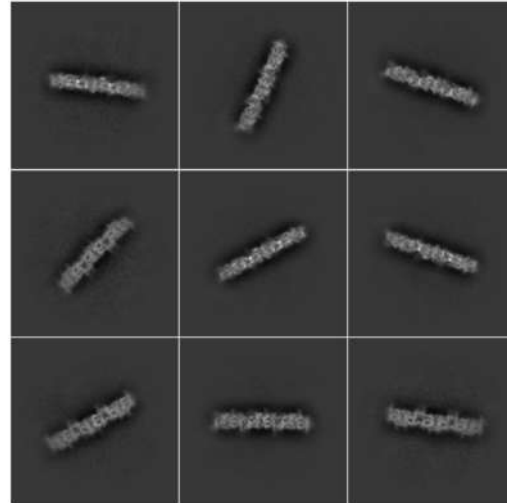


Figure 1. The SPA cryo-EM of human septin hexameric complex. A) A representative cryo-EM micrograph of the SEPT2G-SEPT6-SEPT7 complex dataset. The scale bar represents 50 nm. B) Representative 2D class averages of septin complex particle images.

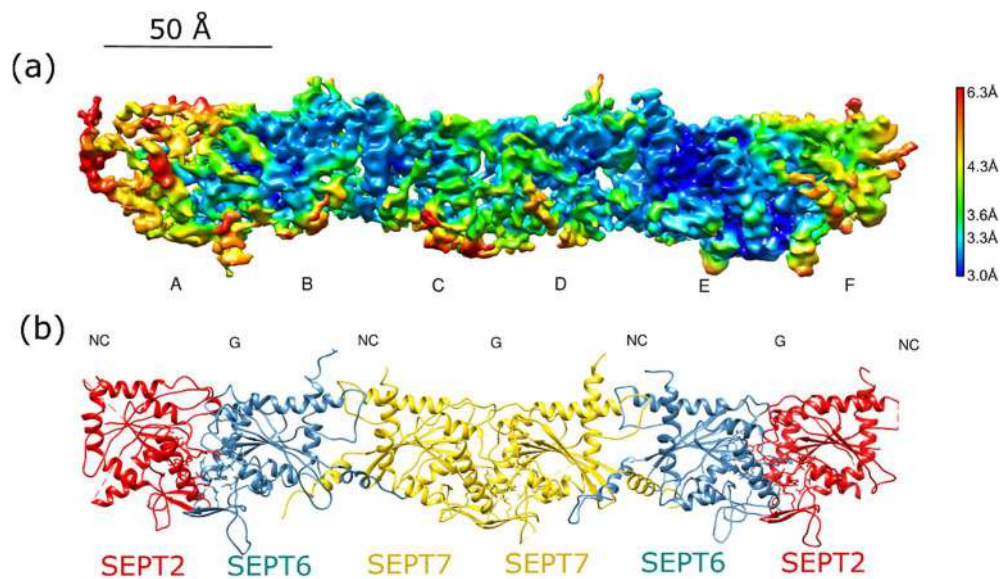


Figure 2. A) Local resolution analysis performed in IMAGIC-4D and visualized in Chimera. Colour keys indicate the local resolution in Å. B) The atomic model of the septin hexameric complex (fitted and adjusted into the Cryo-EM map) in which the monomers are coloured individually and shown as ribbons.



Cryo-EM Structure Of The Mature And Infective Mayaro Virus At 4.4 Å Resolution Reveals Features Of Arthritogenic Alphaviruses

Helder V. Ribeiro-Filho^{1,3}, Lais D. Coimbra^{1,3}, Alexandre Cassago², Rebeca P. F. Rocha¹, João Victor da Silva Guerra¹, Rafael de Felicio¹, Carolina Moretto Carnieli¹, Luiza Leme¹, Antonio Cláudio Padilha², Adriana F. Paes Leme¹, Daniela B. B. Trivella¹, Rodrigo Villares Portugal², Paulo Sérgio Lopes-de-Oliveira¹, Rafael Elias Marques^{1*}.

¹ Brazilian Biosciences National Laboratory, Brazilian Center for Research in Energy and Materials (CNPEM) 13083-970 Campinas, SP Brazil

² Brazilian Nanotechnology National Laboratory, Brazilian Center for Research in Energy and Materials (CNPEM) 13083-970 Campinas, SP Brazil

³ These authors contributed equally to this work: Helder V. Ribeiro-Filho and Lais D. Coimbra

*Correspondence to rafael.marques@lnbio.cnpem.br

Mayaro virus (MAYV) is an emerging arbovirus (arthropod-borne virus) present in Latin America that may cause a debilitating arthritogenic disease named Mayaro Fever. The biology of MAYV and its ability to cause disease are not fully understood and largely inferred from related arthritogenic alphaviruses. Importantly, there are no commercially-available diagnostic tools, specific treatments or vaccines against Mayaro fever. Here we present the structure of MAYV at 4.4 Å resolution, obtained by single particle cryo electron microscopy (Cryo-EM) using the Titan Krios transmission electron microscope (ThermoFisher). Our samples were preparations of mature, infective virions propagated in Vero CCL81 cells, concentrated and purified by ultracentrifugation against a sucrose cushion followed by a Na/K tartrate discontinuous gradient. MAYV presents typical alphavirus features and organization. Interactions between viral proteins that lead to particle formation include those between the structured domains of capsid proteins (C), the anchorage of E2 into a cleft in C and interactions between histidine residues along the ectodomains of E1 and E2. We describe a hydrophobic pocket formed between E1 and E2 spike proteins and conformational epitopes specific of MAYV that may inspire the design of MAYV-specific antibody-based diagnostic tests. We also describe N-glycosylated residues in MAYV E1 (N141) and E2 (N262) that were confirmed and characterized using mass spectrometry. While both N141 and N262 may affect MXRA8 host receptor binding, we observed that N262 forms a molecular “handshake” between MAYV spikes, organized as N262 glycans reaching out to each other from adjacent E2 proteins in separate spikes. The structure of MAYV is suggestive of structural and functional complexity among alphaviruses, which may be targeted for specificity or antiviral activity.

REFERENCES

[1] Ribeiro-Filho, Coimbra et al., Nat Commun 12, 3038 (2021).

[2] This research was supported by grants from FAPESP (2018/03917-6, 2017/15340-2, 2018/00629-0), CNPq (440379/2016-4), CAPES (130767/2016-01) and Serrapilheira Institute, grant number Serra-1709-19681.

ACKNOWLEDGEMENTS

We thank LNNano/CNPEM for the use of electron microscopy facility (TEM-23519, TEM-24308) and for supporting part of computational analyses. We thank Mr. Valber Ferreira for his technical assistance and Prof. Maurício Lacerda Nogueira (FAMERP, Brazil) for providing the MAYV strain used in this study.

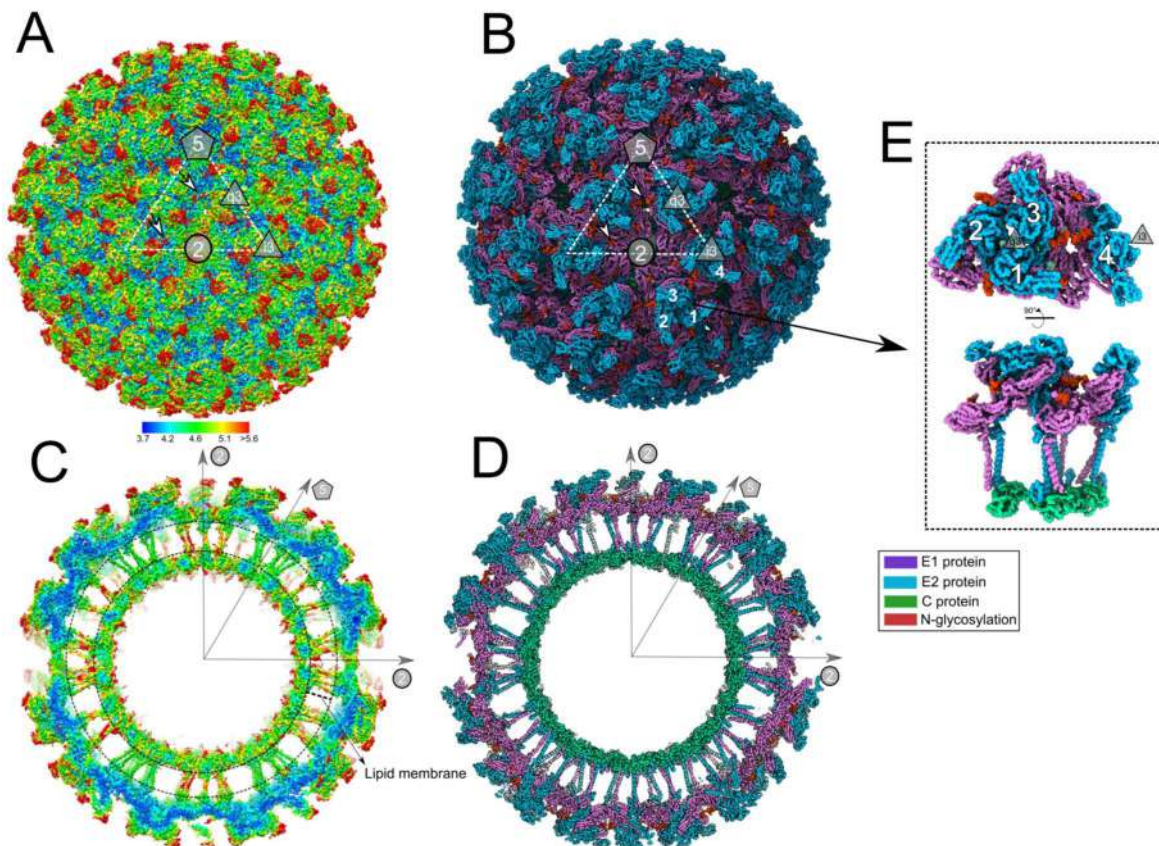


Figure 1. Overall structure of infectious MAYV determined by cryo-EM. (A) MAYV particle showing the external surface with assigned symmetry axes. The white dashed triangle indicates the icosahedral asymmetric unit. Polygons indicate the five-fold axis (pentagon), three and quasi three-fold axes (triangles), and two-fold axis (circle). MAYV density map is in surface representation and coloured by local resolution estimated using $\frac{1}{2}$ -bit threshold criterion in Imagic-4D software system. Scale bar indicates the calculated local resolution. The local resolution values range from 3.7 to 7.8, with median of 4.2 (B) MAYV 3D atomic model fitted into the density map. For clarity, only backbone atoms are presented. The model shows coloured MAYV proteins. 5-3-2 symmetry axes and the asymmetric unit are the same as in (A). (C) and (D) Central cross-section of the MAYV density map or atomic model, respectively. (E) Two rotated views of MAYV asymmetric unit formed by four E1-E2 heterodimers following icosahedral $T = 4$ triangulation. Three and quasi three-fold axes are indicated.



Structural basis of N-glycan demannosylation by the probiotic *Bifidobacterium longum*

Rosa L. Cordeiro¹, Camila R. Santos¹, Mariane N. Domingues¹, Tatiani B. Lima¹, Renan A. S. Pirolla¹, Mariana A. B. Morais¹, Felipe M. Colombari¹, Renan Y. Miyamoto¹, Rafael S. Bezerra¹, Gabriela F. Persinoti¹, Antonio C. Borges², Fabiane Stoffel^{1,3}, Marin van Heel², Rodrigo V. Portugal², Priscila O. Giuseppe¹ and Mario T. Murakami^{1*}

¹ Brazilian Biorenewables National Laboratory (LNBR/CNPEM), Campinas, Brazil

² Brazilian Nanotechnology National Laboratory (LNNano/CNPEM), Campinas, Brazil

³ Department of Chemistry, Federal University of Santa Catarina, Florianópolis, Brazil

Bifidobacteria are among the first colonizers of the human gastrointestinal tract (GIT), being especially abundant in breast-feed infants [1]. Although the proportion of bifidobacteria decreases in adult GIT, their presence has been associated with a positive effect on human health, such as prevention of diarrhea, amelioration of lactose intolerance, or immunomodulation [2]. Therefore, bifidobacteria have been used as component of health-promoting foods. *Bifidobacterium longum* is a very well-adapted bacterium of the GIT, tolerant to gastric acid and firmly attached to intestinal cells through bacterial polysaccharides. Its genome sequence reflects the strong adaptation to the human GIT, with many predicted proteins for catabolism of oligosaccharides released from either plant polymers or host-derived glycoproteins and glycoconjugates [3]. In this context, *B. longum* has enzymes predicted for the breakdown of N-glycans, oligosaccharides present in glycoproteins that control multiple metabolic functions, such as adhesion and cell signaling. In this work, we investigate the molecular mechanisms of demannosylation of N-glycans by the commensal bacterium *Bifidobacterium longum*. Aiming this, we functionally characterized and elucidated the cryo-electron microscopy (Cryo-EM) structure of three key enzymes from this system, ManA, ManB and ManC, which trim α -mannosides from N-glycans. Biochemical assays showed that these enzymes exhibit distinct specificities having a cooperative role in the cleavage of α -mannosyl residues. Cryo-EM structures at high-resolution revealed an oligomeric arrangement for the three enzymes and an active site populated with variable loops that define the substrate preference between these complementary mannosidases. Our data provide insights into the molecular mechanisms of GH38 α -mannosidases and contribute for the understanding on the bacterial-host interface between humans and bacteria from a genus of great importance to human health.

[1] R. Boesten, F. Schuren, K. Ben Amor, M. Haarman, J. Knol, and W. M. de Vos, "Bifidobacterium population analysis in the infant gut by direct mapping of genomic hybridization patterns: Potential for monitoring temporal development and effects of dietary regimens," *Microb. Biotechnol.*, vol. 4, no. 3, pp. 417–427, May 2011.

[2] E. Rosenberg, E. F. DeLong, F. Thompson, S. Lory, and E. Stackebrandt, *The prokaryotes: Prokaryotic biology and symbiotic associations*. Springer-Verlag Berlin Heidelberg, 2013.

[3] M. A. Schell et al., "The genome sequence of *Bifidobacterium longum* reflects its adaptation to the human gastrointestinal tract," *Proc. Natl. Acad. Sci.*, vol. 99, no. 22, pp. 14422–14427, Oct. 2002.

[4] This research was supported by FAPESP (Brazil).

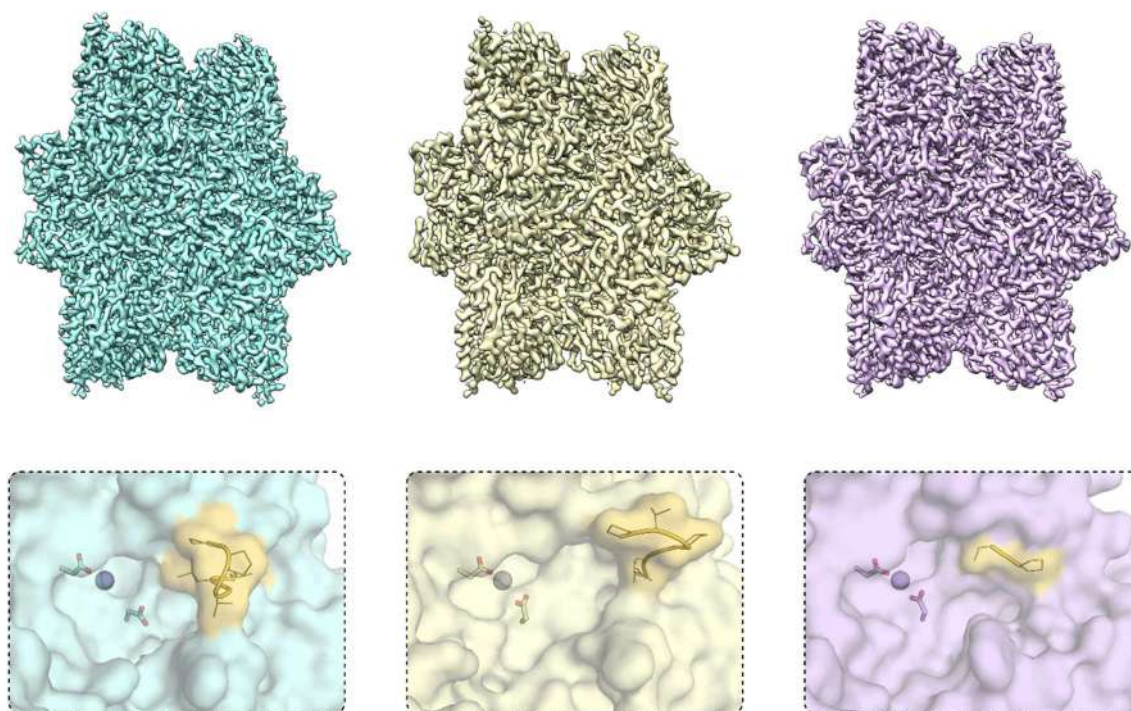


Figure 1. Cryo-EM maps of ManA (blue), ManB (yellow) and ManC (purple) (upper panels) and representation of their respective active sites (bottom panels). Metal ions are represented by spheres, catalytic residues by sticks and the variable loops are highlighted in orange.



Impact of androgenic stimulation on mitochondrial oxygen consumption and organelle distribution in prostatic epithelial cells.

Francisco Breno S. Teófilo^{1,*}, Estela N. B. Busanello², Claudia D. C. Navarro², Anibal E. Vercesi², Hernandes F. Carvalho^{1,3}.

¹ Department of Structural and Functional Biology, Institute of Biology, State University of Campinas (UNICAMP), Campinas, Brazil.

² Department of Clinical Pathology, Faculty of Medical Sciences, State University of Campinas (UNICAMP), Campinas, Brazil.

³ National Institute of Science and Technology on Photonics applied to Cell Biology (INFABiC), Campinas, Brazil.

* f211599@dac.unicamp.br

Puberty is an important stage of prostate development, having as one of its main events the beginning of secretory activity by specialized epithelial cells [1]. Among the secretion components, the high concentration of citrate ion stands out, suggesting a blockage of aconitase, the enzyme responsible for citrate conversion in the citric acid cycle [2, 3, 4]. It is known that during the first postnatal weeks the physiological states of the prostate are tightly regulated by androgens, with an expressive increase in testosterone concentration at puberty [1]. However, morphofunctional aspects of epithelial cell mitochondria in variable conditions of androgenic stimulation are poorly elucidated. Therefore, we aimed to verify the organization of the mitochondrial network of epithelial cells and mitochondrial oxygen consumption in ventral prostate (VP) biopsies of rats belonging to two groups in physiologically distinct phases from normal prostate development: *pre pubertal* and *post pubertal*; opposed to a third one induced to androgenic deprivation: *post pubertal killed on day 3 after surgical castration*. The experimental design, including sample size and procedures, were approved by the State University of Campinas Committee on the Use of Experimental Animals (CEUA), under protocols n°. 5146-1/2019 and n° 5383-1/2019. *Airyscan* microscopy images obtained after staining with MitoTracker Red CMXRos + HOECHST 33342 revealed a disparity in the distribution of mitochondrial content throughout the VP epithelial ducts (proximal, medial and distal regions, according to their position regarding the urethra) (Figure 1). The absence of androgenic stimulation seems to impact the mitochondrial network promoting the appearance of mitochondrial clusters, despite similar aggregates are also present in proximal regions of pre pubertal rats not subjected to castration. Results obtained by high-resolution respirometry [5] indicated an upward trend in the average respiratory rates in the post pubertal group when compared to the prepubertal animals: ADP (26%), oligomycin (20%) and FCCP (24%). Additionally, castration has contributed to a significant decrease in average respiratory rates: ADP (45%), oligomycin (47%) and FCCP (28%) (Figure 2). These observations suggest an association between androgenic stimulation and mitochondrial morphology and physiology in the rat VP, with androgenic deprivation impacting mitochondrial oxygen consumption and promoting morphological changes with the appearance of mitochondrial aggregates.

REFERENCES

- [1] P.S.L. Vilamaior et al., Prostate growth of the ventral prostate in Wistar rats: a stereological and morphometrical study, *Anat. Rec.* 288A (8) (2006) 827-931.
- [2] L.C. Costello et al., Zinc inhibition of mitochondrial aconitase and its importance in citrate metabolism of prostate epithelial cells, *J. Biol. Chem.* 272 (46) (1997) 28875-81.
- [3] L.C. Costello et al., Zinc causes a shift toward citrate at equilibrium of the m-aconitase reaction of prostate mitochondria, *J. Inorg. Biochem.* 78 (2) (2000) 161-5.
- [4] L.C. Costello et al., A comprehensive review of the role of the zinc in the normal prostate functions and metabolism; and its implications in prostate cancer, *Arch. Biochem. Biophys.* 611 (1) (2016) 100-12.
- [5] E.N.B. Busanello et al., Pravastatin chronic treatment sensitizes hypercholesterolemic mice muscle to mitochondrial permeability transition: protection by creatine or coenzyme Q₁₀. *Front Pharmacol.* 8 (185) (2017) 1-11.

ACKNOWLEDGEMENTS

This research was supported by CNPq (Brazil), FAPESP (São Paulo, Brazil) and CAPES (Brazil). INFABiC is co-funded by FAPESP (2014/50938-8) and CNPq (465699/2014-6). FBST was supported by a fellowship from CNPq (140512/2020-9).

FIGURES

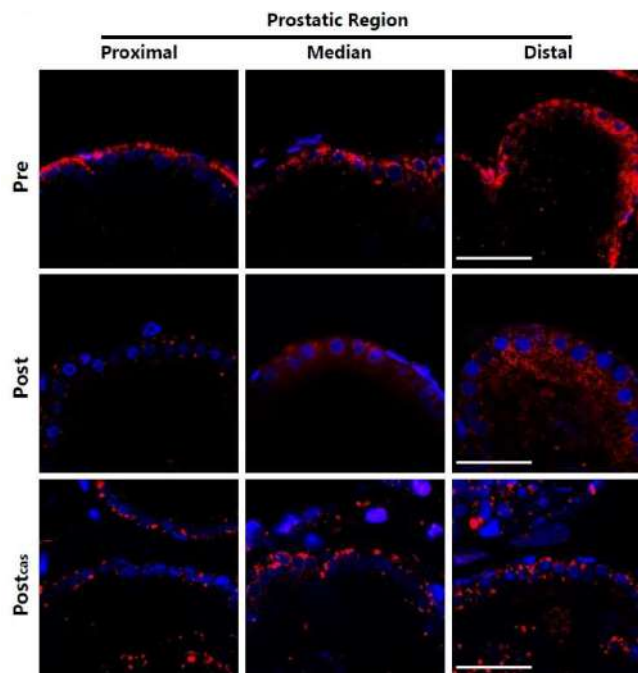


Figure 1 - Disparity in the distribution of mitochondrial content along the VP epithelial ducts. Mitochondrial network in epithelial cells from different regions: proximal (left panels), intermediate (middle panels), and distal (right panels) of the VP in distinct phases: *pre pubertal (Pre)*, *post pubertal (Post)*, and *day 3 after castration (Post_{cas})*. Mitochondrial network stained with MitoTracker Red (red) and HOECHST-stained nuclei (blue). Scale Bar: 40 μ m.

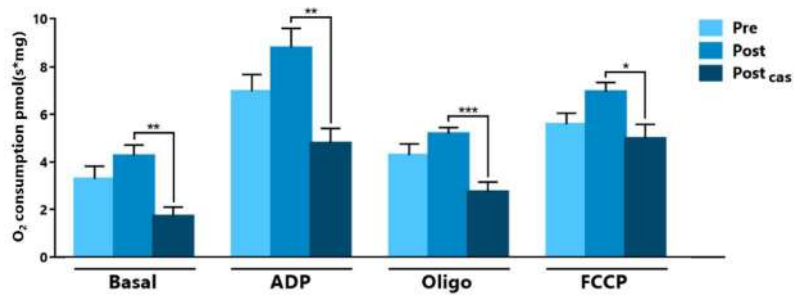


Figure 2 - Oxygen consumption by VP biopsies. Bar graphs showing respiratory in VP biopsies of *pre* pubertal (*Pre*), *post* pubertal (*Post*) and *post* pubertal killed on day 3 after castration (*Post_{cas}*) rats. * $p < 0.05$, ** $p < 0.01$, *** $p < 0.001$, when compared *Post* and *Post_{cas}* (one-way ANOVA, *post-hoc* Sidak test). $N = 3-4$.



Super-Resolution Structured Illumination Microscopy for Analysis of New Chemotherapeutics Against *Toxoplasma gondii*

Carlla Assis Araujo-Silva^{1,2}, Jennifer Mendonça Guimarães^{1,2}, Franz Bracher⁴,
Wanderley de Souza^{1,2}, Erica dos Santos Martins-Duarte³ and Rossiane
Claudia Vommaro^{*1,2}

1. Instituto de Biofísica Carlos Chagas Filho – Universidade Federal do Rio de Janeiro
 2. Instituto Nacional de Ciência e Tecnologia em Biologia Estrutural e Bioimagens, Universidade Federal do Rio de Janeiro, Brasil
 3. Departamento de Parasitologia - Universidade Federal de Minas Gerais, Brasil.
 4. Department of Pharmacy - Center for Drug Research, Ludwig-Maximilians University Munich, Butenandtstr - Munich, Germany
- * vommaro@biof.ufrj.br

Super-Resolution Structured Illumination Microscopy (SR-SIM) was applied in this work to analyze the effects of histone deacetylase inhibitors derived from the selective inhibitor of HDAC6 - Tubastatin A (TST), the compounds used were KV46, KV30 and KV24 [1,2] against *T. gondii* *in vitro*. *T. gondii* is a protozoan parasite that can cause hydrocephalus, uveitis, motor and neurological delay in newborns, and encephalitis in immune compromised individuals. The treatment is restricted to an association of pyrimethamine and sulfadiazine, which are related to side effects and appearance of allergy. The three compounds tested were active against *T. gondii* tachyzoites in human foreskin fibroblasts (HFF) infected for 48h and showed IC₅₀ in the nanomolar range. HFF were treated for 24h with 1 μM of each compound. Afterwards, they were fixed with formaldehyde 4% and carried out for immunofluorescence. Cells were incubated with anti-SAG-1 (surface antigen) and anti-IMC (internal membrane complex) followed by incubation with secondary antibodies conjugated with Alexa 488 and 568, respectively, to elucidate the anti-proliferative effect of these inhibitors. Samples prepared for immunofluorescence were subjected to SR-SIM in an ELYRA PS.1 microscope (Carl Zeiss). Z-stacks of high-resolution image frames were collected in 5 rotations by utilizing an alpha Plan-Apochromat 63×/1.46 oil DIC objective. Images were reconstructed using a structured illumination algorithm in the ZEN software (BlackEdition, 2012). Treated cells showed formation of rounded masses of parasites with the impairment of the budding of daughter cells (Figure 1, arrowheads). The interruption of the cell division process and consequent individualization of new daughter cells are important events in the analysis of new antiparasitic compounds. The results indicate SR-SIM as a powerful tool to analyze the effect of anti-protozoan drugs.

Acknowledgments: The authors thank CENABIO (Centro Nacional de Biologia Estrutural e Bioimagem da UFRJ).

REFERENCES:

- [1] Bougdour A et al., J Exp Med. 13;206(4) (2009) 953.
- [2] Vögerl, K. et al., J. Med. Chem, 62;(3) (2019)1138–1166

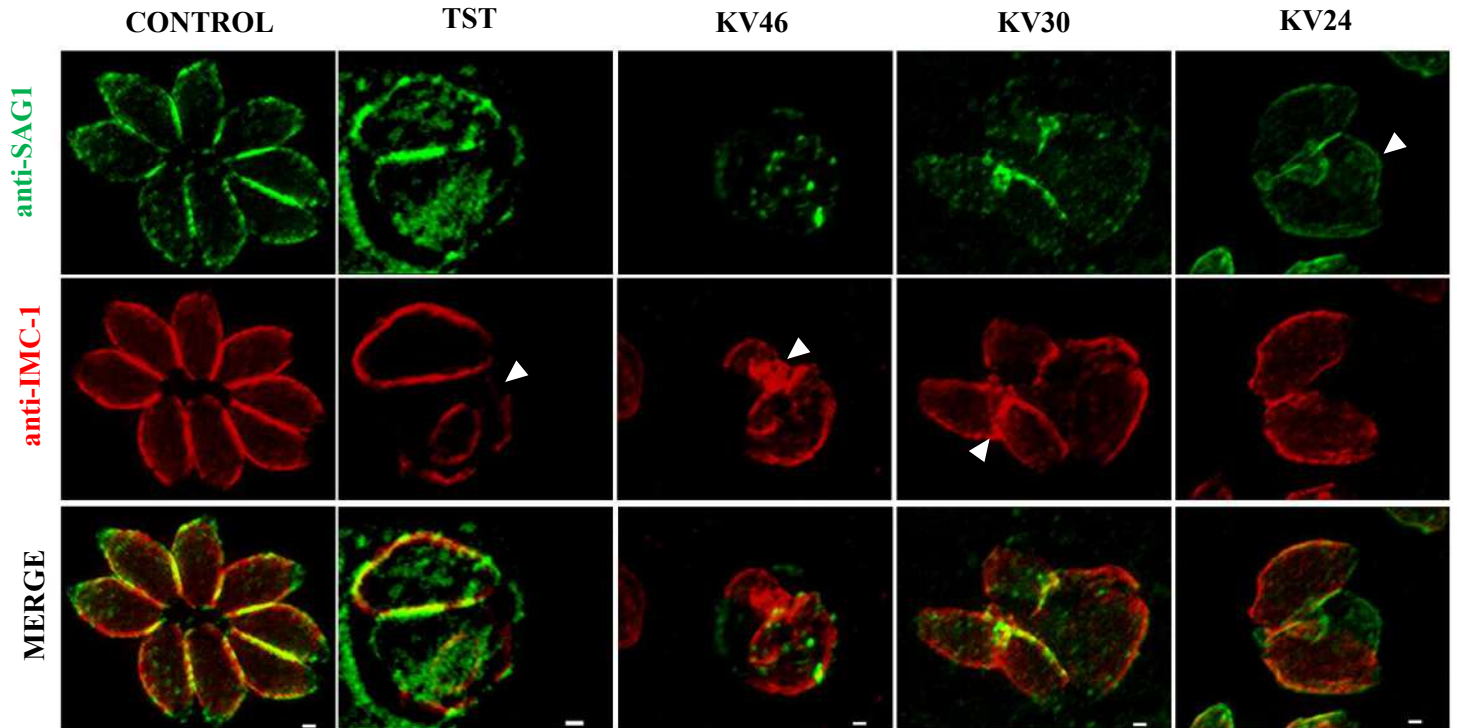


Figure 1- Super-Resolution Structured Illumination Microscopy (SR-SIM). Visualization of the maximum intensity projection (MIP) by the SR-SIM of HFF cells treated with 1 μ M TST, KV46, KV30 or KV24, for 24h. The coverslips were sealed with ProLongTM Gold Antifade Mountant that forms a near-perfect optical path (1.47 RI), at room temperature. The formation of masses of damaged parasites, which did not complete the budding process can be clearly observed (white arrowheads). Anti-SAG-1 (surface antigen - green - Alexa 488) and anti-IMC (internal membrane complex - red - Alexa 568) Scale bar = 0,5 μ m.



Ultrastructural Characterization of *Mabuya nigropunctata* Leukocytes

Brenda Fachetti ^{1,3*}, Máira Turiel-Silva ^{1,3}, Edilene O. Silva ², Ana Paula Drummond ³, José Diniz ³

¹ Universidade do Estado do Pará, Departamento de Morfologia e Ciências Fisiológicas, Centro de Ciências Biológicas e da Saúde, Marabá, Brasil;

² Universidade Federal do Pará, Instituto de Ciências Biológicas, Belém, Brasil;

³ Instituto Evandro Chagas, Seção de Hepatologia, Laboratório de Microscopia Eletrônica, Belém, Brasil.

*brenda.fachetti22@gmail.com

The parasitology of different groups of animals has a biological strand of great interest, which is a parasite-host relationship [1]. The ultrastructural study of leukocytes that are targets of protozoa of the phylum Apicomplexa, as *Saurocytozoon mabuyi* and *Garnia morula*, is of fundamental importance to clarify basic aspects of the structure of these host cells [2]. In order to know the ultrastructure of leukocytes of the lizard *Mabuya nigropunctata*, 10 animals were captured in the Bragantina region of the Pará State, North Brazil (License MMA SISBIO N^o.12420-2). Blood samples were obtained by punctured in the caudal vein of the lizards after anesthesia, posteriorly stained with Giemsa and analyzed by light microscopy. The blood samples were posteriorly processed for transmission electron microscope (TEM). By light microscopy and TEM, monocytes, lymphocytes, thrombocytes, four types of granulocytes (I, II, III and IV) and neutrophil-like cells (NLC) were identified. The monocytes exhibit a large, rounded or reniform nucleus, peripheral heterochromatin and an abundance of euchromatin. Furthermore, vacuoles, Golgi complex (GC), several mitochondria (MIT) and poorly developed endoplasmic reticulum (ER) were observed in the cytoplasm. The lymphocyte showed a typical centralized nucleus with heterochromatin distributed on its periphery with the presence of abundant euchromatin in the central region, which was eventually filled by a scarce heterochromatin. The cytoplasm was homogeneous and sparse with a poorly developed ER and some vacuoles. The thrombocyte presented a central nucleus with peripheral and abundant heterochromatin, oval/elongated shape, limited cytoplasm with some organelles (MIT, ER, vacuoles and cisterns similar to those of ER and GC). Type I granulocytes presented eccentric and small nuclei, cytoplasm with granules of varied shapes and electron density. Type II granulocytes presented bi-lobulated and eccentric nuclei, cytoplasm containing granules with varied shapes and electron density, well-developed ER and a significant amount of MIT. Type III granulocytes had peripheral nuclei with cytoplasmic granules heterogeneous in shapes and electron density. Type IV granulocytes had a peripheral nucleus with a cytoplasm similar to the "blackberry" aspect, conferred by large granules and intense electron density. Some profiles of these granules demonstrated the presence of central electron lucent areas. NLC presents a lobulated nucleus, cytoplasm with heterogeneous granules and varied electron density, presence of MIT and a well-developed ER. These findings may contribute to our understanding of the leukocytes of *M. nigropunctata* and further studies with parasitized cells.



REFERENCES

[1] A. Araújo et al., Memórias Do Instituto Oswaldo Cruz, 98(suppl 1), 5–11 (2003).

[2] S.O. Alberio et al. Tissue Cell. 37(3):193-202 (2005)

This research was supported by Instituto Evandro Chagas and CNPq (Brazil).

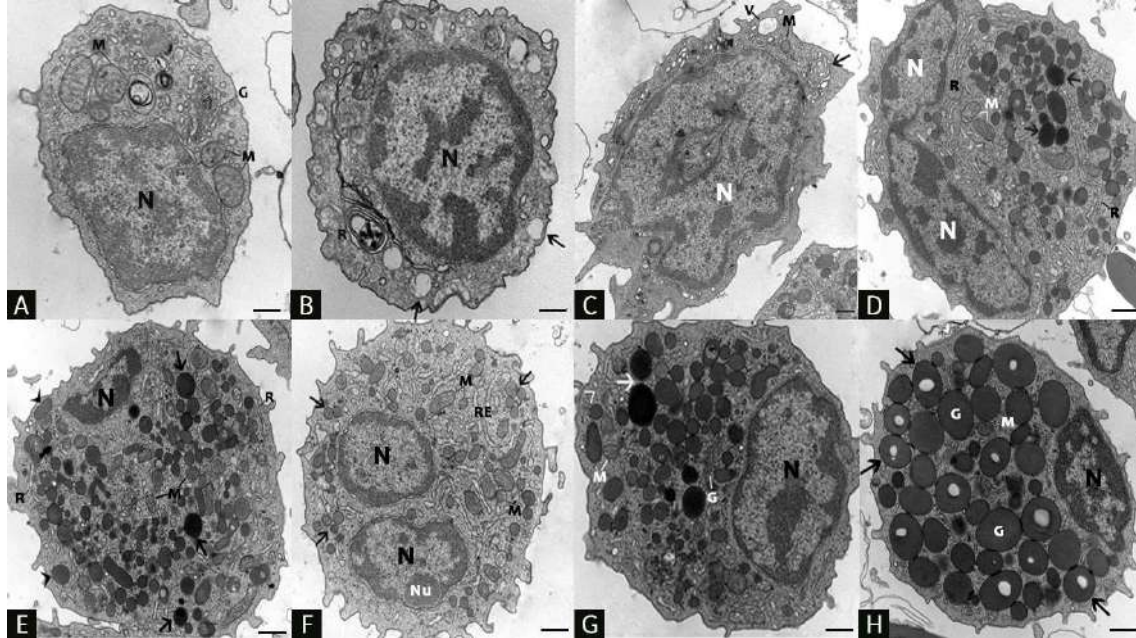


Fig. 1: Electron micrograph of leukocytes from the lizard *Mabuya nigropunctata*. **A:** Monocytes with nucleus (N) rounded shape to the amoeboid; mitochondria (M) and Golgi complex (G); **B:** Lymphocyte. Note nucleus (N) round in shape to the amoeboid; endoplasmic reticulum (R); **C:** Thrombocytes showing nucleus (N) in an amoeboid shape with possible central invagination, mitochondria (M), vacuole (V) and cisterns similar to those of endoplasmic reticulum and Golgi complex (Arrow); **D:** Neutrophil-like cell showing the peripheral nucleus (N) in bi-lobulated format, mitochondria (M), electron-dense granules (arrow). The endoplasmic reticulum is well developed (R); **E:** Granulocytes T1 showing the nucleus (N) in an elliptical shape with an irregular contour. The cytoplasm contains several granules: electron dense granules (arrow), granules (arrowhead), mitochondria (M) and endoplasmic reticulum (ER); **F:** Granulocytes T2, the nucleus (N) appears in two profiles, nucleolar center (Nu), mitochondria (M), ovoid granules (arrows). The endoplasmic reticulum is well developing (ER); **G:** Granulocytes T3 demonstrating the eccentric nucleus (N) with ovoid shape and irregular contours, abundant cytoplasm containing mitochondria (M), Golgi complex (G) endoplasmic reticulum (arrowhead) and heterogeneous electron-dense granules (arrow); **H:** Granulocytes T4 demonstrating the eccentric (N) nucleus, mitochondria (M), electron dense granules (G) and granules with electron lucent profiles (arrow). Scale Bar = 500 nm.



Morphology and Morphogenesis of SARS-CoV-2 in Vero-E6 Cells

Debora Ferreira Barreto-Vieira^{1*}, Marcos Alexandre Nunes da Silva¹, Cristiana Couto Garcia², Milene Dias Miranda², Aline da Rocha Matos², Braulia Costa Caetano², Paola Cristina Resende², Fernando Couto Motta², Marilda Mendonça Siqueira², Wendell Girard-Dias³, Bráulio Soares Archanjo⁴, Ortrud Monika Barth¹

¹Fundação Oswaldo Cruz-Fiocruz, Instituto Oswaldo Cruz, Laboratório de Morfologia e Morfogênese Viral, Rio de Janeiro, RJ, Brasil.

²Fundação Oswaldo Cruz-Fiocruz, Instituto Oswaldo Cruz, Laboratório de Vírus Respiratórios e do Sarampo, Rio de Janeiro, RJ, Brasil.

³Fundação Oswaldo Cruz-Fiocruz, Instituto Oswaldo Cruz, Plataforma de Microscopia Eletrônica Rudolph Barth, Rio de Janeiro, RJ, Brasil.

⁴Instituto Nacional de Metrologia, Qualidade e Tecnologia, Núcleo de Laboratórios de Microscopia, Rio de Janeiro, RJ, Brasil.

*barreto@ioc.fiocruz.br

The coronaviruses (CoVs) called the attention of the world for causing outbreaks of severe acute respiratory syndrome (SARS-CoV), in Asia in 2002-03, and respiratory disease in the Middle East (MERS-CoV), in 2012. In December 2019, yet again a new coronavirus (SARS-CoV-2) first identified in Wuhan, China, was associated with a severe respiratory infection, known today as COVID-19. This new virus quickly spread throughout China and 30 additional countries. As result, the World Health Organization (WHO) elevated the status of the COVID-19 outbreak from emergency of international concern to pandemic on March 11, 2020. The impact of COVID-19 on public health and economy fueled a worldwide race to approve therapeutic and prophylactic agents, but so far, there are no specific antiviral drugs or vaccines available. In current scenario, the development of in vitro systems for viral mass production and for testing antiviral and vaccine candidates proves to be an urgent matter. The objective of this work is study the biology of SARS-CoV-2 in Vero-E6 cells at the ultrastructural level. In this study, we documented, by scanning and transmission electron microscopies and real-time reverse transcription polymerase chain reaction (RT-PCR), the infection of Vero-E6 cells with SARS-CoV-2 samples isolated from Brazilian patients. The infected cells presented cytopathic effects and SARS-CoV-2 particles were observed attached to the cell surface and inside cytoplasmic vesicles. The entry of the virus into cells occurred through the endocytic pathway or by fusion of the viral envelope with the cell membrane. Assembled nucleocapsids were verified inside rough endoplasmic reticulum cisterns (RER). Viral maturation seemed to occur by budding of viral particles from the RER into smooth membrane vesicles (Figure 1). The RT-PCR assay demonstrated an increase in the amount of SARS-CoV-2 RNA copies in the supernatant at least two log₁₀ steps within 72 hours post-infection (Table), suggesting production of viral progeny. Therefore, the susceptibility of Vero-E6 cells to SARS-CoV-2 infection and the viral pathway inside the cells were demonstrated by ultrastructural analysis [1].

REFERENCE:

[1] D.F. Barreto-Vieira et al., Mem. Inst. Oswaldo Cruz, Rio de Janeiro, Vol. 116: e200443, 2021.

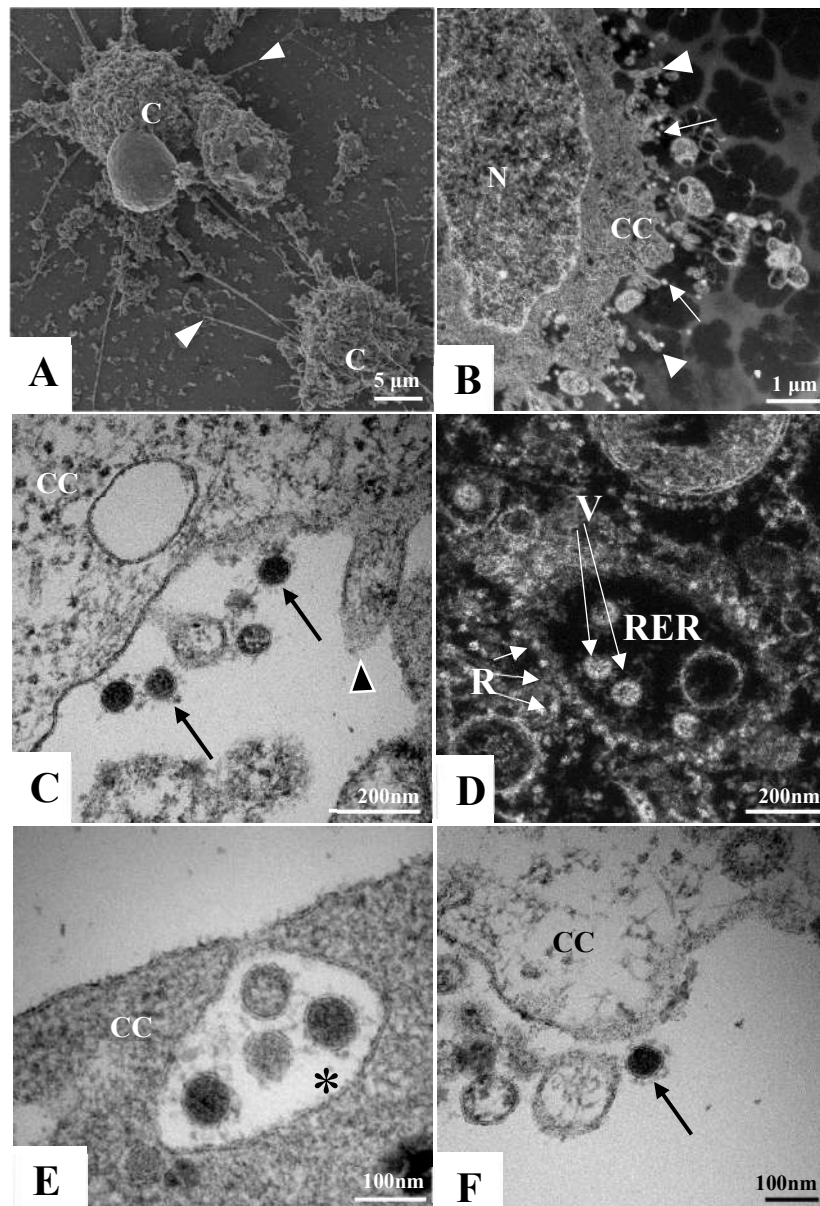


Figure 1: Vero-E6 cell, 72 hours post-infection with SARS-CoV-2, presenting numerous filopodia (head arrow) [A]. Virus particles attached to cell filopodia [B], in cytoplasmic membrane [C], inside rough endoplasmic reticulum cistern with thickened ribosomes [D] and inside smooth vesicles (asterisk) at the periphery of the cell and with your membrane fused with membrane cell were observed [E]. Virus particles presenting spherical morphology, displaying spikes, and a diameter between 80 and 100nm [F]. Cell (C), Cell cytoplasm (CC), nucleus (N), SARS-CoV-2 particles (arrow).



TABLE

Virus RNA quantification (copies/mL)

<i>Virus Isolate</i>	<i>1 hpi (inoculum)</i>	<i>72 hpi (virus growth)</i>
<i>EPI_ISL_415105</i>	1,2 x 10 ^{e4}	1,3 x10 ^{e7}
<i>EPI_ISL_414045</i>	1,3 x10 ^{e5}	1,4 x10 ^{e7}
<i>EPI_ISL_427294</i>	4,7 x10 ^{e3}	1,6 x10 ^{e7}

hpi: hours post infection



Eosinophil cytolytic cell death during human inflammatory diseases: a mechanism underlying release of extracellular traps, granules and vesicles

Vitor H. Neves^{1*}, Cinthia Palazzi¹, Kennedy Bonjour¹, Peter F. Weller², Rossana C. N. Melo^{1,2**}

¹ Laboratory of Cellular Biology, Federal University of Juiz de Fora, Department of Biology, Institute of Biological Sciences, Juiz de Fora, Minas Gerais, Brazil

² Department of Medicine, Beth Israel Deaconess Medical Center, Harvard Medical School, Boston, Massachusetts, USA

*vitor.neves97@gmail.com.com **rossana.melo@ufjf.edu.br

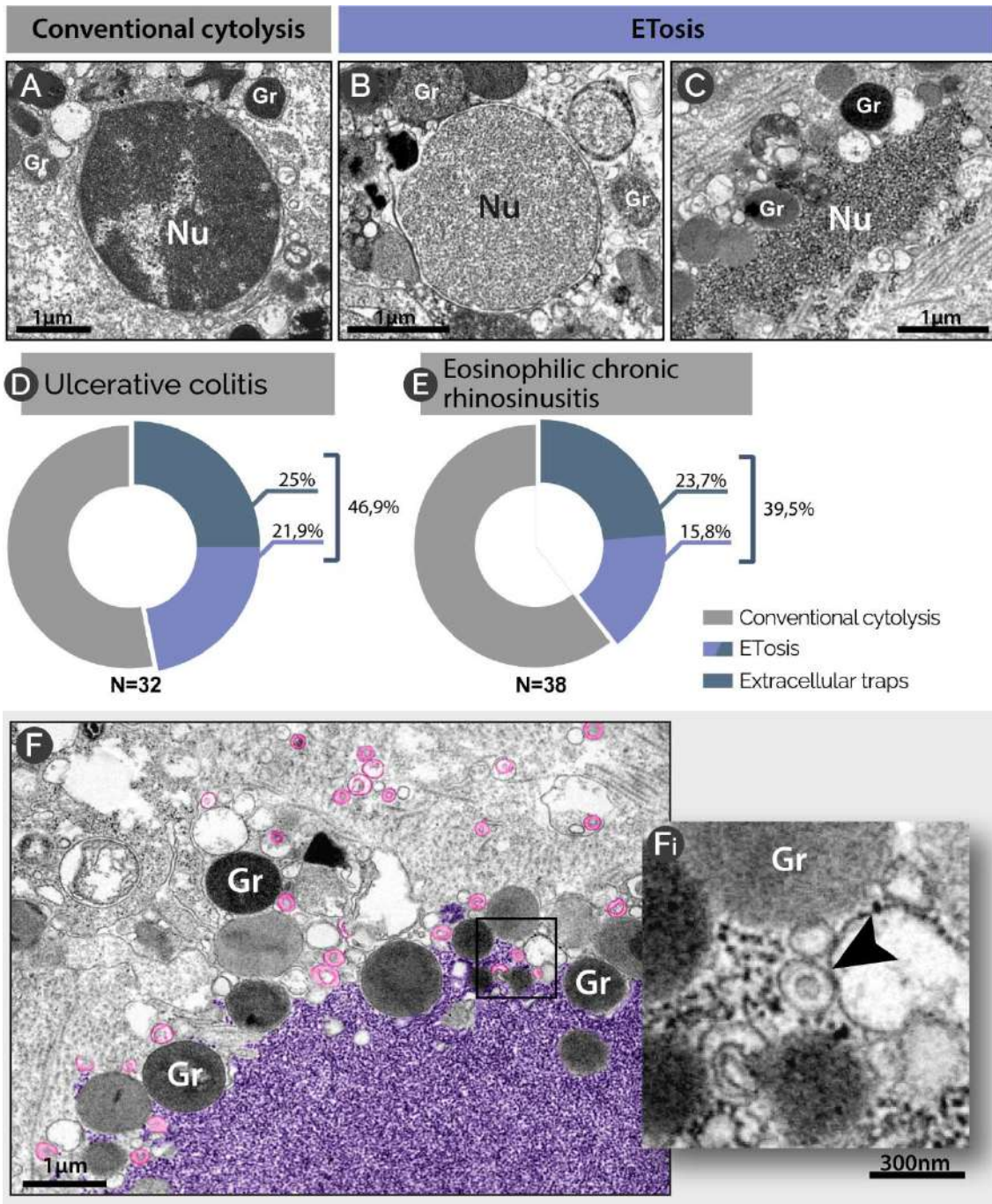
Eosinophils are multifunctional cells from the immune system with activities associated with the secretion of products stored in their cytoplasmic granules. One of the main mechanisms by which this secretion occurs is based on a cell death process, classically named cytolysis [1], which involves plasma membrane rupture with extracellular deposition of intact and functional free eosinophil granules (FEGs) [2]. This process can also generate DNA extracellular traps (ETs), released through ETosis (extracellular DNA trap cell death), a more recently described cytolytic cell death mechanism where there is deposition of decondensed chromatin together with FEGs, in the extracellular matrix [3]. Many questions regarding the ultrastructure of classic cytolysis and mainly ETosis, remain open. This study aimed to investigate, *in situ*, the ultrastructural characteristics of eosinophils undergoing cytolysis during human eosinophilic inflammatory diseases. For this, we applied transmission electron microscopy (TEM), the only technique that allows distinguishing the eosinophil degranulation mechanisms and its subcellular characteristics, to biopsies of patients diagnosed with eosinophilic chronic rhinosinusitis and ulcerative colitis. Our quantitative analyses showed that cytolysis is one of the most frequent secretory mechanisms of eosinophils in the studied diseases and that ETosis (nuclear delobulation, chromatin decondensation, expansion and release) represents a significant portion of these cytolytic eosinophils (~43%). We also identified, for the first time, changes in the nuclear envelope (NE), represented by dilation of the perinuclear space and formation of vesicles derived from the NE. Our analyses showed that the process of ETosis leads not only to the deposition of FEGs, but also to the release of typical vesiculotubular carriers termed Eosinophil Sombbrero Vesicles (EoSvS). Free EoSvS were associated with FEGs, inflammatory cells and ETs. EoSvS remain intact after the cytolytic death of human eosinophils with potential functional implications *in situ*. Our results highlight the mechanisms of cytolytic cell death as an important eosinophil secretory process in eosinophilic diseases and identify other pathways potentially participating in the propagation of the eosinophil response after cell death.

REFERENCES

- [1] Spencer et al., Front. Immunol., 5 (2014) 496.
- [2] Neves et al., PNAS, 105.47 (2008) 18478.
- [3] Ueki et al., Blood, 121.11 (2013) 2074

ACKNOWLEDGEMENTS

This research was supported by CNPq and FAPEMIG (Brazil) and NIH (USA).



Ultrastructural features of eosinophil ETosis observed by TEM during eosinophilic diseases. (A) Nucleus (Nu) of an eosinophil in the process of conventional cytolysis. Note a very condensed chromatin and a preserved nuclear envelope. (B and C) Nuclear (Nu) changes of eosinophils in process of ETosis. In (B), note a highly decondensed chromatin (typical of ETosis) with preserved nuclear envelope. In (C), note extracellular deposit of decondensed chromatin as extracellular DNA traps, with absent nuclear envelope. Free granules (Gr) are observed. (D and E) Quantitative analyses of conventional cytolysis and ETosis. (F) An eosinophil undergoing ETosis shows expanded and released chromatin, (colored in purple) free granules (Gr) and free EoSs (pink). (Fi) Higher magnification of an EoSV (arrowhead) associated with the extracellular chromatin and granules (Gr).



The Exomembrane System of *Cyrtilia lignieresi*-Infected Erythrocytes

Maíra Turiel-Silva ^{1,3*}, Camila Wendt ⁴, Brenda Fachetti ^{1,3}, Edilene da Silva ², Ana Paula Drummond ³, Wanderley de Souza ⁴, Kildare Miranda ⁴, José Diniz ^{3*}

¹ Universidade do Estado do Pará, Departamento de Morfologia e Ciências Fisiológicas, Centro de Ciências Biológicas e da Saúde, Marabá, Brasil;

² Universidade Federal do Pará, Instituto de Ciências Biológicas, Belém, Brasil;

³ Instituto Evandro Chagas, Seção de Hepatologia, Laboratório de Microscopia Eletrônica, Belém, Brasil.

⁴ Universidade Federal do Rio de Janeiro, Instituto de Biofísica Carlos Chagas Filho and Centro Nacional de Biologia Estrutural e Bioimagem, Rio de Janeiro, Brasil;
*mairaturiel@uepa.br

The phylum Apicomplexa consists of many species of obligate intracellular parasitic protozoa, such as *Plasmodium spp* and *Eimeria spp*, which are known to cause important diseases that affect humans and animals, respectively. The genus *Cyrtilia* has received attention due to the description of *Cyrtilia sp.* infection in fishes found in the Amazon region such as *Potamotrygon wallacei* (cururu stingray), where it acts in the control of the invertebrate population as well as a bioindicator [1]. Lainson [2] described *Cyrtilia lignieresi* parasitizing the red blood cells of the fish *Synbranchus marmoratus* from Para State, North of Brazil, transmitted by its definitive host, the leech *Haementeria lutzi*. In a previous work, our group analyzed the structure of *C. lignieresi* trophozoites by transmission electron microscopy [3], revealing fine details of the intracellular organization of the trophozoite stage. In this work, we analyzed structures involved in host-parasite interaction by transmission electron microscopy tomographic techniques (TEM/STEM tomography) and FIB-SEM tomography (slice and view technique) of *C. lignieresi*-infected red blood cells. Results showed that macrogametocyte stage parasites induce the formation of an exomembrane system within the parasitized erythrocyte, with two types of structures: a tubovesicular network and cleft-like profiles. The tubovesicular network has a vesicular and tubular morphology, frequently observed in areas close to the parasitophorous vacuole. In contrast, the cleft-like structures are distinguished as small flattened membranes that are dispersed throughout the host cell cytoplasm. Altogether, results provide new insights on the mechanisms underlying the host cell interaction between *Cyrtilia lignieresi*-infected red blood cells and further studies are underway.

REFERÊNCIAS

- [1] A.T. Oliveira et al., Brazilian Journal of Biology, 77(2), 413–416, (2017).
- [2] R. Lainson, Parasitological topics. London, Canning EU ed, pp 150–158, (1981)
- [3] J.A. Diniz et al., Parasitology Research, 88(7), 593–597, (2002).

This research was supported by IEC, UEPA, CNPq, FAPERJ e FINEP (Brazil).

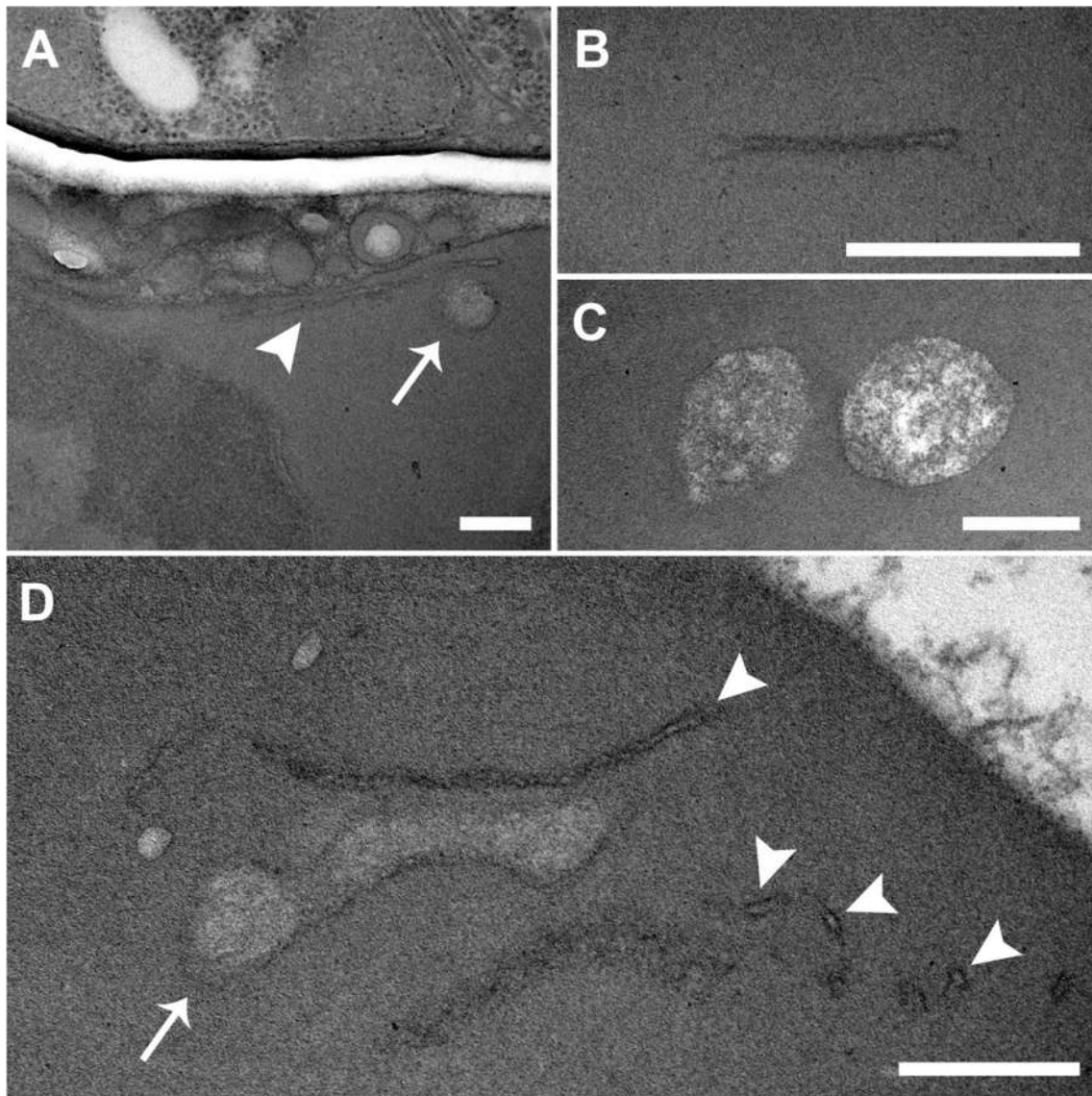


Figura 1: Membranous structures are observed in the cytoplasm of erythrocytes infected with *C. lignieresii*. Images of ultrathin sections obtained by TEM revealed flat membrane profiles (A and D, arrows, B) and circular membrane structures with a particulate material (A and D, arrows, C). Scale bar: 500 nm.



Three-dimensional Characterization of Membrane Fusion Events During Osmoregulation in *Trypanosoma cruzi*

Ingrid Auguto¹, Wendell Girard Dias², Wanderley de Souza^{1,4}, Veronica Jimenez³ and Kildare Miranda^{1,4}

¹Laboratório de Ultraestrutura Celular Hertha Meyer, Instituto de Biofísica Carlos Chagas Filho, Universidade Federal do Rio de Janeiro, Rio de Janeiro, Brasil. ²Fundação Oswaldo Cruz - FIOCRUZ, Rio de Janeiro, Brasil. ³ California State University, Biological Science Department, Fullerton, United States. ⁴Centro Nacional de Biologia Estrutural e Bioimagem (CENABIO), Universidade Federal do Rio de Janeiro, Rio de Janeiro, Brasil. *kildare.miranda@gmail.com

As many protozoa, *T. cruzi* has a contractile vacuole complex (CVC) which arrest the excess of cytosolic water and release it outside of the cell, in a phenomenon called regulatory volume decrease [1]. The CVC in *T. cruzi* is formed by the central vacuole (CV) surrounded by the spongiome, a highly organized and dynamic network of interconnected tubules and vacuoles [2]. In order to investigate the structural changes that take place in the CVC during water uptake and discharge, we used 3D electron microscopy to compare wild type (WT) and mutant epimastigotes which have shown different responses to hypoosmotic stress: (1) super-efficient mutants overexpressing TcVps34, (2) low-efficient mutants overexpressing TcrPDEC2 and (3) knockout parasites for a mechanosensitive channel (TcMscS). Samples were submitted to high-pressure freezing, followed by freeze substitution and imaged by electron tomography and FIB-SEM tomography. The data set was submitted to morphological and morphometric analyses. Results showed fragmented CVCs in TcrPDEC2 low-efficient mutants, when compared to CVCs of WT cells (Fig. 1). On the other hand, the TcVps34 super-efficient mutant showed very interconnect CVCs with a higher capacity to capture and larger volume of water during CVC pulsation (Fig. 1). The PDEC2 is known to be involved in vesicle trafficking and fusion in different organisms, which justify the different efficiency of TcrPDEC2 and TcVps34 mutants [3]. These results demonstrate the importance of the fusion events between spongiome elements and between them with the CVC for cell volume homeostasis. Our data also showed for the first-time ~20 nm to 200 nm-opening fusion pores between the CV and flagellar pocket membrane through the adhesion plaque in WT and TcrPDEC2 cells (Fig. 2). To elucidate the discharge mechanism in *T. cruzi* we evaluate the potential participation of the mechanosensitive channel (MSC) TcMscS in knockout mutants under hypoosmotic stress. We observed fusion pores in WT and mutant groups (Fig. 3), but with more frequency in WT cells. As the TcMscS is localized to the CVC membrane, we hypothesize that it may play a role in transport of ions and small osmolytes which mediates regulatory volume responses and/or in the activation downstream signaling cascades involved in events such as the fluid discharge [4]. Altogether, the results showed evidence of the crucial role of the membrane fusion events for osmoregulation in *T. cruzi*, being important both in uptake and discharge movements of the CVC in epimastigotes. This research was supported by CNPq, CAPES, FAPERJ, and FINEP.

REFERENCES

- [1] Rohloff, P., & Docampo, R. 2008. *Experimental Parasitology*, 118(1), 17–24.
- [2] Girard-Dias, W., et al. 2012. *Histochem Cell Biol*, 138:821–83.
- [3] Gillooly, D. J. et al. 2001. *Biochemical Journal*, 355(2), pp. 249–258.
- [4] Dave, N., et al. 2021. bioRxiv 498469.

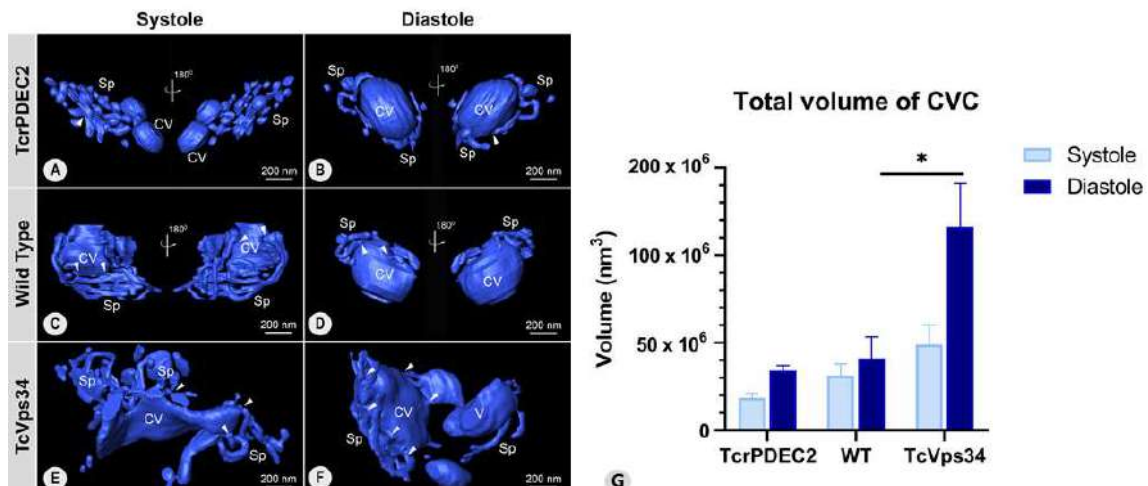


Figure 1. Three-dimensional models of CVC during pulsation cycle. (A - F) 3D models of CVC in overexpressing-TcrPDEC2 mutant, wild type, and overexpressing-TcVps34 mutant at systole and diastole, respectively. The arrowhead points the connections between spongiome with the central vacuole. (G) Quantification of total volume of CVC comparing systole and diastole stages in the different cell groups. Data values are represented by mean \pm SEM. One-way ANOVA test applied. * $p \leq 0.02$. CV - central vacuole, Sp - spongiome.

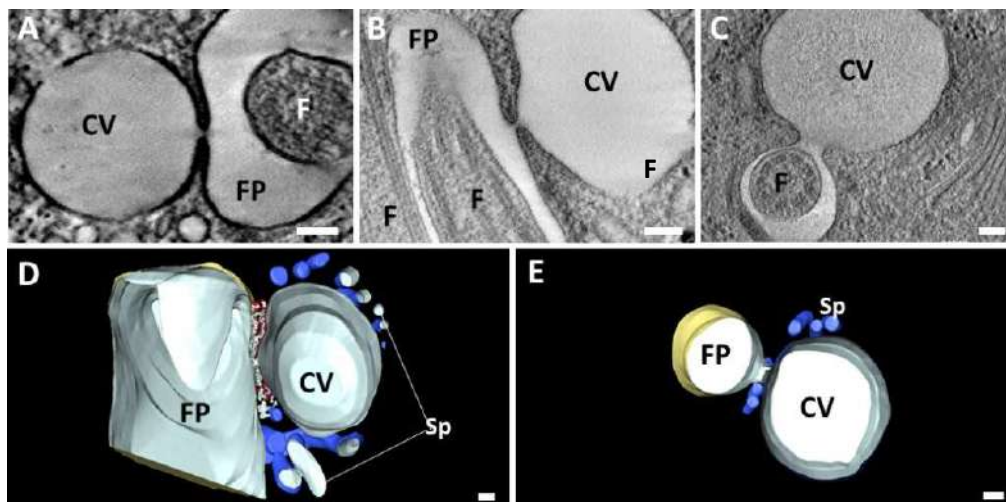


Figure 2. Fusion pores between the central vacuole and the flagellar pocket observed by electron tomography. (A) Pore observed in WT cell. Notice the electron density of the adhesion plaque around it. (B) and (C) Pores of ~ 20 nm and ~ 100 nm observed in TcrPDEC2 mutants. (D) and (E) 3D model of (B) and (C) respectively. CV - central vacuole, Sp - spongiome, FP - flagellar pocket, F - flagellum. Scale bar = 100 nm.

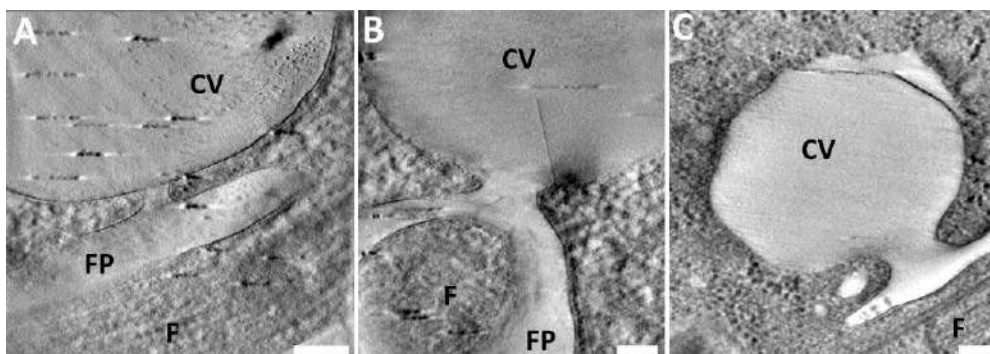


Figure 3. Fusion pores observed in cells under hypoosmotic stress. (A, B) wild type cells showing pores of ~ 50 nm and ~ 100 nm, respectively. (C) Large pore of ~ 180 nm observed in TcMscS KO. CV - central vacuole, FP - flagellar pocket, F - flagellum. Scale bar = 100 nm.



Deciphering the Mayaro virus structure using single-particle Cryo-EM analysis

Helder V. Ribeiro-Filho^{1*}, Lais D. Coimbra¹, Alexandre Cassago², Rebeca P. F. Rocha¹, João Victor da Silva Guerra¹, Rafael de Felício¹, Carolina Moretto Carnieli¹, Luiza Leme¹, Antonio Cláudio Padilha², Adriana F. Paes Leme¹, Daniela B. B. Trivella¹, Rodrigo Villares Portugal², Paulo Sérgio Lopes-de-Oliveira¹ and Rafael Elias Marques¹

¹ Brazilian Biosciences National Laboratory, Brazilian Center for Research in Energy and Materials (CNPEM), Campinas, SP, Brazil

² Brazilian Nanotechnology National Laboratory, Brazilian Center for Research in Energy and Materials (CNPEM), Campinas, SP, Brazil

*helder.ribeiro@lnbio.cnpem.br

Mayaro virus (MAYV) is an emerging single-stranded RNA alphavirus in Central and South America [1]. In Brazil, first MAYV cases were reported in Amazon region. From there MAYV infections have increased and expanded towards urban areas, with identified cases in Central and Southeast regions [2,3]. By using Cryo-Electron Microscopy (Cryo-EM) and Single Particle Analysis (SPA), we determined the 4.4 Å resolution structure of the mature and infective MAYV produced at LNBio/CNPEM. MAYV micrographs in movie-stacks were collected on a 300 kV Titan Krios (LNNano/CNPEM) and the SPA of the Cryo-EM data was performed using the Imagic-4d software system [4,5]. As a pre-processing step, we performed *a posteriori* data normalization and magnification anisotropy correction, since we found an anisotropic magnification difference of around 1.5 %. Then, we performed a contrast transfer function correction by phase-flipping each micrograph. To extract MAYV particles from micrographs, we first picked the particles using rotationally averaged reference particles from the dataset and extracted them with a 800 x 800 box size from the 4096 x 4096 pixel original micrographs to retrieve full dataset information. Next, we aligned the boxed particles and summed each movie stack. To obtain an initial MAYV 3D structure from 2D particles images we determined their relative Euler-angle orientations assuming icosahedral symmetry and starting from random assigned angles. Iterative cycles of angular reconstitution and rotational and translational alignments using reprojections from 3D reconstructions were repeated until 3D resolution convergence was achieved. For the final 3D reconstruction, we used the best 40,179 particles selected by the error associated to the angular reconstitution and to better delineate the Cryo-EM map, we applied a band-pass filter using a normalized amplitude spectrum filter (Figure 1). The final Cryo-EM map was used to fit an initial MAYV 3D atomic model obtained from the homology modelling of MAYV asymmetric unit. To refine the 3D model, we carried out real space refinement cycles with Phenix software suite [6], which include rigid and flexible fitting, as well as global minimization and simulated annealing. From our refined MAYV 3D model we extracted structural information that reveals novel features of arthritogenic alphaviruses [7]. The overall organization of MAYV E1, E2 and capsid proteins are quite similar to other described alphaviruses, but our Cryo-EM map allowed the identification of important protein-protein contacts, mainly involving histidine residues, that can play a key role in MAYV assembly/disassembly. At E1 and E2 ectodomains, we mapped and compared MAYV and CHIKV (Chikungunya virus) residues that are involved in antibody binding and that can be determinant for serological cross-reactivity. In addition, we observed two N-glycosylation sites at MAYV ectodomains. One of those glycans are close to human



receptor binding site and shows a structural pattern that seems to connect the spikes. Between E1 and E2 proteins, close to the lipid bilayer, we found a hydrophobic pocket occupied by an extra density, which cannot be explained by side-chain residues. This pocket may be a putative target of rational drug design. We also described capsid-capsid contacts with MAYV structure that seem to be mainly driven by electrostatic interactions and that may be important for understanding the capsid self-assembly process.

REFERENCES

- [1] Lorenz, C., Freitas Ribeiro, A. & Chiaravalloti-Neto, F. Mayaro virus distribution in South America. *Acta Trop.* 198, 105093 (2019).
- [2] Brunini, S. et al. High Frequency of Mayaro Virus IgM among Febrile Patients, Central Brazil. *Emerg. Infect. Dis.* 23, 1025–1026 (2017).
- [3] Mourão, M. P. G. et al. Mayaro Fever in the City of Manaus, Brazil, 2007–2008. *Vector-Borne Zoonotic Dis.* 12, 42–46 (2012).
- [4] van Heel, M. et al. Four-dimensional cryo-electron microscopy at quasi-atomic resolution: IMAGIC 4D. *Int. Tab. Cryst. F.*
- [5] Afanasyev, P. et al. Single-particle cryo-EM using alignment by classification (ABC): the structure of *Lumbricus terrestris* haemoglobin. *IUCrJ* 4, 678–694 (2017).
- [6] Afonine, P. V. et al. Real-space refinement in PHENIX for cryo-EM and crystallography. *Acta Crystallogr. Sect. D. Struct. Biol.* 74, 531–544 (2018).
- [7] Ribeiro-Filho, H.V., Coimbra, L.D., Cassago, A. et al. Cryo-EM structure of the mature and infective Mayaro virus at 4.4 Å resolution reveals features of arthritogenic alphaviruses. *Nat Commun* 12, 3038 (2021). <https://doi.org/10.1038/s41467-021-23400-9>

ACKNOWLEDGEMENTS

We thank LNNano/CNPEM for the use of electron microscopy facility (TEM-23519, TEM-24308) and we thank Rodrigo Portugal and Marin Van Heel for all supporting in the single-particle Cryo-EM analysis. This study was supported by grants from FAPESP (2018/03917-6, 2017/15340-2, 2018/00629-0), CNPq (440379/2016-4), CAPES (130767/2016-01) and Serrapilheira Institute, grant number Serra-1709-19681.

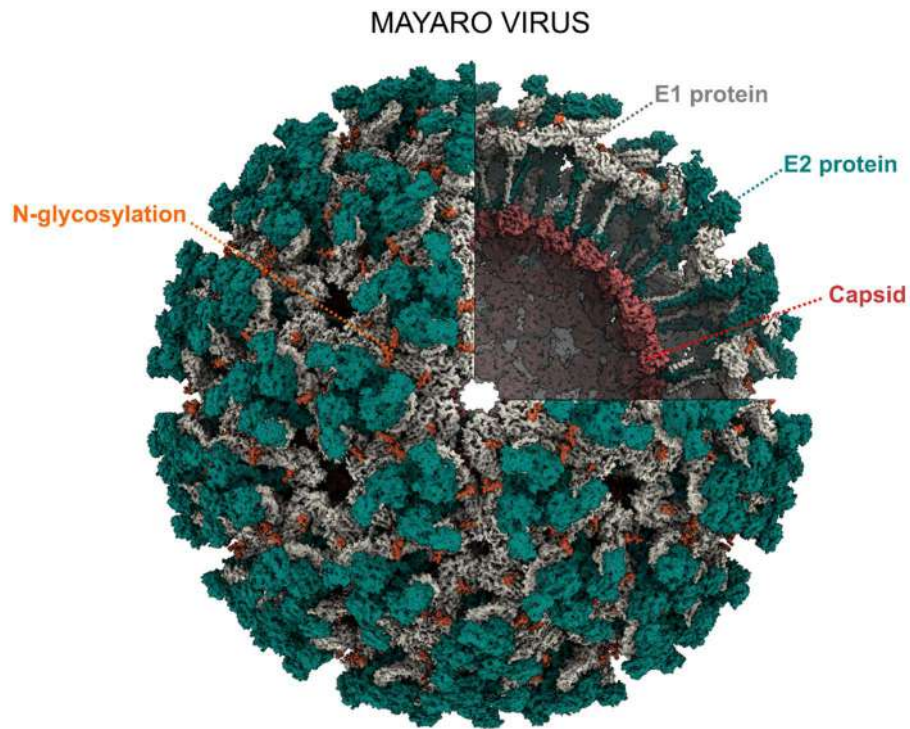


Figure 1. MAYV Cryo-EM map showing structural proteins and N-glycosylation sites with a cutaway in one quadrant to highlight transmembrane and capsid organization. Each color corresponds to a structural protein or glycans.



A Simple and Straightforward Method for Making Holey Carbon Grids

Ingrid Augusto¹ e Kildare Miranda^{1,2*}

¹Laboratório de Ultraestrutura Celular Hertha Meyer, Instituto de Biofísica Carlos Chagas Filho, Universidade Federal do Rio de Janeiro, Rio de Janeiro, Brasil.

² Centro Nacional de Biologia Estrutural e Bioimagem (CENABIO), Universidade Federal do Rio de Janeiro, Rio de Janeiro, Brasil.

*kildare.miranda@gmail.com

The electron microscopy field require high investments in all its steps, from sample preparation to imaging as well as along post-processing. Finding and sharing strategies to minimize its cost, without affecting the quality and accuracy of the analyses is important to increase the accessibility and expansion of electron microscopy techniques between research groups. One of the supplies used in electron microscopy are the grids covered by non-continuous (holey) support films. Employed in methodologies as negative staining and cryo-EM, coated grids by formvar and/or carbon support films are usually commercialized at expensive prices. Holey carbon films are useful to reduce the background noise allowing the samples to be imaged suspended alone (or in vitreous ice) across the holes [1]. In this work, we describe a method for making holey carbon grids (Fig. 1) using a protocol easily accessible to most labs [2]. First, add 10 drops of glycerol 50% in 50 ml of 0.5% formvar. Sonicate the mix inside a beaker at full power. After observing the formation of bubbles, dip a previously cleaned glass slide into the liquid keeping it for 1-3 minutes while sonicating or dip it immediately after the sonication for smallest and more distributed holes. Drain on tissue. The hole size and density can be evaluated by phase contrast or stereo microscopy. (Fig. 2A, D). If not right, adjust the time of sonication procedure. Remove the formvar film by slowly dipping the slide at 45° angle into a container with distilled water. Observe while the colored film lifts off the slide and float at water surface. Drop grids onto the film and collect it with filter paper. After the filter paper dry, soak it with methanol for 30 minutes in a petri dish to remove glycerol. Then, coat the grids with a thick carbon layer. To remove the formvar, load the grids on a soaked fresh filter paper in chloroform inside a closed petri dish. The holes density and size observed in the final grids varied according with the sonication time, allowing to adjust it according with the sample to be analyzed. Slides immersed for long sonication period produced meshes with high density and large holes (Fig 2). The grids holes size range is from 0.5 to 10 μm .

REFERERENCES

- [1] M.J. Dobro et. al., Plunge freezing for electron cryomicroscopy, *Methods Enzymol* (2010) 63-66.
- [2] University of Cape Town, Electron Microscope Unit. Method for making holey grids. <http://www.emu.uct.ac.za/method-making-holey-grids>. Accessed 18 May 2021.

ACKNOWLEDGEMENT

This research was supported by CNPq (Brazil), CAPES, FAPERJ and FINEP.

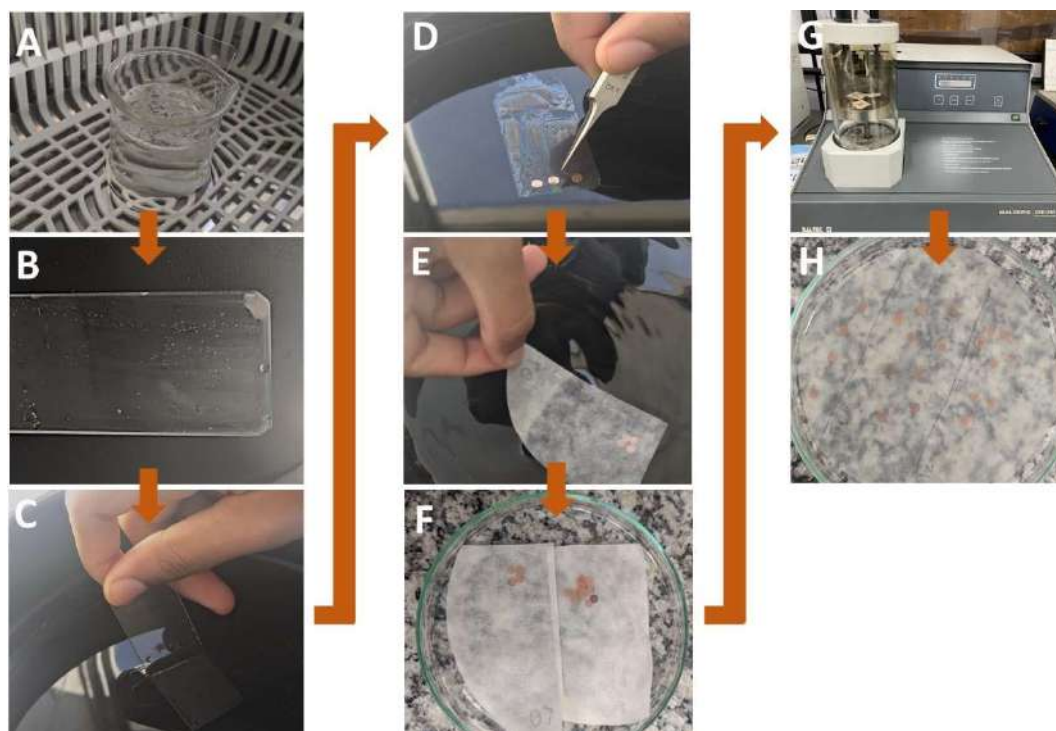


Figure 1. Workflow for holey carbon grid preparation. (A) The glass slide plunged in the mixture of 0.5% formvar with 10 drops of 50% glycerol during sonication. (B) The film adhered to the glass slide. Observe the marks of the formed holes. (C) Removing the film from the slide using distilled water. (D) Loading the copper grids onto the film and (E) collecting it using a filter paper. (F) After the filter paper dried, it was soaked with methanol for 30 minutes in a closed petri dish. (G) The grids are covered with a thick carbon layer and (H) placed on a fresh filter paper soaked in chloroform.

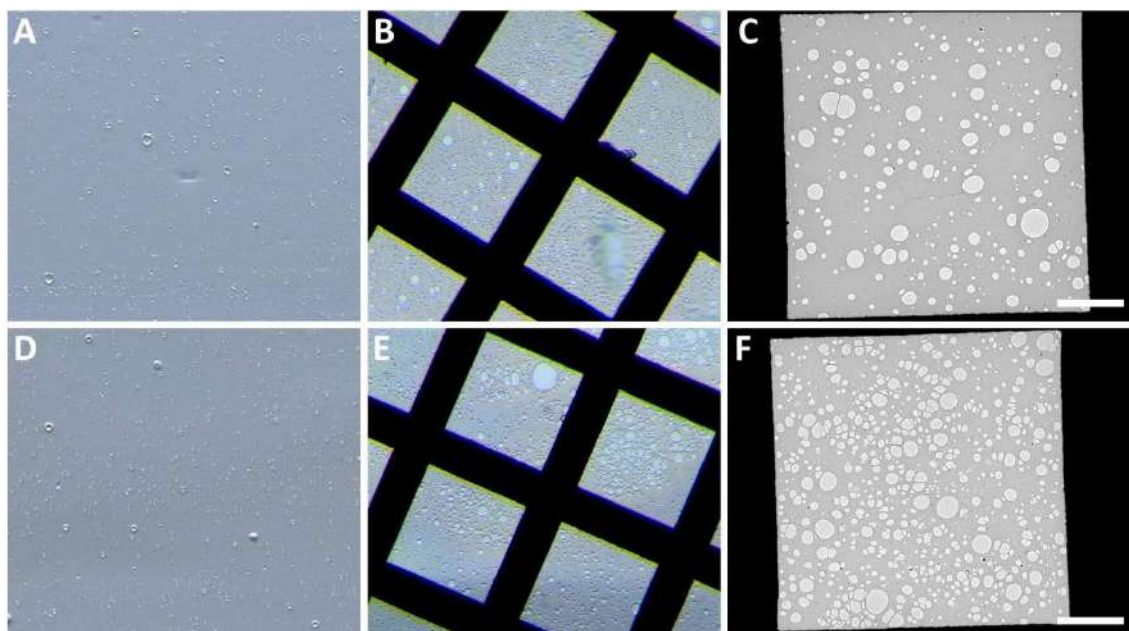


Figure 2. Images from the glass slides and grids produced. It shows two conditions of grids production: i) the glass slide was immersed immediately after the sonication time ended (A – C) and ii) the glass slide was kept immersed during the sonication (D – F). Note the differences in the concentration of the holes in the films, whereas the film formed during the sonication show a high density and more large holes. (A, D) Stereo images from the film adhered to the slide. (B, E) Stereo images from the grids before the carbon coat. (C, F) Transmission electron microscope images from the final grids. Scale bar = 20 μm .



How to Prepare Pathogenic Protists for SEM Using a Simple Low-Cost Chemical Method Without Critical Point Drying

Tuanne Santos Melo^{1*} and Antonio Pereira-Neves¹

¹ Fiocruz Pernambuco, Instituto Aggeu Magalhães – Departamento de Microbiologia, Recife, Brazil. * tuanne_melo17@hotmail.com

Scanning electron microscopy (SEM) is widely used to study parasitic protists, e.g., *Trichomonas vaginalis* (*Tv*), *Leishmania infantum* (*Li*) and *Trypanosoma cruzi* (*Tc*) that cause human trichomoniasis, visceral leishmaniasis and Chagas disease, respectively [1]. Drying is a critical stage for SEM sample preparation. Most current protocols use critical-point drying (CPD) with liquid carbon dioxide; however, this method requires an expensive equipment with high maintenance cost, which can be impractical for small laboratories on an individual scale. In addition to longer preparation time, CPD is not a glitch-free method; a minor change in the parameters may lead to membrane damage, resulting in substantial and irreversible deformation of fragile and sensitive cell surface structures [2]. An alternative, low-cost method for drying biological samples is the use of chemicals such as hexamethyldisilazane (HMDS). HMDS has been used to prepare bacteria, plants, insects, and mammal tissues samples for SEM, achieving similar or even better results to those obtained via CPD [2, 3]. The combined properties of low surface tension and protein cross-linking potential are likely to be important factors in the suitability of HMDS as a drying agent for biological specimens, reducing the damage on the surface structures [4]. HMDS is also miscible with acetone and ethanol, increasing its usefulness for drying most of specimens [5]. However, there are few reports on the use of HMDS for preparing parasitic protists for SEM. Here, we described an easy and faster protocol for drying samples of *Tv*, *Li* promastigotes and *Tc* trypomastigotes for SEM using HMDS and compared this chemical procedure with the CPD-dried samples. Parasites were fixed in 2.5% glutaraldehyde in 0.1 M cacodylate buffer, pH 2, post-fixed for 15 min in 1% OsO₄ and dehydrated in ethanol series (7.5%, 15%, 30%, 50 %, 70%, 90%, and three times in absolute alcohol for 10 minutes each). For the chemical drying, after dehydration the samples were incubated in HMDS: ethanol 1:2, 1:1 and 2:1 mixtures (final volume 500 µL) for 10 min each, immersed once in 100% HMDS (final volume 300 µL) for 30 seconds, blotted dry on filter paper and air dried for 30 min. Alternatively, an aliquot of each sample was dried using CPD, as previously described [6]. Both HMDS and CPD dried samples were coated with gold–palladium to a thickness of 15 nm and then observed with a SEM operating at 15 kV. Our results showed that: (a) for *Tv* samples, in contrast to the CPD-dried parasites (Fig. 1a), we found thin protrusions, similar to cytonemes, on the cell surface of many HMDS-treated parasites (Figs. 1b-c). Because both CPD and HMDS *Tv* samples were obtained from the same culture tube, this finding suggests that protrusions could be fragile structures to CPD procedure. (b) For *Li* and *Tc* samples, CPD- and HMDS-dried parasites showed similar results about the quality of cell morphology preservation (Figs. 1d-i). These results indicate that HMDS is a time-saving and inexpensive alternative to CPD for preparing parasitic protists specimens, providing better surface preservation for *Tv* samples, at least [7].

- [1] W. De Souza; M. Attias, *Experimental parasitology*, 190 (2018) 10-33.
- [2] M. A. Koon et al., *Journal of visualized experiments: JoVE*, 143 (2019).
- [3] R. Bhattacharya, et al., *Applied Microscopy*, 50 (2020) 1-6.
- [4] J. L. Nation, *Stain technology*, 58 (1983) 347-351.

- [5] R. J. Lewis, Sr (Ed.). Dicionário de Química Condensada de Hawley. 13ª ed. New York, NY: John Wiley & Sons, Inc. (1997) 573.
[6] Y. R Nieves et al., Mol. Life Sci. 75 (2018) 2211–2226.
[7] This work was supported by CNPq/PROEP Instituto Aggeu Magalhães – FIOCRUZ

Acknowledgement: We thank Dr. Regina Bressan for kindly provide the *L. infantum* and *T. cruzi* cultures.

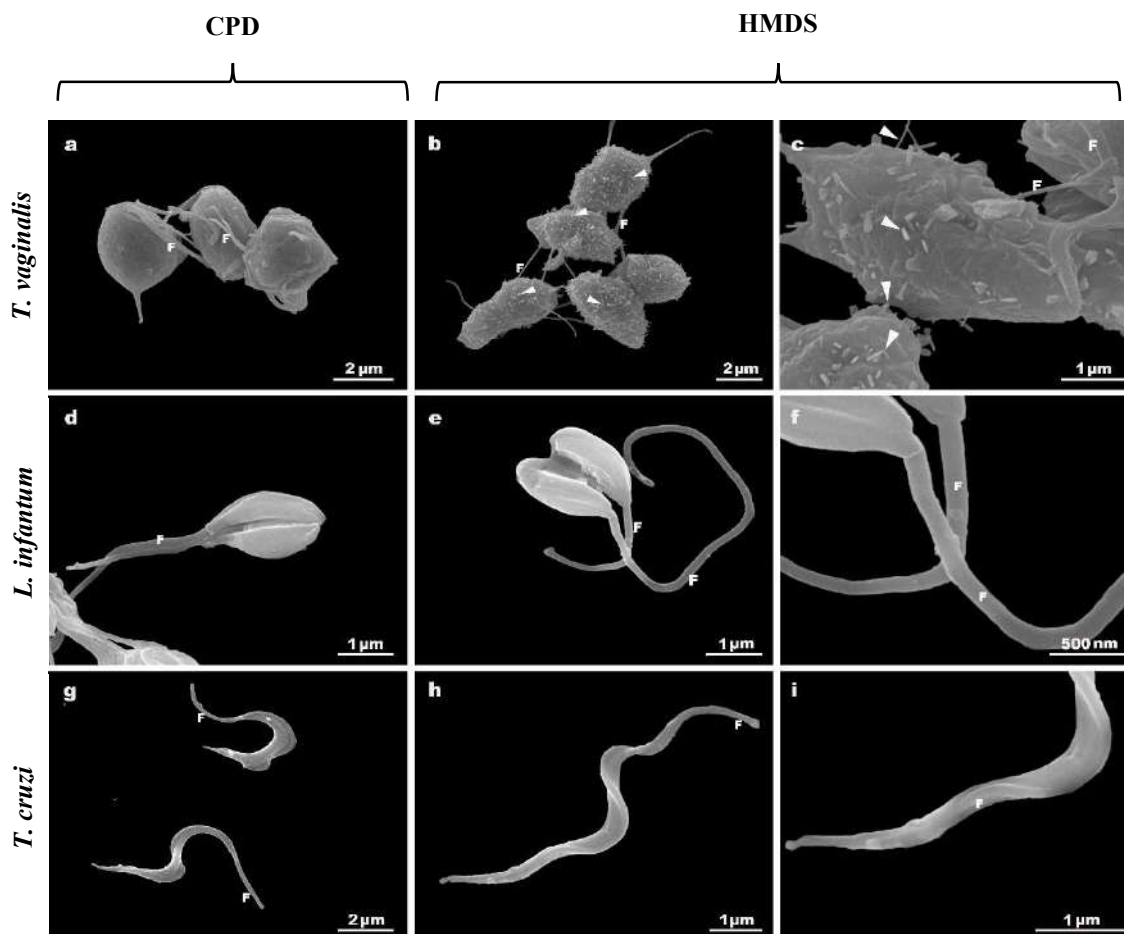


Figure 1. Comparison of the images of *Trichomonas vaginalis* (a-c), *Leishmania infantum* promastigotes (d-f) and *Trypanosoma cruzi* trypomastigotes (g-i) obtained after the CPD (first column) and HMDS (second and third columns) procedures. Note the presence of many protrusions (arrowheads), similar to cytonemes, in *T. vaginalis* after HMDS treatment (b-c). Similar results are observed for *L. infantum* (d-f) and *T. cruzi* (g-i) after CPD and HMDS methods. F, flagella. Bars.: a, b, g, 2 µm; c, d, e, f, h, i, 1 µm; f, 500nm.



High content image-based assays as a tool for experimental chemotherapy

Ana Paula R. Gadelha^{a,b} & Wanderley de Souza^{c, d}

^aDiretoria de Metrologia Aplicada às Ciências da Vida, Instituto Nacional de Metrologia, Qualidade e Tecnologia (INMETRO), Rio de Janeiro, RJ, Brazil

^cInstituto de Biofísica Carlos Chagas Filho, Universidade Federal do Rio de Janeiro, Rio de Janeiro, RJ, Brazil

^bInstituto Nacional de Ciência e Tecnologia em Biologia Estrutural e Bioimagens, and Centro Nacional de Biologia Estrutural e Bioimagens, Universidade Federal do Rio de Janeiro, Rio de Janeiro, RJ, Brazil

High content image-based assays have emerged as a powerful tool for the biological evaluation of potentially therapeutic compounds. This technique is based on an automated fluorescent microscopy system that allows acquiring quickly and sequentially live or fixed cell images [1]. These assays require seeding of cells in multiwell plates, addition of compounds, and labeling with multiple fluorescent dyes. Following image acquisition, the information is extracted via a software that detects and quantifies the emitted signals (Fig. 1). Employing robotic arms, automated liquid handlers, and plate reading devices, high content image-based assays are designed for large-scale screening used for the analysis of pharmacological compound libraries and the identification of targets [2]. Morphological and functional parameters can also be evaluated qualitatively and quantitatively to characterize cell phenotypes and their subsequent alterations after exposure to multiple drugs [3]. Using high content analysis, we analyzed the effects of metronidazole and albendazole, drugs used on the treat of intestinal infection, on intestinal cell lines. Decrease of cell area and shape; alterations on nuclear size and micronuclei formation were observed after treatment (Fig. 2). Data obtained using high content analysis are important for understanding the mechanism of drug action against infectious diseases. High-content imagers are suitable instrumentation platforms for many applications by providing high-throughput multi-wavelength image acquisition at single-cell resolution, coupled with fast image analysis software, thus enabling collection of multiple end-point data in a single study.

References

1. Boutros M, Heigwer F, Laufer C (2015) Microscopy-Based High-Content Screening. *Cell* 163:1314-1325.
2. Lin S, Schorpp K, Rothenaigner I, Hadian K (2020) Image-based high-content screening in drug discovery. *Drug Discov Today* 25:1348-1361.
3. Li and Xia (2019) Review of high-content screening applications in toxicology. *Arch Toxicol* 93:3387-3396.

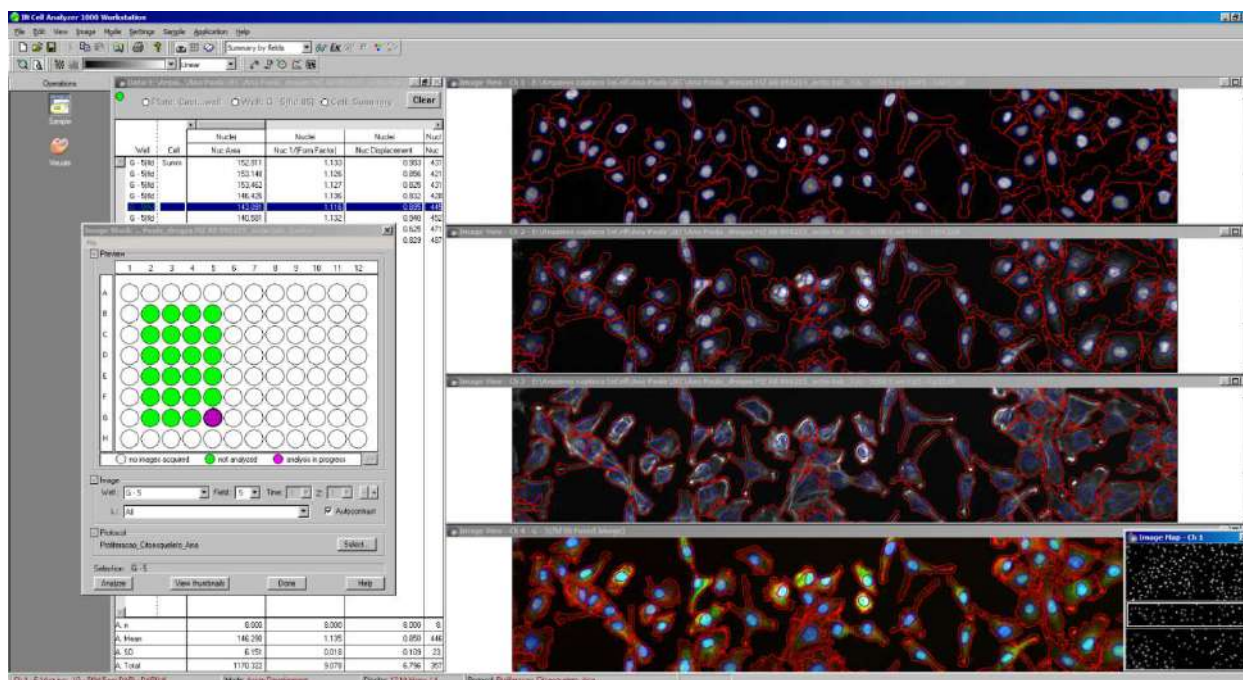


Figure 1: The image analysis program is shown and the user interface following completion of analysis can be observed.

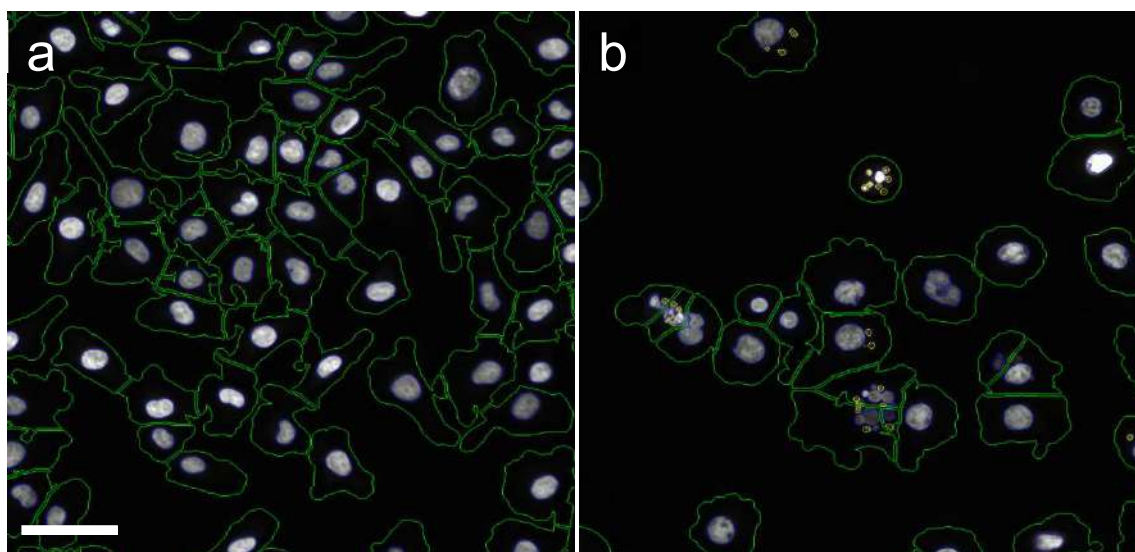


Figure 2: Nuclear channel image of intestinal epithelial cells (IEC-6) stained with Hoechst 33342. **(a)** Analysis overlays show cell nuclei (blue line), cytoplasm boundary (green line) on control culture. **(b)** Analysis overlays show micronuclei boundary (yellow line) on cells treated with albendazole.



The use of thiocarbohydrazide to increase membrane contrast and peroxidase labeling of cellular structures in electron microscopy.

Carolina L Alcantara^{1,2,3}, Narcisa L Cunha e Silva^{1,2,3}, Wanderley de Souza^{1,2,3}

¹Laboratório de Ultraestrutura Celular Hertha Meyer - Instituto de Biofísica Carlos Chagas Filho, Universidade Federal do Rio de Janeiro. Av. Carlos Chagas Filho 373, Centro de Ciências da Saúde, Bloco G, 21941-902, Rio de Janeiro, Brazil

²Centro Nacional de Biologia Estrutural e Bioimagens-CENABIO. Universidade Federal do Rio de Janeiro. Av. Carlos Chagas Filho 373, Centro de Ciências da Saúde, 21941-902, Rio de Janeiro, Brazil

³Instituto Nacional de Ciência e Tecnologia em Biologia Estrutural e Bioimagens-INBEB. Universidade Federal do Rio de Janeiro. Av. Carlos Chagas Filho 373, Centro de Ciências da Saúde, 21941-902, Rio de Janeiro, Brazil

*alcantara@biof.ufrj.br

Thiocarbohydrazide (TCH) is a mordant that has an affinity for osmium tetroxide and proteinaceous structures. In preparation for electron microscopy, it has been shown that the use of TCH between osmium tetroxide incubations (OTO) can increase contrast and preservation of membrane and lipid structures as well as increase contrast of DAB reaction product of HRP cytochemistry [1, 2]. With the significant advances that have occurred in high-resolution scanning electron microscopy (SEM), especially related to methodologies that allow the observation of intracellular structures, that are exposed by successive abrasion with a gallium ion beam as in FIB-SEM, the search for better pre-embedding contrasting methods has regained attention. Here, we report our observations on the use of OTO staining with classical cytochemical methods to facilitate the 3D reconstruction of labeled structures and organelles. We used epimastigotes of *Trypanosoma cruzi*, whose endocytic pathway was labeled with horseradish peroxidase, followed by fixation and detection of the peroxidase activity using the classical diaminobenzidine-osmium method followed by incubation with TCH, which increases the concentration of osmium at the sites where the enzyme is located as well as the contrast of lipid-containing structures. This procedure allowed not only a better visualization of membranous structures and lipid inclusions but could also easily identify the endocytic tracer (HRP) inside the cell by FIB-SEM. All structures involved in the endocytic activity could be traced and reconstructed. Moreover, OTO staining increased the contrast of cytoskeletal structures, also favoring its 3D reconstruction. By this means, OTO staining has been proving to be an old but very efficient method to increase the overall contrast of biological samples, especially those designed for FIB-SEM and electron tomography.

REFERENCES

1. Seligman, A.M., H.L. Wasserkrug, and J.S. Hanker, *A new staining method (OTO) for enhancing the contrast of lipid-containing membranes and droplets in osmium*

- tetroxide--fixed tissue with osmiophilic thiocarbohydrazide(TCH). J Cell Biol, 1966. 30(2): p. 424-32.*
2. Willingham, M.C. and A.V. Rutherford, *The use of osmium-thiocarbohydrazide-osmium (OTO) and ferrocyanide-reduced osmium methods to enhance membrane contrast and preservation in cultured cells. J Histochem Cytochem, 1984. 32(4): p. 455-60.*

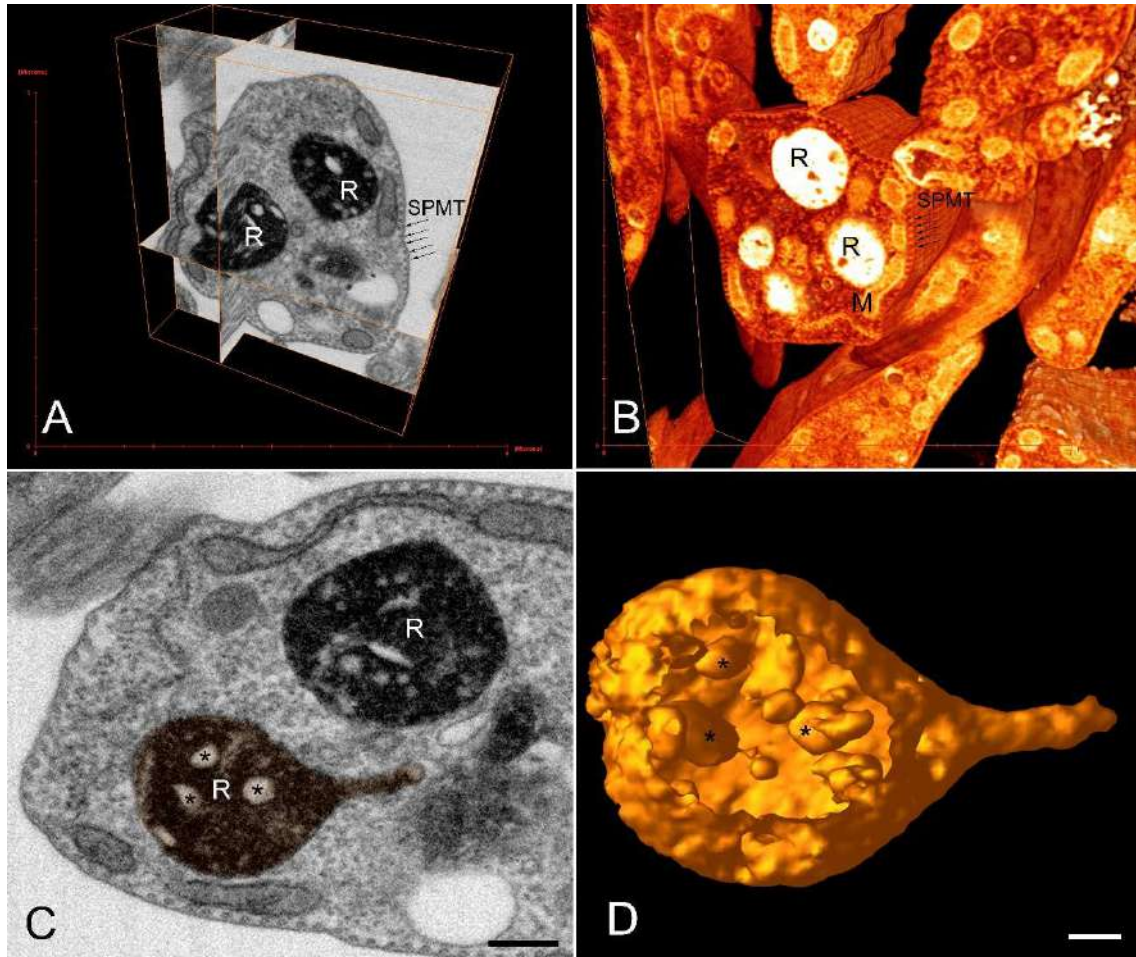


Figure legend) Tridimensional reconstruction of reservosomes after DAB-cytochemistry. A, C. Orthoslice (A) and single Z image (C) view of a FIB-SEM series of epimastigotes submitted to HRP endocytosis and DAB-cytochemistry, showing reservosomes with a dark lumen and electron lucent lipid inclusions (asterisk in C). B, D. The big difference in contrast of cellular structures allows 3D reconstruction software to build automatic 3D models more accurately. B. The Voltex algorithm of Amira software (Fei Company), allowed reconstruction of the volume where it is clear the observation of reservosomes and its lipid inclusions, as well as subpellicular microtubules (arrows, SPMT) below plasma membrane. D. Isosurface rendering algorithm used in 3dmod (University of Colorado) shows automatic reconstruction of reservosomes (highlighted in C) and lipid inclusions inside (asterisk). Bars: C – 500 nm, D – 200 nm



Immunolabeling In Epoxy Resin Embedded Samples

Noêmia Rodrigues^{1,2}, Wanderley de Souza^{1,2}, Marlene Benchimol^{2,3*}

¹ Instituto de Biofísica Carlos Chagas Filho, Universidade Federal do Rio de Janeiro, Rio de Janeiro, Brazil. ,

² Centro Nacional de Biologia Estrutural e Bioimagem (CENABIO),

³ Universidade do Grande Rio – UNIGRANRIO, Rio de Janeiro, Brazil.

* Corresponding author: marlenebenchimol@gmail.com

Electron microscopy is a technique used for obtaining images of biological and non-biological samples with high resolution. Electron microscopy, permit us to detail structures of cell and tissues [1]. However, several events may be missed if conventional studies are not complemented with details concerning the subcellular localization of substances, as proteins, e.g. So, electron microscopy is used in association with various auxiliary techniques as immunolabeling. Immunoelectron microscopy is one of the best methods for detecting and localizing proteins in cells and tissues. This technique principle is the use of antibodies to detect the intracellular location of proteins. Ultrathin sections are labeled with antibodies against a particular antigen and labeled with gold particles in a second step. Usually, we use hydrophilic resin to do this procedure because it allows antibody access to the required antigen [2]. In the present work, we used epoxy resin, which is hydrophobic and does not allow the formation of the complex antibody-antigen. To permeabilize the epoxy resin, we used commercial hydrogen peroxide (H₂O₂) in a concentration of 10 volumes for 10 minutes obtaining the results shown in figures A e B. This method proved effective in samples of contaminated tissues by SarsCov2 and other cells, as Benchimol and colleagues showed in the Golgi complex of *Tritrichomonas foetus* [3].

Protocol: *T. foetus* cells were fixed overnight in 2.5% glutaraldehyde in 0.1 M cacodylate buffer, pH 7.2, and dehydrated in ethanol. Covid19 infected tissues were fixed for 2 hours in 2.5% glutaraldehyde in 0.1 M cacodylate buffer, pH 7.2, and dehydrated in acetone. Whole cells, Golgi fractions, and infected tissues were embedded in Epon. Gold sections were obtained and collected in nickel grids. For immunolabelling, thin sections were quenched in 50 mM NH₄Cl for 30 min and incubated with mAb anti-Golgi 20.3. After several washes in PBS-1% BSA, the sections were incubated with 10 nm gold-labeled goat anti-mouse IgG (BB International, UK). Finally, the samples were washed and observed with an electron microscope.

This process is cheaper than using hydrophilic resin. In addition, if the sample is a rare material or has a small volume, it is essential to prioritize the standard procedure. The described method makes it possible to explore those Epon included samples for immunolabeling and saving time.

REFERENCES

[1] Bozzola, J.J and Russel L.D. (1992) Electron microscopy: principles and techniques for biologists. Jones and Bartlett Publishers.

[2] Griffiths, G. (1993). Fine structure immunocytochemistry. Springer-Verlag Berlin, Heidelberg.

[3] De Andrade Rosa I, Caruso MB, Rodrigues SP, Geraldo RB, Kist LW, Bogo MR, Gonzaga L, DE Vasconcelos AT, Morgado-Díaz JA, Zingali RB, Benchimol M.(2014) New insights on the Golgi complex of *Tritrichomonas foetus*. *Parasitology*. Feb;141(2):241-53. doi: 10.1017/S0031182013001455. Epub 2013 Oct 18. PMID: 24135238.

ACKNOWLEDGEMENTS

This work was developed at LUCHM – Laboratório de Ultraestrutura Celular Hertha Meyer, IBCCF, UFRJ, Brazil, supported by Faperj and CNPq.

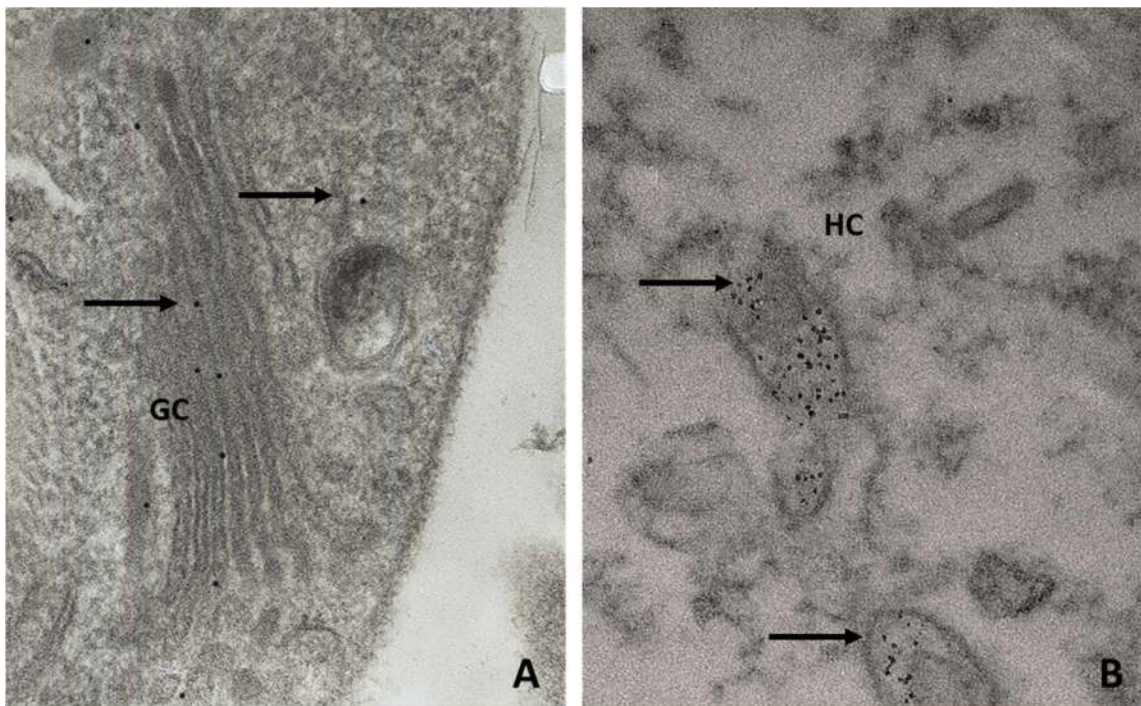


FIG 1: Immunolabeling in epoxy resin embedded samples. A) Antibody anti Golgi complex protein in *Tritrichomonas foetus*. The arrow shows gold particles. **GC** – Golgi complex; B) Immunolabeling in kidney tissue of Covid-19 patient. **HC** – host cell.



Freeze-Fracture Preparation Without Special Equipment

Luis Otavio da Silva Pacheco¹, Márcia Attias^{1,2}, Kildare Miranda^{1,2},

Wanderley de Souza^{1,2}

¹ Universidade Federal do Rio de Janeiro, Instituto de Biofísica Carlos Chagas Filho, RJ, Brasil.

² Centro Nacional de Biologia Estrutural e Bioimagem (CENABIO), RJ, Brasil.

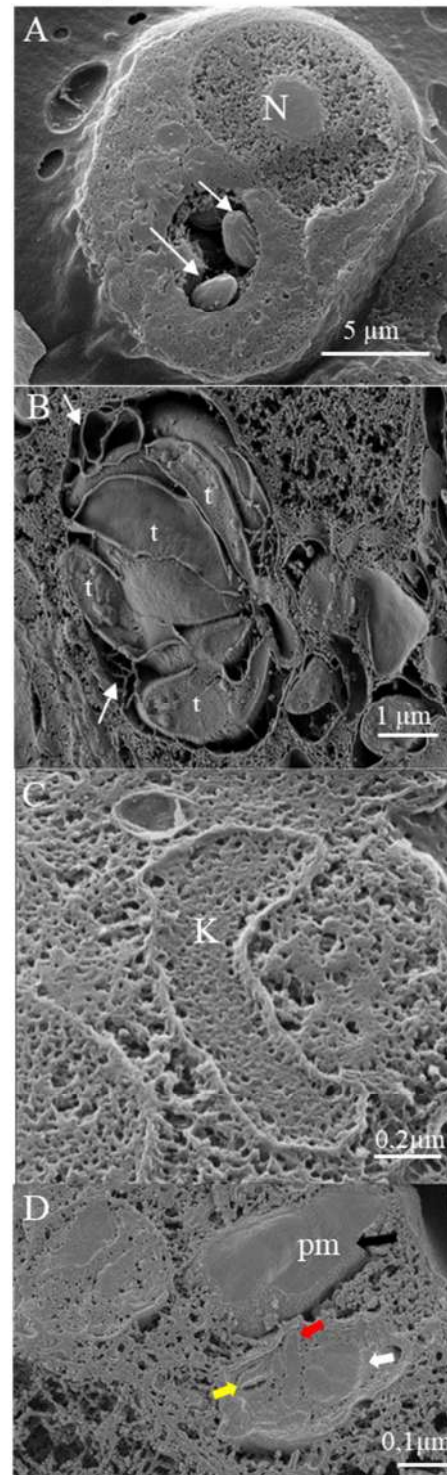
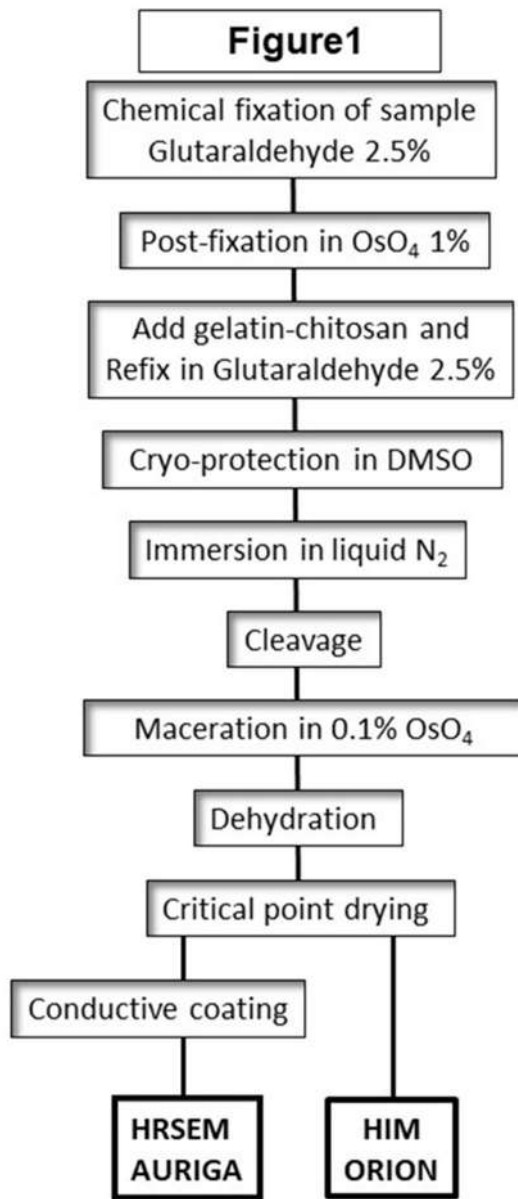
* otaviopachecoluis@biof.ufrj.br

The introduction of High and Ultra High Resolution scanning electron microscopes in life sciences laboratories stimulated the development of new techniques that allow, in addition to the observation of the cell surface, also the intracellular environment. In this new resolution level, intracellular structures associated or not with organelles become visible. In this work, we rescued the method described by Fukudome and Tanaka [1] to analyze different types of biological materials, such as tissues and protist parasites. The main steps of the method include: Fixation in 2.5% of glutaraldehyde, post-fixation in 1% OsO₄, incorporation into a chitosan/gelatin mixture in 1:1 ratio, re-fixation in 2.5% glutaraldehyde, infiltration with DMSO 25% for 30 minutes and 50% for 30 minutes for cryoprotection, pre-freezing in Freon 22, freezing in liquid nitrogen, fracture with a frozen razor blade, cryoprotection removal in a water bath at room temperature. Some samples were also macerated in OsO₄ (0.1%) for 96 hours before dehydration. Next, samples were dried by CO₂ critical point method, received conductive coating for observation in an AURIGA40 Scanning Electron Microscope (Thermo-Fisher) or were observed uncoated in ORION-ZEISS Helium ion scanning Microscope (Fig. 1 is a flowchart of the method). The protocol was tested in epimastigotes of *T. cruzi* cultivated in suspension and in cell cultures infected with *Toxoplasma gondii* or *Trypanosoma cruzi*. Infected cultures were gently trypsinized before fixation. Results and discussion: Using this method, we successfully exposed internal structures of infected cells and tissues. The previous trypsinization of the cell monolayer avoided flattening of the adhered cells. The mixture of gelatin and chitosan kept the individual cells together. Although gelatin is dissolved in the maceration process, chitosan still retains the cells. DMSO was successfully used as cryoprotector. Extraction of soluble cell components occurred during maceration. Cells infected with *T. cruzi* showed two amastigotes in a parasitophorous vacuole (Fig 2). A). The results show the optimization of this protocol as a promising technique to be used as an alternative to freeze-fracture or cryoSEM. Different types of samples may be studied with this technique. Observation of uncoated samples by Helium ion microscopy was also tested with positive results, enhancing resolution of the method since no conductive coating is necessary. Besides, new protocols, using high pressure frozen and freeze-substituted cells are under development. Acknowledgments: CAPES, CNPq, FAPERJ, FINEP. The authors also thank the Division of Material Sciences (DIMAT) at INMETRO for the use of the ZEISS- ORION Helium Ion Microscope.

[1] Fukudome & Tanaka(1986). J. of Microsc. Vol 141(2):171-8



Figure 2





Legends

Figure 1: Flowchart of the protocol developed in this work

Figure 2: (A) Host cell infected with *T. cruzi*. Samples was cleaved but not macerated. A conductive coating of Au was applied on the sample for further observation in routine SEM. Cleavage exposed the intracellular space of the host cell, revealing the amastigote forms of *T. cruzi* (arrow) inside the parasitophorous. The nucleus (N). (B) Rosette of *Toxoplasma gondii* tachyzoites (t) inside a host cell. Intravacuolar network of tubules that stabilizes the tachyzoites in the rosette (arrow). Samples received a 5 nm platinum coating and were observed in Auriga 40 microscope. (C) Kinetoplast (K) of an epimastigote of *T. cruzi* observed uncoated and without maceration in the ORION ion beam microscope. (D) Exposure of three amastigote forms of *T. cruzi* free in the cytoplasm, one non-cleaved and one cut longitudinally. In the cleaved we observe the flagellum (yellow arrow), cinetoplast (red arrow) and the nucleus (white arrow). In the case of the uncleaved parasite, the plasma membrane (black arrow) is observed. Au coating observed in Auriga 40 microscope of high resolution.



Cryo-TEM specimen preparation of concentrated polymeric micelle

Laura C. E. da Silva¹, Antonio C. Borges², Marcelo G. de Oliveira¹, Marcelo A. de Farias^{2*}

¹ Institute of Chemistry, University of Campinas, UNICAMP, 13083-970 Campinas, SP, Brazil

² Brazilian Nanotechnology National Laboratory (LNNano), Brazilian Center for Research in Energy and Materials (CNPEM), 13083-970 Campinas, SP, Brazil

*marcelo.farias@lnnano.cnpem.br

Pluronic®F127 micellar hydrogels are of growing interest to the biomedical field due to their versatility as drug delivery systems [1]. Pluronic®F127 is a symmetric and amphiphilic triblock copolymer which in aqueous medium self-assembles into micelles that pack together with increasing temperature or concentration, leading to non-flowable hydrogels [2]. The microstructure of these hydrogels is usually investigated by small-angle X-ray scattering, which is not a readily available technique. Conversely, cryo-TEM is a widespread technique used for investigating the morphology of aqueous systems. In the case of Pluronic®F127 micellar systems, the elevated viscosity poses a significant challenge for specimen preparation and, consequently, for cryo-TEM observation. Herein, we show a trustworthy, inexpensive and readily available methodology for preparing specimens of highly viscous micellar solutions and non-flowable hydrogels using an automated vitrification system. Two important issues were addressed: how to obtain specimens that are sufficiently thin for imaging, in spite of the elevated viscosity of the samples and how to ensure that the supramolecular structure observed was not an artifact of sample preparation. We concluded that the critical gel temperature (cgt) is a key parameter to be considered. In terms of specimen ice thickness, the best results are obtained when the sample is pre-cooled to a temperature just below the critical micelle temperature (cmt), where the sample is a low viscosity liquid, and blotted at a temperature above the cmt and below the cgt. In terms of microstructure observation, homogeneous regions of intermediary thickness provide the best results. Thus, with this methodology we were able to visualize not only the morphology of individual Pluronic®F127 micelles but also the supramolecular structure evolution as a function of concentration. We believe that this protocol is a suitable alternative for imaging micellar hydrogels and it might be easily replicated on any cryo-TEM facility.

References

- [1] T.H. Epps, R.K. O'Reilly, *Chem. Sci.* 7 (2016) 1674
- [2] M.A. Rodrigues, *Thin Solid Films*, 6 (2000) 1192.

Acknowledgments: FAPESP [grant number 2016/02414-5 and 2018/14142-5], LNNano/CNPEM.

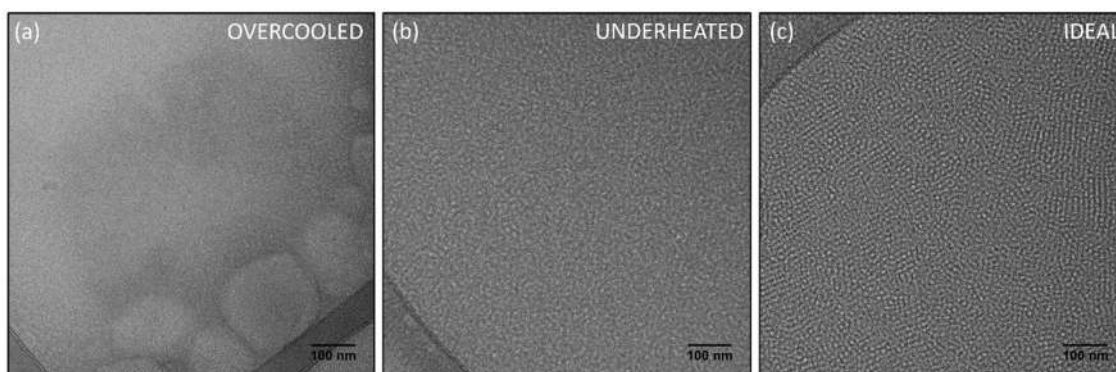


Fig. 1. Temperature influence on specimen preparation. TEM micrographs of a 15 wt% sample under (a) prolonged pre-cooling, showing poor self-assembly on the grid; (b) short post-blot heating periods, showing poor micelle packing; (c) ideal conditions (15 min of pre-cooling and 5 min of oven heating), showing well-defined micelles and regions of ordered domains.

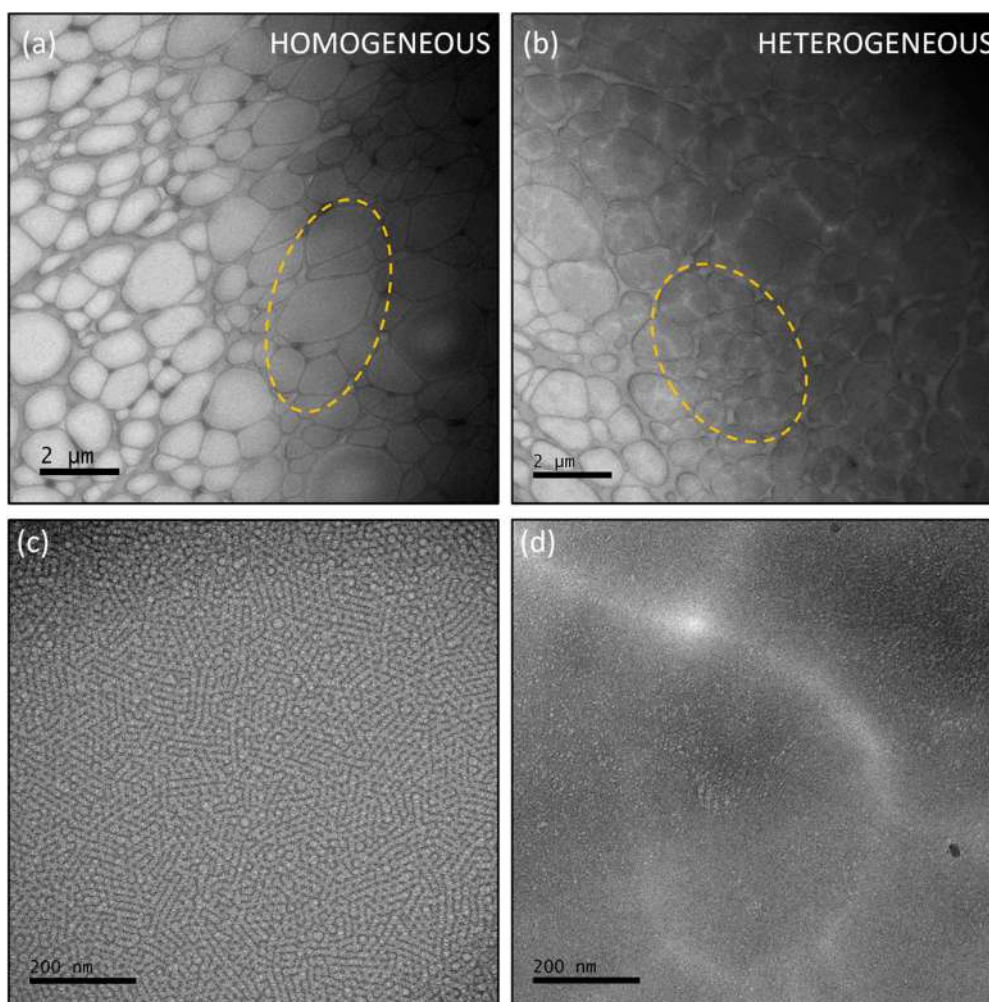


Fig. 2. Ice thickness guidelines. (a) and (b) show low magnification micrographs. The ideal ice thickness is highlighted by the yellow dashed lines in (a), while the yellow dashed lines marked in (b) highlight a region of approximately the same ice thickness as the one marked in (a), however, in a heterogeneous region of the grid. Possibly, the heterogeneous regions are due to the aggregation of amorphous matter that has not yet underwent self-assembly. (c) and (d) show representative higher magnification micrographs of the highlighted regions of (a) and (b), respectively.



Protocol for Cellulose Nanomaterials Size and Morphology Characterization by TEM.

Laura C. E. da Silva^{1*}, Alexandre Cassago² Liliane C. Battirola¹, Maria do Carmo Gonçalves¹ and Rodrigo V. Portugal^{2*}

¹ Institute of Chemistry, University of Campinas (UNICAMP), P.O. box 6154, 13083-970, Campinas, SP, Brazil

² Brazilian Nanotechnology National Laboratory (LNNano), Brazilian Center for Research in Energy and Materials (CNPEM), 13083-100, Campinas, SP, Brazil.

*rodrigo.portugal@lnnano.cnpem.br

Cellulose nanomaterials morphology, size and dispersibility are key parameters for their application in polymer nanocomposites, gels and foams. Transmission electron microscopy (TEM) is the most suitable technique for the morphological characterization of these particles; however, the intrinsic low contrast of cellulose nanomaterials in TEM is a major drawback. Even though it is widespread knowledge that negative staining using uranyl acetate is the best approach for intensifying cellulose contrast, up to now few have succeeded in obtaining high quality images and reliable size measurements. Herein we present an optimization of the standard uranyl acetate protocol commonly used for biological specimens, which was developed to suit cellulose nanomaterials [1]. Notably, few alterations in the standard uranyl acetate protocol were needed, revolving mostly around the sample application on the grid and the grid preparation, not the staining itself. Even though some authors have already shown that CNC concentration and dispersion are key to achieving good quality images, to the best of our knowledge none has attempted to provide clear and concise guidelines for both, specimen preparation and aspect ratio measurements. Figure 1 shows a summary of the results obtained using this protocol through triplicate measurements of commercial cellulose nanocrystals (CNC). These results were used to validate the reliability and reproducibility of the CNC aspect ratio calculation. The guidelines we provided herein also allowed to perform high-quality imaging of cellulose nanocrystals embedded in different polymer matrices [2,3], as illustrated in Figure 2. In summary, this protocol provides cost-effective and readily available guidelines for successfully performing TEM imaging and aspect ratio calculation of cellulose-based nanomaterials.

REFERÊNCIAS

- [1] L.C.E. da Silva, A. Cassago, L.C. Battirola, M.C. Gonçalves and R.V. Portugal, Cellulose (2020)
- [2] L.G.L. Germiniani, L.C.E. da Silva, T.S. Plivelic, M.C. J. Mater. Sci. (2019)
- [3] M.I. Santos, L.C.E. da Silva, M.P. Bomediano, D.M. Catori, M.C. Gonçalves, M.G. de Oliveira, Soft Matter (2021).

ACKNOWLEDGEMENTS

This research was supported by FAPESP, CNPq and the National Institute of Science, Technology and Innovation in Complex Functional Materials (Inomat/INCT). We also acknowledge LNNano/CNPEM for the access to the electron microscopy facility, proposals TEM-20485, TEM-21412.

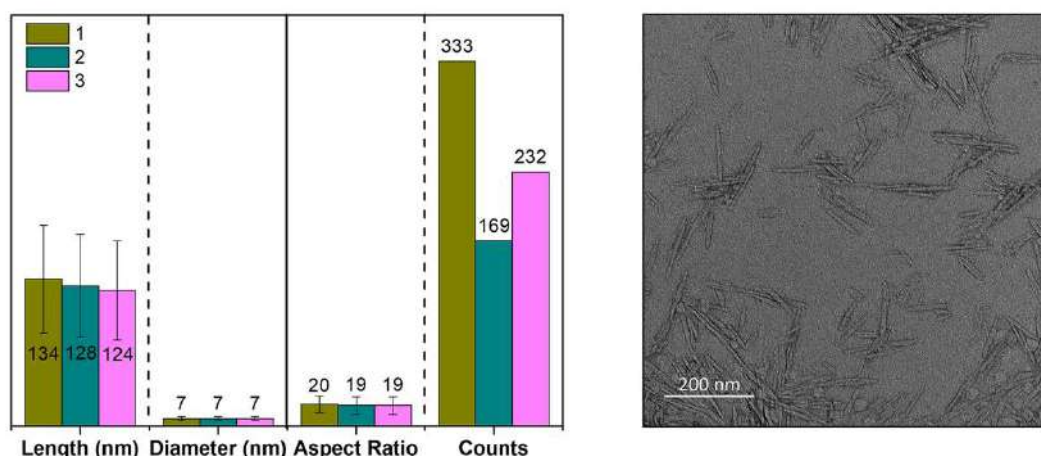


Figure 1: On the left, commercial CNC size characterization: average length, diameter, aspect ratio, as well as the number of particles counted for each triplicate measurement. On the right, representative TEM micrograph of the commercial CNC used for validating the protocol.

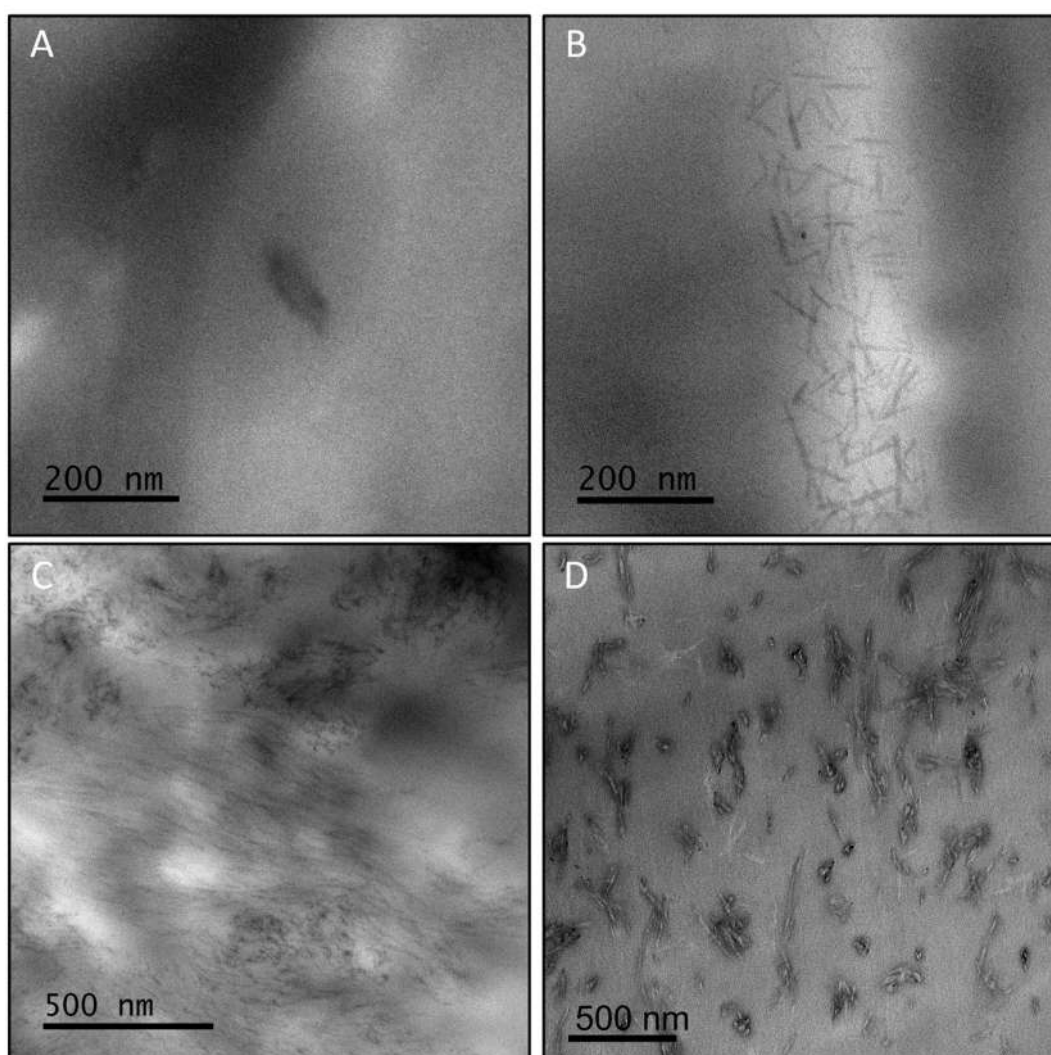


Figure 2: TEM micrographs of cellulose nanomaterials embedded in polymer matrix: polycaprolactone matrix 5 wt% CNC stained from the section side of the grid (A) or the opposite side (B); solvent-cast polycaprolactone with 25 wt% CNC (C) [2]; photopolymerized poly(acrylic acid) with 5 wt% CNC (D) [3].



Using free software to produce 3D models of helminth eggs

Dias Y^{1,2}; Freitas, EO³; Machado, LP⁴; Lopes-Torres EJ^{1*}

¹ Laboratório de Helminologia Romero Lascasas Porto, Departamento de Microbiologia, Imunologia e Parasitologia – UERJ-RJ

² Programa de Pós-graduação em Ensino em Biociências e Saúde, IOC, Fiocruz-RJ

³ Centro Universitário Universus Veritas - RJ

⁴ Departamento de Ensino de Ciências e Biologia – UERJ-RJ

*e-mail: eduardo.torres@uerj.br

Didactic models of microscopic structures can contribute to innovate existing teaching methodologies, as well in health education activities [1]. While commercial software are usually more polished and have more functions, free software can be excellent tools to create didactic models based on 3D microscopy [2]. The aim of this work was to make three-dimensional didactic models of helminth eggs, based on microscopy images, using free software. The models were based on images acquired by light microscopy (DIC) of *Trichuris muris* and *Ascaris lumbricoides* eggs (Fig. 1). The vectorization and segmentation of images was performed using the Inkscape software, based on microscopy images. Inkscape is free and open source software that allows editing and creating vectorized images. In this software, it is possible the transform the raster images, acquired by light microscopy, into high quality vectorized images, which can be easily edited and later converted into 3D images.. The images produced with this software were exported in Scalable Vector Graphics (.svg) and imported to TINKERCAD® three-dimensional model creation website (Fig. 2). When importing the vectorized images into TINKERCAD®, the website automatically converted the vectorized images with topography, generating three-dimensional images. After this step, we have a virtual three-dimensional model that can be freely shared, 3D printed, or edited using this website or other software. While the resulting models were accurate to reproduce the microscopy images, we chose to make a second version of the egg-shell with the software Sculptris, which allows to freely sculpt a 3D models and to create a more true to life representation of this structure (Fig. 3). In our results it was possible to represent details of the egg-shell layers of *T. muris* egg and the larvae (L1) showing internal structures, such as, rudimental esophagus and germ cells (Fig. 3). The 3D model of *A. lumbricoides* egg highlighted the texture of the egg-shell with a irregularly undulations over its whole surface (Fig. 3). Didactic models have a high potential to contribute to the production of knowledge about the control and biological characteristics of several intestinal parasitosis. The use of microscopy images and free drawing and 3D modeling software proved to be excellent tools for the creation of these didact models.

[1] AUGUSTO, I. et al. Virtual Reconstruction and Three Dimensional Printing of Blood Cells as a Tool in Cell Biology Education. PLoS ONE 11(8): e0161184. 2016.

[2] AGUIAR, L. C. D. Um processo para utilizar a tecnologia de impressão 3D na construção de instrumentos didáticos para o Ensino de Ciências. Bauru: Universidade Estadual Paulista, 2016. 226p. Dissertação de Mestrado.

ACKNOWLEDGEMENTS: FAPERJ-JCNE, EIC-UERJ, CNPq, FINEP.

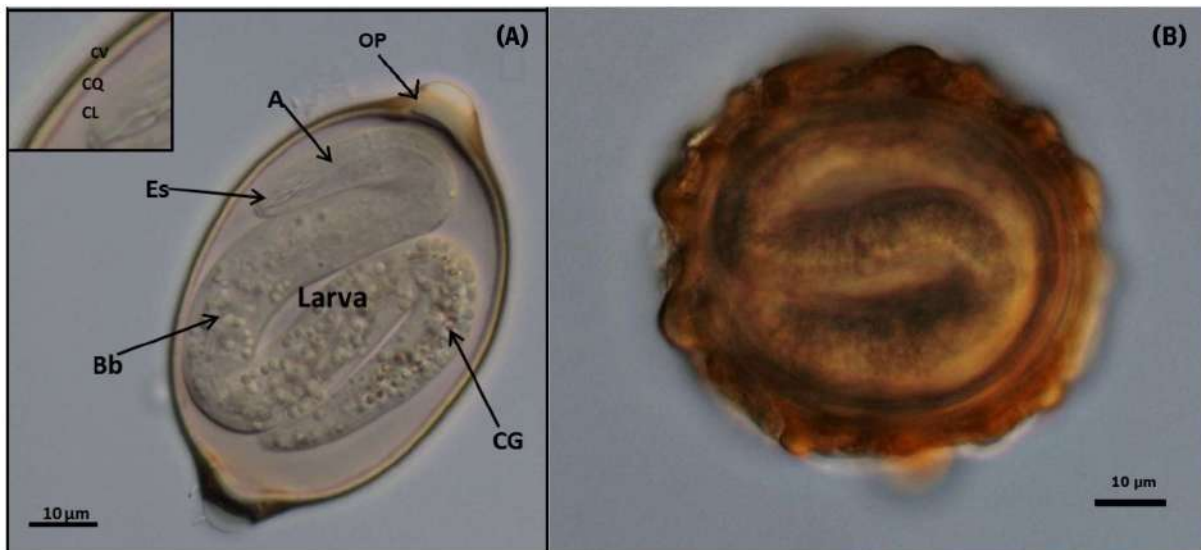


Fig. 1 – Examples of light microscopy of *Trichuris muris* (A) and *Ascaris lumbricoides* (B) eggs. *Trichuris muris* egg structures: Bright field showing the polar plug (OP), larva L1 with esophagus (Es) and germ cells (CG) associated with the formation of the bacillary band (Bb) and digestive system. Inset: Detail of the eggshell layers (CV: Vitelline, CL: Cuticulin and CL: Lipid). *Ascaris lumbricoides* egg structures: Fertile egg observed by light microscopy in interferential system (DIC) and it is possible to observe the oval shape (almost spherical), the nipple membrane (outer layer) and thick and irregular shell.

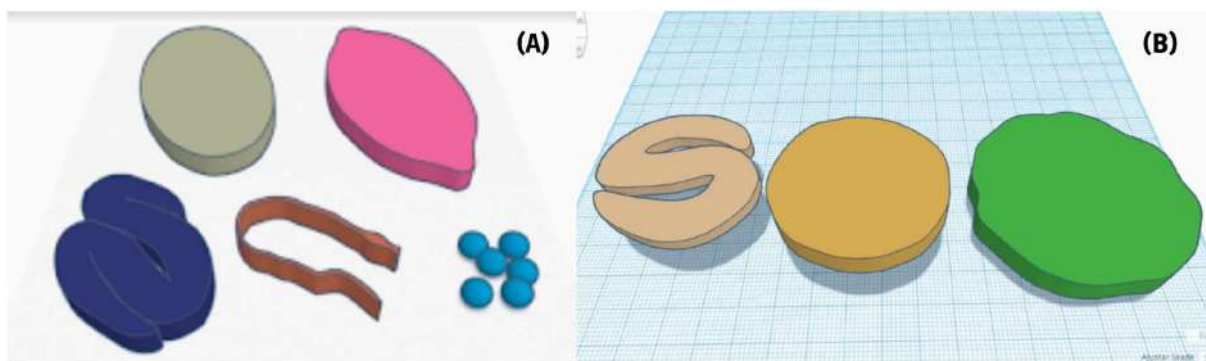


Fig. 2 – Three-dimensional modeling of all detached structures of the egg and L1 larva of *Trichuris muris* (A) and Three-dimensional modeling of all detached structures of the *Ascaris* egg and L1 larva (B).

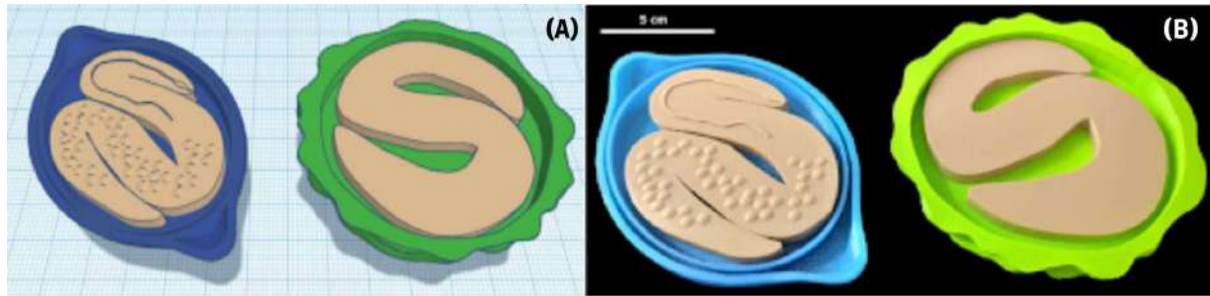


Fig. 3 – Finished virtual (A) and 3D printed models (B). Grouping of different segments of *Trichuris* eggs (left) and *Ascaris* (right) finalized on the Tinkercad website (A). Photograph illustrating the inside of the final result of the printed 3D models of *Trichuris* eggs (left) measuring 20cm x 12cm and *Ascaris* egg (right) measuring 17.14cm in diameter (B)



1nm Resolution With 0.1m Wavelength: Using Twisted Bilayer Graphene Moiré Patterns To Evaluate The Limits Of Near Field Immersion Microscopy.

Douglas A. A. Ohlberg¹, Diego Tami^{1,2}, Andreij C. Gadelha³, Eliel G. S. Neto⁴, Fabiano C. Santana³, Daniel Miranda³, Wellington Avelino², Kenji Watanabe⁵, Takashi Taniguchi⁵, Leonardo C. Campos³, Jhonattan C. Ramirez⁶, Cássio Gonçalves do Rego⁶, Ado Jorio^{2,6}, Gilberto Medeiros-Ribeiro^{1,2,6*}

¹ Microscopy Center, Universidade Federal de Minas Gerais, Belo Horizonte, MG 31270-901, Brazil.

² Electrical Engineering Graduate Program, Universidade Federal de Minas Gerais, Belo Horizonte, MG 31270-901, Brazil.

³ Physics Department, Universidade Federal de Minas Gerais, Belo Horizonte, MG 31270-901, Brazil.

⁴ Instituto de Física, Universidade Federal da Bahia, Campus Universitário de Ondina, Salvador - BA, 40170-115 Brazil.

⁵ National Institute for Materials Science (NIMS), 1-2-1 Sengen, Tsukuba-city, Ibaraki 305-0047, Japan.

⁶ Department of Electronic Engineering, School of Engineering, Universidade Federal de Minas Gerais, Belo Horizonte, MG, Brazil.

⁷ Computer Science Department, Universidade Federal de Minas Gerais, Belo Horizonte, MG 31270-901, Brazil.

*gilberto@dcc.ufmg.br

Hooke in 1679 made observations that enhancing magnification of microscopes was achieved upon spreading fluids onto the surface of a sample and gently elevating it until the liquid touched his microscope lens [1]. The gain in resolving power due to liquid-lens contact gave birth to liquid immersion microscopy. Yet, imaging at molecular and atomic scales required the development of electron and scanning probe microscopies to surpass the physical limits dictated by diffraction [2]. Nano-infrared experiments [3] and picocavity tip-enhanced Raman spectroscopy imaging later demonstrated that radiation in the visible range [4] can surpass this limit by using scanning probe tips to access the near-field regime [5]. With a relative permittivity $\epsilon_r = \epsilon / \epsilon_0 \sim 80$. (ϵ and ϵ_0 as the water absolute permittivity and vacuum permittivity), and a refractive index n of about 9 at 3GHz frequencies, the effect of water can enhance near-field operation in the microwave regime. Here we show that ultimate resolution can be obtained by using scanning microwave imaging microscopy (sMIM) to reveal structures with feature sizes down to 1nm using a radiation of 0.1m in wavelength. The sMIM system (see figure 1 below) comprises of an add-on microwave heterodyne detection bridge commercialized by PrimeNano Inc. The simultaneously measured Atomic Force Microscopy (AFM) images and sMIM images allows us to precisely position the tip in a non-contact, attractive mode, conducive to water meniscus formation and control. As a test material we use twisted bilayer graphene, which is not only a very important recent topic due to the discovery of correlated electron effects such as superconductivity [6] and localization of lattice dynamics [7], but also because it provides a sample where we can systematically tune a superstructure moiré pattern's modulation from below one up to tens of nanometers. sMIM is implemented as a 3GHz microwave signal coupled to an Atomic



Force Microscope (AFM) probe tip that works as a waveguide and performs as an apertureless near-field microscope [8]. By analyzing the tip-sample distance dynamics, ambient humidity and water meniscus nucleation kinetics we demonstrate that this ultimate 10^8 probe-to-pattern resolution can be achieved by using liquid immersion microscopy concepts and exquisite force control exerted by AFM tips on water menisci [9]. We also discuss the contrast mechanisms and by means of a full-wave model for the electro-magnetic fields we developed a lumped element model that describes the meniscus effect. We summarize extracting the real and imaginary parts of several images of twisted bilayer graphene at selected angles, and show the perspectives of a vector-based microscopy tool can impact the study of 2D van der Waals systems.

REFERENCES

- [1] R. Hooke. *Lectioes Cutlerianae, Or A Collection of Lectures, Physical, Mechanical, Geographical & Astronomical: Made Before the Royal Society on Several Occasions at Gresham Colledge [i.e. College] : to which are Added Divers Miscellaneous Discourses.* J. Martyn, Printer to the Royal Society, London, (1679)
- [2] Microscopium: or, some new discoveries made with and concerning microscopes, p. 98.
- [3] E. Abbe. 1(3) (1881) 388.
- [4] J. Chen et al. *Nature*, 487 (2012) 77.
- [5] J. Lee et al. *Nature*, 568 (2019) 78.
- [6] E. Synge. 6(35) (1928) 356.
- [7] U. Zondiner et al. *Nature*, 582(2020) 203.
- [8] A. C. Gadelha et al., *Nature*, 590 (2021) 405.
- [9] O. Amster et al. Practical quantitative scanning microwave impedance microscopy. *Microelectronics Reliability*, 76-77 (2017) 214.
- [10] D. A. A. Ohlberg et al., *Nature Comms* 12 (2021) 2980.
- [10] This research was supported by CNPq, FINEP, FAPEMIG and CAPES (Brazil).

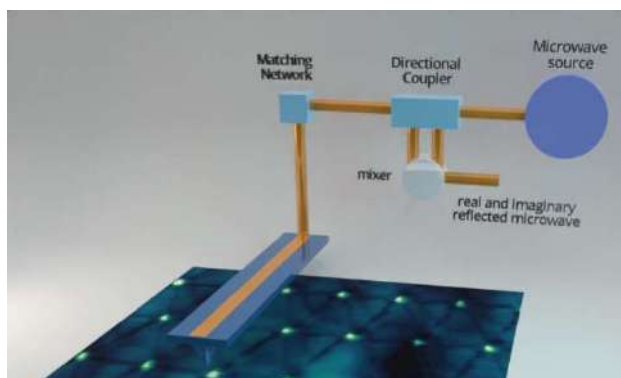


Fig. 1: Experimental set-up: an AFM tip, acting as a microwave waveguide coaxes the microwave fields to the end of the tip. A detection scheme separates in real and imaginary parts by a heterodyne bridge. The AFM tip also measures the force and by conventional feedback loop allows us to operate in the attractive, non-contact mode.

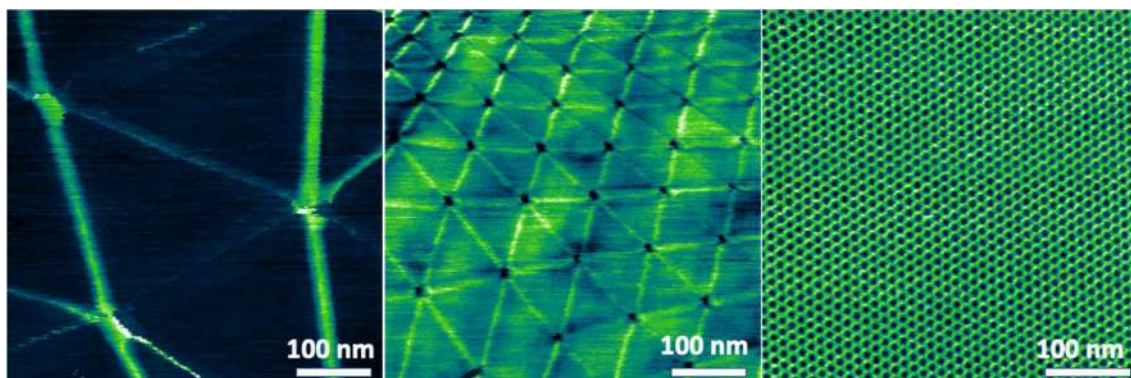


Fig. 2: Microwave conductivity images of twisted bilayer graphene rotated by 0.04, 0.15 and 1.2 degrees from left to right respectively. Scan sizes of 500nm, 500nm and 400nm.



Using atomic force microscopy and self-assembled monolayers to reveal crystal orientation and grain boundaries in 2D materials.

Mariana C. Prado^{1*}, Regiane Nascimento², Luciano Moura², Camilla K. B. Q. Oliveira³, Barbara E. N. Faria², Matheus J. S. Matos¹, Mario C. Mazzoni², Luiz G. Cançado², Helio Chacham² and Bernardo R. A. Neves²

¹Universidade Federal de Ouro Preto, Physics Department, Ouro Preto - Brazil.

²Universidade Federal de Minas Gerais, Physics Department, Belo Horizonte - Brazil.

³Universidade Federal do Paraná, Physics Department, Curitiba - Brazil.

*mariana.prado@ufop.edu.br

Following the realization of single-layer graphene atop silicon oxide, much attention has been drawn towards two-dimensional (2D) materials. Graphene is a semimetal, hexagonal boron nitride (hBN) is an insulator, and single-layer molybdenum disulfide (MoS₂) is a semiconductor with a direct bandgap. Besides those, there are numerous other two-dimensional nanosheets of a variety of materials including other transition metal dichalcogenides and phyllosilicates [1]. Characterizing these 2D materials is a challenge that must be addressed so they can fulfill their potential to revolutionize the industry with their outstanding mechanical, optical and electrical properties. Here, we present a simple way to reveal the crystallographic orientations of graphene, MoS₂, and hBN without the need of acquiring atomic resolution microscopy images. Octadecylphosphonic acid (OPA) is a linear alkyl chain organic molecule that forms self-assembled monolayers (SAM) on top of the cited materials and that keeps registry with the crystallographic directions of the substrate beneath it. An atomic force microscopy (AFM) image easily detects the period of the 2D molecular crystal that forms atop the flake, revealing the substrate's crystallographic orientation. *Ab initio* calculations reveal that the molecular crystal's ripples (detected in the AFM image, both in topography and phase contrast channels) are aligned with MoS₂ [2], hBN [3], and graphene's [4] armchair direction. Figures 1 and 2 illustrate the results. For MoS₂, we have also found that our samples, purchased from SPI supplies, presented ripples of the molecular crystal forming 12° angles that did not reflect the substrate's hexagonal symmetry. Interestingly, Stone-Wales-type defects have been predicted to cause 12°-angled grain boundaries in MoS₂ and WS₂. Thus, the SAM deposition followed by standard AFM analysis on ambient conditions proposed in this work enables the direct localization of MoS₂ grain boundaries. For graphene, *ab initio* calculations and Raman spectroscopy measurements also show that OPA induces p-type doping of $\sim 10^{13}$ cm⁻². Summing it up, spin coating OPA ethanolic solution on 2D materials is a facile way of discovering flake orientation, characterizing grain boundaries of MoS₂ samples, and achieving chemical doping of graphene.

[1] P. Miró et al., Chem. Soc. Rev. 43, (2014) 6537-6554

[2] M. C. Prado et al., Nanotechnology 26, (2016) 47.

[3] C. K. Oliveira, C et al., Nano Research 8 (5) (2015) 1680-1688.

[4] M. C. Prado et al., ACS Nano 5 (1) (2015) 394-398.

[5] This research was supported by CNPq, CAPES, FAPEMIG, Rede Nacional de Pesquisa em Nanotubos de Carbono, Instituto Nacional de Ciência e Tecnologia (INCT-Nano-Carbono), National Energy Research Scientific Computing Center (NERSC) (Brazil).

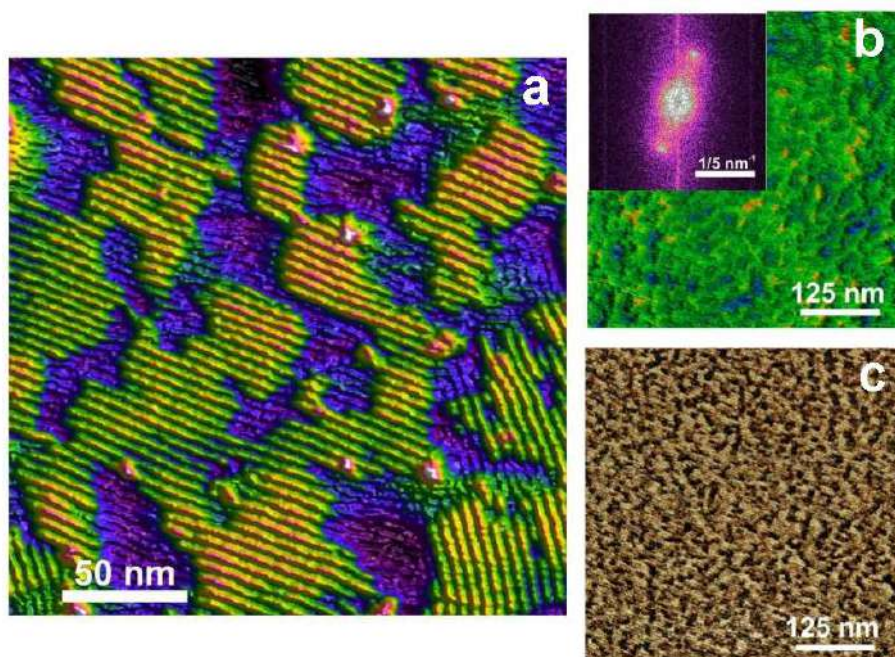


Figure 1 – OPA deposition on graphite (a) and graphene (b and c). Panels (a) and (b) are AFM topographic images of OPA ripples formed on graphite and single layer graphene. In (b), the rippled domains are somewhat masked by the substrate (SiO_x) rugosity, but the fast Fourier transform shown in the inset reveals the periodic nature of the molecular decoration. The ripples are in graphene's armchair direction. Panel (c) is a phase contrast image acquired simultaneously with (b) evidencing the high coverage of the OPA SAM.

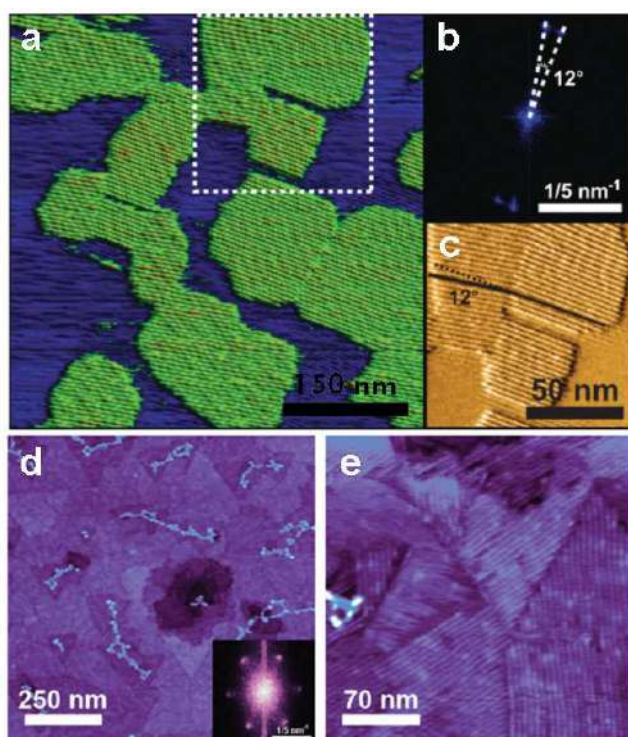


Figure 2 – OPA deposition on MoS_2 (a, b, and c) and h-BN (d, and e). Panels (a), (d) and (e) are AFM topographic images of OPA ripples formed on MoS_2 and h-BN. The FFT (b and inset on d) reveals the periodic nature of the OPA SAM. The 12° grain boundary on MoS_2 is evidenced in the amplitude error image (c), taken from the region marked in (a) by the dashed square.



Gypsum: An Environment-Friendly, Inexpensive And Robust Height Calibration Standard At Nanometer-Scale For Atomic Force Microscopy

Ana P. M. Barboza^{1*}, Joyce C. C. Santos², Elisângela Silva-Pinto³ and Bernardo R. A. Neves²

¹ Department of Physics/ Instituto de Ciências Exatas e Biológicas, Universidade Federal de Ouro Preto, Ouro Preto, Brasil.

² Department of Physics/ Instituto de Ciências Exatas, Universidade Federal de Minas Gerais, Belo Horizonte, Brasil.

³ Instituto Federal de Minas Gerais, Ouro Preto, Brasil.

*ana.barboza@ufop.edu.br

Since its development in the late 1980s and early 1990s, atomic force microscopy (AFM) has played an important role in the advance of nanoscience and nanotechnology [1, 2]. More recently, it has also been omnipresent in the research and development of the so-called low-dimensional (0D, 1D and 2D) materials [3, 4]. The ability to measure height variations with sub-angstrom sensitivity is at the core of the AFM applicability in these fields [1–4]. However, such sub-angstrom sensitivity does not translate into sub-angstrom accuracy straightforwardly. In other words, height standards are required to calibrate AFM setups and validate their measurements.

REFERENCES

- [1] W. A. Goddard et al., Handbook of Nanoscience, Engineering, and technology, Boca Raton, CRC Press, 2007.
- [2] B. Bhushan Springer Handbook of Nanotechnology, Berlin, Springer, 2004.
- [3] F. J. Owens et al., The Physics and Chemistry of Nanosolids, Hoboken, NJ: Wiley, 2008.
- [4] F. J. Owens, The Physics of Low Dimensional Materials, Singapore, World Scientific, 2017.
- [5] NanoAndMore <https://nanoandmore.com/afm-accessories-height-calibration-standards> AsylumResearch <https://afmprobes.asylumresearch.com/accessories-ApexProbes> <https://apexprobes.uk/afm-calibration-standards/> all accessed on 16/September/2019
- [6] L.A. Nagahara et al., J. Vac. Sci. Technol. B 12 (1994) 1694.
- [7] A. P. M. Barboza et al., Nanotechnology 31 (2020) 11570.
- [8] The authors acknowledge financial support from Brazilian funding agencies: CNPq, Fapemig, Capes and INCT-NanoCarbono. APMB also acknowledges the support from UFOP- Grant Custeio 2017. The authors are thankful to Mr Antônio Pinto G L Neto for the mineral samples, to Professor Ananias B Alencar (UFVJM—Brazil) for the help with figures and to Mr Alexandre M Moreira and the Crystallography Laboratory (LabCri, Physics Department, UFMG, Brazil) for the x-ray diffraction experiments.

Several companies sell Si/SiO₂-based height standards (with step heights varying from tens to hundreds of nanometers) with their price ranging from several hundreds to a few thousand dollars each [5]. Alternatively, at the nanometer level, an often-used calibration standard is etched mica [6]. Although its fabrication does not require sophisticated and



expensive lithographic techniques, it still employs harsh chemicals (hydrofluoric acid), requiring strict safety routines and creating contamination risks [6]. Therefore, it is easy to infer that an inexpensive, environment-friendly and robust height calibration standard at the nanometer level would be a nice add-on to any AFM laboratory. Here we use plain water as etchant, gypsum flakes readily review 0.75 nm tall terraces which are easy to image (lateral dimensions from tens to hundreds of nanometers) and robust against time in ambient conditions as showed in figure 1. Therefore, the present work demonstrates a new height standard alternative which is easily-available for all AFM microscopists around the world [7].

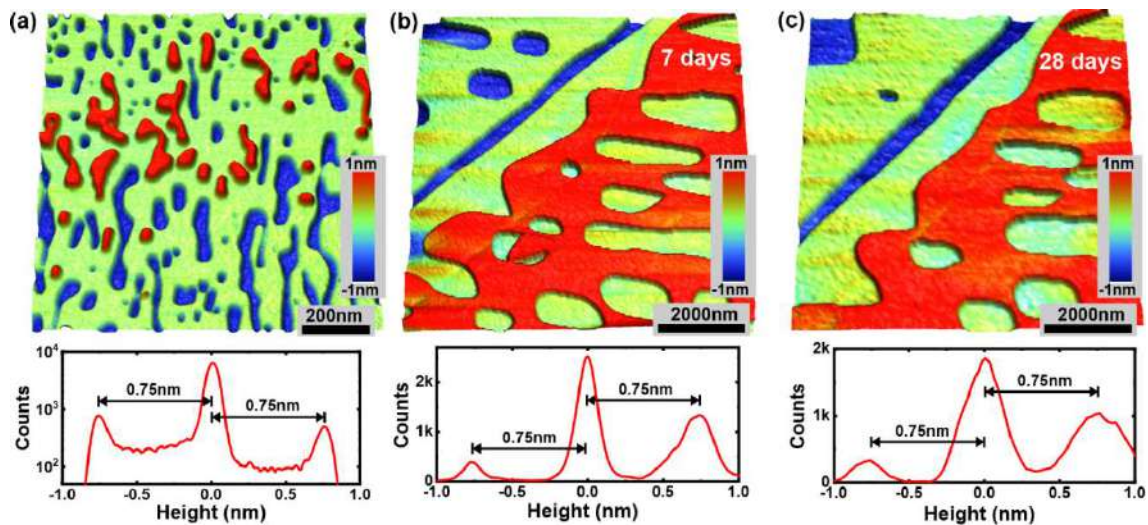


Figure 1. AFM images and their respective height distribution histograms of gypsum flakes prepared via (a) water immersion (immersion time: 300s), (b) droplet casting (dwell time: 300s) after 7 days and (c) the same region after 28 days. In all AFM images black and colored scale bars indicate lateral and vertical dimensions, respectively. In all histograms, black arrows indicate appropriate step heights (vertical distances) [7].



Atomic Resolution From Friction Force Microscopy Using The Jarzynski Equality

Yasmin Watanabe^{1*}, Rodrigo Capaz² and Renata Simão¹

¹ Departamento de Engenharia Metalúrgica e de Materiais – COPPE/UFRJ, Rio de Janeiro, Brasil.

² Departamento de Física dos Sólidos, IF/UFRJ, Rio de Janeiro, Brasil.

*yasmin@nano.ufrj.br

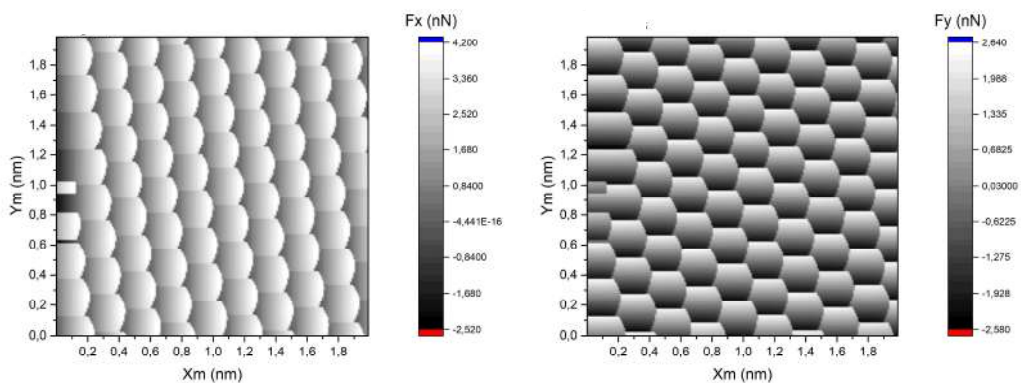
Along with the development of the Atomic Force Microscopy (AFM), there was an increase in the number of studies regarding surface properties in atomic scale, both experimentally, taking advantage of the versatility presented by the AFM, and theoretically, through modeling and computer simulations [1]. In the present work we simulate the scanning process of an AFM in Friction Force Microscopy mode (FFM), using the Tomlinson model and Langevin dynamics. The tests were performed on graphene surface, using different scanning speeds, temperatures and contact forces. The results of our simulations were compatible with FFM images from experimental works found in literature [2]. With the variation of the simulation parameters, it was possible to observe two distinct types of interactions between the tip of the microscope and the surface of sample: the well known “stick-and-slip” movement, characterized by a discontinuity in tip movement during scanning, and the thermolubricity regime, that occurs under lower scanning velocities and higher temperatures [3]. At last, we use the Jarzynski equality to map the potential energy of graphene in both cases. Although in the “stick-and-slip” case it was only possible to use Jarzynski’s equation in a portion of the distance between two energy minimums, the whole potential curve was mathematically fitted and the energy barrier was shown to be in agreement with the reference values. For the thermolubricity mode, we were able to obtain the surface potential for the entire scanning distance, which indicates it may be possible to apply these results in order to obtain FFM images with better resolution.

[1] U. D. Schwarz et al., ACS Nano. 10, 38 (2016).

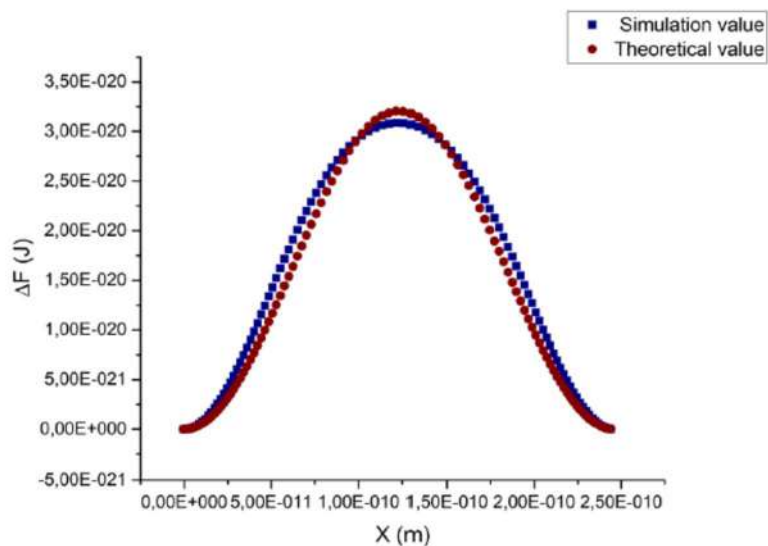
[2] H. Holscher et al., Phys. Rev. B, 57, 4 (1997).

[3] F. Pellegrini et al., Phys. Rev. B 99, 075428 (2019).

The authors would like to thank CNPq (Brasil) for the financial support.



Simulation results for the lateral force measured in the horizontal direction (left) and the vertical direction (right).



Energy profile along the distance between two potential minimums of graphene surface calculated using the Jarzynski equality (blue) and compared with reference value (red).



Electrostatic Force Microscopy Measurements Of The Local Dielectric Constant Of A Biological Nanostructured System

Wescley Walison Valeriano^{1*}, Rodrigo Ribeiro Andrade², Juan Pablo Vasco³, Angelo Malachias¹, Bernardo Ruegger Almeida Neves^{1,2}, Paulo Sergio Soares Guimarães¹, and Wagner Nunes Rodrigues^{1,2}.

¹ Departamento de Física, ICEx, Universidade Federal de Minas Gerais, Av. Antônio Carlos 6627, 31270-901 Belo Horizonte, Minas Gerais, Brazil

² Centro de Microscopia, Universidade Federal de Minas Gerais, Av. Antônio Carlos 6627, 31270-901 Belo Horizonte, Minas Gerais, Brazil

³ Institute of Theoretical Physics, Ecole Polytechnique Fédérale de Lausanne EPFL, CH-1015 Lausanne, Switzerland

*wescleyvaleriano@gmail.com

Natural photonic crystals are exciting nanostructured systems in which the dielectric properties play a fundamental role [1]. Many of them are biological systems [2]. Studies of the origin of physical colors in insects are numerous in the literature and the most used tools are non-local optical reflectance, electron microscopies, and scanning probe microscopies, which give support to theoretical models aiming to describe the measured optical properties [3]. However, all these techniques directly reveal only the structure with nanometric resolution, the local dielectric response is indirectly inferred from the model [4]. Despite the large number of studies, the local dielectric properties of natural photonic crystals remained essentially undetermined due to the great difficulties in measuring the dielectric response at the nanometric scale [5]. Until now the nanometric local relative permittivity of a natural photonic crystal had not been directly measured.

Fumagalli et al. [6], and Riedel et al. [7] developed several techniques of Electrostatic Force Microscopy (EFM) to extract the relative permittivity at the nanoscale, allowing new fields to be explored. Here we use EFM to map the relative permittivity of the nanometric layers that make up the wings of the *Chalcopteryx rutilans* damselfly [8,9]; structure which make it a natural photonic crystal. We obtain quantitative information about the wing structure and its local relative permittivity properties. We also simulate the optical reflectance using the extracted spatial profile of the relative permittivity and compare it with the measured reflectance in the visible range, obtaining a good correlation. In this way, we can provide a full description of the origin of the colors of the *Chalcopteryx rutilans* damselfly male posterior wings. [10]

REFERÊNCIAS

- [1] Joannopoulos, J. D.; Johnson, S. G.; Winn, J. N.; Meade, R. D. Photonic Crystals;
- [2] Teyssier, J.; Saenko, S. V.; Van Der Marel, D.; Milinkovitch, M. C. Nat. Commun. 2015, 6, 1–7. doi:10.1038/ncomms7368
- [3] Vukusic, P.; Stavenga, D. G. J. R. Soc. Interface 2009, 6, S133-48. doi:10.1098/rsif.2008.0386.focus
- [4] Stavenga, D. G.; Leertouwer, H. L.; Hariyama, T.; De Raedt, H. A.; Wilts, B. D. PLoS One 2012, 7, 1–8. doi:10.1371/journal.pone.0049743
- [5] Gabriel, C.; Gabriel, S.; Corthout, E. Phys. Med. Biol. 1996, 41, 2231–2249. doi:10.1088/0031-9155/41/11/001



- [6] Gomila, G.; Toset, J.; Fumagalli, L. J. Appl. Phys. 2008, 104, 024315. doi:10.1063/1.2957069
- [7] Riedel, C.; Arinero, R.; Tordjeman, P.; Ramonda, M.; L vque, G.; Schwartz, G. A.; De Oteyza, D. G.; Alegria, A.; Colmenero, J. J. Appl. Phys. 2009, 106, 1–6. doi:10.1063/1.3182726
- [8] Valeriano, W. W. Cores Estruturais Da Asa Da Lib lula *Chalcopteryx Rutilans*, Universidade Federal de Minas Gerais, Brazil, 2015
- [9] Wesley Walison Valeriano, Rodrigo Ribeiro Andrade, Juan Pablo Vasco, Angelo Malachias, Bernardo Ruegger Almeida Neves, Paulo Sergio Soares Guimar es and Wagner Nunes Rodrigues. Beilstein J. Nanotechnol. 2021, 12, 139-150. <https://doi.org/10.3762/bjnano.12.11>
- [10] This research was supported by FAPEMIG, CNPq, CAPES and FINEP.

The authors would like to thank Prof. Angelo Machado for his generosity and enthusiasm for this work, supplying us with the precious specimens of damselflies studied here. We acknowledge the Center of Microscopy at the Universidade Federal de Minas Gerais for providing the equipment and technical support for experiments involving electron and scanning probe microscopies.

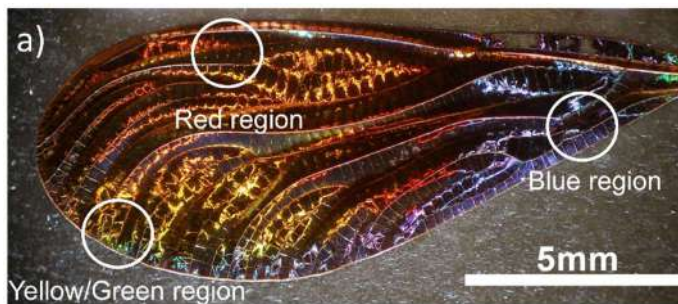


Fig1. Optical images of the iridescent hind wing of the male damselfly *Chalcopteryx rutilans* (Rambur) (Odonata, Polythoridae).

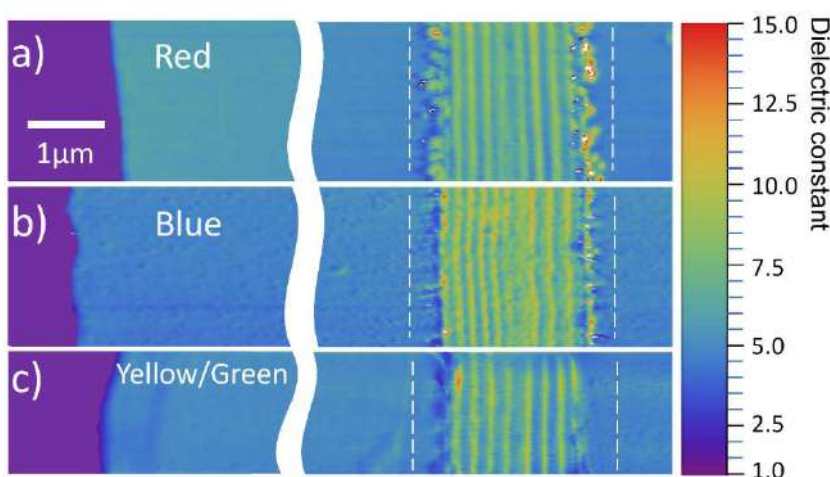


Fig2: Relative permittivity image of three colored regions of the hind wings of *Chalcopteryx rutilans*, Red region (a), Blue region (b), Yellow/Green region (c). The color scale on the right side gives the values of the relative permittivity. On the left side, with the purple color, we have the Au/Cr surface. The areas which appear bluish in the images ($\epsilon_r \sim$ around 4) correspond to the polymerized resin wrapping the wing.



Microfabrication of Pyramidal Nanoantennae for TERS (Tip Enhanced Raman Spectroscopy)

Fabiano C. Santana^{1*}, Vitor P. Monken¹, Bruno S. Oliveira², Thiago L. Vasconcelos²,
Wagner N. Rodrigues¹, Luiz Gustavo Cançado¹, Ado Jório¹

¹ Departamento de Física, Instituto de Ciências Exatas, Universidade Federal de Minas Gerais, Belo Horizonte, Brazil.

² Divisão de Metrologia de Materiais, Instituto Nacional de Metrologia, Qualidade e Tecnologia, Rio de Janeiro, Brazil.

*fabianocs7@gmail.com

Near-field optical microscopy/spectroscopy is a new technique that allows optical characterization with high spatial resolution, either by Raman scattering analysis (TERS, Tip-enhanced Raman Spectroscopy), or photoluminescence (TEPL, Tip-enhanced Photoluminescence) [1,2]. The technique consists of amplifying the optical signal through the use of near-field information, evanescent optical waves, by the use of an optical antenna (structure that presents localized surface plasmon resonance - LSPR), allowing to obtain chemical and structural information of a sample with nanometric resolution [3]. For this, a nanoantenna is positioned in the laser focus region of the optical system by using a scanning probe microscopy system. High spatial resolution is so obtained, typically around 10 nm, and allows the characterization of the entire class of nanomaterials [4]. Currently these antennae are handcrafted manufactured, which has prevented the dissemination of the technique. The use of microfabrication and processing techniques can turn the fabrication of these antennae into an industrial process. In this work we use these techniques to obtain silicon molds (Figures 1 and 2) for the extraction of microfabricated nanoantennae called PTPP [5] (Pyramidal Plasmonic Tunable Tip) as shown in Figure 3, necessary for the TERS technique. An improvement in the TERS system performance is also expected, with an increase in the signal captured by the TERS microscope, when using PTPP antennae such as those manufactured in this work, compared to other antenna formats currently used. [6] This work is part of an effort carried out at UFMG and INMETRO to develop a robust and high-performance TERS spectrometer. There is still no commercially available system with these features. [7]

REFERENCES

- [1] L. Novotny, B. Hecht; Principles of Nano-Optics, Cambridge University Press, 2012.
- [2] M. A. Paesler, P. J. Moyer; Near-Field Optics: Theory, Instrumentation, and Applications; Wiley, 1996.
- [3] L. G. Cançado, A. Jorio, A. Ismach, E. Joselevich, A. Hartschuh, and L. Novotny; Phys. Rev. Lett. 103, 186101, 2009.
- [4] Indhira O. Maciel, et al; Nature Materials 7 (2008) 878.
- [5] T. L. Vasconcelos, et. al, Adv. Optical Mater. 2018, 6, 1800528. [10] T. L. Vasconcelos, et. al, ACS Nano. 2015, 9, 6297– 6304
- [6] Gadelha, A.C., Ohlberg, D.A.A., Rabelo, C. *et al.* Localization of lattice dynamics in low-angle twisted bilayer graphene. *Nature* **590**, 405–409 (2021).
- [7] This work was supported by FAPEMIG, CNPq and FINEP.

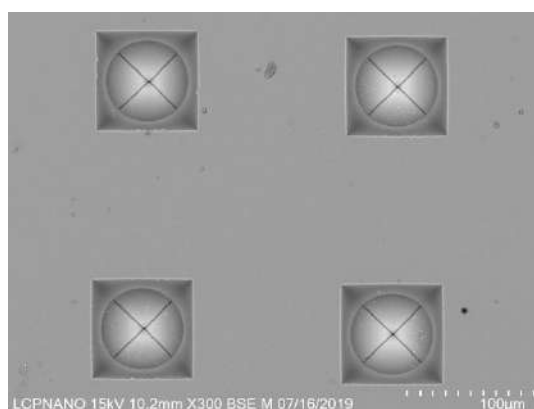
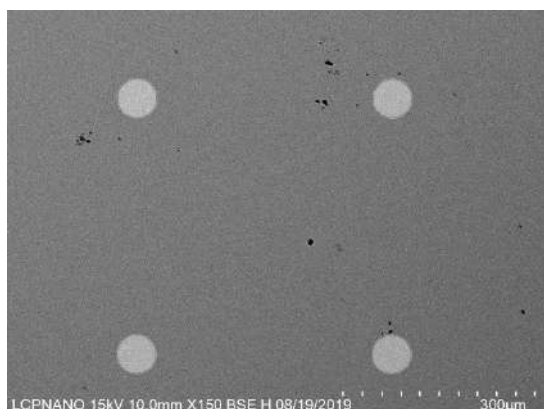


Figure 1 First microfabrication process. **a)** Plasma opened windows at SiNx, exposing the silicon layer. **b)** Pyramidal shaped cavities formed after wet etching with KOH.

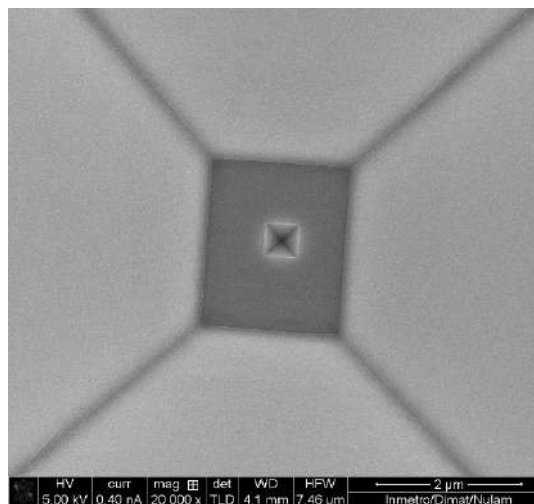
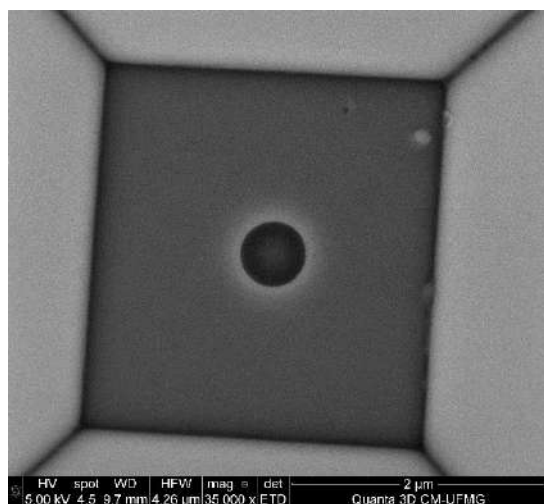


Figure 2 Second microfabrication process. **a)** Window opened by FIB on the bottom plateau of the cavity. **b)** Wet-etched nanopyramid at the bottom plateau.

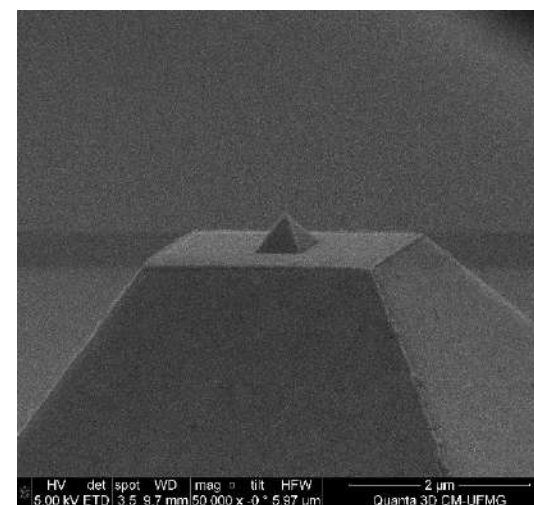
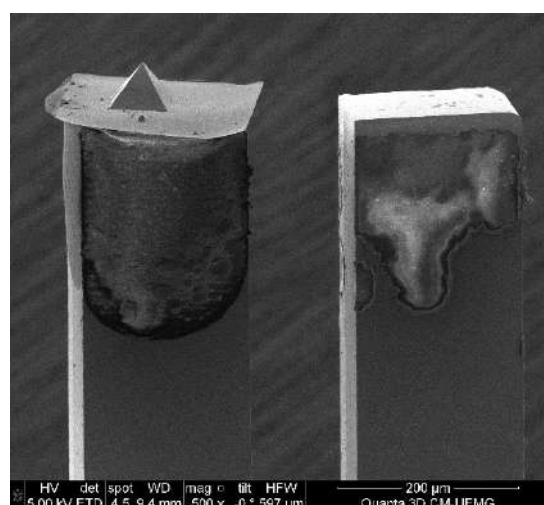


Figure 3 Extracted PTPP nanoantenna from silicon mold. **a)** Full view of the entire antenna on the tuning fork with the micropyramid; **b)** Close view of nanopyramid at the apex of micropyramid.



Engineering New 2D Functional Materials at Surfaces: from Doped Graphene to Metal-Organic Frameworks

Abner de Siervo¹

¹ Departamento de Física Aplicada, Instituto de Física “Gleb Wataghin”, Universidade Estadual de Campinas, 13083-859, Campinas, SP, Brazil.

*asiervo@ifi.unicamp.br

The so-called *2D materials* emerged in the last decades as an exciting new area for research that discovered new physical phenomena as well as plenty of room for technological applications. These materials can be divided into different classes that involve (1) one-atom-thick layers, like the graphene “celebrity”, twisted graphene layers, and other members such as h-BN, borophene, phosphorene, stanene, and so on; (2) layered materials like transition metal dichalcogenides (TMDs), and topological insulators; and (3) 2D functional organic-networks [1,2]. These materials have shown new interesting physical phenomena like linear-electronic dispersion, quantum-hall effect, outstanding photonic properties, unexpected magnetic, superconductor, ferroelectric, and piezoelectric behaviors [1,2]. All these physical phenomena have driven the community to propose applications for these materials in many different areas such as new supports for catalysts, supercapacitors, sensors, energy production (e.g solar cells) and storage, electronic and photonic devices, among others. Our group in Campinas has been working during the last years on the epitaxial growth of different members of these families (graphene, h-BN, h-BNC alloys, TMDs, and 2D-organic frameworks) [3-10] to better understand the electronic and atomic structure of these materials. In this seminar, I will show recent examples where we have applied different growth and functionalization strategies to produce new epitaxial functional *2D materials*. The electronic and atomic structure of these materials were characterized by combing different synchrotron-based techniques, such as x-ray photoemission and absorption spectroscopies with other surface science techniques, for instance, scanning tunneling microscopy and spectroscopy, as well as the support of theoretical calculations based on density-functional theory (DFT) to improve the understanding of the materials at an atomic scale.

- [1] Mengqi Zeng, et al. *Chemical Reviews* 118 (13), 6236-6296 (2018).
- [2] Akinwande, et al. *Nature* 573, 507–518 (2019).
- [3] L.H. de Lima et al., *Physical Review B* 87, 081403(R) (2013).
- [4] L.H. de Lima et al., *Chemistry of Materials* 26 (14), 4172-4177 (2014).
- [5] Rodrigo C.C. Ferreira et al., *Chemistry of Materials* 30 (20), 7201-7210 (2018).
- [7] Juan Carlos Moreno-López et al., *Chemistry of Materials* 31, 3009-3017 (2019).
- [8] Alisson Ceccatto dos Santos, et al., *Chemistry of Materials* 32, 2114-2122 (2020).
- [10] Nataly Herrera-Reinoza, et al., *Chemistry of Materials* 33, 2871-2882(2021).

These works are financially supported by FAPESP, CNPq, and CAPES from Brazil.

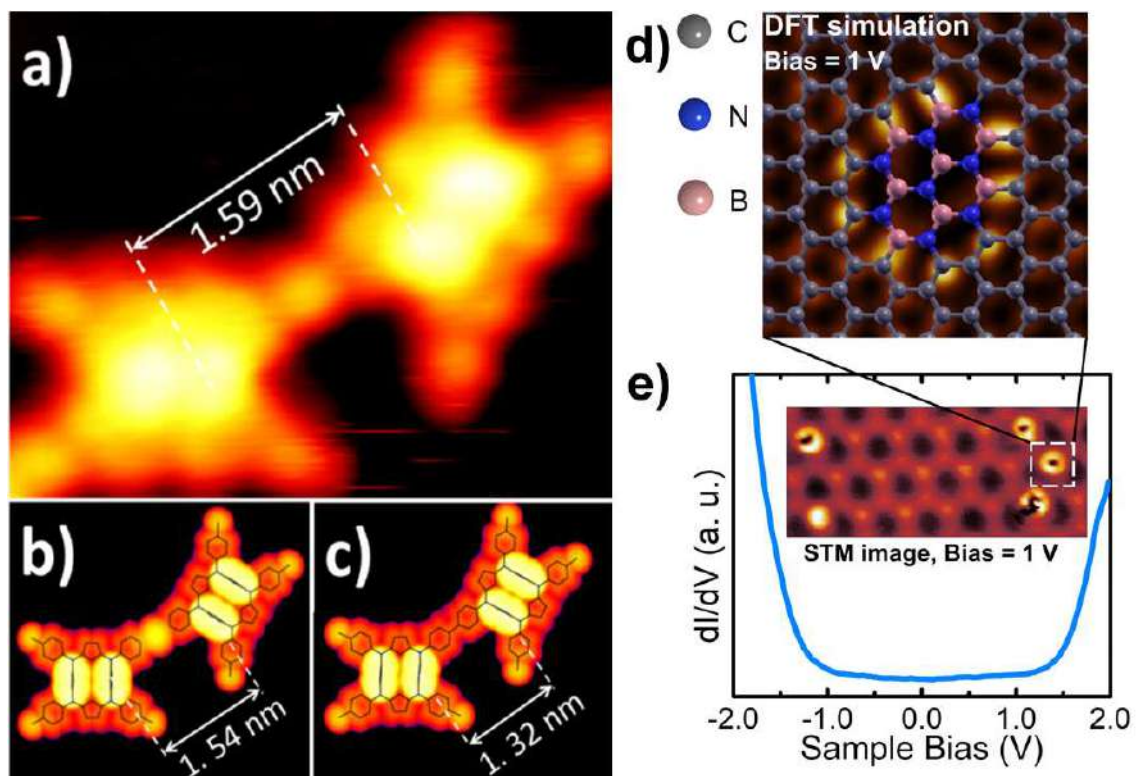


Fig 1 – a) High-resolution STM image of an organometallic bonding (C-Cu-C) between two tetraphenyl porphyrins followed by DFT simulations considering two models: b) organometallic and c) covalent bonding (adapted from ref.7). d) and e) STM image and DFT simulation of a graphene semiconductor based on h-BN nanoclusters doping (adapted from ref.10).



Local (Cross) Information Density: Powerful Practical Tools for Interpreting 3D Structures, Especially in Cryo-EM.

Sayan Bhakta^{12*}, Rodrigo V Portugal¹, Michael Schatz³ and Marin van Heel¹

¹ Brazilian Nanotechnology Nat. Lab. (LNNano/CNPem), Campinas, SP, Brazil.

² CSIR - Indian Institute of Chemical Biology, Kolkata, India.

³ Image Science Software GmbH, Berlin, Germany.

*sayan.bhakta@lnnano.cnpem.br // 19sayanbhakta89@gmail.com

The resolution assessment of an imaging instrument has traditionally been measured by metrics such as the Abbe or Rayleigh criterion. However, such *instrumental resolution* metrics are a property of the instrument, independent of whether it is even being used to image an object or not. To assess the reproducible global resolution one has achieved in a data collection experiment, the Fourier Ring Correlation (FRC) and the Fourier Shell Correlation (FSC) criteria were introduced in the 1980s [1]. These metrics assess the *results resolution* achieved in an experiment, especially when coupled to an information-based threshold criterion [2]. These are now accepted also universally in X-ray tomography, X-ray crystallography, super-resolution light microscopy. However, recent insights indicate that the most universal metrics to assess the *results resolution* are local metrics [3,4]. They allow us to use the same metric and threshold functions for global as well as for the local resolution on the same scale. These metrics are especially good at comparing the results of independent experiments. Fully new in concept are the local information densities and associated metrics [4]

Preliminary tests confirm the potential of the approach. We could highlight transmembrane helices within an encapsulating phospholipid bilayer. We successfully imaged glycosylations on the exterior of large complexes such as alpha viridae. Applications include visualising dynamic interactions of factors with the ribosome, and structural differences between species-specific ribosomal components (**Fig 1**). The insights obtained may inspire the development of new antibiotics. During the current Covid-19 pandemic, a large number of SARS-CoV-2 spike protein structures have been/are being deposited in the public Electron Microscopy Data Bank (EMDB). The inter-comparability of these structures with the new metrics, may become an important tool for interpreting the dynamics of corona-virus spike trimers (**Fig 2**).

[1] G Harauz and M. van Heel: **Exact filters for general geometry three-dimensional reconstruction**, *Optik* 73 (1986) 146-156.

[2] M van Heel and M Schatz: **Fourier shell correlation threshold criteria**, *J. Struct. Biol.* **151** (2005) 250-262.

[3] M van Heel and M Schatz: **Information: to harvest, to have and to hold**. *arXiv* (2020) <https://arxiv.org/abs/2009.03223>

[4] DC Mendonça, et al., and Garratt RC: **An atomic model for the human septin hexamer by cryo-EM**. *Journal of Molecular Biology* (2021) 167096

[5] M. Shasmal and J. Sengupta: **Structural diversity in bacterial ribosomes: Mycobacterial 70S ribosome structure reveals novel features**, *PLoS One* (2012) 7 (2) e31742

[6] This research was supported by Image Science Consulting Ltd (London, UK and Berlin/Germany); and by FAPESP (Sao Paulo, Brazil).

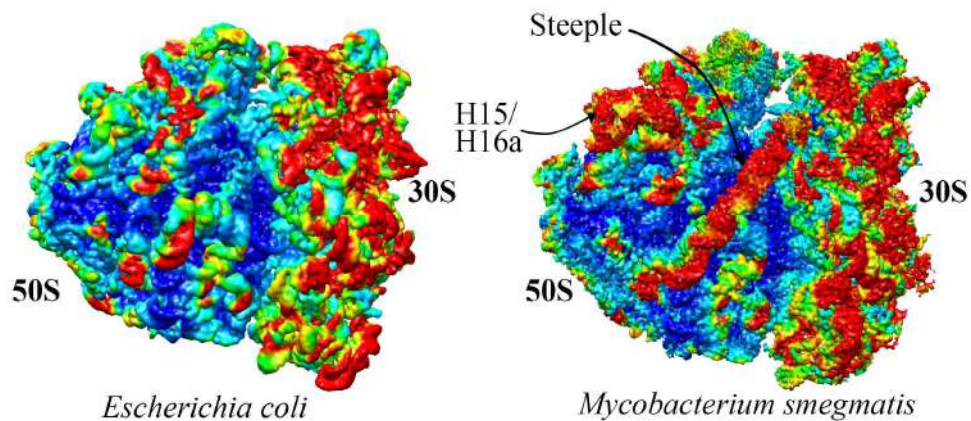


Figure 1: Ribosomes from *Escherichia coli*, a gram-negative bacterium, and *Mycobacterium smegmatis*, an actinobacterium, are very different although they share a similar core structure. *Mycobacterium* ribosomes [EMD-3751] contain extra rRNA helices [5], not present in *E. coli* ribosomes [EMD-3493]. Two main additional rRNA helices the “steeple” helix and helix 15/helix 16A (H15/H16A) are marked. The local cross-information density (LCID) between these maps highlights the differences as shown in red, while the similar core structures are depicted in blue.

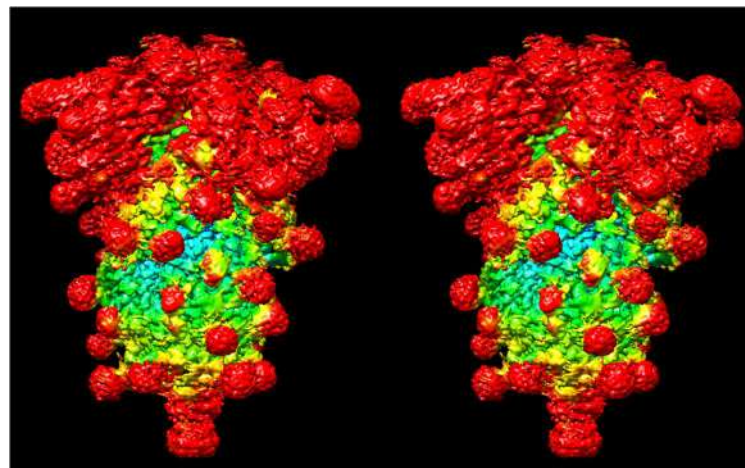


Figure 2: Stereo Pair of a Local Cross-Information Density (LCID) view of SARS-CoV-2 spike protein derived from EMD entry EMD-21452). The image has been coloured using the LCID metric between spike-structure entries (EMD-21452 and EMD-11332). The comparison reveals details of the glycosylation of this corona virus spike trimer whereby the level of glycan visualisation can be adapted using different threshold levels [3].

We thank Ralf Schmidt of Image Science GmbH, Berlin, Germany, for his programming contributions.



Use of Deep Convolutional Neural Networks in Automatic Recognition and Classification of Coal Macerals

Magalhães Santos, R. B.^{1*}; Paciornik, S.¹; Augusto K.S.¹; Alvarez Iglesias, J.C. ²;
Rodrigues, S.³; Esterle, J.S.³; Domingues, A.L.A.⁴

¹ PUC-Rio, Departamento de Engenharia Química e de Materiais (DEQM), Rio de Janeiro, Brasil.

²Strategy, Analytics and M&A, Deloitte, Rio de Janeiro, Brazil.

³University of Queensland, School of Earth and Environmental Sciences, Brisbane, Australia

⁴Vale S.A., Centro de tecnologia de ferrosos (CTF), Belo Horizonte, Brasil

* rbryan2008@hotmail.com

Macerals are the individual constituents of organic matter and have an influence on the quality of the coals, which can be recognized by microscopic analysis. Thus, the microstructural characterization of coal by optical microscopy is a fundamental tool, allowing the identification of the macerals by reflectance, color, morphology, among others [1]. The analysis of these macerals is traditionally performed by a trained petrographer visualizing the polished surface of a specimen under an optical microscope. A fraction of each maceral is estimated counting a statistical number of points, sweeping the entire sample surface (Figure 1). Macerals are identified by their size, shape, color, reflectivity, texture, fungal presence, degradation, degree of gelification, fluorescence and even their relative position to other macerals. There is no clear set of easily extractable parameters that can be used to define a maceral, rendering traditional image analysis and machine learning ineffective [2]. This generates a motivation for the use of deep learning methods, which have proven to be extremely efficient for classifying and recognizing patterns. This work employs a Mask R-CNN model, which is a very elaborate recent architecture of neural network that is currently the state-of-art for instance segmentation. It consists of 2 stages. The first one scans the image and proposes possible bounding boxes for identified objects which are then refined and fed to the second stage. The second stage analyzes the individual bounding boxes and can choose pixels belonging to the object and which ones belong to the background, with the idea that a bounding box contains only a single whole object, even when it overlaps with a different one [3] [4]. After one year and 10 months of intensive work to build a databank with previously classified images, some preliminary results have been achieved. The databank consists of manually tagged macerals with supervision from a professional coal petrographer; the classification of the tagging is made at 3 different levels: Maceral level, Maceral Sub-group level and Maceral group level. The aim is to reach successful segmentations for both sub-group and group level. At group level, the classes consist of: vitrinite, inertinite and liptinite. At sub-group level, the classes consist of: gelovitrinite, telovitrinite, detrovitrinite, geloinertinite, teloinertinite, detroinertinite and liptinite. Currently, the databank is still being expanded to include more samples of different origins and coalification ranks, in the hopes of creating a more generic network capable of tackling a wide array of coal samples. Figure 2 shows a promising segmentation and classification of many macerals at sub-group level.

- [1] Suárez, I., R.; Crelling, C.; Applied Coal Petrology-The Role of Petrology in Coal Utilization-DOI- <https://doi.org/10.1016/B978-0-08-045051-3.X0001-2> (2008).
- [2] Taylor, G.H.; Teichmüller, M.; Davis, A.; Diessel, C.F.K.; Littke, R.; Robert, P.; Organic Petrology 14th edition 1998.
- [3] Girshick, R.; Fast R-CNN, arXiv: 1504.08083v2, (2015).
- [4] He, K.; Dolla, P.; Girshick, R.; Gkioxari, G.; Mask R-CNN. arXiv:1703.06870v3 (2018)
- [5] This research was supported by CAPES, CNPq and FAPERJ (Brazil).

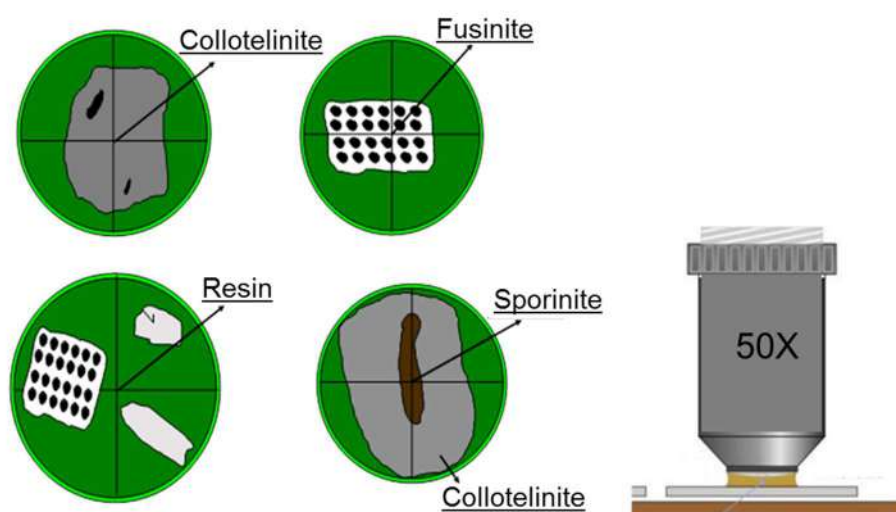


Figure 1- Illustration of the point count analysis use for maceral estimation.

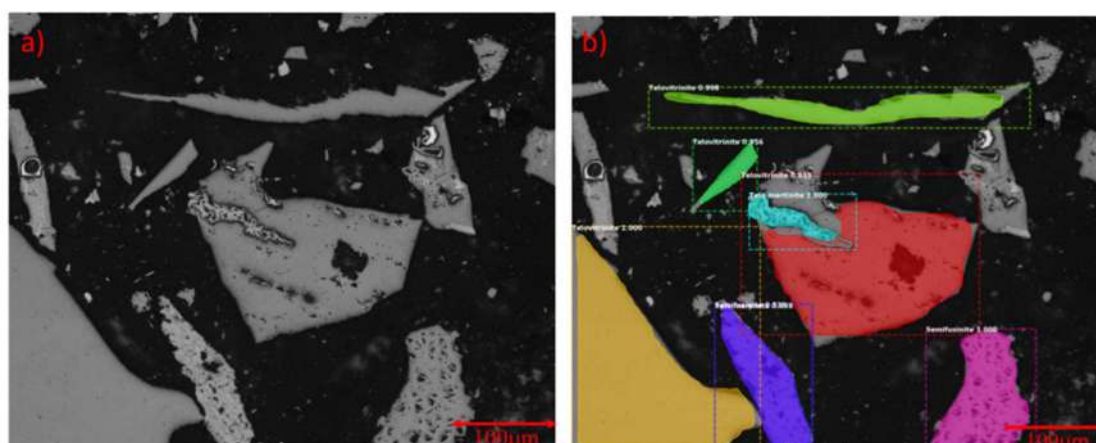


Figure 2- Preliminary result. a) Original image. b) Automatic classification of macerals at subgroup level.



Elemental and structural analysis of granular deposits in the bone growth zone of fin bony rays of zebrafish (*Danio rerio*)

Marcos Farina^{1*}, Jacques Werckmann², Andréa P.C. Campos³ Mair M.M. de Oliveira¹
and Ovidiu Ersen⁴

¹ Programa de Bioengenharia e Terapia Celular/Instituto de Ciências Biomédicas-UFRJ, Rio de Janeiro, RJ, Brasil.

² Centro Brasileiro de Pesquisas, Rio de Janeiro, RJ, Brasil.

³ CNRS, Centrale Marseille, FSCM (FR1739), CP2M, Aix Marseille Univ, 13397 Marseille, France

⁴ Institut de Physique et Chimie des Matériaux de Strasbourg (IPCMS), UMR 7504 CNRS, Université de Strasbourg, 23 rue du Loess, 67034 Strasbourg, France

*marcos.farina.souza@gmail.com

Bone tissue has been intensely studied for a long period of time which has produced a vast literature on its biology and structure, including anatomy, histology, and other aspects. Progress in the knowledge of bone as an organ or specific tissues got a huge development recently specifically due to state of the art imaging methods such as micro computed tomography, analytical and ultrahigh resolution methods such as transmission electron microscopy and atom probe tomography. Concerning the morphological organization of bone, new findings on its hierarchical organization in different length scales have been proposed as a fractal like pattern [1] and a new mechanism of mineralization associated with bone cells in vivo constituted by amorphous calcium phosphate (ACP) granules extruded by osteoblast cells [2]. The zebrafish (*Danio rerio*) has been used as a model for the study of some organs and tissues as the bone (Fig. 1A), due to similarities with other vertebrates along its development. It was described recently that besides matrix vesicles and mineralization directly associated to collagen or collagen-associated molecules, intracellular granules containing amorphous calcium phosphates (ACP), could participate as additional sources of calcium and phosphate ions after being outsourced by the osteoblast cells to the extracellular milieu [2]. In this work we analyzed the ACP granules from the bone growth zone (bgz), situated between the cell layer and the mineralization front in transverse sections of the middle region of fin ray bones (Fig. 1B). We found two types of granular deposits (Fig. 1C and inserts c1 and c2), both containing calcium detected by EELSpectroscopy (Fig. 1D). One granule has a smooth texture and is similar to those previously described (c1) [2], while the second one is composed by an aggregation of needle like particles (c2), corresponding probably to mineralized collagen fibrils present in the bgz. These original findings show that, although bgz contains many ACP granules in transit to the mineralization front, it can also contain some collagen fibrils isolated from the bonny region capable to mineralize independently.

References

[1] Reznikov et al., *Science* 360, 507 (2018)

[2] J. Mahamid et al., *Cells Tissues Organs* (2011)194:92–97.

Acknowledgements:

CNPq and Faperj Brazilian agencies and by the LIA project from CNRS – France.

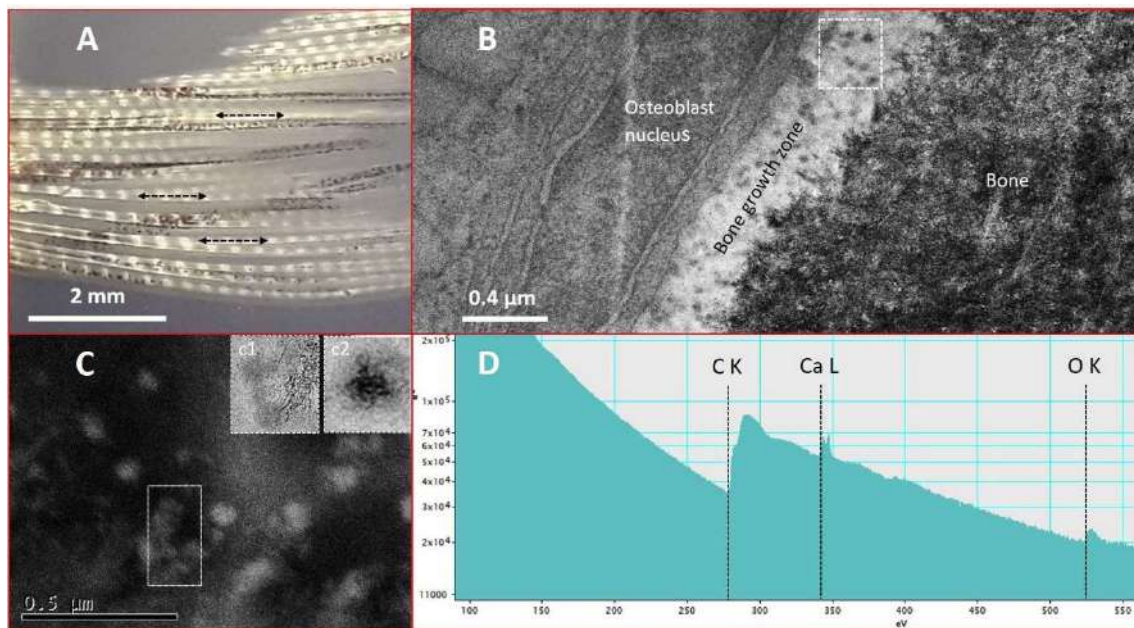


Fig. 1: Multiscale analytical analysis of fin bones of the zebrafish. A) Polarization light microscopy of part of the fin from zebrafish where several bonny rays belonging to the intermediate region (more near the fish's body, located in the left side of the figure) are observed; B) Transmission electron microscopy (TEM) image of an ultrathin section transverse to the bonny rays, from a region similar to the previous figure. Three main regions are indicated. In the bone growth zone (*bgz*), several dark-grey or dark regions are seen (e.g.: inside the square with a dotted contour); C) High Angle Annular Dark Field (HAADF) enlarged image of a region composed by granules from a *bgz*. Insert c1: granules with a dark-grey appearance near newly formed nanocrystals (needle-like particles); Insert c2: black regions composed of groups of elongated deposits; D) Electron energy loss spectrum obtained from the region delimited by the rectangle in C), showing the presence of calcium and oxygen, corresponding to dark-grey amorphous granules, which are expected to act as a source of ions for the bone formation.



Insight by In Situ-TEM Into the Nucleation and Crystallization Processes of Calcium Phosphate Nanoparticles

Gisele Dalmônico¹, Dris Ihiawakrim², Nathaly Ortiz², Marcos Farina³, Ovidiu Ersen² and André L. Rossi^{4*}

¹ Centro Nacional de Pesquisa em Energia e Materiais (CNPEM/LNNANO) - Brasil.

² Institut de Physique et Chimie des Matériaux de Strasbourg (IPCMS) - France.

³ Universidade Federal do Rio de Janeiro (UFRJ/ICB) - Brasil.

⁴ Centro Brasileiro de Pesquisas Físicas (CBPF) - Brasil.

*alinhares@cbpf.br

Calcium phosphates (CaP) are a class of materials that attracts strong interest in many research areas. They are the main inorganic constituents of the calcified tissues of vertebrates (bones and teeth) and can be used in bone implants due to their remarkable biocompatibility and bioactivity. Among the multitude of calcium phosphates, hydroxyapatite (HA) is the most stable phase under body fluid conditions. The processes involving nucleation and growth of HA are under intense debate as the technical difficulties to interpret and conclude about these events are related with the reaction times and particles dimension. In-situ TEM (Transmission Electron Microscopy) is a unique technique for the study of CaP crystallization in aqueous medium at the nanoscale. In this work HA was synthesized by using calcium hydroxide and phosphoric acid solutions prepared just before the analyses. In a previous work we performed a detailed characterization of the synthesis and products by using Cryo-TEM [1]. A Protochips liquid cell holder (Poseidon Select 550) was used in a JEOL 2100F/Cs(S) TEM. The reaction was followed in the microscope during 15 h and three main steps were observed and recorded: (1) dissolution of Ca(OH)_2 and formation of a dense liquid phase; (2) formation of amorphous calcium phosphate and; (3) formation of HA needles. The needle or plate-like morphologies are typical of synthetic and biological HA observed edge-on and thus a strong indication of HA formation. Only two works until now investigated the nucleation and growth of biomimetic CaP by using In Situ-TEM but the exact moment of the needle-like crystals formation was not recorded. This information was registered in the present work.

[1] Dalmônico et al., *Materials Chemistry and Physics* (2019) 237.

[4] This research was supported by CNPq and FAPERJ (Brazil).

Acknowledgments: The authors wish to thank LABNANO/CBPF, CAPES, CNPq and FAPERJ and International Associated Laboratory (LIA-CNRS).



Intrinsic Antitumor Properties of Gum Arabic-Gold Nanocomposites

Jenifer P Gonçalves¹, Anderson F da Cruz¹, Ábner M Nunes², Mario R Meneghetti², Heloise R de Barros³, Beatriz S Borges⁴, Lia CAS de Medeiros⁴, Maurilio J Soares⁴, Gustavo R Rossi¹, Daniel L Bellan¹, Stelée MP Biscaia¹, Aline M Cristal¹, Edvaldo da S Trindade¹, Fernanda F Simas¹, Izabel C Riegel-Vidotti³, Carolina C de Oliveira^{1*}

¹ Laboratory of Inflammatory and Neoplastic Cells, Cell Biology Department, Universidade Federal do Paraná (UFPR), Curitiba, Brazil.

² Catalysis and Chemical Reactivity Group, Institute of Chemistry and Biotechnology, Universidade Federal de Alagoas, Maceió, Brazil.

³ Macromolecules and Interfaces Research Group, Chemistry Department, UFPR, Curitiba, Brazil.

⁴ Laboratory of Cell Biology - Instituto Carlos Chagas (ICC/Fiocruz), Curitiba, Brazil.

*krokoli@ufpr.br

Physicochemical properties of gold nanoparticles makes them a simple platform for functionalization. It is known that shapes and sizes affect their effects in a biological environment. However, their intrinsic antitumor action still needs clarification [1]. Therefore, here we investigated gold nanospheres (AuNS) and nanorods (AuNR), functionalized with the natural heteropolysaccharide Gum Arabic (GA), as possible antitumor agents. GA-AuNS and GA-AuNR were chemically synthesized [2,3] and their morphologies were confirmed by transmission electron microscopy (fig.1 A and B). Melanoma cells (B16-F10) and fibroblasts (BALB/3T3) were exposed *in vitro* for 96h to different concentrations of GA-AuNS and GA-AuNR, and cell number and endomembranes viability were evaluated through colorimetric assays (fig. 1 C). For both groups, cell number decreased in a concentration-dependent manner compared to GA alone. An opposite trend was observed for endomembrane viability, indicating that the higher concentration induced vesicles accumulation, which resulted in higher incorporation of the neutral red dye. TEM images revealed both nanocomposites attached to the cell membrane, intracellularly in the cytosol and inside intracellular vesicles (fig. 1 D), corroborating nanoparticles internalization. Primary tumor and experimental lung metastasis experiments were performed in mice (C57BL/6) by B16-F10 cells subcutaneous and intravenous injection. Treatment with GA-AuNS and GA-AuNR was initiated after 5 days and was maintained for 10 consecutive days. GA-AuNS treatment did not affect tumor growth (fig. 1 E) or lung metastasis (data not shown). However, GA-AuNR showed reduction in both parameters, factors that contribute to a better prognosis. These results showed that even with similar *in vitro* results only GA-AuNR was able to impair *in vivo* melanoma progression, being a good candidate as a new antitumor agent.

REFERENCES:

- [1] Part of this abstract is published at GONÇALVES, J. P. et al., Eur J Pharm Biopharm, 157 (2020)
- [2] SILVA, M. G. A. et al. Comptes Rendus Chimie, 16 (2013).
- [3] DE BARROS, H. R. et al. RSC Advances, 6 (2016).

ACKNOWLEDGEMENTS:

CAPES for student fellowship and Electron Microscopy Center of UFPR (CME-UFPR) and LabCet (ICC/Fiocruz) for kindly providing the BALB/3T3 cells.

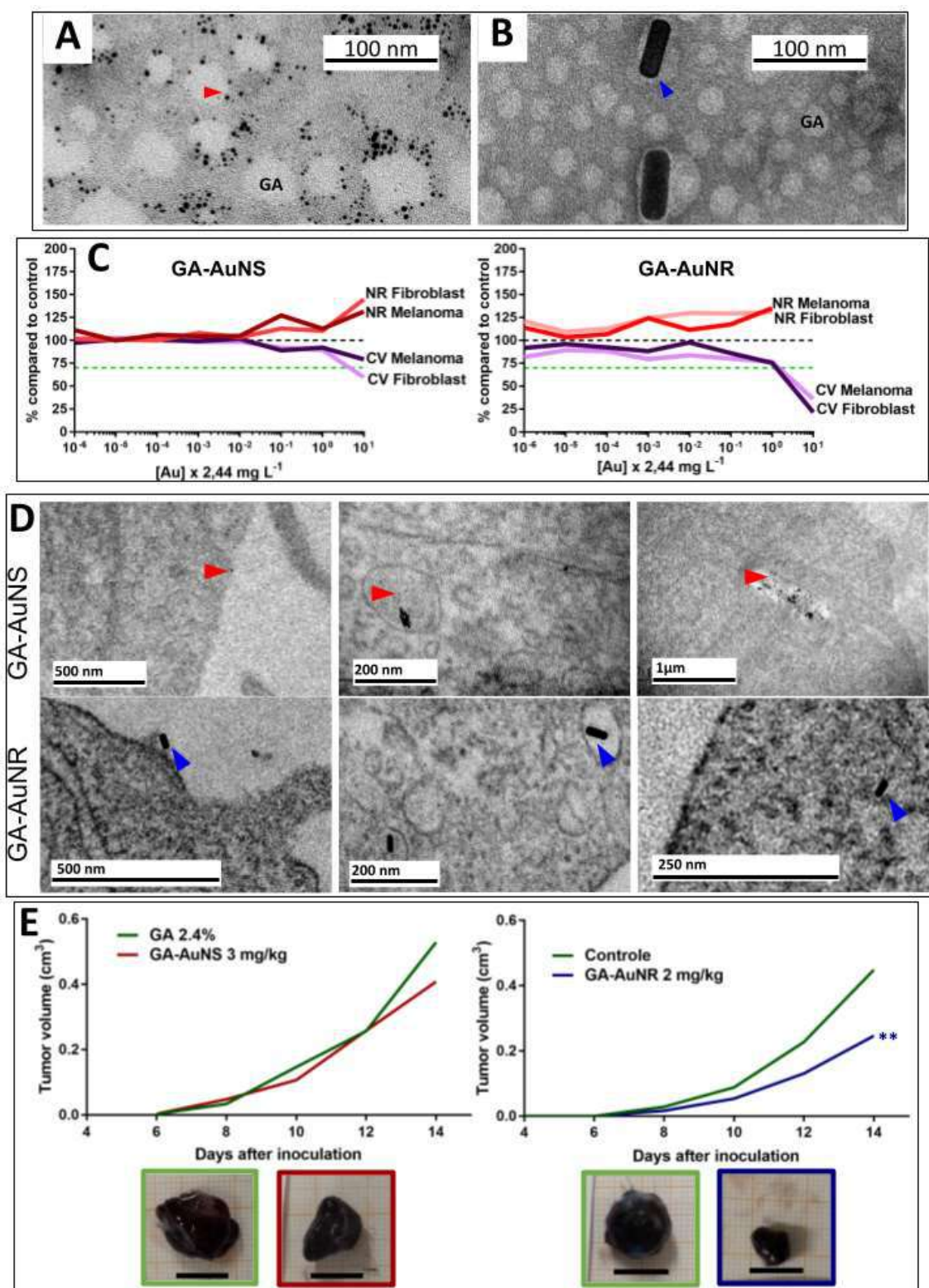


Figure 1. Results from *in vitro* and *in vivo* experiments. (A and B) TEM of GA-AuNS and GA-AuNR. (C) Colorimetric assays of melanoma and fibroblasts exposed to the nanocomposites. (D) TEM sections of melanoma cells treated with nanocomposites. (E) *In vivo* assay: Difference in tumor evolution after treatment with the nanocomposites and representative tumor for each group, scale bar = 1cm. Red sets indicate GA-AuNS and blue indicate GA-AuNR.



Conjugation of Spike and Nucleocapsid Proteins of SARS-CoV-2 with Gold Nanoparticles

Luis Alberto Contreras¹, Wanderson Juvencio Keijok¹, Jairo Pinto de Oliveira¹ and Marco Cesar Cunegundes Guimarães^{1*}

¹ Laboratory of Functional Nanomaterials. Federal University of Espirito Santo, Av Marechal Campos 1468, Vitória, ES 29.040-090, Brazil.

* e-mail: marco.guimaraes@ufes.br

The coronavirus disease (COVID-19) caused by the new coronavirus named as severe acute respiratory syndrome coronavirus 2 (SARS-CoV-2) has spread rapidly around the world causing a serious pandemic [1]. The alarming growth of this pandemic makes it necessary to know and implement reliable diagnostic methods to properly detect and treat patients, which will help slow the spread of the disease. The Spike (S) protein and the Nucleocapsid (N) protein of coronaviruses are known to be the main targets of the humoral immune response (that is to say, antibody) and are therefore used in most tests to detect antibodies to SARS-CoV-2 [2]. In this work we report the bioconjugation of two viral proteins, protein S and protein N, to gold nanoparticles (AuNPs). Successfully showing the formation of bioconjugates for their use as biosensors in different devices (paper platforms, microfluidic chips) allowing a reliable diagnosis of the SARS-CoV-2 that causes Covid-19.

A synthesis of AuNPs was performed using a variation of the Turkevich method [3]. For the characterization of the AuNPs, UV-Vis spectroscopy and transmission electron microscopy were used, obtaining monodisperse AuNPs of approximately 20 nm. Viral proteins were linked to AuNPs by covalent bonds using: thiolated mercaptohexadecanoic (MUA), 1-ethyl-3-(3-dimethylaminopropyl) carbodiimide hydrochloride and N-hydroxysuccinamide (EDC / NHS) [4]. The formation of the bioconjugate was verified with the Bradford test by measuring the absorbance at a wavelength of 595 nm on the UV-vis spectrophotometer. In addition, Raman spectroscopy was performed on the bioconjugate, confirming the presence of the viral proteins on the surface of the AuNPs.

Keywords: Bioconjugate, Protein Spike, Protein Nucleocapsid, Gold Nanoparticle.

Bibliography:

- [1] SHENG, N., Xue-Ping, M., Shu-Yun, P. A. N. G., Qin-Xin, S. O. N. G., Bing-Jie, Z. O. U., & Guo-Hua, Z. H. O. U. (2020). Research Progress of Nucleic Acid Detection Technology Platforms for New Coronavirus SARS-CoV-2. *Chinese Journal of Analytical Chemistry*, 48(10), 1279-1287.
- [2] Sheikhzadeh, E., Eissa, S., Ismail, A., & Zourob, M. (2020). Diagnostic techniques for COVID-19 and new developments. *Talanta*, 121392.
- [3] J. Turkevich; P.C. Stevenson; S. Hiller *Discuss. Faraday Soc.*, 1951,11, 55.
- [4] Oliveira, J. P., Prado, A. R., Keijok, W. J., Antunes, P. W. P., Yapuchura, E. R., & Guimarães, M. C. C. (2019). Impact of conjugation strategies for targeting of antibodies in gold nanoparticles for ultrasensitive detection of 17 β -estradiol. *Scientific reports*, 9(1), 1-8.



Acknowledgements:

Foundation for Amparo Research and Innovation of Espírito Santo - FAPES
Laboratory of Functional Nanomaterials of the Federal University of Espírito Santo.
Laboratório de Ultraestrutura Celular Carlos Alberto Redins - LUCCAR of the Federal University of Espírito Santo.

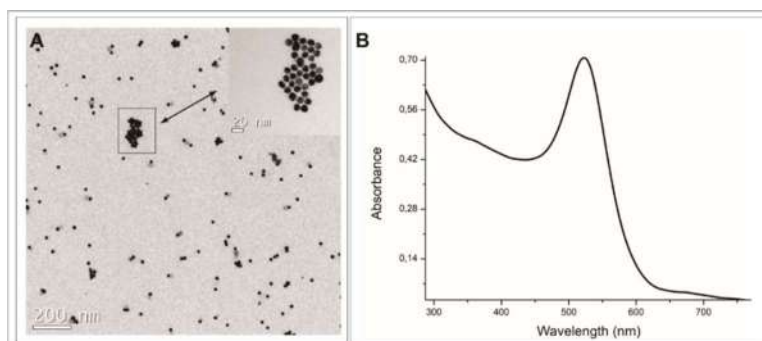


Figure 1. Gold nanoparticles of approximately 20 nm using Transmission electron microscopy (A). UV-Visible absorption spectroscopy for the synthesized gold colloid showing the characteristic plasmonic peak at 522nm (B).

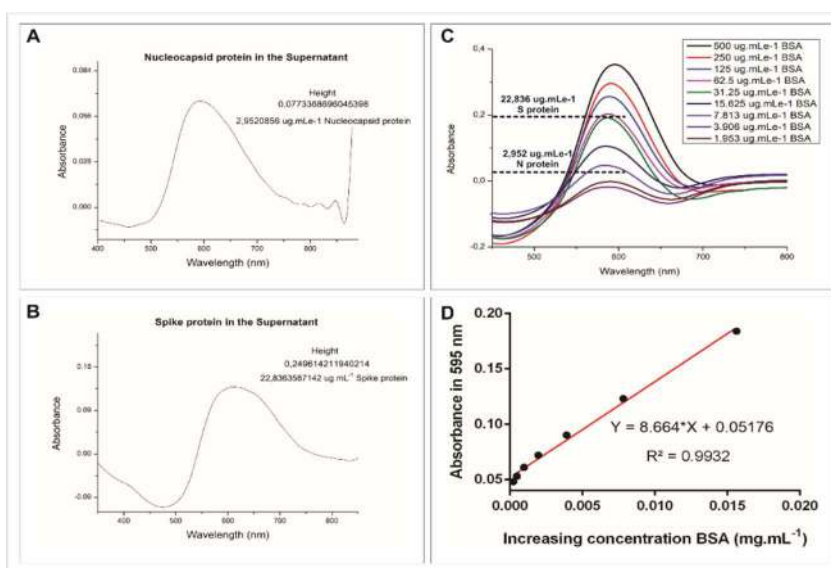


Figure 2. UV-Visible absorption spectroscopy of total protein dosage with Bradford (595 nm) supernatant from the bioconjugation of gold nanoparticles with protein N (A) and protein S (B). UV-Visible absorption spectrum in the detection of BSA (C). Adequate obtained in options 500 to 1.953 $\mu\text{g mL}^{-1}$ (D).

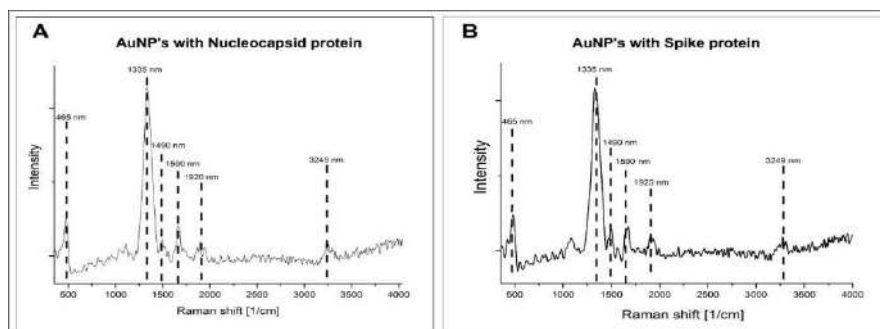


Figure 3. Raman spectroscopy of AuNPs with protein N (A) and protein S (B).



High Quality Quantitative Structural Analysis of Nanosystems using Pair Distribution Function (PDF) based on Precession Electron Diffraction (PED)

Leonardo Corrêa^{1*}, Murilo Moreira¹, Varlei Rodrigues¹ and Daniel Ugarte¹

¹ Inst. de Física “Gleb Wataghin”, Univ. Estadual de Campinas, Campinas-SP, Brazil
*lmcorra@ifi.unicamp.br

Nanoparticles (NPs) attract great interest in the research community due to the possibility of obtaining unique properties due to size-induced effects. The control of NP structural properties demands characterization techniques capable of providing quantitative and representative information that is not always possible using conventional experimental methods. Pair Distribution Function (PDF) has proved to be an excellent option to perform quantitative structural analysis in nanosystems [1]. Electron-based PDF (ePDF) is an alternative to study nanovolumes of materials due to the strong electron-matter interaction; unfortunately, multiple scattering renders the quantitative evaluation of electron diffraction (ED) intensities rather complex and time consuming. But, Precession Electron Diffraction (PED) yields diffraction patterns with a “quasi-kinematical” character, such that modeling and intensity interpretation can be performed using the simple single scattering calculation used for x-ray (kinematical approximation) [2]. Here, we describe the implementation of a methodology to derive ePDF from PED data, and show that the quantitative comparison with kinematical models attain residues values very close to the ones derived from synchrotron-based experiments [3]. We have developed a software in Python language, which perform all the ED processing steps and structural refinement based on the ePDF curve. We have analyzed metal (AuAg) NPs generated by home-made cluster source (see Fig. 1a) and TEM experiments were made in a TECNAI G2 microscope (200 keV) coupled with CCD camera and ASTAR precession system, (LCE-DEMa-UFSCar). The best description of our measurement (e.g., see Fig. 1b) has been obtained for decahedral NPs of 3 nm in diameter (\emptyset). Our results show that PED is best suited for PDF analysis, improving residues for all analyzed cases in relation to the traditional selected area electron diffraction (SAED). The obtained small residue values are associated to the use of PED and to a careful subtraction of amorphous carbon substrate background. The inclusion of size dispersion to our Dh model resulted in a residue of 15% (Fig. 2), similar to synchrotron values for metal NPs [3]. The NPs show complex polycrystalline structures. However, we have been able to derive quantitatively several structural information that cannot be obtained from atomic resolution images. Electron diffraction were measured for a region with ~ 2000 NPs (below a pictogram of sample material), with electron dose of $\sim 10 \text{ e}^-/\text{\AA}^2$. So, we anticipate that PED-based PDF will become a reliable approach to analyze quantitatively the statistical properties of complex NPs samples, including polycrystalline and beam sensitive materials [4].

References

- [1] T. Egami et al., *Underneath the Bragg Peaks Structural Analysis of Complex Materials*, Elsevier, Oxford, 2003.
- [2] P. A. Midgley et al., *IUCrJ*, 2 (2015) 126.
- [3] S. Banerjee et al., *J. Phys. Chem. C*, 122 (2018) 29498.

[4] This research was supported by CNPq, CAPES and FAPESP (Brazil).

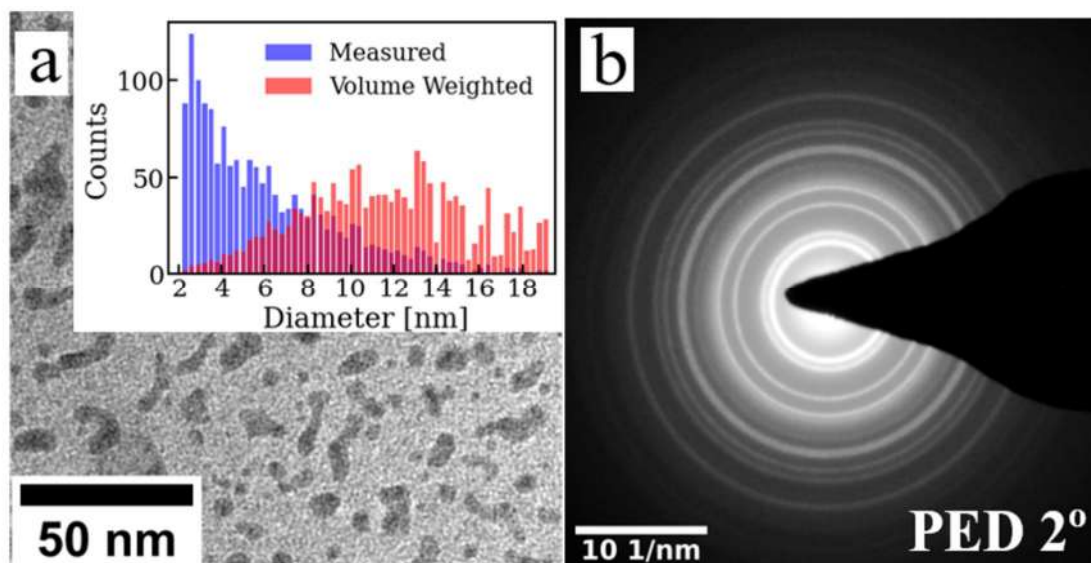


Figure 1: a) TEM image of the measured AuAg NPs. Inset: measured size distribution and it weighted by volume as diffraction is volume sensitive. b) PED pattern utilized in our analysis.

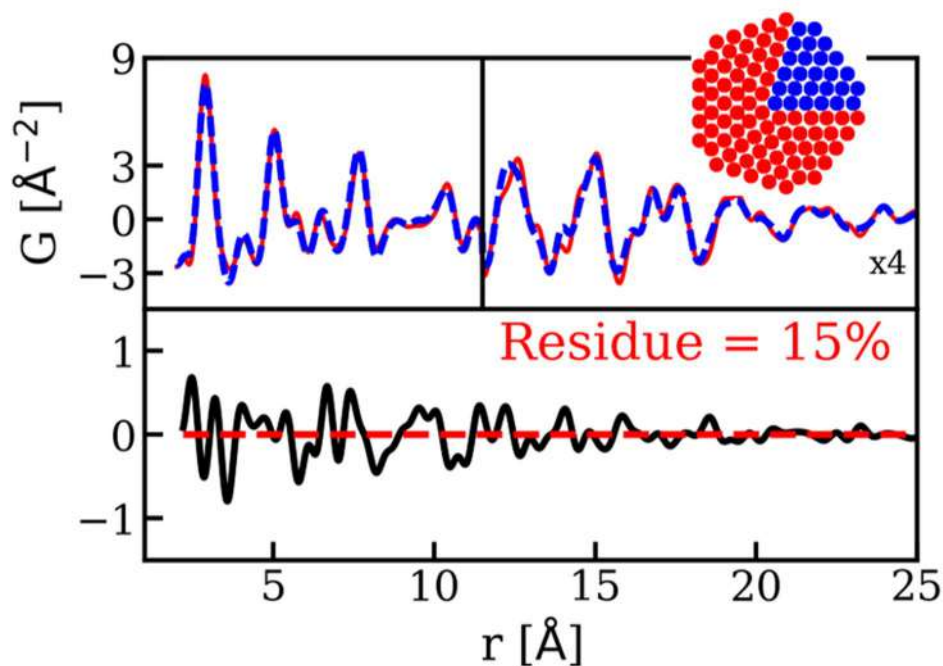


Figure 2. Comparison between the measured PED ePDF (continuous line) and optimized ePDF for the Dhs with size distribution (dashed line). The region after 11.5 Å is multiplied by a 4 factor to improve visualization. The difference curve is plotted at the bottom.



Finding Hidden Correlations in EDS Hyperspectral images: Elemental Distribution Inside of small Bimetallic Nanoparticles.

Murilo Moreira^{1,2*}, Matthias Hillenkamp², Varlei Rodrigues¹, Daniel Ugarte¹

¹ Univ. Estadual de Campinas, Inst. de Física “Gleb Wataghin”, Brazil.

² Univ. Claude Bernard Lyon I, Inst. of Light and Matter, France.

*moreiraz@ifi.unicamp.br

Bimetallic nanoparticles (BNPs) can display different types of structures and adopt different morphologies and even chemical order. By controlling the size and chemical composition, different physical and chemical properties can be obtained due to quantum and surface-induced phenomena. Hence, it is of great interest to establish reliable methods for the characterization of chemical composition and elemental distribution of single small BNP (sub-10 nm). STEM-based methods have allowed measurements with a high degree of reliability and reproducibility, generating huge sets of 3D or 4D data, called hyperspectral images (HSIs). In this way, new and advanced statistical tools from machine learning have been employed to better exploit the dataset information. For example, Nonnegative Matrix Factorization (NMF), an unsupervised method to find hidden correlations, can be used as blind source separation (BSS) [1], allowing evaluate the signals such as different chemical phases in HSIs without human bias. In this work, we will describe the measurement of the chemical composition of benchmark AgAu BNPs using Energy-dispersive X-ray Spectroscopy (EDS) combined with Scanning Transmission Electron Microscope (STEM), in a Titan-Themis Cubed operated at 80 kV. In particular, we have explored the use NMF to find elemental distribution hidden in nanoalloys to measure element segregation. By combining experimental data analysis and simulations, we have been able to reveal the complete signal separation of an alloy core of AgAu from an Ag-rich shell, meaning chemical segregation, as can be seen in Figure 1. Besides the apparently elemental mixing observed in raw image spectra, NMF enhances the identification of an Ag shell between 0.5 and 1 nm depending on the BNP system analyzed. Additionally, from the signal associated with the core of the BNPs it is possible to retrieve the quantitative information as demonstrated by the simulations. Therefore, we measured a core chemical composition average of ~70% in Au atoms, while the full BNPs chemical composition average is ~50%. Efforts are still being performed to estimate an uncertainty interval such that the analysis of signal-to-noise-ratio improvement by data reconstruction from the NMF decomposed components. These results thus demonstrate the possibility of measurement of chemical composition distribution inside small BNPs, on the single-particle level and open the way for further studies concerning elemental patterns (random, gradients, coreshell, Janus, etc.) in small BNPs.

REFERENCES

[1] O. Nicoletti, et al., Nature 502 (2013): 80-84.

[2] Brazilian Agencies FAPESP, CNPq and CAPES are gratefully acknowledged for financial support. Funding European Union Seventh Framework Program is gratefully acknowledged.

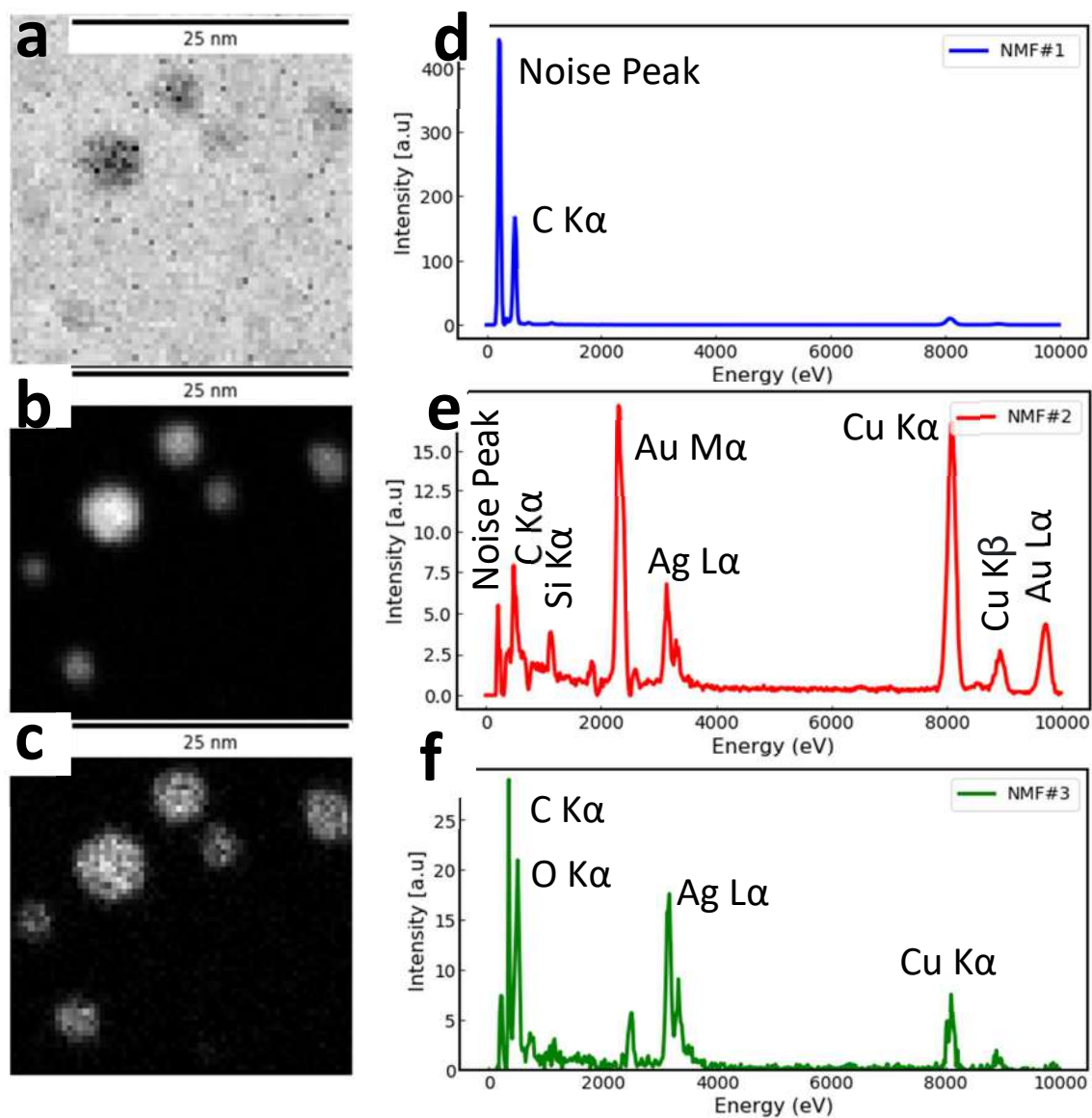


Figure 1 – NMF decomposition results of a HSI obtained by STEM-EDS of small AgAu BNPS. Spatial components associated to a) background, b) AgAu core, c) Ag oxide shell and respective spectral components in d), e) and f) addressing the chemical signature.



Phase Identification in NaNbO_3 Perovskite Nanoribbons by STEM - DPC

Beatriz Canabarro^{1*}, Sebastian Calderon², Paulo Ferreira² and Paula Jardim¹

¹ DEMM-COPPE/UFRJ, Rio de Janeiro, Brazil.

² INL, Braga, Portugal.

*canabarro@metalmat.ufrj.br

Perovskites are a well-known group of oxide ceramics (ABO_3) that can exhibit many different phases depending on the temperature, due to octahedral distortions in their structure. In the case of NaNbO_3 , Megaw *et al.* (1974) [1] have described the presence of seven different phases, although recently more phases have been found. One interesting ferroelectric phase (Q) is metastable at room temperature and can be induced from the P phase (antiferroelectric and stable at room temperature) by large electric fields, doping, or mechanical stress [2]. In this study, we investigate the phase(s) present in nanoribbons of NaNbO_3 , when grew over metallic niobium platelets and evaluate their microstructure. For this purpose, high-angle annular dark-field (HAADF), annular bright-field (ABF), and differential phase contrast (DPC) scanning transmission electron microscopy (STEM) was used. The images were collected using an aberration-corrected Titan Themis 80-300 operated at 200 kV with a convergence semi-angle of 21 mrad. The experimental images obtained were compared with multislice computer simulations. We have considered three different zone axis ([100], [010] and [001]) (Figure 1) using Dr. Probe V1.9 software [3]. The structure models of P (s.g.: P₆mm - PDF code 33-1270) and Q phases (s.g.: P₂1ma - PDF code 38-1249), an acceleration voltage of 200kV, 100 frozen lattices and the microscope setups reported by Haas *et al.* (2019) [4] were used. The simulated images show that a distinction between the P and Q phases is possible along the [010] zone axis, using the ABF or DPC detectors, due to the position of the oxygen atomic columns. Yet, when ABF and DPC images are compared, it is clear that the latter is much more sensitive, particularly when iDPC images are used (Figure 2). Under these conditions, we observed that apparently the Q phase is present in the nanoribbons, and that the Na and O atoms show displacement with respect to the Nb atoms, which indicate local spontaneous polarization. This result corroborates the hypothesis that the nanometric form also stabilizes the metastable phase.

REFERENCES

- [1] H. D. Megaw, *Ferroelectrics*, 7 (1974) 87.
- [2] H. Zhang *et al.*, *Acta Mater.*, 179 (2019) 255.
- [3] J. Barthel, *Ultramicroscopy*, 193 (2018) 1.
- [4] B. Haas *et al.*, *Ultramicroscopy*, 198 (2019) 58.

Acknowledgments:

The authors acknowledge the financial support by Coordenação de Aperfeiçoamento de Pessoal de Nível Superior (CAPES) - Finance Code 001.

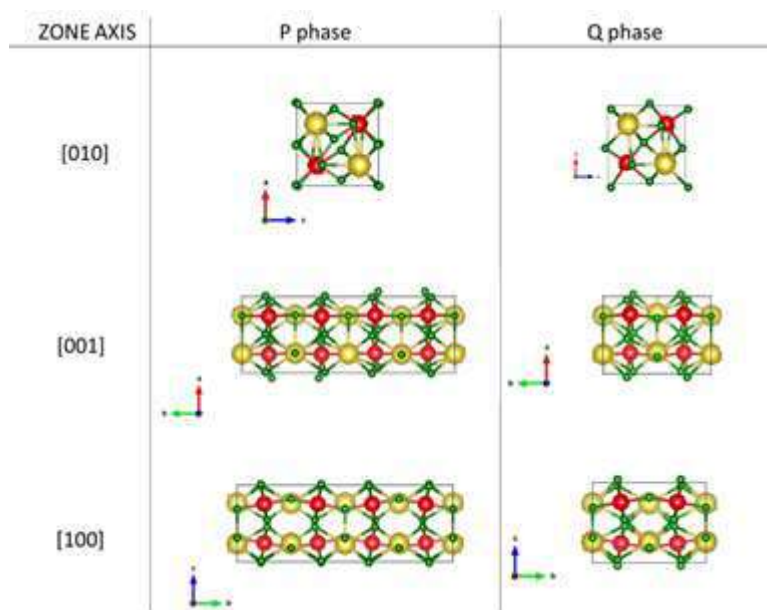


Figure 1- The unit cell structure models of P (s.g.: $Pbma$ - PDF code 33-1270) and Q phases (s.g.: $P2_1ma$ - PDF code 38-1249) seen in the three different zone axis ([100], [010] and [001]) chosen to be simulated. The Nb atoms are represented in red, the Na in yellow, and the O in green.

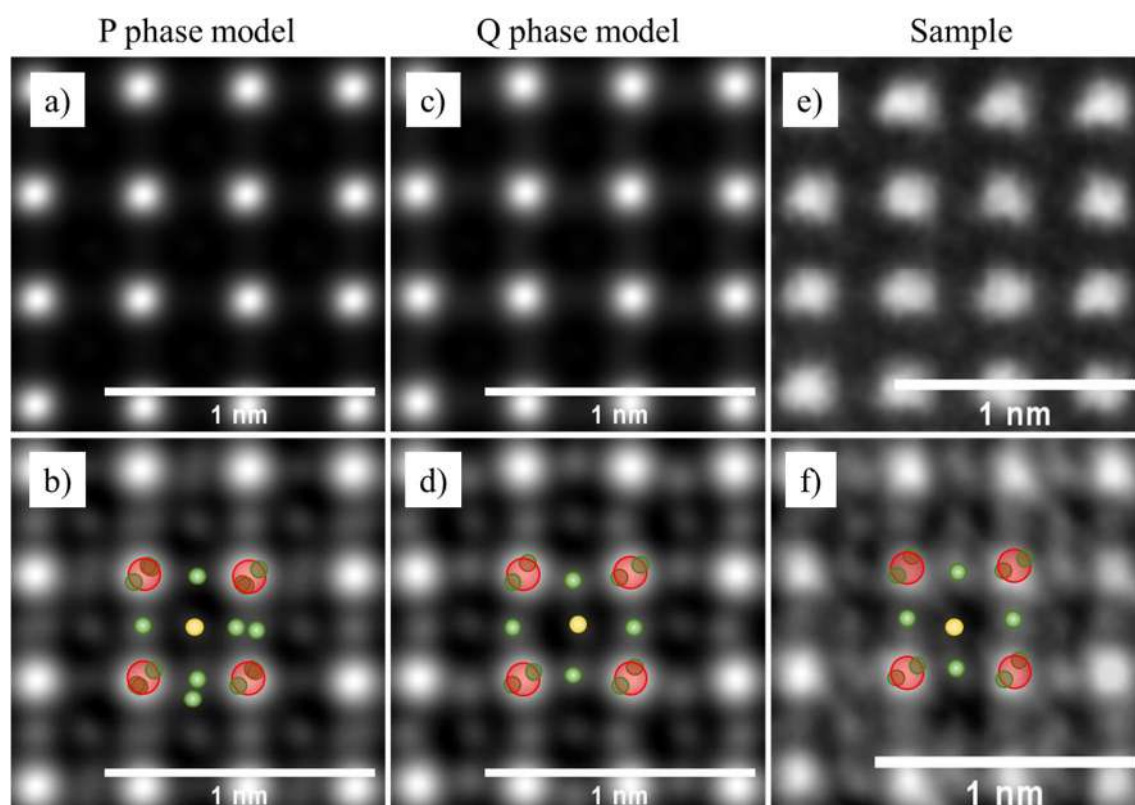


Figure 2 – HRSTEM HAADF and iDPC images of P phase model (a,b), and Q phase model (c,d) simulated using Dr. Probe compared to sample images (e,f). Over the iDPC images, there is the representation of the atoms in the zone axis [010] (the Nb in red, the Na in yellow, and the O in green).



Experimental Evaluation of the Stacking Fault Energy of a Fe-Mn Alloy Through the Measurement of the Partial Dislocations Distance

Lucas B. Otani^{1*}, André L. Vidilli¹, Claudio S. Kiminami², Walter J. Botta², Francisco G. Coury², Guilherme Zepon² and Claudemiro Bolfarini²

¹ Graduate Program in Materials Science and Engineering (PPGCEM), Federal University of Sao Carlos (UFSCar), Sao Carlos, SP, Brazil

² Department of Materials Engineering, Federal University of Sao Carlos (UFSCar), Sao Carlos, SP, Brazil

*lucasbotani@gmail.com

One of the main parameters to determine the mechanical behavior of an FCC metallic alloy is the Stacking Fault Energy (SFE). This parameter is associated with the strain hardening capacity of the material and it is often correlated to some mechanisms as the Transformation Induced Plasticity (TRIP) and Twinning Induced Plasticity (TWIP) effects. Both phenomena are described as efficient in increasing both the strength and elongation at fracture of the material. High-Mn steels are alloys that belongs to the second and third generation of the well-known Advanced High Strength Steels (AHSS), in which the TRIP and TWIP effects may be present, directly impacting the final mechanical behavior of the material [1]. There are three main methods to obtain the SFE of an alloy: ab initio approach, thermodynamic calculations, and the experimental determination of the partial dislocations by Transmission Electron Microscopy (TEM). The second method is the most used due to its ease of use and relatively simple calculations. However, there is a non-negligible difference by the models that are currently being applied in the literature to determine the SFE via thermodynamic calculations [2-5]. From all the above, the objective of this work was to experimentally determine the SFE through the partial dislocations distance measurement and confront this value with the thermodynamic models present in the literature. A completely recrystallized Fe-36.9%Mn-0.02%C alloy was processed and submitted to a cold rolling step with a thickness reduction of less than 1% to induce the presence of dislocations. One sample was prepared by grinding until 80 μm of thickness and stamped into 3 mm discs. The final preparation was made by a Precision Ion Polishing System (PIPS) operating at 5 keV. A Tecnai G² F20 (FEI, Hillsboro, OR, USA) TEM operating at 200 kV and equipped with a field emission gun (FEG) was used for this study. The Weak-Beam Dark Field (WBDF) technique was used to determine the distance from the partials in a g(4g) condition with the beam direction near the [111] zone. Four different pairs of partial dislocations were observed and measured by image analysis. An equation was used to correlate the partial distances and the SFE [6]. The experimental value was 28.1 ± 8.6 mJ/m². In the end, five different sets of equations present in the literature were used to calculate the SFE of the composition through the thermodynamic approach and compared to the experimental results. The main conclusion is that for the composition studied in this work, just two of the models appeared to have a better correlation to the experimental results.

[1] B. De Cooman et al., Acta Mater. 142 (2018) 283.

[2] A. Saeed-Akbari et al., Metall. Mater. Trans. A 40 (2009) 3076.

- [3] O. A. Zambrano, J. Eng. Mater. Techn. 138 (2016) 041010.
 [4] S. Lee et al., J. Alloys Compd. 617 (2014) 588.
 [5] L. B. Otani et al., Metals 10 (2020) 352.
 [6] D. T. Pierce et al., Acta Mater. 68 (2014) 238.

The authors thank the Laboratory of Structural Characterization (LCE/DEMa/UFSCar) for the general facilities. This study was financed in part by the Coordenação de Aperfeiçoamento de Pessoal de Nível Superior - Brasil (CAPES) - Finance Code 001; São Paulo Research Foundation (FAPESP), grant 2017/14805-1 and 2013/05987-8; and Conselho Nacional de Desenvolvimento Científico e Tecnológico, grant 141053/2017-8.

Equation 1 – Correlation between the SFE and the distance between the partial dislocations [1].

$$SFE \left(\frac{mJ}{m^2} \right) = \frac{\mu_{eff} b_p^2}{8\pi d_{actual}} \frac{2 - \nu_{eff}}{1 - \nu_{eff}} \left(1 - \frac{2\nu_{eff} \cos 2\beta}{2 - \nu_{eff}} \right)$$

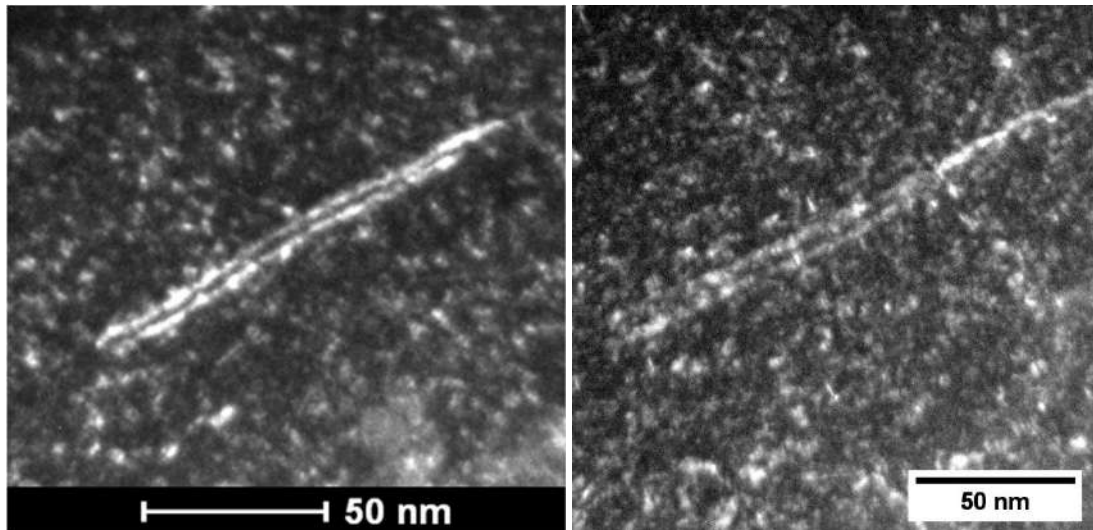


Figure 1 – Examples of partial dislocations images acquired through WBDF-TEM technique.

Table 1 – Distance of the partial dislocations evaluated through WBDF-TEM and the respective SFE value considering its character angle.

	Distance of the partials	Character Angle	SFE (mJ/m ²)
Dislocation 1	4.67 x 10 ⁻⁹ m	90°	35.3
Dislocation 2	6.01 x 10 ⁻⁹ m	36°	19.7
Dislocation 3	4.57 x 10 ⁻⁹ m	80°	35.6
Dislocation 4	6.55 x 10 ⁻⁹ m	55°	21.6
			28.1 ± 8.6 mJ/m ²

Table 2 – Thermodynamic models present in the literature [2-5].

	Model 1	Model 2	Model 3	Model 4	Model 5
SFE (mJ/m ²)	63	61	68	32	31



Production and Characterization of Nb-Ni-WC-Cu Alloys via Spark Plasma Sintering

Yara Daniel Ribeiro^{1*}, Alexandre Candido Soares¹, José Izabel Liberato Júnior¹ and Gilberto Henrique Tavares Álvares da Silva¹

¹ Rede Temática em Engenharia de Materiais (REDEMAT) - Universidade Federal de Ouro Preto, Ouro Preto, Brasil.

*yaradanielr@hotmail.com

The development of new materials is linked to technological innovations, mainly due to applications at increasingly higher temperatures [1]. In this scenario, niobium alloys are promising candidates due to their high melting points, low densities and high mechanical properties at high temperatures [2], [3]. As a result, they are considered ideal for application in parts of jet engines and other components of the aerospace industry [4]. The aim of the present work was to produce Nb-based alloys via spark plasma sintering (SPS). For this purpose powders of Nb, Ni, Cu and WC were used to manufacture alloys with compositions Nb-15Ni-2%WC-2%Cu. The powders were then mixed for 2 hours in a high energy mill and sintered via SPS at temperatures 1000, 1100 and 1200°C, with uniaxial pressure of 30 MPa. The sintered specimens analyzed by X-RD and SEM-EDS. By analyzing the diffractograms shown in Figure 1, it was possible to identify the formation of the NbO, NbC, Nb₂C, δ -Ni₃Nb (orthorhombic), γ "-Ni₃Nb (tetragonal), (Nb,W) and W phases at all studied temperatures. Figure 2 shows the micrographs obtained by SEM of the sintered samples, it is possible to observe that the microstructures are very similar in all prepared conditions, it is clear that there was no formation of very distinct phases, with only a light gray matrix appearing. and some dispersed phases with a slightly darker coloring. In addition, it is noted that in all specimens produced there is the presence of pores, but it is visible that with the increase in sintering temperature this presence is reduced. On the other hand, the EDS revealed that there was an increase in the homogeneity in the distribution of the elements as the sintering temperature rose, as can be seen in Figure 3. It was concluded that the proposed alloy was successfully manufactured via SPS, and when performing the analysis by X-RD it was possible to identify the formation of both solid solutions between components and intermetallic ones, already by MEV-EDS it is concluded that with the increase in the sintering temperature there was a reduction in the pores and an increase in the homogeneity in the distribution of the elements.

REFERENCE

- [1] S. H. Zhu *et al.*, "Structural and electronic properties of Nb-Cr-Si based alloys: First-principles calculations," *Phys. B Condens. Matter*, 2019.
- [2] P. Zhang *et al.*, "Preparation and moderate temperature oxidation behavior of Ti- and Al-doped NbSi₂-Si₃N₄ composite coatings on Nb alloy," *Surf. Coatings Technol.*, 2019.
- [3] C. Cui *et al.*, "Portevin-Le Châtelier effect in wrought Ni-based superalloys: Experiments and mechanisms," *J. Mater. Sci. Technol.*, 2020.
- [4] L. Sun *et al.*, "Comparison investigation of hot corrosion exposed to Na₂SO₄ salt and oxidation of MoSi₂-based coating on Nb alloy at 1000 °C," *Surf. Coatings Technol.*, 2020.

ACKNOWLEDGMENT

This work was carried out with the support of the Coordination for the Improvement of Higher Education - Brazil (CAPES).

FIGURES

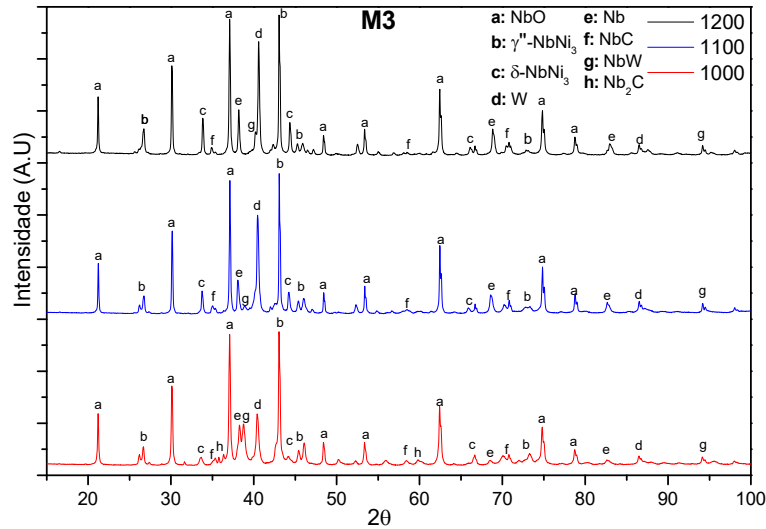


Figure 1 – X-RD diffractogram of the specimens at temperatures of 1000, 1100 and 1200°C.

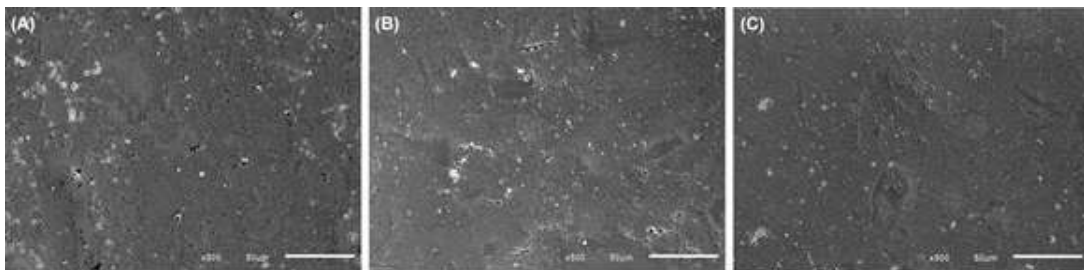


Figure 2 - Micrograph of the alloy sintered at (A) 1000°C, (B) 1100°C and (C) 1200°C with 500X increase in SEM. Source: The author.

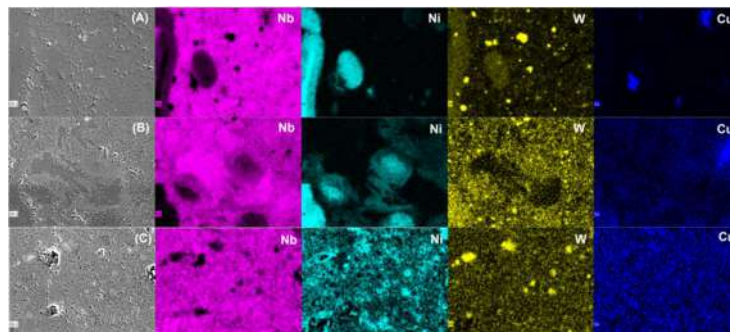


Figure 3- Elementary EDS mapping for the sintered alloy at (A) 1000°C, (B) 1100°C and (C) 1200°C. Source: The author.



Production and Characterization of Nb-10W-15(Ti6Al4V) - 1Cu Alloy Via Spark Plasma Sintering

Alexandre Candido Soares^{1*}, Yara Daniel Ribeiro¹, José Izabel Liberato Júnior¹ and Gilberto Henrique Tavares Álvares da Silva¹

¹ Rede Temática em Engenharia de Materiais (REDEMAT) - Universidade Federal de Ouro Preto, Ouro Preto, Brasil.

*alexandre.csoares@hotmail.com

The use of Niobium based alloys (Nb) has been gaining prominence due to the combination of its high melting point and low densities, when compared with other refractory metals, demonstrating great potential for applications in high temperature environments, surpassing Ni super alloys commonly used [1]. Thus, the present study aimed to develop and characterize the Nb-10W-15(Ti6Al4V)-1Cu alloy, with percentages by weight. The mixture was homogenized for 2 hours and sintered via spark plasma sintering (SPS). For this, axial pressure of 30 MPa was used and temperatures of 1400 and 1500°C, performed in triplicate. In the characterization of the sintered samples, by XRD, on Figure 1, it was identified the solid solution (Nb,W), already expected due to the interaction between these elements [2]. The formation of the β Ti phase was observed, as the W and Nb are stabilizers of this phase [3]. The formation of the AlTi₃ intermetallic is related to the low reaction rate between Al with Nb and W, forming a phase only with Ti. In addition, this interaction of Al with Ti justifies the formation of α Ti, since the element stabilizes this titanium phase [4]. TiO₂ and TiC is justified by the high affinity of Ti for these elements [5]. By SEM together with EDS, presented in Figure 2, the microstructures and homogenization of the elements were studied. It was possible to observe a light colored matrix, composed of (Nb,W) with islets of titanium alloy, dark colored, dispersed throughout the matrix. Furthermore, it is noticed the low presence of pores and no formation characteristic of microstructural transformations. The low presence of titanium in the matrix is due to the greater diffusivity of Nb into Ti, which created a barrier for the diffusion of Ti to Nb [6]. Another fact observed is the protection against effective oxidation of niobium by titanium, since most of the oxygen comes from the rich phases has Ti, with the oxygen almost imperceptible in the matrix (Nb,W) [7]. In relation to copper, it is possible to notice the formation of small islets distributed throughout the alloy, probably accumulated in the macropores, due to the formation of liquid and its low solubility in the matrix (Nb,W) [8]. Finally, it was concluded that SPS sintering was effective and very promising for the manufacture of Niobium based alloys with a high melting point, due to the low surface porosity and the good homogenization of the elements based on the SEM and EDS presented.

REFERENCES

- [1] C. R. M. Afonso *et al.*, "Characterization, corrosion resistance and hardness of rapidly solidified Ni–Nb alloys," *J. Alloys Compd.*, 2020.
- [2] O. N. Senkov *et al.*, "Ductile Nb alloys with reduced density and cost," *J. Alloys Compd.*, 2019.
- [3] Y. Li *et al.*, "Microstructure and isothermal oxidation behavior of Nb-Ti-Si-based alloy additively manufactured by powder-feeding laser directed energy deposition," *Corros. Sci.*, 2020.
- [4] H. Z. Niu *et al.*, "Fabrication of a powder metallurgy Ti₂AlNb-based alloy by spark plasma sintering and associated microstructure" *Mater. Des.*, 2016.
- [5] Y. Li *et al.*, "Phase equilibria in the Nb–Ti side of the Nb–Si–Ti system at 1200 °C and its oxidation behavior," *J. Alloys Compd.*, 2017.
- [6] Y. Liu *et al.*, "Kinetic modeling of diffusion mobilities in bcc Ti-Nb alloys," *J. Alloys*



- Compd.*, 2009.
- [7] X. Liu *et al.*, “Mechanisms of Ti and B on improving weld metal toughness of a Nb-alloyed steel,” *Mater. Sci. Eng. A*, 2020.
- [8] F. A. Da Costa *et al.*, “Effect of high energy milling and compaction pressure on density of a sintered Nb-20%Cu” *Int. J. Refract. Met. Hard Mater.*, 2015.

ACKNOWLEDGMENT

The present work was carried out with the support of the Coordination for the Improvement of Higher Education - Brazil (CAPES).

Figure 1 - Diffractograms of the Nb-10W-15(Ti6Al4V)-1Cu alloy. Source: author.

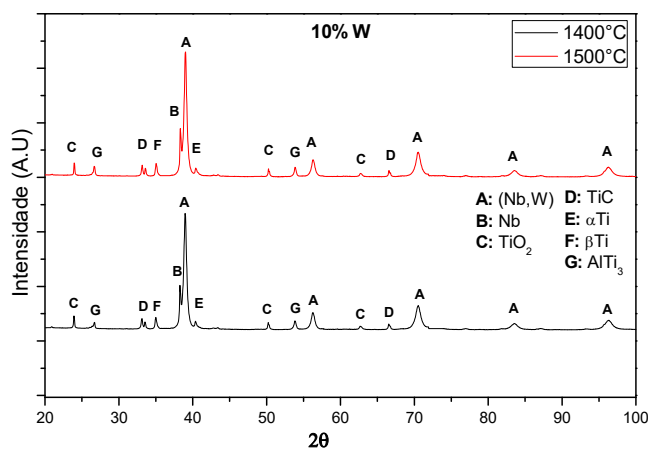
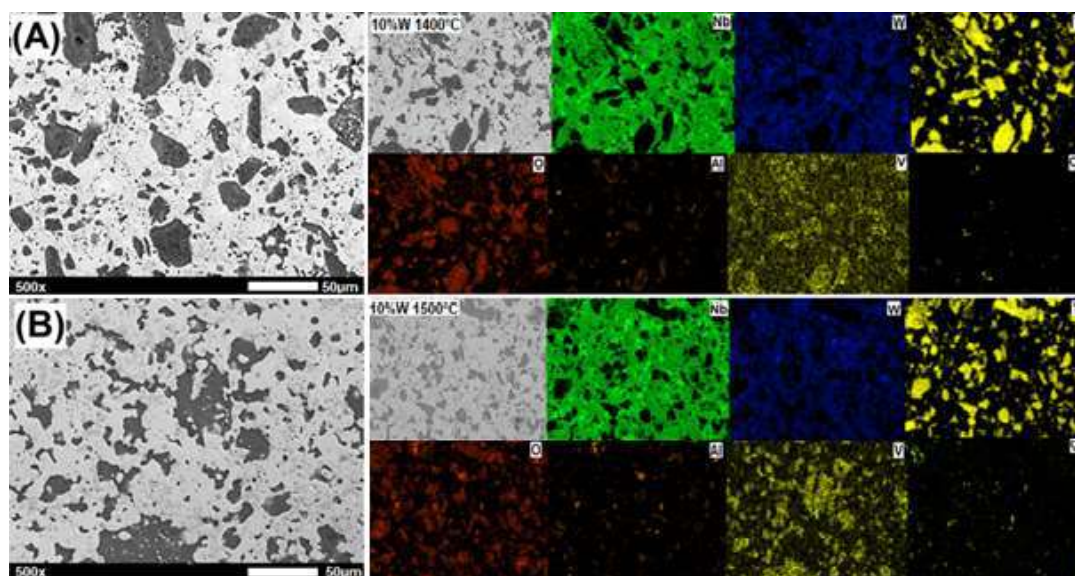


Figure 2 - Micrograph and EDS of the Nb-10W-15(Ti6Al4V)-1Cu alloy, sintered at (A) 1400°C, (B) 1500°C with 500x magnification. Source: author.





Nanomechanical characterization of organic matter and clay mineral using AFAM in shale

D. L.P. de Lacerda^{1*}, R. Prioli², Y. M. Parizek-Silva¹ and G. F. Vasquez¹

¹ Centro de Pesquisas & Desenvolvimento Leopoldo Américo Miguez de Mello/Petrobras, Rio de Janeiro/Brazil

² Departamento de Física/Pontifícia Universidade Católica, Rio de Janeiro/Brasil.

*douglas.lacerda@petrobras.com.br

Shales are the most frequent sedimentary rock on the surface and are important for petroleum systems, as they can be found as source rocks of hydrocarbons or cap rocks that limits the accumulations of hydrocarbons [1, 2]. Its macroscopical mechanical properties are important to determine its structural stability and are the link between the petrophysical properties and the geophysical observables [3]. The mechanical properties of the clay minerals and organic matter, commonly found in shales, are not well known. This represents a serious limitation to the full understanding of the macroscopical shale properties. The mechanical properties of these important constituents have been studied by atomic force microscopy acoustic modes and with peak force mode [4,5,6,7,8,9]. In this work, we have implemented an atomic force acoustic microscopy (AFAM) with a combination of small equipment modifications and imaging processing. In this setup, the sample is fixed on a piezoelectric ceramic while an AFM tip is held in contact under constant force. A sinusoidal signal is used to introduce a vibration on the surface, the registered AFM signal is sent to a lock-in amplifier that register the osculation amplitude of the AFM cantilever. The amplitude registered by the lock-in is also registered by the AFM controller and can be imaged as the tip scans the surface. Several oscillation amplitude images are registered for different frequencies and are post processed in order to find the resonance amplitude (figure 1). A mechanical model that represents the resonance frequency as function of the mechanical properties of the surface and the cantilever are used to calculate the Indentation modulus of the material under study. After this procedure, we were able to produce an Indentation modulus map (figure 2) and measure the mechanical properties of clay and organic matter previously identified on the imaged region using energy dispersive x-ray.

REFERENCES

- [1] A. C. Aplin et al., AAPG Bulletin, 95 (2011) 2031
- [2] K. Bjørlykke. *Petroleum Geoscience: From Sedimentary Environments to Rock Physics*, chapter Capítulo 6 - Shales, Silica Deposits and Evaporites, Springer Berlin Heidelberg, 2010.
- [3] J. Yang et al., *Nature Communications*, 8 (2017) 2179.
- [4] M. Prasad et al., *Geophysical Research Letters*, 29 (2002) 1172
- [5] M. Eliyahu et al. *Marine and Petroleum Geology*, 59 (2015) 294
- [6] T. M. Wilkinson et al., *Journal of Materials Science*, 50 (2015) 1041

[7] S. Zargar et al., Geophysics, 81 (2016) M1

[8] C. Li et al., Fuel, 233:894–910 (2018)

[9] C. Li, et al., Marine and Petroleum Geology, 96 (2018) 128

ACKNOWLEDGEMENTS

The authors would like to thanks Petrobras for the samples and the mineralogical analysis.

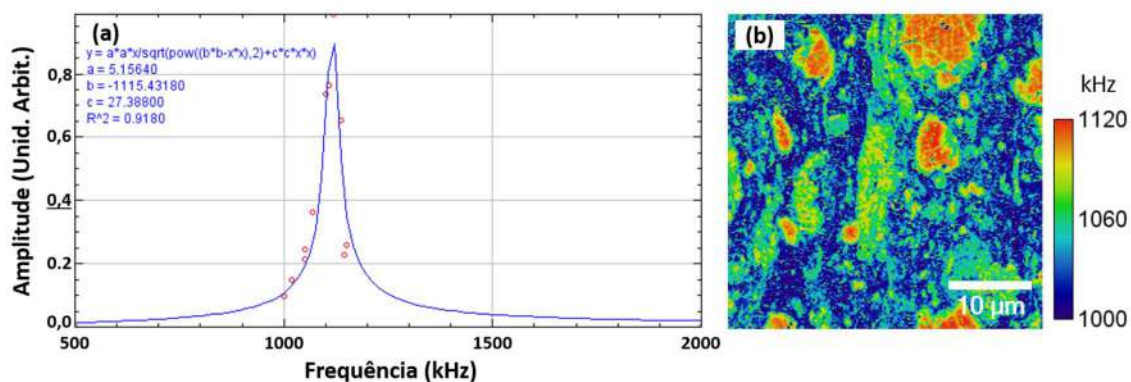


Figure1 - (a) Lorentzian function fit to a measurement on a point in sample (b) resonance map after fit in all measured points.

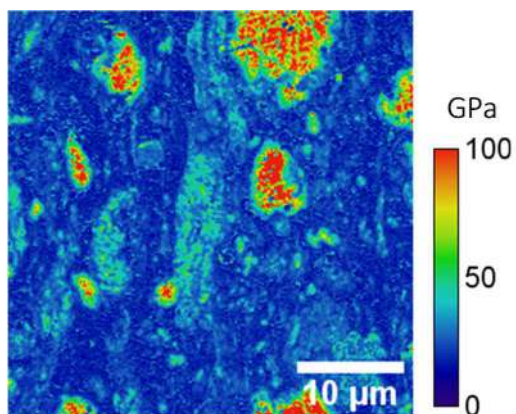


Figure 2 - Indentation modulus map.



Characterization of Sandstones Through Image Analysis and Simulations

Rafael da Silva Vianna^{1*}, André Maués Brabo Pereira¹, Ricardo Leiderman¹, Janine Domingos Vieira².

¹ Institute of Computing, UFF, Niterói, Brazil.

² School of Engineering, UFF, Niterói, Brazil.

*rafaelvianna@id.uff.br

Image analysis and simulations are increasingly applied to characterize sandstone samples as a complementary analysis to laboratory tests due to their capability to overcome many difficulties presented in physical testing. Some of the advantages are their non-destructive characteristic, low cost, ease of performing repeatable analyses, and possibility to perform analyses that cannot (or are very difficult to) be performed in experimental tests. By means of image analysis and simulations it is possible to extract the constituent's contents of sandstones, porosity, pore connectivity, effective properties and others. Accurate results are expected to be obtained with realistic models, which may be generated by means of imaging technologies on several scales (e.g., microcomputed tomography (micro-CT)). Therefore, in this work, we aim to characterize samples of sandstones through image analysis and simulations using micro-CT images. The characterization of sandstones using micro-CT images involve several steps as presented in Figure 1: sample preparation, micro-CT acquisition and reconstruction, image processing and segmentation, mesh generation, and numerical simulations. In the image processing and segmentation step, we use a machine learning approach. Machine learning is very efficient to segment phases that the traditional techniques of segmentation would not be able to do. The segmented images are used to obtain the volume fraction of the material phases. The contents of phases are compared to experimental results validating our approach. Additionally, effective properties of the material are obtained by computational simulations based on numerical methods. This is an attractive alternative to laboratory tests to assess effective properties of porous materials, since this methodology can consider the material internal structure through realistic virtual models as presented in [1-5].

[1] Andreassen, E.; Andreasen, C.S. How to Determine Composite Material Properties Using Numerical Homogenization. *Comput. Mater. Sci.* 2014, 83, 488-495.

[2] Aarnes, J.E.; Gimse, T.; Lie, K.A. An Introduction to the Numerics of Flow in Porous Media using Matlab. In *Geometric Modelling, Numerical Simulation, and Optimization*; Springer: Berlin/Heidelberg, Germany, 2007.

[3] Sheng, X.Y.; Zhi, X.X. A New Numerical Method for the Analysis of the Permeability Anisotropy Ratio. *Chin. Phys.* 2002, 11, 1009-1963.

[4] Akanji, L.T.; Matthai, S.K. Finite Element-Based Characterization of Pore-Scale Geometry and Its Impact on Fluid Flow. *Transp. Porous Media* 2010, 81, 241-259.

[5] Yang, L.; Yang, J.; Boek, E.; Sakai, M.; Pain, C. Image-Based Simulation of Absolute Permeability with Massively Parallel Pseudo-Compressible Stabilized Finite Element Solver. *Comput. Geosci.* 2019, 23, 881-893.

This research was carried out in association with the ongoing R&D project registered as ANP n° 21289-4, “Desenvolvimento de modelos matemáticos, estatísticos e

computacionais para o aperfeiçoamento da caracterização petrofísica de reservatórios por Ressonância Magnética Nuclear (RMN) " (UFF/Shell Brasil/ANP), sponsored by Shell Brasil under the ANP R&D levy as “Compromisso de Investimentos com Pesquisa e Desenvolvimento”.

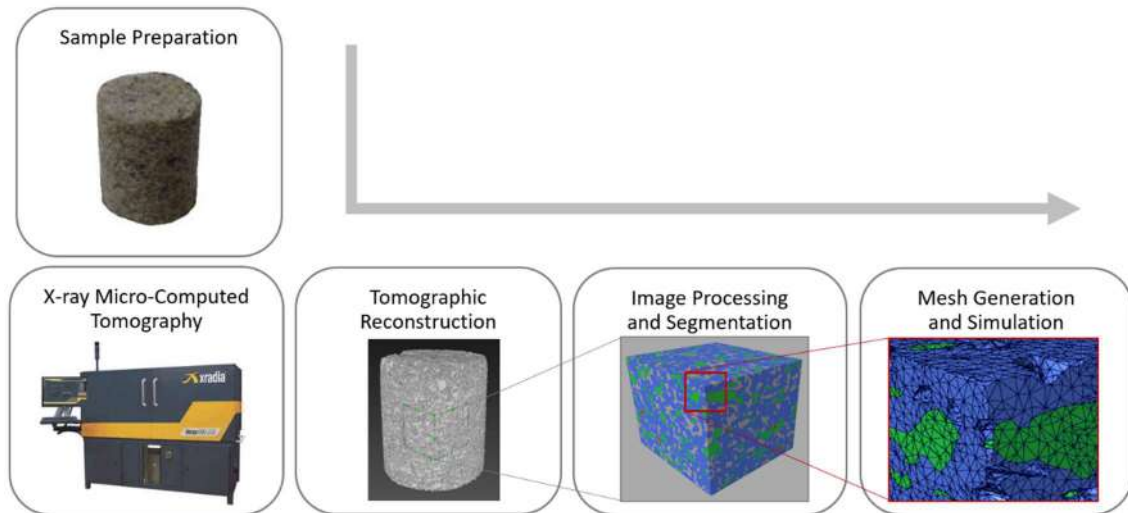


Figure 1 Workflow in virtual material characterization, from sample preparation to numerical simulation, embracing micro-CT acquisition, tomographic reconstruction and image processing and segmentation.



Digital Volume Correlation (DVC) applied to in-situ microCT Images of Strain-Hardening Cement-Based Composites (SHCC)

Renata Lorenzoni^{1*}, Iurie Curosu², Sidnei Paciornik¹, Viktor Mechtcherine², Flavio A. Silva³ and Giovanni Bruno⁴

¹Department of Chemical and Materials Engineering, PUC-Rio, Rio de Janeiro, Brazil.

²Institute of Construction Materials, Technische Universität Dresden, Germany.

³Department of Civil and Environmental Engineering, PUC-Rio, Rio de Janeiro, Brazil

⁴BAM-Berlin. E-mail: renata.lorenzoni@aluno.puc-rio.br

SHCC are fiber-reinforced cementitious materials that achieve significant deformations through multiple cracks formation [1]. Their mechanical behavior is strongly linked to the cracks opening behavior. In this scenario, DVC is a powerful method by which cracks can be analyzed in 3D throughout the interior of the specimen. DVC is a technique that estimates full-field strain in 3D over the entire volume of the specimen by correlating imaging volumes of the specimen in unloaded and loaded states [2]. It comprises three main steps: acquisition of 3D images; pattern-matching correlation procedure to measure a displacement vector field; calculation of the strain field from the measured displacements. In this work, images of SHCC specimens were acquired by in-situ microcomputed tomography (microCT), that provided six 3D datasets in different states of loading during a tensile test, from STEP_0 (unloaded) to STEP_5 (end of test). Image pre-processing was performed before DVC calculation: all five loaded datasets were aligned according to STEP_0 and a sub volume was cropped resulting in six datasets with 224 slices with 336 x 336 pixels each (Figure 6). Displacement and strain were calculated by the open source code Software for the Practical Analysis of Materials (SPAM) [3]. The pattern-matching correlation between the images before and after is made in a sub volume, traversing the image at a given step size. Here, a sub volume was defined as $(32 \text{ voxels})^3$ and the step size was 8 voxels. The code was run five times with input from two subsequent steps. First, Step 0 was defined as a reference image and Step 1 as a deformed image and in the last run, the reference and deformed images had Steps 4 and 5, respectively, as input. The result of displacement was plotted as arrows colored according to the magnitude (Figure 7), and it shows a tendency of displacement towards the positives x and y-axis, characterizing a torsion during the test, in addition to the tensile effort (y-axis). Figure 8 shows the y-axis strain (ϵ_{yy}) results. Until step 2, the first formed crack concentrates greater strain. From step 3, when the top crack appears, the strain decreases in the cracks below and the strain in the cracks above becomes more prominent. This means that there is a relaxation in the bottom crack and the strain concentrates in the upper crack, where the rupture occurs.

The authors would like to acknowledge the financial support offered by agencies CNPq, CAPES and FAPERJ, as well as by the German Academic Exchange Service – DAAD.

[1] V. C. Li, “On Engineered Cementitious Composites (ECC) A Review of the Material and Its Applications,” *J. Adv. Concr. Technol.*, vol. 1, no. 3, pp. 215–230, 2003.

[2] B. K. Bay, T. S. Smith, D. P. Fyhrie, and M. Saad, “Digital volume correlation: Three-dimensional strain mapping using x-ray tomography,” *Exp. Mech.*, vol. 39, no. 3, pp. 217–226, 1999.

[3] O. Stamati *et al.*, “spam: Software for Practical Analysis of Materials,” *J. Open Source Softw.*, vol. 5, no. 51, p. 2286, 2020.

FIGURAS

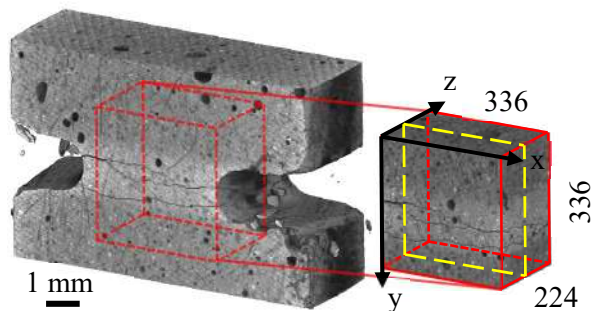


Figure 6. Highlight of a cropped volume used as input for the SPAM code.

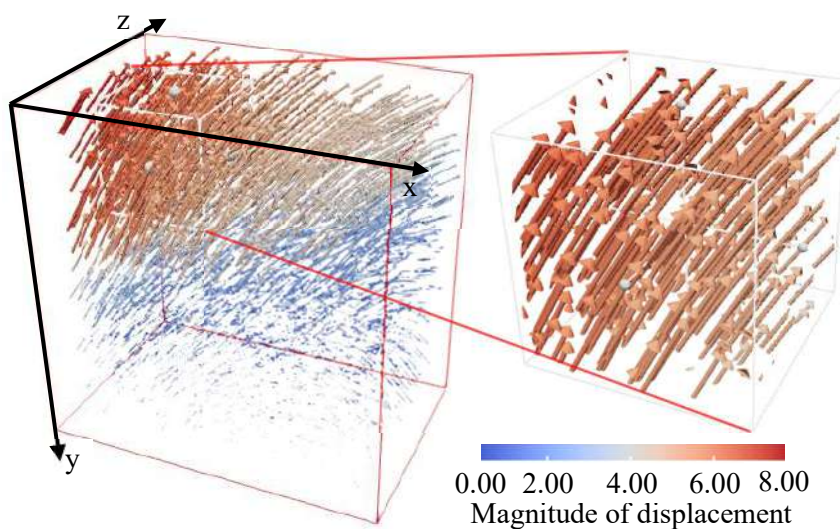


Figure 7. Displacements from step 2 to step 3 obtained by SPAM code represented by arrows.

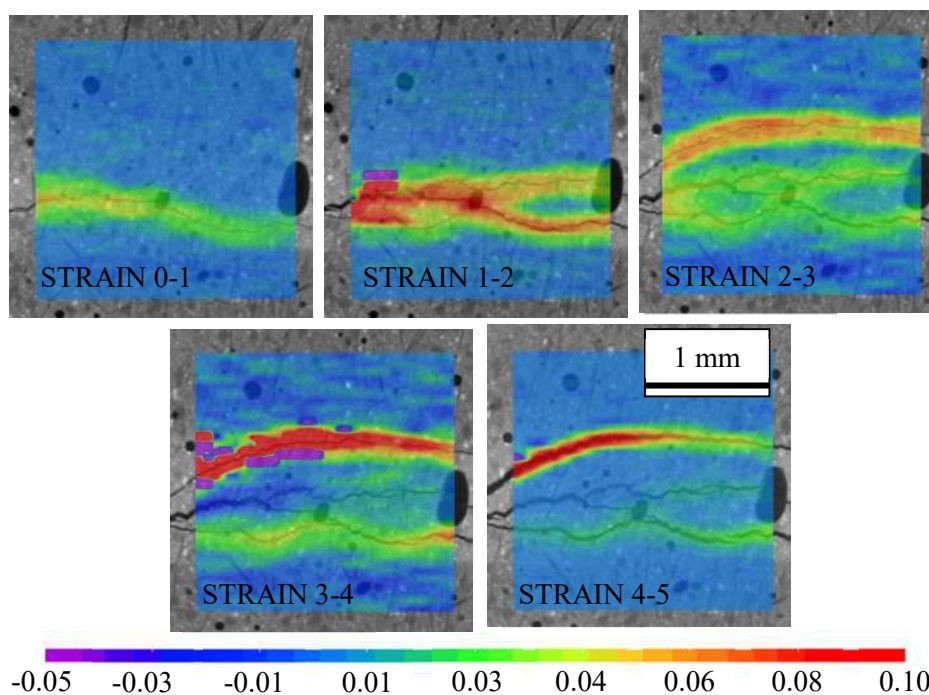


Figure 8. Plotted y-axis strain (e_{yy}) obtained by SPAM overlapped on the final loading dataset of each analysis.



Microstructural characterization of maraging steels Fe-13Ni-15Co-(7.5-15)Mo-(0.06-0.88)Ti (wt.%) after aging

Daniela Passarelo Moura da Fonseca^{1*} and Angelo Fernando Padilha¹

¹ Universidade de São Paulo, Escola Politécnica, PMT, São Paulo, SP, Brasil.

*danipassarelo@usp.br

Maraging 400 steels are ultra-high-strength steels with low carbon content ($< 0.01\%$), whose base composition is Fe-13Ni-15Co-10Mo (wt.%) with small additions of Ti and Al. Their mechanical strengths are mainly achieved by precipitation hardening of intermetallic compounds, which occurs during the aging heat treatment applied after austenitization followed by cooling in air. When it comes to in-depth studies on the physical metallurgy of this steel, the literature is scarce and limited to works prior to the 1990s [1, 2]. More recently, some groups have studied the particularities of precipitation hardening of these ultra-high-strength maraging steels and have shown, after aging, the repeated presence of two types of precipitates with nanometric dimensions: $(\text{Ni,Fe})_3(\text{Mo,Ti})$ and the Laves phase $(\text{Fe,Co})_2(\text{Mo,Ti})$. [3–6] Thus, the objective of this work was to perform the microstructural characterization of maraging 400 steels, varying composition and aging time. A non-commercial maraging 400 was fabricated by vacuum induction melting (VIM) and electroslag remelting (ESR), following by homogenization at 1250°C for 5 hours, forging and hot rolling. Tab. 1 shows the chemical composition of each sample, varying the percentage of Mo (increases from D to E) and Ti (increases from A to C). After received, the samples were solution annealed at 900°C for 1h and quenched in water. Then they were aged at 480°C for 3h and 6h. The microstructure was characterized using a SEM/EDS (FEG FEI-Inspect 50), XRD (Philips X'Pert-MPD, $\text{CuK}\alpha$, $20^\circ \leq 2\theta \leq 100$), quantitative stereology (image J) and Vickers hardness (Shimadzu HMV-2, 15s, 1 kgf). Fig. 1 shows SEM image for each sample and aging time. Samples A, B, C and E in the non-aged condition (0h) presented micrometric precipitates (light contrast) rich in Mo (EDS) and identified as Fe_3Mo (by XRD). After aging, the initial precipitates remained with the same size and morphology. Fig. 2.a shows the Vickers hardness vs aging time, even with the presence of micrometric Fe_3Mo precipitates, there was precipitation hardening by nanometric precipitates. These precipitates are too small to be observed by SEM and their peaks coincide with the martensite peaks (from matrix), which makes not possible to identify them with XRD as well. Sample E (highest Mo content) presented larger and less precipitates ($0.29 \pm 0.2 \mu\text{m}$, $2.47 \text{ precip./}\mu\text{m}^2$) than samples A, B and C ($0.21 \pm 0.1 \mu\text{m}$, $3.51 \text{ precip./}\mu\text{m}^2$), which presented values similar between them. This indicates that the Mo content in the alloy influences not only austenitization kinetics, but also dissolution kinetics of Fe_3Mo , the more Mo, higher the temperature required. Assuming this same behavior during the aging precipitation process, it can be inferred that, for higher Mo content, longer it will be the diffusion time of the atoms, from the position of solid solution to the sites of formed nanometric precipitates. That is, the Mo can influence the precipitation kinetics and, in this case, the difference between the hardness values of the samples, for the same aging time, can represent different stages in the aging curve, as illustrated in Fig.2b. For example, in aging for 6h, samples A, B and C would be close to the hardness peak, while sample E (in black) would have already crossed that point and sample D (in pink) would still be rising. The microstructural characterization indicated that: a) the solubilization temperatures usually used for other classes of maraging steels do not apply to maraging 400, due the higher contents of Mo and Co; b) the compositions A, B and C proved to be technologically

promising, presenting high levels of mechanical resistance; c) there is a great influence of the Mo in the phase transformations and d) it is necessary to study using advanced high resolution techniques such as TEM and high energy XRD.

- [1] Hornbogen, E.; Rittner, K.. *Steel Research*, v. 58, n. 4, p. 172–177, 1987.
- [2] Menzel, J.; Klaar, H.-J. *Steel Research*, v. 61, n. 1, p. 30–38, 1990.
- [3] Alves, T. J. B. et al. *Hyperfine Interactions*, v. 238, n. 1, p. 1–9, 2017.
- [4] Sun, L. et al. *Acta Materialia*, v. 149, p. 285–301, 2018.
- [5] Niu, M. et al. *Acta Materialia*, v. 179, p. 296–307, 2019.
- [6] da Fonseca, D. P. M. et al. *Materials Research*, v. 24 (1), p. 1-11, 2021.

This research was supported by USP-Poli and CNPq.

Tab. 1 – Chemical composition (%wt) of the maraging steels studied

Liga	Ni	Co	Mo	Ti	Al	C	Si	Mn
A	12.61	14.49	11.12	0.060	<0.01	0.021	0.190	0.220
B	14.11	14.27	11.40	0.400	0.01	0.014	0.060	0.030
C	13.08	15.35	11.30	0.88	0.05	0.024	0.080	0.050
D	13.40	14.96	7.51	0.250	0.06	0.023	0.150	0.160
E	14.06	15.21	15.02	0.240	0.04	0.021	0.060	0.040

Fig. 1 – SEM image of samples A, B, C, D and E in the non-aged condition (0h), aged at 480 °C for 3h and aged at 480 °C for 6h. Secondary electrons, chemical attack by immersion in Vilella

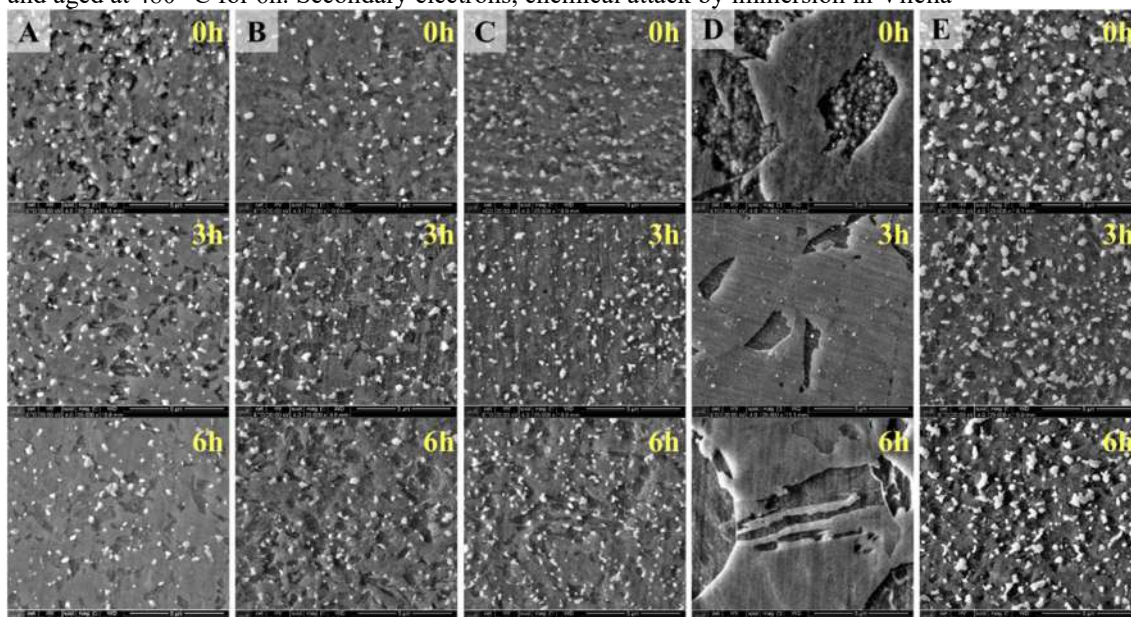
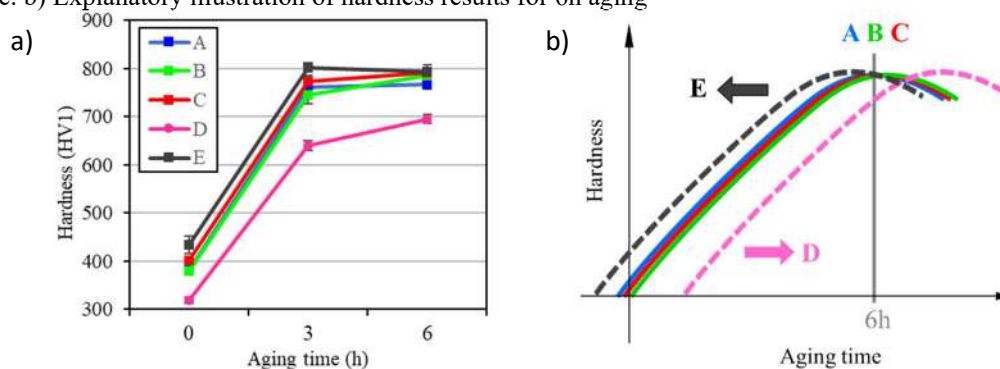


Fig. 2 – a) Vickers hardness (HV1) of samples A, B, C, D and E (aged at 480 °C) as a function of aging time. b) Explanatory illustration of hardness results for 6h aging





Effect of Heat Treatment on the Microstructure of Polycrystalline Superconducting Ceramic $\text{SmBa}_2\text{Cu}_3\text{O}_{7-d}$.

Carlos A. C. Passos^{1*}, Raoni C. Barbieri¹, João V. S. Chagas¹

¹ Grupo de Física Aplicada, Departamento de Física, Universidade Federal do Espírito Santo, Vitória, Brasil.

*email-do-carlos.passos@ufes.br

In this work, we prepare $\text{SmBa}_2\text{Cu}_3\text{O}_{7-d}$ superconducting ceramics through the solid state reaction method with different calcination routes. Our goal was to evaluate the influence of synthesis parameters on ceramic microstructure. Briefly, the heat treatment parameters are summarized in Table 1. We then subjected all samples to the same sintering treatment with the parameters: heating rate of $4^\circ\text{C}/\text{min}$ to a temperature of 960°C whose time in this isotherm was of 72 hours, the cooling rate was $1^\circ\text{C}/\text{min}$ to 520°C , where the time at this plateau was 24 hours and, finally, the samples were cooled at a rate of $1^\circ\text{C}/\text{min}$ to room temperature. All sintering process was under constant oxygen flow were $1.4\text{ cm}^3/\text{s}$. After that, we determine the densities (ρ_{ap}) of the samples by Archimedes Principle. From these data, we calculated porosity of each sample with the following equation:

$$\text{Porosity} = 1 - \frac{\rho_{ap}}{\rho_{teo}} \quad (2)$$

where $\rho_{teo}=6.8716\text{ g/cm}^3$ which is the theoretical density of the orthorhombic crystal structure of ceramic [1].

The samples were also fractured into two pieces. One of the pieces was embedded in cold epoxy resin. For the sanding procedure, we used silicon carbide (SiC) sandpaper with a particle size of 800, 1200, 2500 and 5000. For the polishing of the samples, we used a polishing machine with a diamond paste of a particle size of $1\text{ }\mu\text{m}$. Then, we analyzed the polished and unpolished samples in a JEOL JSM6610LV Scanning Electron Microscope.

We analyzed all micrographs of polished and unpolished samples with ImageJ2 software [2]. First, we did a pre-processing applying the **Trainable Weka Segmentation** (TWS) [3,4] plugin to sanded and polished samples in order to quantify the porosity. We chose two classes for segmentation: ceramic and pores. Using the drawing tool, we selected several representative regions of each class. We apply the **Fast Random Forest** classifier to perform multitasks in parallel. We chose the following image features in classifier training: **Bilateral and Anisotropic diffusion** (for noise removal), **Gabor and Sobel Filter** (for edge detection), and **Entropy** (for texture determination). The filter parameters were minimum sigma = 1.0, maximum sigma = 32.0 and balanced classes. To correct errors after each training, the selected regions were modified or deleted, and the classifier was retrained. The performance of successive trainings was evaluated using the **Out of bag error** [4]. After this training on the micrograph, the classifier and segmentation data were saved so that we could use it in other images.

Post-processing was performed on the ceramic class maps from the application of **Threshold** command. Then, to improve the identification of areas, the **Dilate** filter was applied, to close the pore contours, and the **Fill Holes** filter, to fill the interior of the closed



regions. With the treated micrographs, we obtained the fraction of pore area that was compared with the results obtained by the Archimedes method, as shown in Table 2.

Our results indicate that the ImageJ2 software is an important tool for evaluating the microstructure of ceramics and allowed us to automate the process of segmentation of digital images. Furthermore, it allowed us to quantify the pore fraction and densities of ceramics with relative errors lower than 3.60%.

REFERENCES

- [1] I. Hamadneh, et al. *Journal of Superconductivity and Novel Magnetism*, v. 29 (3) (2016) 829–834.
- [2] J. Schindelin, et al. *Nature Methods*. 9, (7), (2012) 676–682.
- [3] I. Arganda-Carreras, et al. *Bioinformatics*. 33 (15) (2017) 2424–2426.
- [4] R. C. Barbieri, J. V. S Chagas, L. G. S. Nunes. *Blucher Proceedings*. In: *Anais do X Encontro Científico de Física Aplicada*, (2019) 1–4.

ACKNOWLEDGMENT

The authors would like to thank CAPES for granting the scholarship.

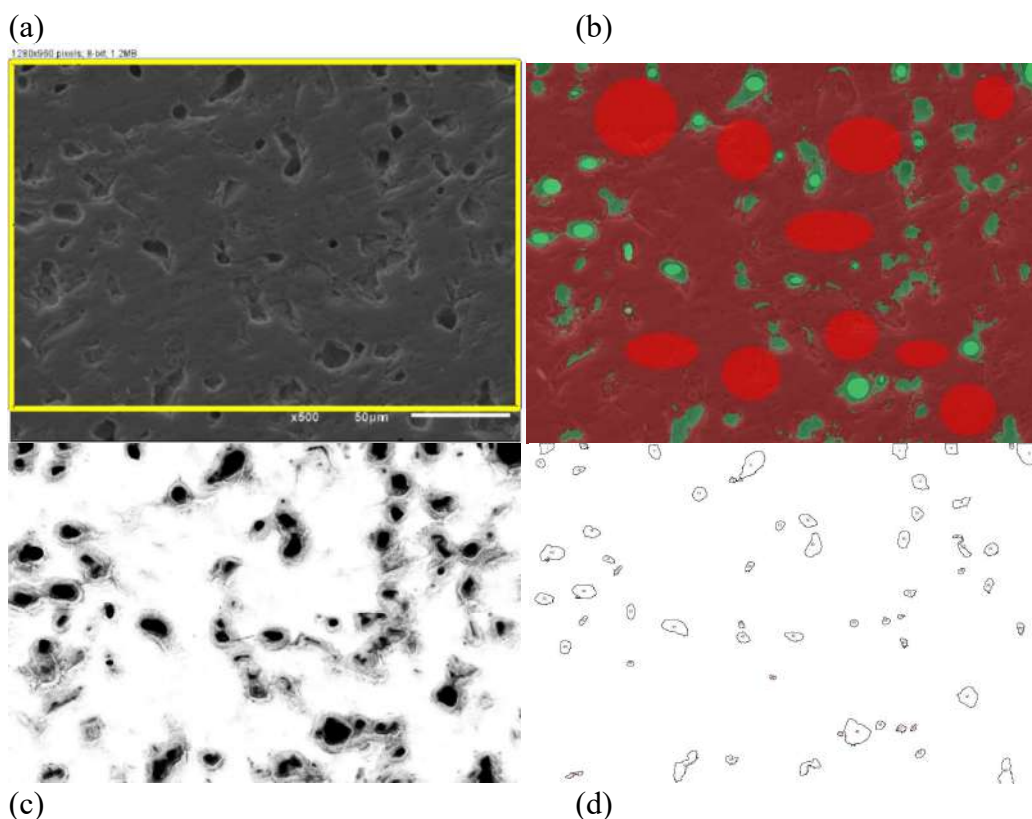


Figure 1: (a) Micrograph of the Sm-123 (A1-960) sample sanded and polished at 500x magnification. (b) Image segmentation was performed by TWS plugins. Red represents the segmented regions as ceramic and the color green as pores. Stronger colored regions are the input data provided by the user to the classifier, and the other regions have been segmented by TWS. (c) The probability map was generated at the end of the segmentation by TWS. The intensity of the pixels in the image indicates the probability that these pixels belong to the map class. (d) Outline of particles identified as sample pores.

Table 1: Heat treatment parameters of SmBa₂Cu₃O_{7-d} polycrystalline ceramics.

Sample	Calcination Temperature (°C)	Time of Isotherm (h)	Cooling Rate (°C/min)
A1-930	930	40	10
A2-930	930	80	10
A2-960	960	80	10
A3-930	930	40	1
A3-960	960	40	1

Table 2: – Porosity was estimated by analyzing the images obtained from the SEM. Porosity was defined as the area fraction of the regions segmented with the pore class. Sample A1-960 could not be analyzed by the method because its wear was not sufficient to even out the surface.

Sample	Average Porosity Fraction from Images	Average density from images (g/cm ³)	Density (g/cm ³)	Relative Error (%)
A1-930	9,63	6,21	6,28	1,14
A2-930	9,42	6,22	6,36	2,15
A2-960	11,42	6,09	5,94	2,45
A3-930	10,76	6,13	5,92	3,56
A3-960	15,60	5,80	5,90	1,73



Oxidation Assisted Intergranular Cracking of Alloy 718 associated to γ'' grain boundary dynamic precipitation

Amanda Varela^{1*}, Luiz Henrique de Almeida¹

¹. Programa de Engenharia Metalúrgica e de Materiais/UFRJ, Rio de Janeiro, Brasil.

*amandavarela@coppe.ufrj.br

Alloy 718 has a high technological importance in aerospace and power industries, since it was designed to operate under elevated pressures, temperatures and oxidizing environments [1]. This is a result of the slow kinetic precipitation of the metastable phase γ'' (Ni_3Nb) and the formation of protective oxides [1,2]. However, the oxidation assisted intergranular cracking (OAIC) manifestation at about 650°C leads to a dramatic decrease in ductility of alloy 718, evidencing a change in the type of fracture and making its application at higher temperatures unfeasible [1-3]. Figure 1 illustrates a typical dimpled ductile fracture transitioning into a faceted surface in the OAIC temperature interval. The phenomenological and kinetic characterization related to this effect does not have a consensus in the literature [1,2]. Since niobium is a critical element of the microstructure, representing up to 5,5% at, being a carbide former, known for its oxygen affinity and prone to segregation, the most recurrent explanation associates the decomposition of the intergranular (Nb, Ti)C to form a brittle oxide Nb_2O_5 on the grain boundaries. In fact, this theory does not stand when one analyzes the kinetics of the phenomenon [2]. Although there is evidence of the niobium surface enrichment in the given conditions to form the oxide, there is no confirmation of the NbC as its source or a clear characterization of Nb_2O_5 [2,4]. On the other hand, previous results show correspondence between the minimum ductility and the fastest precipitation rate of the γ'' strengthening phase temperatures, besides an incompatibility between OAIC kinetics and reported NbC decomposition times [2]. Driven by these facts, this work makes an effort towards the understanding of this theory by hot tensile testing and image characterization by SEM, targeting the critical role of Ni_3Nb . The tensile samples were solution annealed at 1050°C for 1h and then overaged at 800 and 900°C for 32h. These specimens had nearly all Nb available for precipitation in solid solution consumed in the form of γ'' and/or δ [5], the most stable form of Ni_3Nb , and they were tested at 850°C, representing the minimum ductility temperature at a strain rate of $3,2 \times 10^{-2} \text{s}^{-1}$. Figure 2 shows SEM images of the fractured surfaces and longitudinal sections of two overaged samples tested at 850°C. Both aging temperatures show intense resolved δ precipitation and their surface fracture reveal a notable increase in ductility, compared to the solution annealed condition, which was also verified quantitatively. It is proposed that the OAIC embrittlement mechanism is, in fact, primarily related to the dynamic γ'' precipitation during deformation, especially in the boundary driven segregation of niobium, prior to the precipitation itself.

REFERENCES

- [1] A. de Vasconcelos Varela et al., J. Mater. Res. Technol., 7 (2018) 319-325.
- [2] A. de Vasconcelos Varela, (2017). UFRJ, Rio de Janeiro, Brazil.
- [3] M. Rezende et al., J. Alloy. Compd., 643 (2015) S256-S259.
- [4] K. Al-Hatab et al, Oxid. Met. 75 (2011) 209-228.
- [5] M. Rafiei et al, Vaccum, 178 (2020) 109456.



This research was supported by CAPES and FAPERJ (Brazil).

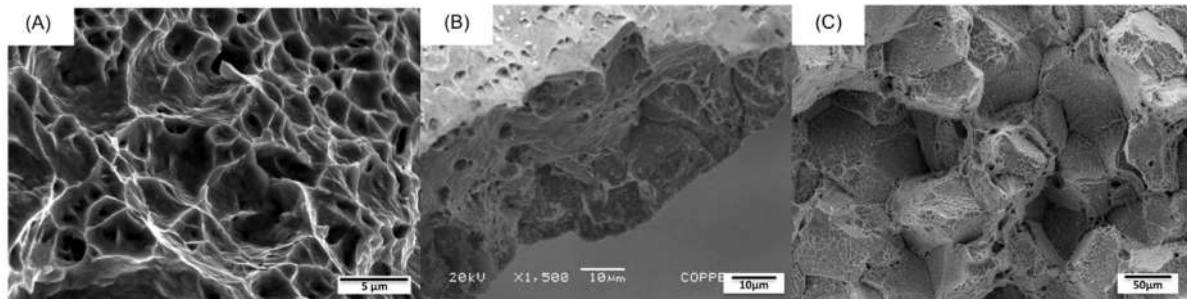


Figure 1 – SEM/SE images of the fracture surfaces of solution annealed samples tested at (a) 600, (b) 650 and (c) 850°C. The fractures reveal a change in the fracture mode, going from 100% ductile at 600°C to 100% brittle at 850°C.

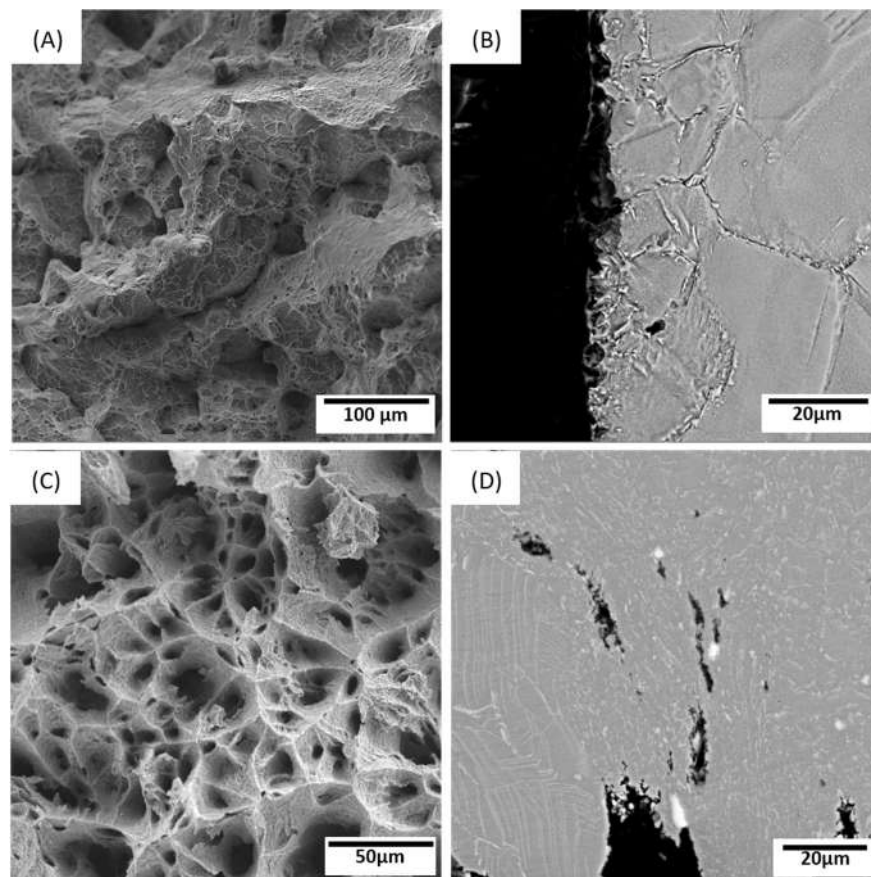


Figure 2 – SEM/SE images of fractured surfaces of samples aged at (a) 800 and (c) 900°C for 32h, showing ductility recover with (a-c) an increasing loss of intergranular facets and (c) even dimples. Also SEM/BSE images of the longitudinal sections of these samples aged at (b) 800 and (d) 900°C for 32h, showing (b-d) the Nb-rich precipitation at the boundaries and (d) even (Nb,Ti)C carbides. All samples were tested at 850°C under secondary vacuum of 1.7×10^{-2} mbar, at a $3,2 \times 10^{-2} \text{ s}^{-1}$ strain rate.



Application of Electron Pair Distribution Function (ePDF) for Characterization of Beam-sensitive NaREF₄ Nanoparticles

Leonardo Corrêa^{1*}, Flávia S. Ferreira², Fernando Sigoli² and Daniel Ugarte¹

¹ Instituto de Física “Gleb Wataghin”, UNICAMP, Campinas-SP, Brazil

² Instituto de Química, UNICAMP, Campinas-SP, Brazil

*lmcorra@ififi.unicamp.br

NaREF₄ (RE: rare-earth) nanoparticles (NPs) are promising materials due to the possibility of fine-tuning their properties through control of size, composition and formation of core@shell structures [1]. The compounds may appear as cubic (α) or hexagonal (β) phases that can be combined for the generation of unique properties [1]. This material is rather sensitive to electron beam irradiation, so their study with TEM methods must be realized with extreme care. In order to obtain a high resolution image the required electron dose is $>1000 \text{ e}^-/\text{\AA}^2$, what can damage their structure. Here, we describe a structural study of NaREF₄ NP based on Pair Distribution Function (PDF) derived from Selected Area Electron Diffraction (SAED). PDF allows for quantitative structural analysis of NPs and fulfils reasonably well the low electron doses requirement (usually a few $10 \text{ e}^-/\text{\AA}^2$) [2]. A TECNAI G2 microscope (200 keV), coupled with a CCD camera (14 bits, 2048x2048 pixels) was utilized (LCE-DEMa-UFSCar). We have developed a software in Python language, which perform all the SAED processing steps and structural refinement based on the ePDF curve. Our sample was composed of α -NaDy_{0.15}Y_{0.85}F₄@ α -NaYF₄, the NPs mean diameter (\emptyset) by image was $\sim 10 \text{ nm}$ (see Fig. 1a), the measured SAED can be seen in Fig. 1b. Both α and β phases are present in the sample (see Fig 2a). Clearly, the PDF is sensible to the β phase (commonly found as an impurity) as show by the residue values (40% without β and 27% with β , see Fig. 2b). The quantitative refinement revealed a proportion of 0.7 α and 0.3 β , this information is an important tool to improve structural control. We could not identify the presence of a α -NaYF₄ shell and \emptyset values are much lower than the ones expected from images. Such discrepancy may be due a polycrystalline shell, surface amorphization by oxidation or carbonization, but also may be due to the weak scattering power of this rather low atomic number sample. We are confident that the quality of the fit will improve with the use of Precession Electron Diffraction (PED), that will reduce dynamical diffraction effects in the measurements [3]. PED can be performed with same instrument used here, and these experiments will soon allow further improvement of this study [4].

References

- [1] D. Zhao et al., *RSC Adv.*, 4 (2014) 13490.
- [2] T. Egami et al., *Underneath the Bragg Peaks Structural Analysis of Complex Materials*, Elsevier, Oxford, 2003.
- [3] P. A. Midgley et al., *IUCrJ*, 2 (2015) 126.
- [4] This research was supported by CNPq, CAPES and FAPESP (Brazil).

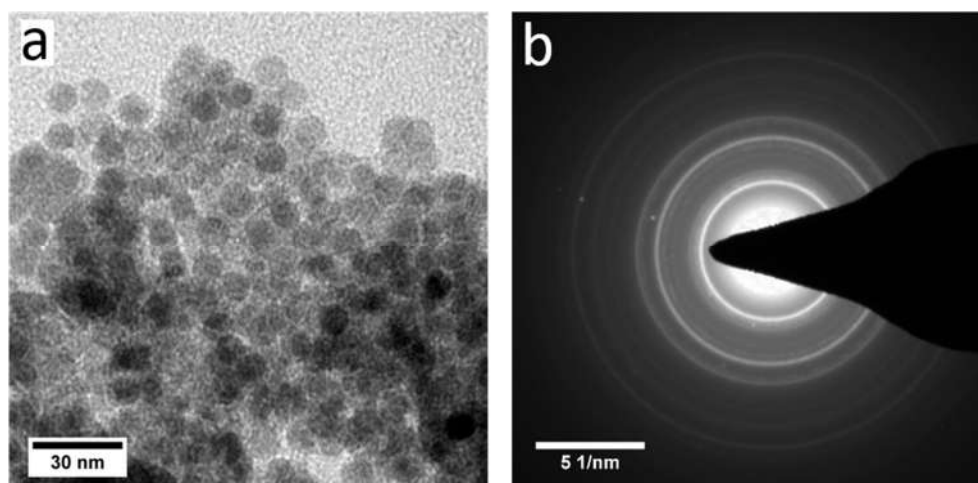


Figure 1: a) TEM image of the α -NaDy_{0.15}Y_{0.85}F₄@ α -NaYF₄ NPs. b) SAED pattern utilized in our analysis.

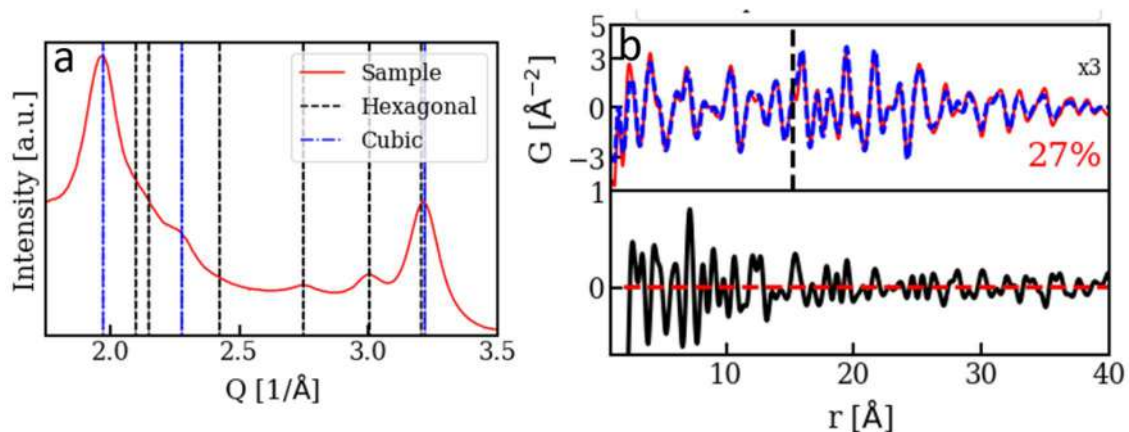


Figure 2: a) Azimuthally integrated pattern extracted from (Fig. 1b); we have superposed the expected position of the peaks for the α and β phases. b) Comparison between the measured ePDF (continuous line) and optimized ePDF for the α plus β model (dashed line; region $r > 15$ Å is multiplied by a 3x factor to improve visualization). The lower part of (b) shows the difference curve.



Microstructural characterization of the $\text{Cr}_{29.7}\text{Co}_{29.7}\text{Ni}_{35.4}\text{Al}_{4.0}\text{Ti}_{1.2}$ precipitation-hardened multi- principal element alloy

Diego de Araujo Santana^{1*}, Claudio Shyinti Kiminami², and Francisco Gil Coury³

¹ Postgraduate Program in Materials Science and Engineering, Federal University of São Carlos, São Carlos, Brazil.

² Department of Materials Engineering, Federal University of São Carlos, São Carlos, Brazil.

³ Department of Materials Engineering, Federal University of São Carlos, São Carlos, Brazil.

*Corresponding author: diegodeasantana@ppgcem.ufscar.br

Since 2004 some alloys with equiatomic or near equiatomic compositions and interesting properties have been reported in the literature. These new metallic materials were initially named High Entropy Alloys (HEA) or Multicomponent alloys. Recently, the term Multi-principal Element Alloys (MPEAs) is being increasingly more used. In the early studies of these concentrated alloys, many works were focused on the development of single-phase compositions with optimized properties. Some of the initial thoughts were that solid solutions would be the most stable phases and that intermetallic compounds could be detrimental to mechanical properties. However, nanometric second-phase intermetallic particles dispersed in a ductile matrix acts as a barrier to dislocation motion and, consequently, improve the mechanical properties of an alloy. Therefore, recent studies on MPEAs have been broadened to multi-phase compositions. In this context, we have designed a new precipitation-hardened MPEA, namely $\text{Cr}_{29.7}\text{Co}_{29.7}\text{Ni}_{35.4}\text{Al}_{4.0}\text{Ti}_{1.2}$ (at. %). This alloy was developed to have a concentrated CrCoNi face-centered cubic matrix (FCC) containing nanometric L_{12} precipitates. The alloy was produced by conventional casting, cold-rolled, solution-treated, and aged at 850 °C for different times. The microstructural evolution of precipitates size as a function of aging time was analyzed through Transmission Electron Microscopy (TEM)-dark field images taken using the superlattice reflections of the L_{12} phase. The volume fraction of the precipitates was determined through an established relationship for projected images [1], where the TEM-foil thickness was measured by the electron energy-loss spectrometry (EELS) method [2]. The chemical composition of the matrix and the precipitates was determined using Energy Dispersive X-Ray Spectroscopy (EDS). The results showed a good agreement with thermodynamic calculations performed using the CALPHAD method and PanHEA2020 database [3] via the software Pandat.

REFERENCES

- [1] E.E. Underwood, Quantitative Stereology, Addison-Wesley, 1970.
- [2] D.B. Williams, C.B. Carter, Transmission Electron Microscopy, 2nd ed., Springer, 2009.
- [3] PanHEA: Thermodynamic database for high-entropy transition metal alloys, CompuTherm LLC (www.compuTherm.com).



ACKNOWLEDGEMENTS

This work was financed in part by the Coordenação de Aperfeiçoamento de Pessoal de Nível Superior - Brasil (CAPES) - Finance Code 001, Conselho Nacional de Desenvolvimento Científico e Tecnológico (CNPq) and by grant number #2018/26390-3, São Paulo Research Foundation (FAPESP). The authors thank the Laboratory of Structural Characterization (LCE/DEMa/UFSCar) for the general facilities.



Image and Diffraction Artifacts in TEM Analysis of a Cr-Co-Ni Multi-Principal Element Alloy

Gustavo BERTOLI^{1*}, Claudio S. KIMINAMI² and Francisco G. COURY²

¹ Federal University of São Carlos, Graduate Program in Materials Science and Engineering, Rod. Washington Luis, km 235 SP-310, 13565-905, São Carlos, SP, Brazil.

² Federal University of São Carlos, Department of Materials Engineering, Rod. Washington Luis, km 235 SP-310, 13565-905, São Carlos, SP, Brazil.

*gustavo.bertoli@estudante.ufscar.br

The present work studied a face-centered cubic (FCC) multi-principal element alloy (MPEA) with low stacking fault energy (SFE), the Cr₄₀Co₄₀Ni₂₀ MPEA, which demonstrated a promising mechanical behavior. During microstructural characterization, the electron diffraction analysis revealed some additional spots prohibited for the FCC phase (indicated by white arrows in Figure 1(c)). Based on this, we investigated the possibility of a dual-phase microstructure, constituted by the FCC phase and a small fraction of martensitic phase formed upon cooling, which would be undetectable by conventional X-ray diffraction, but it possibly impacts the mechanical behavior through interface hardening [1-3]. This investigation is relevant in the study of strengthening mechanisms and related topics, so that in the future it will be possible to design stronger alloy with a set of desired properties. As shown in Figure 1(a-c), transmission electron microscopy (TEM) analysis revealed an FCC matrix with annealing twins and stacking faults. Some spots of the diffraction pattern are corresponding to the hexagonal close-packed (HCP) phase, but this phase could not be indexed. In a high-resolution TEM (HR-TEM) analysis (Figure 1(d,e)), lamellae with periodic contrast at every three atomic layers were observed. Fourier transforms (Figure 1(f)) confirm that these lamellae are responsible for all additional spots in the diffraction pattern. The periodic contrast of the HR-TEM images and the additional spots can be explained in two ways [4]:

REFERÊNCIAS

- [1] J. Li et al., *J. Mater. Sci. Technol.* 57 (2020) 85–91.
- [2] Q. Li et al., *Adv. Mater.* 30 (2018) 1–9.
- [3] Z. Li et al., *Nature*. 534 (2016) 227–230.
- [4] E. Abe et al., *Philosophical Magazine A*. 75 (1997) 975–991.
- [5] W. Wu et al., *Intermetallics*. 96 (2018) 104–110.
- [6] B. Amin-Ahmadi et al., *Appl. Phys. Lett.* 102, 071911 (2013).

AGRADECIMENTOS

The authors acknowledge the Fundação de Amparo à Pesquisa do Estado de São Paulo - Brasil (FAPESP) [Grant number 2019/00229-4] and the Conselho Nacional de Desenvolvimento Científico e Tecnológico - Brasil (CNPq) [Grant number 424645/2018-1] for financial support. This study was financed in part by the Coordenação de Aperfeiçoamento de Pessoal de Nível Superior - Brasil (CAPES) - Finance Code 001. The authors thank the Laboratory of Structural Characterization (LCE/DEMa/UFSCar) for the general facilities.



(1) from the overlapping of the FCC matrix and a twin in an incoherent interface, which would generate additional spots by double diffraction; or (2) by the formation of the so-called 9R phase. The 9R phase is formed by dissociating incoherent twin boundaries $\Sigma 3\{112\}$ into two other boundaries, which delimit a 9R phase region [5,6]. Dissociation occurs by the emission of a set of stacking faults at every three $\{111\}$ planes of the FCC structure, generating the 9R structure with a specific stacking of nine close-packed planes (ABC/BCA/CAB) [1,6]. Since its formation depends on the existence of stacking faults, the 9R phase is most commonly reported in FCC metals with low SFE. Some studies argue that the 9R phase can contribute to interface hardening and increase the work hardening rate [1,2]. In a detailed analysis of the results, mainly through the position of additional spots in the diffraction pattern [4], it was defined that the lamellae are not 9R phase. This definition is important for the study of strengthening components in this alloy since the 9R phase can contribute to strengthening, while the other possibility, an image artifact, does not exist with real interfaces, and does not contribute to strengthening. Therefore, the nanometric lamellae with periodic contrast observed in this work are an image artifact produced by the overlapping of the FCC matrix and twins, and not the 9R phase. The promising mechanical behavior of the $\text{Cr}_{40}\text{Co}_{40}\text{Ni}_{20}$ MPEA has no contribution from the interface hardening component by the 9R phase. Thus, the other strengthening components (solid solution, grain refining, etc.) and related topics can be properly studied without the conclusions being compromised by misinterpretations from image artifacts.

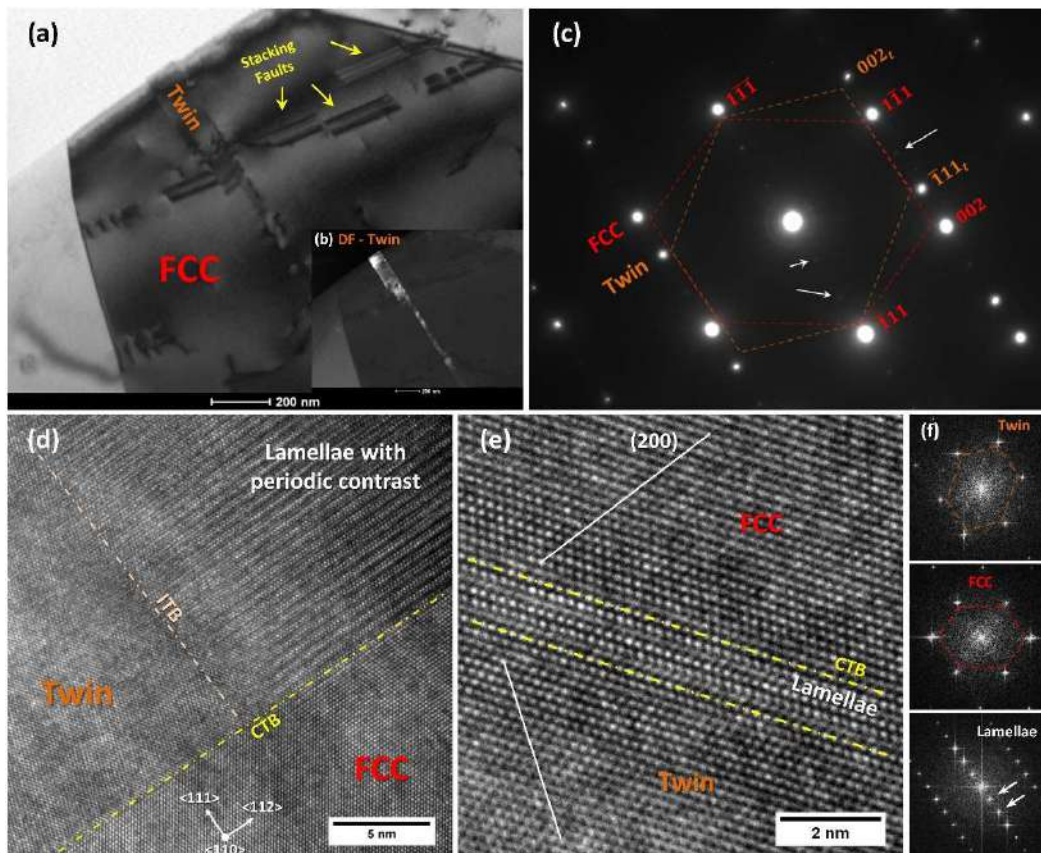


Figure 1 – TEM analysis of the recrystallized $\text{Cr}_{40}\text{Co}_{40}\text{Ni}_{20}$ MPEA (900 °C/0.5 h). (a) Bright field image along the $\langle 110 \rangle$ zone axis; (b) dark field (DF) acquired using the $\{111\}$ spot of the twin; (c) selected area diffraction pattern from $\langle 110 \rangle$ zone axis, indexed with FCC phase and twin with additional spots. (d,e) HR-TEM images and (f) Fourier transforms (FFT) showing the FCC phase, twin, lamellae with periodic contrast, coherent (CTB) and incoherent (ITB) twin boundaries.



Pair Distribution Function Obtained from Electron Diffraction – ePDF: An Advanced Structural Characterization Tool.

João Batista Souza Junior¹, Gabriel Ravanhani Schleder^{1,2}, Adalberto Fazzio^{1,2}, Edson Roberto Leite^{1,3} and Jefferson Bettini^{1,*}

¹ Brazilian Nanotechnology National Laboratory (LNNano), Brazilian Center for Research in Energy and Materials (CNPEM), 13083-970, Campinas, Brazil

² Federal University of ABC (UFABC), Santo André, São Paulo, Brazil ¶

³ Department of Chemistry Federal University of São Carlos, 13565-905, São Carlos, SP, Brazil.

* jefferson.bettini@lnnano.cnpem.br

Atomic-scale structure determination has become crucial to understand nanomaterials properties and develop new technologies. Although Pair Distribution Function (PDF) analysis by neutron and X-rays scattering profile have been used to study nanomaterials, electron diffraction can offer some advantages to characterize the atomic structure of clusters, small nanoparticles, and amorphous samples. Electrons have higher scattering power than X-rays, allowing to obtain PDF from electron diffraction (ePDF) for small sample amounts and time-efficient data acquisition. The number of electron microscopes available worldwide is another advantage. Nowadays, with the rise of methodologies and specific software for ePDF data analysis, the scientific community can benefit from advanced transmission electron microscopy (TEM) structure determination integrating commonly available TEM analyses (size, distribution, shape, and high-resolution TEM atomic visualization) with ePDF atomic structure determination both for core and surface configurations. Therefore, ePDF has the potential to become one routinely and advanced characterization tool for nanomaterials science. In this work, ZrO₂ nanoparticles with an average size of 2,8 nm (Figure 1) [1] have been characterized by ePDF to investigate the structural coherence changed after the ligand exchange, and the structure of amorphous glassy water has also been analyzed by ePDF and compared to other results in the literature (Figure 2) [2]. A Joel JEM 2100F microscope and an Orius 600 CCD camera were used to acquire the electron diffraction patterns for ZrO₂ nanoparticles study. The amorphous glassy water was prepared by traditional cryo sample methodology, and the electron diffraction patterns obtained using a Talos 200C microscope, a cryo sample holder, and a CETA camera.

References

[1] Schleder, G. R.; Azevedo, G. M.; Nogueira, I. C.; Rebelo, Q. H.; Bettini, J.; Fazzio, A.; Leite, E. R. Decreasing Nanocrystal Structural Disorder by Ligand Exchange: An Experimental and Theoretical Analysis. *Journal of Physical Chemistry Letters* 2019, 10,

[2] Souza Junior, J. B.; Schleder, G. R.; Colombari, F. M.; de Farias, M. A.; Bettini, J.; van Heel, M.; Portugal, R. V.; Fazzio, A.; Leite, E. R. Pair Distribution Function from Electron Diffraction in Cryogenic Electron Microscopy: Revealing Glassy Water Structure. *The Journal of Physical Chemistry Letters* 2020, 11, 1564–1569, PMID: 32023063



Acknowledgement

This work was supported by Brazilian agencies Fundação de Amparo à Pesquisa do Estado de São Paulo FAPESP (Grant Nos. 2018/051591, 2013/07296-2, 2017/18139-6, 2017/023172) and Conselho Nacional de Desenvolvimento Científico e Tecnológico CNPq (INCTCarbono).

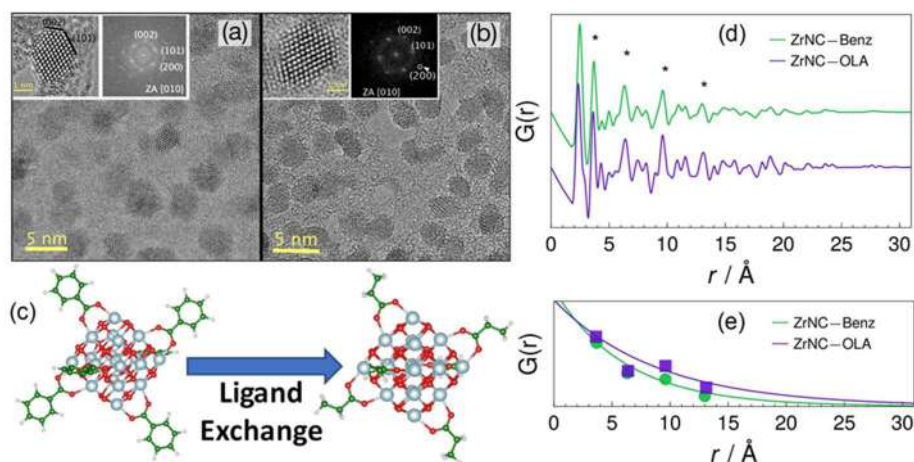


Figure 1 - HRTEM images of ZrO_2 nanocrystals having (a) benzoic acid ($ZrNC_{Benz}$) and (b) oleic acid ($ZrNC_{OLA}$) as surface ligands. (c) Scheme of the ligand exchange process displaying the structural models of the ZrO_2 cluster with the aromatic ligands and with aliphatic chain (C_2H_5-) ligands obtained from DFT calculations. (d) ePDF of $ZrNC_{Benz}$ and $ZrNC_{OLA}$ samples. The asterisks indicate the first Zr-Zr peaks. (e) Exponential fitting used to obtain the finite length of structural coherence ($LSC = 2/\alpha$) by using the equation $\exp(-\alpha r)$ to Zr-Zr peaks.

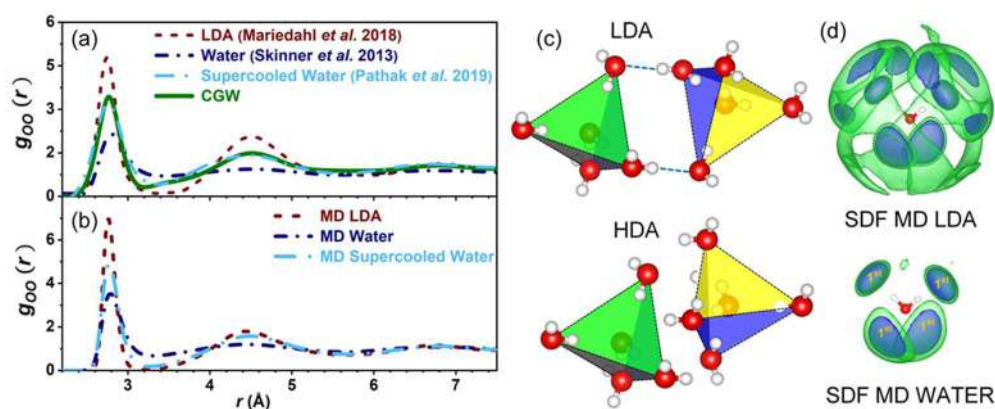


Figure 2 - Amorphous ePDF $g(r)$ for (a) thin Cryo-EM glassy water (CGW) support membrane compared to X-ray PDF for the LDA phase (Mariedahl et al.31), liquid water (Skinner et al.32), and supercooled water (Pathak et al.33). CGW ePDF was also compared to (b) $g(r)$ calculated from molecular dynamics for LDA, liquid water and supercooled water. (c) Water tetrahedra schemes showing the LDA short-range order (SRO; top) with two nearest neighbor tetrahedra connected by two hydrogen bonding interactions (blue lines), and the high-density amorphous (HDA) SRO (bottom) that do not keep the local structure, allowing H_2O molecules to approach another tetrahedra thus increasing local density. (d) Spatial distribution function (SDF) of the LDA ice (top) and



liquid water (bottom), obtained by molecular dynamics. Two isosurfaces are shown indicating larger (blue) and lower (green) spatial concentration of molecules.



Pitting Corrosion Initiation in Super Duplex Stainless Steel Investigated by EBSD

Ribeiro, T.G.M.^{1*}, Spadotto, J.C.^{1,2}, Labre, C.³ and Bott, I.S.¹

¹ Department of Chemical and Materials Engineering, PUC-Rio, Rio de Janeiro, Brazil.

² Materials Performance Centre, School of Materials, The University of Manchester, UK.

³ Brazilian Center of Research in Physics, CBPF, Rio de Janeiro, Brazil.

*Corresponding author: thiagogmr@yahoo.com.br

The microstructure of Duplex stainless steels (DSS) has an approximately equal balance of ferrite (δ) and austenite (γ) phases, which results in excellent mechanical and corrosion properties. When applied upon in practical conditions such as welding and heat treatment around 1000 °C and 1100 °C, these steels show significant microstructural changes. These changes range from the volume fraction of the phases, chemical composition, precipitation of intermetallic phases, and the formation of interfaces having different orientation relationships (O.R.), such as Kurdjumov-Sachs (K-S) and Nishiyama-Wassermann (N-W) [1]. Depending on both the microstructural evolution and morphology of the phases, different responses to a particularly corrosive environment can be developed. Therefore, the application of such structural materials in work environments can be compromised [1,2]. The steel studied in this work is the DSS UNS 32750, which was aged in temperatures of 1000 °C and 1100 °C for 24 and 240 h. All samples were water quenched after aging, followed by corrosion testing according to the ASTM G48 standard (24 h at 60 °C in a 6% FeCl₃ solution). The microstructure characterization was conducted by scanning electron microscopy (SEM JEOL-JSM 7100F) equipped with a Si drift detector (SDD) for X-ray energy dispersive spectroscopy (XEDS) (Oxford Instruments X-Max 80) and electron backscatter diffraction (EBSD) detector (Nordlys Max2). EBSD analysis confirmed the influence of heat treatment on the microstructural balance and morphological evolution of the phases. It was identified the effect of the exposure time in the formation of interfaces having the K-S and N-W O.R. EBSD phases and Inverse Pole Figure (IPF) maps in **Figure 1a e Figure 1b** shows the distribution of the ferrite, austenite, and sigma (σ) phase resulting from the aging at 1000 °C for 240 h. The latter is considered highly harmful in stainless steel due to its high hardness, low corrosion resistance, and high formation kinetics. The formation of such deleterious phase occurs at grain boundaries and preferential sites of supersaturated elements of the ferritic and austenitic matrix [2]. **Figure 1c** displays the solute partitioning of Fe, Cr, Ni, Mo, and Si between the identified phases identified by XED spectrum images. This figure confirmed that the σ phase was enriched in Cr and Mo and contained Fe, Si, and Ni. EBSD phase map in **Figure 2a** indicates the susceptibility of the pitting initiation at the phase boundary regions. Based on this figure, it is identified the pitting did not start close to an interface with the O.R. K-S (yellow lines – indicated by the arrows). This analysis is in accordance with the literature in which planes with higher atomic density have greater interfacial energy, promoting excellent resistance to corrosion [3,4]. **Figure 2b** shows the IPF map of the steel after heat treatment of 1100 °C for 24 h submitted to corrosion testing, where the location of the pitting is preferred at the grain boundaries, however away from the O.R. N-W (black line – indicated by the arrow) [4]. The present research is still under development to clarify the influences of crystallography with susceptibility to pitting.

References:

[1] R. N. Gunn, Duplex Stainless Steels: Microstructure, Properties and Applications, **Woodhead Publishing Limited: Cambridge**, 1nd ed. 1997

- [2] Haghdad, N. et al. **Materials Letters**, v. 196, pp. 264–268, 2017.
 [3] Zhang, L. et al. **Metall Mater Trans B**, Vol. 49, pp. 919–925, 2018.
 [4] Shahryari A. et al. **Corrosion Science**, Vol. 51, pp. 677-682, 2009.
 [5] The authors are grateful to CBPF-Brazil for the access to the LabNano Electron Microscopy facilities and to the *Coordination for the Improvement of Higher Education Personnel – CAPES/Brazil*.

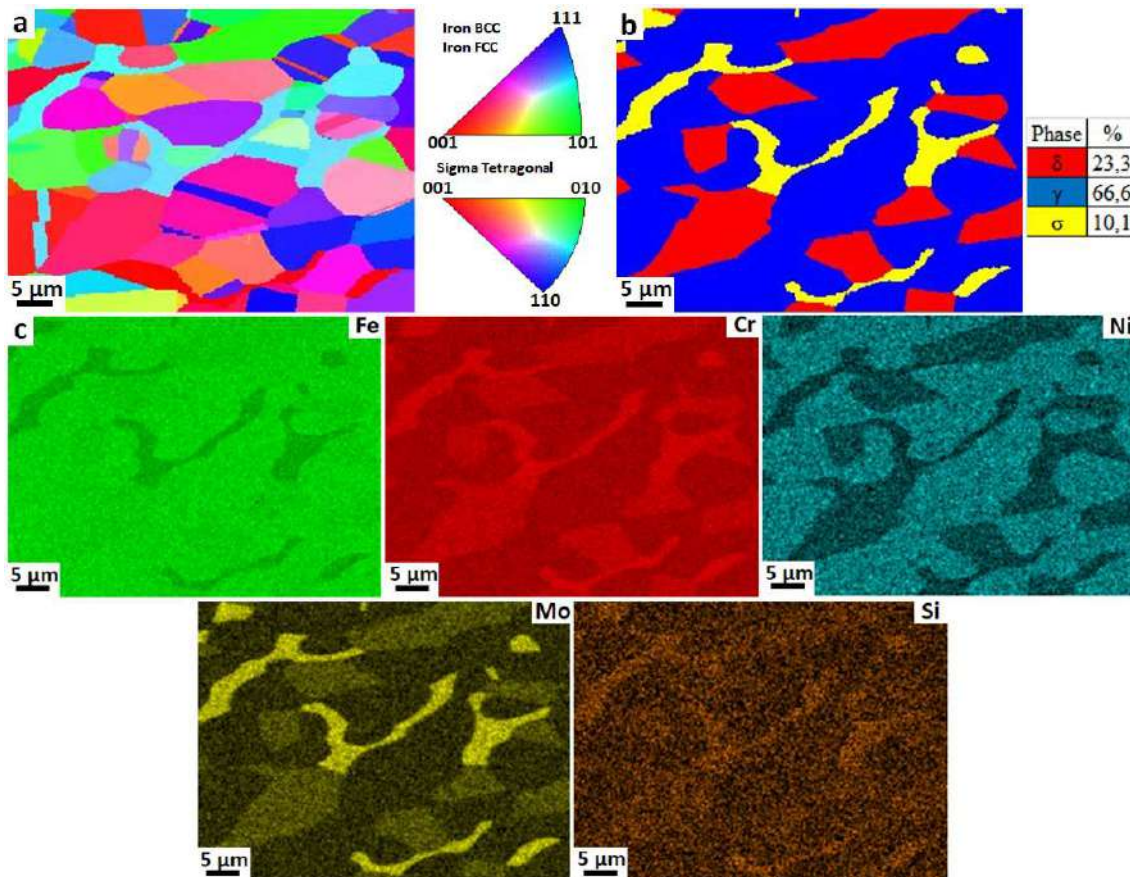


Figure 3. Microstructure of DSS UNS 32750 aged at 1000 °C for 240 h. (a) IPF map; (b) phase map showing the balance phase of ferrite, austenite, and σ phase; and (c) corresponding XED spectrum images of Fe, Cr, Ni, Mo, and Si. Electrolytic polishing.

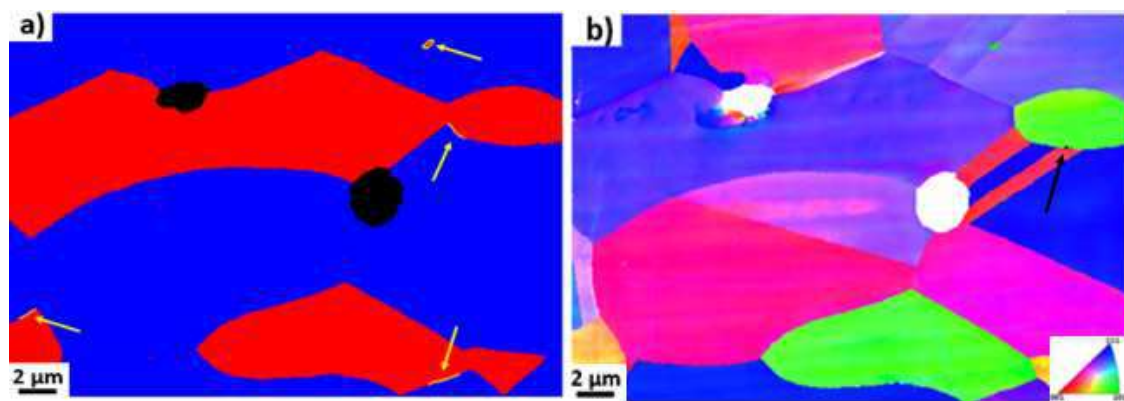


Figure 4. (a) EBSD phase map (ferrite = red and austenite = blue) of UNS 32750 aged at 1000 °C for 240 h showing the pitting located far from the O.R. K-S (indicated by arrows yellow) and (b) corresponding IPF map and showing O.R. N-W (indicated by arrow black). Mechanical Polishing.



Eta phase characterization in HP40 steels after long-term exposure in service conditions

M.C. Mendes¹, M. Nascimento², L.S. Araújo², L. Mallet³, J. Dille^{2,3}, L.H. de Almeida²

¹ Federal Center for Technological Education of Rio de Janeiro (CEFET-RJ)
matheus.mendes@cefet-rj.br

² Federal University of Rio de Janeiro (UFRJ)

³ Free University of Brussels

Reformer furnaces have been largely applied in the petrochemical industry to produce hydrogen gas. Under operational conditions, this process can reach 950°C at about half of height of the radiant tubes [1]. The use of centrifugally cast stainless steels in these components, particularly HP grade, has been well-established, being the tubes designed for a nominal life of 100.000hs under creep deformation [1]. As a critical factor, a decrease in creep resistance after long-term aging has motivated an improvement on the performance of HP steels in recent years. In this context, Nb and Nb plus Ti were added to the chemical composition of the normal grade to increase microstructural stability, resulting in the micro-alloyed HP steels [2]. During long-term service, the microstructural evolution promotes a progressive reduction of creep resistance and ductility, mainly due the coarsening of the primary and secondary carbides, and partial transformation of the primary NbC and (Nb,Ti)C to an intermetallic G-phase (Ni₁₆Nb₆Si₇) [3]. The occurrence of this silicide in HP steels is associated with the instability of the niobium carbides in a temperature range between 700 and 1000°C during long-time operational exposure. Although there is an adequate knowledge about the presence of G-phase (FCC structure), some studies have identified another intermetallic for long-term aged HP steels, the eta-phase. [3]. A little information about eta-phase (DC structure) in these alloys is available, but its stoichiometry is proposed as NiCrSi and its formation supposed occurs due an instability of the G-phase in temperatures above 900°C [3]. In this work, in-service aged HP steels with two different chemical compositions have been studied using several techniques to investigate the G-phase instability and, consequently, the eta-phase presence. The microstructure has been characterized by analytical electron microscopy (SEM-EDS) combined with electron back-scattered diffraction (EBSD) technique and the crystallography by transmission electron microscopy (TEM). In only one of the two samples, two distinct Si rich phases, easily identified by the EDS spectra (Fig1), were found. However, the diffraction pattern similarity between the FCC and DC structures makes the crystallographic identification difficult and could lead to an interpretation error due to double-diffraction spots on the pattern. In order to unambiguously identify the correct crystal structure, it is mandatory to have a diffraction pattern corresponding to a [001] zone axis. In this context, a <100> direction-oriented Si-rich particle was selected by EBSD and, then, correctly oriented in the SEM to be able to obtain a FIB cross-section perpendicular to one of the two other <100> directions. In this way, the measurements on the electron diffraction pattern, having a [001] zone axis, showed values that correspond to the diamond-cubic eta-phase (Fig3).

[1] I.U. Perez et al., J Fail. Anal. and Preven. 13 (2013) 779.

[2] J. Laigo, et al., Mater Charact. 59 (2008) 1580.

[3] E.A. Kenik, et al., Scr. Mater. 49 (2003) 117.

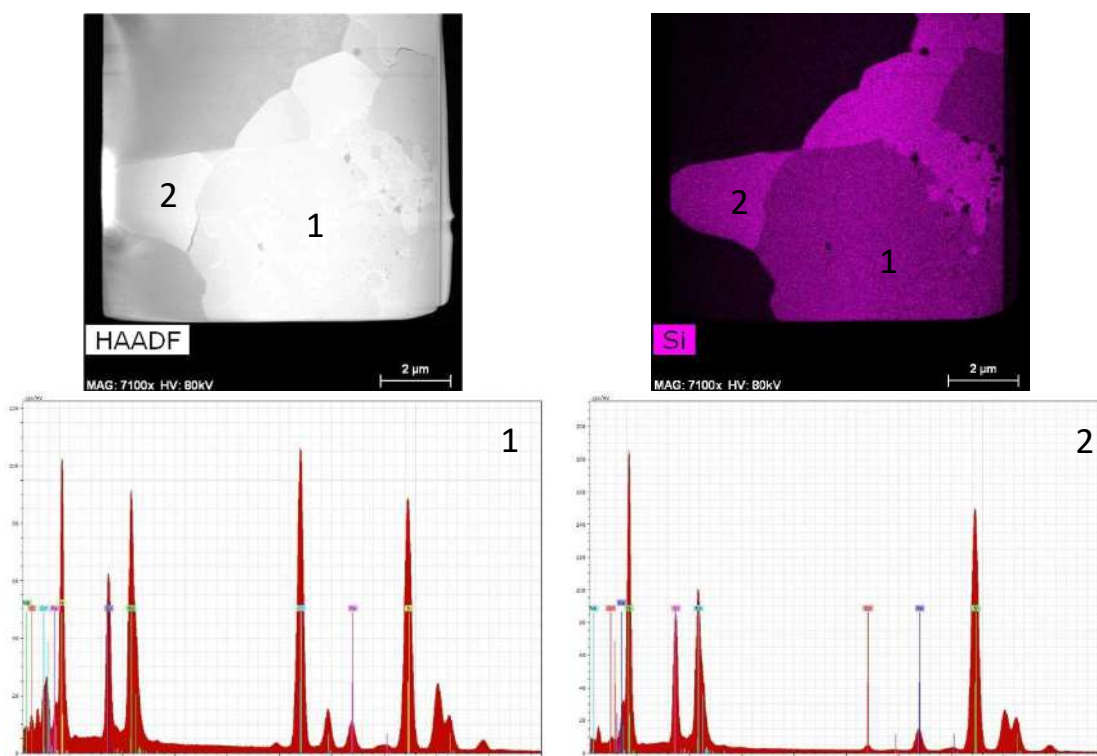


Fig1. HAADF-TEM image and EDS-TEM mapping showing Si-rich intermetallic particles on TC sample. EDS spectra showed two different particles, in (1) high Cr and N, corresponding to eta phase and in (2) low Cr and no N, corresponding to a G-phase.

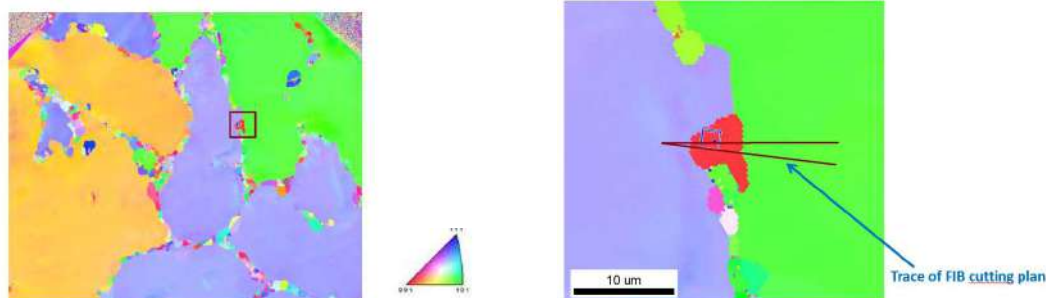


Fig2. SEM-EBSD mapping showing the $\langle 100 \rangle$ direction-oriented Si-rich particle and the FIB cross-section region.

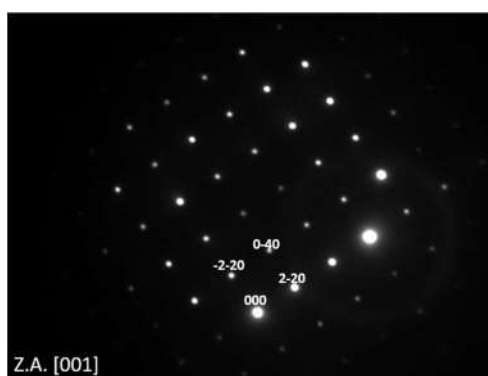


Fig3. Electron diffraction pattern of the diamond cubic eta-phase.



Assessment of Crystallographic Orientation Relationships Between δ -phase and γ -matrix in Alloy 718 by Electron Backscattered Diffraction

Flávia da Cruz Gallo^{1*}, Luiz Maurício Barreto de Azevedo¹, Cilene Labre², Loic Mallet³, Leonardo Sales Araújo¹, Luiz Henrique de Almeida¹

¹Programa de Engenharia Metalúrgica e de Materiais (UFRJ), Rio de Janeiro, Brazil,

²Centro Brasileiro de Pesquisas Físicas (CBPF), Rio de Janeiro, Brazil,

³Université Libre de Bruxelles (ULB), Brussels, Belgium.

*flacruz@metalmat.ufrj.br

Literature shows that the physical metallurgy on δ -phase precipitation in alloy 718 still arouses interest to fully understand its precipitation driven force and growth kinetics. Particularly focusing on high-temperature precipitation of δ phase, different orientation domains or variants within one intergranular precipitate were observed in strain free alloy 718, aged above γ'' solvus temperature [1,2]. Crystallographic information based on TEM analysis evidenced an orientation relation (OR) between γ matrix and δ precipitate corresponding to $\{111\}\gamma//\{010\}\delta$ and $\langle 11\bar{0}\rangle\gamma//\langle 100\rangle\delta$, showing that δ is a coherent precipitate with the $\{111\}\gamma$ habit plane [1,3,4]. The majority of studies focusing on establishing crystallographic orientation relationships between phases is based on transmission electron microscopy (TEM), selected-area diffraction patterns (SADPs) and high-resolution transmission electron microscopy (HRTEM) analysis. Despite newly achieved advances in TEM characterization capabilities, results are thoroughly dependent on high-quality sample preparation, which actually configures the chokepoint in a nanoscale research. The present work investigated intergranular precipitation of δ -phase in alloy 718 aged at 900°C as a function of time, using SEM-EBSD, focusing on the differentiation of the precipitation behavior at grain boundaries with different characters. Fig. 1 shows SEM/BSE images of samples aged at 900°C for different times. Small step size EBSD scans provided enough resolution to detect different orientation domains within each δ precipitate. Raw data processed by MTEX generated inverse pole figures (IPF) as well as phases orientation distribution function (ODF). This technique proved to be a very efficient alternative to obtain crystallographic information from the precipitates and matrix when compared to TEM analysis and SADPs. The possibility to access larger areas, and consequently, more significant statistical populations of precipitates and grains, makes this EBSD-based analysis advantageous over TEM. Not to mention time consuming is an issue for TEM sample preparation. The obtained results showed that the crystallographic orientation of δ -phase relative to the neighbor grain reflects the orientation relation previously observed in literature [1,3,4]. Additionally, it was verified using EBSD scans that all δ precipitates contain at least two variants, both of which follow strictly the OR with the matrix. Fig. 2 shows the IPF of alloy annealed at 900°C for 4h, with an intergranular δ particle in a random high-angle boundary (RHAB). All variants of the precipitate follow the OR with only one neighboring grain (γ_1). Precipitates formed at an incoherent $\Sigma 3$ twin boundary follow the OR with both neighboring twinned orientations (Fig. 3).

[1] M. Sundararaman et al., Metall. Trans. A, **19**, 453 (1988).

[2] M. Dehmas et al., Adv. Mater. Sci. Eng., **2011**, 1 (2011).

[3] G. H. Cao et al., Mater. Charact., **136**, 398 (2018).

[4] S. Azadian et al., Mater. Charact., **53**, 7 (2004).

This research was supported by CAPES and FAPERJ. Authors thank to Villares Metals for the material.

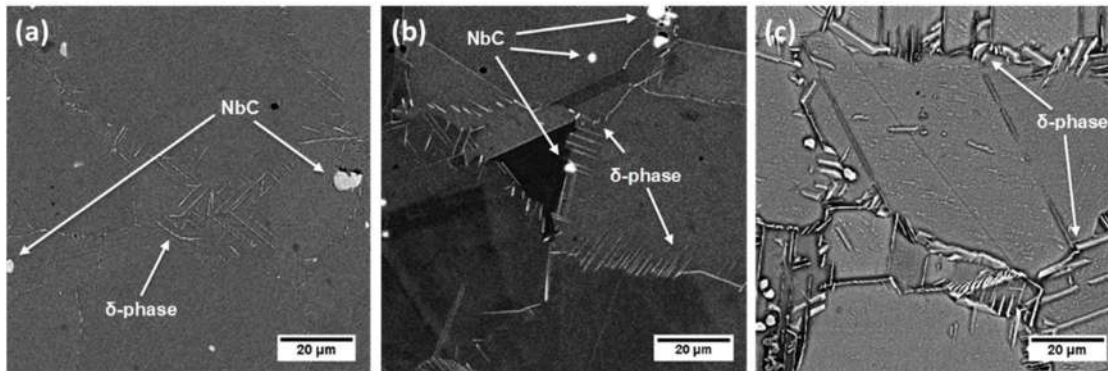


Fig. 1 – SEM/BSE images of samples aged at 900°C for (a) 2 h, (b) 4 h and (c) 6 h, showing δ-phase precipitation evolution and MC-type carbides (glyceregia / 90 sec).

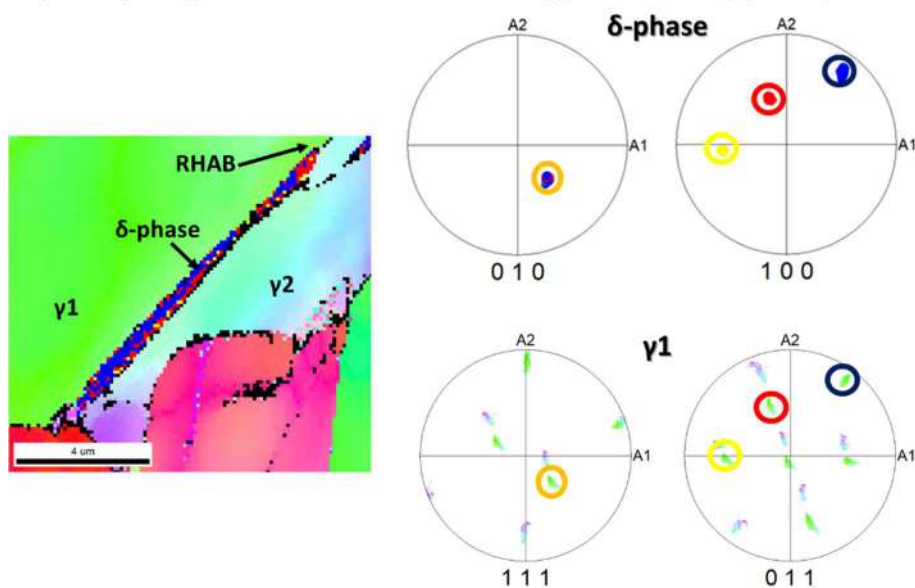


Figure 2 – IPF of alloy 718 annealed at 900°C for 4 h, showing an intergranular δ particle in a RHAB. ODF of δ-phase evidencing different variants. All variants coincide only with matrix γ1 in grain 1.

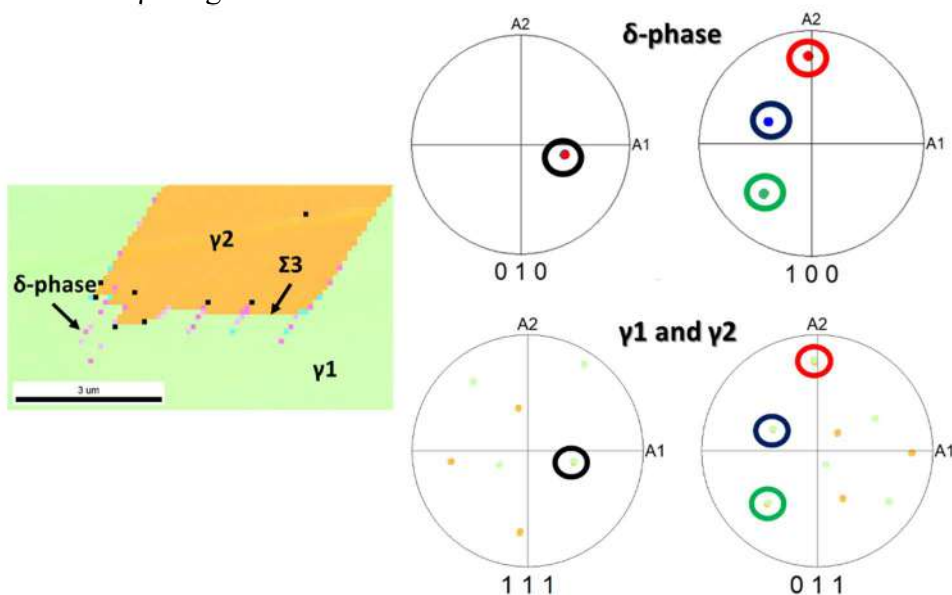


Figure 3 – IPF of alloy 718 annealed at 900°C for 4 h, showing an intergranular δ particle in an incoherent Σ3 twin boundary. All δ-phase variants coincide with both grain 1 and 2 (γ1 and γ2).



Evaluation of the Twinning Induced Plasticity Effect on a FeMnAlC Steel during Cyclic Deformation

André L. Vidilli^{1*}, Lucas B. Otani¹, Witor Wolf², Claudio S. Kiminami³, Walter J. Botta³, Francisco G. Coury³ and Claudemiro Bolfarini³

¹ Graduate Program in Materials Science and Engineering, Federal University of São Carlos (UFSCar), São Carlos, SP, Brazil.

² Department of Metallurgy and Materials, Federal University of Minas Gerais (UFMG), Belo Horizonte, MG, Brazil

³ Department of Materials Engineering, Federal University of São Carlos (UFSCar), São Carlos, SP, Brazil

*andre.vidilli@gmail.com

The Fe-Mn-Al-C steels have been considered a promising candidate for automotive application as it can offer low density, ultra-high strength, it presents good formability due to its high ductility, and presents high-energy absorption capability, which is essential for passenger safety [1]. The excellent combination of mechanical properties of these alloys is associated with the Twinning Induced Plasticity (TWIP) effect, which the twins nucleated during the plastic deformation act as obstacles to the dislocation motion, reducing the mean free path, leading to high strain hardening rates [2]. A critical resolved shear stress must be reached for mechanical twins nucleation. It is reported in the literature different deformation modes during monotonic and cyclic tests of TWIP steels. While it was observed a massive fraction of twins during tensile test, the absence on cyclic loading is commonly reported [3]. The present work aims to evaluate the mechanical behavior of Fe-25wt.%Mn-3wt.%Al-0.4wt.%C during tensile and fatigue tests, focusing on the presence of deformation twins and their possible effects on both tests. The steel was processed by spray forming, resulting in a deposit with high microstructural homogeneity. Then, the deposit was swaged at 800 °C, generating bars that were annealed at 900°C for 20 min, resulting in a fully recrystallized austenitic microstructure with 15 µm average grain size. Specimens were machined from the bars for tensile and fatigue tests. The first was carried out up to failure under a strain rate of 10⁻³ s⁻¹. The fatigue evaluating was performed on a stress-controlled mode, under a 20 Hz frequency, R = 0.1, a run-out of 5.10⁶ cycles and the fatigue limit was determined by staircase method. A Philips XL-30 FEG SEM was used for microstructural evaluation of the longitudinal sections of the fatigue specimens. The transmission electron microscopy (TEM) was used to identify the TWIP effect after tensile and fatigue tests through a FEI Tecnai G²F20 operating at 200kV. One TEM foil of the fatigue crack propagation area was prepared by the Focused Ion-Beam technique using a Ga-ion source in a Quanta FEG 3D FEI microscope. The current steel showed an outstanding ductility during the tensile test with 73% of elongation at fracture and a high density of nanometric deformation twins was observed by TEM distributed throughout the specimen. The fatigue limit was 387 MPa and mechanical nanotwins were identified both in the surface of the specimens and in grains in which occurred the fatigue crack stable propagation. This result indicates that the critical stress has been reached on the surface, as it is a region with stress concentrating effect, and in the fatigue crack propagation path due to the stress field associated with the plastic zone ahead of the crack tip. The main conclusion is that the TWIP effect is not

only active during cyclic loading, but can also influence the nucleation and crack propagation stages for the fatigue behavior [4].

- [1] S. Chen et al., Prog. Mater. Sci. 89 (2017) 345.
- [2] R. Kalsar et al., Scripta Mater. 154 (2018) 207.
- [3] A. S. Hamada et al., Mater. Sci. Eng. 517 (2009) 68.
- [4] A. L. Vidilli et al., J. Alloys Compd. 831 (2020) 154806.

The authors thank the Laboratory of Structural Characterization (LCE/DEMa/UFSCar) for the general facilities. This study was financed in part by the Coordenação de Aperfeiçoamento de Pessoal de Nível Superior – Brasil (CAPES) – Finance Code 001; São Paulo Research Foundation (FAPESP), grant 2018/04142 and 2013/05987-8; and Conselho Nacional de Desenvolvimento Científico e Tecnológico, grant 130825/2018-2.

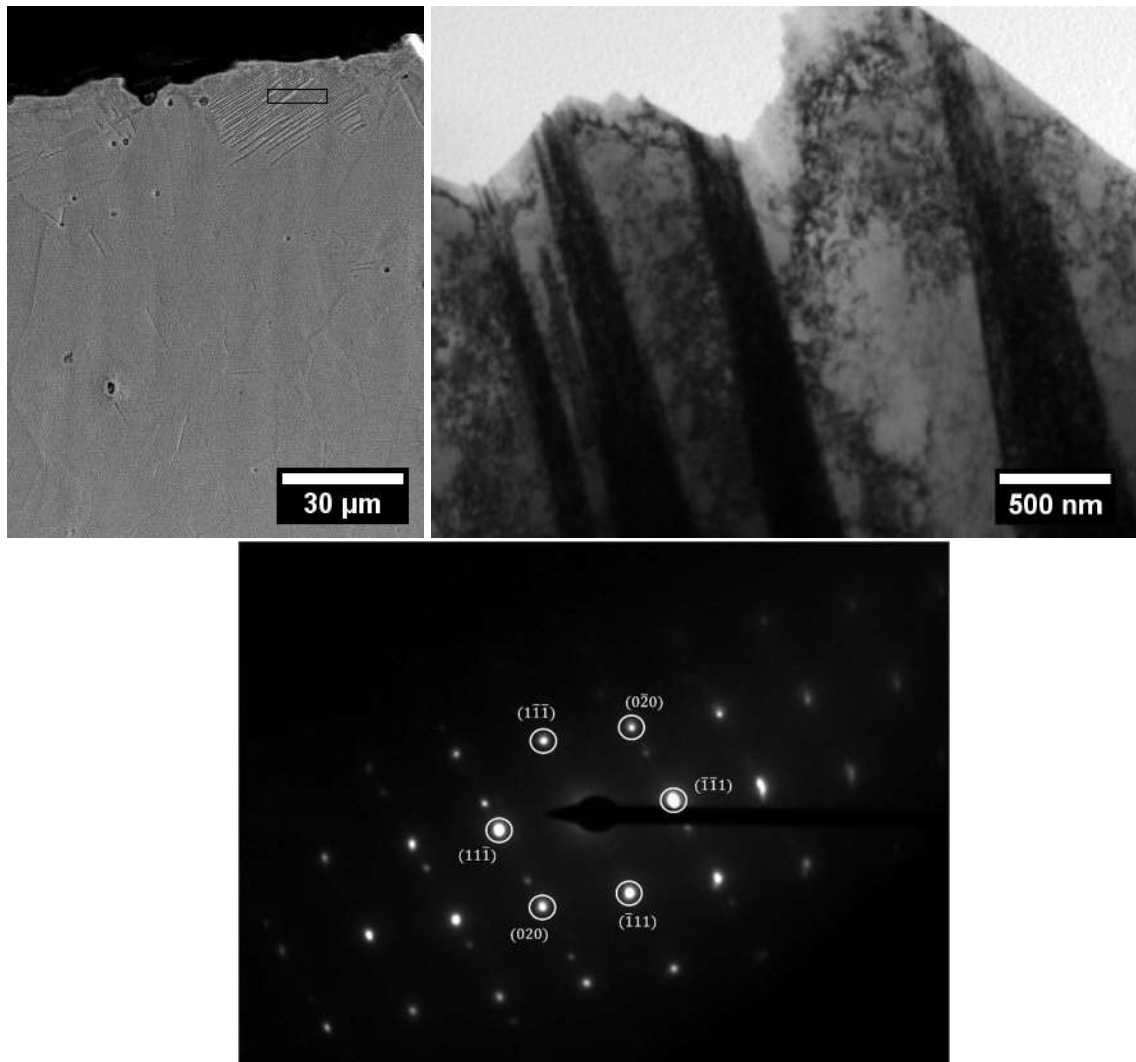


Figure 1 – SEM – SE image of a section of the fatigue crack stable propagation region; TEM-BF image from the FIB-extracted sample corresponding to the region highlighted by the rectangle in SEM image; The selected area diffraction pattern of the [110] zones axis showing the matrix and twin reflections.

DOI:
ISSN:



28º CONGRESSO DA SOCIEDADE BRASILEIRA
DE MICROSCÓPIA E MICROANÁLISE
12 a 15 JUL 2021

on-line

50anos
SOCIEDADE BRASILEIRA DE
MICROSCÓPIA E MICROANÁLISE





Ultrastructural Analysis of Flagellar Ectosomes-Like Structures in *Tritrichomonas foetus*

Abigail Miranda-Magalhães^{1*} and Antonio Pereira-Neves¹

¹ Fiocruz Pernambuco, Instituto Aggeu Magalhães – Departamento de Microbiologia, Recife, Brazil.

*abimiranda00@gmail.com

Tritrichomonas foetus (*Tf*) is a flagellated protist that colonizes the reproductive tract of cattle and the large intestine of cats [1]. *Tf* has three anterior flagella and one recurrent flagellum that runs toward the posterior region of the cell, forming an undulating membrane [1]. In addition to cell movement and sensory functions, the eukaryotic flagella can send information via ectosomes (ECs), a type of extracellular vesicle (EV) that protrude and shed from the cell surface [2]. There are few studies about EV in *Tf* [3] and neither of them reports the presence of flagellar ECs structures. Consequently, the aim of this study is to identify flagellar ECs-like structures in *Tf* after interaction with Alcian blue and host cells. To this, *Tf* was cultivated in a TYM (trypticase, yeast extract and maltose) medium, supplemented with 10% fetal bovine serum for 24 h at 37°C [4]. For Alcian blue assays, *Tf* was incubated in 1% Alcian blue-coated coverslips for up to 2 h at 37°C. For parasite-host cells interaction assays, *Tf* was incubated with fresh bovine preputial epithelial cells (PECs) at 5:1, parasite: host cell rate, for to 15 minutes at 37°C. All samples were prepared for scanning electron microscopy (SEM), as previously described [5]. Alternatively, parasites were settled onto Alcian blue-coated carbon film nickel grids and negatively stained with 1% aurothioglucose, as previously described [5]. SEM revealed ECs-like structures ranging in diameter from approximately 50 nm–200 nm closely apposed the flagella under all experimental conditions (Figs. 1- 2). Vesicular structures that seems to be in process of budding directly from the flagellar membrane were also observed using negative staining (Fig. 1c). After interaction with PECs, it was noticed parasites connected to each other through the flagella with numerous ECs on that region (Fig. 2a). In addition, we found flagellar ECs in contact with PECs (Fig. 2b). Quantitative SEM analysis showed that approximately 7.5% of *Tf* grown in axenic culture (control) exhibited flagellar ECs. Similar result was found after Alcian blue interaction; however, the *Tf* percentage with flagellar ECs was 12-fold higher after PEC interaction, suggesting that ECs are being formed in response to host cell exposure (Fig. 3a). Interestingly, no significant difference was found in the relative number of ECs per flagella between all experimental conditions (Fig. 3b). Our data demonstrate the presence of flagellar ECs-like structures in *Tf* and highlight a role for the ECs in the cell-to-cell communication and *Tf* pathogenesis; however, further studies are necessary for better characterization of these structures and their role in the parasites' biology [6].

[1] J. Dabrowska, J. Vet. Res., 63 (2019) 533

[2] J. Wang et al., Essays Biochem, 62 (2018) 205

[3] W. De Souza et al., Parasitol. Res., 119 (2020) 2005

[4] L. Diamond, The Journal of Parasitol., 43 (1957) 488

[5] M. Benchimol et al., Biocel, 45 (2021) 259

[6] This work was supported by CNPq/PROEP Instituto Aggeu Magalhães-FIOCRUZ, nº 39/2018

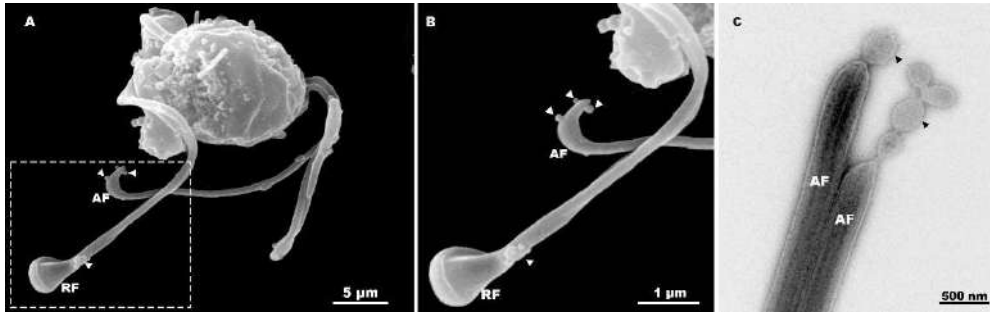


Figure 1. (a-b) SEM of flagellar ectosomes-like structures (arrowheads) in *T. foetus* after Alcian blue interaction. (c) Negative staining showing ectosomes - like structures in process of budding from the flagellar membrane. RF, recurrent flagellum; AF, anterior flagella. Bars.: a, 5 µm; b, 1 µm; c, 500 nm.

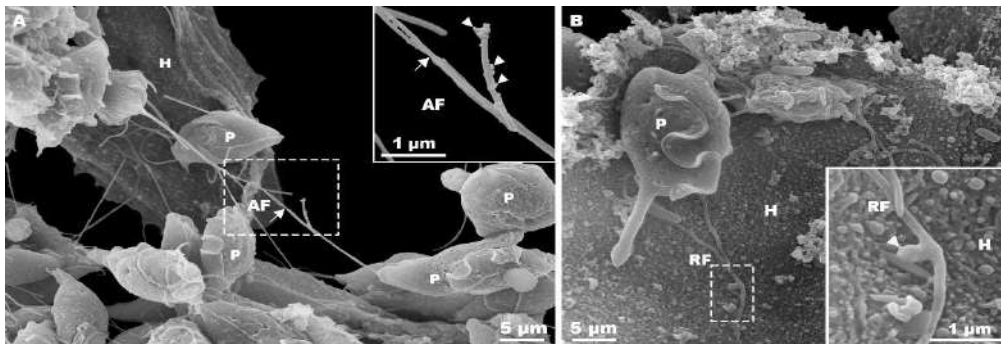


Figure 2. Flagellar ectosomes-like structures (arrowheads) in *T. foetus* after interaction with fresh bovine preputial epithelial cells (H). (a) Parasites are connected to each other through the flagella (arrow) with numerous ectosomes (ECs) on that region. (b) A flagellar ECs in contact with host cell (H) can be noticed. RF, recurrent flagellum; AF, anterior flagella; P, parasite; H, host cell. Bars.: a-b, 5 µm; insets, 1 µm.

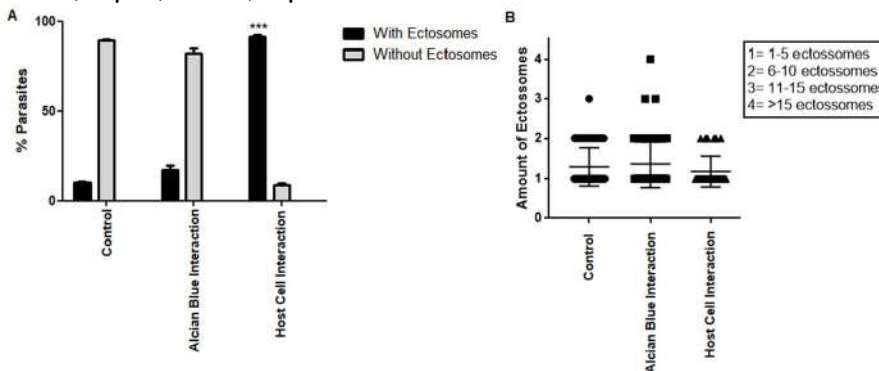


Figure 3. Quantitative analysis of flagellar ectosomes (ECs) in *T. foetus*. Control: parasites grown in axenic culture; Alcian Blue Interaction: parasites incubated in Alcian blue-coated coverslips; Host cell Interaction: parasites coincubated with bovine preputial epithelial cells. The result was determined from counts of at least 100 parasites randomly selected per sample using SEM. The values are expressed as the means \pm S.D of two independent experiments, each performed in duplicate. (a) Percentage of parasites displaying ECs; The *Tf* percentage with flagellar ECs was 12-fold higher after PEC interaction, suggesting that ECs are being formed in response to host cell exposure. *** $p < 0.001$ as compared with control using ANOVA test. (b) The relative number of ECs per flagella. Scale: (1) from 1 to 5 ECs; (2) from 6 to 10 ECs; (3) from 11 to 15 ECs; and (4) > 15 ECs. No significant difference was found between all experimental conditions.



Scanning Electron Microscopy of Testicular Maturation of *Baryancistrus xanthellus*

Ivana K.S.Viana¹, Alex S. Paiva^{2*}, Leocyvan Nunes¹, Yanne A. Mendes², Renata S. Oliveira¹, Yuri W.M. Favacho², João M. S. Rodrigues¹, Liziane A. B. Gonçalves¹, Rossineide M.Rocha¹

¹ Laboratório de Ultraestrutura celular, Universidade Federal do Pará, Instituto de Ciências Biológicas, Belém, Brasil

² Laboratório de Imunohistoquímica, Universidade Federal do Pará, Instituto de Ciências Biológicas, Belém, Brasil

* alexsousa27@gmail.com

Brazil stands out as the third country in the world that sells the most ornamental fish for the aquarist market [1]. *Baryancistrus xanthellus* is a species of the loricarideo family, endemic to the Amazon region, known as "amarelinho" and of high economic value in the international market [2]. However, the reproductive and morphological characteristics of the testicular maturation of this species are unknown, in which this knowledge is important to support studies for captive breeding and preservation of the species' genetic material. Thus, a total of 30 males of *B. xanthellus* were caught in bimonthly collections in 2016 and 2017 from the Xingu River in northern Brazil. Testis fragments were fixed in Karnovsky's solution for 3h, post-fixed with 1% osmium tetroxide solution, dehydrated in a graded ethanol series, and critical point dried using CO₂. Specimens were mounted on stubs, coated with gold and analyzed using a LEO 1430 Scanning Electron Microscopy (SEM). The testes of *B. xanthellus* are located in the dorsal region of the coelomic cavity are paired and lobular shape. The testes are fused caudally, forming a single sperm duct leading to the urogenital papilla (Fig 1 A,B). Four stages of testicular maturation were observed: Immature presents a regular outer covering (Fig. 1C) and little apparent tubules without organization of spermatogenic cysts (Fig. 1D); In maturation with irregular testicular surface and seminiferous tubules with spermatogenic lineage cell cysts (Fig. 1E,F); Mature with irregular testicular surface, well-defined cell cysts and in greater quantity (Fig. 1G,H); Spermatized with slightly irregular external surface and seminiferous tubules with some cell cysts (Fig. 1I,J). By SEM it was possible to evidence the organization of the tissue structure of the testis whose data subsidize information for the characterization of reproductive biology and future cryopreservation techniques.

References:

[1] G. Prang. Uakari,3 (2007) 7.

[2] M.O. Camargo et al., Entre a Terra, as águas e os pescadores do Médio Rio Xingu: Uma abordagem Ecológica. 1ª ed. Belém 2009.

Acknowledgement

Coordination for the Improvement of Higher Education Personnel (CAPES) for financial support

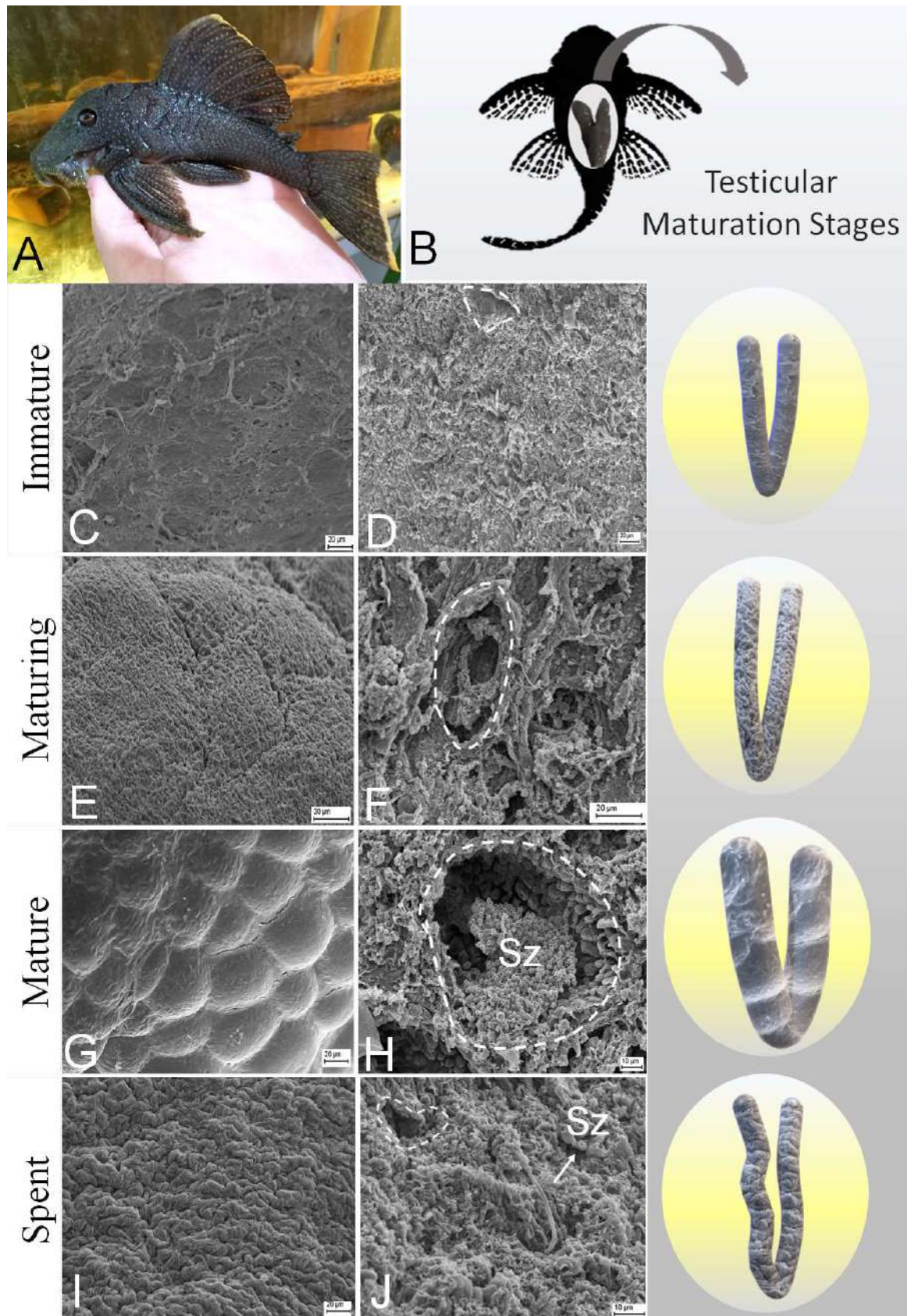


Figure 1 A: Photograph B. *xanthellus* B: Schematic of testicular maturation stages C,D: immature testis E,F: maturing testis G,H: mature testis I,J: spent testis. Sz: sperm, dashed line: seminiferous tubule.



Activity of the Synthetic Compound 4-[[[(4-fluorophenyl)amino)methyl]-5-(4-nitrophenyl)-3-[N'-(pyridin-2-ylmethylene)hydrazinecarbonyl]-isoxazole on *Leishmania amazonensis*

Amanda Beatriz Kawano Bakoshi^{1*}, Rayanne Regina Beltrame Machado¹, Hélito Volpato¹, Samara Mendes de Souza Melo², Fernanda Andreia Rosa³, Tania Ueda-Nakamura¹, Sueli de Oliveira Silva¹, Celso Vataru Nakamura¹ and Danielle Lazarin-Bidóia¹

¹ Laboratory of Technological Innovation in the Development of Drugs and Cosmetics, Universidade Estadual de Maringá, Maringá, Brazil.

² Department of Chemistry, Universidade Estadual de Maringá, Maringá, Brazil.

*amandabakoshi@gmail.com

Leishmaniasis, a disease caused by protozoa of the genus *Leishmania*, remains endemic in nearly 100 countries [1]. Current treatment is inadequate due to the toxicity and drug resistance [2]. Thus, it is evident that new studies must be conducted to discover less toxic and more effective leishmanicidal drugs. Therefore, this study aimed to investigate the *in vitro* activity of a new synthetic compound 4-[[[(4-fluorophenyl)amino)methyl]-5-(4-nitrophenyl)-3-[N'-(pyridin-2-ylmethylene)hydrazinecarbonyl]-isoxazole (**35-a**) on intracellular amastigotes of *Leishmania amazonensis* and to evaluate the morphological and ultrastructural changes induced by **35-a**. The antiproliferative activity against amastigotes was performed using J774A.1 macrophages infected with promastigotes (1:10 ratio) for 24 h and treated with increasing concentrations of **35-a** for 48 h. The survival index was obtained after Giemsa staining by counting the number of infected cells and amastigotes per macrophage, and the IC₅₀ was determined. Cytotoxicity of **35-a** in J774A.1 macrophages and L929 fibroblasts was evaluated after 48 h using the MTT colorimetric assay, and the CC₅₀ was determined. For SEM, amastigotes treated with IC₅₀ and 2xIC₅₀ of **35-a** for 48 h were fixed with 2.5% glutaraldehyde in 0.1 M cacodylate buffer at 4 °C for 24 h, dehydrated, critical point dried in CO₂, sputter-coated with gold and visualized in a FEI SCIOS™ dual-beam microscope. For TEM, cells were treated and fixed, post-fixed, dehydrated, embedded in EPON™ epoxy resin and polymerized. Ultrathin sections were obtained and examined in a JEOL JEM 1400 TEM. Table 1 shows that **35-a** exhibited an excellent activity against amastigotes (IC₅₀=0.96 μM), and low cytotoxicity in J774A.1 macrophages (CC₅₀=196.1 μM) and in L929 fibroblasts (CC₅₀=232.1 μM). Figure 1 shows amastigotes treated with 0.96 μM of **35-a**. SEM and TEM analysis of treated amastigotes revealed a reduction in the number of intracellular amastigotes (Figure 2A) and an increase of autophagic vacuoles and lipid droplets accumulation (Figure 2B). Taken together, these findings suggest that the isoxazole **35-a** is active against *L. amazonensis* and stands out as a promising candidate for further investigations regarding treatment of leishmaniasis.

REFERENCES

- [1] M. Akhoundi et al., PLOS Neglected Tropical Diseases. 10 (2016) 6.
- [2] E. Torres-Guerrero et al., F1000 Research. 6 (2017) 750.

ACKNOWLEDGEMENTS

This study was supported by grants of CAPES, CNPq, FINEP, Fundação Araucária and COMCAP-UEM.

Table 1. *In vitro* activity of the isoxazol **35-a** against *Leishmania amazonensis*.

	IC ₅₀	J774A.1 macrophages CC ₅₀	SI	L929 fibroblasts CC ₅₀	SI
Intracellular Amastigotes	0.96 ± 0.028	196.1 ± 8.3	204.27	232.1 ± 6.2	241.77

Data were expressed in μM , mean \pm standard deviation. Selective index (SI) was calculated by the equation: $\text{SI} = \text{CC}_{50} / \text{IC}_{50}$.

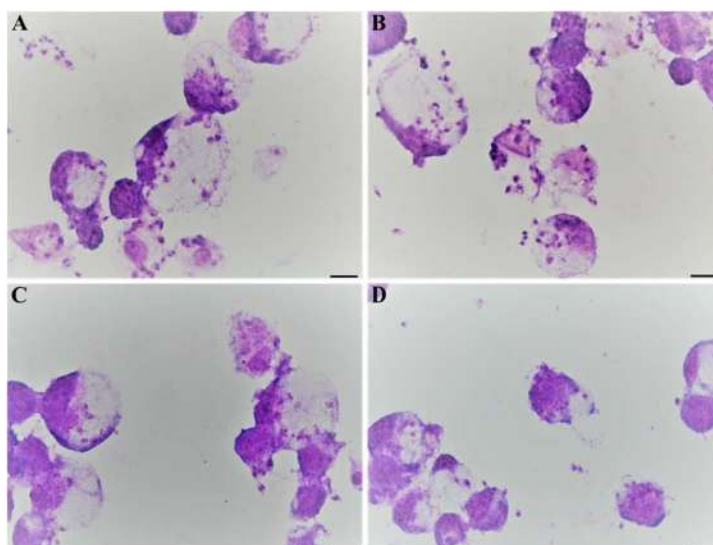


Fig. 1. Light microscopy of J774A.1 macrophages infected with *Leishmania amazonensis* amastigotes and treated with the isoxazol **35-a** for 48 h. Untreated parasites (A, B). Amastigotes treated with 0.96 μM (IC₅₀) of **35-a** (C, D). Bars: 10 μm .

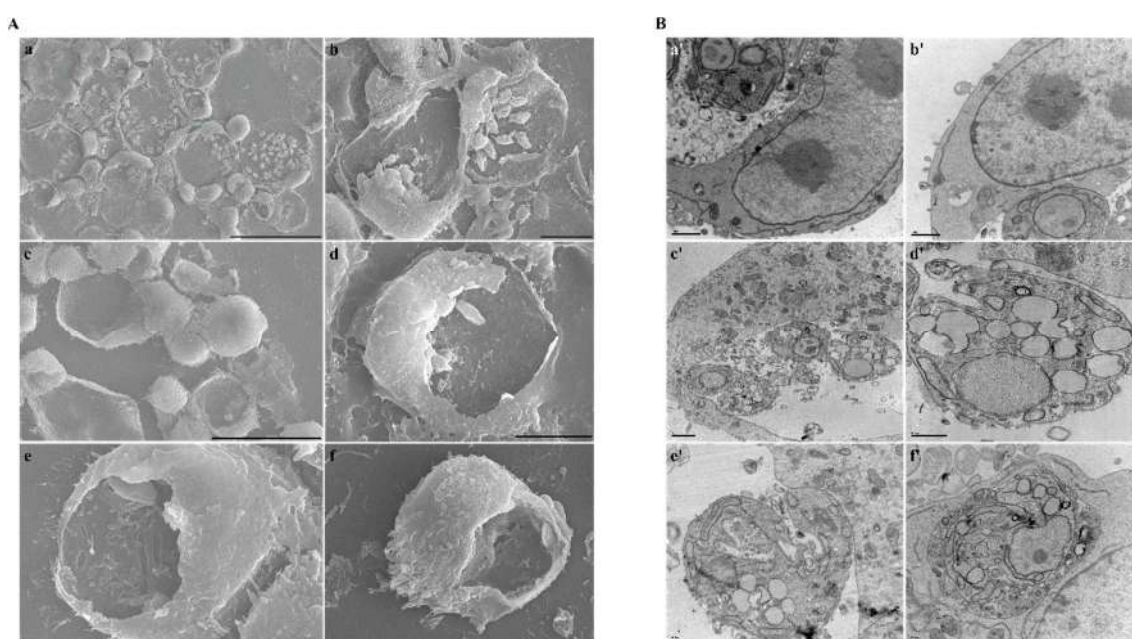


Fig. 2. Scanning electron microscopy (A) and transmission electron microscopy (B) of J774A.1 macrophages infected with *Leishmania amazonensis* amastigotes and treated with **35-a** for 48 h.



Untreated parasites (a, b, a', b'). Amastigotes treated with 0.96 μM (IC_{50}) (c-e, c'-e') and 1.92 μM (2xIC_{50}) (f, f') of **35-a**. Bars: 50 μm (a), 10 μm (b, d, f), 30 μm (c), 5 μm (e), 1 μm (a'-c'), 0.5 μm (d'-f').



The KAP7 importance to cell proliferation, mitochondrial DNA arrangement and repair in the trypanosomatid

Angomonas deanei

Camila Silva Gonçalves^{1,2*}, Carolina Moura Costa Catta Preta^{2,4}, Bruno Repolês³, Jeremy Mottram⁴, Wanderley de Souza^{1,2}, Carlos Renato Machado³ and Maria Cristina Machado Motta²

¹. Centro Nacional de Biologia Estrutural e Bioimagem, IBCCF - UFRJ, RJ, Brasil.

². Laboratório de Ultraestrutura Celular Hertha Meyer, IBCCF- UFRJ, RJ, Brasil:

³. Laboratório de Genética Química, ICB, MG, Brasil.

⁴. Centre for Immunology and Infection, University of York, York, United Kingdom.

*camilabiof@gmail.com

Trypanosomatids contain unusual structures, as the kinetoplast, the portion of the single branched mitochondrion that harbours the mitochondrial DNA (kDNA), a network composed by thousands of topologically interlocked DNA circles (minicircles and maxicircles) [1]. The kDNA presents a unique and intriguing array that varies according to trypanosomatid species and stages of development [2]. Such variations on the network arrangement are related to the presence of histone like-proteins that associate to kDNA and are known as KAPs (Kinetoplast Associated Proteins). Furthermore, such proteins neutralize the negatively charged kDNA, thus influencing the activity of mitochondrial enzymes involved in DNA replication, transcription and repair. In *Angomonas deanei* kDNA fibers are disposed in a looser arrangement that fulfills the matrix of the trapezoid shape kinetoplast [3] (Fig. 1b), thus facilitating the identification of kDNA alterations after using compounds that target KAPs [4]. In this work we used microscopy techniques to investigate *A. deanei* cells that had *kap7* genes deleted by CRISPRCas9 system. The mutant protozoa had a reduced cellular proliferation in relation to wild type (WT) cells (Fig. 1a). Transmission Electron Microscopy (TEM) revealed that mutant cells present alterations on the kDNA network, that was seen densely packed especially in the region facing the basal body (brackets) (Fig. 1e-g). Analysis by Scanning Electron Microscopy (SEM) showed that mutants presented a reduced length of the cell body and flagellar shortening when compared to control protozoa, as well as, multiples cell body indicating division impairment (Fig. 1h-j). Regarding cytokinesis, mutant cells exposed to genotoxic agents, as ultraviolet radiation, presented exacerbated phenotypes (Fig. 1n-p) in relation to WT cells (Fig. 1k-m). Taken together, our data indicate that *Angomonas deanei* KAP7 presents important roles in cell proliferation, mitochondrial DNA arrangement and is possibly involved in kDNA repair.

REFERENCES:

[1] Lukes J, Guilbride DL, Votýpka J *et al.*, Eukaryot Cell., Aug;1(4):495-502, 2002.

[2] Cavalcanti DP, Shimada MK, *et al.*, BMC microbiology, v. 9, p. 120, 2009.

[3] de Souza SS, Catta-Preta CM, *et al.*, PLoS ONE 12(11): e0187516, 2017.

[4] Cavalcanti DP, Fragoso, S. P. *et al.*, Parasitology Research, v. 94, p. 439-448, 2004.

This research was supported by CNPq (Brazil), FAPERJ, CAPES. Acknowledgements to CENABIO.

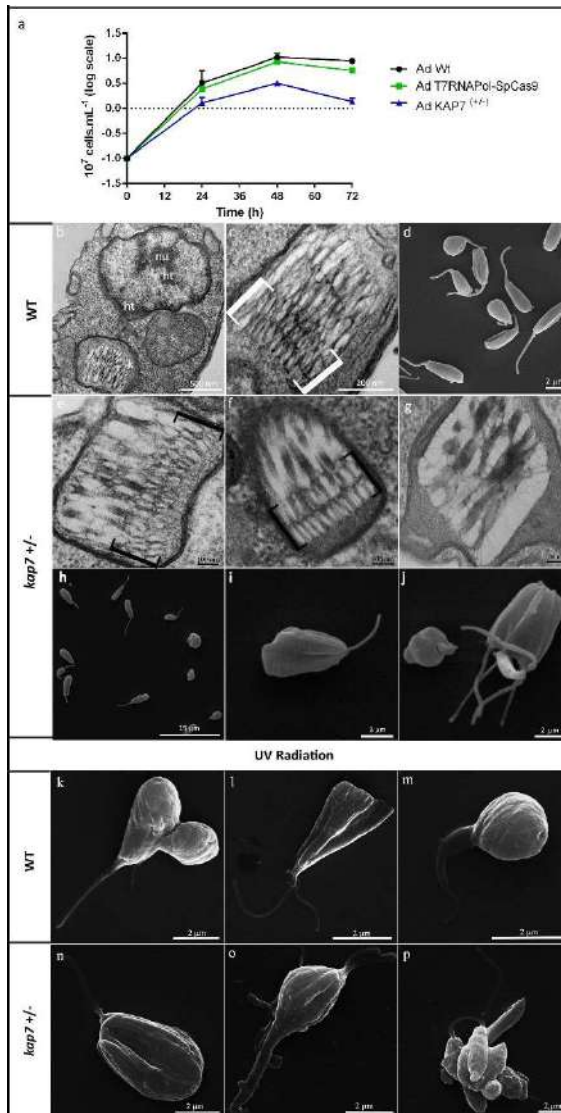


Figure 1. (a) Growth curve for 72 h showed that *KAP7* mutants present a reduced proliferation in relation to WT and T7RNAPol-SpCas9 strains. (b-d) The ultrastructure and morphology of *A. deanei* WT. (e-g) Different levels of compaction was observed in Ad *KAP7*^(+/-) kinetoplast. (h-j) Morphologic analyses showed reduced length of the cell body and flagellum. Multiples cell body were observed indicating division impairment. (k-m) WT exposed to genotoxic treatment by ultraviolet radiation presented different phenotypes. (n-p) Ad *KAP7*^(+/-) showed phenotypes more exacerbated regarding to cytokinesis impairment when compared to WT protozoa. nu-nucleolus, ht-heterocromatin, k-kinetoplast, s-simbiont.



Interactions of TiO₂ Microparticles in Sunscreens with Lettuce Plants (*Lactuca Sativa* L.)

Ana Kamila Medeiros Lima^{1*}, Thaiz B. A. R. Miguel² and Emilio de Castro Miguel³

¹ Doutoranda no Programa de Pós Graduação em Sistemática, Uso e Conservação da Biodiversidade, Departamento de Biologia, Fortaleza, Brasil.

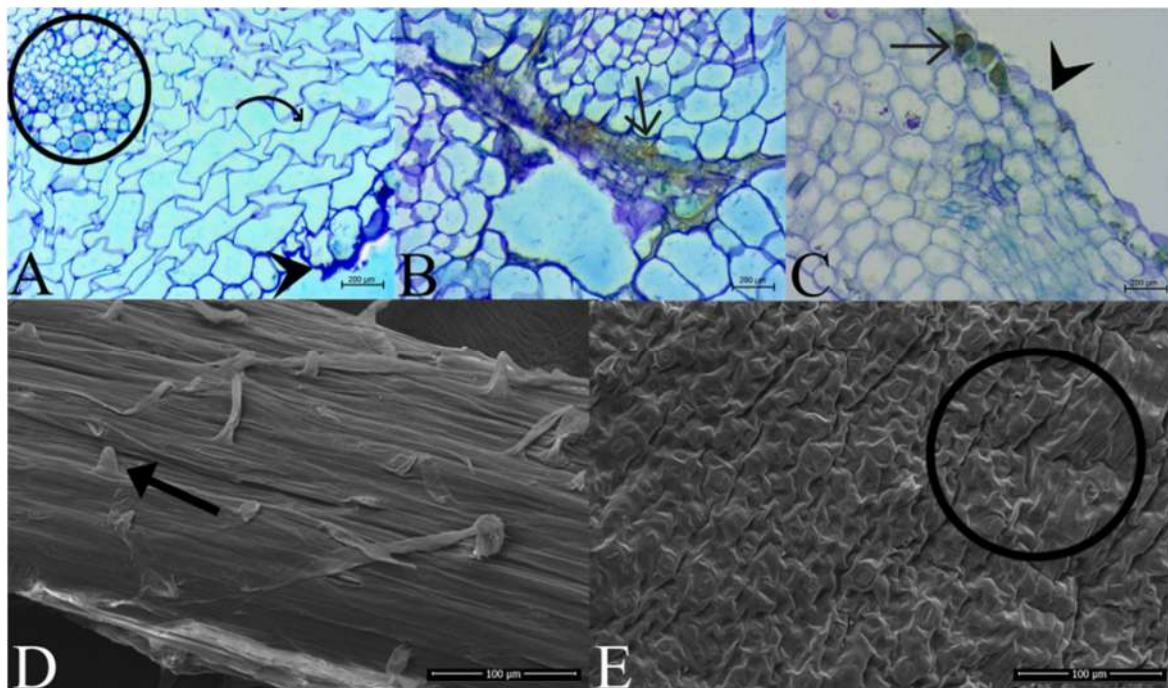
² Laboratório de Biotecnologia, Depto. de Tecnologia de Alimentos, Fortaleza, Brasil

³ Docente no Programa de Pós Graduação em Sistemática, Uso e Conservação da Biodiversidade, Departamento de Eng. Metalúrgica e Materiais, Fortaleza, Brasil.

*kamilamedeiroslimaa@gmail.com

Sunscreens are a class of compounds that protect the skin from ultraviolet radiation in the UVA and UVB range. They are divided into two main classes, organic and inorganic. The second has as main components zinc oxide (ZnO) and titanium dioxide (TiO₂). They act by dispersing and reflecting radiation and are of the order of nanoparticles [1]. With the growth of commercial and industrial use of these particles and the increase in production of titanium dioxide due to its great scientific innovation in the technology of inorganic sunscreens [2] in addition to the accumulation of residues from sunscreens and the need for studies relating the toxicity of these compounds to other groups of organisms, lettuce (*L. sativa* L.) was chosen as an experimental model to carry out further tests and understand the behavior of these MPs, contributing to the elucidation of the effects that the indiscriminate use of this type of product can bring to ecosystems. The aim of this work was explore in more details the relationship between MPs of titanium dioxide and lettuce. The experimental design took place as follows: the lettuce seeds were exposed for two hours to different concentrations of TiO₂ and their growth was monitored for 7 days. Samples collected on the 7th day were processed for optical microscopy and scanning electron microscopy. The main damages were: thickening of the cell wall, presence of inclusions in the tissues, disruption of the vascular bundle, cellular morphological irregularity, little quantity and density of root hairs and irregularity in the epidermis. These damages were found in the concentration of 50 ppm and will be discussed below. An early thickening of the cell wall was observed, as in [3], without appearing in the control being possible an indication of stress [4]. Cytoplasmic changes were seen as cell damage prior to cell death [4]. One of the evidences of toxicity is the small amount, the length of the root hairs, and the absence of them [5]. It was observed that the titanium particles do not have a homogeneous size [6]. In addition, they were visualized as aggregates in the vacuole, cytoplasm and between the cell wall and the plasma membrane [8]. Exposure to MPs during root elongation is associated with the appearance of abnormal cells, as can be seen in Figure 1 [5] [9]. The inclusions, described as oily bodies and with peripheral disposition [7], gradually increased to the maximum in the treatment of 50 ppm. The morphological evidence of cell irregularity and swelling of the epidermis in some points is supported by [5]. Presence of NPs inclusions, accumulation in the rhizoderm, penetration into the cell wall and even translocation is possible [9]. In addition, transcriptional repression of root development genes predicted an altered root phenotype in plants exposed to MPs (including TiO₂) [10]. Studies carried out using TiO₂ and ZnO showed that these particles were able to reach the fruits of tomato plants analyzed regardless of the exposure method [10]. The damage brought here is a potential indicator of bioaccumulation and therefore should be carefully studied.

Figure 1. Optical and electron microscopy for scanning the radicle, hypocotyl, piliferous zone and cotyledons of *Lactuca sativa* on the 7th day after sowing in treatment of 50ppm of titanium dioxide.



A: Curved arrow radicle: cellular morphological irregularity. Circle: the disruption of the vascular bundle. Arrowhead: thickening of the cell wall. B: Hypocotyl. Thin arrow: the presence of inclusions in the vascular bundle. C: Cotyledon. Thin arrow: the presence of inclusions in the epidermis. Arrowhead: cell wall thickening. D: Piliferous zone. Arrow: the small amount and small size of the root hairs. E: Cotyledon. Circle: cell irregularity and swelling.

REFERENCES

- [1] Serpone, N., Dondi, D. and Albini, A. (2007). Inorganic and Organic UV Filters: Their Role and Efficacy in Sunscreens and Suncare Products. *Inorganica Chimica Acta*, 360, 794-802.
- [2] FLOR, J.; DAVOLOS, M. R.; CORREA, M. A. Protetores solares. *Revista Brasileira de Medicina*, v. 65, n. SPEC. ISS. OCT., p. 6-11, 2008.
- [3] MANESH, R. R.; GRASSI, G.; BERGAMI, E.; MARQUES-SANTOS, L. F.; FALERI, C.; LIBERATORI, G.; CORSI, I. Co-exposure to titanium dioxide nanoparticles does not affect cadmium toxicity in radish seeds (*Raphanus sativus*). *Ecotoxicology and Environmental Safety*, v. 148, n. May 2017, p. 359-366, 2018.
- [4] BEGUM, P.; IKHTIARI, R.; FUGETSU, B. Graphene phytotoxicity in the seedling stage of cabbage, tomato, red spinach, and lettuce. *Carbon*, v. 49, n. 12, p. 3907-3919, 2011.
- [5] BEGUM, P.; FUGETSU, B. Phytotoxicity of multi-walled carbon nanotubes on red spinach (*Amaranthus tricolor* L) and the role of ascorbic acid as an antioxidant. *Journal of Hazardous Materials*, v. 243, p. 212-222, 2012.
- [6] BELLANI, L.; MUCCIFORA, S.; BARBIERI, F.; TASSI, E.; RUFFINI CASTIGLIONE, M.; GIORGETTI, L. Genotoxicity of the food additive E171, titanium dioxide, in the plants *Lens culinaris* L. and *Allium cepa* L. *Mutation Research - Genetic Toxicology and Environmental Mutagenesis*, v. 849, n. January, p. 503142, 2020.
- [7] CHICHIRICÒ, G.; POMA, A. Penetration and toxicity of nanomaterials in higher plants. *Nanomaterials*, v. 5, n. 2, p. 851-873, 2015.
- [8] GARCÍA-SÁNCHEZ, S.; BERNALES, I.; CRISTOBAL, S. Early response to nanoparticles in the *Arabidopsis* transcriptome compromises plant defence and root-hair development through salicylic acid signalling. *BMC Genomics*, v. 16, n. 1, 2015.
- [9] RALIYA, R.; NAIR, R.; CHAVALMANE, S.; WANG, W. N.; BISWAS, P. Mechanistic evaluation of translocation and physiological impact of titanium dioxide and zinc oxide nanoparticles on the tomato (*Solanum lycopersicum* L.) plant. *Metallomics*, v. 7, n. 12, p. 1584-1594, 2015.
- [10] ZHANG, P.; MA, Y.; ZHANG, Z.; HE, X.; LI, Y.; ZHANG, J.; ZHENG, L.; ZHAO, Y. Species-specific toxicity of ceria nanoparticles to *Lactuca* plants. *Nanotoxicology*, v. 9, n. 1, p. 1-8, 2015.



Characteristic of Human Milk Powder Obtained by Lyophilization.

Otávio Augusto Silva Ribeiro^{1,2}, Karla Veloso Gonçalves Ribeiro^{1,3*}, Cristiane do Carmo Cesário^{1,3} and Jane Sélia dos Reis Coimbra¹

¹ Universidade Federal de Viçosa, Departamento de Tecnologia de Alimentos, Viçosa, MG - Brasil.

² Universidade Federal do Acre, Centro Multidisciplinar, Cruzeiro do Sul, AC - Brasil.

³ Universidade Federal de Viçosa, Núcleo de Microscopia de Microanálise, Viçosa, MG - Brasil. *karla.goncalves@ufv.br

INTRODUCTION: The storage of expressed human milk (EHM) in a human milk bank (HMB) is a high-cost operation because EHM must be stored under freezing temperature (-18 °C). An alternative solution for storage cost reduction would be the production of powdered EHM. Thus, the objective of this work was to produce and characterize human milk powder grains obtained by freeze-drying, as their characteristics are necessary to determine the EHM solubility. **MATERIAL AND METHODS:** Six samples of pooled EHM were obtained from the HMB at the São Sebastião Hospital in Viçosa city. Each sample was processed using holding pasteurization and subsequently frozen for later lyophilization to obtain the powdered EHM. After the freeze-drying, the lyophilized samples were macerated with mortar and pestle for 5 minutes, covered with gold (15 nm thick) (Quorum, Q150RS, United Kingdom) [1], and analyzed for their characteristics under a scanning electron microscope (Carl Zeiss, LEO 1430 VP, United Kingdom) at 15 kV. **RESULT AND DISCUSSION:** Grains of powdered EHM (Fig. 1-A; 1-B; 1-C) were heterogeneous in shape, with an average area of 6345 μm^2 , with a maximum of 30187 μm^2 and a minimum of 413 μm^2 , an average diameter of 148.56 μm , with a maximum and minimum diameter of 483.52 μm and 24.7 μm respectively. The diameter of powdered milk influenced its reconstitution in water because the smaller the diameter, the greater the contact surface with the solvent, which enhanced its wettability [2]. Orifices were observed in the grains at several points due to the water sublimation process during lyophilization. The presence of pores in the powder allows water diffusion to the inner, thus increasing its solubility [3]. The formation of agglomerates in the powder, which favors its solubilization, was also observed [4]. **CONCLUSION:** Lyophilization can be a good option for obtaining human milk expressed in powder due to the good morphological characteristics of the powder that affect some properties, as solubility.

REFERENCES

- [1] Berger LRR, et al. Cowpea resistance induced against *Fusarium oxysporum* f. sp. *tracheiphilum* by crustaceous chitosan and by biomass and chitosan obtained from *Cunninghamella elegans*. *Biol Control* 92:45–54, 2016.
- [2] Birchal VS, et al. Effect of Spray-Dryer Operating Variables on the Whole Milk Powder Quality. *Drying Technology*, 23:611–636, 2005
- [3] Zhou Y, et al. Freeze-drying of “pearl milk tea”: A general strategy for controllable synthesis of porous materials. *Scientific Reports*, 2016.
- [4] Chever S, et al. Agglomeration during spray drying: Physical and rehydration properties of whole milk/sugar mixture powders. *LWT - Food Science and Technology*, 2017.

ACKNOWLEDGEMENT

CAPES, CNPQ, FAPEMIG, Departamento de Tecnologia de Alimentos da Universidade Federal de Viçosa and Núcleo de Microscopia e Microanálise (NMM) from Universidade Federal de Viçosa.

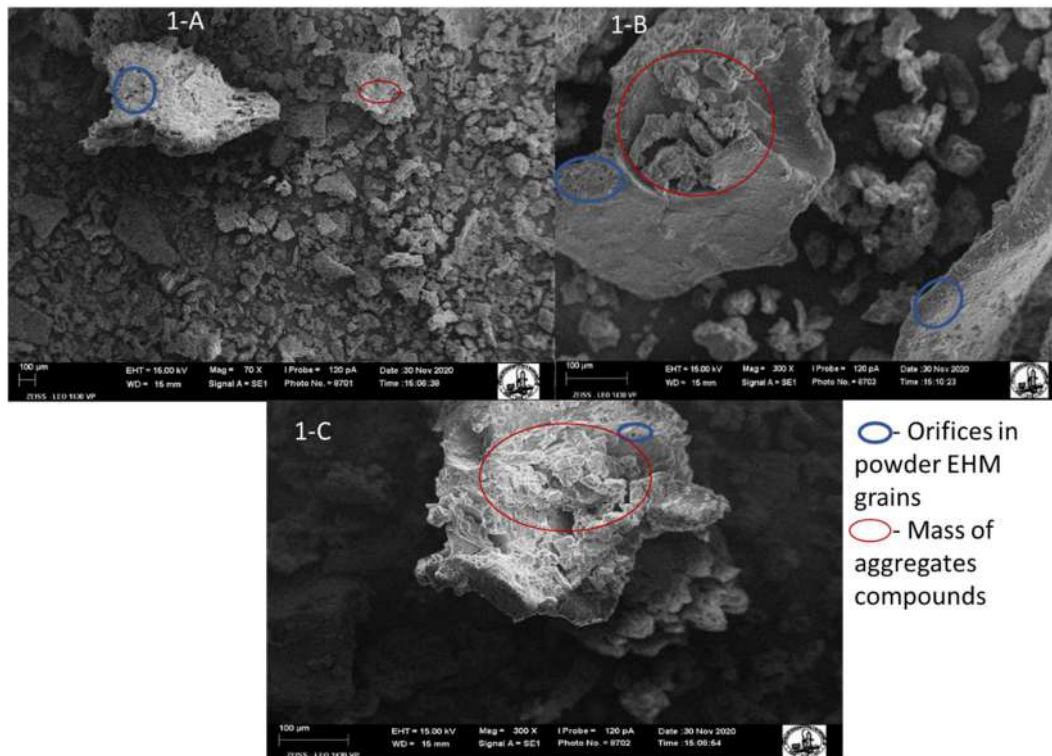


Fig. 1 - A, B e C: Micrograph of human milk expressed in powder, obtained by the same method of freeze-drying with standardized maceration by pistil with 5 minutes; In blue, we see the holes formed by the exit of water during freeze-drying; In red we see the aggregate masses in the powdered human milk grains.



Effect of Buparvaquone as Antifungal Agent

Luana Pereira Borba-Santos^{1*}, Thayná Lopes Barreto², Kelly Ishida², Sonia Rozental¹.

¹Laboratory of Fungal Cell Biology, Institute of Biophysics Carlos Chagas Filho, Federal University of Rio de Janeiro, Rio de Janeiro, Brazil.

²Laboratory of Antifungal Chemotherapy, Department of Microbiology, Institute of Biomedical Sciences, University of São Paulo, São Paulo, Brazil.

*luanaborba@biof.ufrj.br

Repurposing of drugs already available is an alternative to the development of new antifungal agents [1]. Based on this, we evaluated *in vitro* and *in vivo* antifungal activity of buparvaquone, a safe antiprotozoal drug that is commercially available as an intramuscular injection for veterinary application. We used as a model of fungi with medical relevance the dimorphic species *Sporothrix brasiliensis*, which is the main etiological agent of sporotrichosis in Brazil, a subcutaneous mycosis that affects thousands of cats and humans in our country [2]. The *in vitro* activity of buparvaquone was evaluated according to minimum inhibitory concentrations (MIC) determined against a collection of twenty feline-borne isolates of *S. brasiliensis*. To determine the selectivity of buparvaquone toward *S. brasiliensis*, the concentration of this compound that elicited 50% cytotoxicity (CC₅₀) toward mammalian cell line was also estimated. Additionally, we explored the possible mechanism of action of buparvaquone in *Sporothrix* yeast cells, using scanning electron microscopy and cytometry analyzes. The *in vivo* activity of buparvaquone was evaluated using the *Galleria mellonella* model. Buparvaquone inhibited *in vitro* fungal growth at concentrations 1.83-fold lower than itraconazole (the first-choice antifungal used for sporotrichosis) and was 416.7 times more selective for *S. brasiliensis* than mammalian cells (**Table 1**). Scanning electron microscopy images of yeasts treated with a subinhibitory concentration of buparvaquone revealed that this drug altered cell wall integrity and induced cell disruption (**Figure 1Aii**). Treated cells also exhibited mitochondrial dysfunction, ROS and neutral lipid accumulation, and impaired plasma membranes (**Figure 1B-E**). *In vivo* experiments revealed that buparvaquone (single dose of 5 mg/kg) was more effective than itraconazole against infections with *S. brasiliensis* yeasts (**Figure 1F**). Our results indicate that buparvaquone has a great *in vitro* and *in vivo* antifungal activity against *S. brasiliensis*, and induced pronounced morphophysiological alterations in fungal cells. Thus, buparvaquone has a potential application as an alternative treatment for feline sporotrichosis.

This research was supported by CAPES, CNPQ, FAPERJ, and FAPESP (Brazil).

REFERENCES:

- [1] Katragkou A, Roilides E, Walsh TJ. 2016. Expert Opin Pharmacother 17: 1179-1182.
- [2] Rossow JA, Queiroz-Telles F, Caceres DH, Beer KD, Jackson BR, Pereira JG, Ferreira Gremião ID, Pereira SA. 2020. J Fungi (Basel) 6:247.



Table 1. Antifungal activity and selectivity of buparvaquone (BPQ) against *Sporothrix brasiliensis* compared to itraconazole (ITC).

Compounds	<i>Sporothrix brasiliensis</i> (n=20)		LLC-MK ₂ cells	Selectivity Index
	MIC _{range}	MIC _{median}	CC ₅₀	
BPQ	0.015-0.5	0.06	25	416.7
ITC	0.007-0.23	0.11	> 100	>909.1

Results are expressed in μM . MIC, minimum inhibitory concentration that inhibits $\geq 50\%$ of fungal growth. CC₅₀, concentration that elicited 50 % of cytotoxicity. Selectivity Index, ratio between CC₅₀ and MIC_{median}.

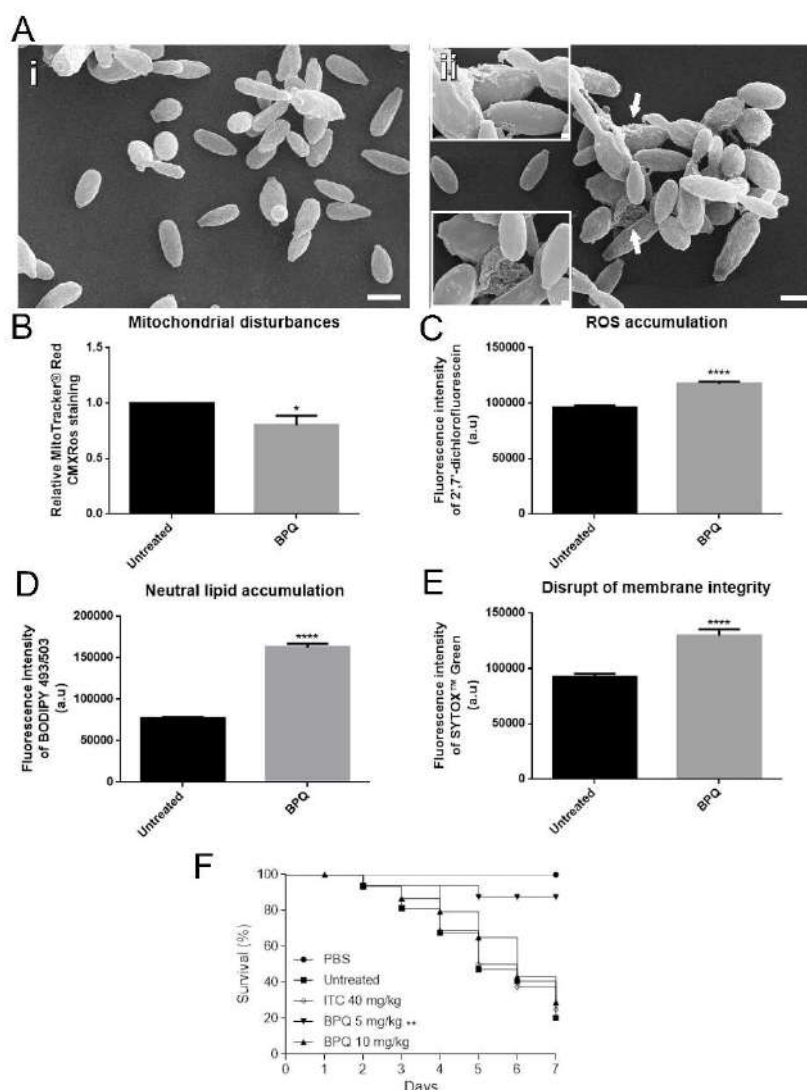


Figure 1. Antifungal effect of buparvaquone against *Sporothrix brasiliensis*. (A) Scanning electron microscopy images of *S. brasiliensis* CBS 133006 yeasts treated with 0.25 μM buparvaquone (BPQ) showed alterations in cell wall integrity and cell disruption (arrows and insets in ii). Yeasts analyzed by flow cytometry exhibited a significant decrease in mitochondrial activity (B), increased cytoplasmic ROS (C), an increase in neutral lipid (D), and a disrupted plasma membrane (E). (F) The survival curve after *Galleria mellonella* treatment indicated that 5mg/kg of BPQ improves the survival of larvae. Scale bars: 2 μm and 200 nm (insets). Data represent mean \pm SEM values. * $p < 0.05$, ** $p < 0.01$, **** $p < 0.0001$ when compared with the untreated group.



Investigation of Silver Nanoparticles Penetration Into Dentinal Tubules By FIB-SEM

Maria Clara Müller de Andrade¹, Aronita Rosenblatt² and André Galembeck¹

¹ Departamento de Química Fundamental, Universidade Federal de Pernambuco (dQF/UFPE), Recife – PE, Brazil

² Faculdade de Odontologia de Pernambuco, Universidade de Pernambuco (FOP/UPE), Recife – PE, Brazil

*andre@ufpe.br

The World Health Organization (WHO) recognizes dental caries as the most prevalent disease in the world. It is estimated that nearly 90% of the population will be affected during their lifetime [1]. It has been reported that pathogenic bacteria can penetrate dentinal tubules when they are exposed due to caries lesions, leading to the rapid advance of the injuries [2]. The effectiveness of silver nanoparticles (AgNP) formulations in caries arrestment have been demonstrated in clinical trials by our research group [3]. Besides the release of Ag⁺ ions from AgNPs have been acknowledged for their antibacterial activity [4], the mechanisms underlying the long-term effects are yet to be elucidated. The present work aimed to investigate the AgNP penetration into dentinal tubules using a focused ion beam combined with scanning electron microscopy (FIB-SEM). The dentin specimens were prepared by removing the incisal enamel of human teeth samples with a rotating diamond disk. The specimens were treated with two different AgNP colloids: (i) spherical nanoparticles (7.5 nm) and (ii) a mixture of spherical (24.3 nm), triangular (33.8 nm), and rod-shaped (40.1/18.8 nm) nanoparticles, as shown in Figure 1. The AgNP samples were directly dropped on the dentin surface and allowed to rest for different times before the analyses. FIB allowed exposing the inner part of the dentinal tubules (Figure 2). It was observed that AgNPs do penetrate dentinal tubules and adhere to their walls, reaching depths of up to 17.1 μm. The penetration depth depends on the exposure time of the dentin surface to the colloid and the nanoparticle size. The total silver amount corresponding to the AgNPs observed in the intra-tubular dentin is within the concentration range expected to inhibit *streptococcus mutans* growth, according to previous results [5].

REFERENCES

- [1] WHO, Oral health 2020. <https://www.who.int/news-room/fact-sheets/detail/oral-health> (accessed April 23, 2020).
- [2] Love RM, Jenkinson HF. Invasion of dentinal tubules by oral bacteria. *Crit Rev Oral Biol Med* 2002;13:171–83.
- [3] Dos Santos VE, et al. 2014. A new “silver-bullet” to treat caries in children - Nano Silver Fluoride: A randomised clinical trial. *J Dent*. 42:945–51.
- [4] Noronha VT et al. 2017. Silver nanoparticles in dentistry. *Dent Mater*. 33(10):1110–1126.
- [5] Targino AGR, et al. 2014. An innovative approach to treating dental decay in children. A new anti-caries agent. *J Mater Sci Mater Med*. 25(8):2041–2047.

ACKNOWLEDGEMENTS

LNnano/CNPEM for the FIB-SEM facility, the human teeth bank of UFPE for providing the sample teeth and, CNPq and CAPES for financial support.

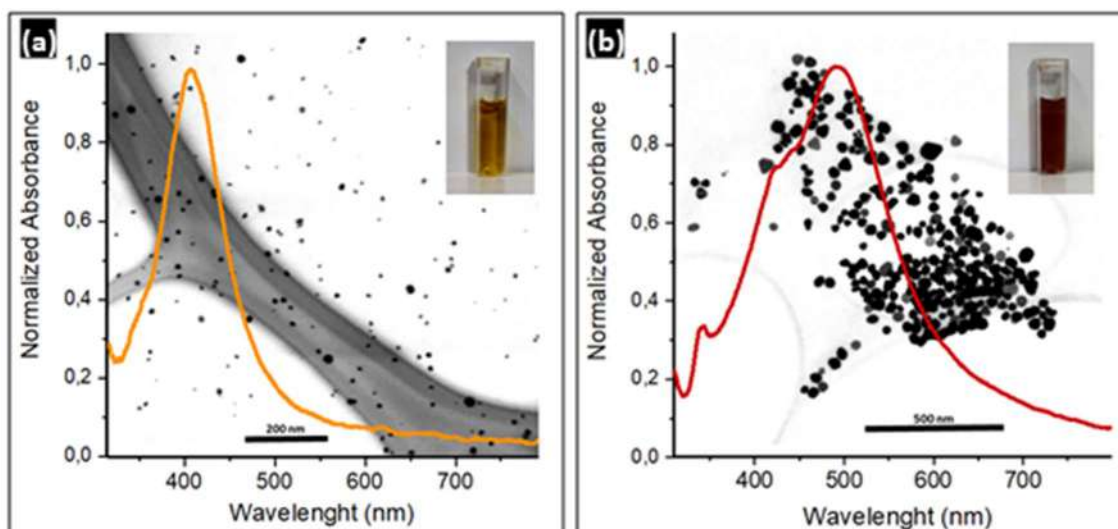


Figure 1. Superposed UV-vis absorption spectra and STEM images of the AgNP colloids. (a) Sample S1 - spherical particles; (b) Sample S2 - spherical, triangular, and rod-shaped nanoparticles.

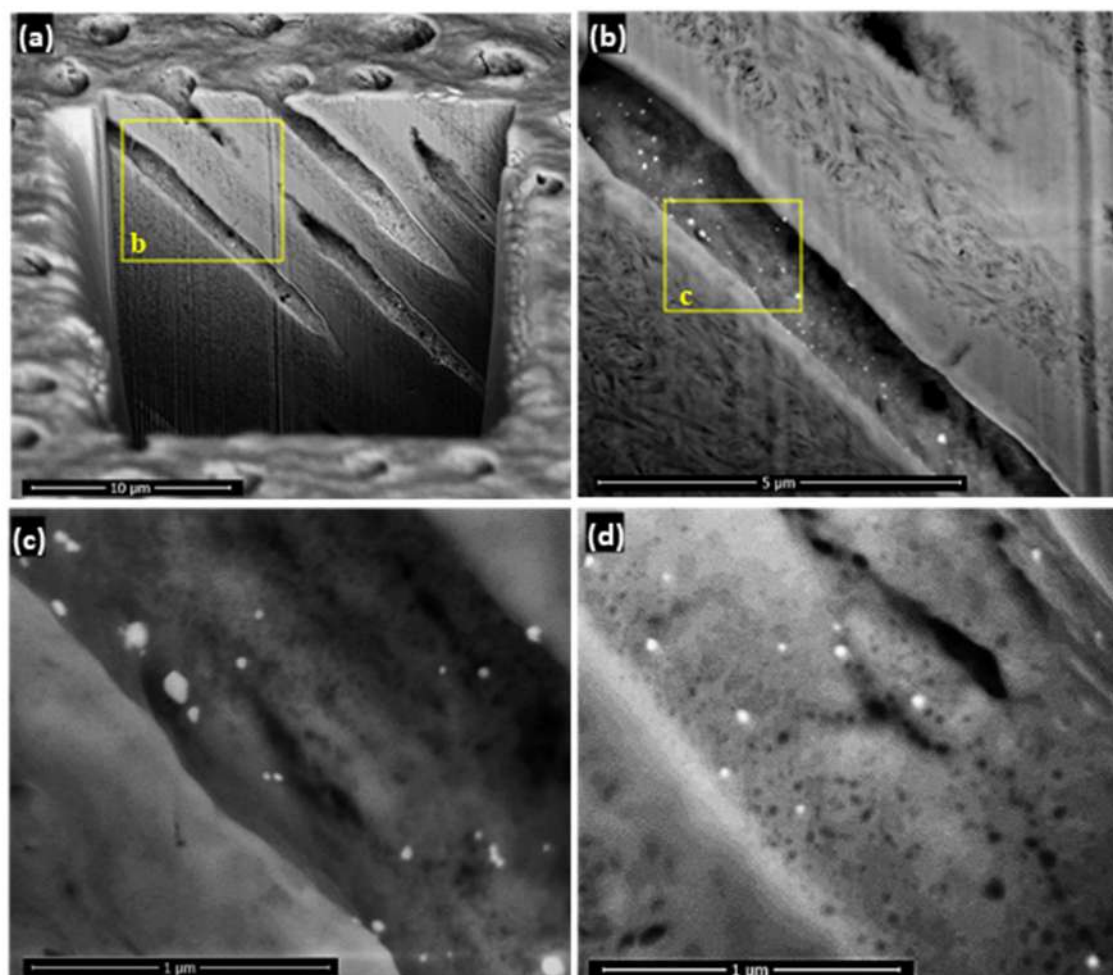


Figure 2 - (a) SEM image of a FIB-excavated region of sample TS2-30 (dentin surface treated with the S2 AgNP colloid for 30 min). Cross-sections of the dentinal tubules were exposed, revealing the AgNPs dispersed through their walls (b,c); (d) SEM image of a dentinal tubule inner region in sample TS1-03 (dentin treated with S1 AgNP colloid for 3 min).



Toxicity of Poly Lactic-co-Glycolic Acid (PLGA) Nanoparticles in *Artemia salina* (Crustacea, Brachiopoda).

Marlos de Medeiros Chaves^{1*}, Vanessa Pinheiro Gonçalves Ferreira¹, Sergimar Kennedy de Paiva Pinheiro², Thaiz Batista Azevedo Rangel Miguel³, Roberto Nicolete¹, Wilson Savino⁴ and Emílio de Castro Miguel²

¹ Laboratório de Nanotecnologia, Fundação Oswaldo Cruz, Eusébio, Ceará, Brasil.

² Laboratório de Biomateriais, Departamento de Engenharia Metalúrgica e de Materiais, Universidade Federal do Ceará, Fortaleza, Ceará, Brasil.

³ Laboratório de Biotecnologia, Departamento de Engenharia de Alimentos, Universidade Federal do Ceará, Fortaleza, Ceará, Brasil.

⁴ Laboratório de Pesquisas sobre o Timo, Departamento de Imunologia, Instituto Oswaldo Cruz, Rio de Janeiro, Brasil.

*marlos.chaves@fiocruz.br

Nanoparticles have potential application in various sectors of the economy. Understanding how these interact with biological systems has aroused great interest from researchers in the last decade. Among the nanoparticles of interest in biomedical applications, an important polymer from the polyester family stands out: poly lactic-co-glycolic acid (PLGA). Its main application is in drug delivery systems as it has excellent biocompatibility and satisfactory biodegradation under physiological conditions [1]. The aim of this study was to determine toxic effects of PLGA nanoparticles on *Artemia salina* [2]. Acute toxicity assays in *A. salina* were carried out [3, 4] with evolutionary stages nauplii 1 and 2 with 24 and 48 hours of hatching interval (in triplicate) in a 24-well culture plate with 2mL of final volume. The concentrations of PLGA tested were 6×10^6 , 6×10^4 , 6×10^2 and 60 particles/mL, in addition to artificial seawater as a negative control and potassium dichromate ($K_2Cr_2O_7$) as a positive control. Aiming to evaluate possible changes in the morphology of the artemias during the experiment, specimens were collected during the toxicity test 24h after each challenge step with PLGA nanoparticles. Observation and image collection was performed with an optical microscope equipped with a digital camera. Nauplii 2 (48h) were collected and fixed after the toxicity experiment. Later, these were dehydrated, dried using Hexamethyldisilazane (HMDS), mounted on stubs and metallized for observation under a scanning electron microscope. In the test performed with nauplii 1, no significant toxic effect was observed after 24h and 48h of exposure. The positive control was lethal in all individuals, in contrast to the negative control. In the trial with nauplii 2 (48h), dead individuals were observed in all groups, including the control. This difference was significant between the exposure time (24h and 48h). However, it did not show significance when analyzed between groups for the 48h exposure period. In the groups treated with PLGA, no visually significant differences were observed, with the exception of the group with the concentration of PLGA 6×10^6 particles/mL. The abdomens of these specimens appeared slightly more wrinkled when viewed under scanning electron microscopy. The findings indicate that the highest concentration of PLGA tested was able to cause morphological changes in the cuticle of the specimens. However, not enough to cause a toxic effect. Histological studies will be performed in order to determine possible microscopic changes in the digestive tract of the artemias.

REFERENCES

- [1] I. Bala, et al., Crit Rev Ther Drug Carrier Syst. 21(5) (2004) 387-422.
- [2] P. Sorgeloos et al., Ecotoxicol. Environ. Saf. 2 (1978) 249-255.

- [3] S.A. Johari et al., Toxicol. Mech. Methods. 29(2) (2019) 95-109.
 [4] T.B.A.R., Miguel et al. Food Bioproc Tec. 14 (2021) 702-716.

ACKNOWLEDGMENTS

The authors would like to thank the Central Analítica-UFC, funded by Finep-CT-INFRA, CAPES-PróEquipamentos and MCTI-CNPq-SisNano2.0 for microscopy measurements.

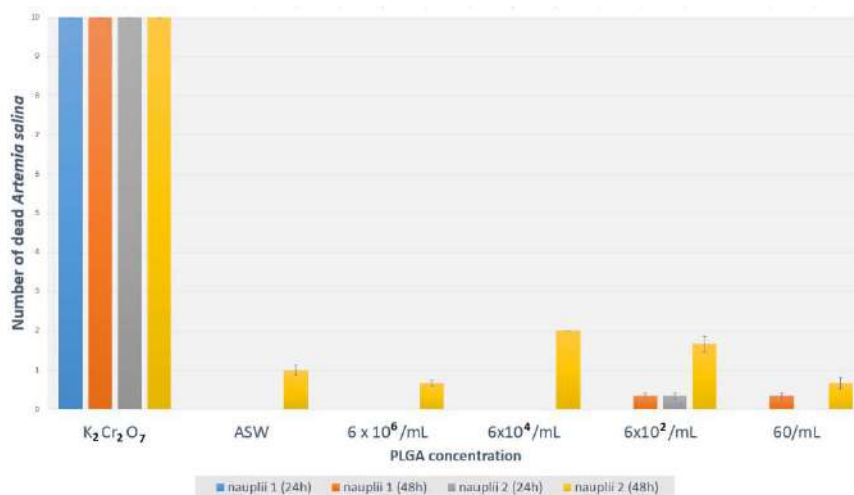


Figure 01. Acute toxicity in brine shrimp. Number of dead individuals in nauplii life stages 1 and 2, with 24h and 48h, using different concentrations of PLGA. K₂Cr₂O₇: Potassium Dichromate; ASW: Artificial Sea Water.

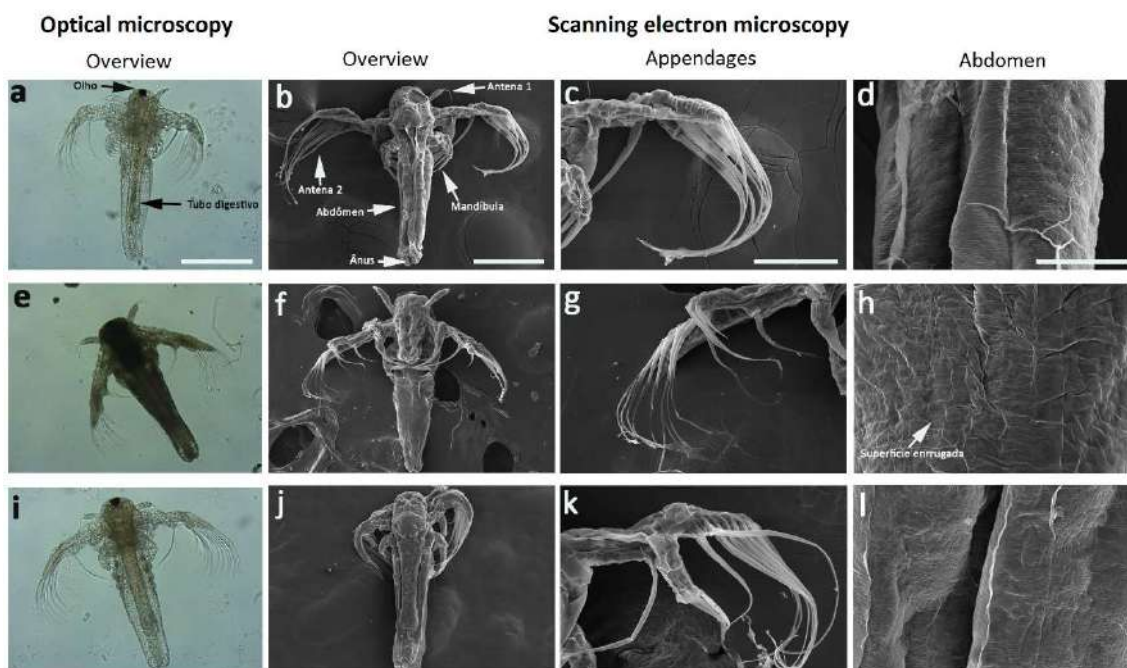


Figure 02. Scanning electron microscopy in *Artemia salina* nauplii 2 48h. A, B, C, D: negative control. E, F, G, H: positive control. I, J, K, L: 6x10⁶ PLGA/mL exposure. C,G,K: no significant changes in the appendages. H: very wrinkled abdominal surface. I: wrinkled abdominal surface. Bars: A, B, E, F, I, J: 200µm; Bars C, G, K: 100µm; Bars D, H, L: 30µm.



Ultrastructural and Morphological Alterations Induced by a New Synergic Ternary Combination on Promastigotes of *Leishmania amazonensis*

Rodolfo Bento Balbinot^{1*}, Danielle Lazarin-Bidóia¹, Tania Ueda-Nakamura¹, Sueli de Oliveira Silva Lautenschlager¹ and Celso Vataru Nakamura¹

¹ Laboratory of Technological Innovation for the Development of Pharmaceuticals and Cosmetics, Department of Basic Health Sciences, State University of Maringá, Maringá, Brazil.

*rodolfoalbinot@hotmail.com

Neglected diseases are a group of infectious diseases that mainly affect low-income populations in developing countries. Among them we can mention leishmaniasis, a complex of diseases caused by protozoan parasite *Leishmania* that affect approximately 12 million people worldwide [1]. Current therapies available have variable efficacy and high toxicity. In this context, are necessary studies for the development of new alternatives of treatment for leishmaniasis, and drug repositioning and combination are therapeutic approaches that have stood out in recent years [2]. In previous studies, our research group has already shown that the compounds LITDFC1, LITDFC2 and LITDFC3 when used in combination (**COMB123**) have a synergistic effect against *L. amazonensis* promastigotes, with IC₅₀ of 312 µM, 0.78 µM and 295 µM, respectively, after 72 h of treatment. Thus, the aim of this study was to evaluate the ultrastructural and morphological changes in *L. amazonensis* promastigotes treated with the **COMB123** ternary combination. For this, promastigotes treated with IC₅₀ of the compounds alone or in combination for 72 h, were fixed in 2.5% glutaraldehyde in 0.1 M cacodylate buffer for 24 h at 4 °C. For SEM, the parasites were dehydrated, critical point-dried in CO₂, sputter-coated with gold and observed using a FEI Scios. For TEM, parasites were postfixated, dehydrated, embedded in Polybed 812 resin, obtained ultrathin sections, contrasted with uranyl acetate and lead citrate, and observed in JEOL JEM 1400. Additionally, the analysis of the ultrathin sections was also performed in FEI Scios in STEM mode. Our results demonstrated that the untreated cells exhibited a normal elongated body with a prominent flagellum and a smooth and intact cell surface, in addition to presenting well-preserved cell structures. Promastigotes treated with LITDFC1, LITDFC2 and LITDFC3 did not show clear morphological changes, but an increase in lipid bodies, autophagic vacuoles, mitochondrial swelling and nuclear disorganization were observed. Promastigotes exposed to **COMB123** suffered rounding of the cell body, shortening and/or loss of flagellum. With regard to cellular organization, **COMB123** also caused intense mitochondrial swelling and nuclear disorganization, in addition to the exacerbated increase of lipid bodies and autophagic vacuoles. Our results support further studies, such as mechanism of action and *in vivo* studies, and may open the way for the development of new chemotherapeutic agents against *L. amazonensis*.

References:

- [1] A. Badirzadeh et al., PLOS Negl. Trop. Dis., 14 (2020) e0007843.
- [2] R.L. Charlton et al., Parasitology, 145 (2018) 219.

Acknowledgments: The authors acknowledge founding from CAPES, CNPq, COMCAP-UEM and FINEP.

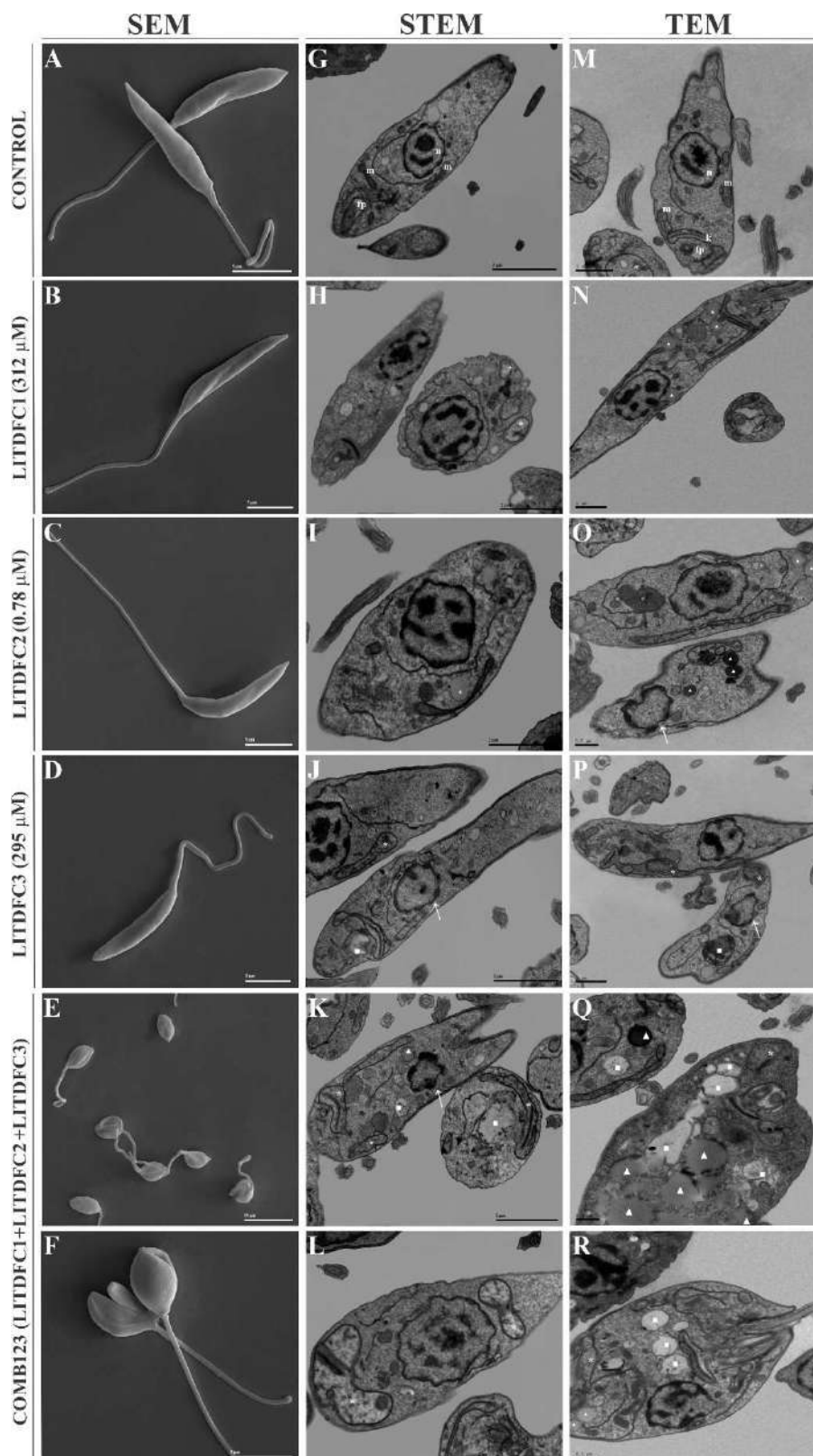


Figure 1. Morphological and ultrastructural analysis of *Leishmania amazonensis* promastigotes treated with **COMB123** and isolated compounds for 72 h. (A-F) Scanning electron microscopy. (G-L) Scanning-Transmission electron microscopy. (M-R) Transmission electron microscopy. *, mitochondrial swelling; ▲, lipid bodies; (arrow), nuclear disorganization; ■, autophagic vacuoles; fp, flagellar pocket; k, kinetoplast; m, mitochondria; n, nucleus. Bars = 10 μM (E), 5 μM (A-D, F), 3 μM (G), 2 μM (H-L), 1 μM (M-N, P) and 0.5 μM (O, Q R).



Tubulization Technique Using Polycaprolactone And Fibrin Biopolymer Promotes Axonal Growth And Functional Recovery After Peripheral Nerve Injury.

Muller, S. K.¹, Leite, A. P. S.², Tibúrcio, F. C.², R. S., Pinto, C. G.², Matsumura, Y. C.³ and Matheus, S. M. M^{3*}.

¹Instituto de Biociências de Botucatu, Biologia Estrutural e Funcional/IBB, Botucatu/SP, Brasil.

²PPG em Bases Gerais da Cirurgia/FMB, Botucatu/SP, Brasil.

³ Departamento de Biologia Estrutural e Funcional (Setor de Anatomia), Instituto de Biociências de Botucatu – UNESP, Botucatu/SP.

*selma.matheus@unesp.br

Peripheral Nerve Injuries (PNI) constitute a common clinical scenario, as peripheral nerves are fragile structures and are often stricken by traumas[1]. PNI lead to complex neural and muscle degeneration and entail several morphofunctional changes in the tissue[2]. Complete functional recovery still hasn't been achieved, as the classic technique (neurorrhaphy) by itself doesn't achieve optimal recovery, and many other variants apart from reconnection are still a challenge for recovery. Thus, new therapies are being studied in order to enhance regeneration and repair[3]. Among them, tubes or conduits are an attractive option, as they can be made of various materials and provide a conduit for stable axonal growth. Combined with these tubes, several adjuvants can be tested, seeking to mimic multiple aspects of the regeneration microenvironment. Here, we highlight the Heterologous Fibrin Biopolymer (HFB), developed by CEVAP/UNESP/Botucatu, as an emerging option, since it has shown positive results in skin and nerve injuries in the last years. Our objective was to evaluate the association of HFB with PCL conduits in nerve reconstruction after PNI, focusing on nerve morphology and morphometry and functional recovery. For that, 32 adult male Wistar rats (CEUA/FMB:1244/2017) were divided into 4 groups (n=8/group): Sham Control (S), Denervated Control (D), PCL Conduit (PCL), PCL Conduit + HFB (FB). In C group, the right ischiatic nerve was only visualized and debrided. In D, PCL and FB groups, neurotmesis (complete section) was performed followed by the removal of an 8mm nerve gap. In PCL and FB groups, the nerve stumps were inserted in 12mm PCL tubes with one 10-0 suture point, and in FB group, 500µL of HFB was subsequently added to the tube. Before and every fifteen days after surgery, the movement of the animals was evaluated using catwalk software, the following parameters were analyzed: fibular functional index, print area, stand rate, max contact area rate and average run duration. After 90 days, all animals were euthanized and the ischiatic nerves were collected and submitted to histological procedures. The number of axons, myelin sheath thickness, G Ratio and diameter of axons and nerve fibers were quantified using the ImageJ software. The functional analysis of the fibular index showed no difference between the groups. In all other variables analyzed, experimental groups did not reach group S ($p \leq 0,05$), when comparisons were made between groups. For print area and max contact area rate the only experimental group that did not achieve similar results as before surgery is the D group. Regarding morphological aspects, S group showed intact axons with normal myelin

sheath (Fig. 1- A). Degenerated axons and fibers were identified in all injured groups, with classic Wallerian degeneration characteristics (Fig.1- B, C, D). In PCL and FB groups, there was a notable increase in extracellular matrix and heterogeneity of the area of regenerated nerve fibers (Fig. 1- C, D). Morphometric analyses showed that the values of PCL group were smaller than S ($p \leq 0,05$), regarding the area of axons and average diameter of axons and nerve fiber. There was no statistical difference between the groups regarding to the number of axons, myelin sheath thickness and G Ratio. Most parameters showed similarity between S and treated groups, supporting nerve regeneration. This occurred even in the D group, since both proximal and distal stumps were included in analysis, and even with mutual degeneration, the proximal stumps regenerated faster [4]. Although there was no difference between the groups, both PCL and HFB, emerge as supportive options to neurorrhaphy, as they provide a stable environment for axonal growth and functional recovery.

Financial Support: FAPESP (2017/06472-2).

- [1] M. Asplund et al., Neuroepidemiology. (2009). 32; 217-228.
- [2] T. Gordon, Int. J. Mol. Sci. (2020). Vol 21; 1-24.
- [3] G. Hussain et al., Int. J. Mol. Sci. (2020). Vol 16;116-134.
- [4] I. Rishal et al., Nat. Rev. Neurosci. (2014).Vol 15; 32-42.

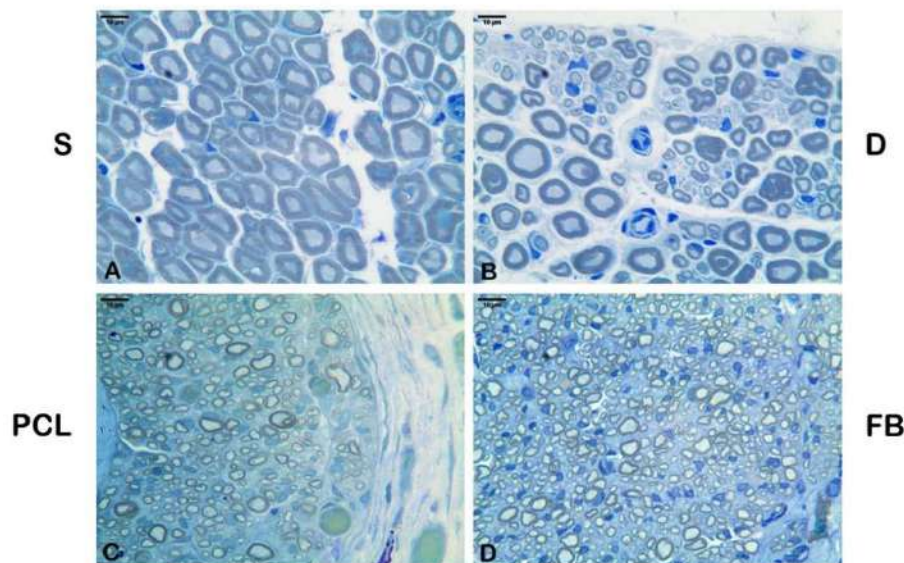


Fig 1: Cross sections photomicrographs of sciatic nerve for each experimental group (staining: osmium tetroxide and toluidine blue). Sham Control (S), Denervated Control (D), PCL Conduit (PCL), PCL Conduit + HFB (FB).



Mayaro virus sample preparation to cryo-EM data collection.

Lais Durço Coimbra^{1*}, Helder Veras Ribeiro-Filho¹, Alexandre Cassago², Rebeca de Paiva Froes Rocha¹, João Victor da Silva Guerra¹, Rafael de Felício¹, Carolina Moretto Carnieli¹, Luiza Leme¹, Antonio Claudio Padilha², Adriana Paes Leme¹, Daniela Baretto Barbosa Trivella¹, Rodrigo Villares Portugal², Paulo Sérgio Lopes-de-Oliviera¹, Rafael Elias Marques¹

¹ Brazilian Biosciences National Laboratory, Brazilian Center for Research in Energy and Materials (CNPEM), Campinas, SP, Brazil

² Brazilian Nanotechnology National Laboratory, Brazilian Center for Research in Energy and Materials (CNPEM), Campinas, SP, Brazil.

*lais.coimbra@lnbio.cnpem.br

Arboviruses are infectious agents transmitted by arthropods that cause millions of cases of febrile illnesses on a yearly basis. Disease caused by arboviruses may manifest as encephalitis, hemorrhagic fever, or arthritis [1]. Mayaro virus (MAYV) is an arthritogenic alphavirus whose biology is not fully understood [2]. We have recently elucidated the structure of MAYV at 4.4Å resolution using cryo-electron microscopy (cryo-EM), aiming at a better understanding of MAYV and Alphavirus biology while searching for rational approaches for the development of antiviral treatments and vaccines. Here we described how high-quality MAYV samples were prepared for Cryo-EM purposes. We improved and adapted protocols for enveloped virus propagation and purification, based on the original protocol provided by Prof. Richard Kuhn (Purdue University). Standard MAYV stocks propagated in Vero CCL81 cells reach up to $1,2 \times 10^6$ infectious viruses per mL of supernatant (PFU/mL), which is insufficient for Cryo-EM analysis. We generated up to 500mL of virus-containing cell culture supernatant and added polyethylene glycol (PEG-8000) at a final concentration of 8% w/v to promote virus aggregation and precipitation. MAYV pellets were recovered by standard centrifugation and purified by ultracentrifugation through a 22% w/v sucrose cushion. A MAYV pellet recovered from beneath the cushion was further purified by ultracentrifugation against a Na/K tartrate gradient (10-35%), resulting in the collection of a single virus band. The quality of purified MAYV particles was calculated in infectious viruses in PFU/mL, samples were tested for protein content using a colorimetric Bradford assay, run through a denaturing SDS/PAGE and observed by transmission electron microscopy using negative staining. Final confirmation of sample quality was established on the observation of Cryo-EM grids prepared with purified MAYV particles plunge-frozen for data collection, under over a dozen different conditions set for the Vitrobot equipment. We obtained infectious and purified MAYV at 2×10^{10} PFU/mL, with approximately $2 \mu\text{g}$ of protein per μL of sample and no protein contaminants, observing only MAYV C, E1 and E2 proteins in gels. As demonstrated in the following structural studies, the cryo-EM data acquisition was successful using our purified samples, which also allowed a detailed characterization of glycosylation both in structure and composition. We conclude this protocol is suitable for the generation of high-quality samples for Cryo-EM and could be adapted for the preparation of other enveloped arboviruses of interest, which lack structural and functional data [3].



REFERÊNCIAS

- [1] Weaver S.C and Reisen W.K, Present and future arboviral threats. *Antiviral Research.* (2010); 85(2): 328.
- [2] Diagne C.T. et al. Mayaro virus pathogenesis and transmission mechanisms. *Pathogens.* (2020); 9 (738).
- [3] This research was supported by FAPESP, CNPQ, Capes and Serrapilheira Institute. (Brazil).

AGRADECIMENTOS

We thank Mr. Valber Ferreira for his technical assistance. We thank LNNano/CNPEM and LNBR/CNPEM.

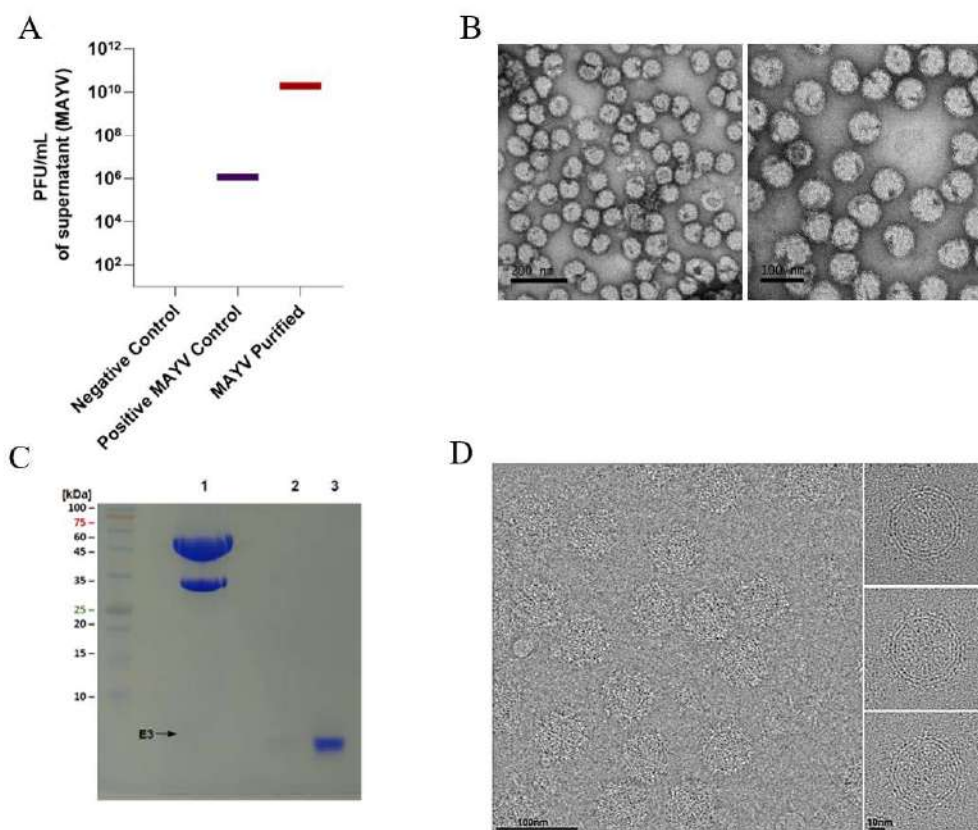


Figure 1 – High and purified titles of infective Mayaro virus for cryo-EM after purification protocol. A) Plaque assay to measure a concentration of infective viral particles of MAYV stock (purple) and purified MAYV (red) produced in Vero CCL8. **B)** Representative image of transmission electron microscopy using negative staining to purity evaluation of MAYV sample. **C)** Analysis of purified MAYV in SDS-PAGE gel. **D)** Representative micrograph of MAYV cryo-EM data collection.



Bovine coronavirus. Detection by transmission electron microscopy techniques.

Catroxo, M.H.B.^{1*}, Martins, A.M.C.R.P.F.¹, and Santos, E.M.¹

^{1*} Electron Microscopy Laboratory, Biological Institute, São Paulo, SP, Brazil
e-mail: marcia.braga@sp.gov.br

Coronaviruses infect humans and a wide diversity of animal species causing respiratory, enteric, neurologic and hepatic disorders. They constitute a zoonotic risk to global public health because their ability to adapt to new species and establish spillover events [1]. Several human CoVs associated with acute gastroenteritis were of suspected zoonotic origin including spillover from cattle [2]. Bovine Coronavirus (BCoV) belongs to the genus *Betacoronavirus* and *Coronaviridae* family. It is an enveloped, RNA virus with a genome size of 32 kb, encoding five main structural proteins, the nucleocapsid, the hemagglutinin esterase, the membrane, the spike (S), and the envelope proteins [3]. BCoV has been implicated in severe diarrhea in neonatal calves from 1 day to 3 months of age, winter dysentery in adult cattle and respiratory infections in calves and feedlot cattle. Animals become infected through the faecal-oral route or inhalation of aerosols. Diseases caused by BCoV leads to significant economic losses both in beef and dairy industry worldwide due to mortality, reduced growth and drastic reduction in milk yield [4]. During the period from 2011 to 2021, approximately 430 samples of bovine feces or small intestine fragments from clinical cases were sent to the Electron Microscopy Laboratory of the Biological Institute of São Paulo, SP, Brazil, for viral diagnostic. The samples were processed for transmission electron microscopy utilizing, negative staining (rapid preparation), immunoelectron microscopy and immunocytochemistry techniques. For the negative staining, the clinical samples were suspended in phosphate buffer 0.1 M and pH 7.0 and placed in contact with metallic grids. Next the grids were blotted with filter paper and negatively stained at 2% ammonium molybdate, pH 5.0 [5]. For the immunoelectron microscopy technique, the screens were incubated with a virus-specific antibody and with viral suspension drops. Upon the screens were contrasted at 2% ammonium molybdate [6]. For the immunocytochemical detection [6], the screens were placed in contact with viral suspension and with primary polyclonal antibody drops. The grids were subsequently incubated in protein A drops in association with 10 nm gold particles (secondary antibody). Grids were then contrasted at 2% ammonium molybdate [7]. Using a Philips EM 208 transmission electron microscope all the samples were analyzed by negative staining technique and a great number of coronavirus particles (Fig.1), pleomorphic, rounded or elongated shaped, with characteristic radial projections forming a corona and measuring 80-140 nm in diameter (Fig. 1, arrow) were observed in 314 (73%) samples. The presence of aggregates formed by antigen-antibody interaction, characterized the positive result obtained, at the immunoelectron microscopy technique for coronavirus (Fig. 2). In the immunocytochemistry technique, the antigen-antibody reaction was strongly enhanced by the dense colloidal gold particles (Fig. 3, arrow). The techniques used are greatly effective for a rapid diagnosis of bovine coronaviruses and can be used in routine procedures to identify the viral agent of this important disease.

References

- [1] K. Dhama, et al., *Clin.Microbiol. Rev.*, 33 (2020) 1-48
- [2] S. Su et al., *Trends Microbiol*, 24 (2016) 490-502
- [3] T. Suzuki et al., *Viruses*, 12 (2020) 183
- [4] M.J. Boileau, S. Kapil, *Food Anim. Practice*, 26 (2010) 123-146

- [5] S. Brenner, R.W. Horne, *Biochem. Biophys. Acta*, 34 (1959) 103.
- [6] M.A. Hayat, S.E. Miller. *Negative Staining*. Mc. Graw-Hill Publ. Company. New York, 1990.
- [7] S. Knutton, *Methods Enzymol.*, 253 (1995) 145-58.

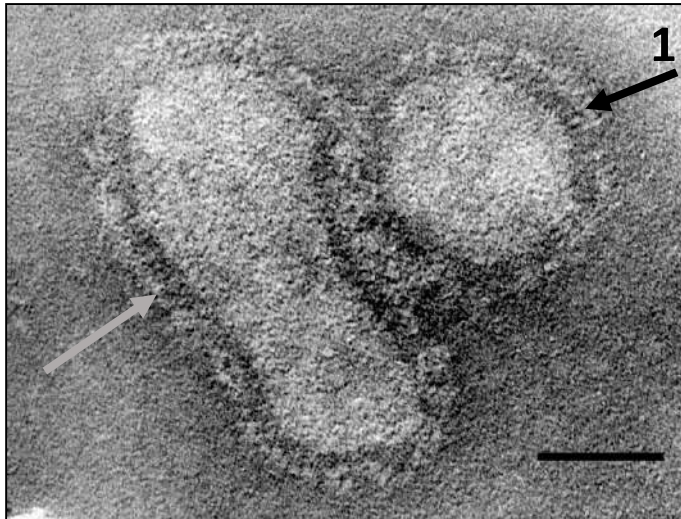


Fig. 1 - Negative staining of coronavirus particles, rounded and elongated, containing characteristic envelope in the shape of a solar corona (arrows). Bar: 54 nm.

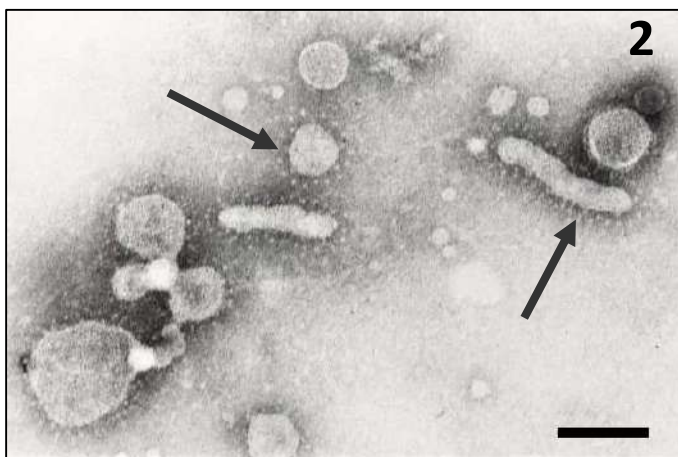


Fig. 2 - In the immunoelectron microscopy technique the coronavirus particles were aggregated by antigen-antibody interaction. Observe thin, wispy, and widely spaced spikes forming the envelope (arrows). Bar: 130 nm.

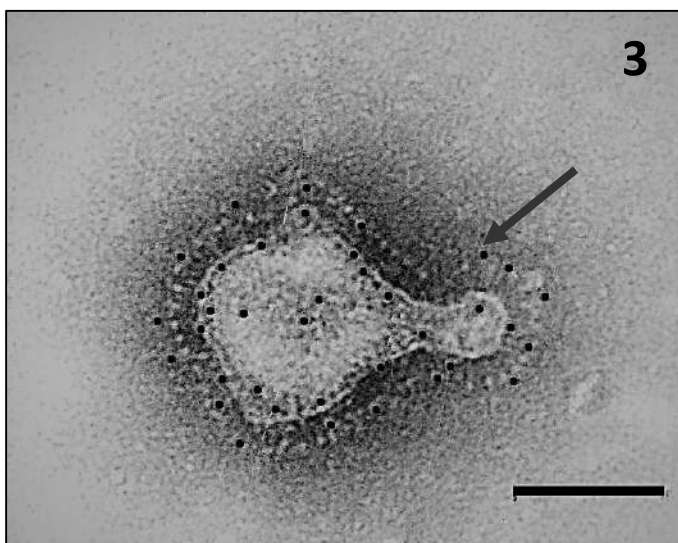


Fig. 3 - Antigen-antibody interaction strongly enhanced by the dense gold particles over the coronaviruses (arrow). Bar: 100 nm.



Cellular and Metabolic Reprogramming by TGF- β Increases V-ATPase Expression and Tumor Malignancy.

Brunna Xavier Martins^{1*}, Enrico Cossi Arantes¹, Anna Lvovna Okorokova Façanha²
Milton Masahiko Kanashiro³ and Arnaldo Rocha Façanha¹.

¹ Universidade Estadual do Norte Fluminense- UENF-Laboratório de Biologia Celular e Tecidual – LBCT, CBB, Campos dos Goytacazes- Brasil.

² Universidade Estadual do Norte Fluminense- UENF-Laboratório de Fisiologia e Bioquímica de Microorganismos – LFBM, CBB, Campos dos Goytacazes- Brasil.

³ Universidade Estadual do Norte Fluminense- UENF- Laboratório de Biologia do Reconhecer– LBR, CBB, Campos dos Goytacazes- Brasil.

*brunnaxmartins@gmail.com

Melanoma emerges by melanocytes transformation with several oncogenes' mutations, consisting in the most lethal form of cutaneous neoplasm, for which the death incidence and therapy resistance have been gradually increased in the last 20 years [1,2]. Melanoma cells express and secrete high quantities of the TGF- β 1 isoform, eliciting melanoma EMT-like changes (epithelial to mesenchymal transition), invasion and bone metastasis [3]. V-ATPases are ATP-dependent proton pumps organized in a multi-subunit complex, which pump H⁺ ions into the lumen of acidic cellular compartments and/or to the extracellular matrix. The expression of these enzymes has been shown to be upregulated in several cancers, including melanoma [4]. The upregulation of V-ATPase specific subunits has been correlated with TGF- β signaling in mammary gland cells and renal kidney diseases [5,6]. In this study, the V-ATPase expression and activity was investigated in human melanoma cells in close relationship with the control of the progression, invasion, and metastasis, to understand the mechanisms of cancer metabolic reprogramming. The hypothesis is that TGF- β can act in V-ATPase enzyme and this interaction alters the ion homeostasis and energy metabolism in melanoma cells. To test this hypothesis, TGF- β was incubated in melanoma cells and we observed the enhance of V-ATPase activity by coupling efficiency and disturbance of energy gradient cell metabolism, through immunostaining and confocal microscopy. In addition, bioenergetics disturbances were detected by measuring the proton fluxes through the cell membrane and by following the acid compartment labeling of melanoma cells *in vivo*. Altogether, our result suggests that TGF- β can affect V-ATPase enzymes and this fact increase the tumoral malignancy in melanoma. These results add an additional layer to the complex bioenergetics network, which might have important therapeutic implications.

References:

- [1]-Siegel R, *et.al. CA Cancer J Clin.* 2019.69:7-34. doi:10.3322/caac.21551
- [2]-E.J. Lelliott *et.al. Front. Immunol.* 2021. 12: 661737. doi:10.3389/fimmu.2021.661737.
- [3]-Wang HX, *et. al. Cell Research.* 2015.1-16. doi: 10.1038/cr.2015.17
- [4]-Martinez-Zaguilan R, *et. al. Am J Physiol.* 1993. 265:1015-1029. doi:10.1152/ajpcell.1993.265.4.C1015
- [5]-Cao X, *et. al. J Physiol Renal Physiol.* 2011. doi:10.1152/ajprenal.00278.2011.

[6]- S. Pamarthy, *et. al. Cell Death Dis.* 2016. 3:7 e2443. doi:10.1038/cddis.2016.347.

Acknowledgment

This work was supported by CAPES, CNPq and FAPERJ.

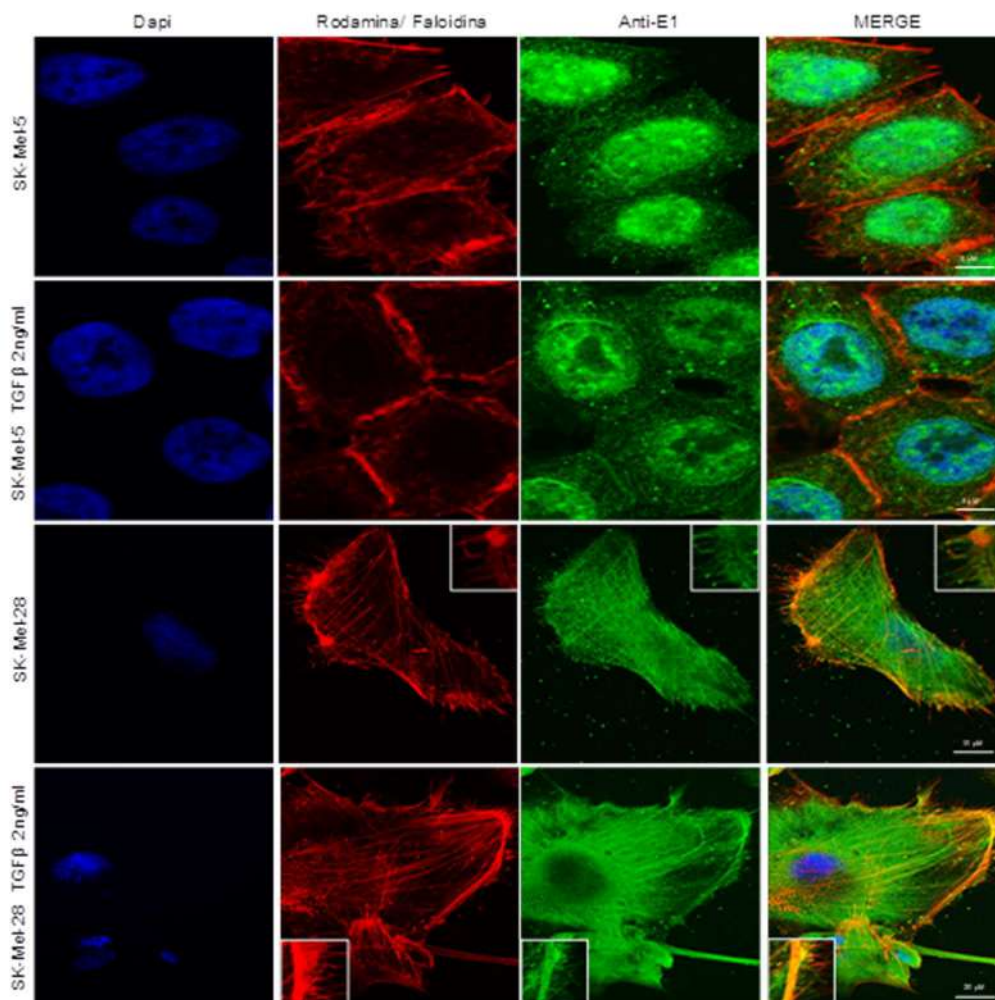


Fig. 1. Immunofluorescence Analysis were used to identify the increase of V-ATPase subunits after the treatment, E1-V-ATPase (green), actin (red) e DAPI (blue). Melanoma cells were treated with TGF- β 2ng/ml. The scale bar represents 5 and 10 μ M.

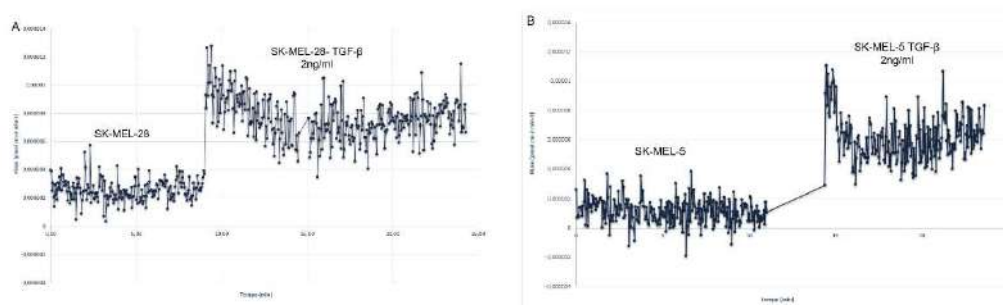


Fig 2. Determinations of the H⁺ fluxes by using a 3D vibrating probe SIET system. Two human cell lines, SK-MEL-5 (A) and SK-MEL-28 (B) were analysing after treatment with TGF- β 2 ng/mL. The proton pump activity increased from 3.5 and 4 times more, respectively.



Melanoma Three-Dimensional Model: Refining *in vitro* Models Aiming Treatment Efficacy Prediction.

Gabriel Henrique Barbosa da Costa Salkovski^{1*}, Anderson Fraga da Cruz¹, Fernanda Fogagnoli Simas¹, Edvaldo da Silva Trindade¹ and Carolina Camargo de Oliveira¹

¹ Laboratory of Inflammatory and Neoplastic Cells, Cell Biology Department, Universidade Federal do Paraná (UFPR), Curitiba, Brazil *krokoli@ufpr.br

Bidimensional (2D) and tridimensional (3D) *in vitro* cell culture are common methodologies used in pre-clinical drug tests. Especially in tumor research, some conditions such as cell-cell and cell-matrix interactions that influence cell mechanisms as adhesion, and differentiation are important to be recreated *in vitro*. Additionally, the tumor microenvironment is composed of different cell types including fibroblasts, macrophages, and tumor cells. Therefore, including two or more cell types in the same 3D *in vitro* system could improve mimicking the *in vivo* tumor microenvironment, being this the main objective in this work. To produce murine and human spheroids two methodologies were used: (1) low attachment surface (LAS), by growing cells on a 96 wells plate coated with agarose, and (2) *hanging drop* (HD), where cells were grown in a drop inside of a *Petri* dish lid for 3 days and then transferred to a 96 well plate coated with agarose for up to 10 days. Murine melanoma expressing green fluorescent protein (B16-F10/GFP), and fibroblasts (BALB/3T3); as well as two human melanoma (CHL-1, and MeWo) and monocytic (THP-1) cell lines in different proportions and initial cell densities were used. Human cells were added simultaneously and 5ng /mL PMA was added to differentiate THP-1 cells into macrophages. For the murine model, cells were either simultaneously plated or added 2 days later, after melanoma spheroid formation. Spheroids were observed every other day by phase contrast microscopy (Carl Zeiss Inverted Microscope Axiovert 40), and murine cells derived-spheroids were observed under fluorescence and confocal (A1R MP+ Nikon) microscopy, by transferring them to a glass bottom plate and adding 10 µg/mL Hoescht for nuclei staining. Murine spheroids were produced by both LAS and HD using 20/80 melanoma/fibroblast % simultaneously (20.000 initial cells) (Figure 1 A-D). Although inner cells visualization (confocal) was impaired due to spheroid size, it was possible to observe melanoma cells surrounded by fibroblasts (both in the surface and the center) (Figure 1 B and D), resembling the architecture present in *in vivo* tumors. Tumor is formed in a tissue with healthy cells, such as fibroblasts, in its surroundings, with the melanoma cells interacting with fibroblast cells, leading to some fibroblast to act as cancer-associated fibroblast (CAFs), that can be recruited by the melanoma cells to get inside the tumor, helping with the tumor progression. For human cells, 70/30 and 90/10 melanoma/macrophage % with 6000 initial cells were plated. HD method produced MeWo/THP-1 (Figure E-F) and LAS method produced CHL-1/THP-1 (Figure G-H) spheroids. Cells localization will be the next step, as well as cell phenotyping (CAFs population, for the murine model, and tumor-associated macrophages (TAMs in the human model). Drugs that have already had their *in vitro* and *in vivo* profile described will also be tested, to analyze the capacity of the model to mimic the effects of the *in vivo* model, in a more credible way in relation to the 2D monoculture model. ACKNOWLEDGEMENTS: CAPES and UFPR/TN for student fellowship and CTAF-UFPR for microscopy services; LabCet (ICC/Fiocruz) for kindly providing the BALB/3T3 cells.

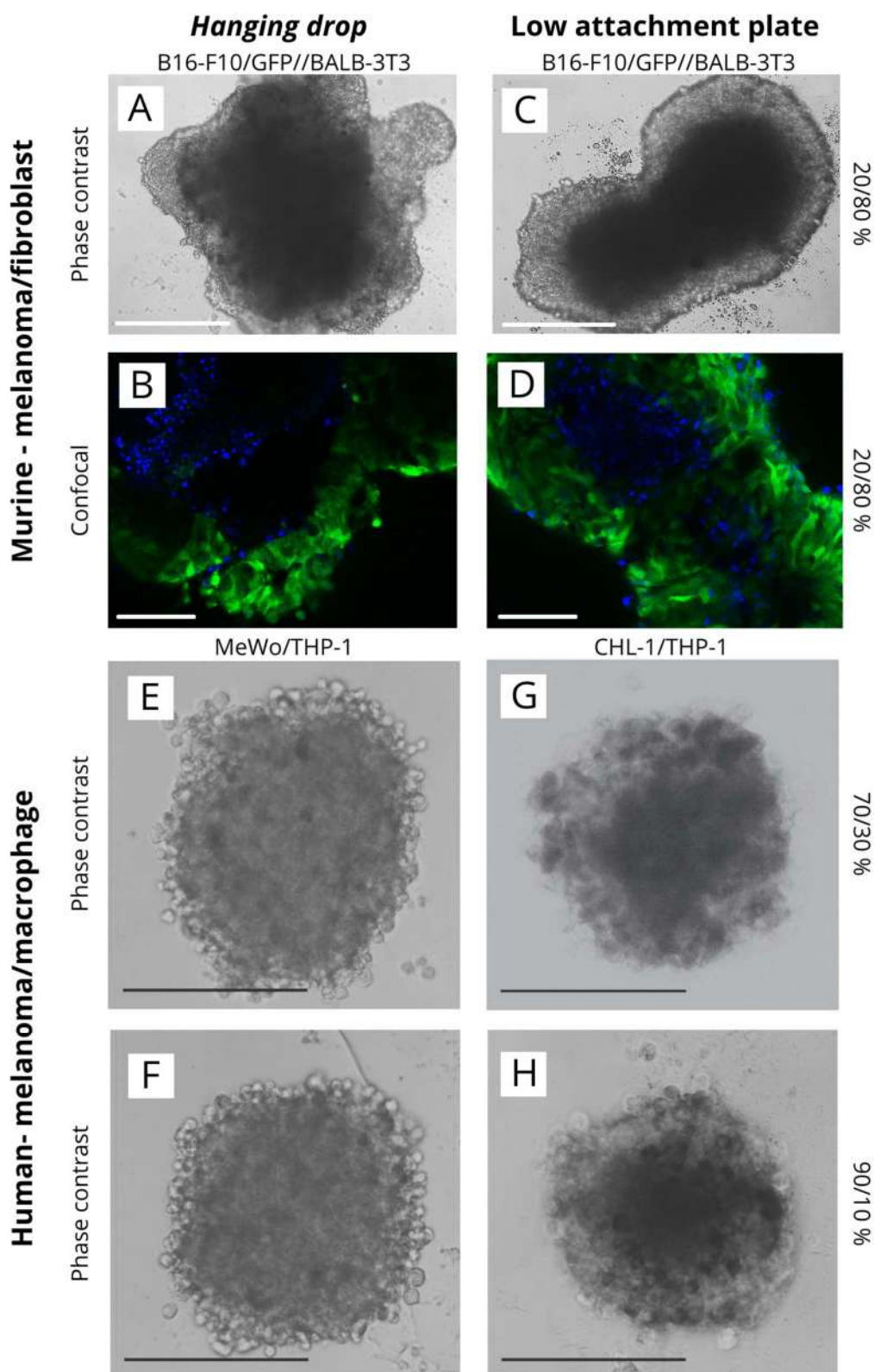


Figure 1 - Coculture spheroids. Murine B16/F-10/GFP//BALB/3T3 in 20/80 density % produced by HD (A and B) and LAS (C and D). Phase contrast image (A and C) and confocal images (B and D) of the same spheroid. Human MeWo/THP-1 produced by HD in 70/30 (E) and 90/10 density (F). CHL-1/THP-1 produced by LAS in 70/30 (G) and 90/10 density % (H). Scale 200 μ m.



Localization of Beta-NGF Receptors (P75 and Trk) In Cumulus Cells and Bovine Immature Oocytes.

Natália Cristina Sossai Arle¹, Muller Carrara Martins², Lucas Melo Gonçalves³ and
Marcelo Emílio Beletti^{1*}

¹ Biology of Reproduction Laboratory, Instituto de Ciências Biomédicas, UFU,
Uberlândia, Brazil.

² Graduate Program in Veterinary Science, Faculdade de Veterinária, UFU, Uberlândia,
Brazil.

³ Undergraduate student in Veterinary Medicine, Faculdade de Veterinária, UFU,
Uberlândia, Brazil.

*mebeletti@ufu.br

It has been identified that Beta-NGF when administered to females during insemination, improves the function of the corpus luteum [1]. Likewise, a positive correlation was also found between the amount of Beta-NGF in sperm and the rates of cleavage and blastocyst in the *in vitro* production of embryos, indicating possible action during the initial embryonic development [2]. More recently, the Reproductive Biology Laboratory at UFU identified that the addition of Beta-NGF to the *in vitro* maturation medium of bovine oocytes results in greater efficiency in the *in vitro* production of embryos. The aim of this study was to verify whether the action of Beta-NGF is directly on the oocyte, cumulus cells or both. As two types of Beta-NGF receptors (p75 and Trk) have already been described, the existence of both in immature oocytes and in their cumulus cells was assessed using immunocytochemistry. Fifteen immature oocytes aspirated from antral follicles, all from slaughterhouse-collected ovaries were fixed in 4% paraformaldehyde and placed individually on silanized slides. After permeabilization with Triton X-100, antigenic recovery in Sodium Citrate solution (pH 6) and blocking of nonspecific sites with Bovine Fetal Serum, the slides were then divided into 3 groups: 1) incubated with polyclonal rabbit anti-primary antibody p75 receptor (NGFR-p75 Sigma N3908), 2) incubated with primary polyclonal rabbit antibodies and anti-Trk receptor (Pan-Trk Abcam EPR17341, and 3) control slide, incubated with Fetal Serum Bovine. Subsequently, all slides were incubated with secondary antibody (A11012 Alexa Fluor 594 Invitrogen). Yo-Pro-1 Iodide (Y3603 Invitrogen) was used as a nucleus marker. The slides were mounted with buffered glycerin and a cover slip and sealed with nail polish. Fluorescence was analyzed using the Zeiss LSM 510-meta laser scanning confocal microscope. Immunofluorescence demonstrated the presence of both receptors in immature oocytes (Fig. 1) and in cumulus cells (Fig. 2). Immature oocytes that were not incubated with primary antibody did not show significant fluorescence. Therefore, the improvement in the efficiency of *in vitro* embryo production when Beta-NGF is added to the oocyte maturation medium should be both by direct action on the oocyte and cumulus cells.

[1] Y. Feng et al., *Reprod Biomed Online*, 36 (2018) 584.

[2] R.T. Silva, *Proteoma nuclear e micro-RNAs de espermatozoides de bovinos férteis e subférteis*, UFU, Uberlândia, 2018.

The authors acknowledge the support of the CNPq, CAPES and FAPEMIG

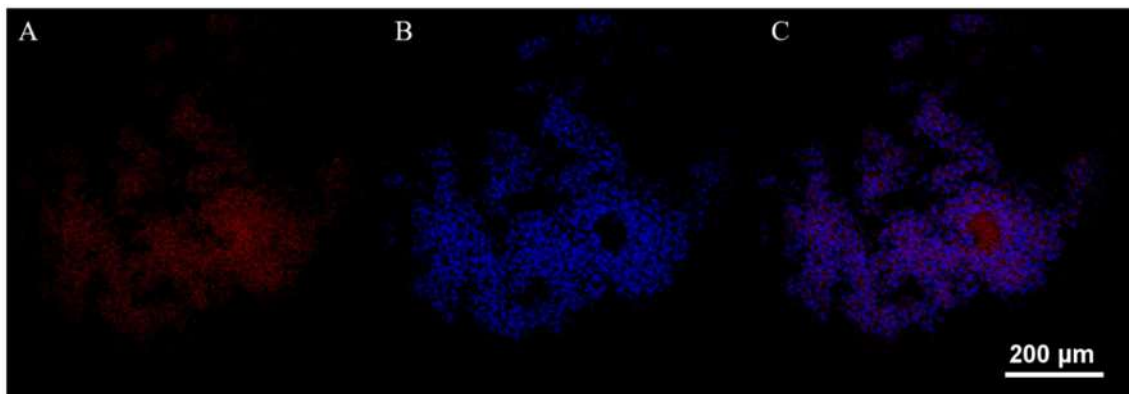


Fig 1: Immature oocyte and cumulus cells. A: p75 receptors marking (red), B: nuclei marking with Yo-Pro-1 (blue), C: Merge.

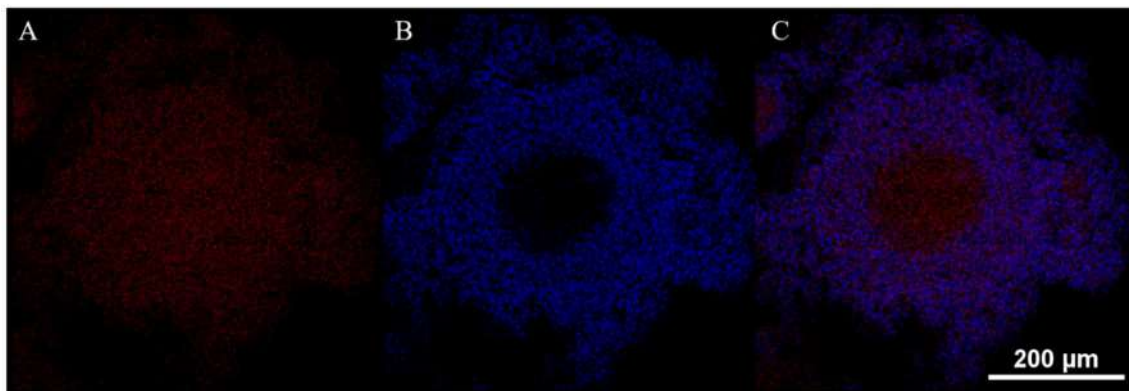


Fig 2: Immature oocyte and cumulus cells. A: Trk receptors marking (red), B: nuclei marking with Yo-Pro-1 (blue), C: Merge.



Effect of lead, cadmium, and perfluorooctanoic acid, in single and combined exposures, on the development of the cephalic region of *Gallus gallus*.

Mariliza Cristine Vieira da Costa^{1*}, Melyssa Kmecick¹ and Claudia Feijó Ortolani-Machado¹

¹ Laboratory of Embryotoxicology. Department of Cell Biology. Federal University of Paraná, Curitiba – PR, Brazil
*marilizacvcosta@gmail.com

Living organisms are exposed to a mixture of environmental pollutants that may interact and generate additive, synergistic or antagonistic effects [1] [2]. Lead (Pb), cadmium (Cd), and perfluorooctanoic acid (PFOA) are potentially toxic to humans and animals. Exposure to these isolated chemicals is known to disturb chicken embryo development and cause malformations in the nervous system [3] [4], but few studies report its effects under mixtures at realistic concentrations, mainly on the cellular mechanisms of its neurodevelopmental toxicity. This study aimed to evaluate the effects of Pb, Cd, and PFOA, *in ovo*, on the migration of cephalic neural crest cells (NCC), proliferation and apoptosis of cells in the brain region, as well as the dispersion of metals at early development of *Gallus gallus* embryos (stages HH10 and HH14). Different concentrations of Pb (0.0015, 0.015, and 0.15 $\mu\text{g}\cdot\text{ml}^{-1}$), Cd (0.05, 0.5, and 5 $\mu\text{g}\cdot\text{ml}^{-1}$), PFOA (0.5, 5 and 50 $\text{ng}\cdot\text{ml}^{-1}$), and the mixtures of two and three chemicals in the intermediate concentrations were tested. Immunolabeling was performed to evaluate the cellular processes after exposure, and the bioavailability of the metals *in situ* was evaluated by autometallography (AMG). A significant reduction in the proliferation and apoptosis of cells in the cephalic region was observed, as well as in the number of neural crest cells and the migration distance of these cells when exposed to almost all the contaminants, isolated and combined. All groups of isolated contaminants showed a significant reduction in a concentration-dependent manner in, at least, one of the evaluated processes. Furthermore, an additive effect occurred in the reduction of proliferation in all the mixture-exposed groups of embryos at the HH10 stage. Also, it was found a higher deposition of metals in the highest concentrations of Pb and Cd. Another interesting morphological finding was the presence of atypical cell groups, detaching from the neural tube epithelium and invading its lumen, regardless of the metal concentration. To date, there are no reports in the literature about the impact of these contaminants on the development of the brain region or NCC. The cell toxicity of these contaminants can occur through different pathways. However, changes in Ca^{2+} homeostasis could explain the findings of reduced proliferation, apoptosis, and migration of cephalic NC found in the present study [5] [6]. In almost all embryonic tissues, there is continuous proliferation, death, and/or migration of cells [7], which play an important role in morphogenesis. Once these processes' occurrence is location and time-specific, any disruption can alter normal development. Moreover, the toxic effects of heavy metals such as Pb and Cd are mainly caused by bioaccumulation, and even during development, the accumulation can result in damage to brain tissue [8]. Thus, exposure to these



contaminants in early development is of great concern. Furthermore, alterations in this region could partially explain the many morphological and functional changes observed in other studies after exposure to these contaminants.

REFERENCES

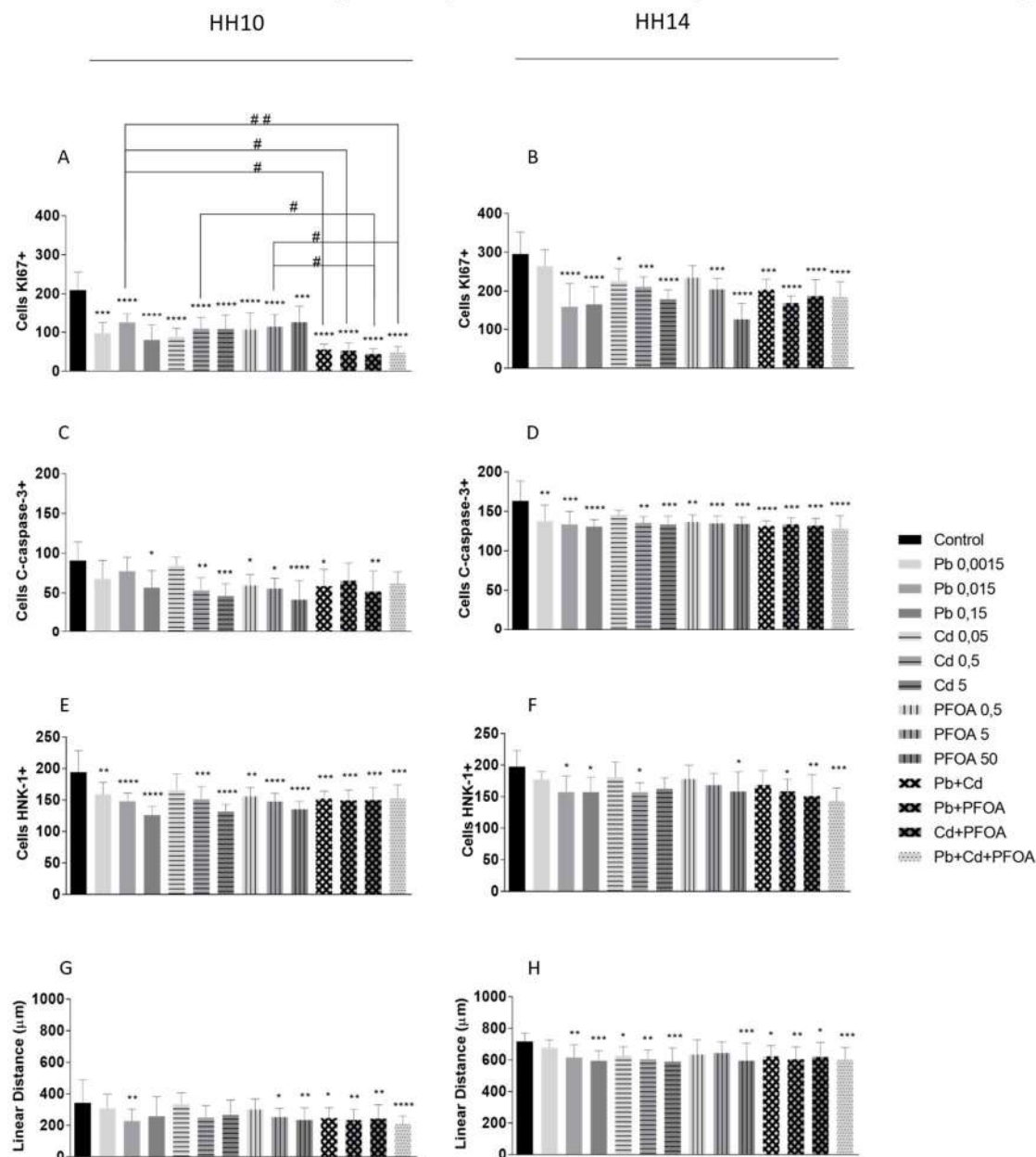
- [1] J. Wilson et al., Effects of defined mixtures of persistent organic pollutants (POPs) on multiple cellular responses in the human hepatocarcinoma cell line, HepG2, using high content analysis screening. *Toxicology and Applied Pharmacology*, 294 (2016) 21-31.
- [2] C. V. Rider et al., Predicting mixture toxicity with models of additivity. In: Rider, C.V.; Simmons, J .E. (Eds.). *Chemical Mixtures and Combined Chemical and Nonchemical Stressors*. Springer, Cham (2018).
- [3] M. C. V. Da Costa et al., Lead exposure affects cephalic morphogenesis and neural crest cells in *Gallus gallus* embryo. *Neurotoxicology and teratology*, 84 (2021) 106948.
- [4] M. Kmecick et al., Morphological evidence of neurotoxic effects in chicken embryos after exposure to perfluorooctanoic acid (PFOA) and inorganic cadmium. *Toxicology*, 427 (2019) 152286.
- [5] G. Choong et al., Interplay of calcium and cadmium in mediating cadmium toxicity. *Chemico-Biological Interactions*, 25 (211) (2014) 54-65.
- [6] Y. Wang et al., Neurotoxic effects of perfluoroalkyl acids: Neurobehavioral deficit and its molecular mechanism. *Toxicology letters*, 305 (2019) 65-72.
- [7] R. Bellairs, M. OSMOND. *The Atlas of Chick Development*. 3. ed. San Diego: Elsevier (2014).
- [8] Y. Zhang et al., Transcriptome analysis reveals the mechanism of common carp brain injury after exposure to lead. *Science of The Total Environment*, 743 (2020) 140796.

ACKNOWLEDGEMENT

We are grateful to Coordenação de Aperfeiçoamento de Pessoal de Nível Superior (CAPES) who supported this work.



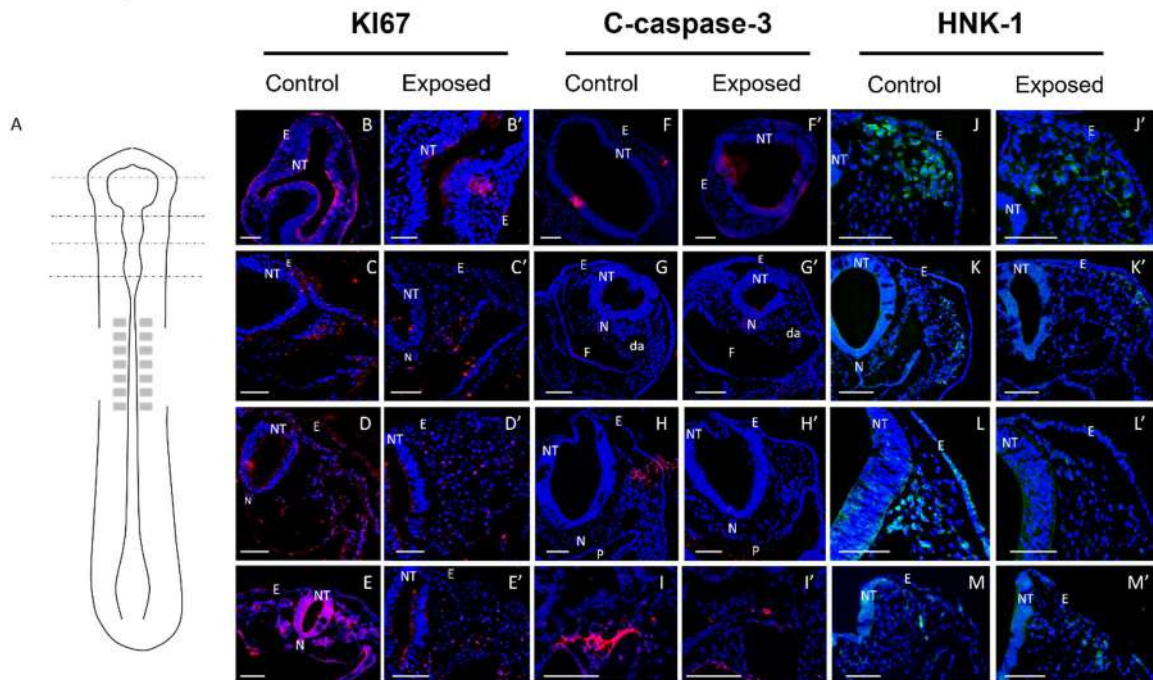
Distribution of Ki67, C-caspase-3 active and HNK-1+ cells, and linear distance of migration of neural crest cells in the cephalic region of chicken embryos at HH10 and HH14 stages



Number of embryos per group: 2. A, C, E, and G: Embryos at stage 10HH. B, D, F, and H: Embryos at stage 14HH. * indicates statistically significant difference compared to the control group: * $p < 0.05$; ** $p < 0.01$; *** $p < 0.001$; **** $p < 0.0001$. # indicates a statistically significant difference between compounds of mixtures: # $p < 0.05$; ## $p < 0.01$. Values = Mean \pm Standard error. One-way ANOVA with Tukey post-test.

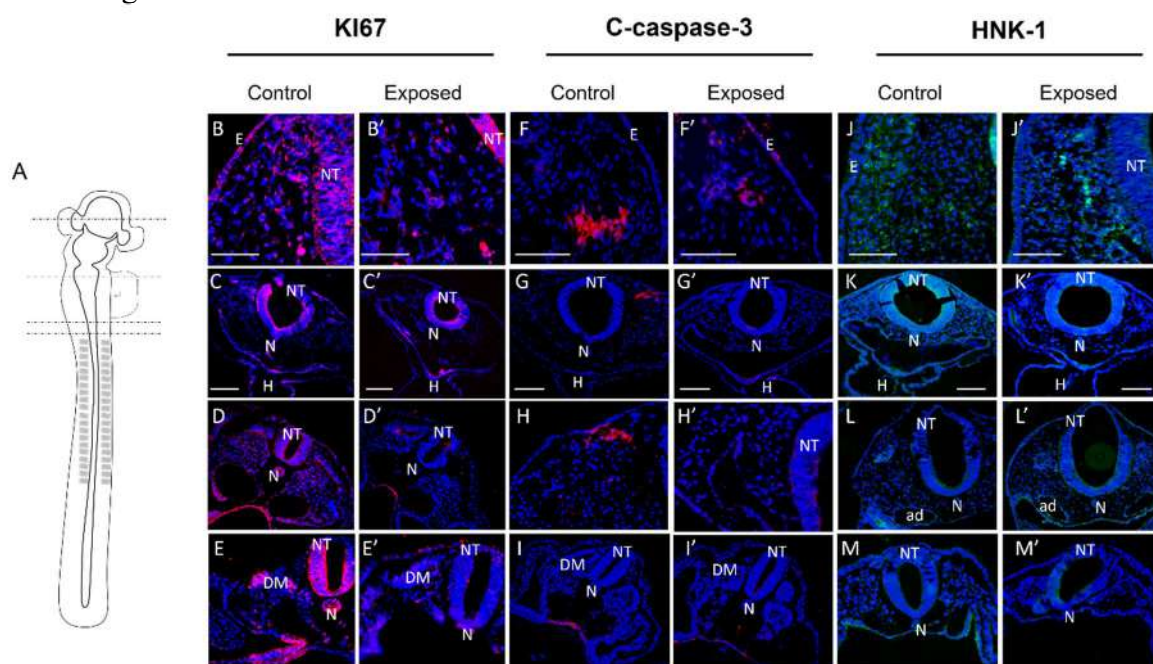


Evaluation of proliferation, apoptosis, and migration of neural crest cells in embryos at HH10 stage



Sections of *G. gallus* embryos at the 10HH stage. A: Schematic drawing showing the different axial levels represented in the board lines. B-M: Control embryos. B', G' and L': Embryos exposed to Pb 0.015 $\mu\text{g}\cdot\text{ml}^{-1}$; C', H' and M': Embryos exposed to Cd 0.5 $\mu\text{g}\cdot\text{ml}^{-1}$; D', I' and K': Embryos exposed to PFOA 5 $\text{ng}\cdot\text{ml}^{-1}$; E', F' and J': Embryos exposed to Pb+Cd+PFOA mixture. NT: Neural tube; N: Notochord; E: Ectoderm; P: Pharynx; da: Dorsal aorta. B – E': Anti-KI67 (red); F – I': Anti-c-Caspase – 3 active (red); J – M': Anti-HNK-1 (green); DAPI (blue). Scale bars: 100 μm .

Evaluation of proliferation, apoptosis, and migration of neural crest cells in embryos at HH14 stage





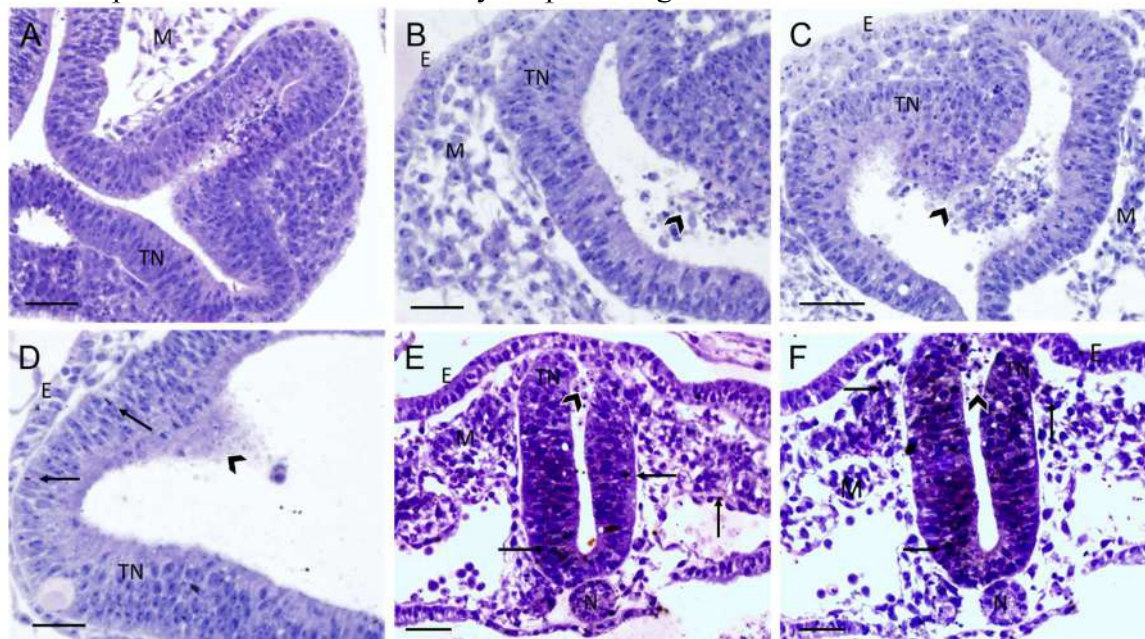
Sections of *G. gallus* embryos at the 14HH stage. A: Schematic drawing showing the different axial levels represented in the board lines. B-M: Control embryos. B', G' and L': Embryos exposed to Pb 0.015 $\mu\text{g}\cdot\text{ml}^{-1}$; C', H' and M': Embryos exposed to Cd 0.5 $\mu\text{g}\cdot\text{ml}^{-1}$; D', I' and K': Embryos exposed to PFOA 5 $\text{ng}\cdot\text{ml}^{-1}$; E', F' and J': Embryos exposed to Pb+Cd+PFOA mixture. NT: Neural tube; N: Notochord; E: Ectoderm; H: Heart; DM: Dermatomyotome B – E': Anti-KI67 (red); F – I': Anti-c-Caspase – 3 active (red); J – M': Anti-HNK-1 (green); DAPI (blue). Scale bars: 100 μm .

Percentage reduction in proliferation, apoptosis, neural crest cells, and their migration after exposure in the cephalic region of chicken embryos at HH10 and HH14 stages

	Proliferation		Apoptosis		NC Cells		Migration	
	HH10	HH14	HH10	HH14	HH10	HH14	HH10	HH14
Pb 0,0015	53,30%	-	-	15,69%	18,04%	-	-	-
Pb 0,015	40,37%	46,14%	-	18,14%	23,65%	20,50%	15,78%	14,12%
Pb 0,15	61,84%	43,87%	37,53%	15,86%	35,04%	20,45%	-	16,96%
Cd 0,05	58,02%	21,30%	-	-	-	-	-	12,66%
Cd 0,5	47,91%	28,70%	41,38%	16,92%	22,06%	20,60%	-	15,53%
Cd 5	48,19%	38,36%	49,03%	18,26%	32,15%	17,57%	-	17,79%
PFOA 0,5	48,96%	-	34,48%	16,43%	19,69%	-	-	-
PFOA 5	45,19%	30,79%	38,88%	17,44%	23,91%	-	26,16%	-
PFOA 50	39,94%	57,46%	54,29%	17,77%	30,45%	19,94%	31,56%	16,94%
Pb+Cd	73,39% ^A	31,00%	40,57%	19,31%	21,54%	-	27,80%	13,16%
Pb+PFOA	74,77% ^A	41,20%	-	18,02%	22,88%	19,74%	31,44%	15,53%
Cd+PFOA	78,75% ^{B,C}	34,78%	42,67	19,00%	22,67%	23,74%	29,02%	13,62%
Pb+Cd+PFOA	77,53% ^{A,C}	37,86%	-	21,70%	21,69%	27,99%	39,46%	16,23%

Reduction percentage compared to control. Pb and Cd ($\mu\text{g}\cdot\text{ml}^{-1}$) and PFOA ($\text{ng}\cdot\text{ml}^{-1}$). Empty field: not significant. A: statistically significant difference compared to Pb. B: statistically significant difference compared to Cd. C: statistically significant difference compared to PFOA.

Metal deposition in the chicken embryo cephalic region



Histological sections of the cephalic region of *G. gallus* embryos at the 10HH stage submitted to autometallography. A: Control; B: Pb 0.0015 $\mu\text{g}\cdot\text{ml}^{-1}$; C: 0.05 $\mu\text{g}\cdot\text{ml}^{-1}$ Cd; D: Pb 0.015 $\mu\text{g}\cdot\text{ml}^{-1}$; E: Cd 5 $\mu\text{g}\cdot\text{ml}^{-1}$; F: Pb 0.15 $\mu\text{g}\cdot\text{ml}^{-1}$. Silver deposition around metal particles (arrows). Abnormal cell grouping in the neural tube (arrowhead). NT: Neural tube; N: Notochord; E: Ectoderm; M: Mesoderm. A-D scale bars: 50 μm ; E-F: 100 μm . Counterstain: HE.



Super-resolution microscopy and 3D modeling of the embryonated egg of *Trichuris muris*

Belém LF ^{1,2}; Durães CG²; Lopes-Torres EJ^{1*}

¹Laboratório de Helminologia Romero Lascasas Porto, Departamento de Microbiologia, Imunologia e Parasitologia – UERJ

²Escola Superior de Desenho Industrial – ESDI/UERJ

*e-mail: eduardo.torres@uerj.br

The species *Trichuris muris* has been widely explored as an experimental model for the study of human and veterinary trichuriasis [1]. Most of results obtained with these experiments contribute to the advances in comprehension of soil-transmitted helminth diseases. Nematodes, especially geohelminths, receive a special attention in the egg characterization, because this structures that are directly associated to the biological behavior of the parasites, involving aspects of the resistance, infection, transmission and epidemiology of these helminthiasis [2]. Morphology and ultrastructure of nematode eggs has been studied using different microscopy techniques, but always based on 2D images results. In this work our main objective was to characterize and modeling the egg structure of *T. muris*, exploring 3D fluorescence microscopy. Fixed embryonic eggs were incubated in Calcein, DAPI and analyzed by super-resolution microscope Zeiss Elyra PS.1 at the CENABIO-UFRJ. Calcein showed a high affinity for egg-shell and polar plugs, allowing details of the plugs and the three layers of the egg-shell (vitellin, chitin and lipid). DAPI allowed the characterization of germ cells of larva (L1) (Fig. 1A). Based on the Z series of images obtained by super-resolution microscopy, we used the Amira software to reconstruct, align and modeling using the "isosurface" algorithm, generating a preliminary model (Fig. 1B). This virtual 3D model was exported to blender software in "stl", allowing adjustments and graphic editions with sculpting and layout tools. Different egg-shell and the plugs were highlighted, detailing and restructuring the triangulation of the model (Fig. 1C). Every process was based on super-resolution microscopy images, showing the importance of these results, improving the morphological characterization of nematode egg. We performed the colorization, rendering and final model for 3D printing (Fig. 1D-F). 3D modeling is the current frontier in structural biology, these results bring an important contribution in parasitology/helminthology. We conclude that another major advance was the integration of the results obtained in our microscopy experiments with graphic design tools. This interaction contributed to the extraction details of our results, especially with the gain in graphic quality of the model. We hope to also contribute to the teaching process in parasitology, mainly by exploring models with a high level of detail and structurally reliable to the biological samples.

[1] Klementowicz JE, Travis MA, Grecnis RK. *Trichuris muris*: a model of gastrointestinal parasite infection. *Semin Immunopathol.* 2012 Nov;34(6):815-28.

[2] Cruz K, Marcilla A, Kelly P, Vandenplas M, Osuna A, Trelis M *Trichuris trichiura* egg extract proteome reveals potential diagnostic targets and immunomodulators. 2021 *PLoS Negl Trop Dis* 15(3).

ACKNOWLEDGEMENTS: FAPERJ-JCNE, PIBIT-UERJ/CNPq, FINEP, CENABIO-UFRJ

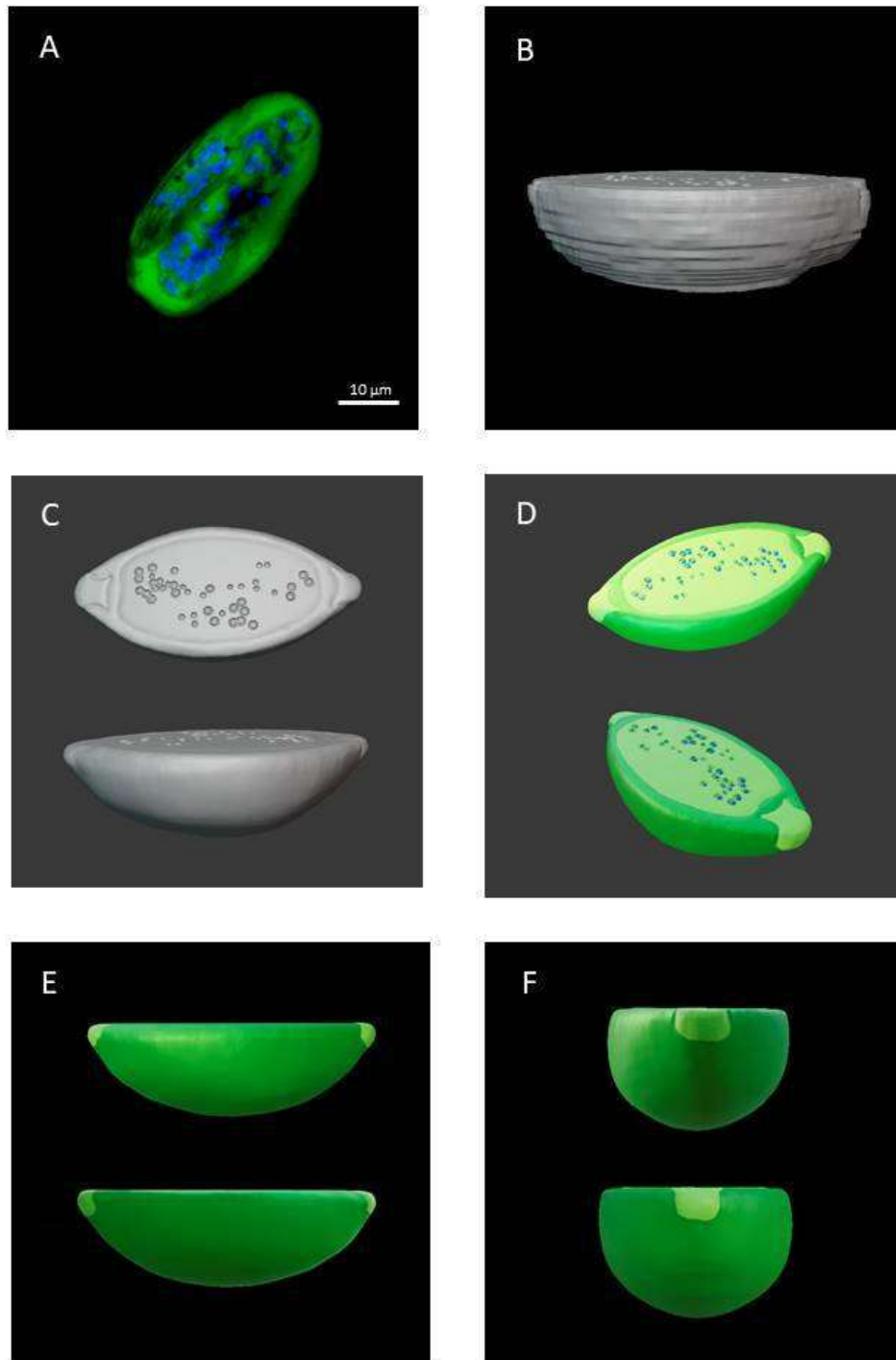


Fig. 1 - *Trichuris muris* egg characterization: (A) Super-resolution image showing egg-shell/egg content (green) and larva germ cells (blue). (B) First model enabled by Amira Isosurface algorithm. (C) Model improved showing the egg-shell layers, polar plugs and germ cells of larva. (D-F) Different angles of the model colored showing the egg structures, including the external surface, internal structures, including the larva cells.



FMRFamide-related Peptides in *Aedes aegypti* Midgut: Neuromuscular Connections and Enteric Nervous System

Raquel Soares Maia Godoy^{1*}, Renata Cristina Barbosa², Breno dos Anjos Costa¹,
Marcelo Jacobs-Lorena³, Gustavo Ferreira Martins²

¹Instituto René Rachou, Fundação Oswaldo Cruz, Departamento de Entomologia, Belo Horizonte, MG, Brazil

²Universidade Federal de Viçosa – Departamento de Biologia Geral, Viçosa, MG, Brazil

³The W. Harry Feinstone, Department of Molecular Microbiology and Immunology and Johns Hopkins Malaria Research Institute, Bloomberg School of Public Health, Johns Hopkins University, Baltimore, MD, USA

FMRFamide-related peptides (FaRPs) are a class of neuropeptides that participate in a variety of physiological processes in invertebrates. All peptides sharing the RFamide C-terminal sequences are currently described as FaRPs. This neuropeptide family includes products of different genes, with the term FaRPs implying the RFamide signature and analogies to FMRFamides rather than genetic family [1-2]. Neuropeptides F (NPF), short neuropeptides F (sNPFs), FMRFamides, myosuppressins, and sulfakinins are members of the FaRPs group [3]. They are involved in physiological roles, such as regulating feeding, development, diapause, and reproduction, and occur in nerves of stomatogastric ganglia and enteroendocrine cells of the insect digestive tract, where they may control muscle functions [4]. However, their direct involvement in muscle function has never been shown in situ. We studied the relationship between FaRPs and midgut muscle during the larval-pupal transition of the mosquito *Aedes aegypti* by confocal and scanning electron microscopies. In late L4, FaRP-positive neuronal extensions attach to the bundles of the external circular muscle layer, and muscle stem cells start to undergo mitosis in the internal circular layer. Thereafter, the external muscle layer degenerates, disappearing during early pupal development, and is completely absent in the adult mosquito (Figure 1). Our results indicate that FaRP-based neural signals are involved in the reorganization of the muscle fibers of the mosquito midgut during the larval-pupal transition. In addition to confirming FaRP involvement in muscle function, we show that the mosquito midgut muscles are largely innervated, and that circular and longitudinal muscles have specific neuron bodies associated with them (Figure 2). Finally, we provide a new interpretation about the neuromuscular connections and enteric nervous system of mosquitoes.

[1] MR Elphick and O Mirabeau. *J Front Endocrinol* (2014) 5:93

[2] K Hao et. al. *Genomics* (2020) 112:1821–1828

[3] MR Strand et al. *Adv Insect Physiol* (2016) 51:145–188

[4] EA Tarr et al. *Cell Tissue Res* (2019) 376:83–96

[5] This work was supported by the Universidade Federal de Viçosa, CAPES, Fapemig, and by the National Institutes of Health (USA) R01AI031478 and the Bloomberg Philanthropies.

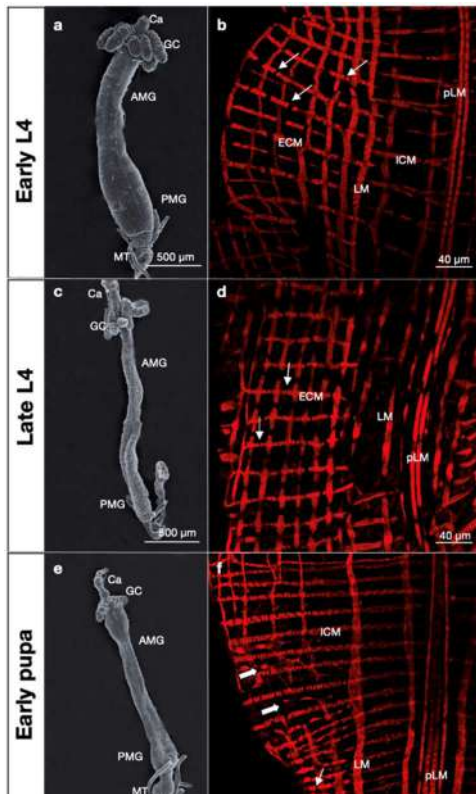


Figure 1: Scanning electron microscopy of the entire midgut of early L4 (a), late L4 (c) and early-1 pupa (e) and confocal images of their respective stages showing the actin filaments (red) of the muscles in the anterior midgut (AMG) (b, d, f). The midgut of early L4 (a) decreases in thickness in the late L4 (c). From late L4 to early pupa (e), the gastric ceca undergo a drastic reduction. b, d, f The external circular muscle layer (ECM) of the AMG presents gaps in actin filaments (thin white arrow) since L4 stage (b), which is maintained in the late L4 (d), and in some portions of the early pupal midgut (f). In other portions of the early pupal midgut, the ECM is not detected or detected as a degenerative structure (full white arrow). Ca: cardia; PMG: posterior midgut; MT: Malpighian tubule; pLM: prominent longitudinal muscle; ICM: internal circular muscle; LM: longitudinal muscle

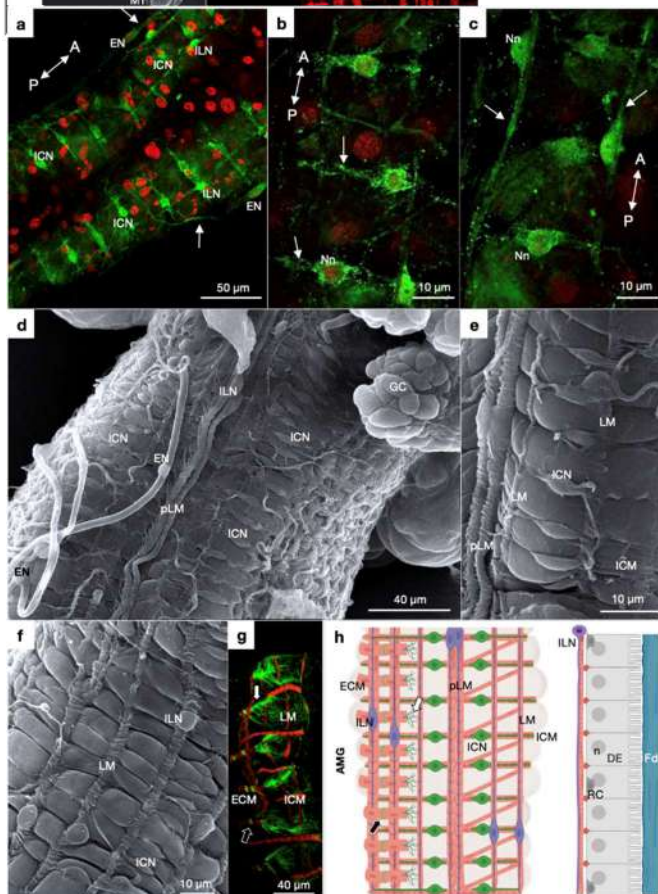


Figure 2: Distribution of three types of neurons in the midgut of immature stages of *Aedes aegypti*. a–c FaRP immunoreactivity (green) in neuron bodies and their ramifications in the midgut of an early pupa. A wide field view is showed in a. Three neuron types can be distinguished, depending on their orientation in the midgut and external/ internal position in relation to the muscles: the external neurons (ENs), the internal circular neurons (ICNs), and the internal longitudinal neurons (ILNs). The thin white arrows show the extensions of the ENs in a, ICNs in b, and ILNs in c. Red: cell nuclei. d–f The midgut neurons in the larva of second instar using scanning electron microscopy. d The localization of the three neuron types in a wide field. e, f Details of the ICN (e) and ILN (f). g, h Redemonstration of the FaRP-positive ring-shaped (black full arrow) and densely branched (white full arrow) structures (g) to generate a scheme model of distribution of the internal neurons and FaRP-positive structures in the anterior midgut (AMG) (h). pLM: prominent longitudinal muscle; LM: longitudinal muscle; ECM: external circular muscle; ICM: internal circular muscle; DE: digestive epithelium; Fd: food in the midgut lumen; RC: regenerative cell; n: digestive cell nucleus



Microanatomical and Secretary Characterization of The Salivary Gland of The *Rhodnius prolixus* (Hemiptera, Reduviidae, Triatominae), a Main Vector of Chagas Disease

Raquel Soares Maia Godoy¹, Ana Carolina Borella Marfil Anhê², Nágila Francinete Costa Secundino¹, Paulo Filemon Paolucci Pimenta¹

¹Instituto René Rachou, Fundação Oswaldo Cruz, Departamento de Entomologia, Belo Horizonte, MG, Brazil

²Universidade Federal do Triângulo Mineiro, Departamento de Engenharia Ambiental, Uberaba, MG, Brazil

Rhodnius prolixus (Hemiptera, Reduviidae, Triatominae) is the principal vector of *Trypanosoma cruzi*, the etiological agent of Chagas disease in American countries. According to estimates, there are 6–7 million individuals infected by this protozoon worldwide, mostly in Latin America, and 90–100 million individuals are exposed to *T. cruzi* infection. These insects are vectors of other harmless protozoa, such as *Trypanosoma rangeli* (Tejera, 1920), which have also been described as likely competent vectors of pathogenic bacteria such as *Serratia marcescens* (Bizio, 1923), *Bartonella* (Gieszczykiewicz, 1939) and *Mycobacterium leprae* (Hansen, 1880) [1]. Female and male Triatominae individuals are hematophagous during all life cycles, and, to antagonize its hemostatic, inflammatory and immune systems, they secrete saliva while feeding on the vertebrate host's blood [2,3]. We investigated characteristic changes of the salivary glands (SGs) that occur during insect development by histological and histochemical techniques, and scanning electron and confocal microscopies. Two pairs of lobules and ducts compose the SG of *R. prolixus*. The organ's size increases over time, but the microanatomical structures are preserved during insect development (Figure 1). Both lobules have a single layer epithelium formed by binucleated cells, which surrounds the saliva reservoir. The principal lobule presents higher polysaccharide and total protein contents than the accessory lobe. A network of external muscle layers is responsible for organ contraction and saliva release (Figure 2). Apocrine, merocrine and holocrine secretion types occur in the secretory epithelium. Dopamine, serotonin and tyrosine-hydroxylase are neural-related molecules that regulate SG function both during and after feeding. The knowledge obtained regarding the dynamics and functioning of the SGs of *R. prolixus* can support future studies aimed at combating the neglected Chagas disease. Further studies can help to better understand the likely release of different secretion types by each of the two SG lobules and their salivary compositions, as well as to aid in determining the exact mechanism that regulates the salivary duct function in *R. prolixus*.

[1] CB Vieira et al. Front. Cell Infect. Microbiol. (2018) 8, 405

[2] J Jurberg J et al. Atlas Iconográfico dos triatomíneos do Brasil (2014) Rio de Janeiro, Brazil: Instituto Oswaldo Cruz

[3] PB Santiago et al. J. Proteom. (2018) 174, 47–60

[4] This work was supported by the following Brazilian agencies FIOCRUZ, CNPq, CAPES, FAPEAM, and FAPEMIG

FIGURES

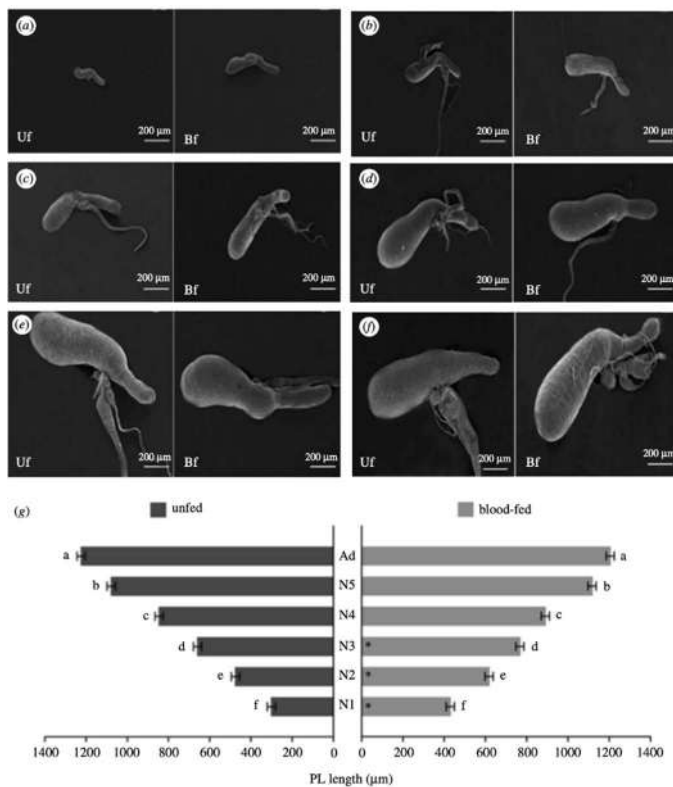


Figure 1: SG of UF and BF *R. prolixus* nymphs and adult. (a–f) The anatomy of SG remains unchanged throughout the life cycle of *R. prolixus*, but their size increases during insect development. (a) First instar, (b) second instar, (c) third instar, (d) fourth instar, (e) fifth instar and (f) adult individual. (g) Lengths of the principal lobule of SGs during insect development. The graph shows the unfolding of the significant interaction ($p < 0.05$) between the explanatory variables used in the model: development stage (with six levels encompassing five juvenile instars plus the adult) and feeding type (with two levels encompassing UF and BF insects). Different letters indicate significant differences among insect development stages within each level of the feeding type using Tukey's test ($p < 0.05$). Asterisks in the bars indicate significant differences between UF and BF insects within each developmental stage of the insect. When comparing UF and BF insects of the same stage, the length of the PL is higher in BF insects in the N1, N2 and N3 nymphs. By contrast, from N4 to adult, there is no difference in size between UF and BF insects. Regarding insect development, there is a progressive increase in the size from N1 to the adult stage

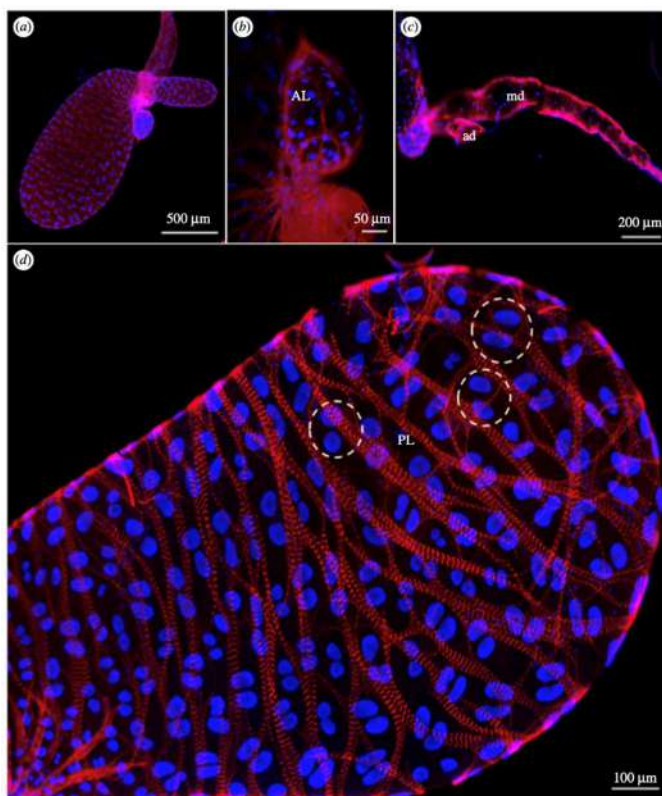


Figure 2: Muscular framework and arrangement of epithelial cell nuclei in the SGs of *R. prolixus*. (a) Overall view. (b) Accessory lobule (AL). (c) Accessory (ad) and main ducts (md). (d) Detail of (a) shows muscle fibres (red) externally coating the SG and the nuclear arrangement of epithelial cells, internally located close to the muscles. Each epithelial cell of the SG has two morphologically similar nuclei (blue), whose pairs are marked by dotted circles.



Action of *Caryocar villosum* oil on the ultrastructure of promastigotes of *Leishmania (Leishmania) amazonensis*.

Adan Jesús Galué Parra^{1*}, Amanda Anastácia Pinto Hage¹, Lienne Silveira de Moraes¹
and Edilene Oliveira da Silva^{1,2}

¹ Laboratory of Structural Biology, Institute of Biological Sciences, Federal University of Pará, Belém, Pará 66075-110, Brazil.

² National Institute of Science and Technology in Structural Biology and Bioimaging (INCT-INBEB), Rio de Janeiro 21941-901, Brazil.

*email– adangalue@gmail.com

ABSTRACT

Leishmaniasis are neglected diseases caused by protozoa of the genus *Leishmania*. They present effective but limited treatment, which makes the search for alternative treatments necessary [1]. Studies with substances of natural origin, which are potentially less toxic to the cell and are selective to the protozoan have been developed. The fruit of *Caryocar villosum* has important pharmacological properties such as: anti-inflammatory, antioxidant, anti-tumor and healing [2]. Thus, the aim of the study was to evaluate the action of oil obtained from the fruit of *C. villosum* (OCV) on *Leishmania (Leishmania) amazonensis* promastigotes. Different microscopy methods were used for analyze the action of the OCV on the morphology of the parasite. Light microscopy (LM), promastigotes stained with Giemsa, scanning electron microscopy (SEM), cells were fixed, dehydrated in graded ethanol, critical-point dried, coated with gold and examined with a MIRA 3 TESCAN microscope and transmission electron microscopy (TEM), cells were fixed, dehydrated in graded acetone, embedded in epoxy resin and examined in Zeiss 906E microscope. Morphological alterations of the treated parasites were observed compared with untreated cells. The analysis by LM showed alterations in the cellular body and atypical division of promastigotes treated with 100 µg/mL of OCV for 72 h. This result was confirmed by SEM, parasite cell body was frequently multi-septated and the presence of two or more flagella became more evident. Analysis by TEM demonstrated that the treatment with OCV promoted changes in the nucleus, DNA fragmentation, presence of two or more nucleus suggesting a different cell division process. Additionally, accumulation of lipid bodies and presence of multiple vesicles within the flagellar pocket of treated parasites were also observed. Thus, the oil of *C. villosum* can be considered a natural compound with a possible leishmanicidal action against the protozoan *L. (L.) amazonensis*.

REFERENCE

- [1] WHO. World Health Organization (2018). Control of the leishmaniases. Fact Sheets, 375. Updated October 2018.
- [2] L.R. Torres et al., Bioactive compounds and functional potential of pequi (*Caryocar spp.*), a native Brazilian fruit: a review. **Grasas y Aceites** 69 (2): 257, 2018.

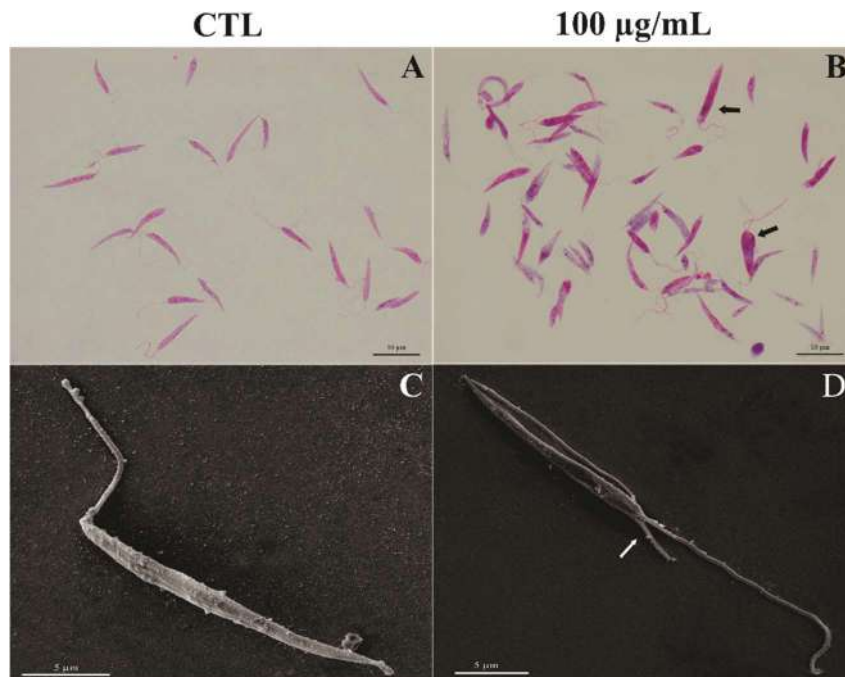


Fig 1. Light microscopy and scanning electron microscopy of promastigote forms of *L. (L.) amazonensis* treated with OCV for 72 h. A-C, Control group; The protozoan morphology was characterized by an elongated cell body and a flagellum emerging from the flagellar pocket B-D, promastigotes treated with 100 $\mu\text{g}/\text{mL}$ of OCV. The arrows indicate parasites with two asymmetric flagella. Note multi-septation of the cell body by SEM.

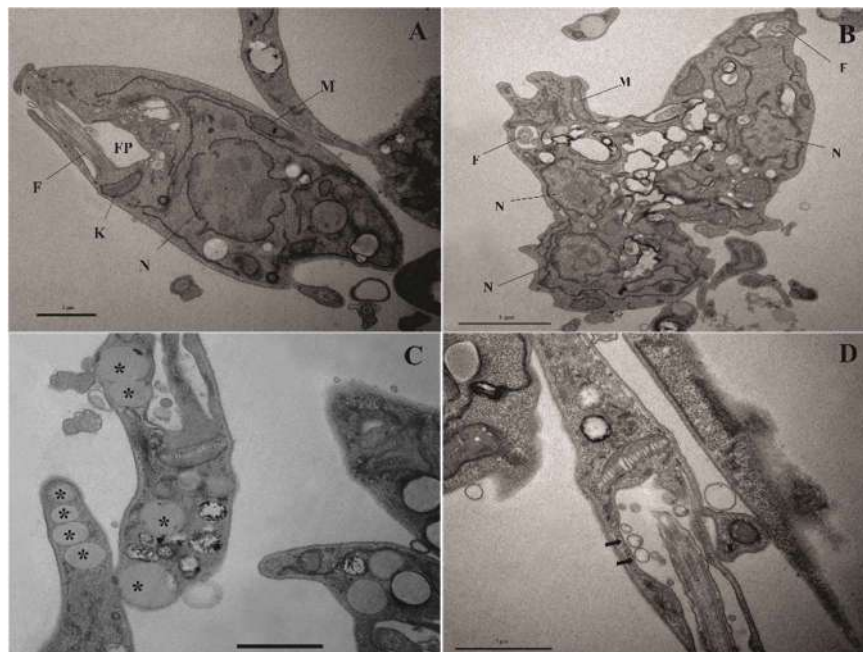


Fig 2. Ultrastructural effects of OCV on promastigotes of *L. (L.) amazonensis*. A, untreated parasite showing typical morphology. B-C-D, promastigotes treated with 100 $\mu\text{g}/\text{mL}$ of OCV for 72 h. B, Note promastigotes forms in apparent atypical division, presenting more than one nucleus, fragmentation of DNA, C, presence of structures similar to lipid bodies (*) and D, observe a large number of vesicles inside the flagellar pocket (arrows).



High Resolution Electron Microscopy Analysis of Hemozoin Crystals

Wendt, C.^{1*}, de Souza, W.^{1,2} and Miranda, K.^{1,2}

¹ Laboratório de Ultraestrutura Celular Hertha Meyer, Instituto de Biofísica Carlos Chagas Filho

² Centro Nacional de Ciência e Tecnologia em Biologia Estrutural e Bioimagem – Universidade Federal do Rio de Janeiro, Rio de Janeiro, Brazil.

* camilawendt@biof.ufrj.br

Malaria is a disease caused by protozoan parasites from the genus *Plasmodium* with the highest impact on public health in endemic areas. Morbidity and mortality of this disease results from the asexual replication of *Plasmodium* in the erythrocyte of the mammalian host [1]. In the course of its intraerythrocytic development, malaria parasites incorporate massive amounts of the host cell cytoplasm. Internalized hemoglobin is digested in a compartment with acidic pH termed the food vacuole, producing aminoacids and others by products, namely heme. Due to its toxic effects, free heme is immobilized and stored in a crystal form known as hemozoin. This mechanism is essential to parasite development and represents a physiological step used as target for many antimalarial drugs [2]. So far, most of the data regarding hemozoin structure and elemental composition has been obtained through the analysis of β -hematin, a synthetic analogue of hemozoin whose structure and physical properties have been the subject of many studies. Fundamental questions regarding crystal growth, immunomodulatory effect and drug inhibition mechanisms, nevertheless, remain unanswered, especially considering crystals obtained from different malaria species. In this work, we used high-resolution electron microscopy approaches to analyze hemozoin crystals obtained from *Plasmodium chabaudi* and *Plasmodium berghei*. Analysis of crystals revealed growing areas on the edge of many crystals, suggesting a preferential mechanism of crystal growth along the z axis direction after crystal formation. This feature was observed on isolated crystals (figure 1) and on crystals located inside the food vacuole of cryopreserved cells (figure 2). In addition, elemental analyses on isolated crystals and crystals inside food vacuoles of intact cells showed iron distribution and its spatial correlation with other ions, such as oxygen and nitrogen. No significant differences on the elemental composition were found, indicating that crystals isolated from different species possess the same chemical nature. Overall, the results contributed to the understanding of mechanisms of crystal growth and the identification of potential areas where antimalarial drugs may bind, affecting hemozoin crystal formation.

References:

- [1] A. F. Cowman *et al.*, Cell 167 (2016) 610.
- [2] P. A. Sigala and D. E. Goldberg, Annu. Rev. Microbiol. 68 (2014) 259.
- [3] This work was supported by CNPq, FAPERJ, FINEP, CAPES (Brazil) and Instituto Nacional de Biologia Estrutural e Bioimagem

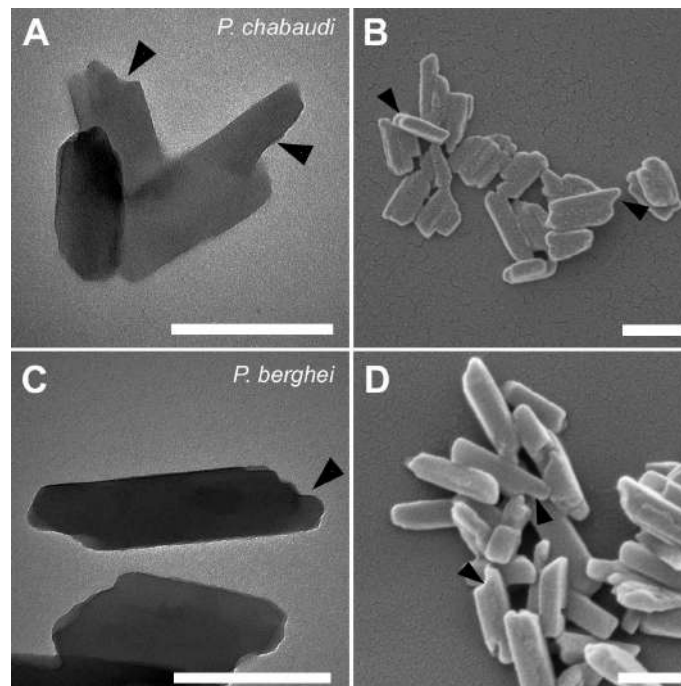


Figure 1: Growing points (arrowheads) were observed in isolated hemozoin crystals from *P. chabaudi* (A-B) and *P. berghei* (C-D). Scale bar: 100nm.

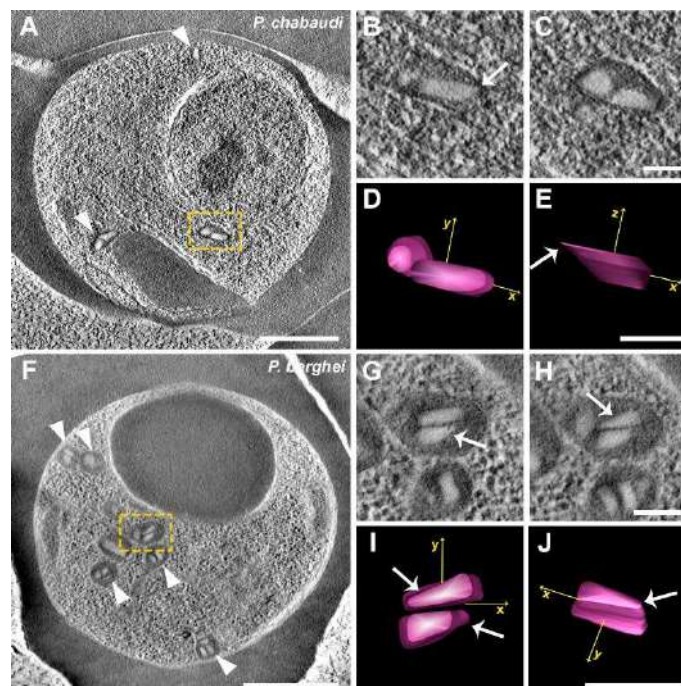


Figure 2: Analysis of hemozoin crystals located inside the food vacuoles of *P. chabaudi* (A-E) and *P. berghei* (F-J) by serial section electron tomography of high pressure frozen and freeze substituted cells. Multiple food vacuoles are seen on parasites cytoplasm (A, F; arrowheads). Analysis of selected food vacuoles (yellow dashed rectangle) along the different z slices shows hemozoin crystals growing points (C-D, G-H; arrows). Different angular rotations of 3D rendered crystals shows brick shape crystals with point ends (D-E, I-J, arrows). Scale bar: 500nm (A, F); 100nm (B-E, G-J).



Ultrastructural characterization of the freshwater microalgae *Tetradismus obliquus* BR003 (Chlorophyta: Chlorophyceae)

Cristiane do Carmo Cesário^{1,2*}, Karla Gonçalves Ribeiro², Jamile Fernanda Silva Cossolin³, José Eduardo Serrão³ and Jane Sélia dos Reis Coimbra¹

¹ Universidade Federal de Viçosa, Departamento de Tecnologia de Alimentos, Viçosa, MG - Brasil.

² Universidade Federal de Viçosa, Núcleo de Microscopia de Microanálise, Viçosa, MG - Brasil.*cristiane.cesario@ufv.br

³ Universidade Federal de Viçosa, Departamento de Biologia Geral, Viçosa, MG - Brasil.

INTRODUCTION: *Tetradismus* (Chlorophyta) is a microalgal genus with biotechnological potential, which exhibits rapid biomass production and high levels of lipids, proteins, carbohydrates, and bioactivity [1]. The knowledge of the morphology and physiology of *Tetradismus* is necessary to optimize its cultivation processes. **MATERIAL AND METHODS:** The *Tetradismus obliquus* BR003 strain was isolated from a freshwater reservoir in Viçosa, Brazil. The cells were fixed in a 2.5% (v/v) glutaraldehyde solution in sodium cacodylate buffer (0.1 M, pH 7.2) containing 2% (m/v) sucrose during 24 h. Then, *T. obliquus* BR003 samples were washed with sodium cacodylate buffer (0.1 M, pH 7.2) three times for 10 min, post-fixed in 1% (w/v) osmium tetroxide for 2 h, washed three times with deionized water, dehydrated using a gradient of aqueous ethanol solution (70%, 80%, 90%, 95 % v/v), and then soaked in LR-White resin (London Resin Company, Basingstoke, United Kingdom) [2]. The ultrathin sections were arranged on copper grids, stained with 5% (m/v) aqueous solution of uranyl acetate for 30 min and lead citrate [3] for 5 min. Then they were analyzed under the transmission electron microscope (Zeiss Libra 120, Carl Zeiss, Germany) at 80 kV. **CONCLUSION:** The cytoplasm of the *T. obliquus* BR003 cells is rich in vacuoles, rough endoplasmic reticulum, mitochondria, and chloroplasts. The nucleus has a predominance of de-condensed chromatin, and the cell wall has three layers. Chloroplasts have many starch granules and can be associated with a spherical central pyrenoid. To the best of our knowledge, this study is the first description with the ultrastructural morphological characterization of the strain *T. obliquus* BR003, grown under standard conditions, to demonstrate specific characteristics of the species.

REFERENCES

- [1] Rizwan M, et al. Exploring the potential of microalgae for new biotechnology applications and beyond: A review. *Renew Sustain Energy Rev* 92:394–404. 2018
- [2] Farder-Gomes CF. Morphology of ovary and spermathecae of the parasitoid *Eibesfeldtphora tonhascai* Brown (Diptera: Phoridae). *Protoplasma* 256:3–11. 2019
- [3] Reynolds ES. The use of lead citrate at high pH as an electron-opaque stain in electron microscopy. *Journal of Cell Biology* 17:208–212, 1963

ACKNOWLEDGMENTS

CAPES, CNPQ, FAPEMIG, Núcleo de Microscopia e Microanálise (NMM) from Universidade Federal de Viçosa.

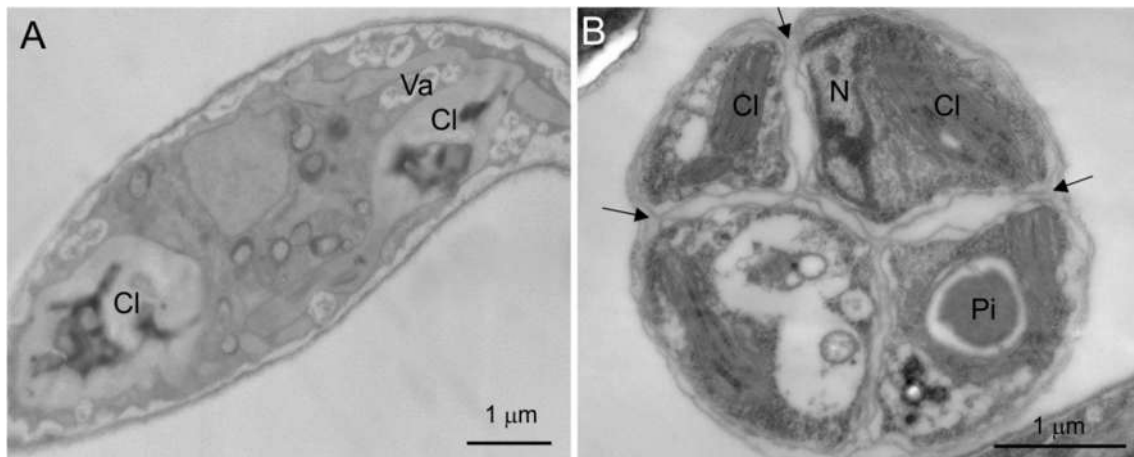


Fig. 1: Transmission electronic micrography of *Tetradismus obliquus* BR003. (A) Overview of a cell in longitudinal section showing chloroplasts (Cl) that occupy most of the cytoplasm and vacuoles (Va). (B) Cross-section of a group of four cells separated by the cell envelope (arrows). All cells are provided with broad nucleus (N) and chloroplasts (Cl) containing pyrenoid (Pi).

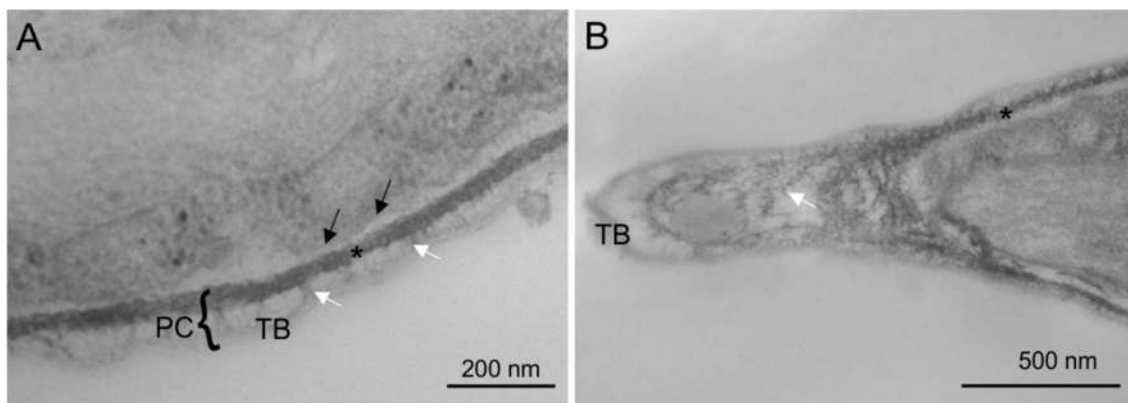


Fig. 2: Transmission electronic micrography of *Tetradismus obliquus* BR003 showing in detail the cell wall (PC). (A) The cell wall is formed by three distinct layers, the outermost is the trilaminar sheath (TB), followed by a layer formed by fibrous material (white arrows) and the innermost has the higher density (*). The innermost layer is in contact with the cell membrane (black arrows). (B) The ends of the microalgae are filled by the fibrous material (white arrow). TB = trilaminar sheath; * = dense cell wall layer.



More than Fixative Solution, Sample Processing is a Differential Step in Cell Ultrastructure Preservation of Porifera

Daniele Stillitani^{1,2*}, Guilherme Muricy², Márcia Attias^{1*}

¹ Instituto de Biofísica/ UFRJ, Rio de Janeiro, Brasil.

² Museu Nacional/UFRJ, Rio de Janeiro, Brasil.

*dstillitani@gmail.com; mattias@biof.ufrj.br.

The preservation of tissues of sponges for observation in Transmission Electron Microscopy (TEM), has always been a challenge. Our aim was to test the quality of preservation of a sponge of the genus *Darwinella* sp. in three types of chemical fixative. MATERIALS AND METHODS: The samples were collected in Cabo Frio, RJ. The sponge was cut in 3 pieces of ~10mm in sea water, and immediately immersed in one of the following combinations of glutaraldehyde 2.5% for 24 hours (Table 1). Samples were washed in the corresponding buffer with osmolarity adjusted with sucrose. All samples were post-fixed in (1:1) 2% OsO₄+ 2.5% potassium ferrocyanide, 10mM CaCl₂ in 0.2M sodium cacodylate buffer for 60 min in the dark, washed, dehydrated in increasing series of ethanol and embedded in Embed 812, and polymerized at 60°C for 48 hours. Ultrathin sections were cut in a Leica UC7 ultramicrotome, collected in copper grids and observed in TEM JEOL 1200 and Fei Tecnai Spirit. RESULTS: All fixatives tested gave a fine preservation of the cells of the mesohyl of the sponge (i, ii and iii). Preservation of the nucleus and nuclear envelope was similar in all solutions. Mitochondria and Golgi complex were slightly better preserved in fixative GlutaSacPHEM fixative. CONCLUSION: Apparently the key factor for a good fixation is to fix and process the samples immediately after collecting with less interference of the buffer and osmolarity in the result. On the other hand, the GlutaSacPHEM fixative generated a better preservation of some cell components. In the same way that the superiority of the PHEM buffer for the Mollusca phylum has already been suggested [1], we also suggest the use of this buffer in the fixative (GlutaSacPHEM fixative) for the Porifera phylum. Finally, we predict more detailed descriptions of the Porifera ultrastructure that may be carried out based on the implementation of the precautions suggested here.

REFERENCES

[1] J. Montanaro et al., PeerJ 4 (2016): e1860. <https://doi.org/10.7717/peerj.1860>.

ACKNOWLEDGMENTS

Coordenação de Aperfeiçoamento de Pessoal de Nível Superior (CAPES), Fundação de Amparo à Pesquisa do Estado do Rio de Janeiro (FAPERJ), Museu Nacional (MNRJ), Centro Nacional de Biologia Estrutural e Bioimagem (CENABIO).

Table 1. Composition and osmolarity of the different fixatives used.

Formula	Glutaraldehyde (concentration and volume)	Buffer (stock concentration)	Buffer (final concentration)	Additions	Total volume	Final osmolarity
i	25%: 1.5mL	PHEM 13.5mL	—	Sucrose 12% (w/v)	15mL	977mOsm
ii	25%: 1.5mL	Sodium cacodylate 0.2M: 12mL	Sodium cacodylate 0.16M	Sucrose 9% (w/v) + Distilled water 1.5mL	15mL	1,025mOsm
iii	25%: 1.5mL	Sodium cacodylate 0.4M: 6mL	Sodium cacodylate 0.16M	Sea water 7.5mL	15mL	1,178mOsm

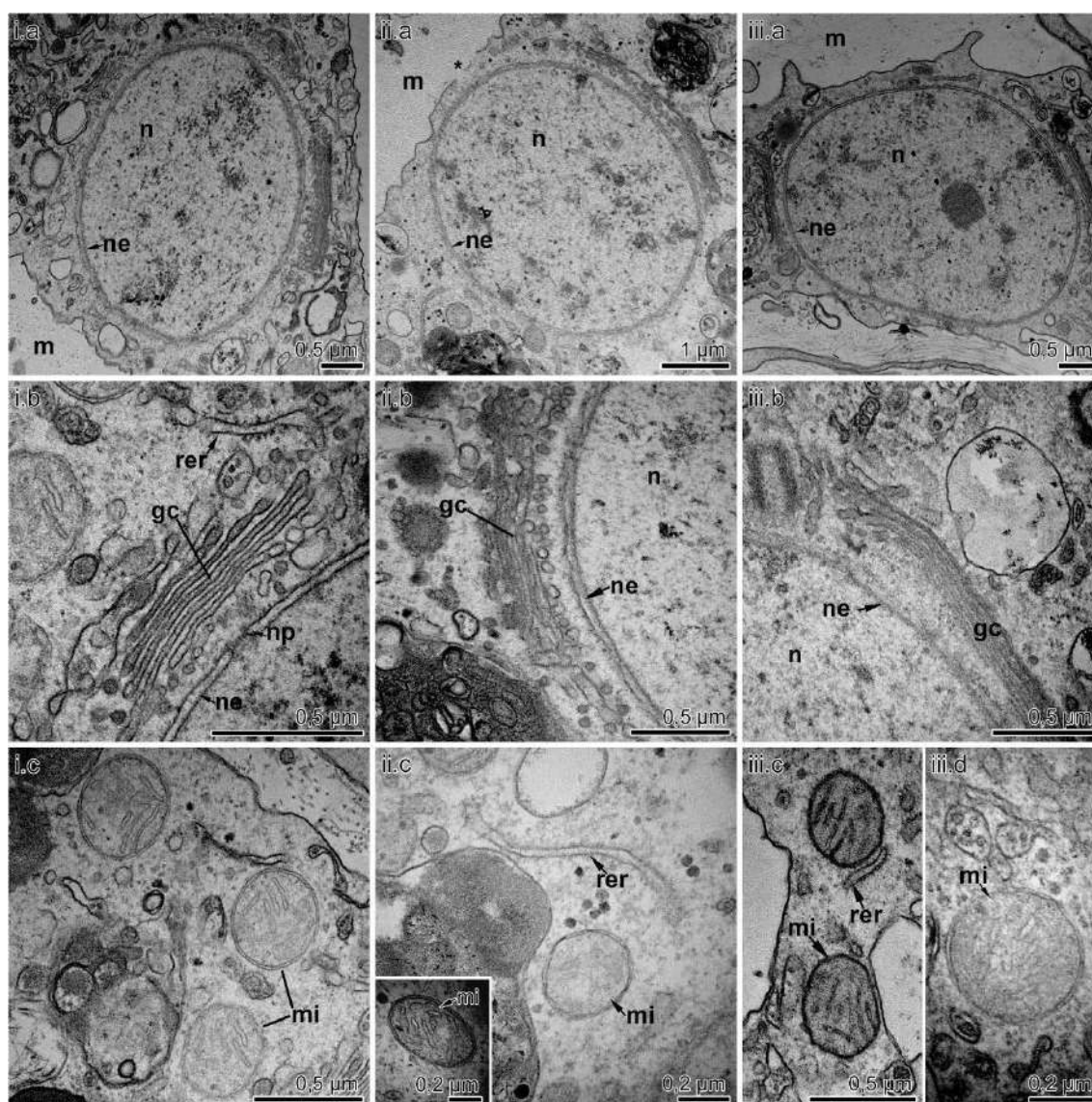


FIGURE 1. Comparison of the ultrastructure of *Darwinella* sp. in each fixative tested. i)- (GlutaSacPHEM); ii)- (GlutaSacCaco); iii)- (GlutaSeaCaco); i.a, ii.a, iii.c)- Good nuclear preservation; i.b, ii.b, iii.b)- Nuclear envelope and Golgi complex preservation. The best preservation was observed in the fixative GlutaSacPHEM; ii.c, iii.c, iii.d, iii.e)- Good mitochondrial preservation. The best preservation was observed in the fixative GlutaSacPHEM. Golgi complex (gc), channel (ch), mesohyl (m), mitochondria (mi), nuclear envelope (ne), nucleus (n), nuclear pore (np), rough endoplasmic reticulum (rer).



Case study of cobalamin F deficiency and hyperchromia: TEM as a key investigation method on the discovery of a novel genetic mutation

Guilherme S. S. S. Tonelli^{1*}, Shelida V. Braz², Patricia N. S. Moretti², Rosenelle A. Benicio^{3,4}, Juliana F. M. Araújo^{2,3,4,5}, Sônia N. Bão¹

¹ Laboratório de Microscopia e Microanálise. Departamento de Biologia Celular, Universidade de Brasília, Brasília, Brasil

² Programa de Pós-Graduação em Ciências da Saúde. Universidade de Brasília, Brasília, Brasil

³ Programa de Pós-Graduação em Ciências Médicas. Universidade de Brasília, Brasília, Brasil

⁴ Faculdade de Medicina, Universidade de Brasília, Brasília, Brasil

⁵ Hospital Universitário de Brasília, Brasília, Brasil

* Guistonelli@gmail.com

A 13-year-old girl was referred from Dermatology to Clinical Genetics due to skin hyperpigmentation and short stature. She is the second child of a consanguineous (third-degree cousins) couple and has an 18-year-old brother and a 5-year-old sister. Her parents and siblings are asymptomatic and there is no history of genetic disorders diagnosed in her family. Since birth, the patient presented hyperpigmentation on cervical skinfolds and on lunulae that turned darker after sun exposure. The patient presents facial asymmetry, short stature, low set ears and prognathism. Her skin was hyperchromic in the following regions: lateral and posterior neck, axillae, hypogastrium, inguinal region, back of hands, fingers and lunulae. She didn't present any mucosal hyperpigmentation, neither tongue abnormalities. Biopsy of hyperpigmented skin showed increased melanin within basal keratinocytes and in numerous melanophages in the papillary dermis. Axillary skin fragment was removed for analysis. Samples were fixed using Karnovsky and post-fixed in Osmium tetroxide, *in bloc* contrasted in Uranyl acetate and gradually dehydrated before embedding in Spurr resin. TEM analysis (Figure 1) revealed heavily melanized melanosomes packed in phagocytic vacuoles. Exome sequencing revealed a novel homozygous indel variant, c.515_516 del (p.Thr172) at *LMBRD1* gene (NM_). Analysis was conducted using Franklin platform (Genoox). This finding implicates on intracellular metabolism errors (Figure 2). The pathogenetic mechanism leading to hyperpigmentation in vitamin B12 deficiency is yet to be defined. The first hypothesis is the oxidation of reduced glutathione due to decrease that would lead to a lack of the normal inhibition of the tyrosinase and the subsequent stimulus of the melanocyte to produce melanin. This explanation would also encompass the findings of the further skin darkening after sun exposure, as ultraviolet would lead to additional depletion of glutathione [1] Another possibility would be an impairment in the melanin transfer between melanocytes and keratinocytes, having as result pigmentary incontinence [1]. Further testing is currently being conducted to better comprehend this rare mutation. The clinical team's supposition of vitamin B12 metabolic defects was confirmed by TEM, hence enabling further hypothesis formulation and guiding the approach on further testing considering the findings of lysosomal deposits.

References: [1] GILLIAM, James N.; COX, Alvin J Arch Dermatol , v. 107, n. 2, p. 231-236, 1973.

Acknowledgements: FAP-DF, CNPq, FINEP and CAPES

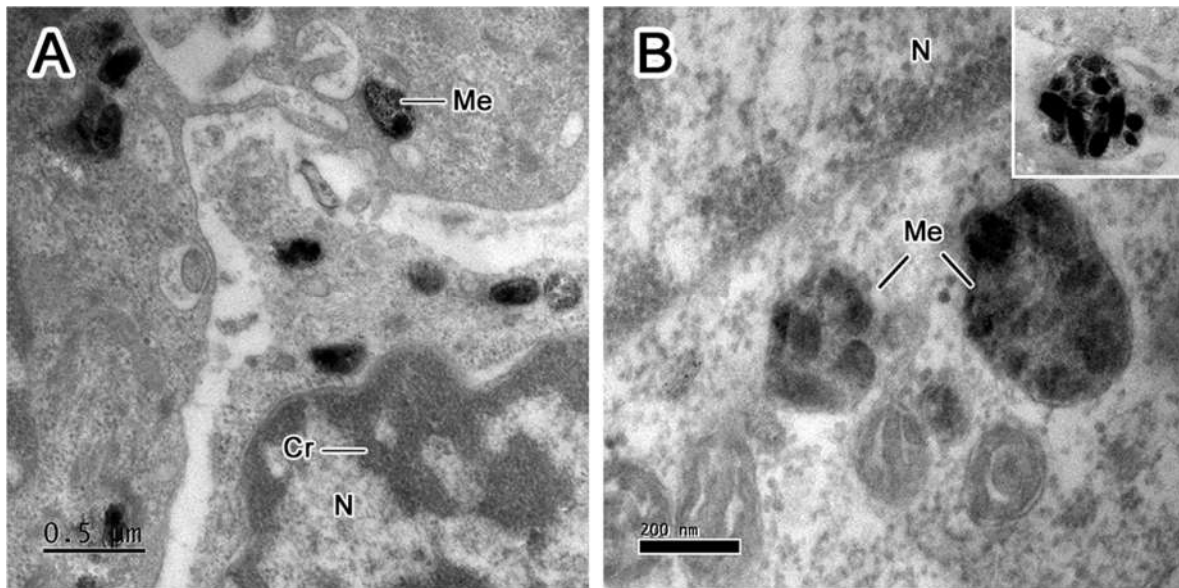


Figure 9. Fibroblast's cytoplasm containing melanosomes (A,B) with irregular electron-dense material. Abbreviations: (N) Nucleus, (Cr) Chromatin, (Me) Melanosomes.

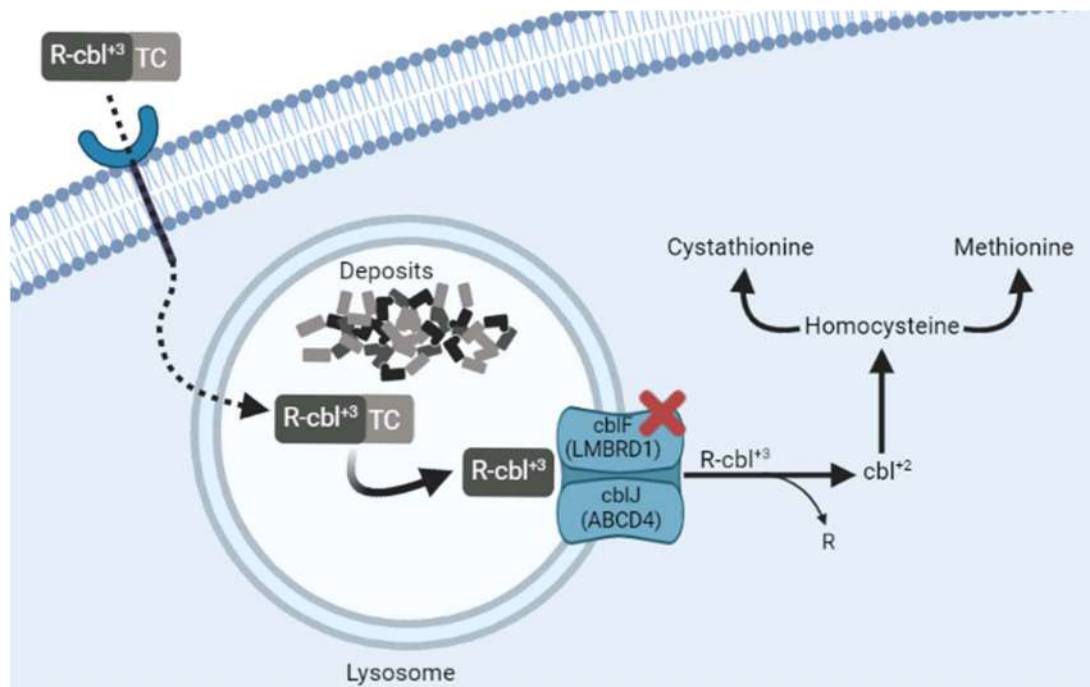


Figure 10. Schematic representation of the patient's cblF metabolism disorder. Cobalamin bound to transcobalamin carrier (TC) enters the cell from the blood. Inside the lysosome, cobalamin is released from transcobalamin. Because of the novel mutation observed, cblF activity is undermined and deposits are formed. The portion of cobalamin molecules that are successfully transported to cytoplasm undergo enzyme-mediated reduction. Created with Biorender software.



Characterization of Hypofractionated Radiation Surviving Cells in Two Colorectal Cancer Cell Lines.

Josiane Weber Tessmann¹, Murilo Ramos Rocha¹, Renata Ivo Vasconcellos¹, Danielle Lazarin-Bidoia², Celso Vataru Nakamura² and Jose Andres Morgado Diaz^{1*}

¹ Programa de Oncobiologia Celular e Molecular, Instituto Nacional de Câncer-INCA, Rio de Janeiro, Brasil

² Laboratório de Inovação Tecnológica no Desenvolvimento de Fármacos e Cosméticos, Universidade Estadual de Maringá, Maringá, Brasil

*jmorgado@inca.gov.br

Radiotherapy (RT) is an effective non-surgical treatment used in several solid tumors, including colorectal cancer (CRC), in order to reduce the risk of local recurrence. In patients with advanced rectal cancer this approach is widely used as a neoadjuvant therapy. However, RT has no impact on metastasis formation, which remains a major obstacle in clinical practice, being responsible for the high mortality rates [1, 2, 3, 4]. In addition, local tumor recurrence after RT tends to be more aggressive, with shorter survival expectancy for the patient [5]. This suggests that the RT surviving cells develop resistance mechanisms that allow their survival and increase metastatic potential. Despite major efforts in this field, the knowledge concerning the post-irradiation behavior and the phenotype of radioresistant cancer cells is still limited and little progress has been made in the treatment of CRC. Therefore, it is important to elucidate what contributes to this phenotype, in order to improve therapeutic success. This study investigated the characteristics of surviving cells of two human CRC cell lines treated with a clinically relevant treatment protocol, hypofractionated radiation. Cells were exposed to 25 Gys delivery in 5 daily fractions. Characterization of this phenotype was performed through phase-contrast light microscopy, transmission and scanning electron microscopy, confocal microscopy of specific markers, and DNA content analysis through flow cytometry. The results show that the surviving cells (ISC) from both cell lines, SW-480 and HCT-116, increase their size, ploidy, the autophagic process, and become resistant to re-irradiation. In addition, the long-term evaluation of the ISC show that HCT-116 lineage does not proliferate again, while the SW-480 ISC enter a transient dormancy state, resuming its growth in about 14 days. These cells generate a heterogeneous progeny, in which was possible to observe three distinct phenotypes: rounded and highly proliferative cells, mesenchymal cells, and the polyploid giant cancer cells. Based on these results, the next step of this study is to identify proteins and pathways differentially regulated in ISCs. Thus, we will contribute to the identification of new therapeutic targets for neoadjuvant therapies, in order to improve the prognosis of CRC patients treated with RT.

REFERÊNCIAS

- [1] R. Sauer et al., *New England Journal of Medicine*, 351 (2004) 17.
- [2] W. Van Gijn et al., *The Lancet Oncology*, 12 (2011) 6.
- [3] S. Engelen et al., *The Lancet Oncology*, 18 (2013) 10.
- [4] V. Banwell et al., *Acta Oncologica*, 58 (2019) 9.
- [5] V. Van Den Brink et al., *Journal of Clinical Oncology*, 22 (2004) 19.

AGRADECIMENTOS. We would like to thank CNPQ, CAPES, FAPERJ and Ministério da Saúde for supporting this work.

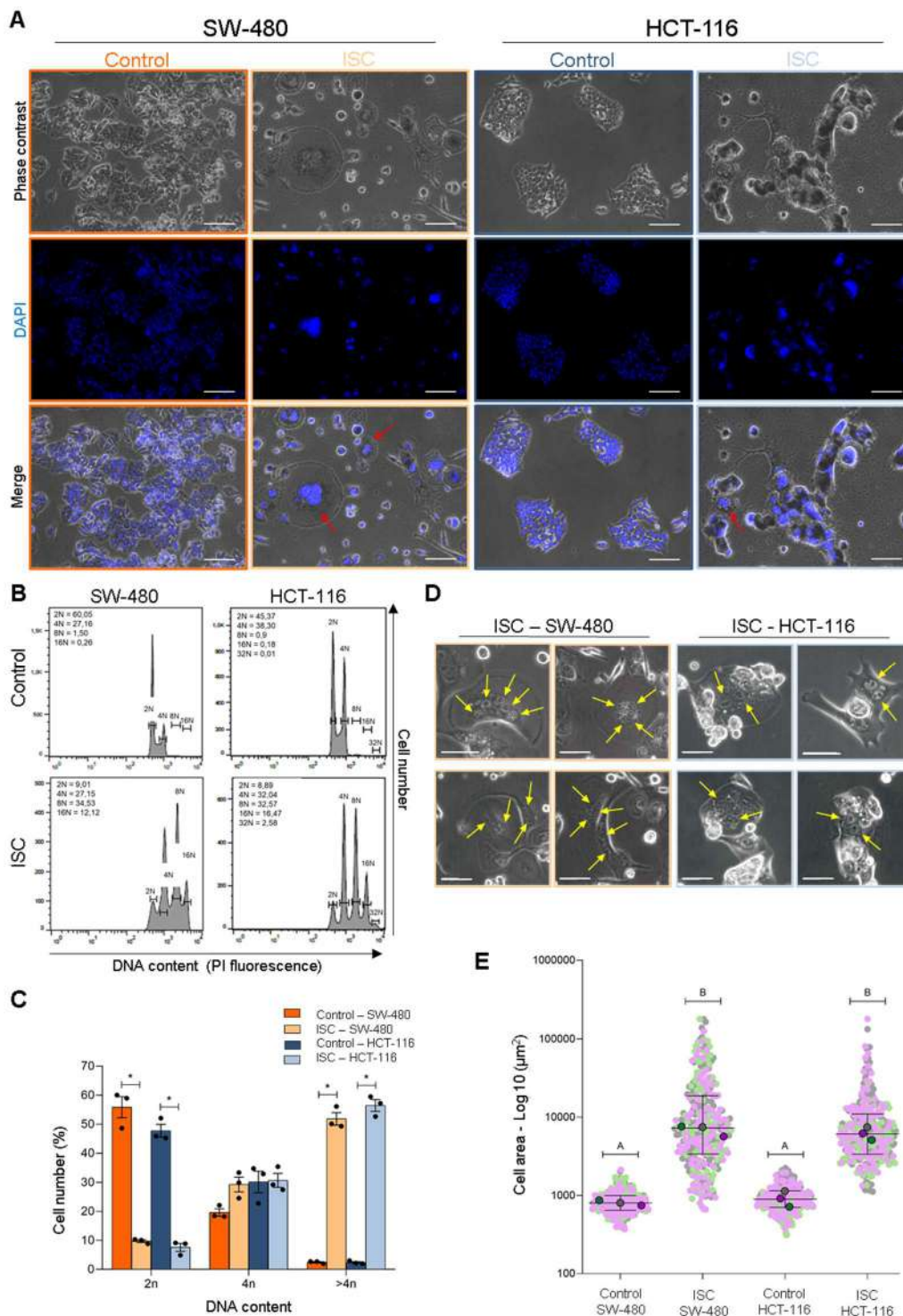


Figure 1 – (A) DAPI stained cells. Red arrows indicate multinucleated polyploid cells. (B, C) Ploidy analysis using flow cytometer. Taking into account that the peak with smaller PI staining would be cells in its usual ploidy (simplified as 2n), we evaluated the amount of genomic content and estimated ploidy of the remaining cells. Data are representative of mean \pm SEM. Statistical significance analysis was performed using the one-way ANOVA with Tukey's post test. (D) Micrographs of cells with yellow arrows indicating multiple nuclei in the ISC cells. (E) Quantification of cell size. Data represent the median and interquartiles. Statistical analysis was performed using the Kruskal-Wallis test with Dunn's post test. Different letters indicate statistical difference. * $p < 0.05$. ISC: irradiation surviving cells. Scale bar: 100 μm



Effect of Sperm Chromatin Defects Identified by Transmission Electron Microscopy on Bovine *In Vitro* Embryo Production.

Lays Oliveira Rocha¹, Paulo Henrique Mazzutti Alves², Sara Hissae Hiraiwa¹ and Marcelo Emílio Beletti^{3*}

¹ Graduate Program in Cell and Structural Biology, Instituto de Ciências Biomédicas, UFU, Uberlândia, Brazil.

² Graduate Program in Veterinary Science, Faculdade de Veterinária, UFU, Uberlândia, Brazil.

³ Biology of Reproduction Laboratory, Instituto de Ciências Biomédicas, UFU, Uberlândia, Brazil.

*mebeletti@ufu.br

When observed under transmission electron microscopy, bull sperm chromatin is usually extremely electron-dense and homogeneous. However, changes from small spots to larger lighter regions are also often observed. The aim of this study was to verify the importance of these sperm chromatin changes identified by transmission electron microscopy on the *in vitro* fertilization and early embryonic development. For this study, five ejaculates from five different Giroland bulls with different levels of fertility were used. Part of each semen sample was used for *in vitro* embryo production (IVEP) routines and part was used for evaluation of sperm chromatin by transmission electron microscopy. One hundred and twenty IVEP routines were performed according to the protocol [1] of the Biology of Reproduction Laboratory of the Universidade Federal de Uberlândia, with approximately 40 oocytes per routine, totaling 4916 oocytes, all from slaughterhouse-collected ovaries. Cleavage rates of experimental bulls were determined 48 hours after *in vitro* fertilization, represented by the percentage of mature oocytes that started cleavage. Blastocyst rates were determined seven days after fertilization and were represented by the percentage of oocytes that started cleavage and reached the blastocyst stage. The rest of the semen samples were used for the evaluation of sperm chromatin by transmission electron microscopy [2]. On average 150 sperm head images of each sample were captured and classified into five grades of defects, as shown in figure 1. Pearson's correlation test was applied between each chromatin defect type and the cleavage and blastocyst rates (Table 1). The high positive and significant correlations between cleavage and blastocyst rates and the percentage of sperm without chromatin defects show that, in general, the absence of changes in sperm chromatin favors the process of fertilization and the early embryonic development. The lack of significant correlation between cleavage and blastocyst rates and milder defects (grades 1 and 2) indicates that these defects have little or no effect on the oocyte fertilization process and that when sperm carriers with this type of chromatin defect fertilized the oocyte, the initial embryonic development is not impaired. The most severe defects (grades 3 and 4) showed significant negative correlations with cleavage and blastocyst rates, indicating that these types of defects can interfere with the fertilization process and when a sperm with these defect types fertilizes the oocyte, the early embryonic development is impaired.

[1] A.C. Lucio et al., *Theriogenology*, 86 (2016) 924.

[2] J.M. Soares; M.E. Beletti, *Braz. J. Vet. Res. An. Sci.*, 43 (2006) 554.

The authors acknowledge the support of the CNPq, CAPES and FAPEMIG

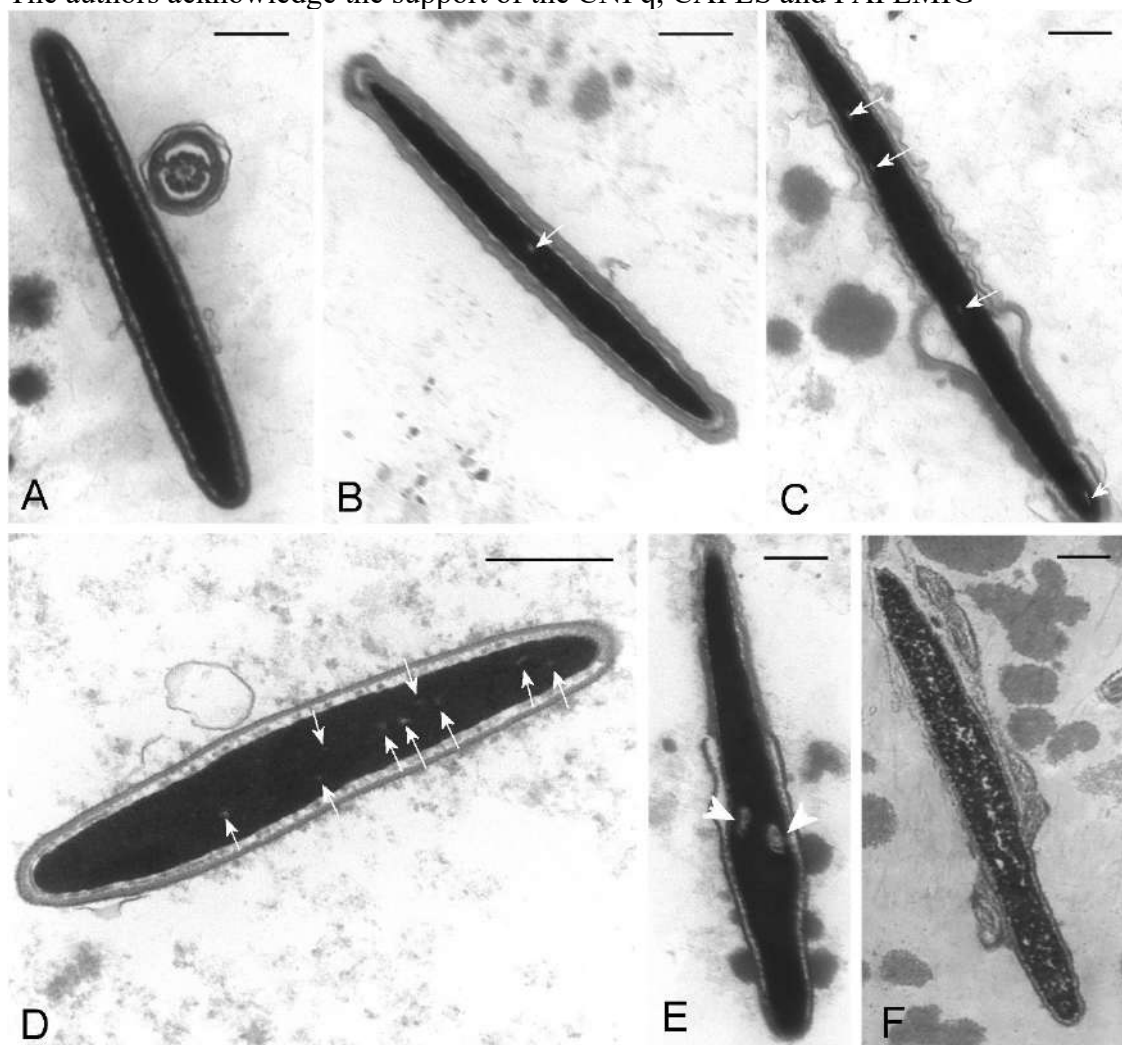


Fig. 1. Examples of sperm heads with each grade of chromatin defect. Grade 0 - absence of chromatin defects (A). Grade 1- presence of up to 3 small bright spots in chromatin (B). Grade 2 - presence of up to 6 small bright spots (C). Grade 3 - presence of several light points (above 6) (D) or lighter region(s) occupying up to a quarter of the sperm head (E). Grade 4 - lighter region(s) occupying above a quarter of the sperm head or large regions with granular chromatin (F). (arrow= bright spot; head arrow= lighter region; bar= 0.5 μ m)

Table 2. Pearson's correlation coefficients and p-value between the grades of chromatin defects and cleavage and blastocysts rates obtained in PIVEs.

Defect category	Cleavage		Blastocyst	
	Coefficient	p-value	Coefficient	p-value
Grade 0	0,91	0,03	0,99	0,0002
Grade 1	0,55	0,33	0,82	0,09
Grade 2	-0,09	0,89	-0,48	0,41
Grade 3	-0,93	0,02	-0,98	0,003
Grade 4	-0,88	0,05	-0,98	0,003



Ultrastructural Studies of Vero-E6 Cells Infected with SARS-CoV-2 and Treated with Antiviral Molecules

Marcos Alexandre Nunes da Silva^{1*}, Maria Eduarda Monteiro², Milene Dias Miranda², and Debora Ferreira Barreto- Vieira¹.

¹ Laboratório de Morfologia e Morfogênese Viral, IOC, Fiocruz Rio de Janeiro, Brasil.

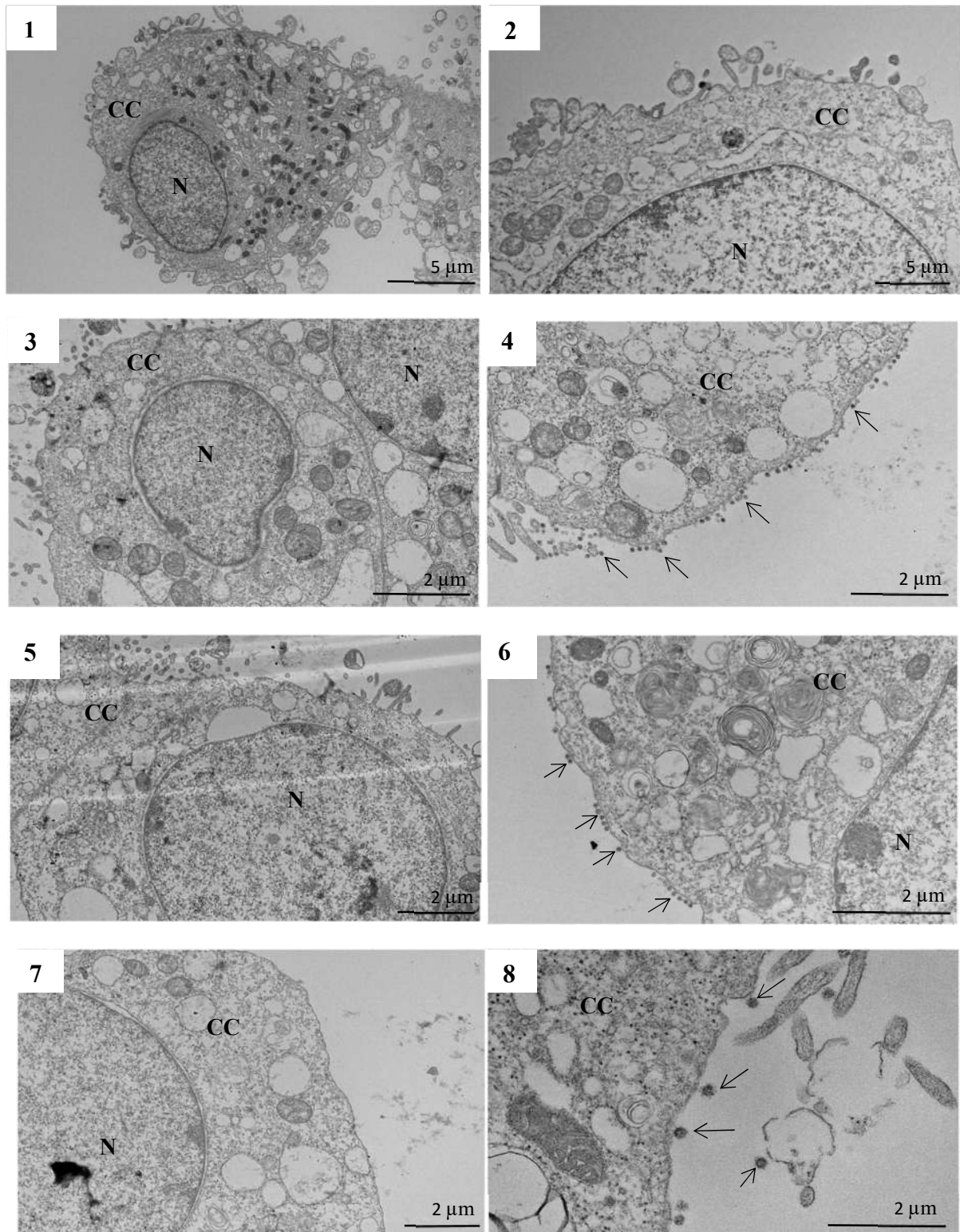
² Laboratório de Vírus Respiratórios e do Sarampo IOC, Fiocruz Rio de Janeiro, Brasil.

*marcos.nunes@ioc.fiocruz.br

Coronaviruses (CoV) drew worldwide attention for causing outbreaks of severe acute respiratory syndrome (SARS-CoV) in Asia 2002-03, and respiratory diseases in the Middle East (MERS-CoV), 2012. In December 2019, more once a new coronavirus (SARS-CoV-2) was first identified in Wuhan, China, it was associated with a serious respiratory infection, known as COVID-19 [1]. This virus spread rapidly throughout China and 30 other countries, resulting on 11 march 2020 in the World Health Organization's upgrading of the SARS-CoV-2 classification for pandemic [2]. A well-characterized standardized in vitro system for the production of viral mass, for testing drug candidates and vaccines against the new coronavirus is extremely interesting in the current scenario. Given the impact on public health worldwide, there is a rush to protocol a therapy, but to date there is no specific antiviral drug. Then, the analyze of impact in SARS-CoV-2 biosynthesis in treated and non-treated cells with anti-viral molecules is pivotal. For this purpose, we evaluated, by transmission electron microscopy, monolayers infected with viral isolate and exposed to drugs that have already been identified as interesting from the point of view of inhibiting the replication of SARS-CoV-2, such as mefloquine and daclatasvir at 10 μ M. The virus was tittered by plaque-forming units assay (PFU/ml) [4,5]. All procedures involving experimental infection have been performed in a safety level 3 laboratories, in accordance with World Health Organization standards [3]. The mefloquine treatment prevented totally the formation of viral progeny with infective capacity in culture supernatant, and the treatment with daclatasvir inhibited viral replication by 80%. Ultrastructural analyzes detected, in cells treated with Daclatasvir, virus adsorbed to the cytoplasmic membrane, and rare particles inside the cell. In cells treated with mefloquine no viral particles were observed. In addition, the data regarding antiviral molecules corroborate the findings already suggested in other studies [4], showing that we use a methodology compatible with the literature and that adds ultrastructural knowledge to the data that will be published, including by other groups, assisting in basic research and applied.

REFERENCES:

- [1] Zhu N, et al. N Engl J Med. V 382(8):727-733 (2020)
- [2] D.F. Barreto-Vieira et al., Mem. Inst. Oswaldo Cruz, Rio de Janeiro, Vol. 116: e200443, (2021).
- [3] Organization, W.H. Geneva, Switzerland, 24 Jan (2020).
- [4] Sacramento CQ, et al. April 21 BioArxiv (2021). DOI: 10.1093/jac/dkab072
- [5] Fintelman-Rodrigues N, et al., Antimicrobial agents and chemotherapy, v. 64, p. 1, (2020).
- [6] This research was supported by CNPq (Brazil); IOC, Fiocruz (Brazil)



Figures 1 and 2: Vero-E6 cells non-infected (cell control) [1: 1 hour of cultivation, 2: 48 hours of cultivation]. **Figures 3, 5 and 7:** Vero-E6 cells 48 hours post-infection treated with 10 μ M of mefloquine; virus particles were not detected. **Figures 4, 6 and 8:** Vero-E6 cells 48 hours post-infection treated with 10 μ M of daclatasvir presenting virus particles (arrow).



The Effect of Amiodarone on *Trichomonas vaginalis*

Tatiana Guinancio de Souza^{1,2}, Wanderley de Souza^{2,3} and Marlene Benchimol¹

¹ Universidade do Grande Rio, Duque de Caxias, Brazil.

² Laboratório de Ultraestrutura Celular Hertha Meyer, Instituto de Biofísica Carlos Chagas Filho, Universidade Federal do Rio de Janeiro, Rio de Janeiro, Brazil.

³ Centro Nacional de Biologia Estrutural e Bioimagens, Universidade Federal do Rio de Janeiro, Rio de Janeiro, Brazil.

*Corresponding Author: marlenebenchimol@gmail.com

Trichomonas vaginalis is a protozoan that causes human trichomoniasis, the most common sexually transmitted infection (STI) on the planet, affecting approximately 278 million people worldwide [1]. Pregnant women with trichomoniasis have a greater chance of miscarriage, premature birth, premature rupture of the placenta, and disorders in pregnancy [1]. The disease can also cause infertility in women and men [2]. In men, the disease is usually asymptomatic. However, in severe cases, it can present inflammation in the urethra and prostate [2]. Infection by *T. vaginalis* is also related to a predisposition to infections caused by human papillomavirus (HPV), [2], human immunodeficiency virus (HIV) [2] in addition to cervical cancer and prostate cancer [2]. The current treatment for human trichomoniasis is metronidazole (MTZ). MTZ 1-(2-hydroxyethyl)-2-methyl-5-nitroimidazole is a compound widely used to treat several infections caused by bacteria such as *Helicobacter*, *Bacteroides*, and *Clostridium* and anaerobic parasites such as *Trichomonas*, *Entamoeba*, and *Giardia* [3]. Although effective to clear the parasite infection, this medication is related to severe side effects, such as nausea, vomiting, dizziness, insomnia [2], and leukopenia and neuropathies in the more severe cases. Because of the toxicity, this therapy cannot be adopted during pregnancy [2]. Besides the toxicity of the treatment, some strains become resistant to 5'-nitroimidazoles, and the development of a new alternative drug for trichomoniasis is necessary. Amiodarone is an antiarrhythmic drug approved in the USA in 1985 used to treat cardiomyopathies [4]. In addition, this antiarrhythmic agent and its derivatives present antiparasitic effects, disturbing Ca²⁺ homeostasis in *Trypanosoma cruzi* epimastigotes and promastigotes and amastigotes in *Leishmania Mexicana*, resulting in an intracellular Ca²⁺ increase [5], blocking the biosynthesis of ergosterol in these parasites [5]. This work investigated the *in vitro* effect of amiodarone on *T. vaginalis* by different microscopy techniques. We noted that the parasites became clustered and presented a high glycogen contents.

REFERENCES

[1] World Health Organization (2012) Global Incidence and Prevalence of Selected Curable Sexually Transmitted Infections – 2008. Geneva: WHO Press.

[2] Midlej V, Rubim F, Villarreal W, Martins-Duarte ÉS, Navarro M, de Souza W, Benchimol M. Zinc-clotrimazole complexes are effective against *Trichomonas vaginalis*. Parasitology. 2019 Aug;146(9):1206-1216.

[3] Edwards DI (1993) Nitroimidazole drugs—action and resistance mechanisms.I. Mechanisms of action. Journal of Antimicrobial Chemotherapy 31, 9–20.

[4] Mason, J. W. Amiodarone. N. Engl. J. Med. **1987**, 316, 455-466

[5] Benaim G, Paniz-Mondolfi AE, Sordillo EM and Martinez-Sotillo N (2020) Disruption of Intracellular Calcium Homeostasis as a Therapeutic Target Against *Trypanosoma cruzi*. *Front. Cell. Infect. Microbiol.* 10:46. doi: 10.3389/fcimb.2020.00046.

ACKNOWLEDGMENT

This research was supported by CNPq (Brazil), Capes and Faperj.

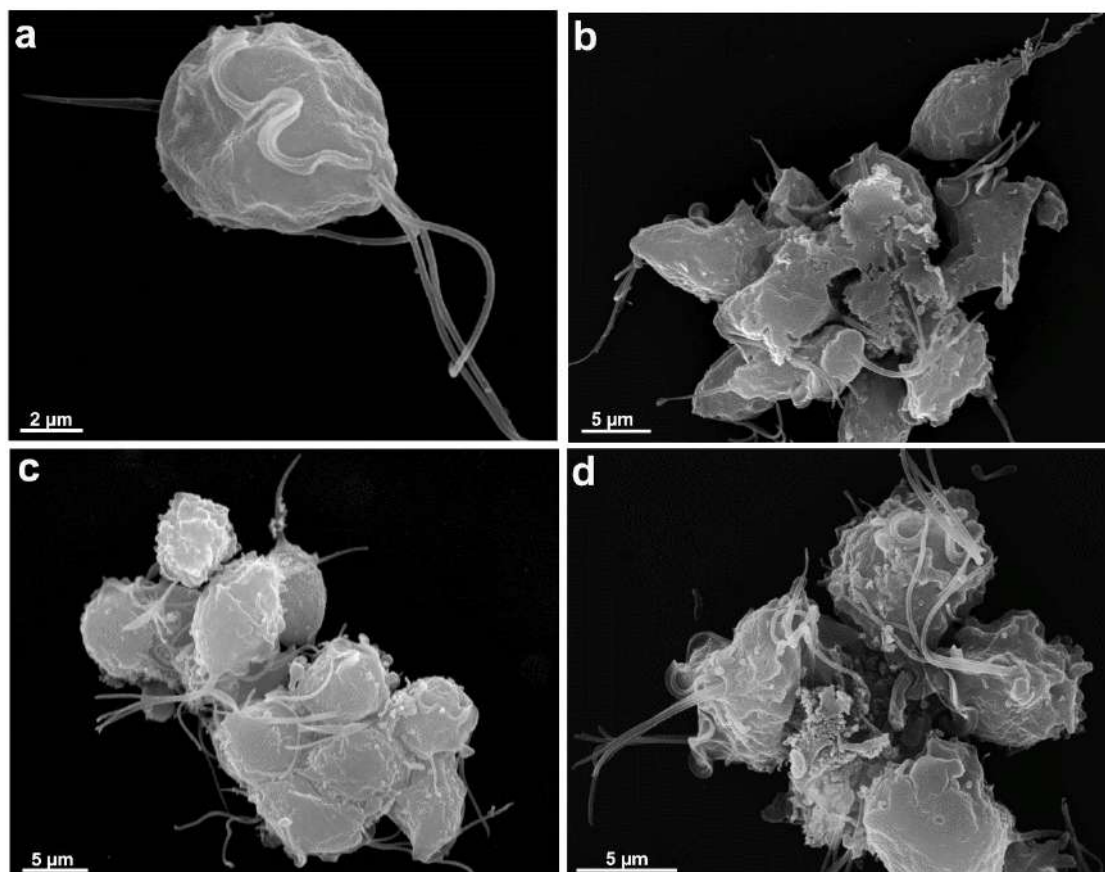


Figure 1. SEM images of *T. vaginalis* treated with 10 µm AMD for 36 h at 37 °C. Control (a) treated with 10 µm AMD for 36 h (b – d) morphological changes, wrinkled and aggregated cells (b - d) (arrows) are observed.



***Trichomonas vaginalis*: secretion of microvesicles and projection of tunneling nanotubes**

Júlio César Santana de Andrade^{1,2*}, Wanderley de Souza^{2,3} and Marlene Benchimol¹

¹ Universidade do Grande Rio, Duque de Caxias, Brazil.

² Laboratório de Ultraestrutura Celular Hertha Meyer, Instituto de Biofísica Carlos Chagas Filho, Universidade Federal do Rio de Janeiro, Rio de Janeiro, Brazil.

³ Centro Nacional de Biologia Estrutural e Bioimagens, Universidade Federal do Rio de Janeiro, Rio de Janeiro, Brazil.

*juliocsntn@gmail.com

Trichomonas vaginalis is the etiologic agent of human trichomoniasis, a highly sexually transmitted infection with the highest frequency worldwide among non-viral and treatable infections associated with HIV and HPV infection, also with premature birth, becoming an important public health problem [1]. The knowledge about the interaction of *T. vaginalis* with host cells is still poorly understood, although the mechanisms of adhesion of the parasite to the cell surface are multifaceted, where several hypotheses are pointed out [2]. Different cell types secrete a heterogeneous group of extracellular vesicles (EVs), including microvesicles (MVs) with a size of 30 to 150 nm. Furthermore, long-range intercellular cytoplasmic bridges, known as tunneling nanotubes (TNTs), are very important elements of communication between cells [3]. Microscopy, particularly scanning electron microscopy (SEM), has been used to analyze the surface of various cell types, including pathogenic protozoa [4]. In recent years, these structures have received important attention in biomedical research. It has been described that EVs can participate in parasite-host cell interaction, transporting several antigens and other specific macromolecules from their cell of origin [5] and engineered TNTs are known to transport biological materials through cytoplasmic bridges between cells [6]. This work aims to characterize morphologically and functionally the MVs and TNTs in the interaction of this protozoan with the vaginal epithelial cells. For this, electron microscopy techniques are used, mainly SEM, both conventional and high resolution. Here, we demonstrate with and without stimulus with calcium ions and ionophores, the secretion of microvesicles and constitutive exosomes that are released with the parasite's membrane. Furthermore, membrane projections, similar to nanotubular structures, already described in other pathogenic protozoa, such as *Tritrichomonas foetus*, were observed.

REFERÊNCIAS

- [1] M. F. K. Aquino, A. S. Hinderfeld and A. Simoes-Barbosa. *Trichomonas vaginalis*. Trends in Parasitology. 36, 646–647, 2020.
- [2] F. Mercer and P. Johnson. *Trichomonas vaginalis*: pathogenesis, symbiont interactions, and host cell immune responses. Trends in Parasitology, 34, 683-693, 2018.
- [3] M. Nawaz and F. Fatima. Extracellular vesicles, tunneling nanotubes, and cellular interplay: synergies and missing links. Frontiers in molecular biosciences, v. 4, p. 50, 2017.

- [4] W. Souza and M. Attias. New advances in scanning microscopy and its application to study parasitic protozoa. *Experimental parasitology*, v. 190, p. 10-33, 2018.
- [5] M. Tkach and C. Théry. Communication by extracellular vesicles: where we are and where we need to go. *Cell*, 164, 1226-1232, 2016.
- [6] T. A. Fykerud, et al. Mitotic cells form actin-based bridges with adjacent cells to provide intercellular communication during rounding. *Cell Cycle*, 15, 2943-2957, 2016.

ACKNOWLEDGMENTS

The authors are grateful for the financial support provided by the Conselho Nacional de Desenvolvimento Científico e Tecnológico (CNPq), Fundação de Amparo à Pesquisa Carlos Chagas Filho do Estado do Rio de Janeiro (FAPERJ) and the Coordenação de Aperfeiçoamento de Pessoal de Ensino Superior (CAPES).

FIGURE

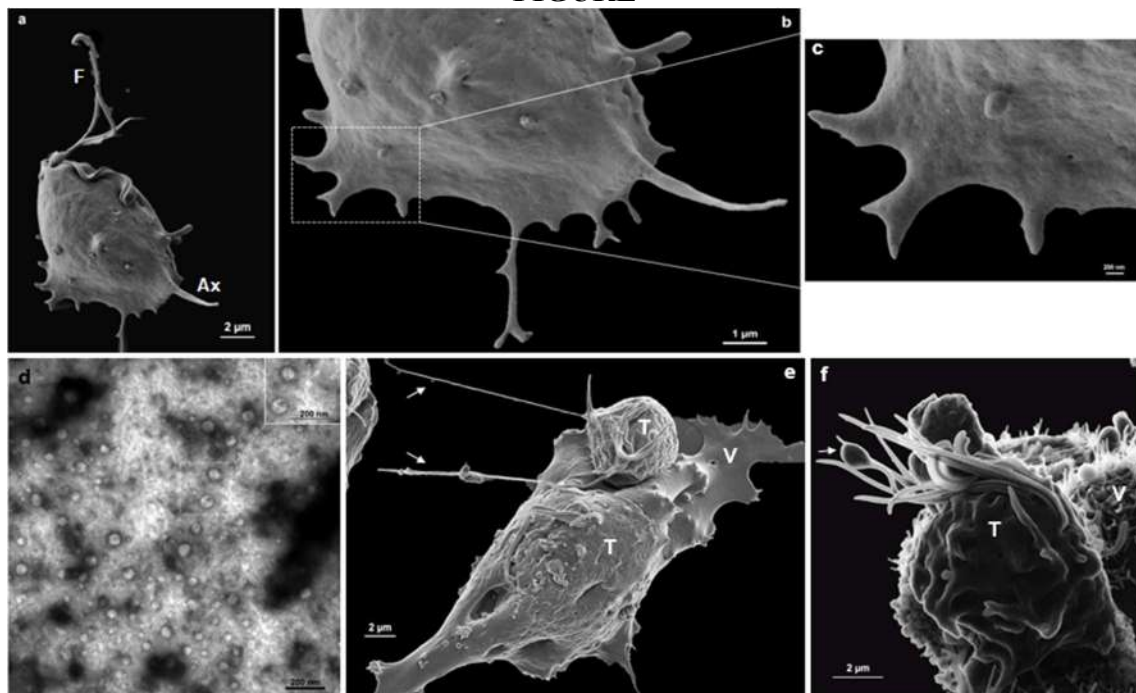


Figure 1. *Trichomonas vaginalis* secreting constitutive microvesicles observed with SEM high-resolution Auriga 40. Samples were coated with 4 nm platinum. **(a)** Control *T. vaginalis*. **(b)** At higher magnification, notice details of the release of microvesicles that sprout from the cell membrane of the parasite. **(c)** inset: higher magnification of the marked area of **(b)**. **(d)** Negative stain TEM (transmission electron microscopy) analysis of an enriched microvesicles sample. Note vesicles with a range size of exosomes. **(e)** Interaction of *T. vaginalis* with a vaginal epithelial cell. The amoeboid-shaped parasites have firmly adhered to the host cell surface. Flagella exhibited nanotubes (arrows). **(f)** Scanning Helium Ion microscopy (HIM) of uncoated *T. vaginalis* in the process of interaction with vaginal cells. We noted the budding of microvesicles on the protozoan cell surface and dilated regions at the tip of the flagella (arrow). **T:** *Trichomonas vaginalis*; **V:** vaginal epithelial cell; **F:** flagella; **Ax:** axostyle.



EXTRACELLULAR VESICLES IN *Tritrichomonas foetus* AFTER PHOTODYNAMIC THERAPY

Amanda Lira G. Albuquerque; Mariela Ines Batista dos Santos, Lais Silva;

Bruno H. Godoi; Cristina Pacheco Soares; Newton Soares da Silva

amanda_lga@yahoo.com.br nsoares@univap.br

Universidade do Vale do Paraíba/Instituto de Pesquisa e Desenvolvimento, Avenida Shishima Hifumi, 2911, Urbanova - 12244-000 - São José dos Campos-SP, Brasil,

Photodynamic therapy (PDT) makes use of a combined photosensitizer and a light source, usually the LASER. In the results of Da Silva et al. (2007) of PDT in *T. foetus*, ultrastructural changes were observed, such as plasma membrane projections, nuclear fragmentation with heterochromatin masses in the periphery, proliferation of the endoplasmic reticulum, intense cytoplasm vacuolization, fragmented pelta-axostilar complex and internalization of the flagella. In recently obtained results, we observed changes in the nucleus similar to apoptosis. The group where the protozoa were incubated with the photosensitizer and after being irradiated showed significant morphological changes with apoptotic characteristics (MARGRAF-FERREIRA, 2017). In the sequence, we carried out studies of the interaction of *T. foetus* after PDT with carbon nanotubes (figure 1) and observed changes in the morphology of the protozoan surface and that vesicles were also being released that modified the morphology of the nanotubes (MACHADO 2014). *T. foetus* from an axenic culture was incubated with the AlPcS4 photosensitizer and then irradiated under a laser source (InGaAlP - Thera Lase-DMC, $\lambda = 685$ nm; P = 26 mW; DE = 4.5 J / cm²; t = 3.52 s). 24 hours after PDT, the protozoa were fixed for at least 1 hour at room temperature, in a 4.0% paraformaldehyde solution, 2.5% glutaraldehyde in 0.1 M cacodylate buffer pH 7.2. After fixation, they were washed in PBS and post-fixed in 1% OsO₄ in 0.1M cacodylate buffer, pH 7.2 with 1% potassium ferrocyanide, and 5mM CaCl₂ at room temperature, in the dark. The cells were then washed in PBS, dehydrated in acetone and embedded in Epon. Ultrathin sections were obtained in an ultramicrotome (Leica Ultracut UCT) and stained with uranyl acetate and lead citrate and observed in a Jeol 1210 Transmission Electron Microscope (ESALQ – Prof. Dr. Eliot Kitajima). In analyzing the images, observed the release of microvesicles that may be related to the protozoan pathogenicity process. In photomicrograph 02, can see that the protozoan *T. foetus* after PDT releases microvesicles in varying amounts and volumes. In figure 2A can see small projections (arrows) on the protozoan membrane. In figure 2B the microvesicles (arrows) are in the process of detaching the membrane. In figure 2C can see a microvesicle already released. The parasite - host cell interaction process involves the secretion of products that can interfere not only in the adhesion process, but mainly in pathogenicity. Communication by secretion products is also recognized that will increase the adhesion of weaker parasites and consequently increase their pathogenesis (COAKLEY; MAIZELS; BUCK; 2015). According to the presented, the study of secretion products of the parasitic protozoan *T. foetus* will contribute to the understanding of the mechanisms not only of the parasite-host cell interaction, but also of the mechanisms of infection and cellular communication.

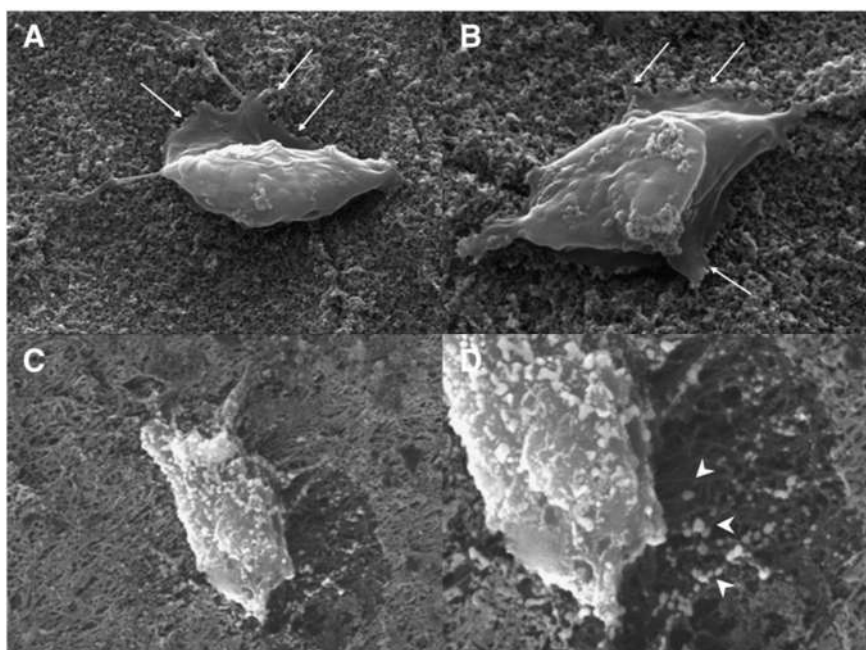


Figure 1 – SEM photomicrograph of the interaction of the protozoan parasite *T. foetus* with a titanium surface coated with VACNT-O2. 1A and 1B are SEM-images of non-PDT treated protozoa. 1C and 1D show images of protozoa after PDT. Arrow - filopodia adhered to the VACNT-O2. Arrowhead - vesicles released by *T. foetus* after PDT (Fig. A, B, and C 5000×; FIG. D 15,000×). (MACHADO, 2014).

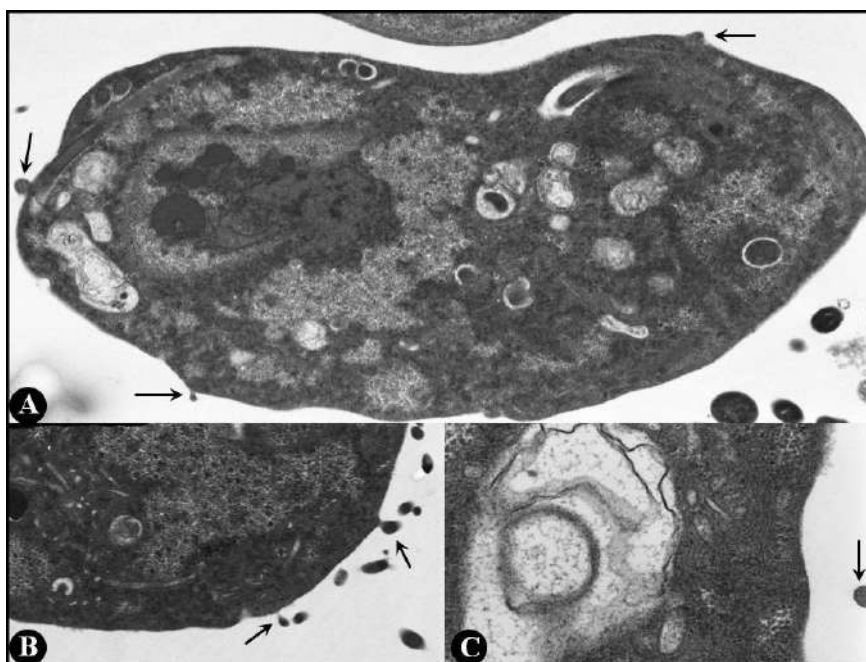


Figure 02 - TEM photomicrograph of the parasitic protozoan *Tritrichomonas foetus* after treatment with PDT. Arrows demonstrate initiation of membrane projections (2A), microvesicles in release (2B) and microvesicles already released (2C). X3000.

Referências Bibliográficas



G. Coakley,; R.M. Maizels; A.H. Buck, Trends in Parasitology, 31 (2015) 477.

N.S.da Silva et al., Veterinary Parasitology, 146 (2007) 175.

S.M. Machado et al., Materials Science and Engineering C, 36 (2014) 180.

A. Margraf-Ferreira et al., Photodiagnosis and Photodynamic Therapy 18 (2017) 193.



Ultrastructural and Biochemical Alterations Induced by ACET-1 on Amastigote Forms of *Leishmania amazonensis*

Rayanne Regina Beltrame Machado^{1*}, Deysiane Lima Salvador², Aline Rufino de Oliveira², Maria Helena Sarragiotto², Tânia Ueda-Nakamura¹, Sueli de Oliveira Silva¹, Danielle Lazarin-Bidóia¹ and Celso Vataru Nakamura¹

¹Laboratory of Technological Innovation for the Development of Pharmaceuticals and Cosmetics, State University of Maringá. Maringá, Brazil

²Department of Chemistry, State University of Maringá – Maringá, Brazil.

*email: raymachado6@hotmail.com

Leishmaniasis represents a serious health public problem and is endemic in tropical and underdeveloped regions. Currently, more than 1 billion people live in areas at risk of infection and the treatment is unsatisfactory [1]. Therefore, is urgently needed the search of new drugs to leishmaniasis treatment. In previous studies, our research group has already shown that the synthetic compound 4-(5'-formyl-[2,2'-bithiophen]-5-yl)but-3-yn-1-yl acetate, **ACET-1**, induced biochemical and ultrastructural unprecedented alterations in promastigotes of *Leishmania amazonensis*, when treated with IC₅₀ (28.9 μM) for 72 h. Reasoned by it, the aim of this study was to evaluate the appearance of these alterations in the intracellular forms, amastigotes. For this, the amastigote-infected J774A.1 macrophages were treated with IC₅₀ (50 μM) and 2xIC₅₀ (100 μM) of **ACET-1** for 48 h at 34 °C and fixed in a solution of 2.5% glutaraldehyde in 0.1 M cacodylate buffer for 24 h at 4 °C. For scanning electron microscopy (SEM), the parasites were dehydrated in increasing ethanol gradient, critical point-dried in CO₂, sputter-coated with gold, and observed using a FEI SCIOS microscope. For transmission electron microscopy (TEM), the parasites were postfixed in a solution of 1% osmium tetroxide, 0.8% potassium ferricyanide and 10 mM CaCl₂ in 0.1 M cacodylate buffer. The samples were dehydrated in increasing acetone gradient and embedded in Polybed 812 resin. Ultrathin sections were obtained, contrasted with uranyl acetate and lead citrate, and observed in JEOL JEM 1400 microscope. To access the reactive nitrogen species (RNS), the parasites were loaded DAF-FM DA and quantified by flow cytometer FACSCalibur, equipped with software Cell Quest. Our results demonstrated that **ACET-1** did not induce morphological changes (Fig. 1), despite proving the reduction in the number of infected macrophages and amastigotes per macrophage. By TEM, **ACET-1** not induced similar changes as observed in promastigotes. However, treated-amastigotes presented nuclear disorganization and autophagic vacuoles in addition to the intense secretory activity of macrophages (Fig. 2). These results agree with the data obtained by biochemical mechanisms, which showed increase of RNS (Fig. 3) that may indicate to oxidative stress caused by **ACET-1** in parasites of *L. amazonensis*.

References:

- [1] W.H.O. Leishmaniasis, Key facts (2021). <https://www.who.int/news-room/fact-sheets/detail/leishmaniasis>, accessed in May 20, 2021.
- [2] This research was supported by CNPq (Brazil)

Acknowledgement: This study was supported through grants from CAPES, CNPq, FINEP, Fundação Araucária, COMCAP-UEM.

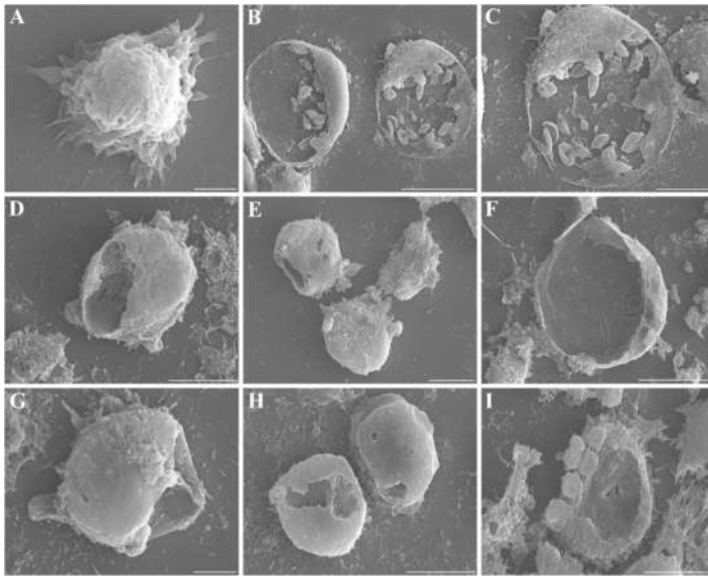


Figure 1: Scanning electron microscopy of amastigotes of *L. amazonensis* treated with ACET-1 for 48 h. (A-C) untreated cells; (D-F) amastigotes treated with IC₅₀ (50 µM); (G-I): amastigotes treated with 2xIC₅₀ (100 µM). Scale bars: (A,G) 5 µm; (C-E,H-I) 10 µm; (B,F) 20 µm.

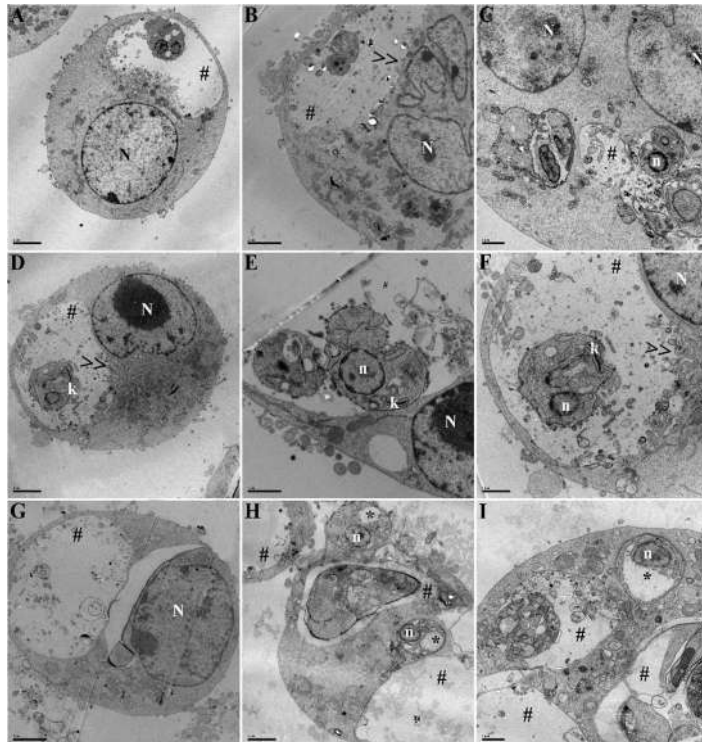


Figure 2: Transmission electron microscopy of amastigotes of *L. amazonensis* treated with ACET-1 for 48 h. (A-C) untreated cells (D-F) amastigotes treated with IC₅₀ (50 µM); (G-I) amastigotes treated with 2xIC₅₀ (100 µM). (n) nucleus; (k) kinetoplast; (*) black autophagic vacuoles (#) parasitophore vacuole (>>) excretory vesicles of macrophages; Scale bars: (A-B,D,G-H) 2 µm; (C,E-F,I): 1 µm.

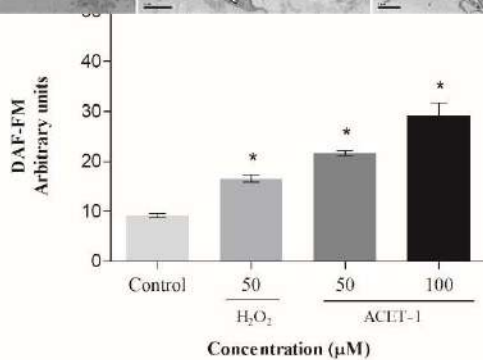


Figure 3. Evaluation RNS production in amastigotes of *L. amazonensis* treated with IC₅₀ (50 µM) and 2xIC₅₀ (100 µM) of ACET-1 for 24 h, using the fluorescent probe DAF-FM diacetate. (*) indicate significant differences in relation to the control group (p < 0.05).



Ultrastructural aspects of the aflagellarepimastigote form of *Trypanosoma caninum*

Kátia C. S. Nascimento¹, Roger M. M. Silva², Francisco O. R. de Oliveira Jr.³, Sandra M. O. Souza³, Suzana Côrte-Real³ and Juliana H. S. Barros^{1,*}

¹Laboratório de Biologia de Tripanosomatídeos, Instituto Oswaldo Cruz/Fundação Oswaldo Cruz, Rio de Janeiro, Brasil

²Plataforma de Microscopia Eletrônica Rudolf Barth, Instituto Oswaldo Cruz/Fundação Oswaldo Cruz, Rio de Janeiro, Brasil

³Laboratório de Biologia Estrutural, Instituto Oswaldo Cruz/Fundação Oswaldo Cruz, Rio de Janeiro, Brasil

*juliana.barros@ioc.fiocruz.br

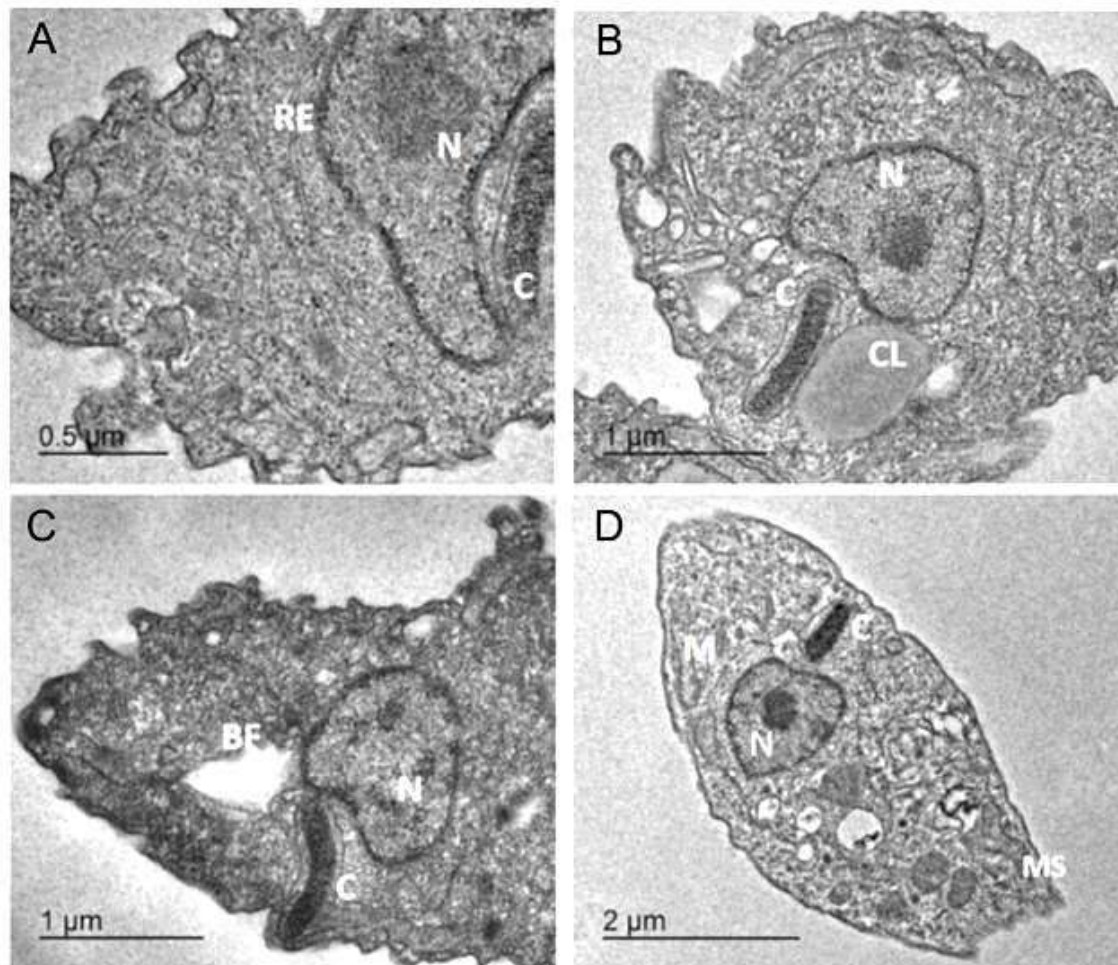
Trypanosoma caninum is a parasite described in the natural infection of dogs and has been isolated exclusively from the healthy skin of these animals. *T. caninum* presents in axenic cultivation, in addition to the classical evolutionary forms, the aflagellar epimastigote form. In order to clarify morphological aspects of this atypical epimastigote form, the objective of this work was to know the ultrastructural aspects of the aflagellar epimastigote form of *T. caninum*. Transmission Electron Microscopy of *T. caninum* was performed under axenic culture conditions of *T. caninum* (COLTRYP 735) after approximately 5 days of culturing in NNN/Schneider medium, at 27°C. To demonstrate the presence of lipid bodies, the parasitic of culture was fixed with 2.5% glutaraldehyde in 0.1 M imidazole buffer for 1 h and then washed with the same buffer and post-fixed with 2% OSO₄ diluted in 0.2 M imidazole buffer, for 30 min. With this methodology, it was possible to visualize lipid bodies and several structures common to trypanosomatids presented. These included (Fig. A) a well-structured nucleus (N), kinetoplast composed of compact genetic material (K), branched mitochondria distended by the parasite body and endoplasmic reticulum distributed throughout the cell body. It's important to emphasize on numerous lipid corpuscles (Fig. B) throughout the body. Lipid corpuscles were very prominent throughout the parasitic body as electron-dense structures of different sizes surrounded only by a membrane. This structure is related to the change in the evolutionary form, with the parasite's nutritional reserve, and may be involved in the modulation of host immune system during infection. These findings suggest that the epimastigote aflagellar evolutionary form may be involved in the biological cycle of *T. caninum*. Subpellicular microtubules (Fig. C) were absent in the flagellar pocket. In fig. D we observed subpellicular microtubules throughout the body *T. caninum*. But to know the role of these lipid corpuscles so abundant in *T. caninum* it will be necessary to carry out studies, among them the research of araquidonic acid present in these structures.

REFERÊNCIAS

[1] Barros, J.H.S. et al., Acta Tropica, 2014, 137: 147-151.

[2] Souza, Wandley de. III. Sociedade Brasileira de Microscopia e Microanálise.

Supported by :CAPES / IOC-FIOCRUZ



Transmission Electron Microscopy (TEM) of *Trypanosoma caninum* from axenic culture in the aflagellarepimastigote form (A-D).

(A): Electron micrograph showing the presence of endoplasmic reticulum (ER), nucleus (N) and kinetoplast (K) with kDNA preserved in the mitochondrial portion close to the nucleus;

(B): In this image, we can see a lipid corpuscle (CL) close to the nucleus (N) and the kinetoplast (K);

(C): In this image, it is possible to identify the flagellar pocket (BF) close to the kinetoplast (K) and nucleus (N);

(D): Electron micrograph showing an overview of the epimastigote form of *T. caninum*, with the characteristic organelles of this parasite: nucleus, k intramitochondrial DNA and subpellicular microtubules



Mitochondrial dynamics during human eosinophil development: an ultrastructural analysis

Cinthia Palazzi¹, Vitor H. Neves^{1*}, Kennedy Bonjour¹, Kássia K. Malta¹, Thiago P. Silva¹, Rossana C. N. Melo^{1,2**}

¹ Laboratory of Cell Biology, Federal University of Juiz de Fora, Department of Biology, Institute of Biological Sciences, Juiz de Fora, Minas Gerais, Brazil

² Department of Medicine, Beth Israel Deaconess Medical Center, Harvard Medical School, Boston, Massachusetts, USA

*vitor.neves97@gmail.com **rossana.melo@ufjf.edu.br

Eosinophils are immune cells involved in allergic and parasitic diseases. More recently, the eosinophil was recognized as a multifunctional granulocyte for its role in several processes such, immunoregulation, maintenance of homeostasis, development and regulation of organs and tissues and fibrosis [1]. Eosinophils pre-synthesize dozens of proteins and store them in secretory granules, termed specific granules, which exhibit unique morphology in terms of their ultrastructure. Several aspects of the secretory pathway of these cells are already elucidated in immune responses [2]. However, little is known about the population of mitochondria, their dynamics and structural organization during the eosinophil development and maturation [3]. In the present study, the ultrastructural features of mitochondria were evaluated during the maturation process of human eosinophils in cultures. Samples of immature and mature human eosinophils from cultures were harvested and processed by transmission electron microscopy (TEM). Different ultrastructural aspects were qualitatively and quantitatively evaluated in electron micrographs such as: area, number, circularity and mitochondria cristae pattern, as well as the occurrence of interaction with other organelles. Our results showed that during the maturation process of human eosinophils, their mitochondria population is drastically reduced. Both the number and the average mitochondrial area are reduced by 50% when immature cells were compared to mature cells. In addition, the maturation process of human eosinophils leads to a significant reduction of the cristae numbers ($P < 0.05$). Considering that the mitochondrial cristae are closely associated with the metabolism/functional activity of these organelles, these data demonstrate that the eosinophil mitochondria respond to the tissue microenvironment with morphological changes in their cristae. In addition, TEM quantitative analyses revealed a close interaction between mitochondria and other organelles, particularly with specific granules, both immature and mature. Altogether, our data indicate that eosinophil mitochondria play an important role in the granulogenesis process with structural changes and interactions with other organelles. Our findings reinforce the role of mitochondria as multifunctional organelles in cells of the immune system.

REFERENCES

- [1] Weller et al., *Nature Reviews Immunology*, 17.12 (2017) 746.
- [2] Melo et al., *Journal of Leukocyte Biology* 104.1 (2018) 85.
- [3] Ilmarinen et al., *International Journal of Molecular Sciences* 15.3 (2014) 3952
- [4] Dvorak, A.; Weller, P. *Human Eosinophils* 76 (2000) 1

ACKNOWLEDGEMENTS

This research was supported by CNPq (Brazil) and NIH (USA).

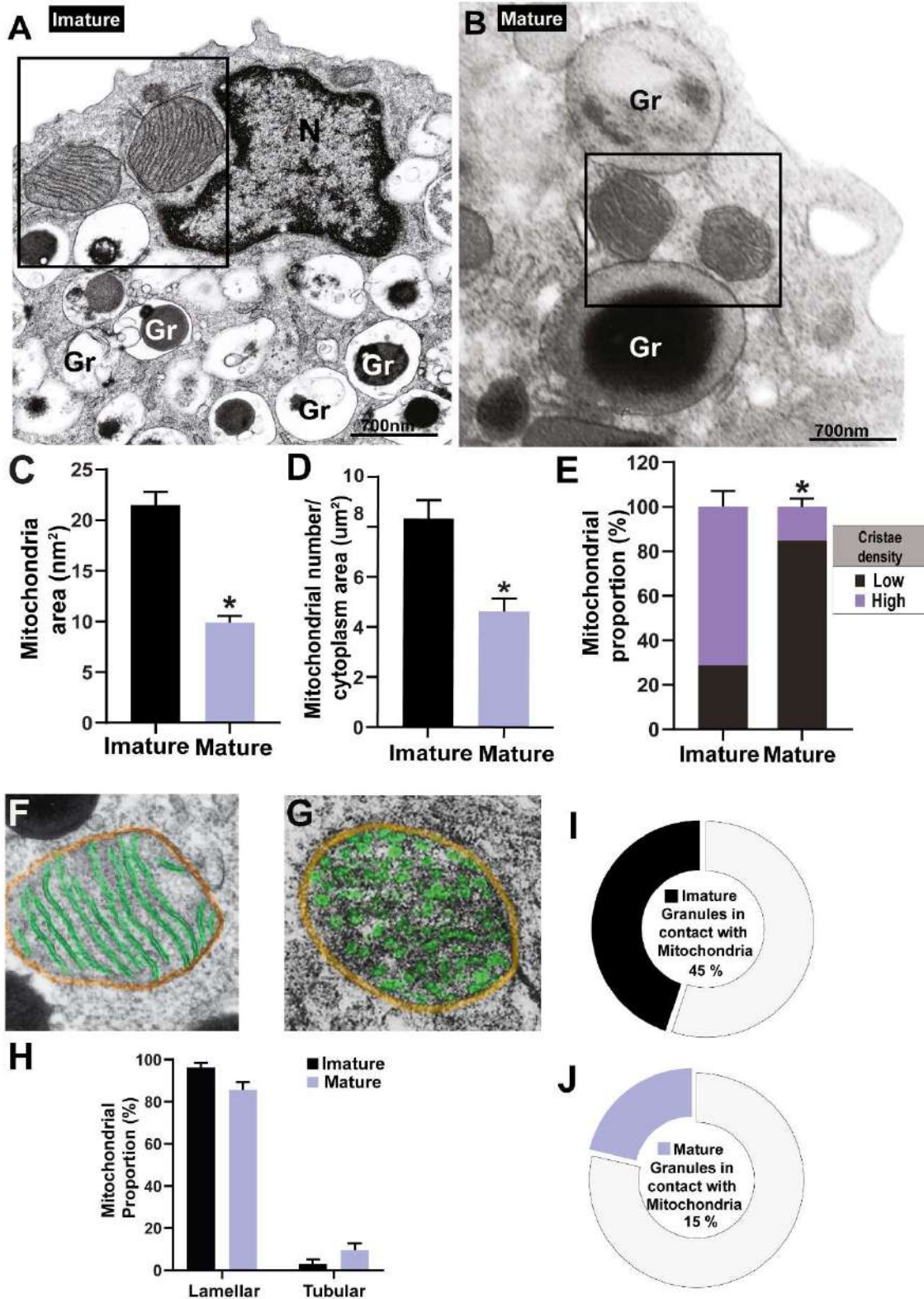


Figure 1: Mitochondrial ultrastructure aspects in mature and immature human eosinophils. (A-E) Mitochondria occupies a larger area of the cytoplasm in immature compared to mature eosinophils and are reduced in number and cristae density during cell maturation. (F-H) Interaction mitochondria-secretory granules (Gr) are observed mainly in immature cells. Cultures of human eosinophils were prepared as described (Dvorak, 2000).



ArtScience applied in microscopy: integration for production a new perspective in parasitology results

Vitoria Meirelles^{1,2}; Eduardo José Lopes-Torres^{1*}

¹. Laboratório de Helminthologia Romero Lascasas Porto (LHRLP), FCM/UERJ, Rio de Janeiro/RJ. ². Escola Superior de Desenho Industrial (ESDI) -UERJ.
*eduardo.torres@uerj.br

Brown and Snelson et al., 2011 published the manifest ArtScience emphasizing that humanity depends on the connection between these areas that have become more and more distant from each other nowadays. Art and science integration results in complex reflections and accounts of life, both reflecting the advances, social changes and historical facts that build the collective memory of humanity, based mainly on virtual or physical images. This reflection is closely linked to our scientific and cultural repertoire, so it is natural that art presents itself as a form of communication, as well as science, highlighted when the microscopy results are explored. Emerging from the wealth of details, representations and interpretations are built on the basis of human life experimentation. Many artistic movements are inspired by the natural sciences, such as: bioart, biomorphism and the re-reading of famous paintings. The re-reading and biomorphism are based on the construction of new materials, in our case, inspired by microscopy results in association with famous works of art. These new materials allow us to take a new look and have new interpretations, having as main screen, images obtained from biological samples and producing new biological forms. From this theory basis we developed this work by integrating ArtScience with microscopy. Our results were obtained by a graphic design student expertise associated with technological knowledge of the helminthology research group. We aim was to produce graphic material based on the interdisciplinarity of Graphic Design and Biological Sciences, focusing on microscopy applied in helminthology. The original images were obtained by Transmission Electron Microscopy (TEM) and Focused Ion Beam scanning electron microscopy (FIB) of bacillary glands of nematode *Trichuris muris*. These images were used as inspiration through its shapes and outlines. For produce our results, we used the “tools as shape” selection, “bitmap tracing” and “colorization of layers” in the free software Inkscape 1.0 and Gimp 2.10.20. The result of biomorphism was obtained using a TEM image (Fig. 1A) and the inspiration was based mainly on the Bioart, where organic and fluid figures were characterized. The creation process included the separation of shapes by its contrast and contours. Then, vectorized figures were drawn, with a contour line and solid colors being used to limit the different shapes (Fig. 1B-F). The rereading of a famous painting was performed from the macro view of a single image obtained by FIB (Fig. 2A). We refer to the painting “The Starry Night”, by Vincent van Gogh (1889). From it, we produced the Glandular Sky (Fig. 2B), through coloring the layers using the same painting's color palette to highlight the lamellar zone - the important structure of nematodes - like van Gogh's stars. Applying this approach to microscopy, the scientific results can be better promoted to the general public. This material can be explored either in parasitology study and in basic science, by integrating different areas of knowledge in education, enabling the use in face-to-face and online learning. Finally, these images can convert in alternative expressions in graphic productions, emphasizing the importance of technical and scientific knowledge and popularizing the ArtScience.

Reference: Adam Brown and Kenneth Snelson. Vol. 44, No. 3, p, 192, 2011. ISAST. Editorial. Acknowledgments: FAPERJ-JCNE, CNPq, FINEP and CENABIO.

Figure 1

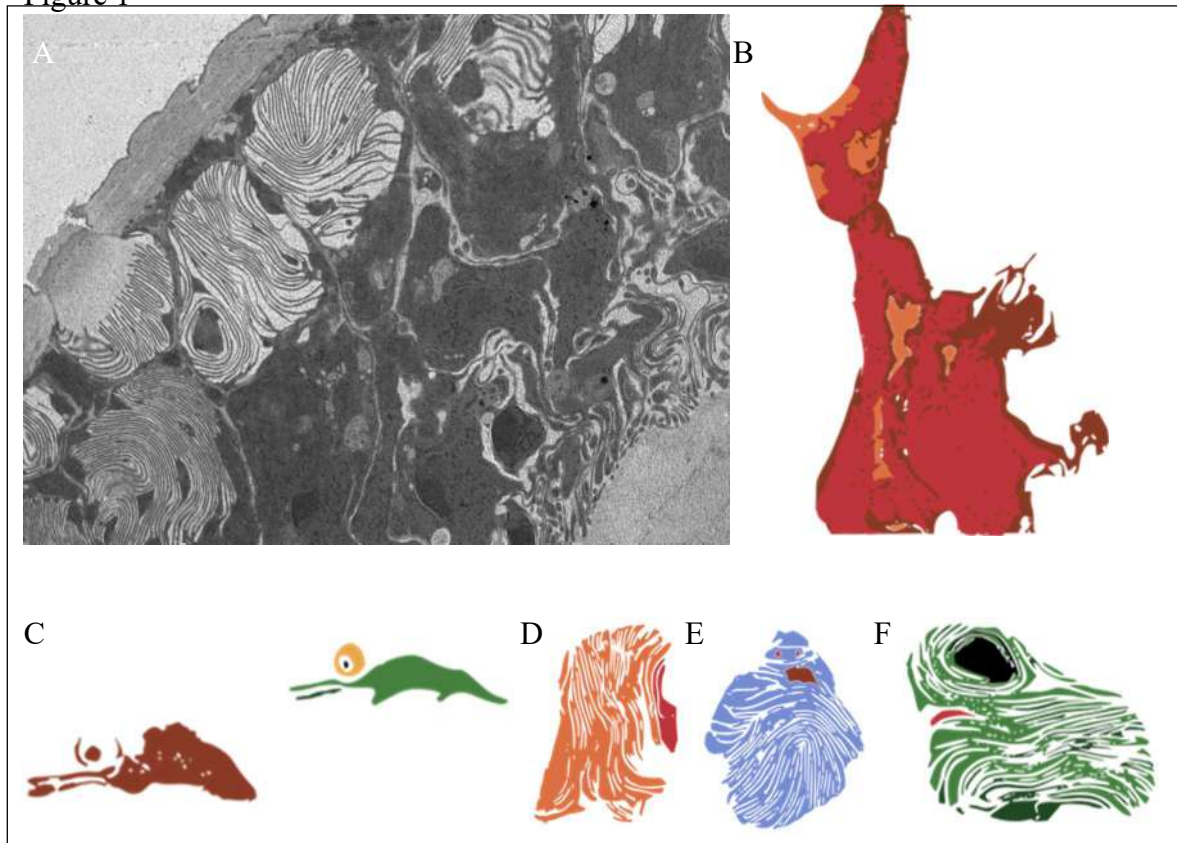


Figure 2

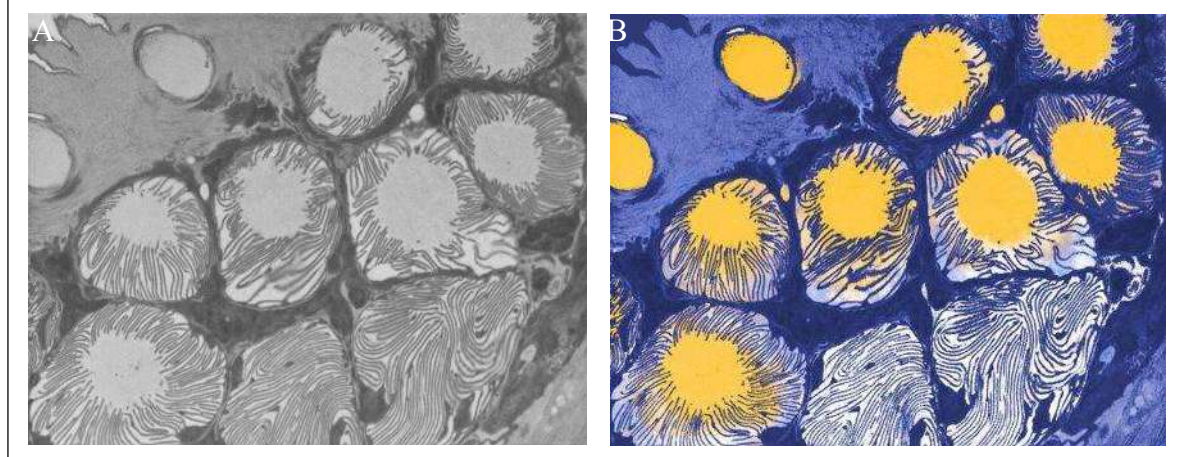


Figure 1: Biomorphism. A- TEM image of a thin section of *Trichuris muris* bacillary band showing bacillary glands; B-F: different shapes morphology inspired in contrast outlines of the original image. B- Fire entity; C- Horizons; D- Face profile; E- Blue mummy; F- Frog. Figure 2: Rereading of The Starry Night - Vincent van Gogh (1889). A- Image of the bacillary glands of *T. muris* obtained by FIB-SEM. B- Glandular Sky, highlighting the lamellar zone (blue) and the glandular chambers (yellow) of different bacillary glands.



Caveolin-1 induces mitochondrial plasticity and chances in inter-organelle communication of hepatic stellate cell.

Mariana Ilha^{1,2}, Leo Anderson Meira Martins^{1,4}, Francieli Rohden¹, Radovan Borojevic⁶, Vera Maria Treis Trindade^{1,3}, Guido Lenz⁵, Fátima C. R. Guma,^{1,3,7*}

¹PPGCB -Bioquímica, ICBS, UFRGS, Porto Alegre, RS, Brasil.

²Institute of Public Health and Clinical Nutrition, Department of Clinical Nutrition, UEF, Finland

³Departamento de Bioquímica, ICBS, UFRGS, Porto Alegre, RS, Brasil

⁴Departamento de Fisiologia, ICBS, UFRGS, Porto Alegre, RS, Brasil

⁵Departamento de Biofísica, IB, UFRGS, Porto Alegre, RS, Brasil

⁶Faculdade Arthur Sa Earp Neto - Faculdade de Medicina de Petrópolis, RJ, Brasil.

⁷Centro de Microscopia e Microanálise, CMM - UFRGS, Porto Alegre, RS, Brasil.

*fatima.guma@ufrgs.br

Caveolin-1 (Cav-1) is an integral membrane protein which may affect mitochondrial flexibility [1]. This work aimed to evaluate the influence of Cav-1 on regulating mitochondrial plasticity and inter-organelle communication in GRX cells [2], a murine model of the hepatic stellate cell (HSC). Previously, we showed that exogenous expression of Cav-1 was sufficient to induce HSC activation [3]. Here we report that GRX cells with exogenous expression or knockdown of Cav-1 changed mitochondrial morphometric parameters and the inter-organelle communication. The GRX cell line was established by [2]. The GRX^{EGFP-Cav1} cell line was established by using the pCav1EGFP [3] and short hairpin RNA (shRNA) lentiviral vectors pLKO.1-NEO-CMV-TurboGFPTMshCav1 were used to silence Cav-1[4]. Cell preparation for TEM analysis was performed as described by [5], ultrastructural imaging was obtained using a JEM 1200 EXII (Jeol, Japan) at an 80-kV acceleration voltage. Measurement of Mitochondrial Area (Å) and Shape Z, analysis of mitochondrial density (grayscale) was performed as described by [6]. The real distance of ER and outer mitochondrial membrane (OMM) were manually traced and quantified (images with 0.2µm - 75k) using the software ImageJ [7]. GRX^{EGFP-Cav1} cells presented a rounded shape mitochondrion, and clear but irregular crests (M*) (Fig.1A). Morphometric analysis showed an increased mitochondrial area in GRX^{EGFP-Cav1} cells and a decreased in GRX^{GFPshCav1} cells (Fig.1B). The Shape Z value revealed that GRX^{EGFP-Cav1} and GRX^{GFPshCav1} presented more rounded mitochondria than GRX cells (Fig. 1C). The grayscale (Fig. 1D) demonstrated no changes in mitochondrial crest density. Another ultrastructural difference between GRX^{EGFP-Cav1} and GRX^{GFPshCav1} cells was the ER morphology and its physical interaction/proximity with the outer mitochondrial membrane (OMM) (Fig 1E). ER in GRX^{EGFP-Cav1} appears to be larger in sheets shape, which may indicate organelle stress (Fig. 1A, yellow arrows), and the physical ER-OMM interaction is reduced (Fig. 1A, red double edge arrows). ER in GRX^{GFPshCav1} is arranged in reduced-stress thin tubules (Fig. 1A, yellow arrows), and the physical ER-OMM interaction seems to be higher (Figure 1A and 1E, red double edge arrows). Considering these results, we hypothesized that Cav-1 can regulate the mitochondrial dynamics, and inter-organelle communication in hepatic stellate cells.

References:

- [1] Fridolfsson, H.N., et al., FASEB J, 2014.
- [2] Borojevic, R., et al., In Vitro Cell Dev Biol, 1985. **21**(7): p. 382-90.
- [3] Ilha, M., et al., J Cell Biochem, 2019, 1-13.
- [4] Thome, M.P., et al., J Cell Sci, 2016. **129**(24): p. 4622-4632.
- [5] Meira Martins, L., et al., Cell Biochemistry and Biophysics, 2014: p. 1-16.
- [6] Lima, K.G., et al., Toxicol In Vitro, 2018. **48**: p. 11-25.
- [7] Sala-Vila, A., et al., Sci Rep, 2016. **6**: p. 27351.

Acknowledgments: The authors thank to CNPq and CMM-UFRGS core facility for transmission electron microscopy.

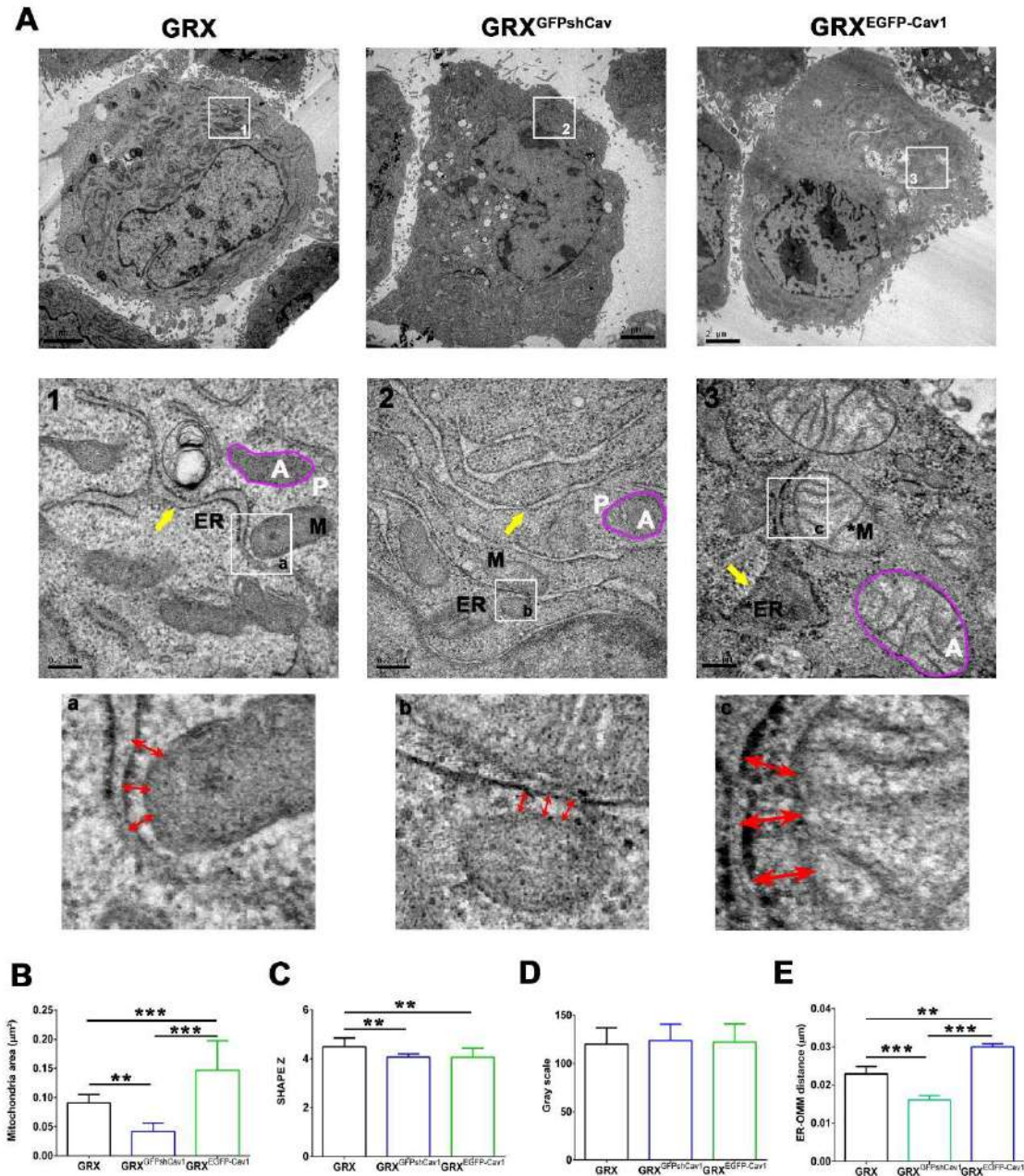


Figure 1: Caveolin-1 changes the mitochondrial morphology and morphometric, ER shape and ER-OMM distance (MAM). (A) Ultrastructural analysis revealed that both exogenous expression and knockdown of Cav-1 changed organelle morphology: mitochondria (M), dilated mitochondria (M*), Endoplasmic reticulum (ER), dilated Endoplasmic reticulum (ER*), white A: area, white P: Perimeter. Red double edge arrows represent the distance between the outer mitochondrion membrane (OMM) and ER membrane (MAM). Yellow arrows show the ER stress (GRX^{EGFP-Cav1}) or without stress (GRX, GRX^{GFPshCav1}). (B) The mitochondrial area in μm^2 . (C) Shape Z coefficient (Shape $Z = P / \sqrt{\hat{A}}$, where P is the perimeter, and \hat{A} is the area). (D) Grayscale representing mitochondrial density. (E) ER-OMM distance in μm by measuring the double edge red



arrows. Data was measured by ImageJ and represent the mean \pm SD from at least fifteen images (n=3 experiments, ** $P < 0.01$ and *** $P < 0.001$ such as indicated by one-way ANOVA followed Bonferroni's post-test.



The Intravacuolar Network of *Cyrtia Lignieresii*-Infected Erythrocytes

Maíra Turiel-Silva ^{1,3*}, Brenda Fachetti ^{1,3}, Camila Wendt ⁴, Edilene da Silva ², Ana Paula Drummond ³, Wanderley de Souza ⁴, Kildare Miranda ⁴, José Diniz ^{3*}

¹ Universidade do Estado do Pará, Departamento de Morfologia e Ciências Fisiológicas, Centro de Ciências Biológicas e da Saúde, Marabá, Brasil;

² Universidade Federal do Pará, Instituto de Ciências Biológicas, Belém, Brasil;

³ Instituto Evandro Chagas, Seção de Hepatologia, Laboratório de Microscopia Eletrônica, Belém, Brasil.

⁴ Universidade Federal do Rio de Janeiro, Instituto de Biofísica Carlos Chagas Filho and Centro Nacional de Biologia Estrutural e Bioimagem, Rio de Janeiro, Brasil;

*mairaturiel@uepa.br

Like many apicomplexan parasites, including *Plasmodium* and *Toxoplasma*, *Cyrtia lignieresii* resides intracellularly, within a specialized compartment named the parasitophorous vacuole (PV) [1], that provides a safe and metabolically active intracellular compartment. The current understanding of the structure of *C. lignieresii* shows that it presents the same characteristics organelles of the phylum apicomplexa [2,3] as well as unique structures found in the course of infection, as is the case of a large number of spherical bodies in the intravacuolar space. In this work, we analyzed *C. lignieresii*-infected red blood cells (iRBCs) by transmission electron microscopy tomographic techniques (TEM/STEM tomography), in order to better understand such structures that seem to have a functional role in the parasite-host interaction. Analysis of *C. lignieresii* iRBC revealed an intravacuolar membranous network (IVN) organized throughout the matrix of the PV. Three distinct structures were observed and characterized: (1) Small vesicles, (2) Multilamellar vesicles and (3) large vesicles containing nanovesicles. The small vesicles are abundant, round-shaped or tubular, measuring on average 90 nm. Three-dimensional reconstruction revealed that the small vesicles seen in profiles are interconnected, forming an IVN. Multilamellar vesicles are electron lucent and exhibit a round-shaped, contain an amorphous content and resemble a myelin structure. The average length of such structures was approx. 580 nm and they seem preferentially located between the small membranous tubules. The large vesicles are oval-shaped, present an average length of 453 nm and, in some cases, it is possible to observe a particulate material within it, very similar to what has been seen in the PV matrix. Moreover, it is possible to observe the presence of nanovesicles inside larger vesicles. Altogether, these results provide evidence for the assembly of an intravacuolar network in the PV in a similar fashion to what has been described in other apicomplexan-infected cells. Whether or not they correspond to functional and structural correlates of known intravacuolar networks is under investigation by our group.

REFERÊNCIAS

[1] A. Bittame et al., Biochemical and Biophysical Research Communications, 459(1), 107–112, (2015).

[2] R. Lainson, R. Parasitological topics. London, Canning EU ed, pp 150–158, (1981)

[3] J.A. Diniz et al., Parasitology Research, 88(7), 593–597, (2002).

This work was supported by IEC, UEPA, CNPq, FAPERJ e FINEP.

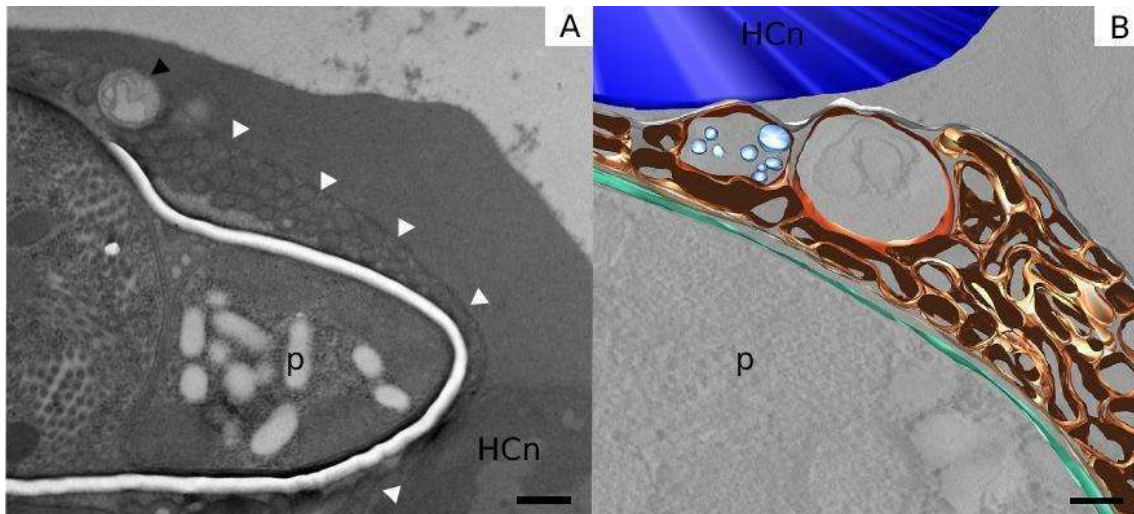


Figure 1: Membranous structures are observed within the parasitophorous vacuole (intravacuolar space), in the cytoplasm of erythrocytes infected with *C. lignieresii*. (A) Image of ultrathin section obtained by TEM revealed small vesicles (white arrowheads) and multilamellar vesicles (black arrowhead) in the intravacuolar space. (B) 3D reconstructions revealed connections between the small vesicles, where they appear as a fully interconnected intravacuolar network (IVN). p: parasite; HCn: Host cell nucleus; Blue: HCn, Light blue: nanovesicles inside a large vesicle; orange: multilamellar vesicle; gold: IVN. Scale bar: 500 nm.



Microbiome Analysis Of The Midgut From Female Adult *Toxorhynchites theobaldi* (Culicidae: Diptera)

Renata C. Barbosa^{1*}, Raquel S. M. Godoy², Juliana S. Silva³, Gustavo F. Martins¹

¹ Departamento de Biologia Geral, Universidade Federal de Viçosa, Minas Gerais, Brazil

² Fundação Oswaldo Cruz, Instituto René Rachou, Fiocruz, Belo Horizonte, Minas Gerais, Brazil

³ Departamento de Microbiologia, Universidade Federal de Viçosa, Minas Gerais, Brazil

*renatabarbose@ufv.br

The mosquitoes are subjected to a wide variety of interactions with environments microorganism in adult stages, including bacteria and fungi. The mosquito non-hematophagous *Tx. theobaldi* feeding nectar, bacteria and fungi often are presents in a flowers [1]. The oral microbiota can be colonized into the organs and tissue including the midgut (the lumen and epithelium). We dissected midgut (n=5) of adult females, aged days 7-14, in following it were incubated in BacLight Green kit (Cat. no. B-35000, Thermo Fisher) at room temperature and scanned using Confocal Laser Scanning Microscope (CLSM) Zeiss 510 Meta at 40x-100x magnification. We examined only the midgut microbiome, which serves as the first barrier to infection, to determine the abundance and diversity of the microbiota. Our results demonstrated the presence of predominantly rod-shaped bacteria throughout the midgut. Midgut bacterial diversity also was assessed by examining the 16S rRNA gene and were amplified by primers PCR, 515F/806R, which amplify the V4 hypervariable region and sequenced on the Illumina MiSeq platform. A total of 127 bacterial genera were identified in the midgut females *Tx. theobaldi*, the most predominant include *Acinetobacter*, *Streptococcus*, *Pseudomonas*, *Asaia*, *Mitochondria*_ge, *Corynebacterium*, *Lactobacillus*, *Sphingomonas*, *Burkholderia-Caballeronia-Paraburkholderia* and *Wolbachia*. In general, bacterial abundance in midgut females of *Tx. toxorhynchites* differed from vector mosquitoes, with the exception of the four genus *Asaia*, *Pseudomonas*, *Staphylococcus* and *Wolbachia* [2,3]. The genus *Wolbachia* can alter pathogen transmission and reduce female fecundity in the hosts mosquitos [4]. In general, we found several bacterial genera in ours samples and, in a very low number, confirming what was observed in CLSM. We conclude that the difference in the composition of the midgut microbiota of adult *Tx. theobaldi* and the hematophagous mosquitoes are due to eating habits.

We thank the Brazilian Federal Agency CAPES (Coordenação de Aperfeiçoamento de Pessoal de Nível Superior) for the financial support to RCB, and the Núcleo de Microscopia e Microanálise (NMM, UFV) for letting us use the confocal microscope.

REFERENCES

1.CANSADO-UTRILLA, Cintia et al. The microbiome and mosquito vectorial capacity: rich potential for discovery and translation. **Microbiome**, v. 9, n. 1, p. 1-11, 2021.

2. COATSWORTH, Heather et al. The composition of midgut bacteria in *Aedes aegypti* (Diptera: Culicidae) that are naturally susceptible or refractory to dengue viruses. **Journal of Insect Science**, v. 18, n. 6, p. 12, 2018.
3. NEPI, Massimo et al. Amino acids and protein profile in floral nectar: much more than a simple reward. **Flora-Morphology, Distribution, Functional Ecology of Plants**, v. 207, n. 7, p. 475-481, 2012.
4. RAZYGRAEV, A. V. A Comparative Study of Catalase Activity in *Culiseta annulata* (Schrank) and *Culex pipiens* L.(Diptera, Culicidae). **Entomological Review**, v. 100, n. 2, p. 162-169, 2020.

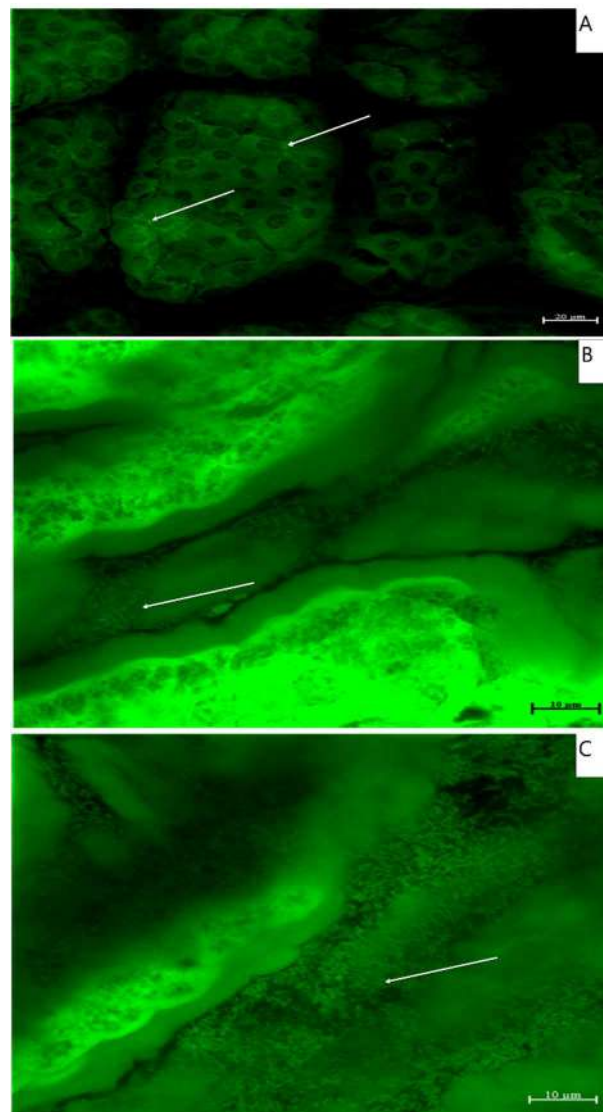


Figure 1 - Immunofluorescence confocal micrographs in dissected midgut of bacterias (rod-shaped) of the *Toxorhynchites theobaldi* (Diptera: Culicidae) using BacLight Green kit (Thermo Fisher). Sections of the female's midgut epithelium *Tx. theobaldi* adult visualized by confocal laser scanning microscope with 40x (**A**) and 100x (**B** and **C**) objectives. The white arrows show the bacterias associated with the midgut lumen.



Histopathology and ultrastructural analyses reveal neurodegeneration and inflammatory process during optic nerve lesion induced by Zika virus infection

Felipe E. O. Rocha¹; Jenniffer R. Martins¹; Matheus R. Gonçalves²; Vivian V. Costa²; Felipe F. Dias^{1*}

¹Laboratory of Cytology, Department of Biological Sciences, State University of Minas Gerais, Ibirité, MG, Brazil.

²Center of Research and Drug Development, Department of Morphology, Institute of Biological Sciences, Federal University of Minas Gerais, Belo Horizonte, MG, Brazil.

*felipe.dias@uemg.br

Zika is a human arbovirose transmitted by *Aedes* genus (*A. Aegypti* and *A. Albopictus*) flies, which triggers severe complications of the Zika congenitus syndrome (ZCS), well known by the microcephaly [1]. Although classically distributed over Africa and SouthEast Asia, brazilian epidemic breakthrough of 2015 comproved virus transmission by gestants placenta, leading to microcephaly and other permanent brain damages to newborn [2]. This condition can be acompanied by other pathologic symptons including hydrocephaly, spinal disraphism, arthrogryposis and oftalmic malformations [3]. Follow up studies of children between 19 to 24 months age during the brazilian epidemy, showed children without microcephaly having disphagia and, motor, auditive and visual commitments [4]. Mild to severe visual deficiencies reached 41.7% of children that didn't developed microcephaly [5] which is corroborated by the increasing of intraocular pression and virus presence in the optic nerve (ON) during experimental models infection [6]. Lesion of the ON, which is composed by retinal ganglionar cells axons, can interrupt the transmission of visual information to the cerebral cortex superior visual centers, leading to variable and progressive levels of visual bleeding [7]. In ON lesions, cells may play effector functions by secreting neurotoxic factors, leading to neurodegeneration of retinal and ON regions by different cell death processes, that orchestrate key events of the ZIKV immunopathogenesis by releasing of Th1 pro-inflammatory cytokines (TNF- α , IFN- γ , IL-1 β , IL-6, IL-10). Despite the knowledge of oftalmic alterations to ZIKV infection, little is known about their immunopathogenesis, mainly the optic nerve neurodegeneration intracellular ways. Here, we used a combination of microscopy techniques to study the development and spreading of the optic nerve lesion induced by ZIKV infection. Two experimental models were infected by ZIKV clinical isolate (HS-2015-BA-01): the first, pregnant C57BL/6 mice were intravenous (i.v.) infected by 1×10^6 /mL ZIKV PFU [N = 6-8; 5.5 days post-coitum (dpc)], with ou without pan-flavivirus antibodies (hibridoma D1.4G2.4.15) and the whole optic nerve of the offspring (12 weeks) were processed to histology, immunohistochemistry and transmission electron microscopy. Alternatively, a second model A129 mice (deficient for IFN-1 alfa/beta receptor) and, high susceptible to ZIKV infection, were used (18). Histopathology and

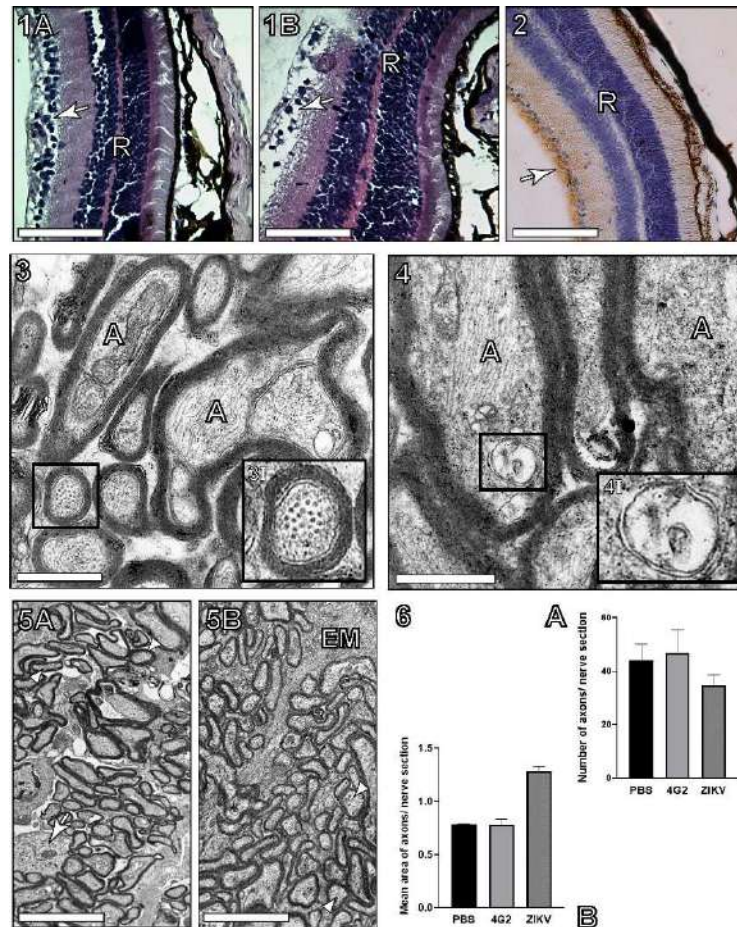


ultrastructural analyses were conducted to evaluate the extension of the lesion and cell neurodegeneration. Histopathology of infected A129 mice eyes showed areas with apoptosis of retinal ganglionar cells compared with non-infected littermates (Fig. 1A, B). To corroborate histopathological results, retinal areas, at the beginning of optic nerve bundle, were immunolabeled by Iba-1 to identify tissue areas indicative of microgliosis (Fig. 2). TEM of the optic nerve demonstrated irregular axons, some of them, with disassembled mitochondria and neurofilaments as autophagosomes formation (Fig. 3, 4). Ultrastructural analyses of ON from infected animals showed areas with reduced number of axons (Fig. 5, 6A) and increasing in size (Fig. 6B), compared with control and 4G2 animals. Our previous study illustrates, for the first time, the basic cellular mechanisms involved in the optical immunopathogenesis of ZIKV infection. However, the impact of these cell death processes and cellular ultrastructural alterations to the disease development awaits further investigation.

References:

- [1] Alvarado *et al.* (2017). *Arch Pathol Lab Med* 141: 26-32.
- [2] Brasil *et al.* (2016); *N Engl J Med* 375: 2321-2334.
- [3] Xavier-Neto *et al.* (2017). *PLoS Negl Trp Dis* 11(2): e0005363.
- [4] Faiçal *et al.* (2019). *BMJ Paediatr Open* 3(1):e000486.
- [5] Freitas *et al.* (2016). *JAMA Ophthalmol* 134(5):529-535.
- [6] Costa e Del Sarto *et al.* (2017). *mBio* 8:e00350-17.
- [7] Selhorst, J.; Chen, Y. (2009). *Seminars Neurol* 29 (01): 029–035.

This research was supported by FAPEMIG, CNPq (Brazil) and Institutional Research Support Program (PAPq) of Minas Gerais State University (UEMG).



Histopathological and ultrastructural analyses of the optic nerve from ZIKV infected experimental models. Fig. 1: Eye tissue from non-infected (A) and ZIKV-infected mice (B) showing retinal (R) empty areas (arrows), indicative of retinal ganglion cell (RGC) death processes. Fig. 2: Iba-1 immunohistochemistry for RGC at the beginning of optic nerve indicate tissue areas of microgliosis. Fig. 3: Ultrastructure of the non-infected optic nerve (ON) identify regular aspect of axons (A) with defined myelin sheath and visible neurofilaments (I) while infected ON showed irregular axons, with disassembled mitochondria and neurofilaments as autophagosomes formation (fig. 4). Ultrastructural analyses of ON from infected animals showing extracellular matrix areas with reduced number of anons (arrowheads) (Fig. 5, 6A) and increasing in size (Fig. 6B), compared with control and 4G2 animals. Arrows (5A): oligodendrocytes. Bars (1A, B, 2): 40 μ m, (3, 4): 500 nm; (3I, 4I): 250 nm; (5A, 5B): 5 μ m.



Cell infection by the Ilheus virus: unraveling the morphogenesis of a neglected arbovirus

Gabriela Cardoso Caldas^{1,2*}, Helver Gonçalves Dias³, Marcos Alexandre Nunes da Silva¹, Vinícius Tadeu Martins Guerra Campos⁴, Flavia Barreto dos Santos³, Alex Pauvolid-Corrêa^{5,6}, Ana Maria Bispo de Filippis⁴ and Debora Ferreira Barreto-Vieira¹

¹ Laboratório de Morfologia e Morfogênese Viral/Instituto Oswaldo Cruz, Rio de Janeiro - Brasil.

² Laboratório de Patologia/Instituto Oswaldo Cruz, Rio de Janeiro - Brasil.

³ Laboratório de Imunologia Viral/Instituto Oswaldo Cruz, Rio de Janeiro - Brasil.

⁴ Laboratório de Flavivírus/Instituto Oswaldo Cruz, Rio de Janeiro - Brasil.

⁵ Laboratório de Vírus Respiratórios e Sarampo/Instituto Oswaldo Cruz, Rio de Janeiro, Brasil

⁶ Department of Veterinary Integrative Biosciences/Texas A&M University, College Station, Texas, United States of America

*gabrielacardosocaldas@gmail.com

Ilheus virus (ILHV) belongs to the genus *Flavivirus* and has been isolated for the first time in 1944 in northeast Brazil. ILHV is maintained in nature through enzootic cycles of transmission involving birds and mosquitoes. Humans are accidental hosts and may present clinical infection ranging from subclinical to severe febrile disease [1]. In this context, the main objective of this study was to describe the general aspects of ILHV infection in cell culture, as well as its morphogenesis. CCL81 Vero cell cultures were inoculated with a multiplicity of infection of 0.01. After the incubation period, 199 Medium, supplemented with 2% fetal bovine serum and penicillin/streptomycin, was added, and the cells were cultured at 37°C in a 5% CO₂ atmosphere. Cytopathic effects were investigated at 24, 48 and 72 hours post-infection (h.p.i.) by inverted light microscopy. For ultrastructural analysis, the monolayer was trypsinized and quickly fixed in 2,5% glutaraldehyde buffered in 0.1M sodium cacodylate, post-fixed in osmium tetroxide, dehydrated in acetone and included in epoxy resin. Sections of 50-70 nm were stained with uranyl acetate and lead citrate and analyzed by transmission electron microscope HITACHI HT7800. **Uninfected cells were used as a negative control (mock group).** No changes were observed in the mock group. Infected cells showed an increase in cytoplasmic vacuoles at 24 h.p.i, presence of few syncytia at 48 h.p.i and considerable cell death at 72 h.p.i. The predominant ultrastructural changes associated with ILHV infection included: ribosome thickening, loss of mitochondrial integrity, formation of syncytium, disturbance in the chromatin distribution pattern, presence of pycnotic nuclei and significant thickening of the rough endoplasmic reticulum (RER) and nuclear membrane. Spherical and enveloped viral particles, approximately 30 nm in diameter, as well as nucleocapsids, were observed inside RER cisterns. These cisterns were surrounded by countless mitochondria and were associated with vesicular compartments (approximately 50 nm in diameter). The initial aspects of ILHV morphogenesis are similar to some already described in other flaviviruses, such as dengue and zika viruses [2,3]. However, some alterations appear to be more intense. In addition, the presence of enveloped particles inside the RER in association with vesicular compartments and mitochondria, suggests that viral assembly occurs in this region. To



our knowledge, this is the first preliminary study to show the dynamics of viral replication and the ultrastructural cellular alterations caused by ILHV.

- [1] L.A.M. Reis & J.P.N. Neto, Brazilian Journal of Development. 4 (2021) 37675-37695
- [2] O.M. Barth, Fundação Oswaldo Cruz. Instituto Oswaldo Cruz. (2000). 126p.
- [3] D.F. Barreto-Vieira *et al.*, PloS One. 9 (2017) e0184397.

This research was supported by CNPq (Brazil) and Oswaldo Cruz Institute.

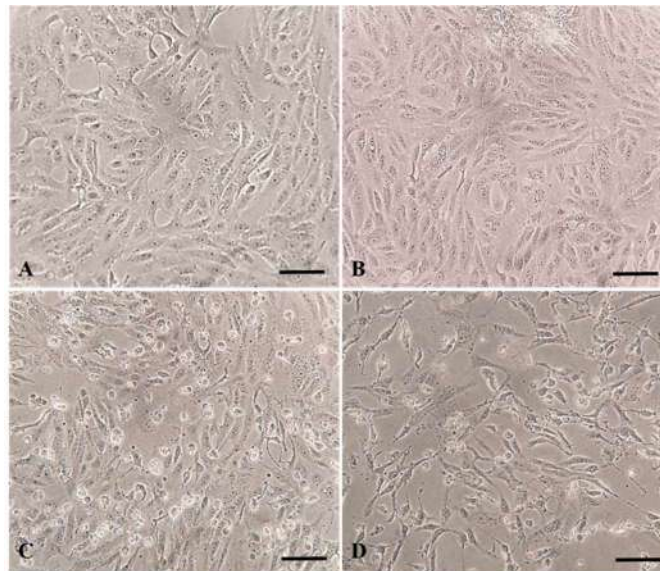


Figure 1. Kinetics of ILHV infection in Vero CCL81 cells (mock [A], 24 [B], 48 [C] and 72 h.p.i [D]) showing the gradual loss of monolayer integrity and cell morphology. Bars = 50 μ m.

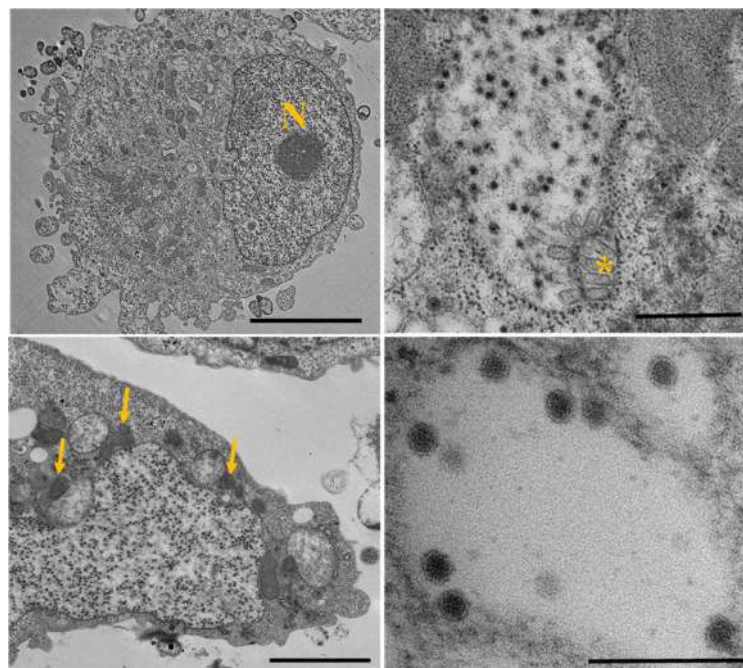


Figure 2. [A] Uninfected Vero cell at 72h of culture. No cellular ultrastructural alterations were observed. Bar = 5 μ m. Vero cells infected with ILHV analyzed by transmission electron microscopy (TEM). [B] RER cistern containing viral particles and presence of vesicular compartments (*). Bar = 500 nm. [C] Thickening of the RER cistern containing numerous nucleocapsids and enveloped particles, surrounded by several mitochondria (arrow). Bar = 2 μ m. [D] Presence of enveloped viral particles inside the RER cistern. Bar = 200nm.



Study of SARS-CoV-2 morphogenesis and interaction with the cell by transmission and high resolution scanning electron microscopy

Lucio Ayres Caldas^{1,2*}, Fabiana Avila Carneiro^{1,2}, Luiza Mendonça Higa³, Fábio Luis Monteiro³, Gustavo Peixoto da Silva⁴, Luciana Jesus da Costa⁴, Ingrid Augusto¹, Edison Luiz Durigon⁵, Kildare Miranda^{1,6}, Amilcar Tanuri³, Wandelely de Souza^{1,6}

¹ Laboratório de Ultraestrutura Celular Hertha Meyer, Instituto de Biofísica Carlos Chagas Filho / Universidade Federal do Rio de Janeiro, Brazil.

² Núcleo Multidisciplinar de Pesquisa em Biologia (NUMPEX), Campus Duque de Caxias Geraldo Cidade / Universidade Federal do Rio de Janeiro, Duque de Caxias, Brazil.

³ Departamento de Genética, Instituto de Biologia / Universidade Federal do Rio de Janeiro, Brazil.

⁴ Departamento de Virologia, Instituto de Microbiologia Paulo de Góes, Universidade Federal do Rio de Janeiro, Brazil.

⁵ Instituto de Ciências Biomédicas, Universidade de São Paulo, São Paulo, Brazil.

⁶ Instituto Nacional de Ciência e Tecnologia de Biologia Estrutural e Bioimagem, Rio de Janeiro, Brazil.

*lucio@biof.ufrj.br

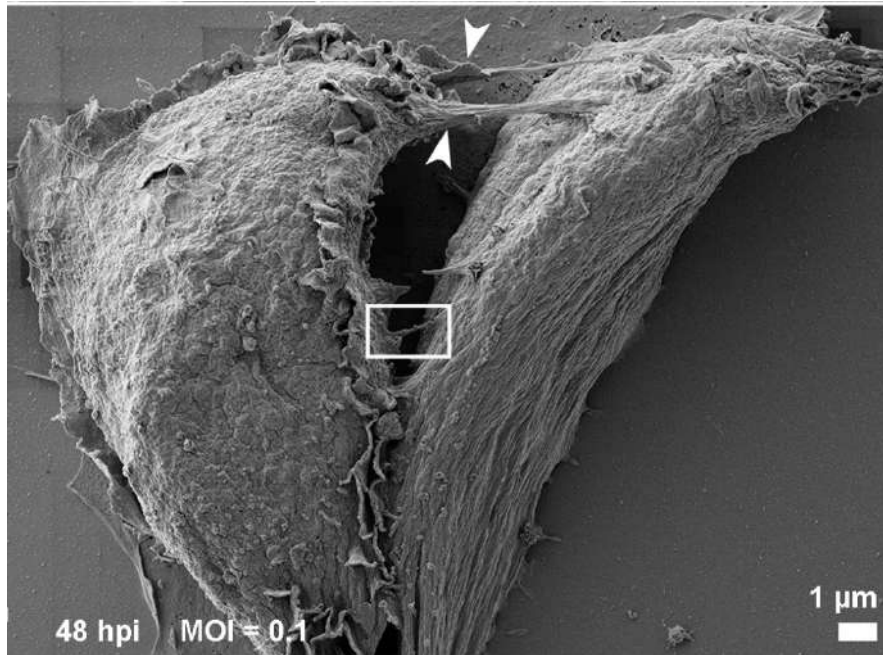
SARS-CoV-2 is a single strand RNA virus, belonging to the *betacoronavirus* genus, within the *Coronaviridae* family. This pathogen, transmitted mainly through droplets and aerosol, is responsible for the COVID-19 [1]. As occur to many of the positive sensed RNA viruses, its cellular cycle involves a robust membranar rearrangement in the cytosol of the infected cells. This structure delimits and protects the locus of replication and morphogenesis of SARS-CoV-2 [2]. In the present study, we approached the main steps of SARS-CoV-2 morphogenesis and interaction with the cell by transmission and high resolution scanning electron microscopy (HR-SEM). The sites of viral replication, and assembly were documented in Vero cells at 24, 48 and 72 hours post-infection by using both electron microscopy modes. In addition, the interactions of this virus with the cell surface, as well as the viral factory and the details of its main components, were also investigated with the aim of HR-SEM, after the removal of infected cells plasma membrane. This allowed the visualisation of unprecedented features of the interactions between this virus and the cell, such as the so-called “virus surfing”, which enables a relatively safe cell-to-cell viral propagation in the tissue [3]. On the other hand, the electron-tomography of these samples showed, for the first time, the presence of SARS-CoV-2 particles in the space between the inner and the outer nuclear envelope. The data obtained in this work contribute to the knowledge of the route of SARS-CoV-2 within the infected cell and the cell biology of their interactions [4].

[1] Zhu, N. et al., N. Engl. J. Med. 382, 727–733 (2020).

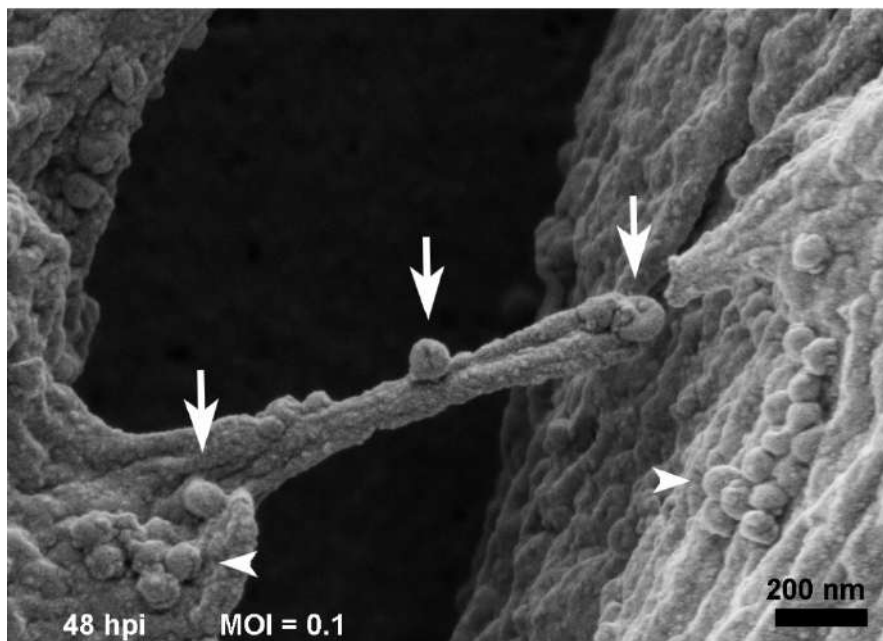
[2] Fehr, A. R. & Perlman, S., Methods Mol. Biol. 1282, 1–23 (2015).

[3] Lehmann, M. J. et al., J Cell Biol 170, 317–325 (2005).

[4] This research was supported by CNPq and FINEP (Brazil).



Communications between two infected cells are indicated with arrowheads. One of the bridges between the cells was depicted in the rectangle. Bar:1 μ m.



A higher magnification of this area showed above displays viral particles (arrows) on their surface. Aggregates of SARS-CoV-2 particles (arrowheads) were also observed on the surface of both cells. MOI = 0.1; Bar: 200 nm.



The Use of 2-hydroxyethyl methacrylate Resin for Histopathology Analysis in the Ocular Toxoplasmosis Model

Carlla Assis Araujo-Silva^{1,2}, Milena Ribeiro Peclat de Araujo^{1,2}, Wanderley de Souza^{1,2},
Rossiane Claudia Vommaro^{*1,2}

1. Laboratório de Ultraestrutura Celular Hertha Meyer, Instituto de Biofísica Carlos Chagas Filho – Universidade Federal do Rio de Janeiro 2. Instituto Nacional de Ciência e Tecnologia em Biologia Estrutural e Bioimagens, UFRJ, Brasil

* vommaro@biof.ufrj.br

The resin 2-hydroxyethyl methacrylate, also called glycol methacrylate (GMA), is widely used for histopathological analysis in light microscopy, because of its miscibility to water and easy handling [1]. Besides, the use of paraffin in tissue processing for microscopy presents some disadvantages, as the shrinkage of tissue structure [2]. In this work we used the Kulzer kit - Technovit® 7100 (GMA), with a 3 hour-fast polymerization protocol at room temperature to process the entire eyes of infected mice with *Toxoplasma gondii*. It was possible to obtain thin slices of the samples for histopathological investigation with particularly good resolution. The mice (C57bl/6 – male 8 weeks) were infected (strain RH) by intraperitoneal injection and euthanized after 5, 10, 18 or 20 days of infection. Both eyes were enucleated and fixed for 24 hours in a solution containing 4% formaldehyde (EMS) and 2% glutaraldehyde (EMS) [3] in 0.1M phosphate buffer, pH 7.2 at 4°C. First, a small cut was made in the cornea region of each infected eye, using a binocular stereoscope (Zeiss, SteREO Discovery.V8). The samples were dehydrated in a crescent series of ethanol 30-100% v:v, incubated in a 1:1 GMA ethanol solution, followed by overnight incubation in pure resin. The samples were embedded in GMA in an improvised mold as seen in Figure 1A to enable tissue orientation. The sections were made with a glass knife in a Reichert-Leica ultramicrotome (Fig. 1B). The sections were collected (Fig. 1C) with tweezers number 3 and placed in a drop of ultrapure water on a slide (Knittel) coated with 0.01% poly-L (Sigma) (Fig. 1D). Afterwards, the slides were placed on a heating plate at 30°C for 5 minutes and the sections were then stained in a 8:2 Giemsa:water solution (Merck), for 1h. The dehydration was carried out with 100% acetone followed by acetone:xylol gradient (50-100%), ending with 100% xylol. Finally, the slides were mounted with Entellan® (Merck). Images were obtained using the Axiobserver Z.1 microscope equipped with an Axiocam HRC (ZEISS) camera. Semi-thin sections processed with GMA and submitted to single-step coloration provided high quality preservation for eye tissue samples for light microscope (Fig. 1 I-IV). The use of GMA in tissue embedding maintained the morphological preservation of mice eye tissue and the semi-thin sections obtained with an ultramicrotome were of better quality (1 - 2.5 µm) than those of paraffin embedded samples obtained in conventional microtomes (thickness from 3 to 5 µm) as found elsewhere in literature. The experimental protocols for animal use were approved by the Institutional Ethics Committee for Animal Use (CEUA/UFRJ: 067/20) . Support agencies: CAPES, FAPERJ and CNPQ.

REFERENCES:

- [1] IJIMA H. et al., Okajimas Folia Anat. Jpn.. 69(1): 15-24, May, 1992.
[2] NAGATO Y. et al., Okajimas Folia Anat. Jpn., 66 (2-3): 145-152, August, 1989.

[3] VELDE J. et al., Histopathology, I, 319-330, April, 1977.

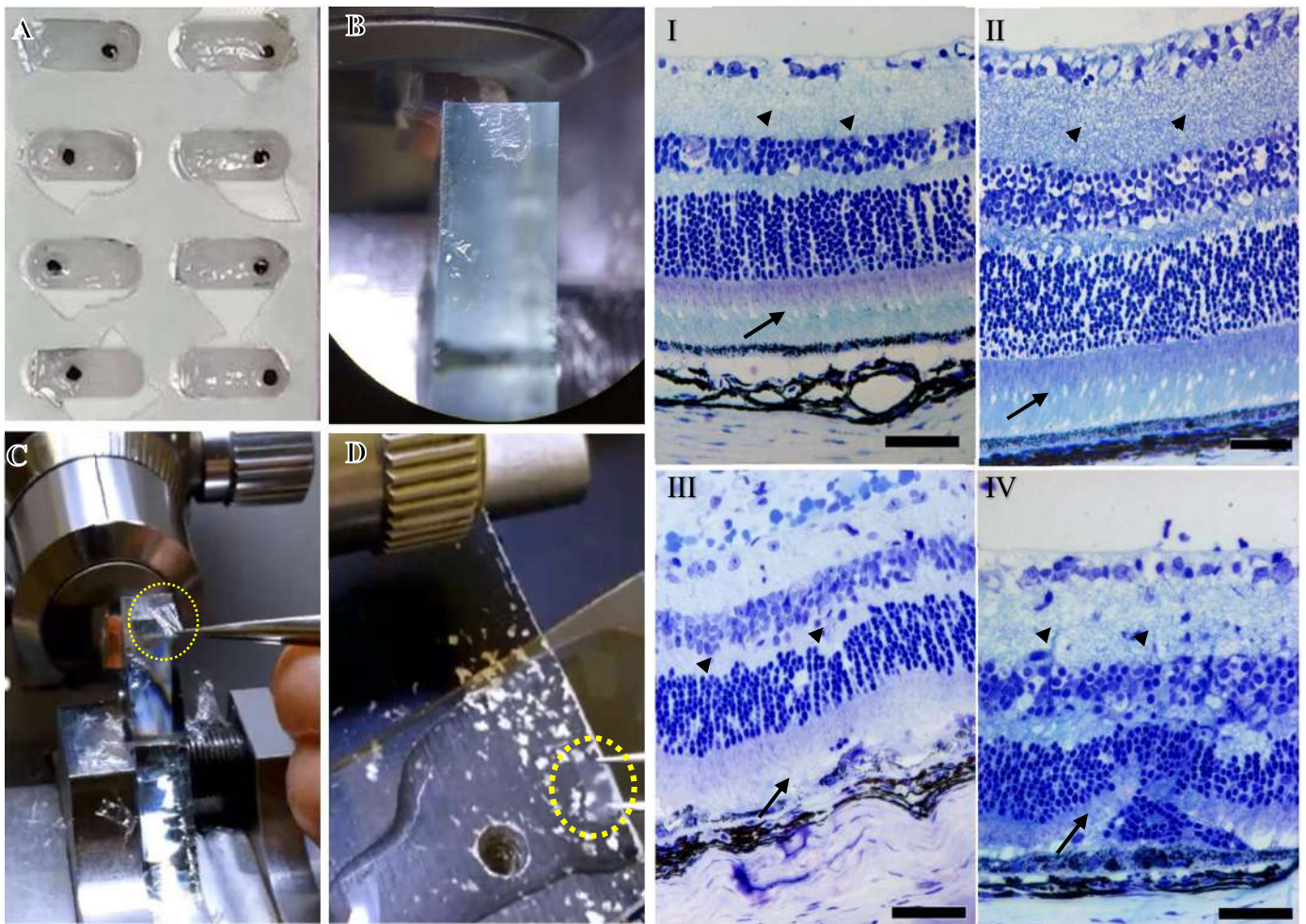


Figure 1 - (A) The eyes were oriented to obtain sagittal sections of the retina, (B) Quality of the edge of the glass knife with a tissue section (C) Proper tweezers were used to collect the sections (yellow circle), (D) The sections were collected and placed in a drop of ultrapure water on a slide (yellow circle). (I- IV) Light microscopy of mice retinas infected with *T. gondii*. (I) 5 days of infection (II) 10 days (III) 18 days and (IV) 20 days. The preservation of delicate structures such as the photoreceptor segments is clearly observed (black arrow in I). As the infection proceeded, the tissue degeneration could be followed (II - IV, black arrows). Cytoplasmic projections were well preserved (arrowheads in I - IV). Scale bar 50 μ m.



Optimization of Lipase Production Using Fungal Isolates from Oily Residues

Letícia Miranda Cesário^{1*}, Rafael Freitas Santos Pereira¹, Jairo Pinto de Oliveira¹

¹Federal University of Espírito Santo, Department of Biology, Vitória, Brazil

*leticiamirandacesario@gmail.com

Lipases are triacylglycerol hydrolases that catalyze hydrolysis, esterification, interesterification and transesterification reactions. These enzymes have been the target of various applications in industry and biotechnology, such as catalysts, detergent production, food, biofuels, wastewater treatment and others [1]. Microbial enzymes are preferable for large scale production due to ease of cultivation and extraction. Several studies have reported that lipases from filamentous fungi are predominantly extracellular and with high activity. However, there are several factors that interfere with enzyme production (pH, temperature, medium composition, agitation, aeration, inductor type and concentration, etc.), making control difficult and burdening the process. This work aimed to optimize the lipase production of four fungal isolates from oily residues (*Penicillium* sp., *Aspergillus niger*, *Aspergillus* sp. and *Aspergillus* sp.). These microorganisms were morphologically characterized by light and scanning electron microscopy. The optimal lipase production time curve was previously determined and the response variable used was the amount of total protein in the medium after cultivation by submerged fermentation. A complete factorial design 3² was performed, evaluating the temperatures (28°C, 32°C and 36°C) and soybean oil inducer concentration (2%, 6% and 10%). Each strain used reacted differently to the conditions tested, the *Aspergillus* sp. (F18) reached maximum lipase production, compared to others, under conditions of 32°C and 2% of oil with a yield of 11007 (µg. ML⁻¹). *Penicillium* sp. (F04) achieved better results at 36°C and 6% oil, for *Aspergillus niger* (F16) was at 36°C and 10% oil and *Aspergillus* sp. (F21) was 32 ° C and 2% oil. Das et al. (2016) optimizing the nutritional conditions of the submerged fermentation of *Aspergillus tamarii* found maximum production of lipases in medium supplemented with coconut oil (2.5%, v/v) approaching the result observed in the present study. The factorial planning used allowed the optimization of the production of fungal lipases from the variables studied.

REFERÊNCIAS

[1] K.E. Jaeger, P.H. Nielsen, Lipases for Biotechnology, Current Opinion in Biotechnology, 2002, p. 390-397.

AGRADECIMENTOS

UFES, MCTIC/CNPqN° 28/2018, FAPES N° 21/2018 e FAPES n° 001/2019.

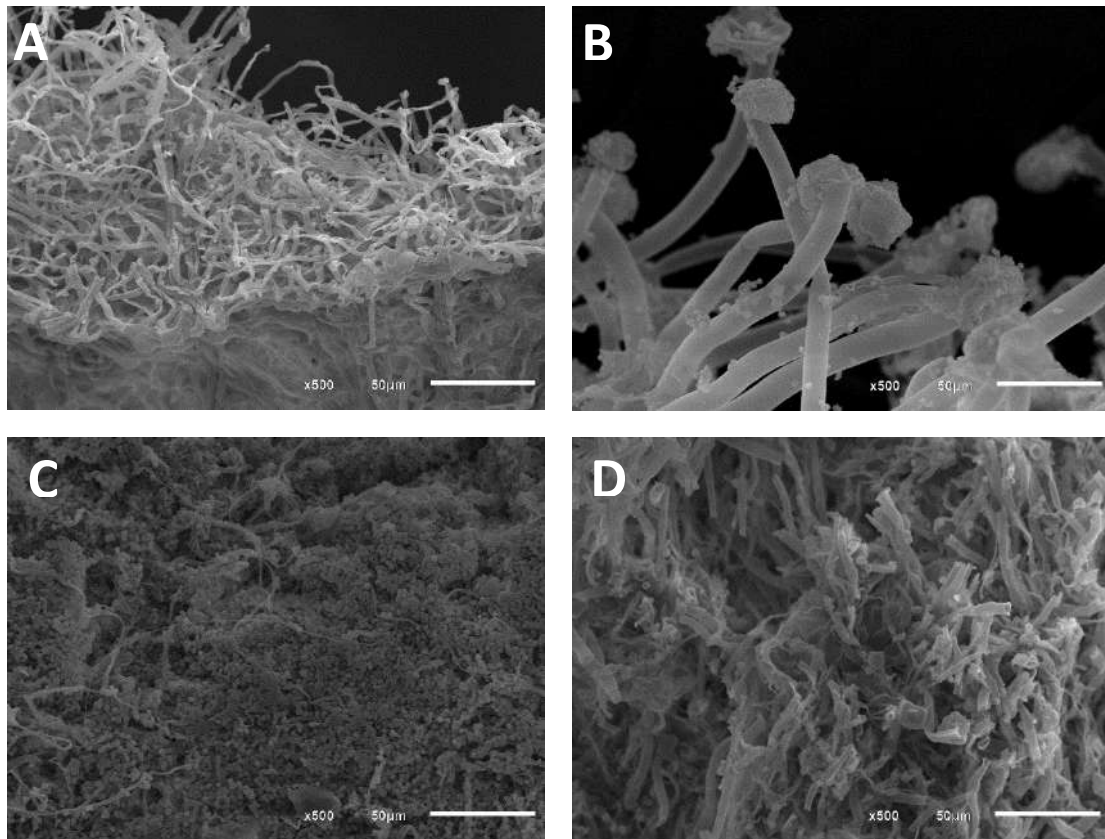


Figura 1. Scanning electron microscopy (SEM) images showing the filaments (hyphae) that form the conidia and spherical bodies (vegetative spores) in *Penicillium* sp. F04 (A), *Aspergillus niger* F16 (B), *Aspergillus* sp. F18 (C) and *Aspergillus* sp. F21 (D).

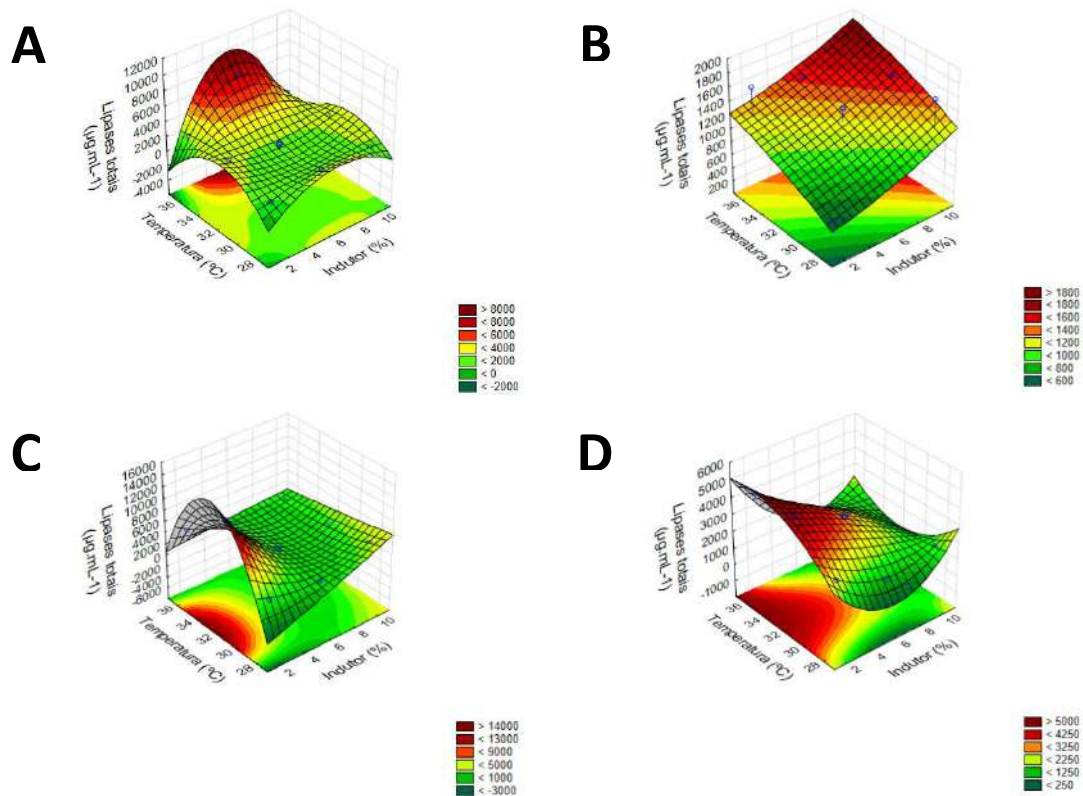


Figura 2. Response surface charts for factorial planning of *Penicillium* sp. F04 (A), *Aspergillus niger* F16 (B), *Aspergillus* sp. F18 (C) and *Aspergillus* sp. F21 (D).



Proposal Of a Rapid And Low-Cost Method To Assess Sublethal Effects Of Pesticides On Bees' Hypopharyngeal Glands.

Murion Monteiro De Godoi^{1*} and Pedro Brito¹

¹ Departamento de Histologia Embriologia e Biologia Celular, Instituto de Ciências Biológicas, Universidade Federal de Goiás, Goiânia, Brazil

*murionmmg@hotmail.com

Bees are important animals in environmental and economical tasks, due to their beekeeping products and participation in the reproductive cycle of various plant species [1]. Studies involving stingless bees grow in numbers over time due to their importance for endemic plant species [2]. Among these bees there is *Frieseomellita varia* (LEPELETIER 1836), a species that is distributed from the Southwest of Mexico to the Southeast of Brazil and an important generalist pollinator. While foraging for nectar and pollen on agricultural systems, bees can be contaminated by pesticides. Monitoring pesticide effects on target bees' organs are essential to understand how these contaminants affect the organism. However, most of cell biology techniques are expensive and/or laborious. Thus, we present a rapid and low-cost method to investigate morphological changes in bees' hypopharyngeal glands. Bees' hypopharyngeal glands are a good study model as they are related to the larval food production, and an alteration on its physiology affect the hive. The hypopharyngeal glands are composed of unicellular acini that attach to a common excretory duct [3]. Our hypothesis is that the ingestion of food contaminated with pesticides makes the unicellular acini irregular shaped, reflecting low secretory activity. To test the proposed methodology, we studied *F. varia* foragers, fed with two sublethal concentrations of the insecticide fipronil. Forage bees from 4 hives were placed in plastic pots, 10 bees each. Three groups were assembled from each hive: C (Control), lc10 (lethal concentration 10%) and lc25 (lethal concentration 25%). Animals were left feeding for 4 hours and euthanized after one hour after feeding. Hypopharyngeal glands were dissected in 0.1M sodium phosphate buffer, pH 7.2 and fixed in 4% paraformaldehyde and 2% sucrose overnight. Then, they were dehydrated in alcoholic series to 70% alcohol. They were photographed in an Olympus BX41 photomicroscope. Fields were analyzed with the Image Pro Plus program. In each gland all possible acini were bypassed, obtaining measurements of area and perimeter. The shape-factor formula ($4\pi A/P^2$) was used to verify the sphericity of the cells. For statistical analyses, the Kruskal-Wallis test was used due the data do not present normal distribution even after logarithmic transformation. After analyzes it was possible to observe that bees from both treated groups presented cells with irregular shapes when compared to the control group ($X^2 = 27.314$, $df = 2$, $p\text{-value} = 1.172e-06$). We concluded that the proposed methodology is effective to investigate morphophysiological changes in the analyzed organ. The methodology is rapid, providing results in few days (~7days) and low-cost using commonly found reagents and equipment. Moreover, the proposed methodology proved to be accurate because it detected significative alterations caused by sublethal concentrations. However, the methodology must be tested with different bee species and pesticides before its broad use.

REFERENCES

- [1] S.A. Corbet et al., *Bee World*, 72(2) (1991) 47
[2] J.A. González-acereto et al., *J. Apic. Res.*, 45(4) (2006) 234.
[3] R.A.C Costa et al. *J.Biosci*, 24(1) (1999) 97.

Acknowledgments: FAPEG (Fundação de Amparo à Pesquisa do Estado de Goiás)

FIGURES



Figure 1: Forager specimen of *Frieseomelita varia*.

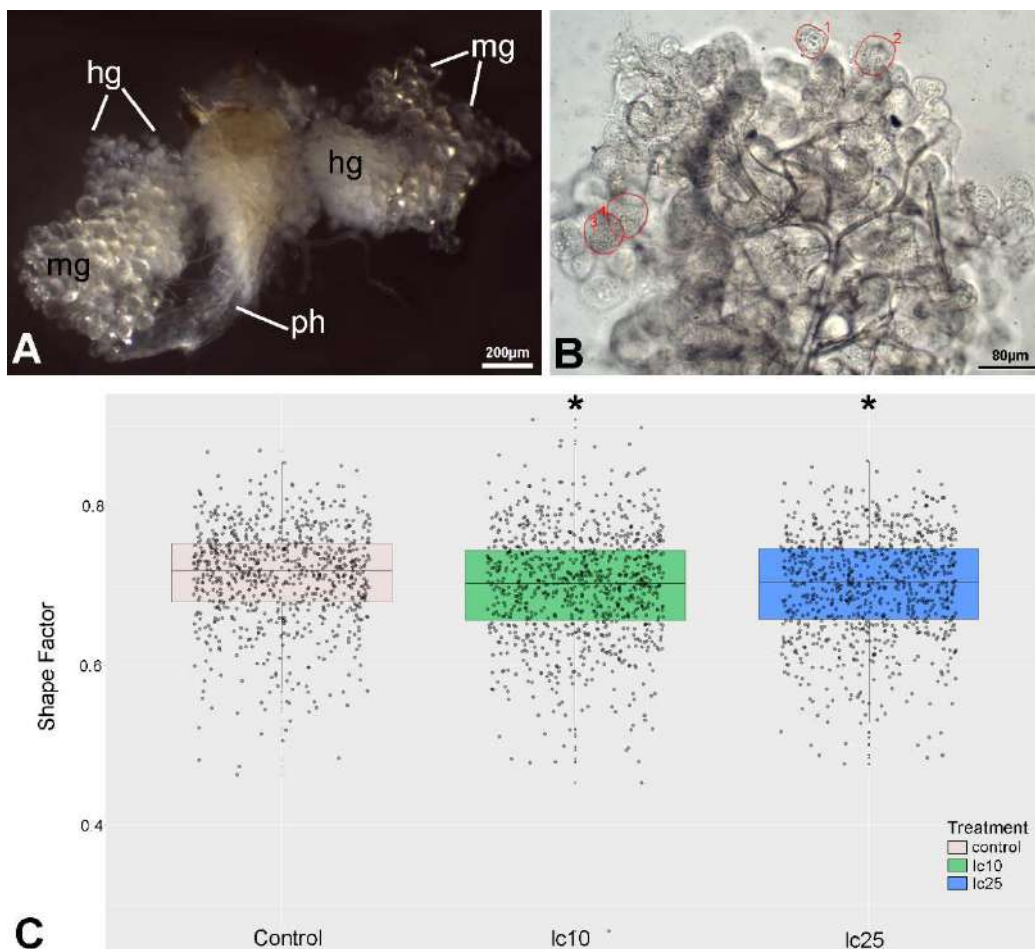


Figure 2: **A)** Stereomicroscopy of the head salivary glands of *F. varia*; (ph) pharynx, (hg) hypopharyngeal glands, (mg) mandibular glands. **B)** Light microscopy of hypopharyngeal gland with four unicellular acini circled. **C)** Boxplot of Kruskal-Wallis test of the Shape Factor ($X^2 = 27.314$, $df = 2$, $p\text{-value} = 1.172e-06$). (*) represents groups with significant difference from Control Group.



Detection Of Autophagy In Secretory Canals Of *Anacardium humile* St. Hill By Immunofluorescence

Shelly Favorito de Carvalho^{1,2*}, Elton Luiz Scudeler³, Daniela Carvalho dos Santos^{1,3} e
Silvia Rodrigues Machado^{1,2}

1. Centro de Microscopia Eletrônica, Instituto de Biociências, UNESP – Botucatu, Brasil.
 2. Programa de pós-graduação em Ciências Biológicas (Botânica), UNESP – Botucatu, Brasil.
 3. Departamento de Biologia Estrutural e Funcional, Instituto de Biociências, UNESP – Botucatu, Brasil.
- *shelly.favorito@unesp.br

Initially described in fungi, autophagy is a preserved process in animals and plants, classified into two main types^{1,2}: macroautophagy and microautophagy, besides mega-autophagy and specific autophagy^{2,8}. Although signs of autophagy have often been reported during the early development of secretory canals in different plant species, including Anacardiaceae members, the autophagic processes have not been adequately explored. The recent development of specific markers for autophagosomes has facilitated the detection of different autophagy pathways in plant cells; in addition, the development of immunostaining methods has allowed important advances in the understanding of autophagy, in particular, in clarifying additional physiological roles of autophagy in plants⁶. Autophagy-related protein 8 (ATG8) is a central component in autophagic machinery related to the formation of autophagosomes and is present in both the inner and outer membranes at the beginning of the formation of the autophagosome (when it is still considered as a phagophore) and remains in the inner membrane until degradation in the vacuole. Because of these characteristics, it is a good marker for tracking autophagy from the early stages to degradation in the vacuole⁷. In this study, we used ATG8 associated with a fluorescent marker observed under a confocal microscope in order to detect the autophagy process in the secretory canals in the aerial vegetative axis of *A. humile*.

- [1] G. Mitou et al., *International Journal of Plant Genomics* (2009).
- [2] W.G. Van Doorn and A. Papini, *Autophagy* 9 (2013) 1922.
- [3] M. Shibata et al., *Journal of Cell Science* 127 (2014) 1161.
- [4] Soto-Burgos et al., *Plant Physiology* 176 (2018) 219.
- [5] Q. Zhang et al., *Planta* 247 (2018) 845.
- [6] D.C. Bassham, *Current Opinion in Plant Biology* 10 (6) (2007) 587.
- [7] D.C. Bassham, *Methods* 75 (2015) 181.
- [8] S.R. Machado and T.M. Rodrigues, *Planta*, 250 (12) (2019).
- [9] This research was supported by FAPESP (Brazil).

Acknowledgments

We thank the Electron Microscopy Center, IBB UNESP and FAPESP for support.

Green markings indicating the presence of autophagosomes were observed in the cells of the secretory epithelium and the parenchyma sheath of the secretory canals in cross sections of aerial stems (Figure 1), confirming the occurrence of autophagy during the development of these secretory structures. The role of autophagy in the differentiation of secretory structures, such as laticifers⁵ and nectaries⁸ has recently been discussed. The results confirm the efficiency of ATG8 as a marker to autophagy in secretory cells. Our finding contributes to deepen the knowledge about the autophagy process and its implications for the development of secretory structures in plants.

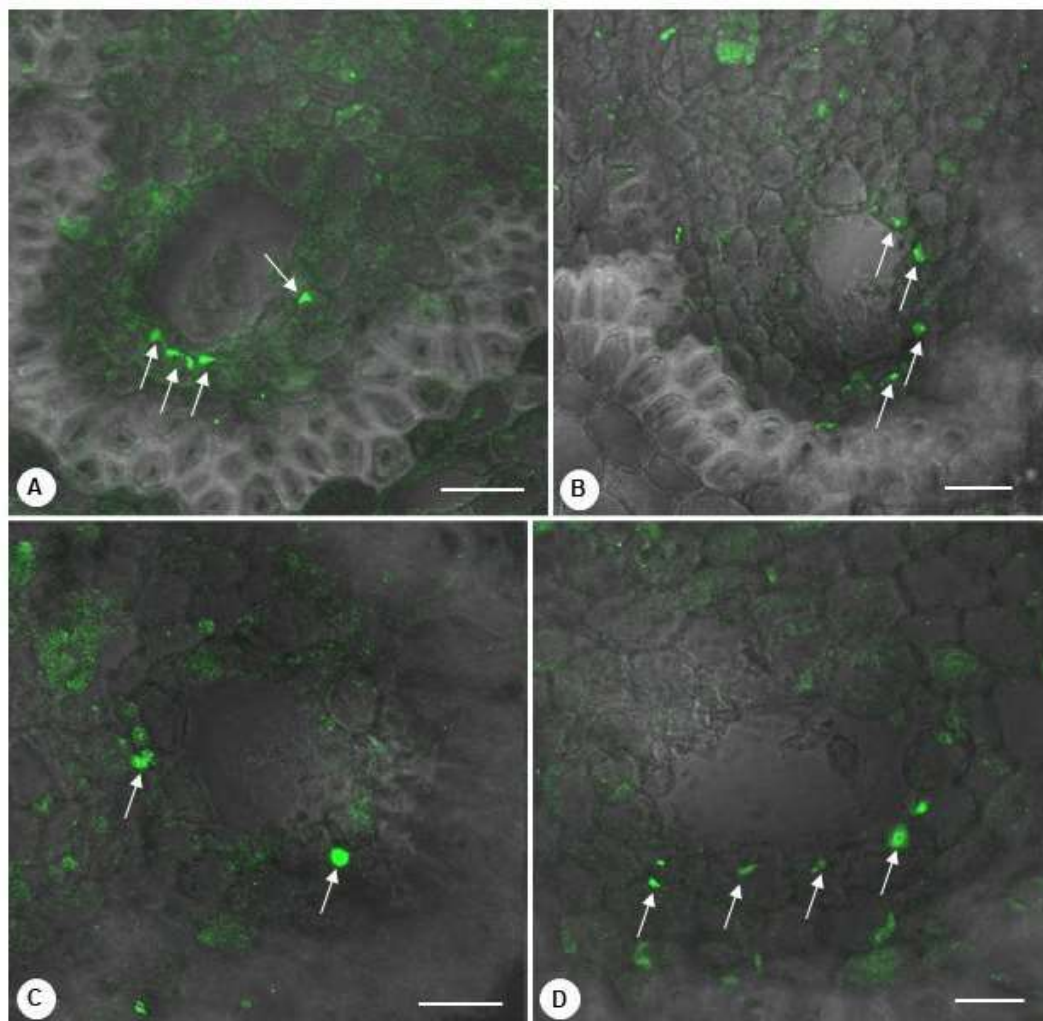


Figure 1. Expression of ATG8a in secretory canals in the aerial stem of *Anacardium humile* observed under the confocal microscope. ATG8a-associated with autophagosomes are observed in green in the secretory epithelium and in the cells of the parenchyma sheath (arrows). Bars: A-B: 20 μ m; C-D: 15 μ m



Antitumoral Activity of a Dibenzylideneacetone Derivative (A3K2A3) Against HeLa Cells

Aline Pinto Zani^{1*}, Zia Ud Din², Edson Rodrigues-Filho², Sueli de Oliveira Silva¹, Francielle Pelegrin Garcia¹, Tania Ueda-Nakamura¹ and Celso Vataru Nakamura¹

¹ Programa de Pós-Graduação em Ciências Farmacêuticas, Laboratório de Inovação Tecnológica no Desenvolvimento de Fármacos e Cosméticos, Universidade Estadual de Maringá, Maringá-PR, Brazil.

² Departamento de Química, LaBioMMi, Universidade Federal de São Carlos, São Carlos, SP, Brazil.

*aline_zani@hotmail.com

Cervical carcinoma (CC) is the fourth most common cancer in women worldwide [1]. Despite efforts to reduce the number of cases of these and other types of cancer, there is still a need for research to find drugs with effective antitumor activity and less toxic effects. In this context, compounds containing chalcones and their derivatives are being extensively studied due to their diverse biological activities [2]. The objective of this work was to investigate the *in vitro* antitumor activity of **A3K2A3**, a new synthetic compound derived from 1,5-diaryl-3-oxo-1,4-pentadienyl, against cervical cells immortalized by HPV 18 (HeLa). For that, cells were plated (2.5×10^5 cells/mL) and treated with **A3K2A3** (1, 10, 50 and 100 μM) for 48 h at 37 °C. Afterwards, cell viability was determined by MTT colorimetric assay. The inhibitory concentration for 50% of the cells (IC_{50}) was determined by linear regression. For morphology evaluation, cells were treated with IC_{50} and $2 \times \text{IC}_{50}$ concentrations of **A3K2A3** and images were taken after 24 and 48 h incubation (Olympus CKX41). To investigate ROS production, HeLa cells were treated and after 24 h, labeled with H_2DCFDA (10 μM). Further, mitochondrial membrane potential was evaluated by TMRE (25 nM). In both experiments, the fluorescence was quantified in a spectrofluorimeter (VICTOR X3, PerkinElmer). Finally, cellular migration was investigated by the wound healing assay. Briefly, after 24 h of plating, a wound was made with a tip, then the cells were treated and observed after 24 and 48 h under a phase-contrast inverted microscope (Olympus CKX41; 4x magnification). **A3K2A3** showed a cytotoxic activity against HeLa cells with an IC_{50} of 18.9 μM and also induced morphological changes such as irregular shape and cellular detachment. Moreover, there was an increase in ROS levels and mitochondrial depolarization in treated cells, indicating oxidative damages. The substance further induced significant inhibition of cell migration when compared with the negative control. Given these results, **A3K2A3** has shown promise as a possible alternative for the treatment of cervical cancer, requiring more studies to better understand its effect against these cancer cell.

[1] INCA. Estimativa 2020: incidência de câncer no Brasil / Instituto Nacional de Câncer José Alencar Gomes da Silva. – Rio de Janeiro (2019).

[2] M. M. A. Hawash et al. Eur. J. Med. Chem., v. 129 (2017) p. 12–26.

Acknowledgments: This research was supported by UEM, Capes, CNPq, FINEP and Pronex/Fundação Araucária.

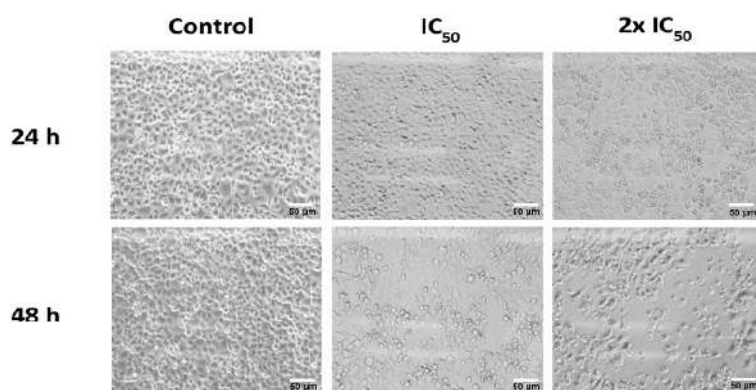


Figure 1- Morphological alterations induced by **A3K2A3** in cervical cancer cell line (HeLa) treated with IC_{50} ($18.9 \mu M$) or $2xIC_{50}$ ($37.8 \mu M$) and analyzed in a phase contrast inverted microscope after 24 and 48 h. Control: untreated cells

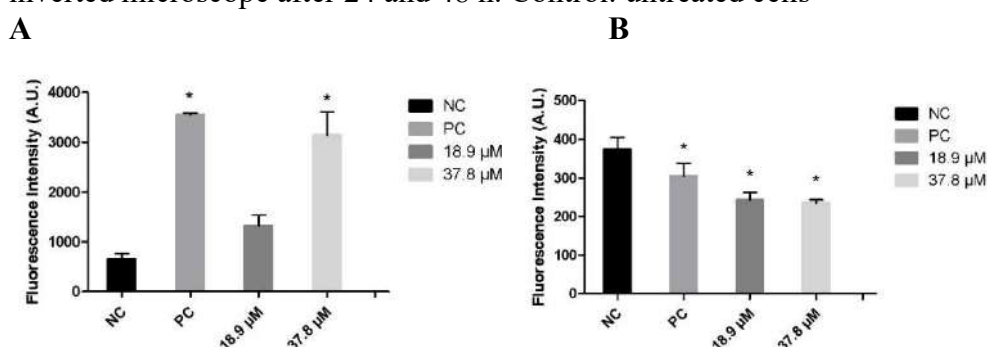


Figure 2 - (A) Production of reactive oxygen species (ROS) using H_2DCFDA fluorescent dye ($10 \mu M$) and (B) assessment of Mitochondrial Membrane Potential by TMRE ($25 nM$) in HeLa cells treated (24 h) with IC_{50} ($18.9 \mu M$) or $2xIC_{50}$ ($37.8 \mu M$) of **A3K2A3**. NC: negative control. PC: positive control (H_2O_2). The data were obtained after performing three independent experiments, and p values ≤ 0.05 , obtained by one-way ANOVA test and Tukey post-test, were considered statistically significant.

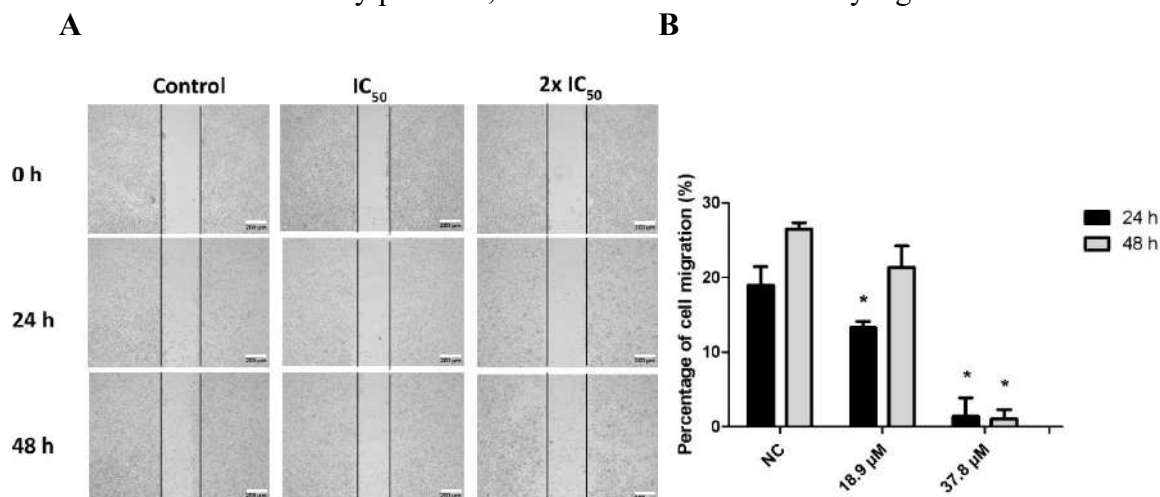


Figure 3- Analysis of cell migration by wound healing assay in untreated HeLa cells (control) and treated with IC_{50} ($18.9 \mu M$) or $2xIC_{50}$ ($37.8 \mu M$) for 0, 24 and 48 h and observed under a phase contrast inverted microscope (A). The data were expressed as a percentage of the wound closure (cell migration) (B) after three independent experiments, p 0.05, compared to the control (untreated cells); through one-way ANOVA test and Bonferroni post-test.



Testicular Morphohistology of the Crab *Sesarma rectum* on the East Coast of Marajó Island, Pará, Brazil.

Álvaro Aragão de Lima^{1*}, Joelly Corrêa dos Santos², Fernanda Simas Corrêa Biancalana² and Adriano Biancalá¹

¹ Federal University of Pará, Marajó-Soure campus, Cellular and Molecular Biology Laboratory, Soure Brazil .

² Federal University of Pará, Marajó-Soure campus, Microbiology and Parasitology Laboratory, Soure Brazil.

*alvarolimabio@gmail.com

Mangroves are coastal ecosystems, serve as a cradle for several species of animals, among the groups of animals most present in these environments we can highlight the crustaceans having as representatives crabs and shrimp, where they perform functions aimed at the cycling of nutrients in the ecosystem, in addition to serve as a base for the feeding of several vertebrates [1], [2], [3]. The municipality of Soure has a wide range of mangroves, where these crustaceans perform their functions, which are vital for the maintenance of this ecosystem. Based on this, the present study aims to describe the reproductive system and the spermatogenesis of the crab *Sesarma rectum*. For this, the specimens were collected in the municipality of Soure (PA) through active collections, taken to the cell and molecular biology laboratory at UFPa - Soure. Initially, the specimens were cryo-anesthetized for 10 minutes, immediately after they were measured and dissected in order to obtain the reproductive system, they were fixed in 10% formalin solution for 24 hours, afterwards this material was preserved in 70% alcohol. With the material preserved, the histological procedures for light microscopy were started, with alcoholic dehydration (70%, 80%, 90%, 100%), later the material was cleared in xylene and embedded in liquid paraffin. 7µm-thick sections were performed. Subsequently, the material was hydrated and stained with Harris Hematoxylin and Eosin (HE). From the analyzes, it was possible to describe the reproductive system and the crab spermatogenesis. The reproductive apparatus macroscopically has the shape of the letter "H". Microscopically, the reproductive system has lobes that are lined by a simple epithelium. Inside these lobes, spermatogenesis occurs. Spermatogenesis consists of a successive series of cell divisions in order to obtain the sperm as the final cell. The first cells of the spermatogenic lineage are the spermatogonias, which were found in two stages A and B, the next cells are the spermatocytes, which can be divided into types 1 and 2, later the next developing cells are the spermatoids that have 3 stages that can be differentiated mainly by the nuclear morphology of these cells, the spermatoids no longer undergo cell divisions, only morphophysiological modifications, in the process called spermyogenesis, resulting in the last cell type the sperm, it is characterized by having the circular nucleus and a central acrossome . Works focused on reproductive biology are extremely important, mainly because they can describe ecological patterns. Thus, the information obtained from this work is important in the elaboration of possible management plans, not only for the species but for the mangrove ecosystem as a whole, in addition to contributing information related to the reproductive biology of these specimens.

REFERENCES

[1] D.S. Castiglioni, M.L. Negreiros-Fransozo. Rev. Bras. de Zool. 23:331-339, 2006.

- [2] D.B Sousa et al., *Sér Zoologia* 105: 339–347, 2015.
[3] G.G Castilho et al., *Acta Zool.* 89, 157–161, 2008.

THANKS

I would like to thank CNPq for the support and funding, also to thank my friends Fabrício Octavio and Pedro Henrique for their help in the collections.

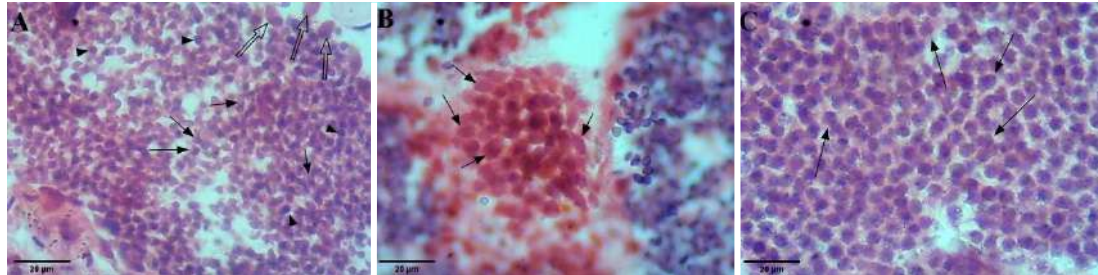


Image 1: cells present in the spermatogenesis process. A) empty arrows point to type A spermatogonia, arrows point to early spermatids, and arrowheads point to secondary spermatocytes. B) the arrows point to type B spermatogonia. C) arrows point to type 1 spermatocytes.

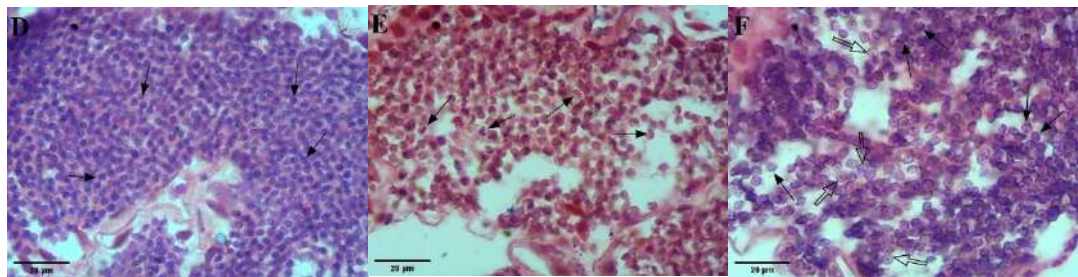


Figure 2: cells present in the spermatogenesis process. D) arrows indicate type 2 spermatocytes. E) sites indicate intermediate spermatids. F) arrows indicate final sperm cells and empty arrows indicate sperm cells.



Investigation On The Occurrence of Microplastics In Mussels Of The Bragantine Estuary (Pará/Brazil)

João M.S. Rodrigues*¹, Juliana C.D. Pantoja¹, Andrews H.F. Leão¹, Alex S. Paiva²,
Yuri W.M. Favacho², Renata S. Oliveira², Liziane A.B. Gonçalves¹ and Rossineide M.
Rocha¹.

¹ Laboratory of Cell Ultrastructure, Federal University of Pará (UFPA), Belém/PA,
Brazil.

² Laboratory of Immunohistochemistry and Developmental Biology, Federal University
of Pará (UFPA), Belém/PA, Brazil.

*jmsrodrigues484@gmail.com

Microplastics (MPs) are ubiquitous on the environment and constitute a rising threat to aquatic ecosystems and global food safety [1]. However, information regarding plastic pollution on amazonian estuaries are still scarce. On the present study we aimed to verify the occurrence of microplastic contamination on sururu (*Mytella spp.*), a mussel with great socioeconomic importance in the Caeté River estuary. A total of 300 specimens were purchased at the free trade fair of Bragança (Pará/Brazil), from October of 2019 to November of 2019. Groups of 10 individuals each were defined and mussels of the same group had their inner contents placed together on flasks containing KOH 10% for digestion during 48 hours. The digested content was filtered using 15 µm nets and analysed in stereomicroscope (Leica M205 A) for visual identification of MPs. Visualized MPs were photographed and classified based on their color and shape [2]. To avoid sample contamination, the use of plastic materials was minimized and negative controls for airborne MPs were set at each analysis. As a result, 63 particles were identified with a concentration of 0.59 MPs/g and 0.21 MPs/individual. Only 5 out of 30 analysed groups did not contain any plastic particle. Fibers of many colors corresponded to almost totality of the findings (N=62), followed by a single blue sphere (Fig. 1). The low number of MPs on the negative controls (N=4) indicates that the results are close to the reality of the region. The concentration of MPs/g in this study was similar to what has been reported for other bivalves sold in markets around the world [3]. This unprecedented record of microplastics contamination of filter-feeding bivalves in the Caeté River alerts to the dissemination of MPs through the estuary and its risks for the local fauna and people.

References

- [1] C. Walkinshaw et al., *Ecotoxicology and Environmental Safety*. 190 (2020) 110066.
- [2] T. Rocha-Santos; A. C. Duarte. *Characterization and Analysis of Microplastics*, 1, (2017) 1.
- [3] Y. Cho et al., *Environmental Pollution*. 245 (2019) 1107.

Acknowledgement: To UFPA by support.

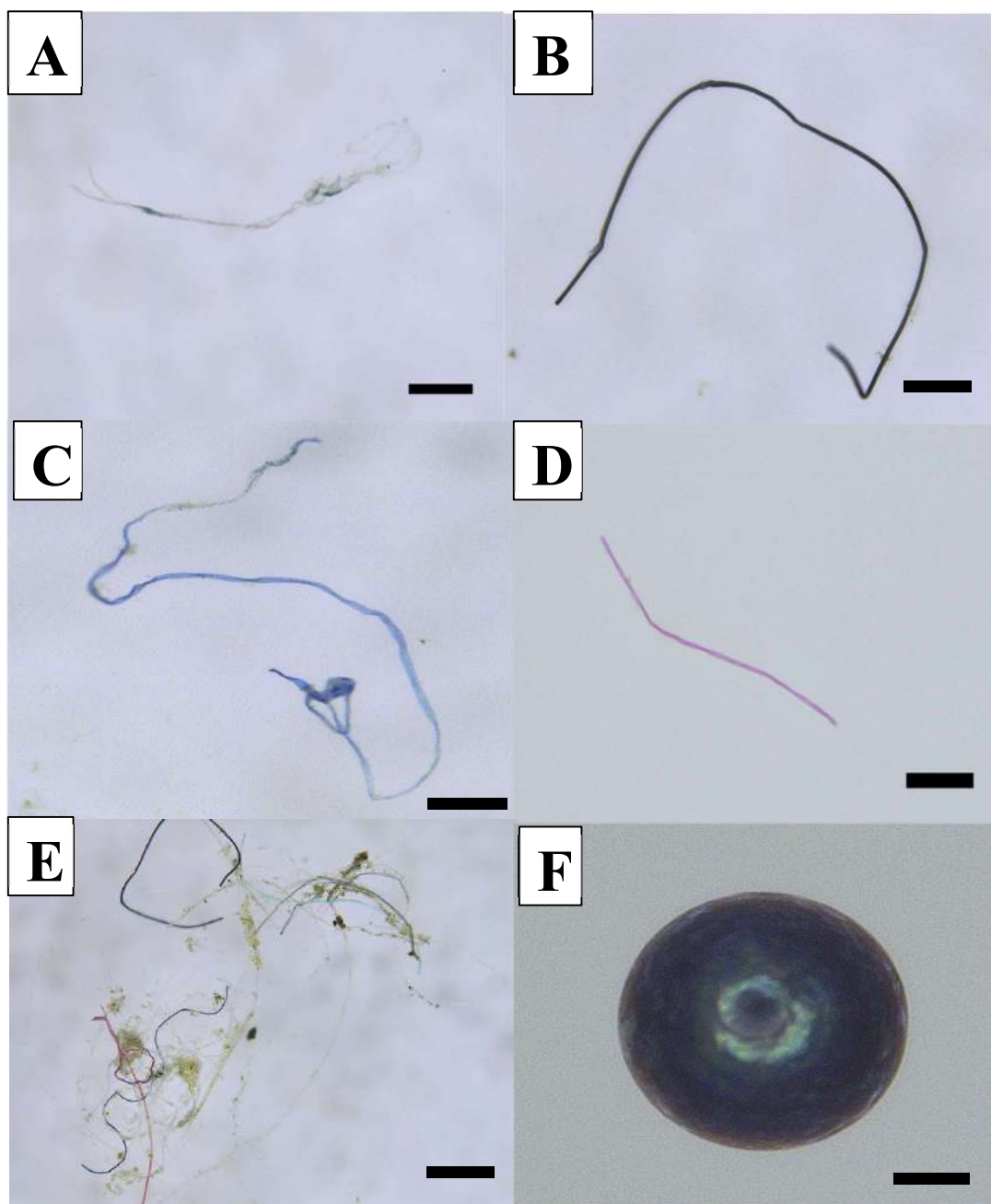


Figure 1: Stereomicrography of microplastics. A – Transparent fiber; B – Black fiber; C – Blue fiber; D – Pink fiber; E – Entangled fibers of different colors; F – Blue sphere. Scale bar: 10 μ m.



Apoptosis In The Hepatopancreas Of *M. amazonicum* From Estuarine Environment

Yuri W.M. Favacho^{1*}, Juliana C.D. Pantoja², João M.S. Rodrigues², Andrews H.F. Leão², Allex S. Paiva¹, Gicelle M. F. Silva¹, Breno R.M. Silva¹, Maria A. P. Ferreira¹.

¹ Laboratory of Immunohistochemistry and Developmental Biology, Federal University of Pará, Belém/PA, Brazil.

² Laboratory of Cell Ultrastructure, Federal University of Pará, Belém/PA, Brazil.

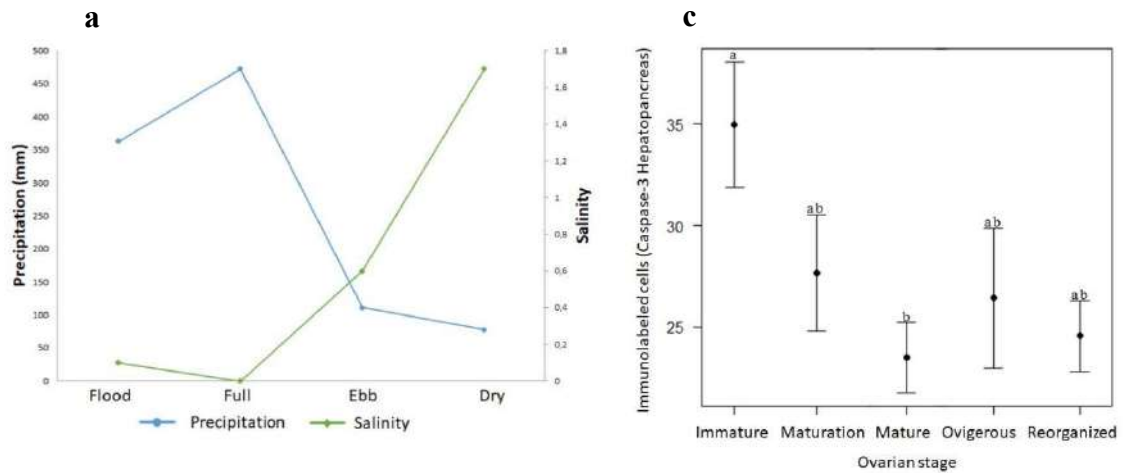
* Email: yuriwellington.mf@gmail.com;

Apoptosis is an active mechanism for regulating homeostasis, embryonic development and elimination of superfluous cells in organisms, occurring by intrinsic or extrinsic pathways, capable activate the Caspase-3 protein and trigger cell death [1]. *Macrobrachium amazonicum* is a specie of freshwater prawn from the Amazon region able to tolerate of the salinity variations in the environment [2,3]. Hepatopancreas is an organ capable of performing digestion and synthesizing proteins that contribute to ovarian maturation [4]. However, there is still no information on the relationship between environment variation and apoptosis in the hepatopancreas. The aim of this study was to describe apoptosis in the hepatopancreas of *M. amazonicum* according maturation ovarian and estuarine environment [5]. Specimens were collected and fragments of hepatopancreas and ovary were fixed in Bouin's solution for 24 hours and subjected to standardized histological procedures for inclusion in paraffin. The replicas of each slide, previously identified, were subjected to immunoperoxidase with primary polyclonal anti-Caspase-3 antibody. Salinity levels were higher in the dry season and lower in the rainy season, which had the highest rainfall [a]. Each hepatopancreatic tubule consists of different cell types, E-cell (embryonic), R-cell (resorptive), F-cell (fibrillar), B-cell (vesicular) and M-cell (basal). The hepatopancreas was analyzed according to the ovarian stage and immunorreaction for cleaved Caspase-3 was frequent in B and R cells, especially in the immature and mature stages [b], with significant differences in the ANOVA / post-Tukey HSD test [c]. The highest frequency of apoptosis occurred during the flood period, the time with the lowest levels of salinity. This study provides information on the cellular dynamics of the hepatopancreas and provides subsidies for future studies of reproductive maturation in environments under anthropic influence.

References

- [1] I. Grivicich et al., Revista Brasileira de Cancerologia 53(3) (2007) 335.
- [2] F.G.Vergamini et al., Contributions to Zoology, 80 (2011) 67.
- [3] G.M.F. Silva et al., Ecology and Evolution,10 (2020) 6536.
- [4] I.B. Franceschini-Vicentini et al., Int. J. Morphol., 27 (2009)121.
- [5] This research was supported by UFPA (Brazil).

Acknowledgment: To UFPA by support.



Figures a: Relation of salinity and precipitation during the hydrological period in the estuarine environment. **c:** Frequency of immunostaining for caspase-3 in hepatopancreas by ovarian stage.

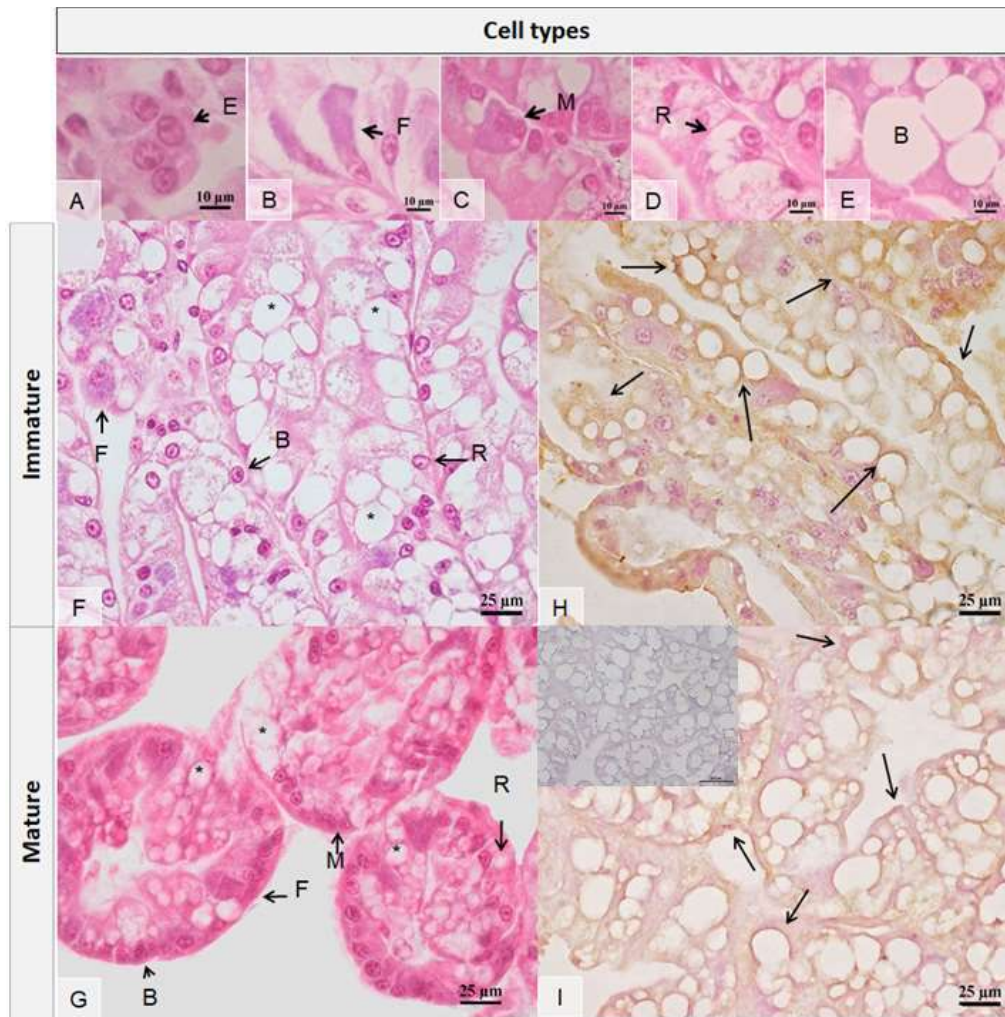


Figure b: Light Microscopy of the hepatopancreas according to the stage of ovarian maturation. A-G (cell types): E, F, M, R, B. H/I: Immunostaining for caspase-3 cleaved hepatopancreatic tubules. F/H: immature. G/I: mature. insert: negative control. E-cell (embryonic), R-cell (resorptive), F-cell (fibrillar), B-cell (vesicular) and M-cell (basal).



On The Tribological Properties Of 2D Materials: A Brief Comparison Between Graphene And MoS₂

Felipe Ptak^{1*}, Clara M. Almeida² and Rodrigo Prioli¹

¹ Departamento de Física, Pontifícia Universidade Católica do Rio de Janeiro, Rio de Janeiro, Brazil

² Divisão de Metrologia de Materiais, Instituto Nacional de Metrologia, Normalização e Qualidade Industrial (INMETRO), Duque de Caxias, Brazil

* ptak@vdg.fis.puc-rio.br

Two dimensional layered materials such as graphene and transition metal dichalcogenides (TMDs) have attracted much attention in recent years due to potential technological applications at the nanoscale, including their use as surface coating and solid lubricants at the nanoscale [1, 2]. In this work, tribological properties of few layer graphene and monolayer molybdenum disulfide (MoS₂) were studied at this scale with the use of an atomic force microscope (AFM) with a silicon nitride tip. Graphene samples were obtained by the exfoliation of bulk highly oriented graphite (HOPG) crystals, while MoS₂ were grown by chemical vapor deposition (CVD). Both samples were deposited onto silicon dioxide (SiO₂) substrates. The role of different parameters were analyzed, such as number of layers, applied load and sliding velocity. By varying the applied load, deformation of such surfaces in contact with the AFM tip, as well as the influence of adhesion is revealed. Data was fitted to the appropriate contact mechanics models, such as the Derjaguin-Müller-Toporov (DMT) and the Johnson-Kendall-Roberts (JKR) models [3]. On the sliding velocity aspect, information on the interaction potential and influence of temperature may be provided using the thermally active Prandtl-Tomlinson (PTT) model [4]. We found that both graphene and MoS₂ samples are better fitted by the JKR model and deformation may play an important role during sliding of both materials. While varying the sliding speed of the tip on the sampled surfaces, friction in graphene increases linearly with the logarithm of velocity up to a certain point, where it then saturates [5]. However, no saturation point was found in MoS₂. Figures 1a and 1b show the topography images of graphene and MoS₂, respectively. Figure 2a and 2b show the measurements of friction with respect to (a) the applied load and (b) sliding speed of the tip, respectively.

REFERENCES

- [1] D. Berman et al., *Materials Today* 17, 31 (2014).
- [2] M. R. Vazirisereshk et al., *Lubricants* 7, 57 (2019).
- [3] R. W. Carpick et al., *Journal of Colloid and Interface Science* 211, 395 (1999)
- [4] M. Evstigneev et al., *Stochastic Modeling and Rate Theory of Atomic Friction*. In: Gnecco E., Meyer E. (eds) *Fundamentals of Friction and Wear on the Nanoscale*. NanoScience and Technology. Springer, Cham. (2015).
- [5] F. Ptak et al., *Scientific Reports* 9, 14555 (2019).

ACKNOWLEDGEMENTS

This work was financially supported by the brazilian funding agencies Coordenação de

Aperfeiçoamento de Pessoa de Nível Superior (CAPES), Conselho Nacional de Desenvolvimento Científico e Tecnológico (CNPq) and Fundação Carlos Chagas de Amparo à Pesquisa do Estado do Rio de Janeiro (FAPERJ). F. Ptak would like to thank Prof. Victor Carozo (PUC-Rio) and Dr. S. H. Safeer (CBPF) for providing the MoS₂ samples.

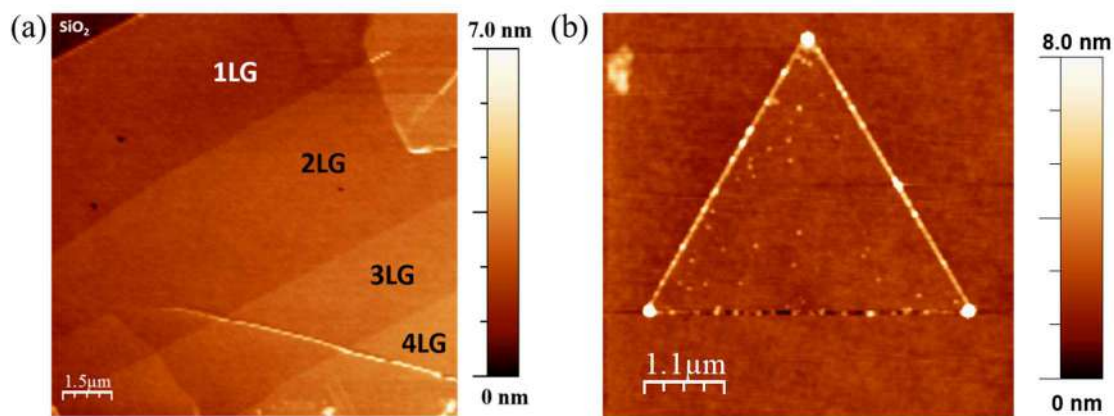


Figure 5: Topography images of (a) few-layer graphene flake and (b) a MoS₂ single crystal.

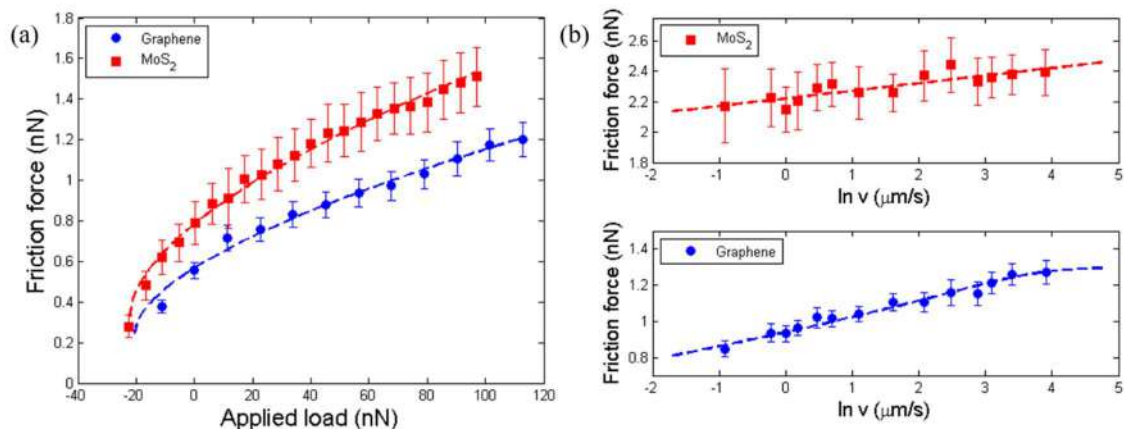


Figure 6: (a) Friction vs load for graphene (blue) and MoS₂ (red). Data was fitted to the JKR model (dotted lines); (b) Friction vs logarithm of sliding velocity for single layer graphene (blue) and MoS₂ (red). Dotted lines indicate the fitted PTT model.



Investigation of Topographical Patterns of Spin Coated GdMnO₃ Thin Films

Cíndel Cavalcante de Souza^{1*}, Heloísa David Yasumura¹, Yonny Romaguera-Barcelay²
and Henrique Duarte da Fonseca Filho¹

¹ Nanomaterials Synthesis and Nanoscopy Laboratory, Physics Department, Federal University of Amazonas, Manaus/Brazil.

² Physics Department, Federal University of Amazonas, Manaus/Brazil.

*cindelcavalcante@hotmail.com

Multiferroic systems have aroused great interest from researchers and industries because they have ferromagnetic and ferroelectric properties in a single phase, and this implies that these materials can be used in technological applications, such as sensors, electronic components, among others [1,2]. Moreover, the perovskite oxides of RMnO₃ type (R is rare earth element) are a novel class of materials exhibiting a set of remarkable interesting properties from the physics point of view, such as superconductivity, ferroelectrics, ferromagnetism, multiferroics and colossal magnetoresistance [3,4]. In this work, GaMnO₃ was synthesized and thin films were produced on Pt(111)/TiO₂/SiO₂/Si substrates using a spin coating apparatus, being sintered at different temperatures. In order to evaluate their spatial patterns as a function of the film's annealing temperature, Atomic Force Microscopy (AFM) technique was used to obtain the topography of the GaMnO₃ thin films. Specific morphological analyzes were performed, such as mean roughness (Sa), mean square roughness (Sq), mean height (Sz), surface asymmetry (Ssk) and kurtosis (Sku) using image processing techniques and mathematical tools. 3D (three-dimensional) topographical images revealed that films annealed at 650°C and 750°C presented the formation of smoother surfaces (Figure 1), but with larger and deeper holes along the surface. On the other hand, films annealed at 850°C had irregular and with sharper peaks, due to the increase in temperature, presenting a rougher surface (~2.97nm). All data can be seen in Table 1. With respect to asymmetry, the sample at 850°C showed a negative asymmetry, while the samples at 650°C and 750°C showed positive asymmetries. As for the kurtosis values, the 650°C and 750°C samples had higher values compared to the 850°C sample, showing that the surfaces present different forms of height distribution.

REFERENCES

- [1] Marti, X. et al. Room-Temperature Antiferromagnetic Memory Resistor. *Nat. Mater.* 2014, 13, 367–374.
- [2] Liu, S.; Yan, S.; Luo, H.; Yao, L.; Hu, Z.; Huang, S.; Deng, L. Enhanced magnetoelectric coupling in La-modified Bi₅Co_{0.5}Fe_{0.5}Ti₃O₁₅ multiferroic ceramics. *J. Mater. Sci.* 2018, 53, 1014–1023
- [3] Asamitsu A, Moritomo Y, Tomioka Y, Arima T and Tokura Y 1995 A structural phase transition induced by an external magnetic field *Nature* 373 407–9
- [4] Tiwari A and Rajeev K P 1999 Electron tunneling experiments on $La_{0.7}A_{0.3}MnO_3$ (A=Ca,Sr,Ba) *Phys. Rev. B* 60 10591–3

ACKNOWLEDGMENTS

The authors thank Fundação de Amparo à Pesquisa do Estado do Amazonas (FAPEAM) for the financial support, as well as UFAM for the Analytical Center infrastructure.

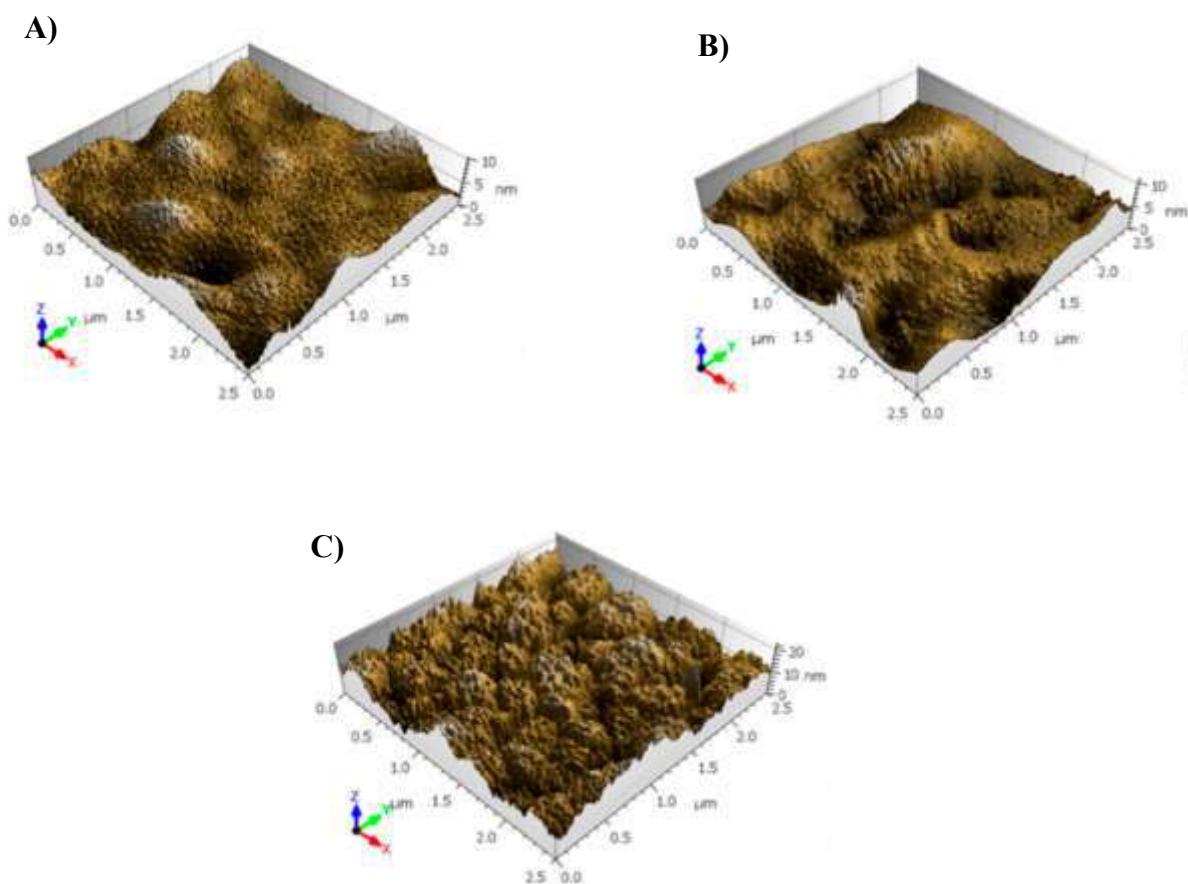


Figure 1: 3D atomic force microscopy (AFM) topographical maps of GdMnO_3 thin films of (A) 650°C , (B) 750°C e (C) 850°C .

Table 1: Height surface parameters of GdMnO_3 thin films

Parameter	GdMnO_3 a 650°C	GdMnO_3 a 650°C	GdMnO_3 a 650°C
Height			
Sa (nm)	1.23 ± 0.21	1.28 ± 0.15	2.97 ± 0.26
Sq (nm)	1.58 ± 0.25	1.65 ± 0.22	3.63 ± 0.30
Ssk	0.44 ± 0.21	0.15 ± 0.27	-0.08 ± 0.08
Sku	3.61 ± 0.42	3.48 ± 0.23	2.63 ± 0.04
Sz (nm)	12.28 ± 2.34	11.88 ± 1.59	29.22 ± 5.59



Scanning Microwave Impedance Microscopy And Raman Spectroscopy As Complementary Tools In The Analysis Of The Structural And Electronic Properties Of Twisted Bilayer Graphene

Douglas A. A. Ohlberg^{1*}, Andreij C. Gadelha², Fabiano C. Santana², Gomes S. N. Eliel³, Jessica S. Lemos², Vinícius Ornelas², Daniel Miranda², Rafael Battistella Nadas², Cassiano Rabelo⁴, Pedro Paulo de Mello Venezuela⁵, Gilberto Medeiros-Ribeiro⁶, Ado Jorio², Luiz Gustavo Cançado², and Leonardo C. Campos²

¹ Microscopy Center, Universidade Federal de Minas Gerais, Belo Horizonte, Brazil.

² Physics Department, Universidade Federal de Minas Gerais, Belo Horizonte, Brazil.

³ Instituto de Física, Universidade Federal da Bahia, Salvador, Brazil.

⁴ Electrical Engineering and Technology Innovation Graduate Programs, Universidade Federal de Minas Gerais, Belo Horizonte, Brazil.

⁵ Instituto de Física, Universidade Federal Fluminense, Niterói, Brazil

⁶ Computer Science Department, Universidade Federal de Minas Gerais, Brazil

* dohlberg@ufmg.br

In the emerging field of twistrionics, the electronic properties of 2D materials are tuned by successively stacking layers of these materials at different rotational (twist) angles relative to the previously deposited layer. These systems became the focus of intense study when superconductivity was first reported in a two layer graphene device fabricated at a “magic” twist angle, and today dozens of articles appear monthly describing the unique properties of new stacks prepared with an endless variety of materials and angles [1]. The “tear and stack” methods commonly used to prepare these systems introduce deviations between the desired and actual twist angles as well as strain gradients and other inhomogenities that require techniques to measure with nanoscale precision the moiré patterns associated with a given twist angle. We have recently shown that the AFM modality known as Scanning Microwave Impedance Microscopy (sMIM) is an effective tool to rapidly screen and map, with 1 nm resolution, bilayers of graphene prepared with a variety of twist angles [2]. Since the contrast mechanism of sMIM images depend on the localized variations in conductance and capacitance of the sample under test, it can readily differentiate the contours of graphene bilayers from the surrounding substrate. Raman imaging also shares this ability, albeit, with a contrast mechanism based on the altogether different mechanism of mapping variations in the spectral peaks uniquely associated with the phonon signatures of a given graphitic structure [3]. Here we investigate by combining Raman spectroscopy [4] and sMIM some of the key essential properties of twisted bilayer graphene systems. The combination of both techniques may shed light in some of the conundrums leading to superconductivity as the twist angle is varied, such as localization, spatial variation of conductivity and disorder. We prepared samples by means of microfabricated truncated pyramids that act as stamps, which by means of a predetermined angle can place a second layer atop a first layer [5]. By means of sMIM, we were able to examine several structures at 1nm resolution. Figure 1 illustrates the essence of our findings. In **a** a microRaman image of a flake containing regions with single layer graphene, exposed hexagonal boron nitride substrates (hBN) and twisted bilayer graphene at angles around 1° and associated spectra in **b**. From **c**. through **g**. capacitance, AFM and conductance images are shown revealing the moiré superlattice and its effect in the material conductivity. We discuss the perspectives of

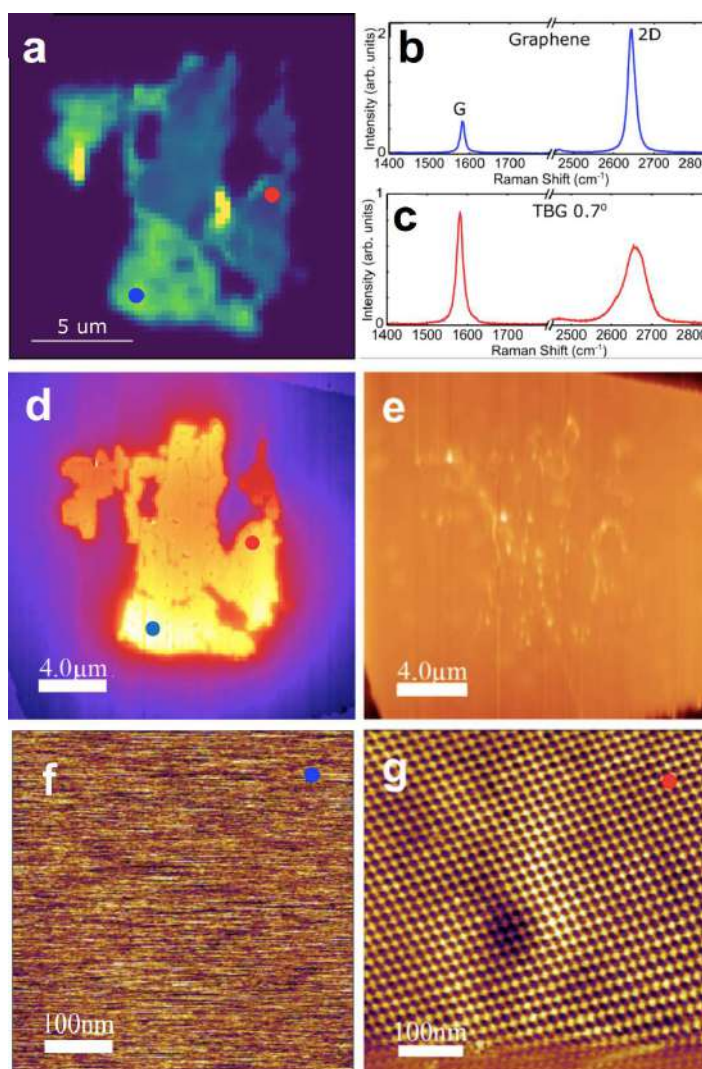


sMIM as an invaluable tool to spatially resolve transport properties of twisted 2D materials.

REFERENCES

- [1] Cao et al., *Nature*, 556 (2018) 43.
[2] Ohlberg et al., *Proc. SPIE, Low-Dimensional Materials and Devices* (2020)114650J.
[3] Jorio et al., *Raman Spectroscopy in Graphene Related Systems*, Wiley-VCH Verlag GmbH & Co. KGaA: Weinheim, Germany, 2011.
[4] A. C. Gadelha et al., *Nature*, 590 (2021) 405.
[5] A. C. Gadelha et al., *ACS Appl. Nano Mater.* 2021, 4, 2, 1858–1866

This research was supported by CNPq, FINEP, FAPEMIG and CAPES (Brazil).





Partially Ordered Porous Structure on Layer-by-Layer PANI/PVS Ultrathin Films: Easy Fabrication of Robust Submicroscopic Patterning

Adriana M. A. Faria¹, Gislayne E. Gonçalves¹, Rodrigo F. Bianchi², Andréa G. C. Bianchi², Carolina Cuba², Bernardo R. A. Neves³, Elisângela Silva-Pinto^{1*}

¹ IFMG - Campus Ouro Preto, Ouro Preto - Brazil.

² UFOP, Departamento de Física, Ouro Preto - Brazil.

³ UFMG, Departamento de Física, Belo Horizonte - Brazil.

*elisangela.pinto@ifmg.edu.br

Films with pores of narrow size distribution have received significant attention in recent years due to their potential applications in tissue engineering, photonic band gap, electronic and optoelectronic devices [1-5]. Among the promising materials for these applications, polymers stand out because they possess both large-scale and low-cost production advantages, as well as the versatility of manufacturing ultra-thin, flexible and elastic films. Hence, a variety of methods have been developed to fabricate these porous polymeric films, such as the templating with colloidal crystal, biotemplating and microphase separation of copolymer methods [5]. In fact, a simple and low-cost method to create structurally ordered porous films is the Breath Figure (BF) method which uses condensed water drops over polymeric films to prepare highly ordered pores structured materials [5]. Polyaniline/poly(vinyl sulfate sodium) (PAni-PVS) is one of the most investigated thin organic semiconducting films due to its promising features such as ease of preparation, acid doping and base undoping processes, and its interest as active material for biochemical sensors [6-7]. The possibility of production thin films with nanostructured surfaces makes the study and commercial research of polymers even more attractive. In particular, in the case of the semiconductive polymers, like PAni-PVS, that allow reversible variation of electrical conductivity from insulation to semiconductor (doping in acid solution and undoping in basic solution), the control of structures with nanopores could give rise to unprecedented devices with mixed electrical and photonic characteristics, with well-defined patterns of recognition or interference, but sometimes insulating or sometimes semiconducting. The present work reports on preparation and characterization of partially ordered porous ultrathin PAni-PVS films on polystyrene substrate using the BF method to easy obtain a robust submicroscopic range structure. To reach this goal, partially porous polystyrene (PS) films was obtained by BF method which was used as a substrate template for layer-by-layer deposition of PAni-PVS. In addition, the BF method was improved with control of deposition parameters of PS, obtained regular and partially organized pores.

[1] V.T. Bui et al., *Polymer*. 74 (2015) 46.

[2] K.J. Rambhia et al., *Journal of Controlled Release*. 219 (2015) 119.

[3] J.D. Joannopoulos et al. *Photonic crystals: molding the flow of light*, Princeton University Press: Singapore, 2008.

[4] E. Ostuni et al., *Langmuir*. 17(2001) 2828.

[5] M.L.K. Hoa et al. *Advances in Colloid and Interface Science*. 121 (2006) 1.

[6] S.W. Kim et al. *Current Applied Physics*. 2 (2002) 335.

[7] M.C. Santos et al. *Polímeros*. 20 (2010) 107.

[8] This research was supported by IFMG (Brazil).

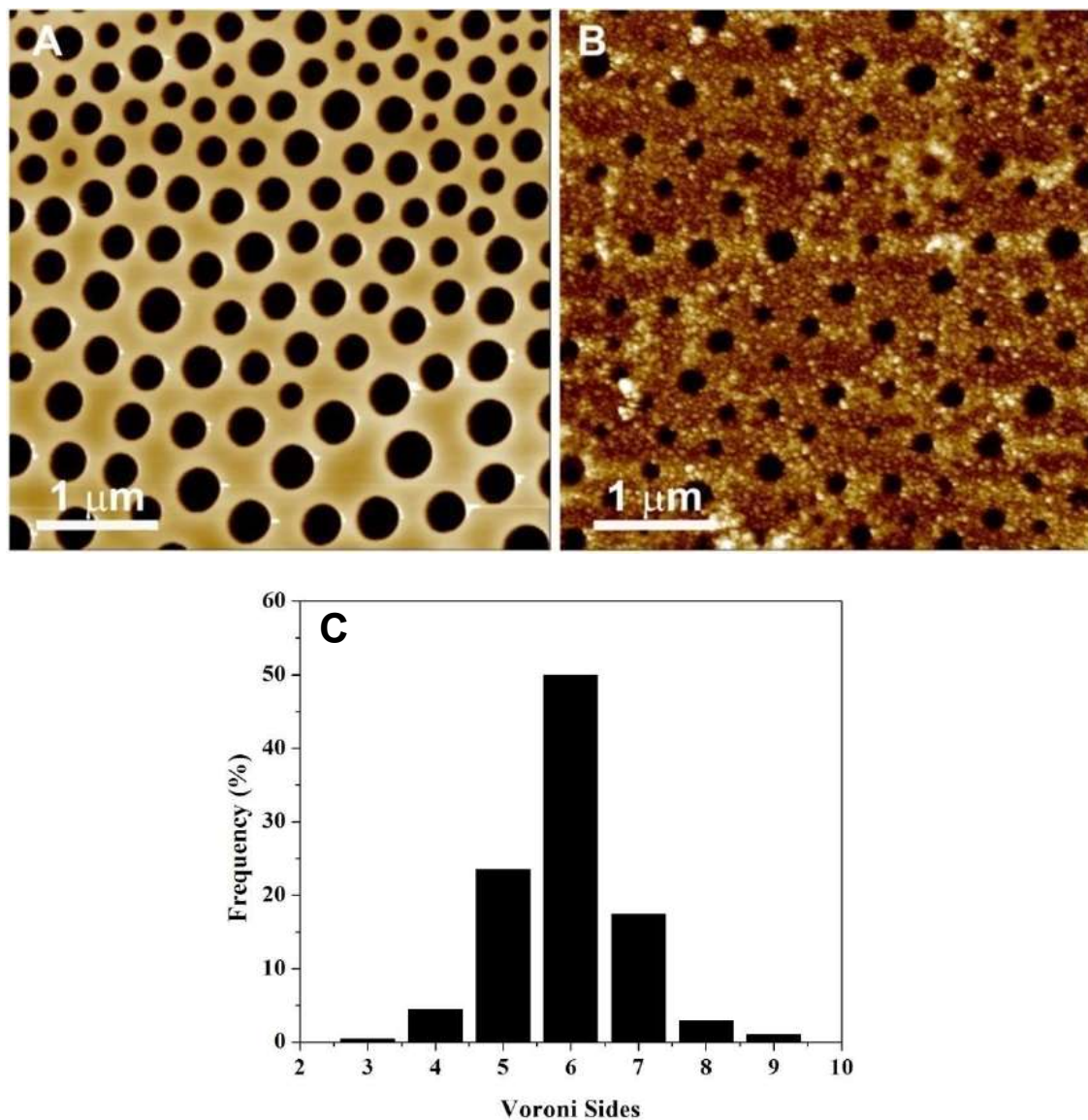


Figure 1: AFM images of A) PS and B) PAni-PVS/PS; C) (b) Histogram of Voronoi sides of sample A.



Two-Dimensional Talc from Waste of Soapstone Industry

Cláudio C. Nascimento¹, Samuel M. de Sousa², Helane L. O. de Moraes², Ariana C. S. Almeida¹, Bernardo R. A. Neves³, Mariana de C. Prado⁴ and Elisângela Silva-Pinto^{1*}

¹ IFMG - Campus Ouro Preto, Ouro Preto - Brazil.

² IFMG - Campus Santa Luzia, Santa Luzia - Brazil.

³ UFMG, Departamento de Física, Belo Horizonte - Brazil.

⁴ UFOP, Departamento de Física, Ouro Preto - Brazil.

*elisangela.pinto@ifmg.edu.br

The extraction of steatite rock, popularly known as soapstone, and the industry that uses it as a raw material, represents important segments of the local economy in Ouro Preto, Brazil. There are several segments of the steatite industry producing utensils, ornaments and cosmetics. However, the disposal of solid waste is one problem that affects the environment. The generated dust is often discarded into the environment, in addition to causing harm to the health of people who work directly in handicrafts or who live in the vicinity of the places where they are discarded. Talc, the main component of steatite, has a crystalline structure, soft texture, high resistance to thermal shock, high oil and grease absorption capacity, low thermal and electrical conductivity, high lubrication and sliding power. In addition, it has a wide range of technological properties, which allows its application in the manufacture of cosmetics, the ceramics industry, the manufacture of paints, rubber, insecticides and fertilizers [1]. On the other hand, the advancement in studies of new materials at the nanoscale shows that natural talc mineral can be mechanically exfoliated down to monolayer flakes with important mechanical properties, such as great resistance to rupture, moderate stiffness and low interaction energy between layers [2]. In this context, this work sought to exfoliate in liquid medium the tailings from the soapstone craft industry, seeking the production of two-dimensional nanostructures of talc. The soapstone tailings collected were characterized by X-ray diffraction and Scanning Electron Microscopy. After exfoliating the tailings in a liquid medium, two-dimensional talc nanostructures were characterized by Atomic Force Microscopy. Two-dimensional nanostructures with an average thickness of 10 nm were obtained. The production of two-dimensional talc structures from the soapstone industry waste proposes a way for its reuse, producing nanostructures with modified mechanical properties that can be used in nanotechnology, such as in reinforcing polymeric films. The possibility of producing a composite with improved properties using low-cost and widely available materials locally is in line not only with what is desirable from an economic and industrial point of view, but also with specific objectives for the development of local communities and the search for sustainable processes.

[1] N.H. Garcia et al., *Holos*. 3 (2014) 69.

[2] A.B. Alencar et al. *2d Materials*. 2 (2015) 8.

[3] Acknowledgments to IFMG for financial supported and Laboratório de Cristalografia do Departamento de Física da UFMG for X-ray diffraction analysis.

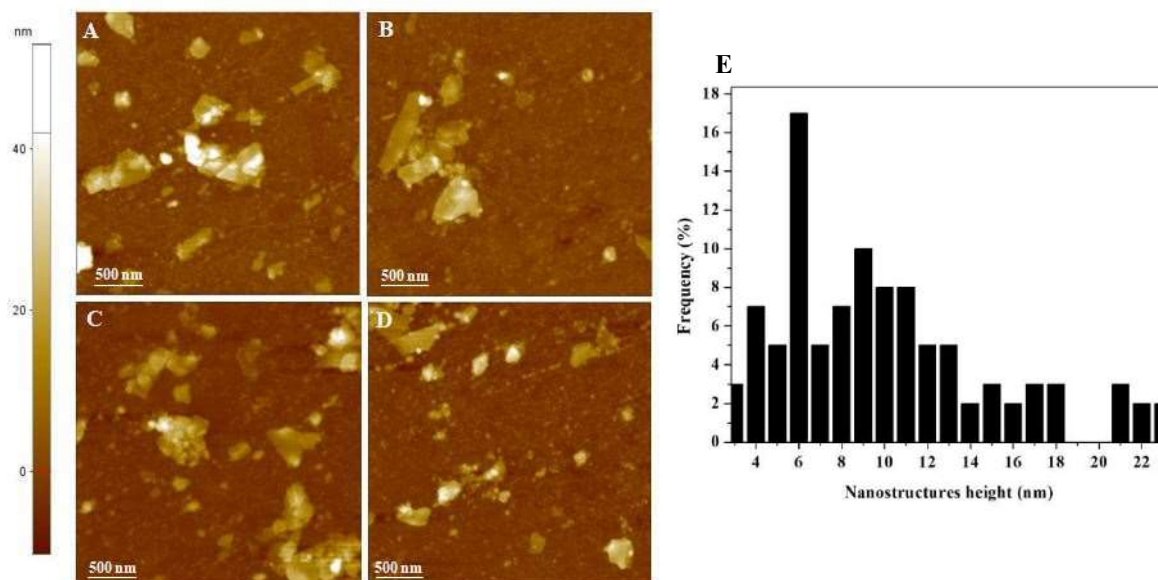


Figure 1: A-D) AFM images of soapstone tailings after exfoliation in liquid medium; E) dispersion of nanostructures height.



EXFOLIATED LEAD SULFIDE CHARACTERIZATION BY SCANNING PROBE MICROSCOPY

Felipe R. G. Beato^{1*}, Elisângela S. Pinto², Fernando G. Araújo¹, Bernardo R. A. Neves³
Mariana C. Prado¹ and Ana Paula M. Barboza¹

¹ Universidade Federal de Ouro Preto, Department of Physics, Ouro Preto, Brazil.

² Instituto Federal de Minas Gerais—Campus Ouro Preto, Ouro Preto, Brazil.

³ Universidade Federal de Minas Gerais, Department of Physics, Belo Horizonte, Brazil.

*felipe.beato@aluno.ufop.edu.br

After the discovery of graphene in 2004, a race began to obtain new two-dimensional materials - those whose thickness is one or a few atoms [1]. These materials have unique properties linked to their dimensions, promising to lead the development of nanotechnology and nanoengineering. In this work, the initial results of the mechanical exfoliation of a new nanomaterial: lead sulfide (PbS), better known as Galena [2], will be presented. We employed Scanning Probe Microscopy (SPM) techniques to characterize the new material. In SPM, an extremely fine tip sweeps the sample surface under inspection [3]. The probe is mounted on the free end of a lever that deflects when interacting with the surface. Different types of interactions can be monitored: mechanical, electrical, or magnetic. The initial results reveal that lead sulfide can be mechanically exfoliated, in nanometric layers, like others two-dimensional materials. Figure 1 shows atomic force microscopy (AFM) images of some PbS flakes investigated in this work. Atomic force microscopy (AFM) measurements [4] of the samples show that the nanometric character of the flakes. Tests were carried out on acidic solutions in an attempt to reduce the contamination generated in the exfoliation process. Analyzes involving Electric Force Microscopy (EFM) [4] and Scanning Kelvin Probe Microscopy (SKPM) [4] were also performed in order to characterize the electromechanical properties of this new nanomaterial. Motivated by a previous theoretical achievement about phase transition pressure-induced in PbS [5] we apply a SPM protocol [3] to further investigate these prediction. Preliminary results shows that it can be possible to see this phase transition using SPM techniques.

REFERÊNCIAS

- [1] N. Briggs, *et al.*, 2D Materials 6 (2) (2009) 022001.
- [2] S. Johnsen *et al.*, JACS 133 (2011) 06.
- [3] A. P. M. Barboza, *et al.*, 23 (2011) 3014.
- [4] V. L. Mironov Fundamentals of scanning probe microscopy. The Russian Academy of Sciences, 2004.
- [5] A. A. Adeleke, *et al.*, J. Chem. Phys. 148 (2018) 104503.
- [6] The authors acknowledge financial support from Brazilian funding agencies: CNPq, Fapemig, Capes and INCT-NanoCarbono. APMB also acknowledges the support from UFOP- Grant Custeio 2017. The authors are thankful to Mr Antônio Pinto G L Neto for the mineral samples and to Mr Alexandre M Moreira and the Crystallography Laboratory (LabCri, Physics Department, UFMG, Brazil) for the x-ray diffraction experiments.

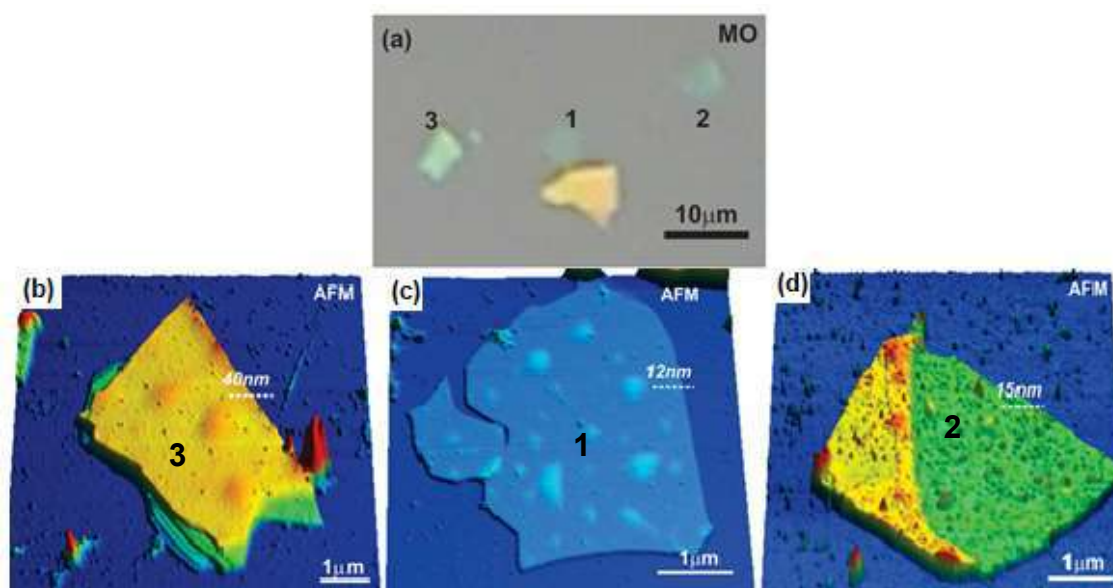


Figure 1 – (a) Optical image and (b)-(d) atomic force microscopy images of different PbS flakes. All samples were prepared by mechanical exfoliation atop SiO_x substrates (in shades of blue).



Topographical Investigation at the Nanoscale of DyMnO₃ Thin Films Produced by Sol-Gel Method.

Heloísa David Yasumura^{1*}, Cíndel Cavalcante de Souza¹, Yonny Romaguera-Barcelay² and Henrique Duarte da Fonseca Filho¹

¹ Nanomaterials Synthesis and Nanoscopy Laboratory, Physics Department, Federal University of Amazonas, Manaus/Brazil.

² Physics Department, Federal University of Amazonas, Manaus/Brazil.

* Correspondence: heloisa.yasumura.3@gmail.com

Perovskite oxides of RMnO₃ type (R = rare earth or ionic transition metal) present an interesting set of technological applications and physical properties,^[1] being especially notable for the DyMnO₃ system, which has photovoltaic applications, spintronic devices, magnetic field sensors, etc.^[2, 3] In this way, we synthesized DyMnO₃ by sol-gel method and thin films were deposited on Pt (111) (150 nm)/Ti (70 nm)/SiO₂ (500 nm)/Si (1 nm) substrate and annealed at different temperatures. In order to assess topographic differences and changes in surface patterns on these films due to heating at different temperatures, Atomic Force Microscopy (AFM) was used. Topographical maps of the DyMnO₃ system were obtained, and these were investigated using processing techniques and mathematical tools. Through these images (figure 1) several analyzes were performed, such as mean roughness (Sa), mean square roughness (Sq), surface asymmetry (Ssk), kurtosis (Sku) and mean peak height (Sz), to understand the evolution of these physical parameters with increasing temperature. The results revealed that the topography at temperatures of 650 °C and 750 °C have smoother surfaces, with deeper valleys and without many defined peaks. From 800 °C, the films have irregular surfaces and more peaks evident, producing a morphology with rougher and denser peaks, suggesting a more uniform surface. The topography showed that films annealed at high temperatures have greater surface roughness (from 1.331 ± 0.226 to 3.988 ± 0.46), negative asymmetries (-0.244 ± 0.166), high kurtosis with leptokurtic behavior, sharper peaks, with sharper and more regular shapes, then having standards for conditions of technological applications. All data can be seen in Table 1.

REFERENCES

- [1] Marques, Igor Hernandes Gomes, et al., *Advanc. Mat. Sci. Eng.*, (2021): 1687-8434.
- [2] Romaguera-Barcelay, Yonny, et al., *Applied Sciences*, 11.9 (2021): 3886.
- [3] Romaguera-Barcelay, Yonny, et al., *Thin Solid Films*, 564 (2014): 419-425.

ACKNOWLEDGMENTS

The authors thank Fundação de Amparo à Pesquisa do Estado do Amazonas (FAPEAM) for the financial support, as well as UFAM for the Analytical Center infrastructure.

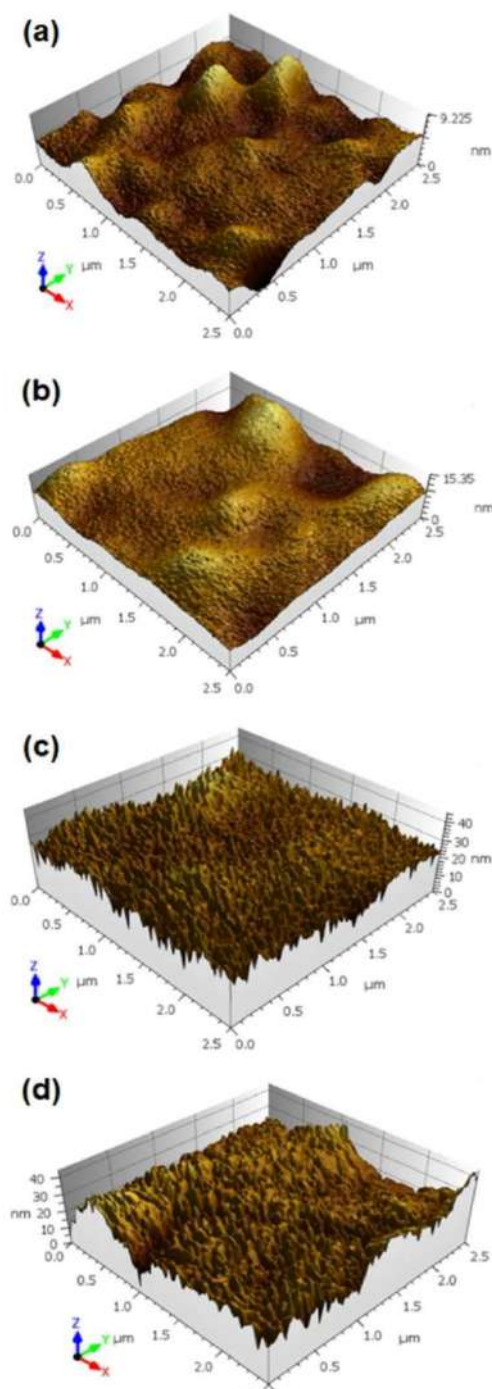


Fig. 1. AFM micrographs of a) DMO650, b) DMO750, c) DMO800, and d) DMO850.

Table 1. Parameters of the nanoscale topography of the samples.

Parameter	DMO650	DMO750	DMO800	DMO850
Sq (nm)	1.331±0.226	1.949±0.188	3.694±0.325	3.988±0.246
Ssk (-)	0.644±0.392	0.167±0.105	-0.102±0.098	-0.244±0.166
Sku (-)	4.931±0.852	5.361±1.071	3.648±0.622	4.015±0.489



Stereometric Analysis of Amazon Rainforest *Anacardium occidentale* L. Leaves

Glenda Quaresma Ramos¹, Heloísa David Yasumura², Cíndel Cavalcante de Souza²,
Henrique Duarte da Fonseca Filho^{2,*}

¹ Postgraduate Program in Tropical Medicine, Fundação de Medicina Tropical, State University of Amazonas, Manaus, AM, Brazil

² Federal University of Amazonas-UFAM, Laboratory of Synthesis of Nanomaterials and Nanoscopy, Physics Department, Manaus, Amazonas, Brazil.

[*hdffilho@ufam.edu.br](mailto:hdffilho@ufam.edu.br)

Cashew tree, more specifically *Anacardium occidentale* L., which is widely distributed in Amazon rainforest regions, belongs to family Anacardiaceae [1], is a strategic plant that has great value in the international food market due to their derived products. Besides this, some biological properties have been widely studied, as antioxidant and antimicrobial activities [2]. In this work, morphology, and power spectrum density of both sides of the *Anacardium occidentale* L. leaf were carefully studied. We used three different microscopy techniques such as scanning electron microscopy, profilometry, and atomic force microscopy for a complete description of the leaf surface morphology. The morphology of the adaxial and abaxial sides revealed a surface composed of striated cuticles and stomata cells, respectively. The height parameters obtained by profilometry revealed that the abaxial side was rougher. However, both sides presented similar Gaussian height distribution and asymmetry. The advanced stereometric parameters obtained by the topographic maps of AFM revealed that the two sides have some singularities due to their different morphologies and roughness, but with similar microtextures. However, average PSD spectra showed that adaxial and abaxial sides are dominated by relatively low and high spatial frequencies, showing that the microtextures, unlike what was shown in stereometric parameters, are different. These results revealed that leaves surface morphology under different aspects and scales and the quantitative parameters confirmed the different spatial patterns displayed, which can be of great interest for the study of the biological behavior of plants from their leaves. This fundamental insight showed that morphology and microtexture of the leaves can be fully explored by microscopy and provide sufficient parameters to differentiate their physical properties. Therefore, our work can help, as a complementary tool, to study the behavior of plants from the morphology and microtexture of their leaves.

REFERENCES

- [1] Ramos GQ, Cotta EA, da Fonseca Filho HD (2016a) Studies on the ultrastructure in *Anacardium occidentale* L. leaves from Amazon in northern Brazil by scanning microscopy. *Scanning* 38:329–335.
- [2] Ifesan B (2013) Antioxidant and Antimicrobial Properties of Selected Plant Leaves. *European J Med Plants* 3:465–473.

ACKNOWLEDGMENTS

The authors thank Coordenação de Aperfeiçoamento de Pessoal de Nível Superior (CAPES) for the financial support, as well as the use of the infrastructure of the Analytical Center of Universidade Federal do Amazonas (UFAM).

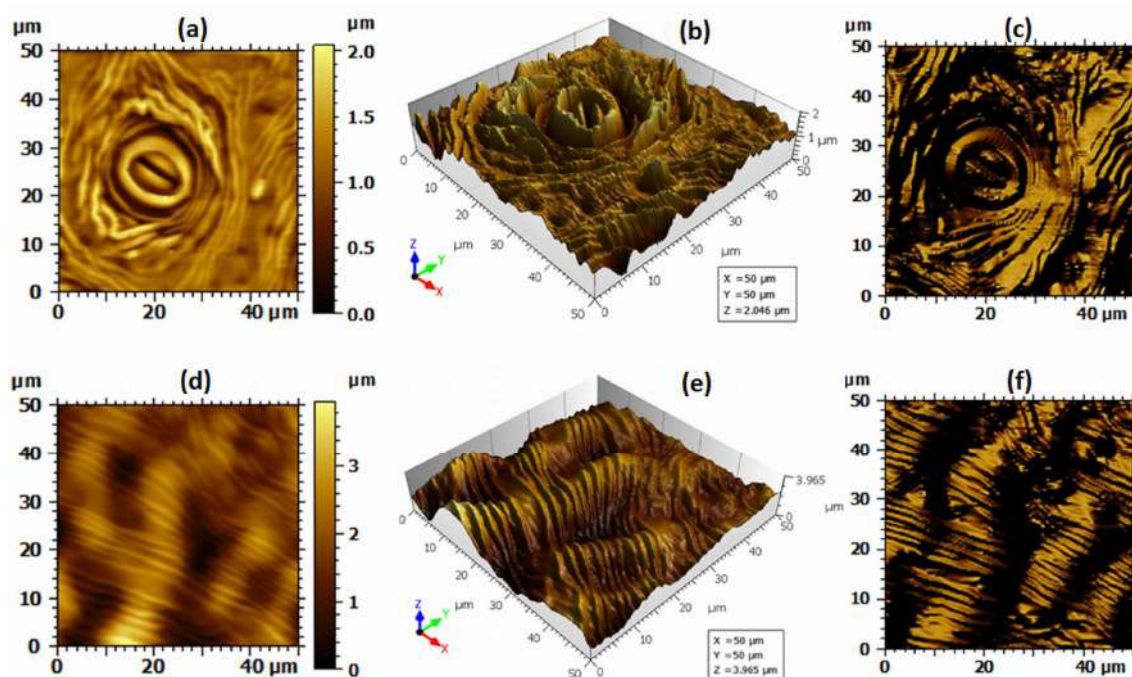


Figure 3. Representative 2D and 3D atomic force micrographs and texture photosimulations ($40 \times 40 \mu\text{m}^2$) of the leaf surface for a-c) abaxial and d-f) adaxial sides.

Table 1. Relevant roughness and height parameters for the abaxial and adaxial leaf surface from profilometry images.

Parameter	Unit	Abaxial	Adaxial
Sq	[μm]	3.294 ± 1.234	1.7535 ± 0.1127
Sa	[μm]	2.72 ± 1.19	1.3829 ± 0.093
Ssk*	[-]	0.127 ± 0.104	0.0772 ± 0.4648
Sku*	[-]	0.202 ± 1.121	1.037 ± 2.132
Sp*	[μm]	12.697 ± 2.13	8.068 ± 3.9961
Sv	[μm]	10.879 ± 1.953	6.472 ± 0.5813
Sz	[μm]	23.576 ± 3.916	14.541 ± 3.790

*Samples without significant difference ANOVA One-Way and Tukey Test ($p < 0.05$).



Hexamethyldisiloxane Plasma Coating On Fabric Surfaces To Be Used In The Manufacture Of Mask Against COVID- 19

Leonardo Pereira Pacheco^{1*}, Sílvia Renata de Souza Marski¹, Audrey Wallace da Costa Barros², Carlos Alberto Achete³, Maíra do Prado¹, Renata Antoun Simão²

¹Curso de Odontologia, Universidade Veiga de Almeida (UVA), Rio de Janeiro-RJ, Brasil.

²Programa de Engenharia Metalúrgica e de Materiais, Universidade Federal do Rio de Janeiro (UFRJ), Rio de Janeiro, RJ, Brasil.

³Divisão de Metrologia de Materiais, Instituto Nacional de Metrologia, Qualidade e Tecnologia -INMETRO, Rio de Janeiro-RJ, Brasil.

*lpachecodr@gmail.com

Respiratory protection and social distance are recommended as a form to prevent COVID-19[1]. The use of fabric masks was recommended to the population in general due to the shortage of respirators and surgical masks [2]. However, studies contest the quality and performance of the mask filtration [3,4]. Hexamethyldisiloxane plasma (HMDSO) has been used to cover surfaces, giving them hydrophobic characteristics, antimicrobial effect with reduced toxicity [5,6]. The aim of this study was to evaluate the HMDSO plasma coating on fabric surfaces to be used in the manufacture of masks, and the effect of washing on the covering. Samples of 400-thread count cotton fabric were used. In experimental group, the fabric was covered with a layer of HMDSO employing the plasma enhanced chemical vapor deposition (PECVD). Optical Microscopy and Atomic Force Microscopy (AFM) were used for topographic analysis. The assessment of the level of hydrophobicity was performed using contact angle measurements, employing the Ramé-Hart goniometer. The absorption time was measured from the moment the drop of water was deposited on the fabric up to 10 minutes. To evaluate the effect of washing on the covering, 7 washing cycles were performed, following a protocol proposed by the World Health Organization. All experiments were performed in triplicate. For the statistical analysis, the Kruskal-Wallis and Dunn tests were used. In the topographic analysis, after covering with HMDSO plasma, a layer of small granules agglomerated on the original surface of the fabric were visualized. The fabric, which initially had a 0° contact angle value, presented angles of 120° after the covering. The water absorption time in the tissue, which was immediate for the tissue, reached the maximum estimated time of 10 minutes after coating. By the seventh wash, the surface remained hydrophobic, with a decrease in the contact angle after the 5th washing and a reduction in the water absorption time in the fabric in the 7th. It was concluded that the use of cotton fabric coated with HMDSO plasma proved to be adequate for the manufacture of protective masks, since the coating made the surface hydrophobic and this property is maintained even after the washes.

Acknowledgements: FAPERJ



References:

- [1] Ha JF. The COVID-19 pandemic, personal protective equipment, and respirator: a narrativereview. *International Journal of Clinical Practice*. 2020.
- [2] Davies A, Thompson KA, Giri K et al. "Testing the Efficacy of Homemade Masks: Would They Protect in an Influenza Pandemic?" *Disaster Medicine and Public Health Preparedness* 2013; 7(4):413–418.
- [3] Clapp, P. W. et al. Evaluation of Cloth Masks and Modified Procedure Masks as Personal Protective Equipment for the Public During the COVID-19 Pandemic *JAMA Intern Med*. 2020 Dec 10; e208168
- [4] Whiley, H. et al. Viral Filtration Efficiency of Fabric Masks Compared with Surgical and N95 Masks Pathogens. 2020 Sep 17; 9(9):762.
- [5] Yang, J. et al. Fabrication of Durably Superhydrophobic Cotton Fabrics by Atmospheric Pressure Plasma Treatment with a Siloxane Precursor. *Polymers (Basel)*. 2018 Apr 22;10(4):460.
- [6] Bastos, D. C. et al. Inducing surface hydrophilization on cornstarch film by SF6 and HMDSO plasma treatment. *Carbohydr Polym*. 2013 Jan 16;91(2):675-81. Epub 2012 Aug 1.

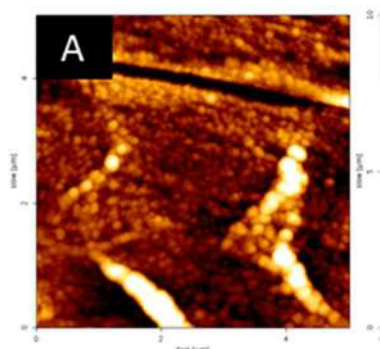


Figure 1 - Topography image (5 x 5 μm^2) of cotton treated with HMDSO plasma.

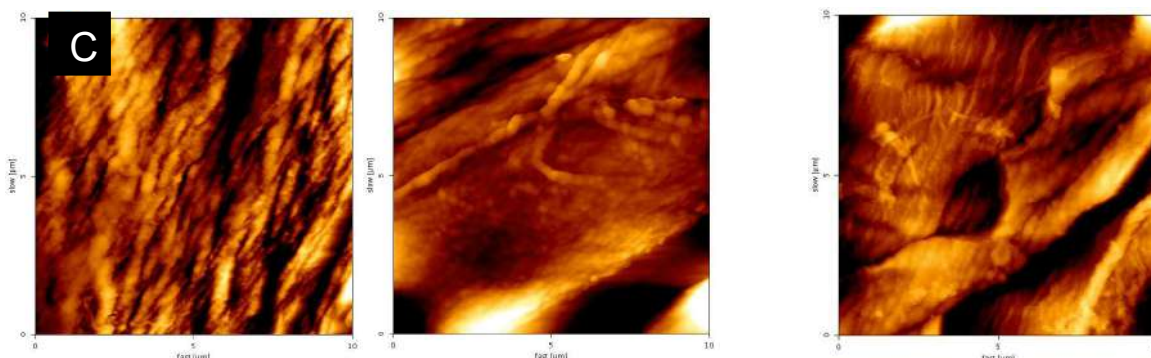


Figure 2 - Topography images of untreated cotton (A), cotton treated with HMDSO plasma (B), and after 7th washes (C).

Table 1: Median values of contact angle measurement (degrees) and absorption time (minutes)

RESULTS								
MEDIAN	HMDSO T0	WASH 1	WASH 2	WASH 3	WASH 4	WASH 5	WASH 6	WASH 7
ANGLE OF CONTACT (°)	124,2 A	122,09 A	113,6 A	122,7 A	115,8 A	102,9 B	103,7 B	99,72 B
TIME OF ABSORPTION (')	10 A	10 A	9,5 A	10 A	5,4 A	4,5 A	3,3 A	4,1 B

Different letters in the row indicate significant values (Dunn's test $p < 0,05$)



2D talc nanosheets obtained via liquid phase exfoliation.

Mariana C. Prado^{1*}, Helane O. Morais², Samuel M. Sousa², Joyce C. Santos³, Ana Paula M. Barboza¹, Elisângela S. Pinto⁴, Bernardo R. A. Neves³.

¹ Universidade Federal de Ouro Preto, Physics Department, Ouro Preto - Brazil.

² Instituto Federal de Minas Gerais, *Campus* Santa Luzia, Santa Luzia - Brazil

³ Universidade Federal de Minas Gerais, Physics Department, Belo Horizonte - Brazil.

⁴ Instituto Federal de Minas Gerais, *Campus* Ouro Preto, Ouro Preto - Brazil

*mariana.prado@ufop.edu.br

The rapid evolution of characterization and production techniques has been enabling the obtention of several new two-dimensional (2D) nanomaterials. This class of low dimensional, nanoscale materials has been in the spotlight since graphene was first obtained isolated on top of a silicon dioxide substrate. A less explored class of materials that yields 2D nano-sheets are the phyllosilicate minerals, which are formed by parallel sheets of silica tetrahedra with a 2:5 Si to O ratio. Among those, talc is a hydrated magnesium silicate with chemical formula $Mg_3Si_4O_{10}(OH)_2$ with numerous industrial applications and abundant in Minas Gerais (Brazil). Alencar et al [1]. reported the experimental and theoretical characterization of nanotalc sheets. Elastic modulus and breaking strength are of the same order of magnitude of the values reported for graphene. In the present work, liquid-phase exfoliation (LPE) was employed to obtain 2D nanosheets of talc. This route enables the production of large quantities of exfoliated material (compared to mechanical exfoliation) and size selection can be performed with the usage of a centrifuge, as reported by Backes et al [2]. Given its scalability, LPE is of considerable interest as a nanomaterial production route for technological applications, but many parameters must be optimized for each material and experimental setup. We investigated talc exfoliation in an ultrasonic bath employing different mediums: aqueous solutions of anionic and nonionic surfactants and organic solvents. The mineral sample was obtained directly from a mining site, milled, and subjected to a simple cleaning process. The nanosheets' suspensions obtained with four different mediums were deposited onto a silicon substrate and atomic force microscopy was employed to characterize the lateral and thickness distribution of the exfoliated flakes. Figure 1 illustrates the results. Flake dimensions were measured in the AFM images and statistics were performed on thousands of flakes for each route revealing minor differences in average flake size. This analysis procedure was reported by Fernandes and co-workers [3]. All routes employed can be used to obtain suspension of few layers nanosheets, with an average thickness of 5 nm or less. As follows, the exfoliation medium can be selected on the desired application demand basis.

[1] A. B. Alencar et al., *2D Materials* 2, (2015) 015004.

[2] C. Backes et al., *Chemistry of Materials* 20 (2017) 243–255.

[3] T. F. D. Fernandes et al., *2D Materials* 7, (2020) 025045.

[4] This research was supported by CNPq, CAPES, FAPEMIG, Rede Nacional de Pesquisa em Nanotubos de Carbono, Instituto Nacional de Ciência e Tecnologia (INCT-Nano-Carbono), and PRPPG-IFMG.

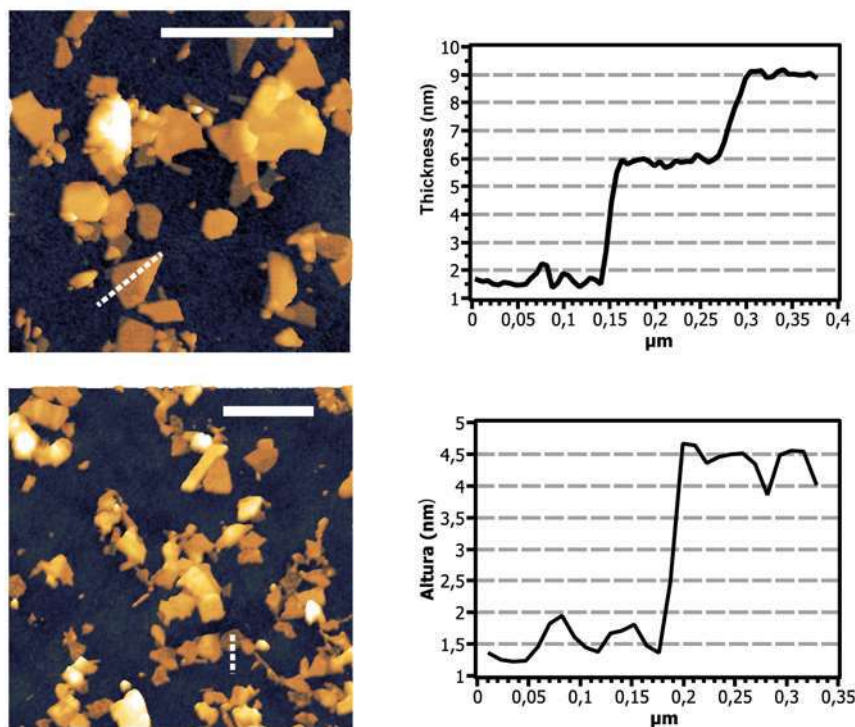


Figure 1 - AFM images illustrating the results for talc exfoliated in 6mg/ml sodium cholate solution (high-density deposition). The dotted white lines in the images correspond to the height profiles shown in the graphics. Most of the flakes in the image are below 10 nm thickness, demonstrating the exfoliation of talc to few-layers flakes. Vertical scale: 20 nm. Scale bar: 750 nm.



Mechanical Properties Characterization of Human Hair Fibers Cortex Region by Multi-parametric Atomic Force Microscopy Mapping

Raissa L. Oblitas^{1*}, Flávio B. Camargo Jr², Wagner V. Magalhães², Maria Cecília Salvadori¹

¹ Instituto de Física, Universidade de São Paulo, SP, Brazil.

² Departamento de Pesquisa e Desenvolvimento, Chemyunion LTDA, Sorocaba, SP, Brazil.

*raissa.oblitas@usp.br

In the development of cosmetic products for hair fibers, macroscopic characterizations of the mechanical properties analysis play an important role. In order to understand the damage caused by treatments or external agents, as well as to evaluate the performance of cosmetic actives, sophisticated techniques have been used. The characterization of nanostructures and organization at the cellular level have been investigated to understand the potential roles of cortex cells in defining the mechanical properties of hair [1-3]. This work shows the evaluation of the effectiveness of a cosmetic active, considering human hair fibers without and with chemical damage caused by bleaching process. For chemically damaged samples, product with and without cosmetic active (placebo and active group) was applied. The fibers were embedded in epoxy resin and cuts were made by ultramicrotomy, for observing cross-sections by Transmission Electron Microscopy (TEM). The resin block surface from the cut with exposed hair fiber cross-section, was used for the characterization by Atomic Force Microscopy (AFM) (Figure 1). Mechanical properties of the fibers cross-section surface were characterized by AFM, in Force Volume (FV-AFM) mode. FV-AFM records a force-distance curve (FC) at each point of the scan, obtaining a 2D matrix of FCs associated with topographic images. Each FC generates adhesion force between probe and sample, maximum sample deformation by the probe and Young's modulus (E) data. The fiber and resin data were obtained simultaneously in a map for the purpose of having the resin data as a reference, to ensure a coherent comparison between the fibers groups. To compare the fibers groups, statistical evaluations were performed using the ANOVA (Analysis of Variance) method, considering the significance level $\alpha = 0.05$ (5%). We found that the fibers group, with chemical damage caused by bleaching process (control group), showed a statistically significant decrease in the natural logarithm of Young's modulus ($\ln(E)$) concerning to the virgin fibers group and, the active group presented an increase of ($\ln(E)$), concerning to the control group and placebo group. Our results demonstrated the fiber degradation of the control group with chemical damage, corroborating with TEM analysis; and the application of the product with active was effective in improving the Young's modulus of the damaged fiber. We also found a radial decrease of $\ln(E)$ along the cross-section of the active group fiber, which is compatible with the results obtained by Confocal Raman Spectroscopy analysis [4], that presented variation of the active permeation along the

depth, starting from the hair fiber surface. It is worth mentioning that the Young's modulus was also determined by Tensile Tester, in which it was not possible to verify statistically significant differences between the groups, evidencing the advantage of the FV-AFM analysis. We also found the prevalence of decrease of $\ln(E)$ for higher adhesion force between tip and sample, using Pearson's correlation coefficient analysis. This result may corroborate with the presence of differentiated adhesive structures (Cell Membrane Complex - CMC with low cystine contents), which have low Young's modulus. Systematic studies using AFM of mechanical properties, identifying nanostructures, would be relevant for the development of cosmetics. The effort to understand better the chemical and physical damage caused by environmental agents or treatments would elucidate interactions between cosmetic active components and internal substructures of the hair fibers [5].

REFERENCES

- [1] H. Kitano et al., *Compos Interfaces*. 16 (2009) 1–12.
- [2] D.P. Harland et al., *J Struct Biol*. 185 (2014) 397–404.
- [3] C. Kunchi et al., *Fibers Polym*. 20 (2019) 1538–1545.
- [4] F. Camargo et al., *29th IFSCC Congress*. (2016)
- [5] This research was supported by Chemyunion Ltda (Brazil) and University of São Paulo. We are grateful to workers at the Laboratório de Filmes Finos of the Institute of Physics, University of São Paulo (LFF - IF USP) for support throughout the experiments.

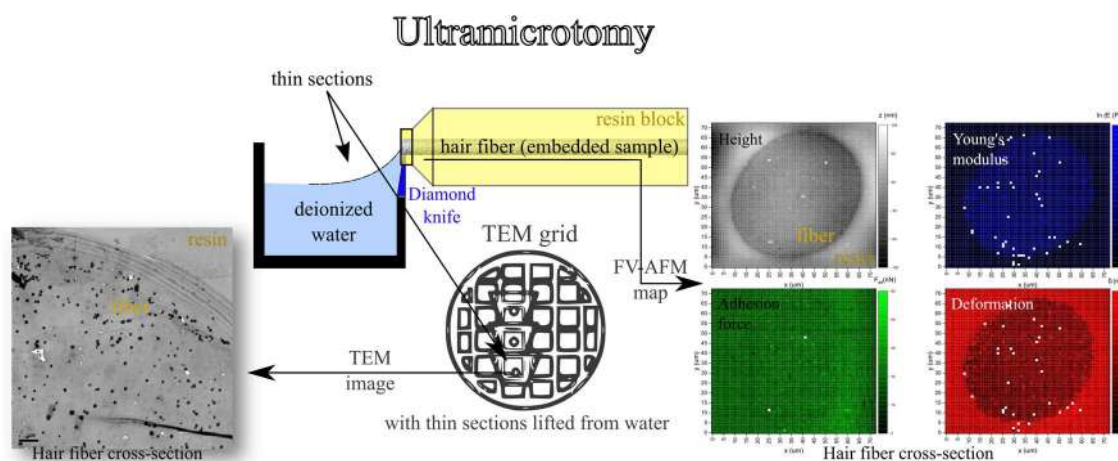


Figure 1: Schematic drawing of sample preparation, obtaining ultrathin sections of hair fiber embedded in epoxy resin, by ultramicrotomy. An example of TEM image and FV-AFM map (topographic image, $\ln(\text{Young's modulus})$, adhesion force between probe and sample and maximum sample deformation by the probe) is shown of hair fiber cross-section.



Analysis of Surface Nanostructures Induced by Slow Highly-Charged Ions in Thin Polymer Films by SFM

R. Thomaz^{1*}, F. V. Filho¹, J. P. M. May¹, M. Schleberger² and R. M. Papaléo¹

¹ Interdisciplinary Center of Nanoscience and Micro-Nanotechnology, School of Technology, Pontifical Catholic University of Rio Grande do Sul, PUCRS, Porto Alegre, Rio Grande do Sul, Brazil

² Fakultät für Physik, Universität Duisburg-Essen, 47048 Duisburg, Germany

*raquel.thomaz@pucrs.br

In this work, surface nanostructures formed by single highly-charged ions (HCI) on ultrathin polymer films were systematically investigated by means of atomic force microscopy (AFM). The size and shape of the impact features produced by 260 keV Xe^{q+} ions ($q=33-40$) on poly(methyl methacrylate) (PMMA) were studied as a function of the thickness h of the layer ($3 < h < 60$ nm). The polymer layers were spin-coated from anisole solutions onto Si substrates (with a ~ 2 nm native oxide layer). Irradiations were performed at the University of Duisburg using the HICS beamline under perpendicular incidence. The size and shape of the single-ion impact features and the thicknesses of the samples were characterized employing scanning force microscopy in the peak force mode under ambient conditions. The tips used were Scan Asyst-air from Bruker with a nominal radius of 2 nm. The linear dimensions of the rims and craters were obtained using the NanoScope software (Bruker Corporation, Santa Barbara, CA). The nanostructures induced by the HCI on thin polymer films are shallow cavities (craters), Figure 1, ~ 10 nm in diameter and roughly 1-2 nm deep, similar to previously reported results [1]. Both crater diameter, D_{crater} , and crater depth, Z_{crater} , showed very little changes even for very thin samples of ~ 3 nm. This behavior was seen for all charge states (potential energy) applied. These findings indicate that the entire potential energy of the HCI is deposited into the first few nanometers close to the surface and that the formation of the nanostructures do not involved material excited deeply in the films. There are, however, some metrological challenges for measuring shallow cavities of diameters close to 10 nm using SFM. The natural roughness of the samples, may look similar to the features created by the individual ion impacts, making the edges of the nanostructures difficult to define with high accuracy. This may introduce distortions in the scaling of the impact features size with film thickness, especially for the ultrathin films, which are also going to be discussed.

REFERÊNCIAS

[1] R. Ritter et al., Europhysics Letters 97 (2012).

AGRADECIMENTOS

O presente trabalho foi realizado com apoio da FAPERGS, da CAPES e do CNPq.

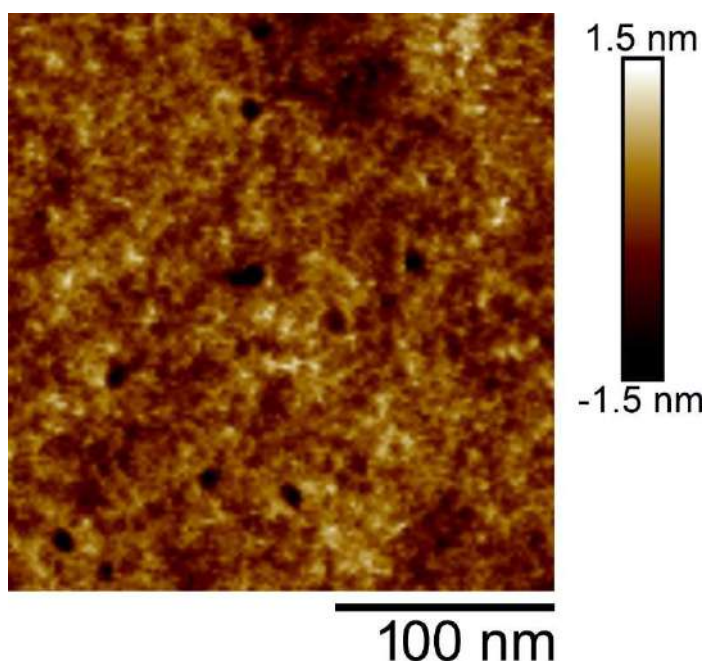


Figure 1 Representative AFM image showing individual impact features (dark circular areas) produced by 260 keV Xe^{33+} highly-charged ions on ~ 50 nm-thick PMMA film.



Instance Segmentation of Quartz in Iron Ore Optical Microscopy Images by Deep Learning

Bernardo Amaral Pascarelli Ferreira^{1*}, Thalita Dias Pinheiro Caldas¹, Karen Soares Augusto¹, Sidnei Paciornik¹ and Julio Cesar Alvarez Iglesias²

¹ Department of Chemical and Materials Engineering, Catholic University of Rio de Janeiro (DEQM-PUC-Rio), Rio de Janeiro, Brazil.

² Strategy, Analytics and M&A, Deloitte, Rio de Janeiro, Brazil.

*bernardoamaral@aluno.puc-rio.br

Iron ore characterization is essential for the mineral industry, since it provides relevant information, such as ores' chemical composition and the textural and morphological aspects of particles, required for designating a proper mineral processing route [1]. Reflected Light Optical Microscopy (RLOM) is typically used in this field, given that the technique allows identification of mineral phases by their different reflectances, in a fast and low-cost procedure. In the last decade, many methodologies based on Digital Microscopy and Digital Image Processing were developed to automate microstructure characterization, in order to improve time-consumption and errors associated with the subjective analysis performed by a human operator [2][3]. However, among other limitations, correct identification of quartz particles became a huge obstacle for simple image segmentation methods, due to the material transparency, property that makes quartz display a similar hue to the resin used for sample mounting. Despite the difficulty for classical image processing techniques, quartz particles can still be visually identified by specialists, which demonstrates that there are features that make its recognition somehow possible. Some studies involving attempts to overcome this difficulty have been made [4][5]. Amid the proposed solutions, the application of Convolutional Neural Networks (CNNs) to categorize images of quartz particles and pure resin regions, revealed excellent and promising results. However, in this procedure, it isn't possible to segment quartz particle in an image containing other mineral classes [6]. Hence, the present work proposes the development of a methodology capable of identifying all quartz particles in iron ore optical microscopy images by instance segmentation employing a state-of-the-art deep learning (DL) algorithm called Mask R-CNN [7]. Figure 1 shows a bright field optical microscopy image of an iron ore sample with quartz particles manually tagged in the VGG Image Annotator (VIA) interface [8]. This tagging process composes the necessary dataset for the training and validation of the model. Until now, the dataset used contains just 535 quartz particles. Even though training DL models requires extensive datasets, the main metrics obtained so far are reasonable: Precision = 72,39%, Recall = 65,19% and F1 Score = 68,6%. Furthermore, Figure 2 displays an excellent detection of quartz particles performed by the generated model, confirming that expanding the training set and optimizing the neural network parameters should provide even better outcomes. It is noteworthy that these are preliminary results, since this research is under development.



REFERENCES

- [1] L. Lu, *Iron Ore: Mineralogy, Processing and Environmental Sustainability*, nº 66. Woodhead Publishing, 2015.
- [2] O. da F. M. Gomes, J. C. A. Iglesias, S. Paciornik, and M. B. Vieira, “Classification of hematite types in iron ores through circularly polarized light microscopy and image analysis,” *Miner. Eng.*, vol. 52, pp. 191–197, 2013.
- [3] J. C. Á. Iglesias et al., “Automatic characterization of iron ore by digital microscopy and image analysis,” *Integr. Med. Res.*, vol. 7, no. 3, pp. 376–380, 2018.
- [4] R. M. Castellanos, J. C. Á. Iglesias, O. da F. M. Gomes, K. S. Augusto, e S. Paciornik, “Characterization of iron ore pellets by multimodal microscopy and image analysis”, *REM - Int. Eng. J.*, vol. 71, nº 2, p. 209–215, abr. 2018.
- [5] I. D. Delbem, R. Galéry, P. R. G. Brandão, e A. E. C. Peres, “Semi-automated iron ore characterisation based on optical microscope analysis: Quartz/resin classification”, *Miner. Eng.*, vol. 82, p. 2–13, 2015.
- [6] J. C. Á. Iglesias, R. B. M. Santos, and S. Paciornik, “Deep learning discrimination of quartz and resin in optical microscopy images of minerals,” *Miner. Eng.*, vol. 138, no. December 2018, pp. 79–85, 2019.
- [7] K. He, G. Gkioxari, P. Dollár, and R. Girshick, “Mask R-CNN,” 2018.
- [8] A. Dutta and A. Zisserman, “The VIA annotation software for images, audio and video,” *arXiv*, pp. 1–8, 2019.
- [9] This research was supported by CNPq, CAPES and FAPERJ.

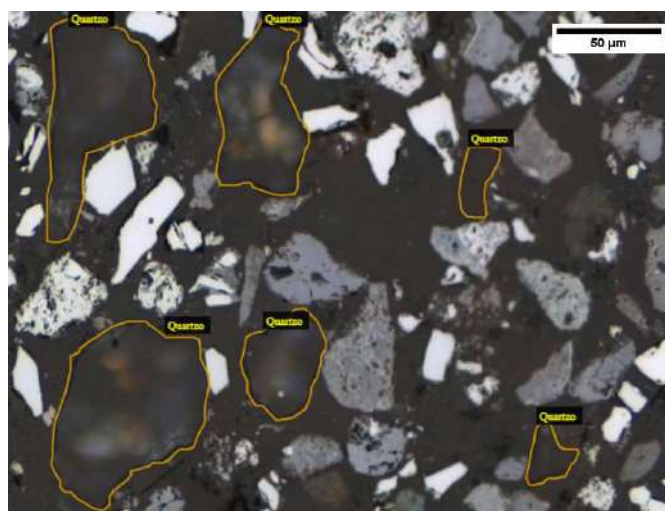


Figure 1 – Iron ore image with quartz particles manually tagged using VIA [8].

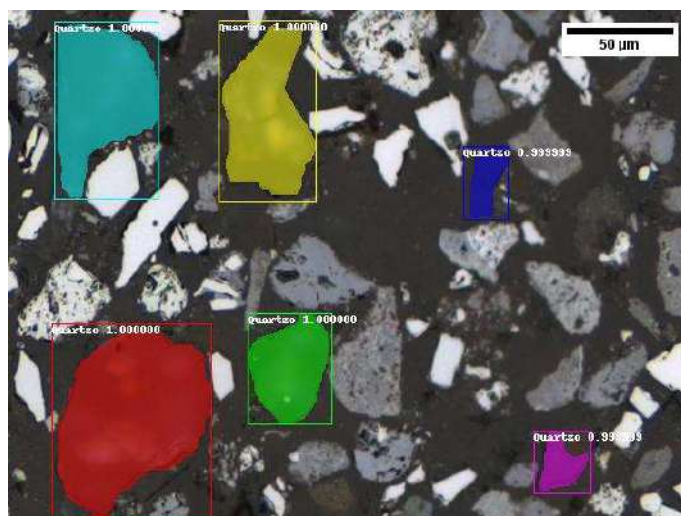


Figure 2 - Detection and instance segmentation of quartz particles performed by the trained deep learning model.



Automatic Iron Ore Characterization by Digital Microscopy and Machine Learning Tools.

Thalita Dias Pinheiro Caldas^{1*}, Bernardo Amaral Pascarelli Ferreira¹, Karen Soares Augusto¹, Sidnei Paciornik¹, Julio Cesar Alvarez Iglesias² and Alei Leite Alcântara Domingues³

¹ Department of Chemical and Materials Engineering, Catholic University of Rio de Janeiro (DEQM-PUC-Rio), Rio de Janeiro, Brazil.

² Strategy, Analytics and M&A, Deloitte, Rio de Janeiro, Brazil.

³ CTF/VALE, Nova Lima, Minas Gerais, Brazil.

*thalitadpc@aluno.puc-rio.br

Iron ore is found in nature as an aggregate of minerals with commercial value. Brazilian ore is mainly composed of hematite, but can also contain magnetite, goethite, and quartz. It has a higher quality than other ores due to the large amount of hematite, as this mineral has a high iron content (69.9%) [1]. Iron ore is typically characterized by reflected light optical microscopy. However, this characterization is not simple due to the wide variety of morphologies and texture of the particles present [2]. For example, hematite, may appear as compact and porous particles. Compact particles can be monocrystalline or polycrystalline. In the case of polycrystalline particles, the internal crystals have different morphologies normally identified as granular, lamellar, and lobular. The porous particles can be microcrystalline or martite [3]. Aiming at automating iron ore characterization, methodologies have been developed using Digital Microscopy and Image Processing and Analysis. However, correct particle segmentation and classification was a recurrent problem. Some studies used machine learning tools to overcome these difficulties [4], but these methods require the choice of non-intuitive parameters for attribute extraction that often depend on a segmentation. Convolutional Neural Networks (CNNs) to segment and classify images have shown excellent results [5][6]. CNNs automatically extract this necessary information through a series of convolutions. The main objective of the present study is to develop a new methodology for mineral characterization using an algorithm called Mask R-CNN [7]. The methodology must be able to detect, classify and segment minerals in the iron ore images. Until now, this method has been trained for the compact hematite, martite and goethite. Figure 11 shows a typical brightfield optical microscopy image of a pellet feed sample manually tagged in the VGG Image Annotator (VIA) [8] interface, with the respective mineral classes to serve as a training dataset for the Mask R-CNN. The training was carried out with 4425 particles of compact hematite, 769 of martite and 519 of goethite. The compact hematite class is the best represented in the training set, but it will still be necessary to increase the number of the other classes. This is reflected in the metrics obtained over the test dataset: precision = 73.59%, recall = 77.72% and F1-score = 75.60%. Figure 12 shows the output of the trained network with a good classification and detection of objects. It is worth mentioning that this research is under development and these results are preliminary, but sufficient to generate good prospects.

REFERENCES

- [1] A. et al Babich, Iron Ore, vol. 66. Brisbane, 2015.
- [2] E. Donskoi, A. Poliakov, J. R. Manuel, M. Peterson, and S. Hapugoda, "Novel developments in optical image analysis for iron ore, sinter and coke characterisation," Trans. Institutions Min. Metall. Sect. B Appl. Earth Sci., vol.



- 124, no. 4, pp. 227–244, 2015.
- [3] J. C. Á. Iglesias et al., “Automatic characterization of iron ore by digital microscopy and image analysis,” *Integr. Med. Res.*, vol. 7, no. 3, pp. 376–380, 2018.
 - [4] O. da F. M. Gomes, J. C. A. Iglesias, S. Paciornik, and M. B. Vieira, “Classification of hematite types in iron ores through circularly polarized light microscopy and image analysis,” *Miner. Eng.*, vol. 52, pp. 191–197, 2013.
 - [5] J. C. Á. Iglesias, R. B. M. Santos, and S. Paciornik, “Deep learning discrimination of quartz and resin in optical microscopy images of minerals,” *Miner. Eng.*, vol. 138, no. December 2018, pp. 79–85, 2019.
 - [6] T. Svensson, “Semantic segmentation of iron ore pellets with Neural Networks,” Lulea University of Technology, 2019.
 - [7] K. He, G. Gkioxari, P. Dollár, and R. Girshick, “Mask R-CNN,” 2018.
 - [8] A. Dutta and A. Zisserman, “The VIA annotation software for images, audio and video,” arXiv, pp. 1–8, 2019.
 - [9] This research was supported by CNPq, CAPES and FAPERJ.

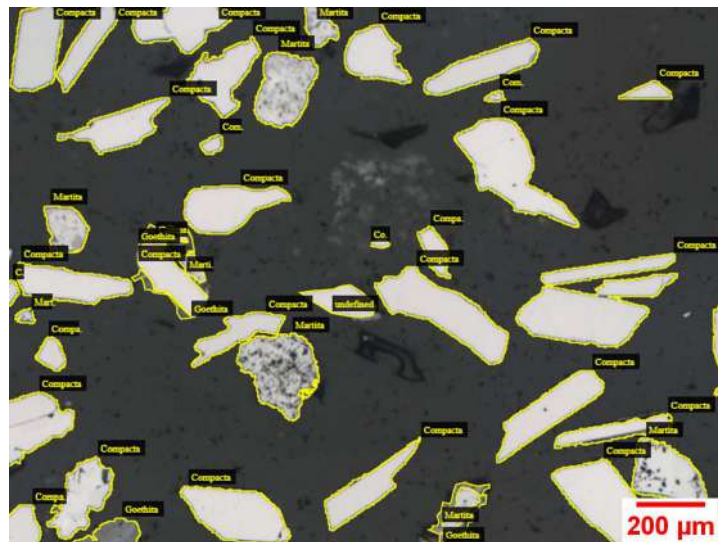


Figure 11 - Iron ore image manually tagged using VIA [8].

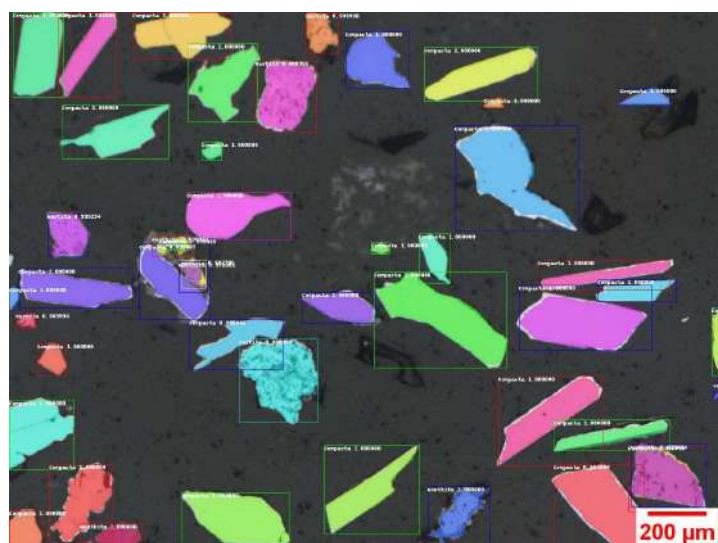


Figure 12 - Iron ore image containing detected, classified, and segmented minerals.



Methylene Blue Associated with Maghemite Nanoparticles has Antitumor Activity in Breast and Ovarian Carcinoma Cell Lines

Ana Luísa G. Silva^{1*}, Natália V. Carvalho¹, Leonardo G. Paterno², Ludmilla D. Moura³, Cleber L. Filomeno², Eneida de Paula³ and Sônia N. Bão¹

¹Department of Cell Biology, Institute of Biological Sciences, University of Brasília, Brasília/DF – Brazil.

²Laboratory of Research on Polymers and Nanomaterials, Chemistry Institute, University of Brasília, Brasília/DF – Brazil.

³Department of Biochemistry and Tissue Biology Laboratory, Institute of Biology, University of Campinas, São Paulo/SP – Brazil.

*iza_gouvea@hotmail.com

Cancer, a group of diseases responsible for the second largest cause of global death, is considered one of the main public health problems today [1,2]. Breast cancer, the second most common type, and ovarian cancer, which has the highest lethality when compared to other types of cancer on the female genital system, are those that stand out in women [2,3]. In this context, nanobiotechnology has been developed for early diagnosis and targeted drug delivery [4]. The present work suggests the association of methylene blue with maghemite nanoparticles (MAGCIT-MB) for the treatment of breast and ovarian cancer. In this work two different human breast carcinoma line (MDA-MB-231 and T-47D) and one ovary cancer line (A2780) were used. MAGCIT-MB was obtained by chemical reaction with maghemite and citric acid. Subsequently was added methylene blue to the solution. MAGCIT-MB presented a hydrodynamic diameter of 60,93 nm with a polydispersity index of 0,199 and zeta potential of -20,9 mV. *In vitro* studies showed that T-47D and A2780 cell lines, with the alamarBlue™ protocol, had a significant reduction in cell viability after treatment with MAGCIT-MB, event not observed in non-tumor lines (HNTMC and HUVEC) and MDA-MB-231. Flow cytometry, suggest that the main mechanism of endocytosis involved in the interiorization of MAGCIT-MB is the clathrin pathway and in transmission electron microscopy demonstrated the nanocomplex accumulated within lysosomes and/or endosomes, invagination of the cell membrane and expansion of the plasma membrane, indicating phagocytosis too. It can be observed by scanning electron microscopy and light microscopy the change in cell morphology. Experiments to evaluate ROS production confirm the cytotoxic mechanism caused by MAGCIT-MB. Studies carried out with separate compounds, show that the association between methylene blue and the magnetic nucleus is responsible for the therapeutic potential of the nanosystem to the treatment of breast and ovarian cancer *in vitro*, considering that methylene blue activity was more evident when coupled to the MAGCIT core.

[1] R. Siegel, et al., CA: A Can. Jou. For Clin. 68(1):7-30, 2018.

[2] P. Webb, et al., B. Prac. & Rese. Clin. Obst. & Gyne. 41:3-14, 2017.

[3] S. Pedraza-Arévalo, et al., The Prostate, 77(15):1499-1511, 2017.

[4] M. Goldberg, et al., Nat. Revi. Cancer, 19(10):587-602, 2019.

[5] This research was supported by CNPq, FAPDF, FINATEC and CAPES.

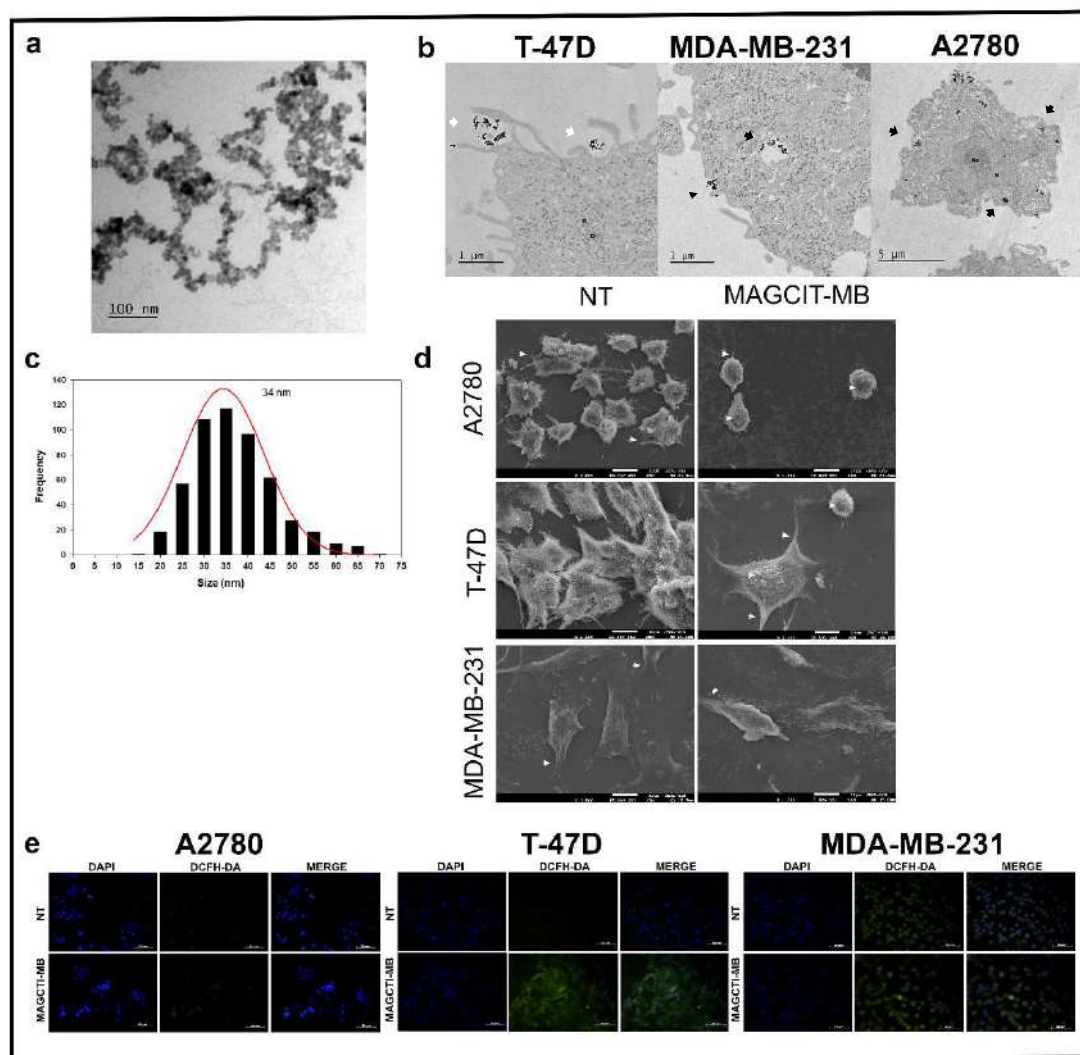


Fig 1. MAGCIT-MB ultrastructure, internalization, and activity in cell morphology. (a) Rounded morphology of MAGCIT-MB assessed by TEM at 80 kV. Scale bar = 100 nm. (b) Cancer cells ultrastructural images, obtained by TEM, demonstrate the localization of MAGCIT-MB in lysosome/endosome (black arrow) in cancer cell lines, in addition to the presence of cytoplasmic prolongation indicating phagocytosis (white arrow). Black arrowhead indicate the invagination of membrane, *N* nucleus, *No* nucleolus, *Er* Endoplasmic reticulum and *R* ribosomes. Scale bars = 5 μm and 1 μm . (c) Nanoparticle size distribution of MAGCIT-MB. (d) Scanning electron micrograph (SEM). NT (cells without treatment) and cells treated with MAGCIT-MB after 48 hours ($0.78 \mu\text{g}\cdot\text{mL}^{-1}$ of MB). Arrows indicate cell adhesion points and arrowheads, changes in the cell surface. Scale bar = 10 μm . (e) DCFH-DA visualized in cancer cell lines by fluorescence microscopy after 6 hours incubated with MAGCIT-MB. DNA counterstained with DAPI (blue) and cytoplasmic ROS generation with DCFH-DA (green). Scale bar = 50 μm .



Polyaniline-Gum Arabic Nanocomposite Compatibility with Physiological-Like Environment and Murine Cells

Jenifer P. Gonçalves¹, Anderson F. da Cruz¹, Carolina C. de Oliveira¹, Edvaldo da S. Trindade¹, Izabel C. Riegel-Vidotti², Marcio Vidotti², Fernanda F. Simas^{1*}

¹ Laboratory of Inflammatory and Neoplastic Cells, Cell Biology Department, Universidade Federal do Paraná (UFPR), Curitiba, Brazil.

² Macromolecules and Interfaces Research Group, Chemistry Department, UFPR, Curitiba, Brazil

* fernanda.simas@gmail.com

Polyaniline (PANI) is a conductive polymer investigated for many biotechnological applications. Colloidal PANI has specific physicochemical properties that make it suitable for topical or physiological applications, but one important limitation is its high hydrophobicity [1]. To increase colloidal stability in a physiological-like environment, PANI can be conjugated with different polymers. Considering that synthetic polymers biosafety is always cause for concern, in this study we used the heteropolysaccharide Gum Arabic (GA), which is a biopolymer extracted from acacia trees exudate and has been previously reported as a great stabilizer and dopant for PANI nanoparticles. For biological applications, studies about its cytotoxic potential are required. Therefore, we investigated PANI-GA compatibility with a biological environment and cultured cells. The PANI-GA nanocomposite was chemically synthesized (Fig. 1A) [2]. To analyze stability, PANI-GA was dispersed in cell culture medium (a protein-rich environment), and incubated in simulated cell culture conditions for 48h, and no aggregation was observed (Fig. 1B). Next, murine fibroblasts BALB/3T3 and macrophages RAW 264.7 were exposed to four concentrations of PANI-GA for up to 48h. Colorimetric assays were used for cell density (crystal violet staining), endomembrane viability (neutral red uptake), and mitochondrial activity (MTT assay) estimation. No significant interference was observed, except for mitochondrial activity in macrophages, which showed a concentration-dependent decrease (Fig. 1C). This result might indicate conducting PANI interference in mitochondrial electrons transport chain. In addition, cell granularity and morphology were analyzed, through flow cytometry and scanning electron microscopy, respectively. Fibroblasts did not show alteration in granularity (data not shown), but their morphology changed when treated with either GA or PANI-GA. In higher concentrations, nanocomposite deposition on top of the fibroblasts could be observed (Fig. 1D). Macrophage's granularity increased in PANI-GA higher concentration (Fig. 1E), indicating increase in nanoparticles uptake. In conclusion, PANI-GA is stable in cell culture conditions and non-cytotoxic for different cell lines.

REFERENCES:

- [1] G. Kashyap et al., *Bioorganic & Medicinal Chemistry Letters*, 29 (2019).
[2] Part of this abstract is published at J. P. Gonçalves et al., *Int J of Biological Macromolecules*, 173 (2021).

ACKNOWLEDGEMENTS: CAPES for student fellowship, Electron Microscopy Center of UFPR (CME-UFPR), and LabCet (ICC/Fiocruz) for kindly providing the BALB/3T3 cells.

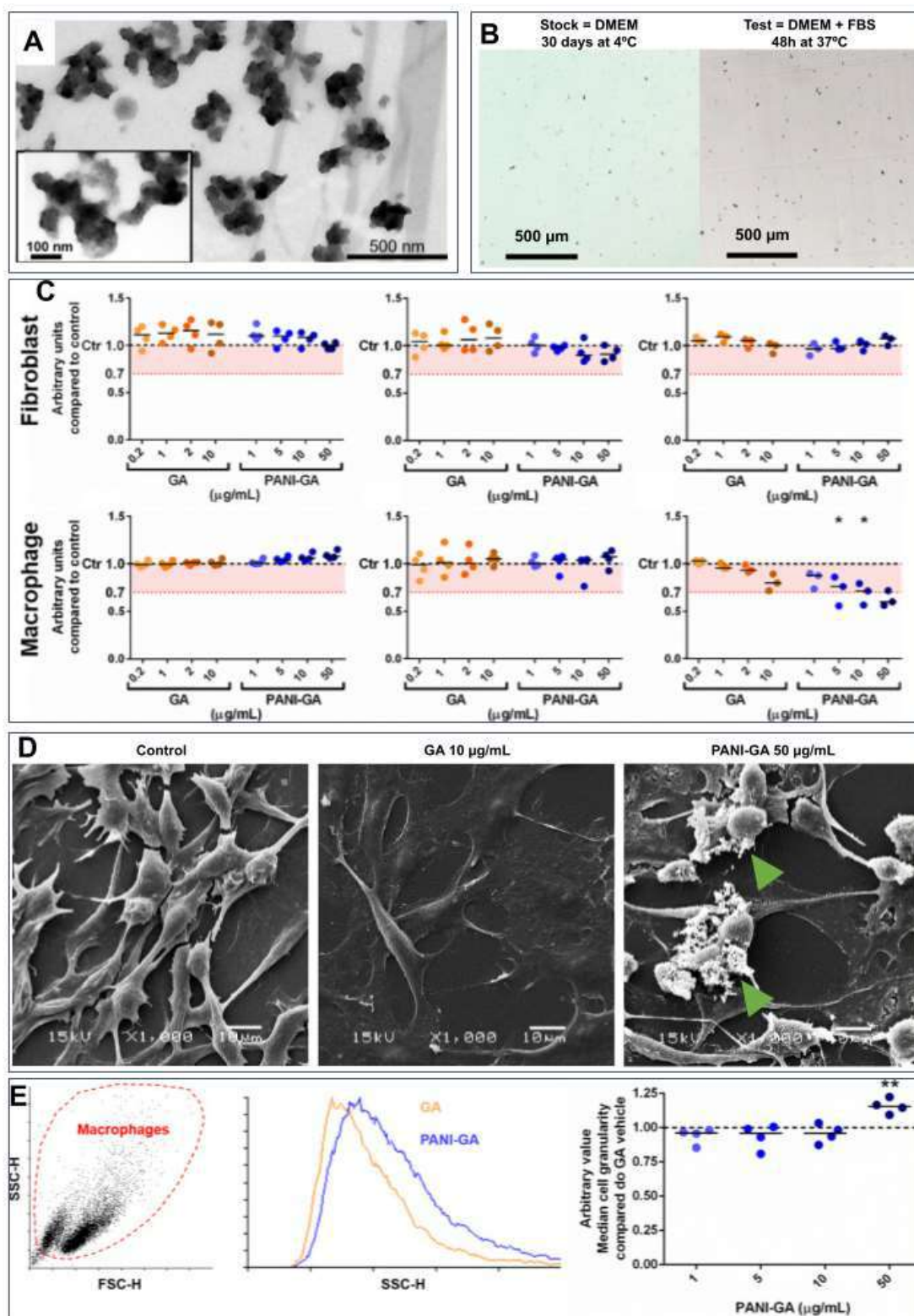


Figure 1. PANI-GA morphology and *in vitro* results. TEM image of PANI-GA (A); Light microscopy images of PANI-GA in stock solution and after incubation in a protein-rich environment (B); Colorimetric assays with fibroblasts and macrophages: PANI-GA treated groups were compared to the respective GA vehicle control (black dashed line, normalized as 1). Unpaired t-test, ** $p < 0.01$ (C); SEM of fibroblasts after exposure to GA or PANI-GA, arrows = sedimented PANI-GA (D); Macrophages granularity (E).



Post-Mortem Changes in Cenozoic Stromatolites from Hypersaline Lagoa Vermelha, Brazil

Carolina N. Keim

Instituto de Microbiologia Paulo de Góes, Universidade Federal do Rio de Janeiro (UFRJ), Rio de Janeiro, Brazil.
cnkeim@micro.ufrj.br

Stromatolites are laminated rocks found throughout the fossil record of the last 3.5 billion years. Observation of present-day growing stromatolites show that they originate from microbial mats, which are complex microbial ecosystems [1]. Once common in shallow aquatic environments, living stromatolites are now rare and restricted to extreme environments [1]. One of these environments was hypersaline Lagoa Vermelha in Rio de Janeiro State coast, Brazil [2]. Older reports accounted for living stromatolites and extensive microbial mats along Lagoa Vermelha beaches [2], although in the last decade only stromatolite skeletons have been observed [3, 4]. In order to unfold why did Lagoa Vermelha stromatolites die, how long they have been dead, and how did they change after death, samples were collected and analysed using microscopy techniques. **METHODS:** For light microscopy, stromatolite samples were air-dried, embedded in Spurr's resin, sliced, polished and mounted. Observation was done using crossed polarizers and epifluorescence. For scanning electron microscopy, samples were cut, polished, air-dried and observed with backscattered electrons (SEM-BSE). **RESULTS:** At fieldwork, upper stromatolite surfaces appeared green and slimy, with scattered barnacles. Barnacle shells were absent within stromatolite cores. Burrows about 1 mm wide occurred up to 1 cm from outer surfaces, whereas abundant microburrows 10 μm in diameter reached less than 1 mm into the stromatolites (Figure 1). Most microburrows were perpendicular to the outer stromatolite surfaces (Figure 1a). In some of them, burrowing microorganisms were lithified (Figure 1b). Fluorescence microscopy showed strong red fluorescence within some microburrows, indicating fresh organic materials and, probably, also chlorophyll (Figure 1c-d). Indeed, SEM showed fresh cell remains within some microburrows, indicating that cells were alive at the time of sample collection. Size, shape, color and fluorescence enabled the interpretation of microburrowing microorganisms as cyanobacteria. Localization at or close to outer surfaces indicate that burrowing cyanobacteria, as well as barnacles and burrowing animals colonised stromatolite surfaces after loss of the microbial mat coat. Microfossils within the stromatolite cores included foraminifera and ostracod shells (Figure 2). Based on ours and previous findings [5], we conclude that Lagoa Vermelha stromatolites died due to eutrophication. It happened a few years before we began fieldwork in 2013, and since their death the stromatolite mineral skeletons became colonised by barnacles, burrowing animals, and filamentous cyanobacteria.

REFERENCES

- [1] E.P. Suosaari et al., *The Depositional Record*, 5 (2019) 489.
- [2] J.A. Höhn et al., *Science of the Total Environment*, 58 (1986) 175.
- [3] L. Laut et al., *PLoS ONE*, 12 (2017) e0184819.
- [4] C.N. Keim et al., *Journal of Sedimentary Research*, 90 (2020) 887.
- [5] S. Pennafirme et al., *Regional Studies in Marine Science* 31 (2019) 100769.

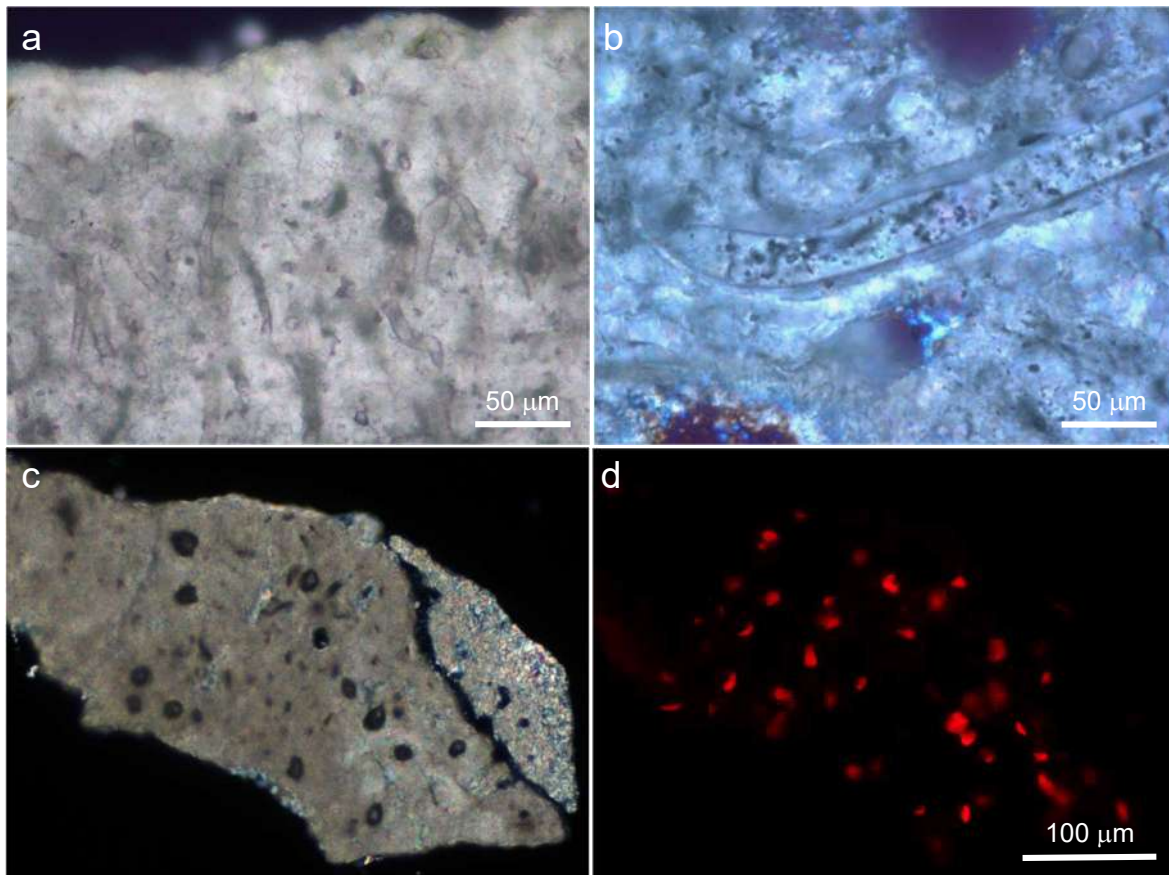


Figure 1: Light micrographs of outer stromatolite surfaces. (a) Microburrows roughly perpendicular to an outer stromatolite surface. (b) Lithified filamentous microorganism reminiscent of a cyanobacterium. (c-d) The same field was observed using polarized light (c) and epifluorescence (d). Note bright fluorescent spots co-localised with microburrows. (a-c) Crossed polarizers. (d) Epifluorescence.

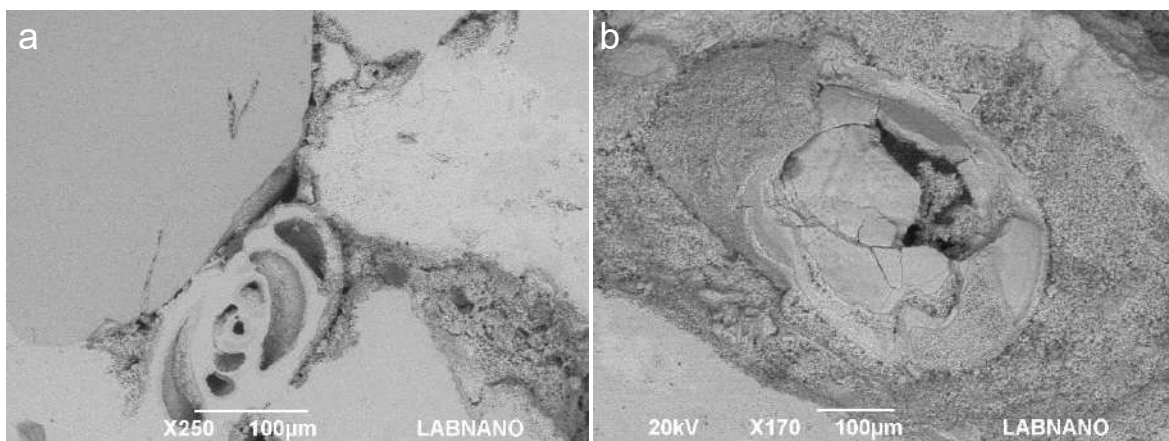


Figure 2: Scanning electron micrographs (SEM-BSE) of inner stromatolite layers showing shells of (a) a foraminifera and (b) an ostracod cemented to stromatolite surfaces by authigenic minerals.



Evaluation of the Antitumor Potential of Copper Oxide Nanorods in MCF-7 Tumor Cells

Giovanna de Carvalho Nardeli Basílio Lôbo^{1*}, Matheus Pereira Sales², Leonardo Giordano Paterno² and Sônia Nair Bão¹

¹ Microscopy and Microanalysis Laboratory, Department of Cell Biology, Institute of Biological Sciences, University of Brasília, Brasília/DF, Brazil.

² Laboratory of Research on Polymers and Nanomaterials, Chemistry Institute, University of Brasília, Brasília/DF, Brazil.

*giovannalobo2012@gmail.com

Cancer is the name of a group of more than 100 diseases that have disorderly cell growth in common. It is one of the main causes of the mortality rate, surpassed only by cardiovascular diseases, thus being considered a serious and complex current public health problem [1]. Conventional treatments for this disease consist of methods that have limitations: they offer risks of damage to healthy tissues or incomplete eradication of malignant cells, in addition to low quality of life for the patient. In this sense, it is necessary to search for new therapeutic modalities capable of promoting a better treatment of this disease. Among other options for therapeutic modalities are the use of nanomaterials as therapeutic platforms. Nanomaterials have been attracting interest due, among other factors, to the high surface area, which allows the anchoring and transport of drugs, biocompatibility and low cost [2]. In view of the development of more effective therapies to fight cancer, this study aims to evaluate the *in vitro* antitumor potential of copper oxide nanorod (CuO-nr) through the cell viability assay. CuO-nr were obtained by alkaline hydrolysis of CuSO₄.5H₂O [3] and subsequent peptization in HNO₃ 0.01 mol L⁻¹. To carry out the study, two cell lines were chosen: HUVEC, as a non-tumor model and MCF-7 as a tumor line. Cells were cultured in accordance with the ATCC (American Type Culture Collection). A 3-(4,5-dimethylthiazol-2-yl)-2,5-diphenyltetrazolium (MTT) bromide assay was performed to analyze the cell viability of the aforementioned strains. The cells were treated, for 24, 48 and 72 hours, with the following concentrations of CuO-nr: 20; 40; 60; 80; [3] [4] [5] and 160 µg mL⁻¹ [6]. The data obtained were analyzed using the Graphpad Prism 5.0 program, submitted to specific tests with 95% statistical confidence, and the Two Way Anova test was used. The *in vitro* cytotoxicity experiments showed that CuO-nr reduced the cell viability of the MCF-7 tumor cell line. The treatment carried out at all times reduced the viability of the cancer cell, an aspect not observed in the non-tumor cell line in lower concentrations compared to the tumor lineage. In the images obtained by Light Microscopy and Scanning Electron Microscopy, it is observed that alterations caused by the nanomaterial caused significant changes in cell morphology. Therefore, the preliminary results show that the therapeutic performance of the nanoparticle has the potential to treat breast cancer cells MCF-7.

[1] SIEGEL *et al.* **CA: A Cancer Journal for Clinicians**, 70, p. 7-30, 2020.

[2] JERONSIA *et al.* **Journal of Medical Sciences**, 36, p. 145, 2016.

[3] ELEMKE *et al.* **J Inorg Organomet Polym Mater**, 30, p. 400-409, 2020.

[4] ABBASI *et al.* **Asian Pacific Journal of Cancer Prevention**, 22, p. 893-902, 2021.

[5] GNANAVEL *et al.* **J Photochem Photobiol B.**, 171, p. 133-138, 2017.

[6] KHAN *et al.* **Colloids and Surfaces B: Biointerfaces**, 153, p. 320-326, 2017.



[7] This research was supported by CNPq, FAPDF, FINEP and CAPES.

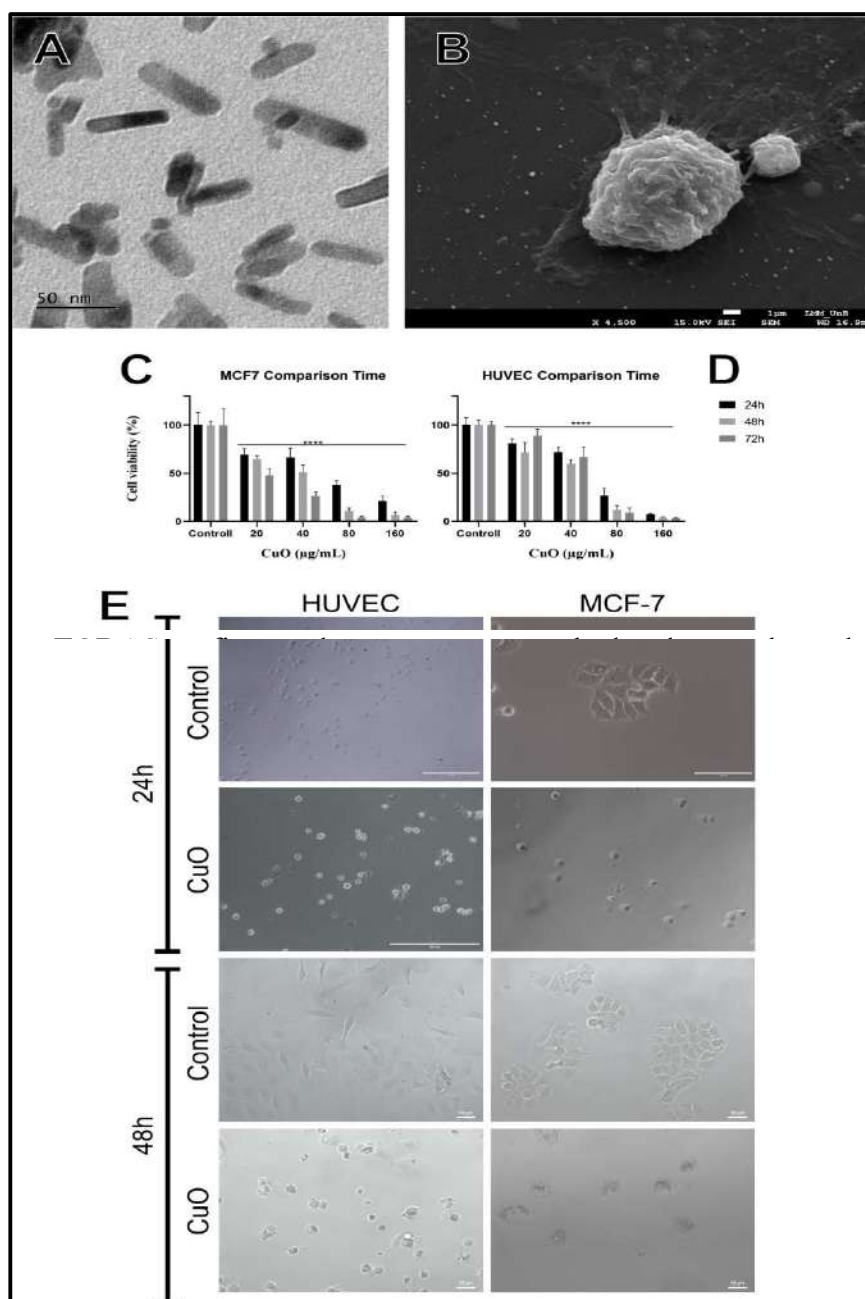


Fig 1. CuO-nr ultrastructure and activity on cell morphology.

(A) Stick-shaped morphology of CuO-nr assessed by TEM at 80 kV. Scale bar = 50 nm. (B) Scanning electron microscopy (SEM) of the non-tumor strain of HUVEC. Scale bar 5µm= (C, D) MTT assay of control and tumor strains at concentrations of 20, 40, 80, 160 µg. mL⁻¹ (E) Inverted light microscopy. NT (untreated cells) and CuO-nr treated cells after 24 and 48 hours (20 µg. mL⁻¹). Scale bar = 50 µm.



Internalization of Emerging Metallic Contaminants from Atmospheric Particulate Matter (PM₁₀) in Human Lung Cells.

Iara da C. Souza^{1*}, Mariana Morozesk¹, Priscila Siqueira¹, Enzo Zini², Iasmini N. Galter², Silvia T. Matsumoto², Marisa N. Fernandes¹

¹ Departamento de Ciências Fisiológicas, Universidade Federal de São Carlos (DCF/UFSCar), Ave. Washington Luiz, Km 235, 13565-905, São Carlos, São Paulo, Brasil.

² Departamento de Ciências Biológicas, Universidade Federal do Espírito Santo (DBV/UFES), Ave. Fernando Ferrari, 514, 29075-910, Vitória, Espírito Santo, Brasil.
*iara@ufscar.br

Atmospheric particulate material from mining and steel industries present several metallic contaminants, which can affect human health. In this study, PM₁₀ from Ilha of Boi, Vitória, Brazil, was collected in a region with a recognized influence of the steel and iron pelletizing industries and a fibroblast lung cell line (MRC-5) was used as a model to investigate cell effects. Particles internalization from PM were observed with transmission electron microscopy (TEM), cytotoxic effects were evaluated with crystal violet and neutral red retention assays and genotoxicity were evaluated through comet assay. Results demonstrate the internalization of aluminosilicate, titanium, bismuth and cerium particles in MRC-5 cells from PM₁₀. Cytotoxic effects were observed from concentrations of PM at 2.5 µg ml⁻¹ in which 20 and 40 µg ml⁻¹ leads to complete cell death. Among five elements observed inside lung cells, three of them are emerging metallic contaminants (EMCs) without governmental regulations. The presence of free nanoparticles in an intracellular environment is a concern due to this bioavailability, indicating that PM contaminants can interact with several biological processes and cell structures with a potential for associated damage not yet understood for human health, which should be further investigated. The present study is the first to demonstrate internalization of Bi and Ce from environmental samples in human lung cells. Finally, as the emerging contaminants are not regulated, results of PM particles internalized in cells contribute to demonstrate the necessity of more efforts of regulatory agencies about PM air pollution. Our results also highlight the need for a reduction of PM emission in industrial and steel industrial area, as well as improvements in PM characterization studies in biological matrix. Financial support: FAPESP Proc. 2021/02906-3, 2019/08491-0, 2016/24257-2;

ACKNOWLEDGEMENTS

The authors are thankful to JUNTOS SOS ES Ambiental for supporting settleable atmospheric particulate sampling and Fernando P. Almeida for his support in size segregation and Material Engineering Department/Federal University of São Carlos for facilities.



AFM characterization of spirulina coated magnetite nanoparticles for magnetic hyperthermia

Lima, I.R.^{1*}; Sampaio, F. A.¹, Pereira, V.G¹, da Silva. H. S². Simão. R. A²., Campos, M. F¹

^{1*}Programa de Pós-Graduação em Engenharia metalúrgica (PPGEM\EEIMVr\UFF)
PPGEM\ Escola de Engenharia Metalúrgica de Volta Redonda. Av. dos Trabalhadores
420-Vila Santa Cecília 27255-125-Volta Redonda –RJ-Brasil

²Programa de Pós-Graduação de Engenharia metalúrgica e de Materiais (COPPE\UFRJ)
Centro de Tecnologia Bloco F - Sala 210\Cidade Universitária\Rio de Janeiro - RJ -
Brasil

e-mail: ingridrussoni@gmail.com

1- Introduction

Magnetite (Fe₃O₄) is the mineral with the strongest magnetic property. Nanoparticles are of use in combating cancer in biomedical applications because they are biocompatible, because they have high saturation magnetization and because of their fast response to the external magnetic field. (Posada, 2020; Liang, 2020). Furthermore, ensuring the biofunctionalization of magnetite nanoparticles is of paramount importance, and inert bioprotective materials, in addition to acting as a stabilizer (Pasechnikv, 2020). Some coatings have already been developed, such as polyethylene glycol, artificial stabilizers and we inserted spirulina, which is a protein that is a protein of vegetable origin obtained from the blue-green alga in a helical manner and does not present toxicity (Rogatto, 2004; Radon, 2020), and which would have the function of increasing the affinity as well as enhancing the protection of nanoparticles acting as a coating and biprotectors of the magnetic core from possible effects common to magnetite, such as the phenomenon of corrosion and possible harmful effects of the biological environment such as biodegradation, acidic pH effects in biological inflammatory processes. Spirulina proves to be quite viable in the application as biprotectors of magnetic nanoparticles because it is a cheap, viable and easily obtainable material, a national product, easy to handle, among others. Thus, this work seeks to obtain, synthesize and carry out the basic procedures for physicochemical characterization of nanoparticles by means of atomic force microscopy (AFM) The production, characterization and study of biofunctionalization is part of the scope of this work in the *in vitro* stage. The investigation involved studies of characterization, affinity perspective and, at the same time, it is bionert in biological media and that have the control of heat release during its application in the human organism as the protein of vegetable origin-spirulina. Synthesis by co-precipitation and physicochemical characterization were performed and analyzed by Nanosite, Hysteresimeter and Modeling in comparison to PEG coating (bioinert coating) in order to ensure the adequacy in relation to size, behavior and increased affinity by the introduction of spirulina. The results suggest having obtained the minimum application parameters as biomaterials in nanoparticles with superparamagnetic behavior. Furthermore, the Atomic force microscopy (AFM) analysis confirms the obtainment of these nanoparticles with potential for application *in vivo*.

References

- [1] A. O. G. Posada, Landínez, D. A., Rojas, T. R.R., Barrado, R., Journal of Materials Research and Technology, 9, Issue 5, (2020) 10597-10607.
- [2] Liane Wu, Ore Geology Reviews, 124, (2020) 103632.
- [3] A. Pasechnikv, Hydrometallurgy, 196, (2020) 105438.
- [4] P. Rogatto, Rev Bras Med Esporte, 10, 4, 2004

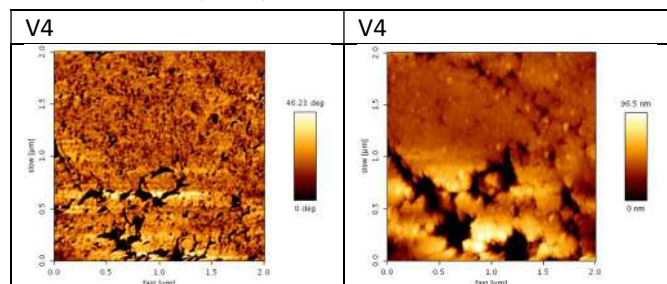


- [5] A. Radon, A., Colloids and Surfaces A: Physicochemical and Engineering Aspects, 607, (2020) 125446, 2020
[6] M.F. Campos, MF, Journal of Physics: Conference Series, 303, (2011) 012049

1- Figures and Tables

1.1- Planejamento Fatorial das Sínteses

1.3- AFM analysis



Amostra	NaOH [g]	Recobrimento*
V4	10	Mistura 1
V7	10	Mistura 2
V11	20	Mistura 1
V14	20	Mistura 2

Planejamento do Recobrimento

Amostra	PEG [g]	Espirulina [g]
Mistura 1	0	8
Mistura 2	4	4

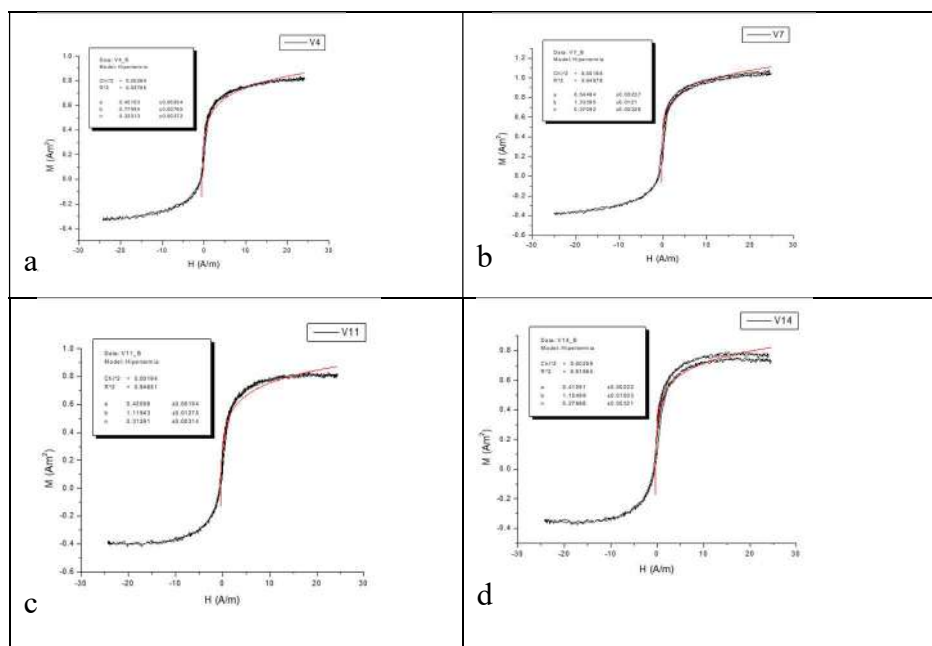
1.2.NTA analysis

S

	D10	D50	D90	MEAN (nm)	REVESTIMENTO	NaOH
V4	28,75	45	86,25	53,25	ESPIRULINA	10 g
V7	40,25	67,5	134,5	79,75	PEG E ESPIRULINA	10 g
V11	29,5	47,5	97	57,5	ESPIRULINA	20 g
V14	27,75	44,5	89	53,75	PEG E ESPIRULINA	20g

Figure 3- NTA obtained from the 4 syntheses of magnetite with spirulina coating

1.4-Modeling from Hysteresis data





High-Resolution *In Situ* Electron Microscopy technique to study biomaterials: Magnetosome thermal stability

Jefferson Cypriano^{1*}, Mounib Bahri², Walid Baazis², Kassioyé Dembelé², Pedro Leão¹, Dennis A. Bazylinski³, Fernanda Abreu¹, Marcos Farina⁴, Ovidiu Ersen², and Jacques Werckmann^{4,5}

¹. Instituto de Microbiologia Paulo de Góes, Universidade Federal do Rio de Janeiro, Brazil

². Institut De Physique Et Chimie Des Matériaux De Strasbourg, Strasbourg, France

³. School of Life Sciences, University of Nevada at Las Vegas, Las Vegas, USA

⁴. Instituto de Ciências Biomédicas, Universidade Federal do Rio de Janeiro, Brazil

⁵. Centro Brasileiro de Pesquisas Físicas, Rio de Janeiro, Brazil

*Jeffcy@micro.ufrj.br

Biom mineralization is a process in which organisms concentrate metal ions and synthesize crystalline structures [1, 2]. Magnetotactic bacteria (MTB) are a group of prokaryotic organisms that biomineralize intracellular single domain crystalline nanoparticles composed of magnetite (Fe₃O₄) or greigite (Fe₃S₄) enveloped by a biological membrane, called magnetosomes [3]. Due to their uniform size and shape, external lipid bilayer and unique magnetic properties, magnetosomes have been studied as tools for biotechnological application [4]. And because these structure stability in certain environments after cell death, they contribute to sediment magnetization as well as are considered fossil records of ancient microbial ecosystems [5]. Therefore, the magnetosomes chemical endurance/change characterization in harsh conditions in different environments is an important issue in biotechnological and paleographic fields. Here we evaluated the magnetosomes thermal stability in a temperature range between 150 and 500°C subjected to oxidizing conditions using *in situ* gas atmosphere STEM, STEM tomography, EDS microanalysis, and EELS. The results showed that magnetosomes are stable and structurally and chemically unaffected at temperatures up to 300°C. When heated between 300 and 500°C, structural damage was observed on the magnetosomes, with cavity formation. The electron energy loss near edge structure spectrum of magnetosome damaged areas indicates oxygen and iron proportion modification. Therefore, the cavity formation in the crystals is most probably associated with the magnetite partial transformation into maghemite due to the nanoscale Kirkendall effect. This study showed that magnetosomes are thermostable in temperatures up to 300°C and displays novel tools to investigate biogenic nanomaterials and potentially, their biosignature relation with environmental changes along geological periods.

References:

- [1] Sogin, ML et al., Proc Natl Acad Sci USA 103 (2006) 12115–12120.
- [2] Pedrós-Alió, C, Ann ver Mar Sci 4 (2012) 449–466.
- [3] Lefèvre CT and Bazylinski DA, Microbiol Mol Biol Rev. 77(3) (2013) 497-526.
- [4] Vargas et al., Molecules 23 (2018) 1–25.
- [5] Kopp and Kirschvink, Earth-Science Rev. 86 (2008) 42–61.

We thank Unidade de Microscopia Multiusuário Padrón-Lins (UNIMICRO), UFRJ and Institut de Physique et Chimie des Matériaux de Strasbourg (IPCMS) for electron microscopy facilities; This work was supported by CNPq, CAPES and FAPERJ.

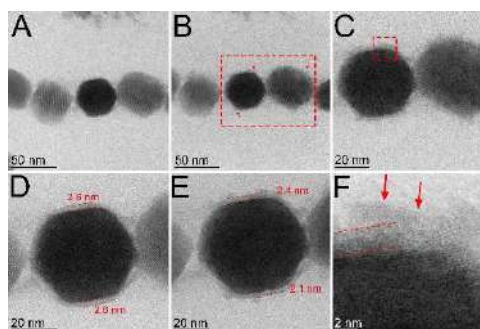


Fig.1) BF-STEM images before and after oxidation treatment at 300 °C. Observation made at room temperature, without the upper membrane which closes the *in situ* chip chamber containing the sample. This greatly increases the signal-to-noise ratio in the image, due to the absence of the interaction of the electrons with silicon nitride cover and with gaseous oxygen atoms. (A,D) Before oxidation treatment, the initial thickness of the membrane is of about 2.6 nm. (B,C) After oxidation treatment, the thickness of the membrane is reduced (arrows in B). (E,F) show details of the thickness (E) and of the structure (arrows in F) of the membrane after treatment.

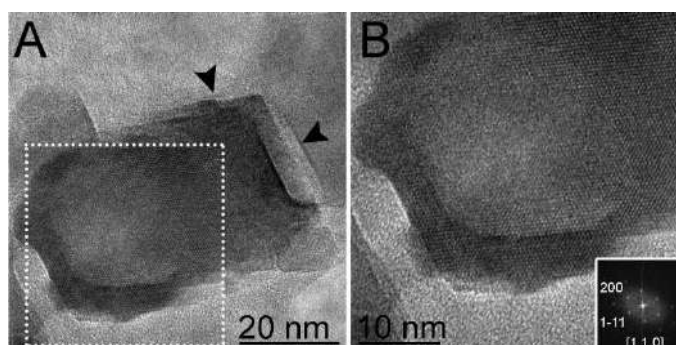


Fig.2) High-resolution CTEM images of magnetosome heated to 500 °C in the *in situ* experiment with O₂. (A) Magnetosome showing a large cavity (area delimited by the white dashed square) and border defects (arrowheads); (B) Higher magnification of magnetosome displayed in (A) showing the damaged crystalline structure and irregular facets in detail. The inset shows an FFT of image in (B) with indexed planes consistent with theoretical angles and distances expected for magnetite or maghemite, based on magnetite cubic pattern with 8.396 Å unit cell parameter and structure of maghemite derived from magnetite structure.

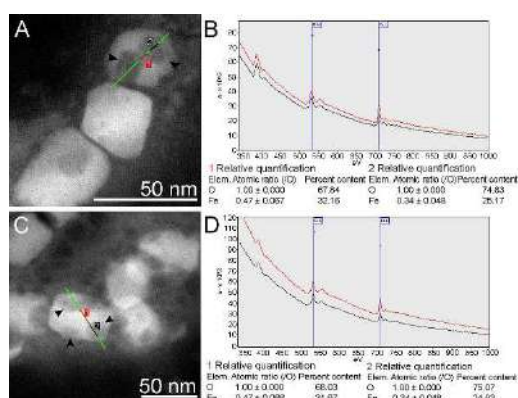


Fig.3) HAADF-STEM images and EELS microanalysis of magnetosomes after heating until 500 °C in the presence of O₂, showing the irregular contrast on magnetosomes and the presence of large cavities. (A) HAADF-STEM image of magnetosomes with cavities. Non-altered regions represented by the red line segment (number 1) and a cavity indicated by the black line segment (number 2) were selected for EELS analysis showed in (B); (B) EELS spectra and relative quantification of regions indicated by red line 1 and black line 2 in (A) for oxygen, O K (540 eV) and iron, Fe L (710 eV); (C) HAADF-STEM image of magnetosomes with cavities. Non-altered regions represented by the red line (number 1) and a cavity, indicated by the black line (number 2) were selected for EELS analysis showed in (D); (D) EELS spectra and relative quantification of regions indicated by red line segment 1 and black line segment 2 in (C) for oxygen and iron.



Nanostructure of calcium phosphate films synthesized by pulsed laser deposition under 1 Torr: effect of wavelength and laser energy

N.R. Checca¹, F.F. Borghi², A.M. Rossi¹, A. Mello¹, A.L. Rossi¹

¹ Brazilian Center for Physics Research, R. Dr. Xavier Sigaud 150, 22290-180, Rio de Janeiro, Brazil.

² Institute of Physics, Federal University of Rio de Janeiro, Brazil
nomifsc@gmail.com

Calcium phosphates (CaP), mainly hydroxyapatite (HA), are biocompatible materials with bioactive properties. They can be used in different forms (powder, films, nanoparticles, scaffold, etc.) for enhancing bone regeneration and improving integration/adhesion of bone in orthopedic/dental implants [1,2]. CaP coatings can be used in metallic implants to reduce toxicity and improve biological responses. CaP coatings synthesized by pulsed laser deposition technique (PLD) were reported since 1970. Nonetheless, the mechanisms of formation and growth of CaP coatings by PLD is still a subject under investigation. In this study, we investigated aspects about the nanostructure of calcium phosphate films formed by PLD under a high-pressure gas (argon) environment (1 Torr) that are not addressed in the literature by using infrared and green laser sources. The plume generated from an ablated hydroxyapatite target was deposited directly over transmission electron microscopy (TEM) grids during 120 s to allow for the use of TEM techniques to investigate the morphology, composition and structure of deposited films from the micron to the nanoscale. The films were found to comprise five different calcium phosphate structures: (1) unstructured amorphous thin film formed by the deposition of ions and molecules over the substrate, (2) dense nanoparticles (< 20 nm) formed over the substrate, (3) low Ca/P ratio spherical particles (< 400 nm) formed on the way to the substrate, (4) rich Ca/P ratio ring-shaped particles (> 400 nm) ejected from the target and (5) crystalline particles (~ 500 nm) removed from the target. Although all samples presented these five structures, the morphology, abundance and size population were all different. This work opens a window to elucidate the complex mechanism underlying calcium phosphate film deposition and growth by pulsed laser deposition.

REFERENCES

- [1] N.R. Checca et al., Applied Surface Science 545 (2021) 148880.
- [2] G.C. Gomes et al., Surf. Coatings Technol. 329 (2017) 174–183.

ACKNOWLEDGMENT

This research was supported by FAPERJ, CNPq and LABNANO/CBPF (Brazil).

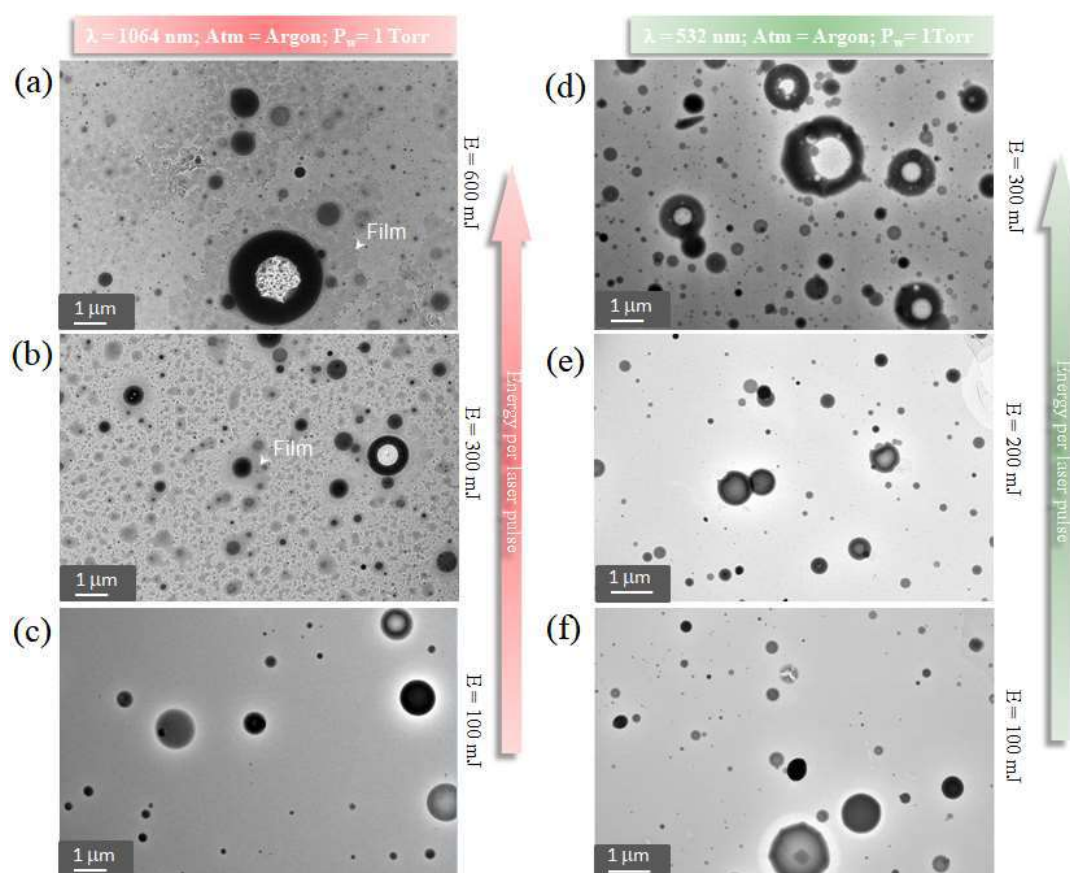


FIG 1. TEM images showing the morphology of IR-600 (a), IR-300 (b), IR-100 (c), G-300 (d), G-200 (e) and G-100 (f). Two types of morphology were identified: spherical and ring-shaped particles. In addition to particles, a thin film was observed covering part of the surface in (a) and (b).

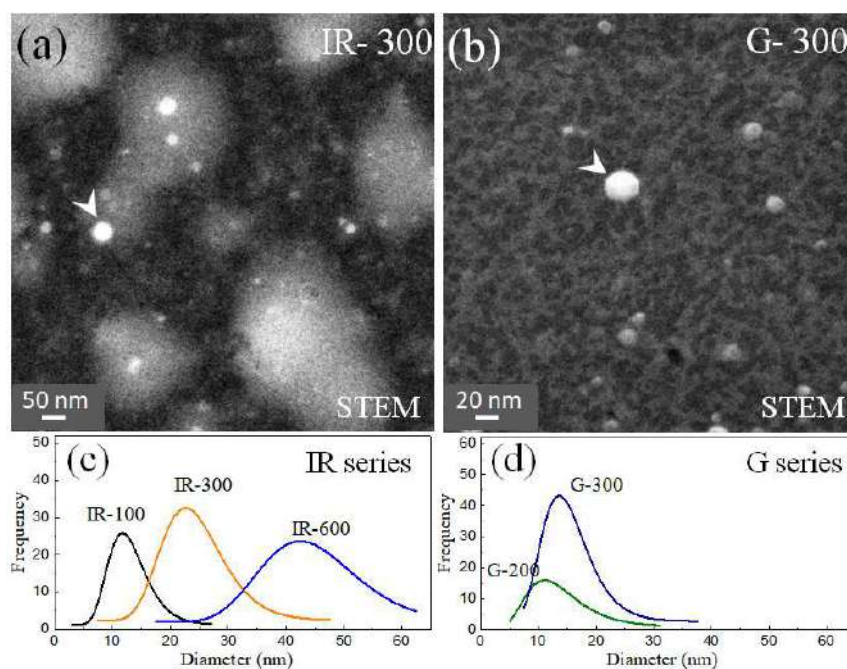


FIG 2. STEM images with high magnification of IR-300 (a) and G-300 (b) showing the difference of the films due to the wavelength, the arrows indicate the nanospheres. (c-d) Mean diameter of nanospheres ($\langle D \rangle$), as a function of laser wavelength and energy.



Less is more: Impact of the conjugation method on enzymatic activity in magnetic nanoconjugates

Thais de Andrade Silva¹ and Jairo P. de Oliveira^{1*}

¹ Federal University of Espirito Santo, Av Marechal Campos 1468, Vitória, ES 29.040-090, Brazil

*jairo.oliveira@ufes.br

The use of enzymes immobilized on nanomagnetic supports has catapulted surprising results in the field of catalysis, mainly due to the increase in surface area and the capacity for recovery and reuse. Although there has been a growing number of publications on immobilization processes in recent years, the meticulous control of this process associated with the lack of reproducibility has made industrial-scale applications unfeasible. This is because the active site of the enzyme may be randomly involved in the conjugation process with nanomaterials. Therefore, the objective of this work was to compare the conjugation strategies of enzymes on nanomagnetic supports through physical adsorption (naked) and by covalent bonding with APTES (NH₂) and MPTS (COOH) ligands. The synthesis of magnetic nanoparticles (NPMs) was performed using a chemical coprecipitation method of iron chlorides II and III (molar ratio 1:2) in the presence of 0.06 M ammonium hydroxide. Functionalization was performed with the linkers 3-aminopropyl trimethoxysilane (APTS) at 0.043 M and 3-mercaptopropyl trimethoxysilane (MPTS) at 0.054 M in an alcoholic solution. The free lipase obtained from *Aspergillus oryzae* was used as a model enzyme. The conjugation was carried out in a reaction medium for 60 min, with stirring at 200 rpm at 28 °C. The total protein dosage was determined by UV-Vis spectrophotometry using a calibration curve and the enzyme activity was determined by the p-nitrophenyl palmitate reduction method. The material was characterized by x-ray diffraction (XRD), transmission electron microscopy (TEM), infrared (FTIR), and Raman scattering. The magnetic nanoparticles had an average size of 20 nm, monodisperse, and with a predominant crystal structure in spinel demonstrated by XRD. Confirmation of bioconjugation can be seen by FTIR analysis (Fig. 1C) where the peak at 1030 cm⁻¹, 2930 cm⁻¹ and 1640 cm⁻¹ confirm the presence of ligands and lipases on the surface of NPMs [1]. The Raman scattering spectra (Fig. 1D) show vibrations at 480 cm⁻¹ that are related to Fe-O interactions [2]. Conjugation by electrostatic attraction was capable of conjugating, on average, 509.49 mg of enzyme per g of NPM, but it had low enzymatic activity compared to covalent binding methods (Fig. 1E and 1F). The MPTS conjugates obtained the best results, as despite having a lower enzyme: NPM ratio of 164.06 mg.g⁻¹, it had the highest enzymatic activity, up to 249.74 U g⁻¹. These results show that the greatest amount of immobilized enzymes is not always the best way to define the conjugation strategy. Understanding these mechanisms is essential for the development of reproducible nanoconjugates with high enzymatic activity



REFERENCES

- [1] SALEHI, Zeinab et al. Journal of Industrial and Engineering Chemistry, v. 35, p. 224-230, 2016.
- [2] SLAVOV, L et al. Journal of Magnetism and Magnetic Materials, v. 322, n. 14, p. 1904-1911, 2010.

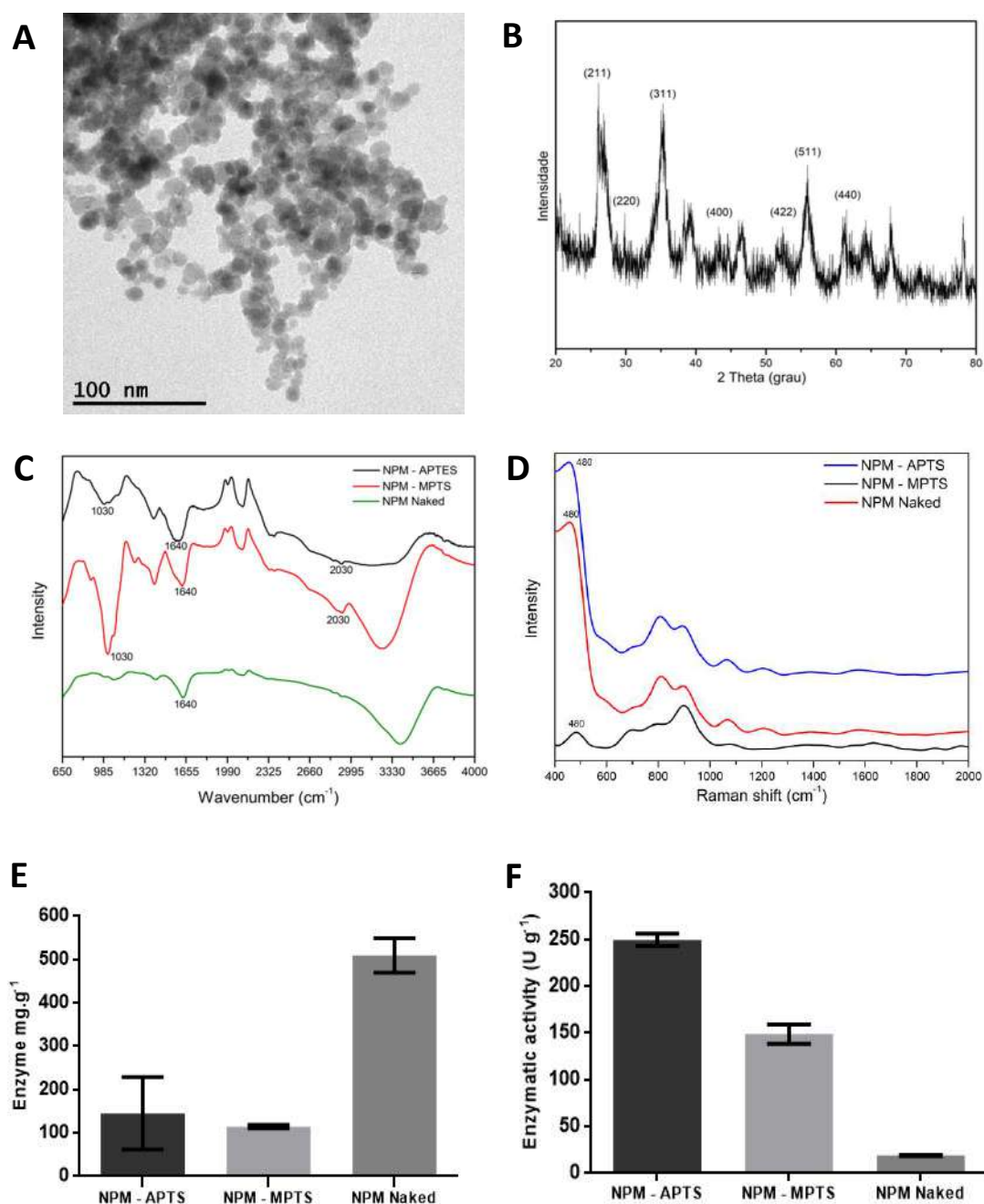


Figure 1. Image of magnetic iron nanoparticles obtained by transmission electron microscopy (A); X-ray diffraction of magnetic nanomaterials (B). Analysis after bioconjugation with enzymes by FTIR (C) and Raman (D). Graph showing the total dosage of enzymes (E) and enzymatic activity (F).



Iron oxide and gold nanoparticles functionalized with Jacalin for IgA purification system

Wanderson Juvencio Keijok¹, Luis Alberto Contreras¹, Jairo Pinto de Oliveira¹ and Marco Cesar Cunegundes Guimarães¹

¹Laboratório de Nanomateriais Funcionais, Universidade Federal do Espírito Santo-UFES - Av. Marechal Campos, 1468, Maruípe, Vitória, E.S. 29.042-755 – Brasil, Tel.: 55. 27.3335 7365,

*e-mail: marco.guimaraes@ufes.br

Nanomaterials are excellent conjugation platforms, being an attractive material for application in a diagnostic system. However, some problems make these systems expensive and with low sensitivity, new diagnostic systems need pre-treatment due to non-specific bindings and treatments that allow the use of the diagnostic system again in other samples. Here, we present the synthesis of jacalin-functionalized iron oxide nanoparticles (FeNP's) these nanomaterials can be controlled by the influence of a magnetic field and are great magnetic nanomaterials capable of separating the desired analyte, in this study FeNP's were used to capture IgA in saliva human, another nanomaterial used in the work was the gold nanoparticles (AuNP's) as sensing that can be analyzed by the alteration in the Localized Surface Plasmon Resonance (LSPR). Understanding these mechanisms is essential for the development of sensors with high sensitivity for immunoassays and that allow reuse using the magnetic field to recover the treated nanomaterial to disconnect the IgA.

Transmission electron microscopy (TEM) was performed to characterize the formation, size and dispersion of FeNP's and AuNPs. EDS were used to confirm the presence of the ligand (3-Mercaptopropyl) trimethoxysilane (MPTS) on the metallic surface of FeNP's. This ligand allows the conjugation of nanomaterials to protein samples and also increased the stability of FeNP's, the zeta potential was used to determine stabilization characterized by self-assembled monolayers (SAM), which demonstrated that it requires a time for binding the binder to the metal surface. Finally, UV-vis spectroscopy was used to quantify Jacalin concentration on MNP and AuNP surfaces using the Bradford A^{595nm}, the decrease in absorbance demonstrates the capture of IgA by FeNP's.

Keywords: iron oxide nanoparticles, gold nanoparticles, jacalin and IgA.

Bibliography:

- [1]. Baghbaderani Y. K., Allgayer R., Schwaminger S. P., García P. F. and Berensmeier S. Magnetic Separation of Antibodies with High Binding Capacity by Site-Directed Immobilization of Protein A-Domains to Bare Iron Oxide Nanoparticles. *ACS Appl. Nano Mater.* v.99, 4956–496348, 2021
- [2]. Skea D. L., Christopoulos P., Plaut A. G., Underdown B. J. Studies on the specificity of the IgA-binding lectin, jacalin. *Molecular Immunology.* V. 25, Issue 1, Pages 1-6, 1988.
- [3] J. Turkevich; P.C. Stevenson; S. Hiller *Discuss. Faraday Soc.*, 1951,11, 55.

Acknowledgements:

The authors thank Brazilian Ministry of Science and Technology and Foundation Support Research and Innovation of Espírito Santo. This work used the equipment facilities at the Laboratory of Functional Nanomaterials, Laboratory of Cellular Ultrastructure Carlos

Alberto Redins and the Laboratory of Biomolecular Analysis (LABIOM) at Federal University of Espirito Santo.

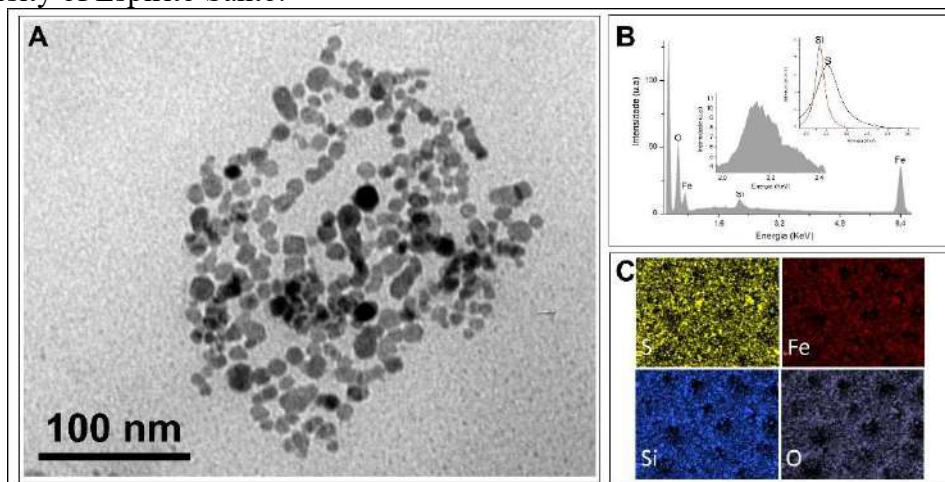


Figure 1. Transmission electron microscopy images of FeNP's, scale bar 100nm (A). Scanning electron microscope (EDS-SEM) energy dispersive spectroscopy of MPTS stabilized FeNP's, the inset shows the area showing two peaks demonstrated by deconvolution (B). The map demonstrates the elementary distribution across the entire sample (C);

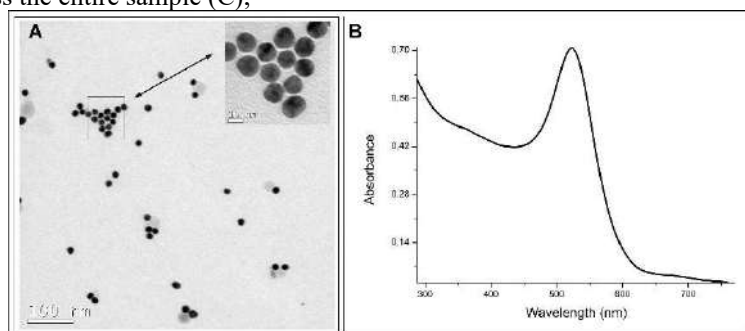


Figure 2. Image obtained by transmission electron microscopy of AuNP's, scale bar 100 nm (A). UV-Visible absorption spectroscopy for the synthesized gold colloid showing the characteristic plasmonic peak at 522 nm (B).

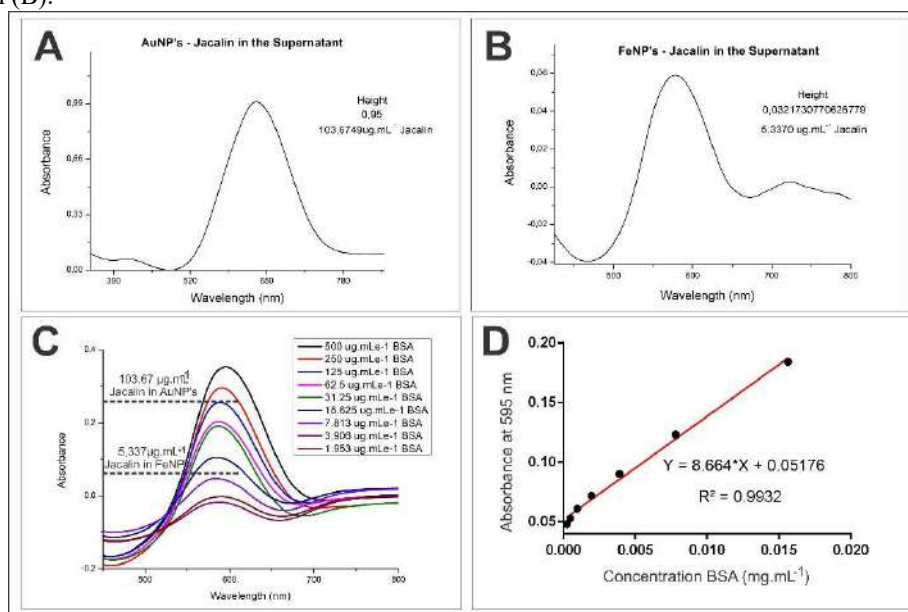


Figure 3. UV-visible absorption spectroscopy of total protein dosage with Bradford, supernatant from the bioconjugation of AuNP's with jacalin (A) and FeNP's with jacalin (B). UV-visible absorption spectrum for the detection of BSA (C) and standard curve obtained at concentrations from 500 to 1.953 µg.mL⁻¹ (D).



Characterization of the Resonance and Morphological Frequency of Hybrid Cantilever Sensors Functionalized With M13 Bacteriophages.

Wellington Silva Ferreira^{1*}, Luís Fernando Hill², Gustavo Miranda Rocha³, Paulo Mascarello Bisch³ and Gilberto Weissmüller⁴

¹ Federal University of Rio de Janeiro, Carlos Chagas Filho Instituto of Biophysics - IBCCF, Rio de Janeiro, Brazil.

² Federal University of Rio de Janeiro, Carlos Chagas Filho Instituto of Biophysics - IBCCF, Rio de Janeiro, Brazil.

³ Federal University of Rio de Janeiro, Carlos Chagas Filho Instituto of Biophysics - IBCCF, Rio de Janeiro, Brazil.

⁴ Federal University of Rio de Janeiro, Carlos Chagas Filho Instituto of Biophysics - IBCCF, Rio de Janeiro, Brazil.

*wellington.silvaferreira@biof.ufrj.br

Sensors are electrical, mechanical, chemical or biological devices that respond to a specific stimulus and send a resulting quantitative impulse as a measurement or operating control [1]. With the advent of nanotechnology, the development of new sensors using nanoscale has grown greatly, mainly because it allows miniaturization, lower power requirements and bigger specificity with the compound [2]. The use of viruses as construction blocks for new devices is very convenient because it has self-assembling properties, and can be genetically engineered or selected, which permits the interaction of the virus with specific analytes [3][4]. A convenient tool to convert the stimulus in information is the Atomic Force Microscopy (AFM), being possible the utilization of the probe (cantilever) natural frequency as a transducer, turning an external signal into a mechanical response, for example, a deflection of cantilever due to adsorption of molecules [1]. We proposed microcantilever functionalization with M13 bacteriophage genetically selected through phage display technique used as a proof of concept in the cantilever sensor. Two chips with three cantilevers were functionalized ($<90^\circ$ and $=90^\circ$) with bacteriophage modified to interact with ethanol. We varied the concentration of humidity and alcohol in the cantilevers. With functionalized cantilever sensors, it was possible to measure resonant frequency shifts due to its exposure to different humidity and ethanol environments. After frequency analysis we characterized a chip functionalized at an angle $<90^\circ$ by scanning electron microscopy (image 2) and a chip functionalized at an angle $<90^\circ$ and $=90^\circ$ by atomic force microscopy (image 3). Frequency analysis showed that cantilever sensors regardless of the form of functionalization have sensitivity to analytes, while the self-assembly properties are only seen on chips functionalized at an angle $=90^\circ$.

REFERÊNCIAS

[1] N.V. Lavrik et al., Rev. Sci. Instrum. 75 (2004) 2229.

[2] F. Sanchez et al., Construction and Building Materials. 24 (2010) 2060–2070.

[3] J. W. OH et al., Nature Communications. 5 (2014) 1–8.

[4] S. H. Yang et al., The Chemical Record. 13 (2013) 43–59.



AGRADECIMENTOS

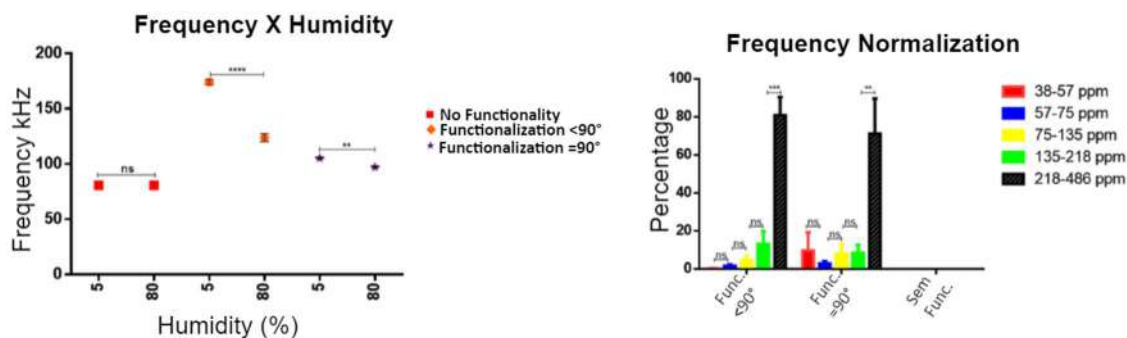


Image 1. (a) quantification of frequencies by varying the humidity (5-80%) on non-functionalized, <math><90^\circ</math> of functionalization, =90° of functionalization M13 bacteriophage cantilevers (b) frequency normalization by varying the ethanol concentration (38-486 PPM) on non-functionalized, <math><90^\circ</math> of functionalization, =90° of functionalization M13 bacteriophage cantilevers. Test one-way ANOVA (** $p<0.01$, *** $p<0.001$ e **** $p<0.0001$).

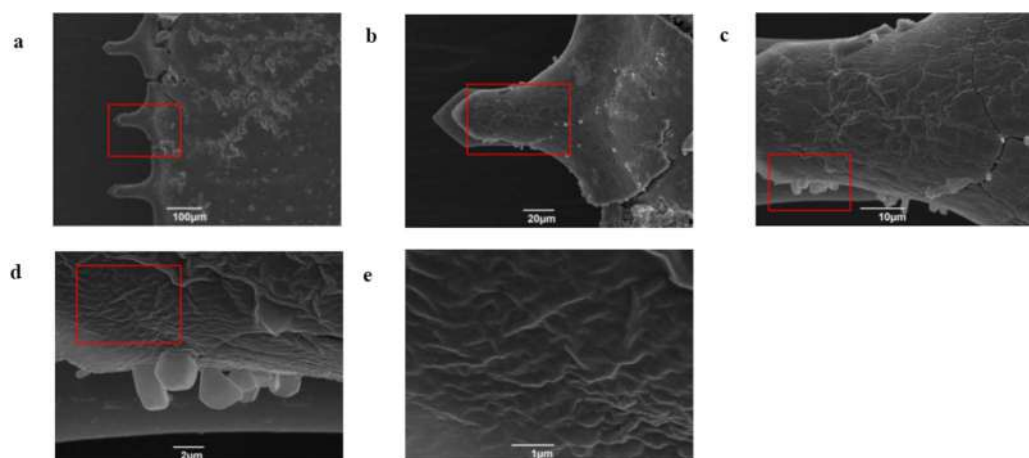


Image 2. Cantilever NSC36/Tipless (MikroMasch USA, Watsonville – CA) with Cr-Au coating. (A) A, B and C cantilever functionalized in the chip (<math><90^\circ</math> functionalization). (B), (C), (D) and (E) shows further cantilever zooming in the cantilever B, where you can see the bacteriophage.

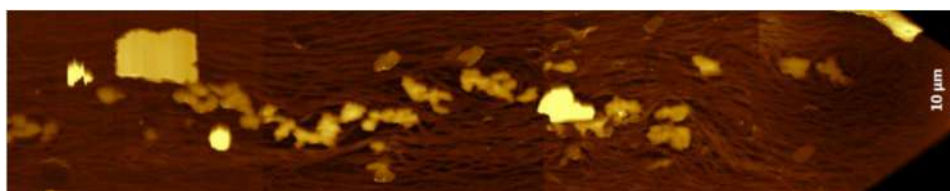


Image 3. Cantilever NSC36/Tipless (MikroMasch USA, Watsonville – CA) with Cr-Au coating. A cantilever functionalized ($=90^\circ$), where you can see the self-assembling properties described in the literature. KeySight equipment, mode tapping, cantilever MSNL-10 Bruker (tip F).



Electron microscopy characterization of nanostructured Mg/Nb₂O₅ composite processed by High Pressure Torsion (HPT) Technique

Caires, A.J^{1*}, Castro, M. M¹, Montoro, L. A.², Figueiredo, R. B¹, Isaac, A. N¹

¹ Departamento de Engenharia Metalúrgica e Materiais, Universidade Federal de Minas Gerais, 31270-901 Belo Horizonte, MG, Brazil.

² Departamento de Química, Universidade Federal de Minas Gerais, 31270-901 Belo Horizonte, MG, Brazil.

*andersoncaires@outlook.com

Nowadays, magnesium alloys are extremely important materials in engineering applications. High-Pressure Torsion (HPT) is widely used as a severe plastic deformation technique for modifying the microstructure of metallic alloys at interfaces, and to promote nanostructuring through grain refinement. [1-2]. This technique promotes deformation in the material structure, accumulating and reorganizing the dislocations, with consequent generation of new grain boundaries (GBs). Additionally, HPT can promote mechanochemical redox reactions between nanostructured oxides and metallic powders. In this work, we report the production of Niobium oxide reinforced magnesium alloys nanocomposites (Mg/Nb₂O₅) processed by HPT and characterized by the HRTEM. Mg/Nb₂O₅ were prepared using commercial magnesium and niobium pentoxide nanowires (Nb₂O₅). Discs of this homogenized mixture, with diameter of 10 mm and thickness 1.2 mm, were submitted to HPT processing at room temperature, pressure of 3.8 GPa, speed of 1 rpm and 10 turns. HRTEM images were used to characterize the microstructure using a 200 kV JEOL[®] JEM-2100Plus. Specimen was prepared by Ar⁺ ion milling using a Gatan[®] precision ion polishing system PIPS[™] II Model 695. The microstructure is characterized by nanocrystalline Mg grains with heterogeneous grain size distribution within nanoscale dimensions (Fig. 1a). The structural characteristics were studied by electron diffraction pattern and dark-field images (Fig. 1b-d). HRTEM analysis was performed in order to find evidence of the redox reactions during HPT processing. Magnesium Oxide (MgO) and Nb precipitates are formed during processing by HPT. Fig. 1e show the bright-field HRTEM image of the Mg/Nb₂O₅ alloy. The dotted circle region is associated with clusters and/or precipitates of Nb with size of about 8–10 nm (Nb with lattice spacing of 2.34 Å). The energy-dispersive X-ray (EDX) spectrum shown in Fig. 1(f) presents the spectroscopic signals corresponding to the elements: Mg K α (1.25 KeV), Nb L α (2.16 KeV), Nb K α (16.57 KeV), O K α (0.52 KeV). Fig. 1g shows a HRTEM image of the region with MgO aggregates inside of Mg grain. The existence of MgO was confirmed by the (002) planes with lattice spacing of 2.6 Å. Fig. 1h shows a HRTEM image of the Nb nanoprecipitates with sizes of 5-10 nm observed in the Mg/Nb₂O₅ alloy and FFT pattern. TEM results show that the HPT-processed samples generated a Mg alloy with nanostructured niobium precipitation. This material may be of interest for future applications in materials engineering.

[1] C. Silva et al., *Materials Characterization*, 162, 2020, 110222.

[2] C. Silva et al., *Materials Science and Engineering: A*, 801, 2021, 140422.

The authors would like to thank CNPq, CAPES and CIT SENAI Institute of Innovation in Metallurgy and Special Alloys for their support.

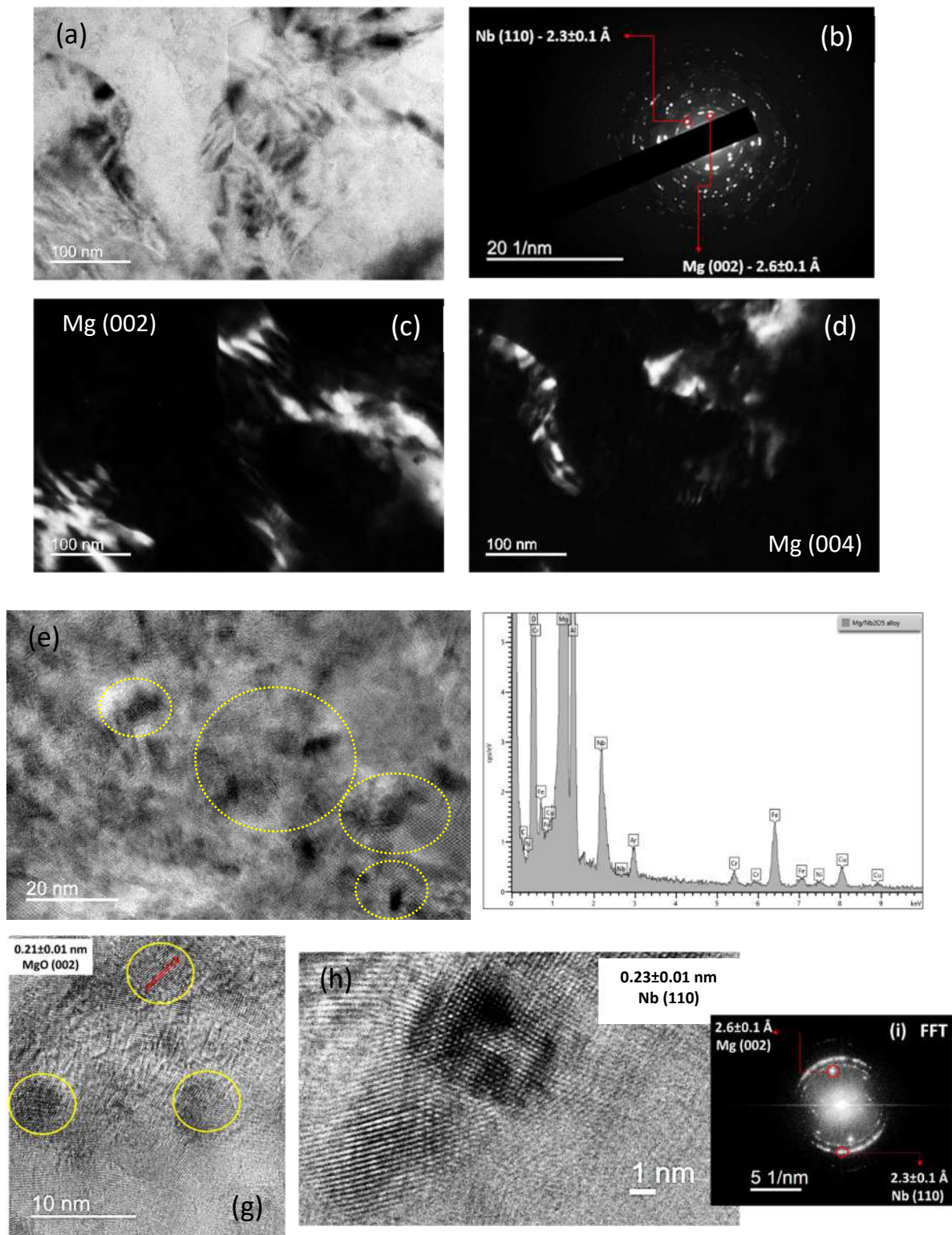


Fig 1 – Microstructure of the Mg/Nb₂O₅ alloy. (a) TEM bright field image. (b) (SAED) pattern and corresponding dark-field images for (c) Mg (002) and (d) Mg (004) from the (Fig. 1a) bright field image. (e) HRTEM image showing a high density of MgO and clusters of Nb precipitates at region near Mg grain contour. (f) EDX spectrum. (g) HRTEM image showing details of MgO aggregates inside of magnesium grain oriented at the (002) planes. (h) HRTEM image showing details of Nb precipitates oriented at the (110) planes (i) FFT pattern (σ : SD).



Observation of Chiral Spin Textures in Pd/Co/Pd Multilayers by Lorentz Transmission Electron Microscopy

C. Labre^{1*}, R. Dutra¹, R. P. Loreto¹, B. G. Silva¹, D. E. Gonzalez-Chavez¹ and R. L. Sommer¹

¹ Centro Brasileiro de Pesquisas Físicas, Rio de Janeiro, Brazil.

* clabre@cbpf.br

Magnetic skyrmions are nanometer-size whirling chiral spin textures and are promising candidates for the next generation of spintronic devices due to their small size, topologically protected structure, and functionality towards the development of room temperature magnetic devices [1]. Lorentz transmission electron microscopy (LTEM) is a powerful tool with an ultrahigh magnetic domain resolution (~ 2 nm); it is thus an ideal method for direct real-space imaging of fine magnetic configurations of ultra-small skyrmions [2,3]. In this work, we investigate the formation of chiral spin textures using LTEM in symmetric multilayers of [Pd(2nm)/Co(t_{Co})/Pd(2nm)] $\times 15$ fabricated by magnetron sputtering technique, where the Pd thickness was fixed at 2 nm and Co layer (t_{Co}) varied from 0.2 to 1.2 nm. The samples were grown both on Si/SiO₂ substrate for magnetization and structural characterization measurements and on 100nm-thick Si₃N₄ electron transparent membranes for TEM imaging and in situ magnetization experiments. High-resolution scanning TEM was performed on a cross-section of the deposited film and showed distinct Pd/Co/Pd layers. The magnetization reversal curve as a function of the magnetic field was acquired by using a vibrating sample magnetometer (VSM) at room temperature. The magnetic anisotropy field H_k increases systematically with a decrease in t_{Co} and the saturation magnetization (M_s), on the other hand, decreases with the decrease in t_{Co} over the entire range. These parameters emerge as a source for the skyrmions stability indicating that the combination of higher PMA and low M_s may allow their formation at zero field [4]. The formation of skyrmions in symmetric multilayers is better described with the assistance of micromagnetic simulations. The micromagnetic simulations were performed using the Mumax3 GPU-accelerated software. The magnetic anisotropy K_u , magnetization saturation M_s , and Dzyaloshinskii-Moriya value D were modified to understand their impact on the skyrmions stability. Figure 1 shows the LTEM image of magnetic domains structure for the sample with Cobalt thickness of 1 nm where the magnetic domains are present. Below 2 nm of Cobalt, the magnetic domains nucleate into skyrmions.

References

- [1] A. Fert et al., Nature Reviews Materials 2 (2017) 1.
- [2] S.D. Pollard et al., Nature Communications 8 (2017) 14761.
- [3] L.C. Peng et al., Chin. Phys. B 27 (Suppl. 6) (2018) 066802.
- [4] J. Brandão et al., Scientific reports 9 (2019).
- [5] I. Kézsmárki et al., Nature Materials 14 (2015) 1116.

The authors thank Labnano/CBPF for technical support and CNPq, Capes, and FACC for financial support.

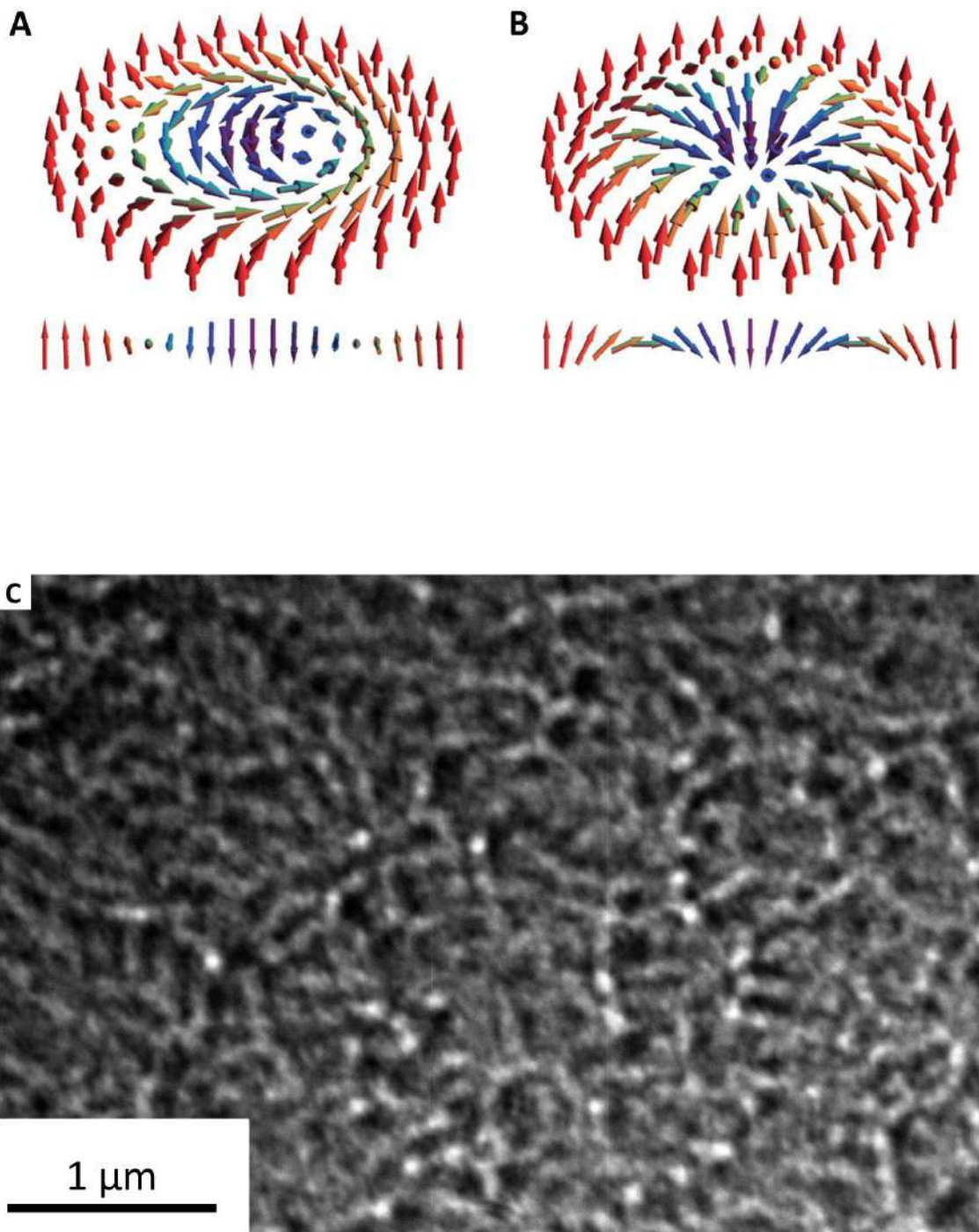


Figure 1 - (A) Bloch and (B) Néel skyrmions with their respective cross-section, extracted from reference [5]. (C) LTEM image of the magnetic domains on the 2 nm thick Cobalt sample.



Solvent Effect in the Crystalline Phase of ZrO₂ Nanocrystals Obtained by Solvothermal Syntheses

Mayara da Silva Santos^{1,2}, Walter Sperandio Sampaio¹ and Cleocir José Dalmaschio^{1*}

¹ Federal Univerity of Espirito Santo, Chemistry Department, Vitória/ES - Brazil

² Helmholtz-Zentrum Berlin für Materialien und Energie GmbH, Berlin, Germany.

*Cleocir.dalmaschio@ufes.br

Metal oxide nanoparticles were widely explored in nanomaterials, once several materials present applications and can be easily obtained in room conditions. However, obtain in a controlled shape, size and phase remain as a challenge for several oxides. Design nanoparticles is a key study for obtaining high functional materials with tunable properties. For that purpose, great progress on chemical methods for controlling the growth of the nanoparticles during the synthesis has been made. However, an important challenge faced by this field of study is to completely understand the crystallization process and the chemical pathways during the syntheses that use growth-controlling agents. Aiming controlling phase, shape and size ZrO₂ nanocrystals were synthesized using three organic solvents, oleic acid, benzyl alcohol and octyl alcohol and adjusting alkoxide reagent concentrations, as Zr precursor, it was obtained functionalized zirconium oxide nanoparticles in three crystallographic phases. To obtain pure phase concentrations were used and purified materials were characterized using X-ray diffraction. Using zirconium butoxide with concentrations 0.25, 0.50 and 0.50 mol L⁻¹ in oleic acid, benzyl alcohol and octyl alcohol were obtained monoclinic, cubic and tetragonal crystalline phase respectively. Transmission electron microscopy was used to analyze the nanocrystals' structure and to assess the crystal size distribution, Figure 1. From images can be proposed that functionalized organic molecules will act as control size as well induce preferential growth, resulting in nanoparticles with phase and size controlled. Thus, it was possible to ascribe the interactions of the solvents with the crystal surface as being responsible for leading to different growth paths and different crystalline phases formation. Additional solvothermal treatments procedure were used to change functionalization molecules and to confirm that crystallographic phase are consequence of synthesis process, keeping the phase after thermal treatment without growth.

REFERENCES

- [1] M. S. Santos, J. C. C. Freitas, C. J. Dalmaschio. *CrystEngComm*, 22, (2020) 1802.
[2] C. Grote, T. A. Cheema, G. Garnweitner, *Langmuir*, 28, (2012) 14395.

ACKNOWLEDGMENT

This study was financed in part by the Coordenação de Aperfeiçoamento de Pessoal de Nível Superior – Brasil (CAPES) – Finance Code 001. The authors also acknowledge the support from: the Brazilian agencies FAPES and CNPq

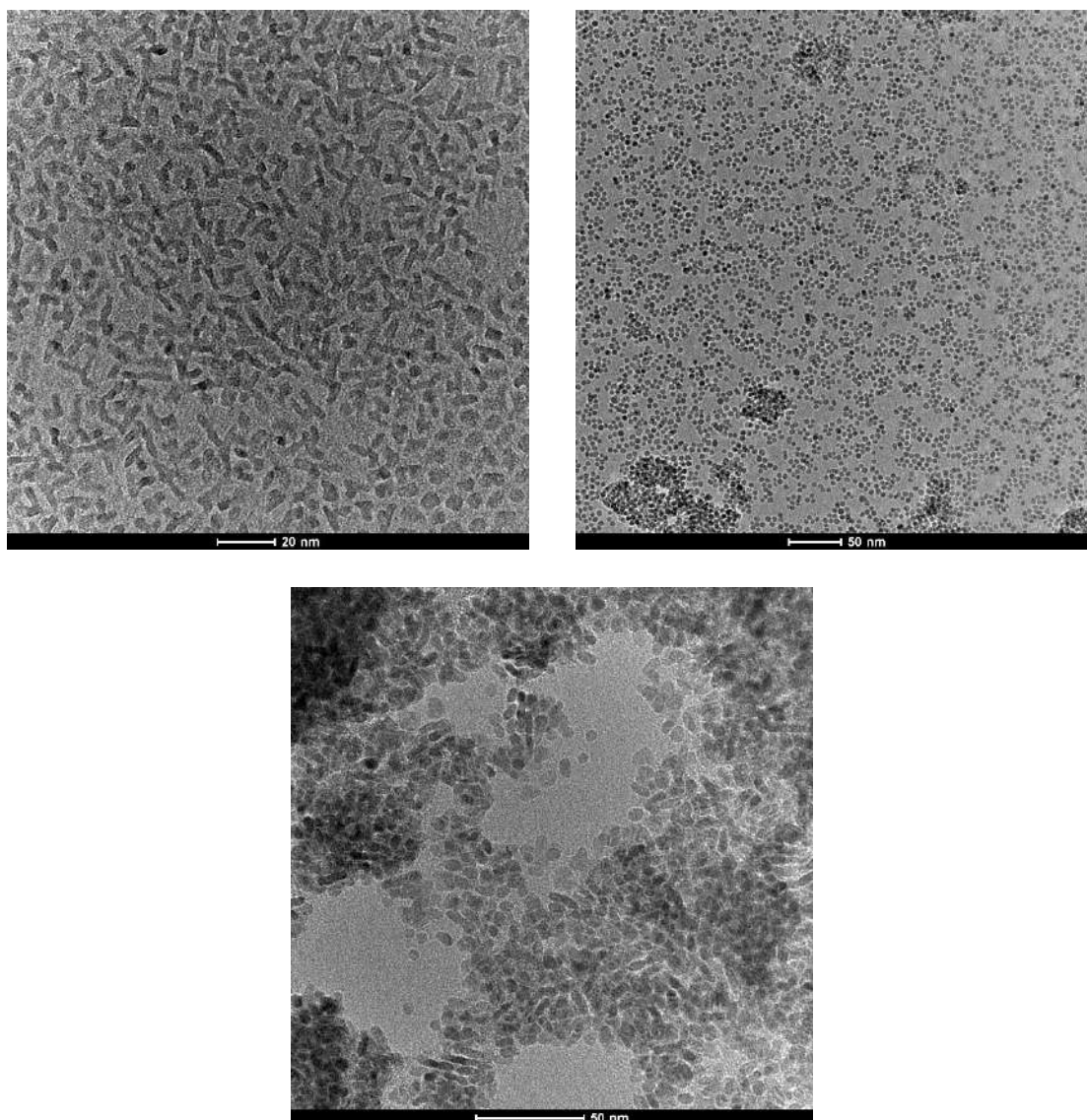


FIGURE 1: Transmission electron microscopy for ZrO₂ nanocrystals obtained in different solvents. A) oleic acid, b) benzyl alcohol and c) octyl alcohol.



Optimizing PCA Denoising of EDS Hyperspectral images: Avoiding Random Noise Bias and Improving Precision and Accuracy of Quantitative Chemical Analysis.

Murilo Moreira¹, Matthias Hillenkamp², Giorgio Divitini³, Luiz H.G. Tizei⁴,
Caterina Ducati³, Monica A. Cotta¹, Varlei Rodrigues¹, Daniel Ugarte^{1*}

¹ Univ. Estadual de Campinas, Inst. de Física “Gleb Wataghin”, Brazil.

² Univ. Claude Bernard Lyon I, Inst. of Light and Matter, France.

³ Univ. of Cambridge, Dept. of Materials Sci. and Metallurgy, United Kingdom

⁴ Univ. Paris Sud - Paris 11, Lab. de Phys. des Solides - UMR 8502, France.

*dmugarte@ifi.unicamp.br

Scanning Transmission Electron Microscopy (STEM) methods have such a degree of reliability and reproducibility that many measurements yield huge 3D or 4D data matrices. These datasets cannot be analysed by conventional means, and advanced statistical tools based on “machine learning” are necessary. These methods exploit redundancies to find hidden correlations, allowing a dimensionality reduction and a much deeper interpretation. Among these processing approaches, Principal Component Analysis (PCA) is probably the most popular and consolidated method to analyse hyperspectral images (HIS), and used to extract meaningful information from big but frequently low signal datasets. Although PCA reconstruction is widely applied for a qualitative improvement of spectroscopic maps, there are still many open issues concerning the fidelity of reconstructions and the occurrence of “biasing” due to random noise or the use of too few principal components for the reconstruction (*underfactoring bias*). This work aims to study the effect of PCA denoising on the quality of quantitative chemical analysis of few-nm-wide bimetallic AuAg nanoparticles (NPs). We have used both experimental measurements and simulations to test the effect of PCA processing on typical energy dispersive x-ray analysis (EDS) HIS of NPs, and perform a detailed analysis of the reliability of chemical quantification. We have estimated the minimal signal-to-noise-ratio (SNR) necessary to avoid random noise biasing of the PCA reconstruction (Figure 1). If these SNR conditions are fulfilled, our study has revealed that PCA reduces the contribution of Poisson noise to the final uncertainty interval, what leads to a net improvement of the precision of quantitative analysis of chemical composition. It is important to mention that this result is not general for all cases, and it is essential to verify carefully the different HIS experimental parameters and the PCA output to get an effective reduction of PCA biasing. We suggest a practical route to optimize PCA denoising improving EDS quantitative analysis both the point of view of both uncertainty and accuracy; also we have suggested some useful quantitative bias estimators. PCA may be extremely helpful tool, but the user must be aware of limitations and pitfalls that need to be avoided in order to reduce artifacts.

REFERENCES

[1] I. T. Jolliffe, *Principal Component Analysis*, 2 ed.; Springer-Verlag: New York, 2002.

[2] Brazilian Agencies FAPESP, CNPq FAEPEX-UNICAMP and CAPES are gratefully acknowledged for financial support. Funding European Union Seventh Framework Program is gratefully acknowledged.

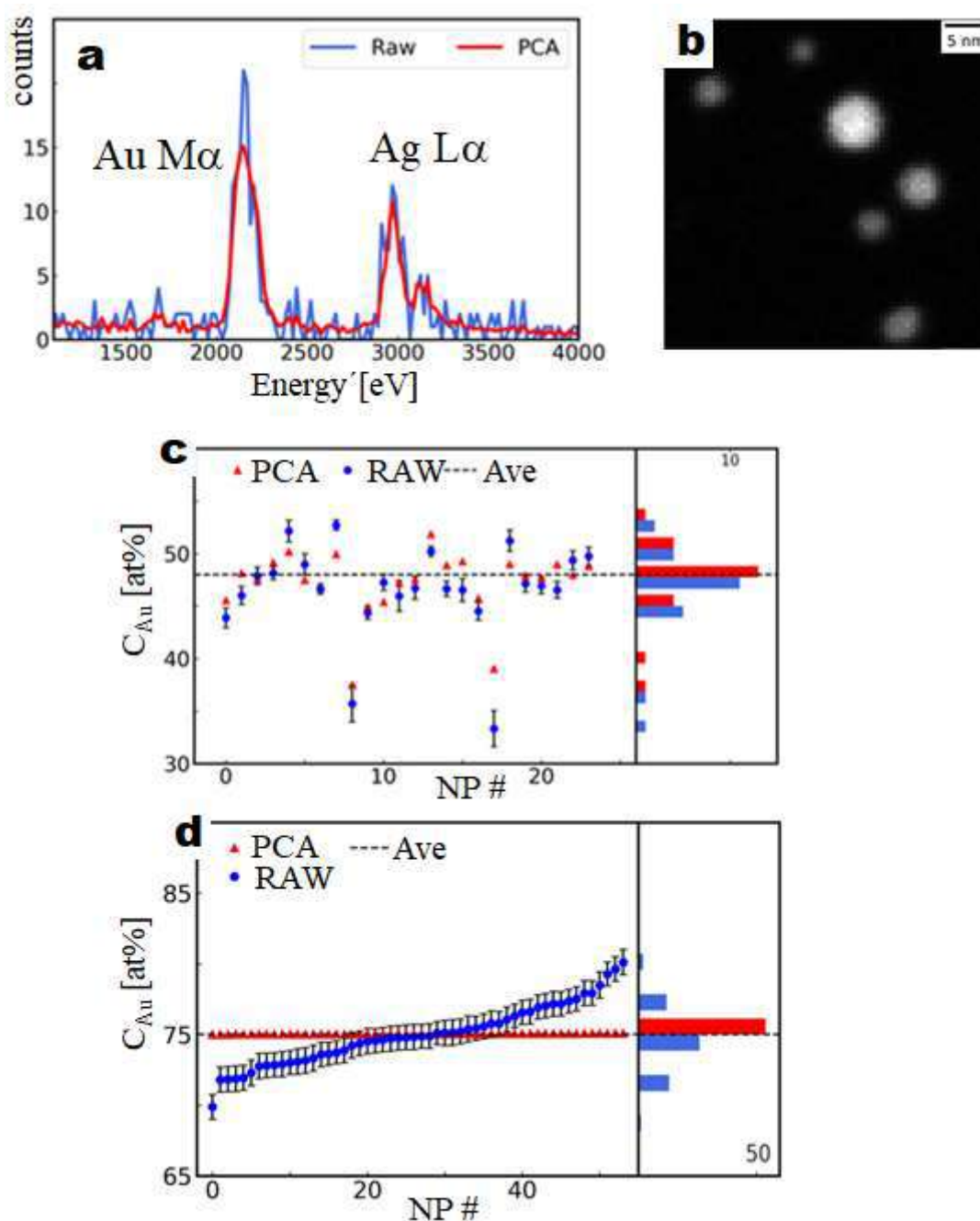


Figure 1. a) Comparison of raw and denoised single-pixel EDS spectrum from a ~ 5 nm NP (AC STEM, Titan Themis, LNNANO-Campinas-Brazil). b) Denoised Au chemical maps. c) Comparison of chemical composition derived using raw and denoised data; note that composition derived from denoised data tend to be closed to sample average composition. d) Simulation of the effect of PCA denoising on the assessment of chemical composition distribution from insufficient SNR (strong random noise bias situation); note that PCA reconstruction can just retrieve the average composition and fails to detect composition dispersion (histograms are displayed along the vertical direction on the right).



Cross-sectional studies in hydroxyapatite crystalline films produced at room temperature by RF magnetron sputtering.

Elvis O. López*, Alexandre Mello, Alexandre M. Rossi, André L. Rossi

Department of Experimental Low Energy Physics, Brazilian Center for Research in Physics (CBPF), Rio de Janeiro, Brazil.

*lopmez@gmail.com/elvis@cbpf.br

In last decades, intense efforts have been devoted to improve the biological performance of dental and orthopedic metal or polymer implants. One critical challenge is the development of bioactive implant coatings that combine long-term stability, mechanical resistance, antibacterial properties, and improved bone regeneration efficiency. Hydroxyapatite (HA, $\text{Ca}_{10}(\text{PO}_4)_6(\text{OH})_2$) has emerged as a candidate material due to its compatibility with components of biological media and blood plasma, osteoconductivity and potential for association with antibiotics and antimicrobials [1,2]. Besides, several chemical and physical techniques for coating implants with this material have been proposed and tested. One of the most used deposition techniques is the radio-frequency magnetron sputtering (RFMS), which have been developed to produce new nanostructured HA coatings for metal implants proposed for biomedical applications [3]. The challenge to use this deposition technique is produce monophasic crystalline HA thin films at room temperature (without need of the use thermal treatment, in-situ or ex-situ). In recent last years it has been possible to perform this challenge by controlling the plasma parameters of deposited ions [4-7]. In this opportunity, a miscellany of results of studies carried out on the interface between HA coatings and substrates will be shown. TEM and HRTEM images at the coating-substrate interface reveal a special crystalline grow, induced by the deposition condition, as well its independence with the substrates used to produce the coatings (Figure 1). Other characterization techniques as: X-ray diffraction by Synchrotron radiation, X-ray photoelectron spectroscopy and Nanoindentation show the high quality of the coating deposited on the Si(100), Ti, TiNx, TiZr and TiZrNx substrates.

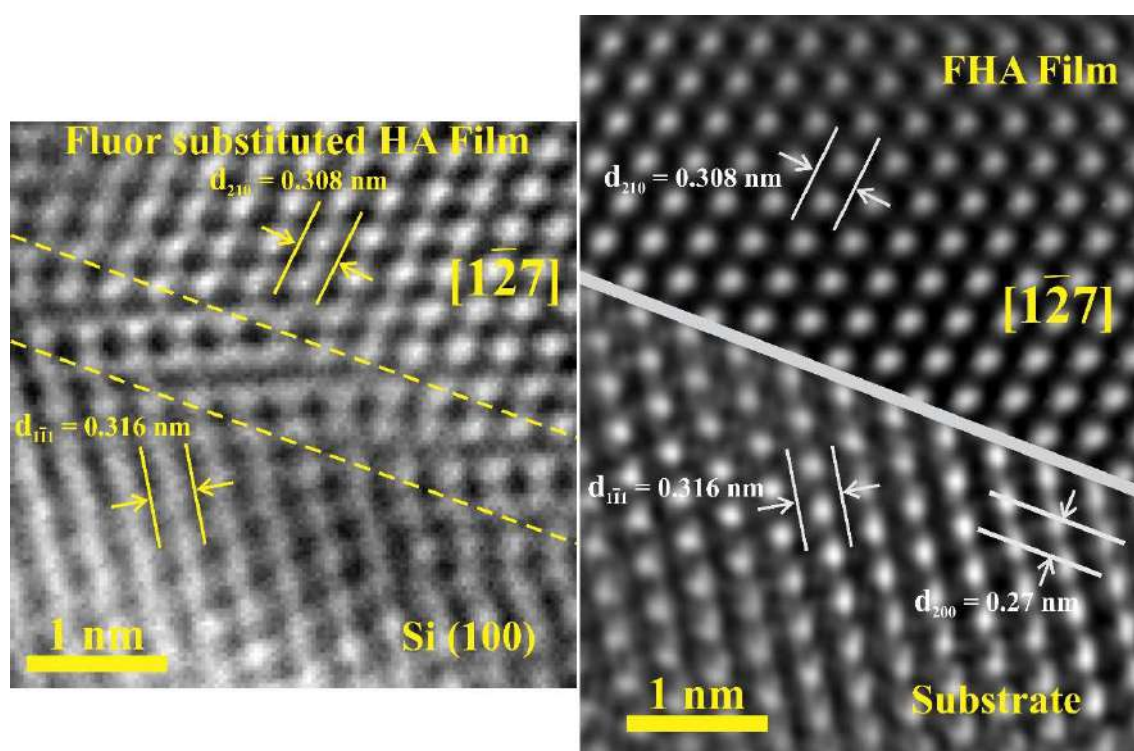


Figure 1: HRTEM image showing the interface between a fluor substituted HA film and Si (100) substrate. The film was produced at room temperature using a right-angle radio-frequency magnetron sputtering (RAMS).

REFERENCES

- [1] L. Wang, G.H. Nancollas, *Chem. Rev.* 108 (2008) 4628.
- [2] V.S. Gshalaev, A.C. Demirchan, Nova Science Publishers, New York, 2012.
- [3] S. Zhang, CRC Press Taylor & Francis Group, New York, 2013.
- [4] E.O. López, A. Mello, H. Sendão, L.T. Costa, A.L. Rossi, R.O. Ospina, F.F. Borghi, J.G. Silva Filho, A.M. Rossi, *ACS Appl. Mater. Interfaces* 5 (2013) 9435.
- [5] E.O. López, A.L. Rossi, B.S. Archanjo, R.O. Ospina, A. Mello, A.M. Rossi, *Surf. Coat. Technol.* 264 (2015) 163.
- [6] E.O. López, A. Mello, M. Farina, A.M. Rossi, A.L. Rossi, *Surf. Coat. Technol.* 279 (2015) 16.
- [7] E.O. López, F.O. Borges, A.M. Rossi, R.M.O. Galvão, A. Mello, *Vacuum* 146 (2017) 233.

ACKNOWLEDGMENT

The authors wish to thank the Synchrotron Light Brazilian National Laboratory (LNLS) for providing beam time at the XRD2, the Nanoscience and Nanotechnology Multiuser Lab (LABNANO) at CBPF for the use of the transmission electron microscopy equipment (TEM) and focused ion beam (FIB) in situ lift-out technique, and the Brazilian government agencies CAPES, CNPq and FAPERJ for the scholarships grant awarded.



Transmission Electron Microscopy Characterization Of Indoor Particulate Matter

H. Coelho-Júnior*, P. E. Santiago Brito and R. L. Sommer

Brazilian Center for Physics Research, Rio de Janeiro-RJ, Brazil.

*hcoelhojunior@cbpf.br

It is estimated that most of the world population live in urban areas, breathing diverse types of pollutants daily [1]. This is because there is an increasing number of vehicles and the most diverse industrial activities present in cities, thus contributing to air pollution [1]. According to the World Health Organization, air quality is one of the main risk factors for human health [2]. Particles with a diameter smaller than $2.5\mu\text{m}$ ($\text{PM}_{2.5}$) are generally more dangerous while ultrafine particles (one micron in diameter or less) can penetrate tissues and organs, posing an even greater risk of systemic health impacts [2]. A recent study has investigated the potential risk of the toxicity of $\text{PM}_{2.5}$ to vascular endothelial cells [3]. In this context, recently [4] a network of North-American universities and research centers launched a research campaign named HOMEChem (House Observations of Microbial and Environmental Chemistry), aimed to investigate the indoor environment especially about the quality of indoor air inside and around buildings and structures aiming health and comfort of its occupants [5]. The idea is that by investigating indoor particulate matter suspended in the atmosphere of houses can help to understand the risk of health problems in closed environments [3]. A research-based on the distribution of $\text{PM}_{2.5}$ estimated by satellite data reveals the importance of adopting more restrictive air quality standards in Brazil [6]. In the present work we investigate the indoor particulate matter collected in São João de Meriti (SJM) city, localized in Rio de Janeiro metropolitan area (Eastern Brazil). In Figure 1 (a) and (b) the arrow indicates the Rio de Janeiro metropolitan area material collection site for the present study, chosen with basis on reference [6] and inspired by reference [4]. As it can be seen in Figure 1 (a), the density of particulate matter in the atmosphere at this site lies in the middle to high-level range (10 to $23\ \mu\text{g}/\text{m}^3$), thus motivating even more research on the subject. After the collection we performed HR-TEM characterization of the indoor particulate matter, motivated by possible new applications in HOMEChem [4] like campaigns and on the assessment of health risk by air pollution in Brazil. The atmospheric material was deposited directly on Ni holey carbon grid accommodated in a house at SJM-RJ and characterized by the TEM from LABNANO/CBPF [see Figure 1 (d)]. HR-TEM micrographs shown in Figures 1 (f) and (g) reveal the crystalline character from the region analyzed with the presence of nanoparticles of $\sim 5\ \text{nm}$ as observed in Figure 1 (g). EDS analysis from the sample is showed in Figure 1 (h) and demonstrated the presence of the following elements: O, Na, Mg, Si, Y, S, K, and Ca. The interplanar spacing indicated in Figures (f) and (g) were indexed and they may be attributed to several structures as: calcite, aragonite, dolomite, calcium silicate, potassium sulfate, sulfur dioxide, and quartz. Our preliminary study shows the presence of indoor nanoparticulate matter and suggest the need for major studies about the possibility for example, of catalysis phenomena, associated with indoor environmental pollutants by the nanocrystals present in indoor air from SJM-RJ. Additionally, TEM can be a useful tool for improving the foundation for PM risk assessments stimulating to HOMEChem campaign [7]. Moreover, our efforts can help to design distributed devices to monitor air quality in smart cities strategies [8,9].

REFERENCES

- [1] V. Van Tran et al, *Int. J. Environ. Res. Public Health*. 17 (2020) 2927.
- [2] World Health Organization. https://www.who.int/health-topics/air-pollution#tab=tab_1 (accessed May 27, 2021).
- [3] W. Xie et al, *J. Appl. Toxicol.* 41 (2021) 713–723.
- [4] J.P.D. Abbatt and C. Wang, *Environ. Sci. Process. Impacts*. 22 (2020) 25–48.
- [5] J. Sundell, *Indoor Air*. 14 (2004) 51–58.
- [6] W.L. Andreão et al, *Environ. Res.* 192 (2021) 110288.
- [7] A. Broström et al, *Sci. Rep.* 9 (2019) 8093.
- [8] M. Carminati et al, *Smart Cities*. 4 (2021) 146–155.
- [9] S. Thomas et al, *Sensors Actuators A Phys.* 244 (2016) 138–145.

ACKNOWLEDGEMENTS

We acknowledge financial support from Brazilian agencies: FAPERJ, FINEP, and CNPq. Additionally, H.C.-J. and P. E. S. B. would like to express your acknowledgments at Programa de Vocação Científica (PROVOC) from CBPF.

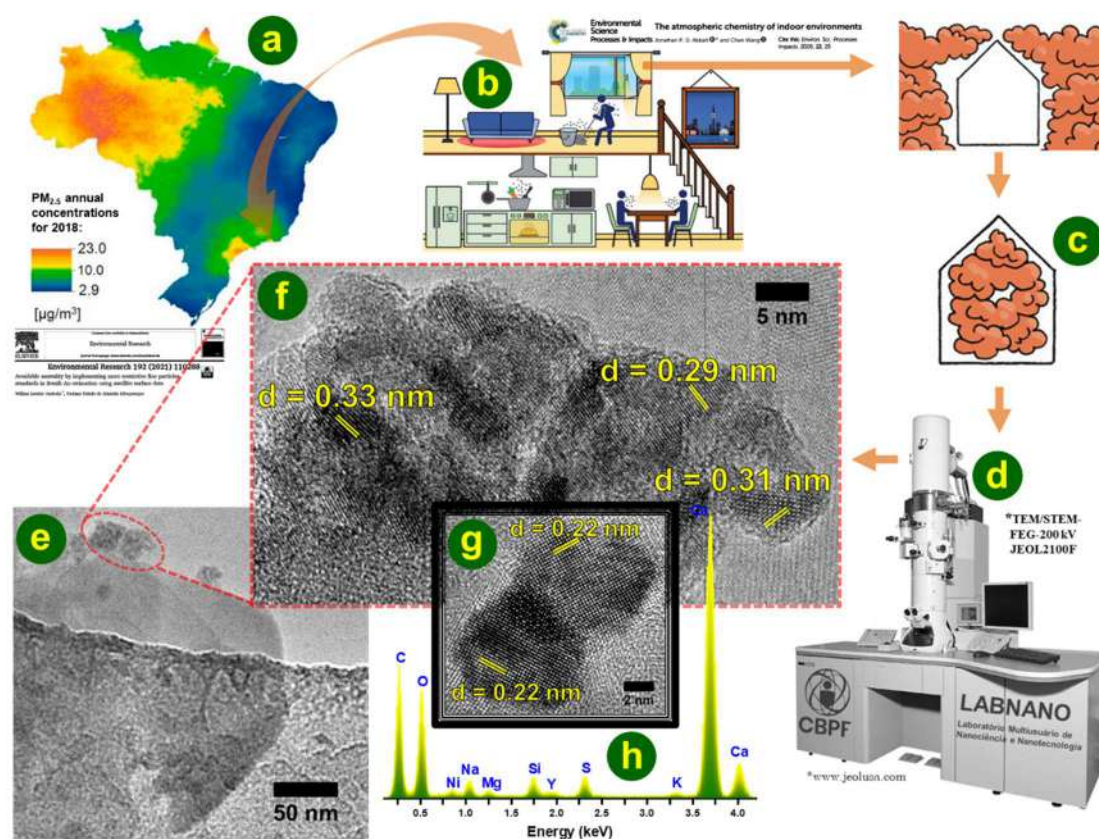


Figure 1: Schematic representing TEM studies of indoor particulate matter from SJM-RJ. (a) indicate the selected region [6] for collection of indoor particulate matter [arrow from (a) to (b)] motivated by the HOMEChem campaign [4]. (b)-(d) we pictorially presented our strategy to collect atmospheric material for analysis by using TEM from Laboratório Multiusuário do Nanociência e Nanotecnologia (LABNANO) from CBPF. In (e) we show a micrograph in lower magnification with HR-TEM (f) from a region its (red dashed line) revealing interplanar spacing respectively indexed. The presence of nanocrystals are observed in (g). (h) is an EDS analysis from the sample studied.



Design of Experiments Approach to nanocellulose production: transforming food waste in nanoproduct

Laryssa Pinheiro Costa Silva¹, Pedro Henrique Cassaro Lirio² and Marco Cesar
Cunegundes Guimarães^{3*}

^{1,2,3}. Federal University of Espírito Santo, Department of Morphological Sciences,
Vitória, Brazil.

*marco.guimaraes@ufes.br

Approximately 40% of all food produced every year goes wasted. The proportion of food and agricultural waste generated at the pre-consumer level represents a significant burden on the environment and remains a global challenge¹. *Cocos nucifera* produces fruits with different applications, however, green coconut fiber is not used². Here, using a statistical tool, a sustainable nanofabrication approach is developed to produce nanocellulose (NC) from cellulose extracted from coconut fiber. A Design of Experiments (DOE), capable of simultaneously analyzing factors that may affect the NC production, time (h) and sample quantity (g). Nanocellulose was produced using mechanical force (glass balls) and water as a solvent. The material obtained was centrifuged and the supernatant and pellet were lyophilized. The samples were structurally characterized by scanning electron microscopy (SEM) and transmission (MET), and the functional groups were confirmed by Fourier-transform infrared spectroscopy (FTIR) and Raman. The optimal conditions for the NC were 15.424h and 0.031g cellulose/mL. The images obtained by SEM and TEM showed that the nanomaterials present in the precipitate are cellulose nanofibers (NCF) (10-20 nm diameter), while in the supernatant they are cellulose nanocrystals (NCC), with diameter 13,95 and 200 nm length. In addition, 92.65% of the material recovered after NC production, corresponds to NCCF and 7.35% to NCC. Thus, the study demonstrated that DOE for optimization is an excellent tool for determining the optimal condition of NC production. Finally, we expected that is possible to produce a high added value nanoproduct from the waste, using only water and mechanical strength.

REFERENCES

- [1] Andler, S.M., et al., *npj Sci Food*, 2 (19), 2018.
- [2] Brainer, Cad. Set. ETENE, 3 (61) 2018.
- [3] This research was supported by CNPq (Brazil), Ministry of Science and Technology, the Ministry of Science and Technology and Foundation Support Research and Innovation of Espírito Santo. This work used the equipment facilities at the Laboratory of Cellular Ultrastructure Carlos Alberto Redins, the Laboratory of Biomolecular Analysis at Federal University of Espírito Santo and the Laboratory of Federal Institute of Espírito Santo, Serra campus.

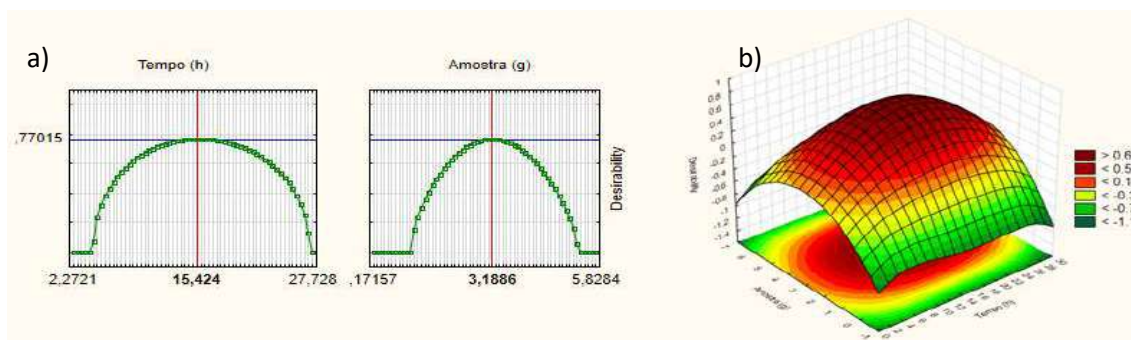


Figure 1. (A) Graph of the desirability function. Maximum response for Nanocrystal (g) and Nanofiber (g). (B) Response surface graph of the desirability function.

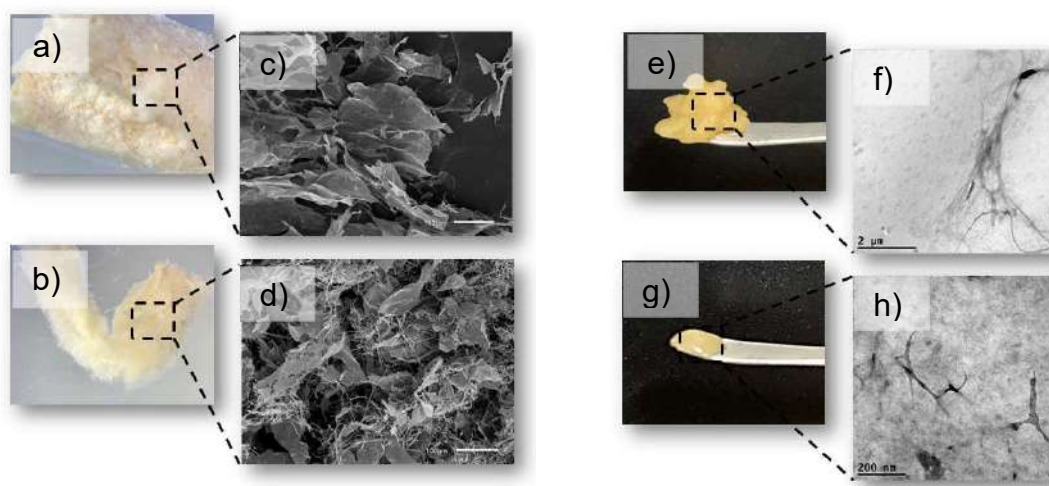


Figure 2. Appearance of the lyophilized precipitate (a) and supernatant (b). Images obtained by SEM of the lyophilized precipitate (c) and supernatant (d). Appearance of the hydrated precipitate (e) and supernatant (g). Images obtained by SEM of the hydrated precipitate (f) and supernatant (h).

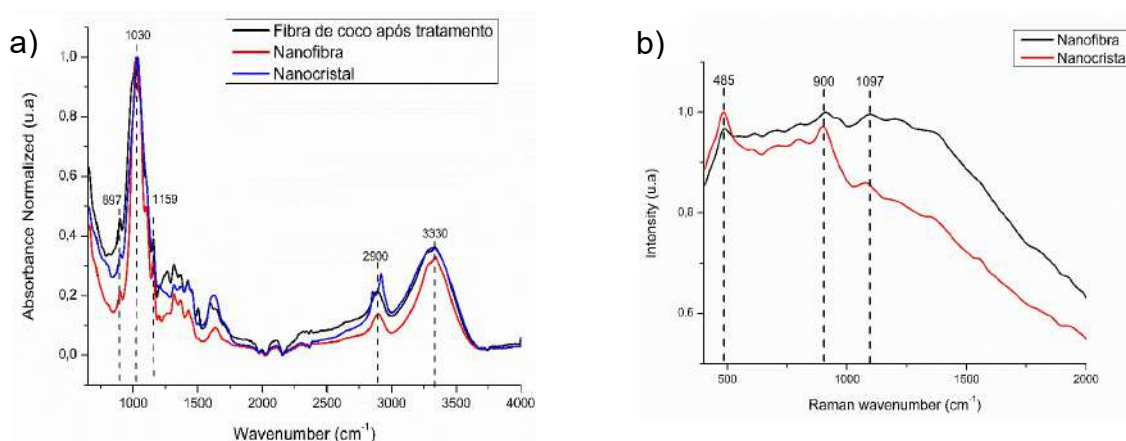


Figure 3. A) FTIR spectra of powdered coconut fibers after the treatment of cellulose extraction (black), nanofiber (red) and nanocrystal (blue). B) Raman spectra of nanofiber (black) and nanocrystal (red).



Influence of Particle Size and Inversion Degree on the Raman Spectra of MnFe_2O_4 Synthesized by the Sol-Gel and Combustion Methods

Mattheus Torquato^{1*}, Eliel Gomes da Silva Neto², Emilson Ribeiro Viana Junior³ and Ronaldo Sergio de Biasi¹

¹ Seção de Engenharia de Materiais, Instituto Militar de Engenharia, 22290-270, Rio de Janeiro, RJ, Brazil.

² Departamento de Física do Estado Sólido, Universidade Federal da Bahia, 40170-110, Salvador, BA, Brazil.

³ Departamento Acadêmico de Física, Universidade Tecnológica Federal do Paraná, 80230-901, Curitiba, PR, Brazil.

*mtorquato@ime.eb.br

Spinel ferrites are ferrimagnetic metal oxides with the general formula AB_2O_4 , where A and B are divalent and trivalent metallic cations, respectively, that can occupy sites with tetrahedral (T) and octahedral (O) symmetry. In the last decades, these materials have been used in electronics and biomedicine due to low fabrication cost and the fact that their magnetic properties can be adjusted by the cation distribution between sites T and O, known as inversion degree (ID), which depends, among other parameters, on particle size [1]. A spinel ferrite is called normal (ID = 0) when divalent cations (A) occupy T sites and trivalent cations (B) occupy O sites, and is called inverse (ID = 1) when A cations occupy half of the O sites and B cations occupy all T sites and half of the O sites. When the occupancy is partial the spinel is called mixed and the ID is a number between 0 and 1. This study proposes a semiquantitative way, using Raman spectroscopy, to evaluate the influence of particle size on the inversion degree, in a manganese ferrite (MnFe_2O_4), from the ratio of the Raman peak intensities of the vibrational mode A_{1g} , related to the presence of Fe^{3+} and Mn^{2+} in the T sites. To reach this goal, four samples were prepared by two combustion methods with two different masses of the fuel, defined by a ratio between the fuel mass and the moles number of the precursor nitrates (2 for iron and 1 for manganese), to obtain different particle sizes. The samples prepared by self-sustained combustion with glycine ($\text{C}_2\text{H}_5\text{NO}_2$) as a fuel were called GN1 and GN2 and the fuel ratio (G/3) were 1 and 2, respectively, while the samples prepared by sol-gel combustion, called ACN1 and ACN2, used citric acid ($\text{C}_6\text{H}_8\text{O}_7$) as a fuel and their ratio (AC/3) were also 1 and 2, respectively. The powders were characterized by X-ray diffraction (XRD), Raman spectroscopy, transmission electron microscopy (TEM) and selected area diffraction (SAD). The XRD and SAD results show the expected crystalline phase MnFe_2O_4 (see Figure 1) with the lattice parameter for ACN1 and ACN2 samples

REFERENCES

- [1] K. Nejati and R. Zabihi. Chemistry Central Journal 2012, 6:23
[2] Z. Surowiec et al. NUKLEONIKA 2015, 60(1):137-141



The authors thanks CNPq, CAPES, Fundação Araucária and FAPEMIG for financial support.

significantly smaller than GN1 and GN2. We also observed different crystallite sizes for each sample, while TEM images confirms different particle size distributions (see Figure 2). The Raman measurements revealed an increase of the intensity ratio between the peaks A_{1g} for Fe^{3+} and A_{1g} for Mn^{2+} as the particle size decreases (see Figure 3 and Table 1), which suggests a higher inversion degree for the samples with smaller particle size. The Raman results also match the reduction in lattice parameter, which is expected when the Fe^{3+} cations move to the T sites [2]. Finally, this study provided a way to estimate the inversion degree and observe the effect of size reduction by Raman spectroscopy.

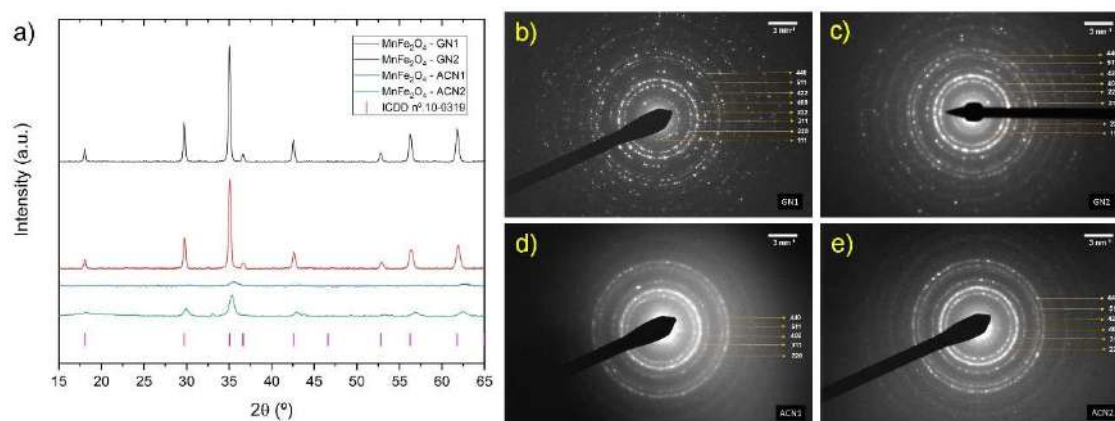


Figure 1 – (a) X-ray diffraction patterns of samples GN1, GN2, ACN1 and ACN2. Selected area electron diffraction patterns of samples (b) GN1, (c) GN2, (d) ACN1 and (e) ACN2.

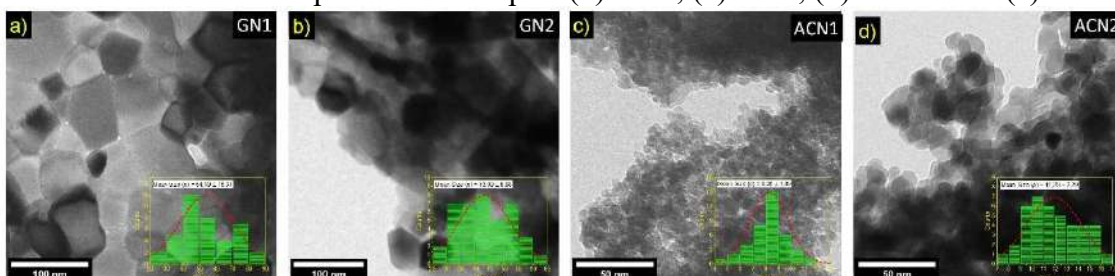


Figure 2 – TEM images and respective particle size distribution histogram (inset) of samples (a) GN1, (b) GN2, (c) ACN1 and (d) ACN2.

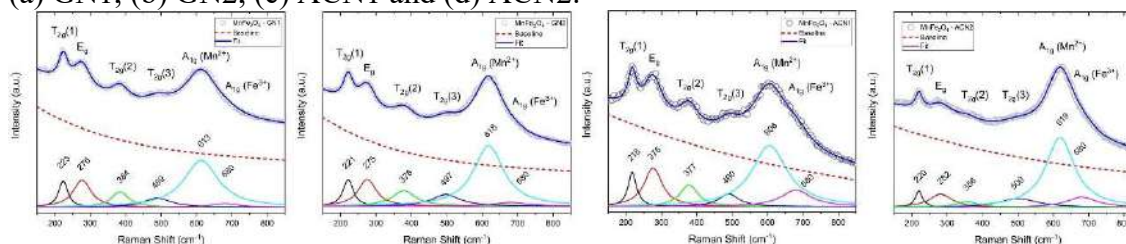


Figure 3 – Raman spectra of samples (a) GN1, (b) GN2, (c) ACN1 and (d) ACN2. The deconvolutions are shown below the experimental curves.

Table 1 – Lattice parameter (a), crystallite size (d), particle size (p) and relative fraction of the vibrational modes A_{1g} of Mn^{2+} and Fe^{3+} .

Sample	a (Å)	d (nm)	p (nm)	$I_{a-A_{1g}-Fe^{3+}} / I_{a-A_{1g}-Mn^{2+}}$ (%)
MnFe ₂ O ₄ – GN1	8.50	36.1	54 ± 16	6.2
MnFe ₂ O ₄ – GN2	8.49	28.1	43.1 ± 9.0	7.1
MnFe ₂ O ₄ – ACN1	8.38	6.2	8.3 ± 1.5	21.5



$\text{MnFe}_2\text{O}_4 - \text{ACN}_2$	8.42	12.8	11.9 ± 2.3	15.7
--	------	------	----------------	------



Characterization of Precipitates in an CuAlNi Shape-Memory Alloy After Aging Thermal Treatments.

Micaela Panizo^{1*}, Fran Bubani², Rosana Gastien³, Eugenia Zelaya⁴

¹ Departamento de Física, Facultad de Ciencias Exactas y Naturales, Universidad de Buenos Aires, 1428 Ciudad Universitaria, CABA, Argentina.

² División Física de Metales, Centro Atómico Bariloche (CAB-CNEA-CONICET) and Instituto Balseiro, UNCuyo, Av. Bustillo 9500, R8402AGP, Bariloche, RN, Argentina.

³ Departamento de Investigaciones en Sólidos, CITEDEF, UNIDEF, J. B. de La Salle 4397, 1603 Villa Martelli, Buenos Aires, Argentina

⁴ División Física de Metales, Centro Atómico Bariloche (CAB-CNEA-CONICET), Av. Bustillo 9500, R8402AGP, Bariloche, RN, Argentina.

*micaela.mpanizo@gmail.com

Shape memory alloys are considered smart materials because of their particular thermo-mechanical properties, which are related to a first order martensitic transformation (MT) between a parent β phase and one or more martensitic phases [1]. Particularly, shape-memory CuAlNi alloys have a high temperature disordered body-centered cubic phase. After quenching, which consists in annealing at 1203K for 1h followed by quenching in water mixed with ice, an ordered β phase can be obtained and kept in a metastable state at room temperature. This β phase can undergo martensitic transformation either by cooling or by applying mechanical stress. It is possible to modify the thermo-mechanical behavior and microstructure of these alloys with isothermal treatments, which are called ageing treatments, at suitable temperatures [2,3]. Transmission electron microscopy images are able to reveal microstructural defects after these ageing thermal treatments, such as precipitation of stable phases (γ , α) and dislocations in the β phase matrix. The aim of the present work is to compare the microstructural evolution of two samples obtained from the same monocrystal, submitted to different ageing treatment procedures at 473K. Both samples were aged for 7.5h. In one of them, the ageing treatment was performed in 8 half-hour cycles, and the other in one single cycle of 7.5h. The microstructural evolution was analyzed by various transmission electron microscopy techniques. α and γ precipitates were observed in both samples and precipitate sizes were compared. The presence of α and γ precipitates in the metastable β matrix was corroborated by the indexation of selected area diffraction patterns consistent with the γ and α structure. Also, γ precipitate size histograms of samples with different heat treatments are compared. Results show that precipitate size distribution is similar in the conditions studied. Scanning transmission electron microscopy (STEM) images obtained with a short camera length show lighter contrast for the alpha precipitates, which have a characteristic cross shape. Moreover, an energy dispersive X-ray spectroscopy (EDS) line scan shows an increase in Cu in the alpha precipitate. An annular dark field image reveals the presence of the order domains around the alpha precipitates and the presence of dislocations. The observation of this kind of dislocations are attributed to a relaxation of the system due to the presence of alpha phase precipitates in beta matrix.

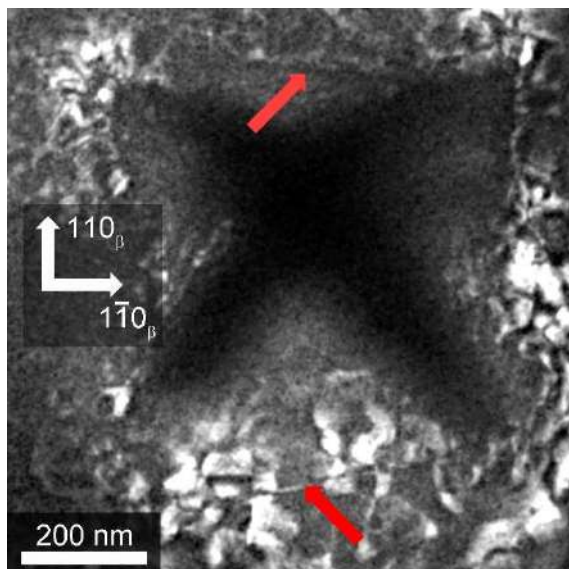


REFERENCES

- [1] Otsuka K., Wayman, C.M. Shape Memory Materials, Cambridge University Press, Cambridge, UK, 1998.
- [2] Gastien R., Corbellani C.E., Araujo V.E.A., Zelaya E., Beiroa J.I., Sade M., Lovey F.C., Mater Charac 84 (2013) 240-246.
- [3] Araujo V.E.A., Gastien R., Zelaya E., Beiroa J.I., Corro I., Sade M., Lovey F.C., J. Alloys Compd, 641 (2015) 155-161.

ACKNOWLEDGEMENTS

Financial support from PICT-2017-0427 (*Agencia Nacional de Promoción de la Investigación, el Desarrollo y la Innovación – Argentina*) and PUE 018-2018 (Consejo Nacional de Investigaciones Científicas y Técnicas, Argentina) is acknowledged.



Distorted L21 order domains around an α precipitate (dark). Centered dark field image. The red arrows point the dislocations.



TEM CHARACTERIZATION OF Ti-12Mo-xNb ($0 \leq x \leq 20$) ALLOYS

Caio Marcello Felbinger Azevedo Cossú^{1*}, Carlos Angelo Nunes¹, Loic Charles Malet²,
Luiz Henrique de Almeida³ e Sinara Borborema⁴

¹ Universidade de São Paulo, DEMAR/EEL, Lorena, Brazil.

² Université Libre de Bruxelles, Brussels, Belgium

³ Universidade Federal do Rio de Janeiro, PEMM/COPPE, Rio de Janeiro, Brazil

⁴ Universidade do Estado do Rio de Janeiro, Departamento de Engenharia Mecânica/
Faculdade de Tecnologia, Resende, Brazil

*sinarab@msn.com

ABSTRACT

Titanium and titanium alloys are the most attractive materials for dental and orthopedic implants due to their light weight, biocorrosion resistance, good biocompatibility and mechanical properties, including low Young's modulus. Titanium alloys can be classified as α , $\alpha + \beta$ and β -type. The beta titanium alloys also can be classified into three categories, stable β , metastable β and near β , as function of the molybdenum equivalent [Mo eq]. If the [Mo eq] is lower than 11 wt. %, martensitic transformation may occur during quenching from temperatures above the β transus. The type of martensite phase formed (α' or α'') depend on the solute concentration in the titanium alloy. The α' martensite phase forms in diluted alloys and has a hcp structure, while the α'' phase is formed in concentrated alloys with an orthorhombic crystal structure. Besides, another metastable ω phase (hcp structure) also may precipitate in the β -Ti matrix during quenching. The aim of this study was to carry out a microstructural characterization of Ti-12Mo-xNb ($0 \leq x \leq 20$) alloys. The alloys were prepared from pure elements through arc melting under argon. The obtained ingots were solution treated at 950 °C under argon atmosphere for 1 h into a tubular furnace and then quenched in water at room temperature. The microstructure of the alloys were investigated by transmission electron microscopy (TEM) under 200 kV. The thin foils were produced using a double jet polishing unit, using a 10% perchloric acid -ethanol solution at -20 °C with a 35V D.C. potential. The TEM bright-field image of Ti-12Mo (Mo eq = 12), Ti-12Mo-3Nb (Mo eq = 12.84) and Ti-12Mo-20Nb (Mo eq = 17.6) alloys are shown in Fig. 1. The dark-field image of the Ti-12Mo shows ω phase precipitated in a β matrix with the diffraction pattern of β and ω phases (Fig. 1a) and martensitic α'' lamellas with the diffraction pattern of β and α'' phases (Fig 1b). The Nb addition resulted in the suppression of α'' phase and decrease of the ω phase, confirming the effect of "Mo eq" on β stabilization. The dark-field image of the Ti-12Mo-3Nb alloy (Fig. 1c) shows ω phase precipitated in a β matrix with the diffraction pattern of β and ω phases. Although the amount of ω phase decreases for higher Nb contents, ω precipitates with a near-spherical morphology can be observed on thin foil of Ti-12Mo-20Nb alloy, Fig. 2d. In conclusion, the microstructure of Ti-12Mo-xNb alloys are sensitive to Nb content. The suppression of α'' phase and the reduction of ω precipitation is in good agreement with the literature, since the increase of the [Mo eq] increase the stability of the β -phase.

ACKNOWLEDGEMENTS: This work was supported by CNPq, CAPES and FAPERJ.

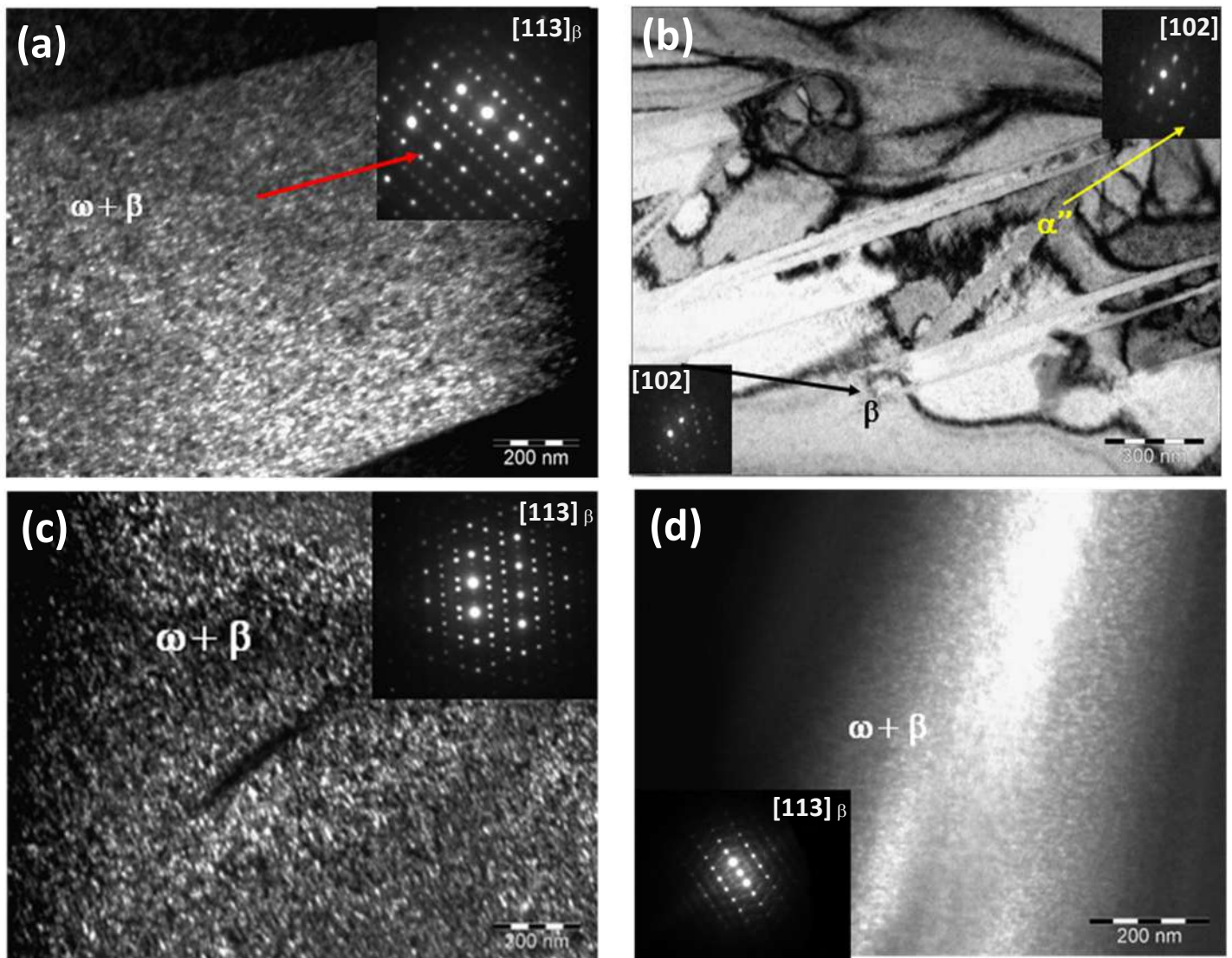


Figure 1 (a) TEM dark-field image of ω phase with a near-spherical morphology precipitated in a β matrix in the Ti-12Mo alloy and SAED pattern of β and ω -Ti with the $[113]_{\beta}$ axis zone, (b) bright-field image of the martensitic α'' lamellas and SAED pattern of β and α'' phases in the Ti-12Mo alloy; (c) and (d) dark-field image of the ω precipitates with a near-spherical morphology in a β matrix in the Ti-12Mo-3Nb and Ti-12Mo-20Nb alloys, respectively.



In vitro* culture and characterization of life cycle of *Metarhabditis blumi

Santos ACB¹; Caracciolo ME^{1,2}; Lopes-Torres EJ,^{1*}

¹ Laboratório de Helmintologia Romero Lascasas Porto (LHRLP), FCM/UERJ, Rio de Janeiro/RJ

² Centro Multiusuário para Análise de Fenômenos Biomédicos da Universidade do Estado do Amazonas (CMA), ESA/UEA, Manaus/AM

* eduardo.torres@uerj.br

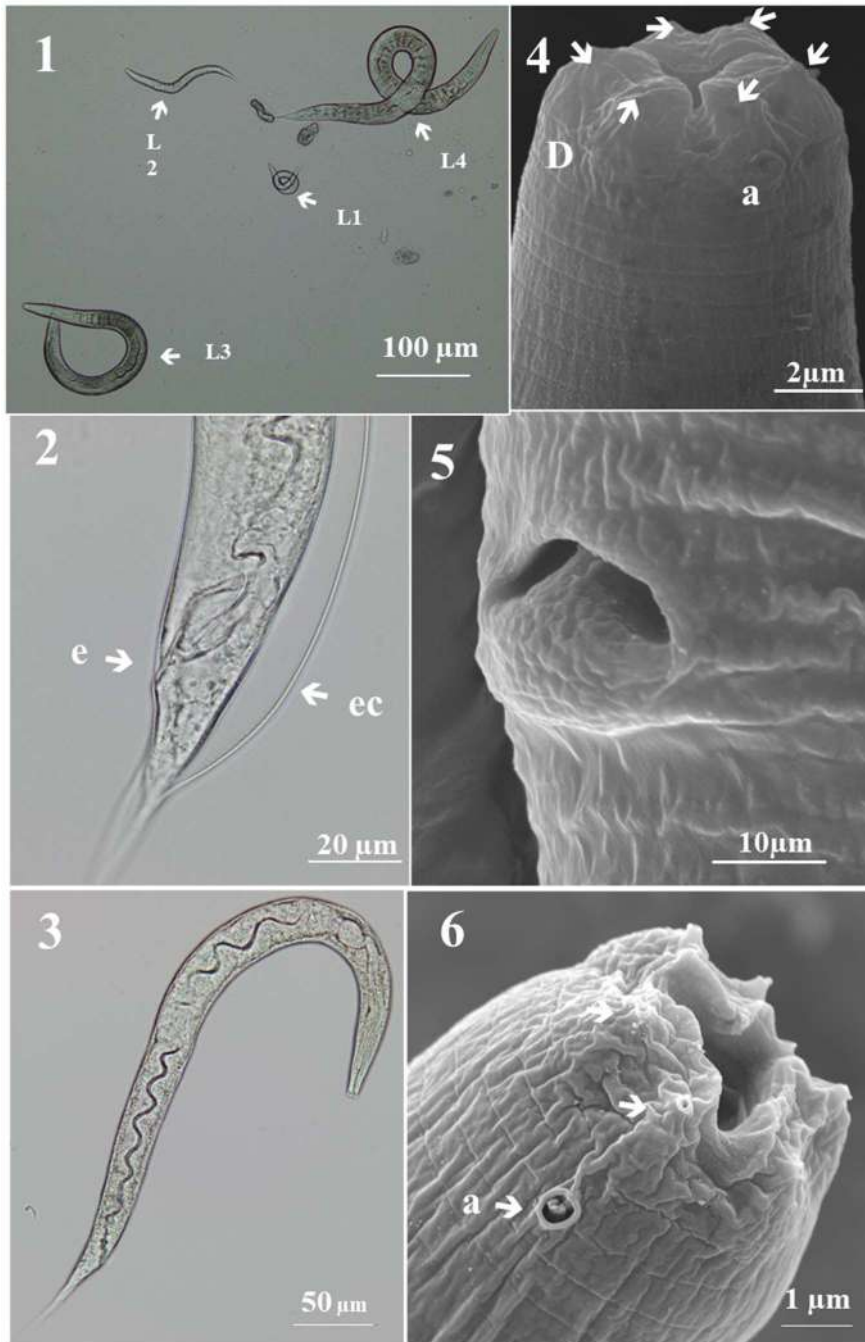
Parasitic otitis in cattle causes serious impact on animal health, mainly in production of dairy herds. Nematodes *Metarhabditis* spp. are associated with this infection [1], developing an intense inflammatory process and, in severe cases, can lead the animal to death [2]. In this work we aimed to establish freezing protocols, and *in vitro* cultivation of the nematode *M. blumi* to characterize and describe the morphology of the larval stages. *M. blumi* strain was acquired from the Caenorhabditis Genetics Center (USA) and maintained in Growth Medium Nematode Culture (NGM) supplemented with *E. coli* OP50 in BOD incubator, following the adapted protocol Stiergnale, 2006 [3]. Nematodes, previously washed in PBS, were frozen by the soft agar method, and kept at -80 ° C for 24 hours to 30 days. For the morphology characterization the parasites were washed in PBS and fixed in Karnovsky solution (4% formaldehyde, 2.5% glutaraldehyde and 0.1 M cacodylate buffer - pH 7.2). For Light microscopy, nematodes were clarified in lactophenol and mounted between in temporary slides with coverslip and observed using Normaski interference contrast. For Scanning Electron Microscopy (SEM), nematodes chemically fixed, were washing in PBS, post fixed in osmium tetroxide (OsO₄) 1% and ferrocyanide in distilled water, dehydrated in ethanol, drying by the CO₂ critical point and sputtered with gold (15-20 nm). Based on our results, we analyzed four larval stages of *M. blumi* development, characterizing as L1, L2, L3 e L4 (Fig.1). Was possible identify the complete digestive system and details of the anterior region (lips, stoma and esophagus) (Fig.3). In the posterior region, we observed the anus (or cloaca) and was possible to identify the genital primordium of the L4 stage showing the cuticle change in molting process (ecdysis) (Fig.2 and 5). Exploring the SEM tool, we detailed the ultrastructure of the anterior region of the nematodes, showing the organization of the lips, the distribution of amphids and cephalic papillae (Fig.3 and 6). The *M. blumi in vitro* culture allows us to add details of morphological structures, enriching the taxonomy information of the group, contributing to biological cycle information of the *Metarhabditis* parasites, enabling the use of these species as an experimental model for improve the strategies of control, including with new pharmacological treatments protocols.

[1] MARTINS W. Jr., Nunes I. J., Ribeiral L. A., Rosaz C. E. E., Nunes V.A. 1971.

[2] BARBOSA J. D., Barbosa J., Henrique D., Henrique L., Araújo V., Loiola L., Alessandra, S., Reis B., Masiero, F., Farias M. DE. 2016.

[3] STIRTNAGHLE, T. Maintenance of *C. elegans*. WormBook, ed. The *C. elegans* Research Community, WormBook. 2006

Acknowledgments: FAPERJ-JCNE and CNPq.



Legends: Light microscopy (Normaski Interference contrast) and Conventional SEM of nematodes larvae of *Metarhabditis blumi*. Fig. 1: Four stages of life cycle showing the difference in size and structural detail of each stage; Fig. 2: Posterior region, highlighting the cloaca, the spicules in developing process (e) and the cuticle exchange; Fig. 3: Larva L2 in lateral-dorsal view showing the body overview highlighting the digestive system developed; Fig. 4: Anterior extremity in laterodorsal view, showing the dorsal (D), lateroventral lips, amphid (a) and cephalic papillae (arrows); Fig. 5: Detail of the opening of the anus or cloaca; Fig. 6: Anterior region in lateral view showing the amphid (a) and cephalic papillae (arrows).



Non-paraxial Theory for the microscope image of Spherical Dielectric Objects and Colloidal Particles

*Fran Gómez¹, Rafael. S. Dutra², Luis. B. Pires¹, Glauber R. de S. Araújo³, Bruno Pontes^{4,5}, Paulo A. Maia Neto^{1,5}, Herch M. Nussenzveig^{1,5}, and Nathan B. Viana^{1,5}.

¹Instituto de Física, Universidade Federal do Rio de Janeiro, Rio de Janeiro, RJ, Brasil.

²LISComp-IFRJ, Instituto Federal de Educação, Ciência e Tecnologia, Rua Sebastião de Lacerda, Paracambi, RJ, Brasil.

³Instituto de Biofísica Carlos Chagas Filho, Universidade Federal do Rio de Janeiro, Rio de Janeiro, RJ, Brasil.

⁴Instituto de Ciências Biomédicas, Universidade Federal do Rio de Janeiro, Rio de Janeiro, RJ, Brasil.

⁵Centro Nacional de Biologia Estrutural e Bioimagem (CENABIO), Universidade Federal do Rio de Janeiro, Rio de Janeiro, RJ, Brasil.

[*frangocar17@gmail.com](mailto:frangocar17@gmail.com)

We derive an explicit partial-wave (Mie) series for the image of a dielectric microsphere collected by a typical infinity-corrected microscope. We model the propagation of the illumination and scattered vector fields through the optical components of the microscope by using the angular spectrum theorem [1,2] with the help of Wigner rotation matrix elements, allowing us to identify the contribution from spin-orbit helicity reversal [3,4]. We consider a high numerical aperture objective well beyond the validity range of the paraxial approximation. The spherical aberration introduced by refraction at the planar interface between the sample and the glass slide is fully taken into account. By comparing our theoretical model with images of colloidal particles placed at different positions with respect to the objective focal plane, we characterize their radii and refractive index. We employ polystyrene microspheres with a known refractive index in order to fit the transverse attenuation length describing the transmission loss of the scattered field. As an application, we measure the radius and refractive index of individual silica beads. We compare the result for the radius with an independent measurement using high-resolution scanning electron microscopy. To validate the result for the refractive index, we develop a second method, independent of the theoretical model, based on the image contrast in glycerin-water solutions. In all cases we find very good agreement between our method and the validation procedures. In addition, the non-paraxial theory provides an excellent description of the images found for all focal plane positions and for both polystyrene and silica microspheres. Our approach allows to use a common optical microscope to measure the refractive index and radius of spherical particles covering the entire size range from the Rayleigh regime to the ray optics one.

REFERENCES



- [1] L. Novotny et al., *Opt. Lett.* 26 (2001) 789.
[2] L. Mandel and E. Wolf, Cambridge University Press, 1995.
[3] K. Y. Bliokh et al, *Nat. Photonics* 9 (2015) 796.
[4] C. Schwartz et al, *Opt. Express* 14, (2006) 8425.

ACKNOWLEDGMENTS

The authors are grateful to Ubirajara Agero and Oscar Mesquita for inspiring discussions. We also thank the Instituto Nacional de Metrologia, Qualidade e Tecnologia (Inmetro) for letting us use their high-resolution scanning electron microscope. We acknowledge support from the Brazilian agencies National Council for Scientific and Technological Development (CNPq-Brazil), Coordination for the Improvement of Higher Education Personnel (CAPES, Brazil), the National Institute of Science and Technology Complex Fluids (INCT-FCx), and the Research Foundations of the States of Minas Gerais (FAPEMIG), Rio de Janeiro (FAPERJ) and São Paulo (FAPESP).

FIGURES:

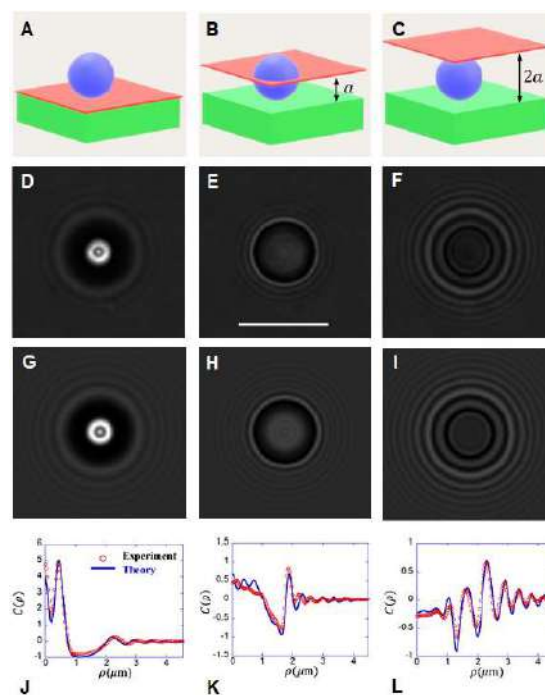


Fig1. From left to right, the image of the polystyrene particle (attached to the glass slide) is brought out-of-focus by driving the microscope stage downwards. As a consequence, the objective focal plane (red) is displaced upwards with respect to the glass slide, as illustrated by panels A, B and C. The corresponding experimental and simulated images are shown in panels D-F and G-I, respectively. Plots of the theoretical (line) and experimental (circles) image contrast versus the distance-to-center ρ are shown in panels J-L. The scale is the same for all images and is indicated by a horizontal bar (5 μm) in panel E.



Sintering of Al-Si Hypereutectic alloy for the production of metal matrix composite via powder metallurgy – a preliminary study

Anderson F. Pereira^{1*}, Paulo Henrique Barreto de Souza de Faria¹, Luciano Monteiro Rodrigues², Bojan Marinkovic² and Paula Mendes Jardim¹

¹ Department of Metallurgical and Materials Engineering, Federal University of Rio de Janeiro, UFRJ, Rio de Janeiro, Brazil.

² Department of Chemical and Materials Engineering, Pontifical Catholic University of Rio de Janeiro – PUC-Rio, Rio de Janeiro, RJ, Brazil

* afpereira@coppe.ufri.br

Aluminum and its alloys occupy an important place in the automotive and aerospace industries due to the association of good mechanical properties and low density, which contribute to the overall weight reduction (i.e., fuel consumption) in vehicles. However, despite the low density of aluminum alloys, their high coefficient of thermal expansion (CTE) still makes it difficult to use these materials as substitutes for steel or cast iron in components where high dimensional stability is required in service. A possible alternative to overcome this limitation is the development of metal matrix composites (MMCs) with CTE close to or lower than that of iron. In this context, we propose the production of a composite of low density and tailored CTE based on a commercial hypereutectic Al-Si alloy (Alumix-231) and ceramics with CTE close to zero or negative, via a powder metallurgy route. Due to the high stability of the Al₂O₃ layer formed spontaneously around powder particles, the sintering of Al alloys requires strict control of the atmosphere to prevent the reoxidation of active metallic surfaces and it usually involves the formation of a persistent liquid phase during the sintering of the material [1]. The present work is in a preliminary phase and aims to study the thermal evolution and sintering behavior of Alumix-231 for future composite fabrication. The processing and sintering route was based on that reported by Heard et al. [3] to optimize the mechanical properties of the alloy. The compaction of the powder was carried out in a uniaxial hydraulic press at 600 MPa and the green-body was subjected to a two-step sintering (delubrication step at 400°C/20min followed by sintering at 560°C/60min) under heating rate of 10°C/min. Differently from the route proposed by Heard et al., the sintering treatment was done under vacuum instead of Nitrogen atmosphere, and the sample was cooled inside the furnace. The powder and sintered compact were analyzed by X-ray diffraction (XRD) for phase identification and the microstructure was observed via scanning electron microscopy (SEM) coupled with X-ray Energy Dispersive Spectroscopy (XEDS). XRD results showed that the alloy in the as-received and sintered condition are both constituted mainly of α -Al and Si with a small fraction of Al₂Cu intermetallic phase. The SEM analysis of Alumix-231 revealed the as-received powder is composed of a mixture of micrometric particles of pure Al and a high-Si master alloy with the presence of Cu and Mg (Figure 1), where the distribution of Si in the alloyed particle relates to the formation of pre-eutectic silicon crystals and the brighter regions observed inside the alloyed particles - Figure 1(a) - are enriched in Cu (Figure 1(c)). Analysis of the sintered sample (Figure 2) indicated the presence of regions of Al, Si and regions rich in Cu (indicative of Al₂Cu). The microstructures observed were consistent with the reported in the literature for this alloy [2,3]. The distribution of the Cu-rich phases in the sintered compact (figure 2) shows that the sintering was efficient to promote



homogenization of the chemical composition. The presence of micropores regions associated with a high oxygen concentration along the particle boundaries (Figure 2 (a, e)) indicates that the sintering step, despite being effective in homogenizing the chemical composition of the material, did not reach 100% densification (which is suggested to be associated with the occurrence of oxidation during this step) and points to the need for greater control of the sintering atmosphere. A sample of the compact after the delubrication step was also analyzed and showed a change in the morphology of the Al₂Cu intermetallic phase when compared to the master-alloy particles, but the distribution of phases was similar to that of the pristine material (powder) as distinct regions of pure-Al and hypereutectic Al-Si-Cu were still observed. Further analyses are in progress to investigate the densification process during sintering (dilatometry of green-body) and the liquid phase evolution (by means of DSC) under nitrogen atmosphere for both the pure alloy and composites with different contents of ceramic reinforcements.

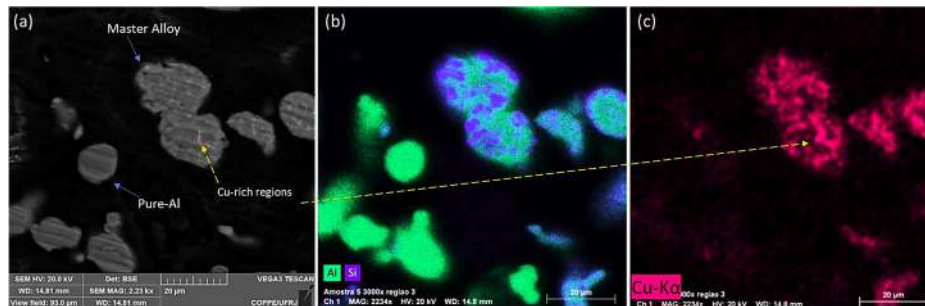


Figure 1 - Backscattered electron SEM images (a) of Alumix-231 powder particles cold-mounted in epoxy and XEDS mappings (b-c) showing the distribution of Al (green), Si (purple) and Cu (pink).

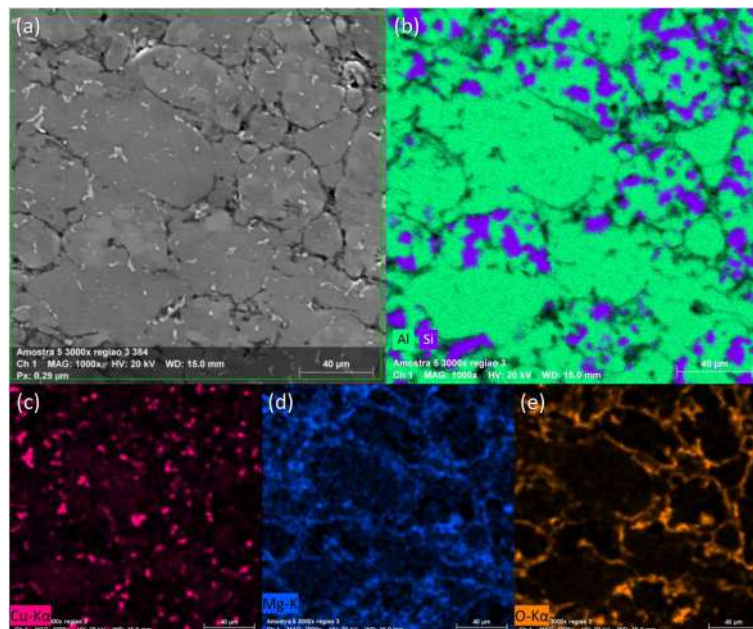


Figure 2 - Backscattered electron SEM images (a) of Alumix-231 sintered compact and XEDS mapping (b-e) showing the distribution of Al (green), Si (purple), Cu (pink) and Mg (blue) and O (orange).



Characterization of Polyurethane Foams Synthesized from Biopolyols

Camila Gomes Peçanha de Souza^{1*}, Sidnei Paciornik¹, José Roberto Moraes d'Almeida¹, Lorenleyn De la Hoz Alford¹, Brenno Santos Leite²

¹ Dept. of Chemical and Materials Engineering (DEQM), PUC-Rio, Rio de Janeiro, Brazil.

² Institute of Exact and Technological Sciences, UFV-Florestal, Minas Gerais, Brazil.

*camilagpsouza@gmail.com

Polyurethane foams are materials with a wide range of applications and of great interest for the market, mainly for their thermal, mechanical, acoustic and low-density properties. Furthermore, there is a growing search for the manufacture of more sustainable polymers, due to the global interest in reducing the use of raw materials derived from fossil fuels. In recent years, there has been an increase in research and also in the production of PU foams of natural and renewable origin. In this context, the present work seeks to characterize the cell microstructure of different types of PU foams, produced from biopolyols derived from agricultural biomass residues, namely: avocado pit, lemon bagasse and cassava skin. Figure 1 shows a first analysis of the foam cells by scanning electron microscopy, where it is possible to identify that the cells of the cassava and avocado foam are considered open cells, and the cells of the lemon foam, closed. The samples were also analyzed in MicroCT, with pixel sizes of 3 μm and 15 μm , in order to observe the three-dimensional structure of the cells. After a sequence of image processing and analysis, it was possible to extract quantitative and qualitative parameters. From the segmentation of the walls of the 3 μm tomographic images, it was possible to make a comparison between the number of cells and the percentage of walls of each foam, as can be seen in Table 1. The image obtained by tomography with 3 μm pixel size refers to an approximately central subvolume of the sample. Figure 2a shows, by way of example, the three-dimensional appearance of the lemon foam cells in terms of volume. The aspect ratio and the average feret diameter were also calculated. For comparative purposes, Figure 2b shows a boxplot of the foam cells volumes. It is noted that the dispersion of data is asymmetric for the volume parameter, evidenced by the difference between the mean and the median and by the difference in the bars the upper and lower limits. The presence of outliers with more expressive values that end up shifting the mean upwards in these distributions is also notorious. As for the lemon and cassava foams, the volume of the cells is similar. Therefore, this series of analysis and characterizations using different techniques of image acquisition and image processing shows that it is possible to have a better understanding of the cellular structure of polyurethane foams, in order to later be able to correlated their microstructure with their mechanical behavior.

REFERÊNCIAS

- [1] S. A. F. Leite et al., Biopolyol and Foam Production from Lemon Bagasse Liquefaction. Congresso Internacional de Biomassa. (2018)
- [2] F De. Pascalis, Quantitative characterization of low-density, high performance polymeric foams using high resolution X-ray computed tomography and laser confocal microscopy. NDT and E International, v. 83, p. 123–133. (2016)

- [3] N. Mills, Polymer Foams Handbook: Engineering and Biomechanics Applications and Design. (2007)
- [4] N.V. Gama et al., Polyurethane foams: Past, present, and future. Materials, v. 11, n. 10. (2018)
- [5] This research was supported by CAPES, CNPq and FAPERJ.

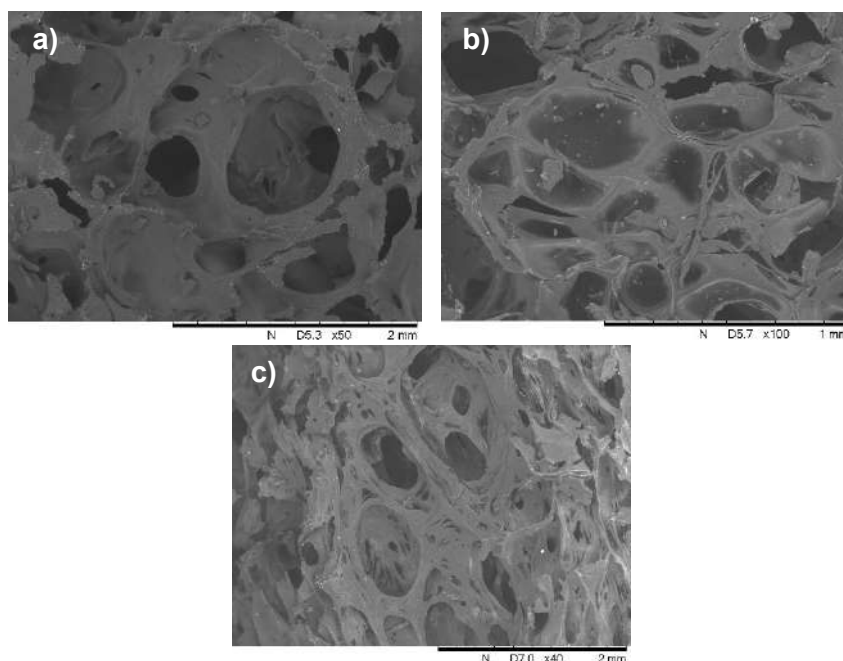


Figure 1: Scanning Electron Microscopy images of: a) Cassava; b) Lemon; c) Avocado.

Table 1 - Number of cells and percentage of walls: Avocado pit, lemon bagasse and cassava skin.

Foam	Avocado	Lemon	Cassava
Number of cells	1317	2709	847
% of walls	5,81	3,19	15,97

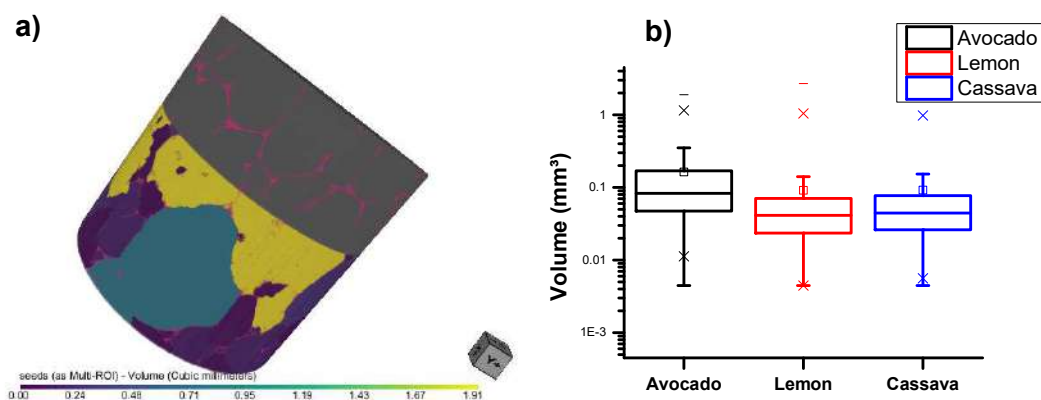


Figure 2: a) Color coded cell volume measurements; b) Comparative boxplot graph of cell volume for lemon, avocado and cassava foam.



Morphologic Study of Polymeric Nanofibers Obtained by Electrospinning: Influence of Technique Variables for Producing Antimicrobial Tissues

Giovanna Picoli Libel^{1*}, Bárbara Stephani Caldas¹ and Eduardo Radovanovic¹

¹ Department of Chemistry of State University of Maringá (UEM), Maringá, Brazil.

*picoligiovanna@gmail.com

Due to the current pandemic situation, it has been noticed a great concern with dissemination of pathogens such as bacteria, fungi and viruses that can cause several and serious diseases and which may not respond to known drugs, characterizing the increase in microbial resistance over the time. For then, the development of antimicrobial materials has been significantly studied to help contain microbial spread in hospital settings and among humans with the production of protective fabrics that can be used in the manufacture of masks, personal protective equipment and in fabrics that can cover surfaces in common environments prone to contact and proliferation of microorganisms. The electrospinning technique allows the production of polymeric nanofibers with large surface areas, different diameters (from a few micrometers to a few nanometers) and degrees of porosity, which can encapsulate antibacterial, antifungal and antiviral compounds [1] to act according to their release in the environment and direct contact with microorganisms. It is a simple, versatile and low cost methodology, in which a polymer solution is ejected from a syringe and stretched with the aid of a high tension applied between the needle and a metallic collector [2]. During the process, the solvent is evaporated and the polymer is deposited as solid fibers. The morphology of the produced fibers depends on the characteristics of the polymer solution used (solvent chosen, polymer molecular weight, concentration, conductivity and viscosity of the prepared solution), on the parameters inherent to the electrospinning technique (applied voltage, solution flow rate, distance between needle and collector) and the conditions of the working environment (temperature, relative humidity) [3]. For this reason, scanning electron microscopy (SEM) is essential for the characterization and study of each parameter described. From this, it is possible to optimize the conditions to obtain tissues that can act as an efficient physical and chemical barrier against the pathogens in question. In this experiment, two different polymeric solutions of poly(vinylalcohol) (PVA) with citric acid and poly(ϵ -caprolactone) (PCL) were prepared with the addition of the ionic liquid 1-hexadecyl-3-methylimidazolium ($C_{16}MimCl$) as an antimicrobial agent [4] and submitted to electrospinning technique for the production of tissues with antimicrobial properties. The scanning electron microscopy images of the produced fibers are presented below, in which it is possible to observe the change in the morphology and in the average diameter of the fibers with the variation in the electrospinning parameters.

References

- [1] H. Rodríguez-Tóbias et al., *Materials Science and Engineering C*. 101 (2019).
- [2] J. Xue et al., *Chemical Reviews*. 119 (2019).
- [3] A. Haider et al., *Arabian Journal of Chemistry*. 11 (2018).



[4] J. Sommer et al., International Journal of Molecular Sciences. 19 (2018).

Acknowledgements

To State University of Maringá (UEM).

Table 1: Parameters for the preparation of polymer solutions.

Polymer	Concentration of Polymer	Concentration of $C_{16}MimCl$	Solvent
PVA	12% (W/V)	1000 $\mu\text{mol L}^{-1}$	Water
PCL	10% (W/V)	$1,9 \times 10^{-3} \text{ mol L}^{-1}$	formic acid/chloroform (3:1 v/v)

Table 2: Parameters inherent to the electrospinning process.

Solution	Applied Voltage	Flow Rate	Distance Needle – Collector	Temperature	Humidity
PVA	20 kV	0,5 mL/h	15,0 cm	21,5°C	53%
PCL	12 kV	1,0 mL/h	10,0 cm	26,7°C	24%

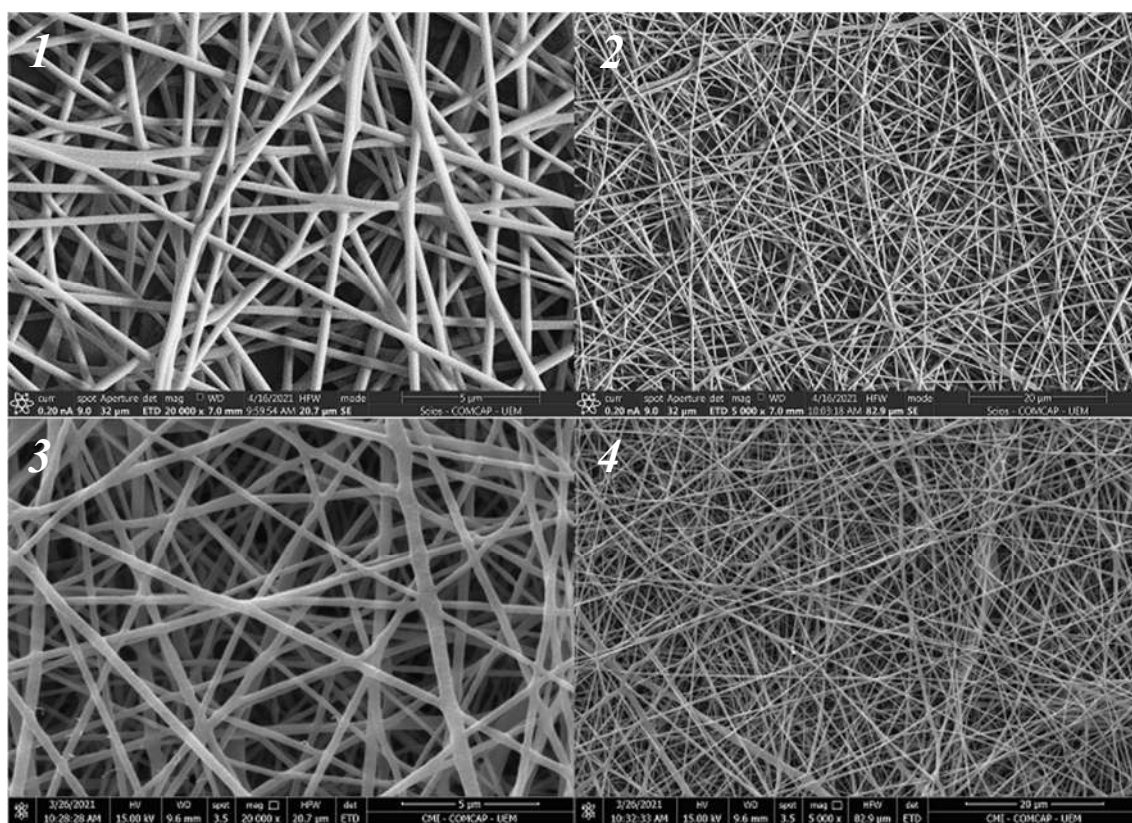


Figure 1: Scanning Electron Microscopy (SEM) images of PVA/CA (1,2) and PCL (3,4) fibers with ionic liquid $C_{16}MimCl$.

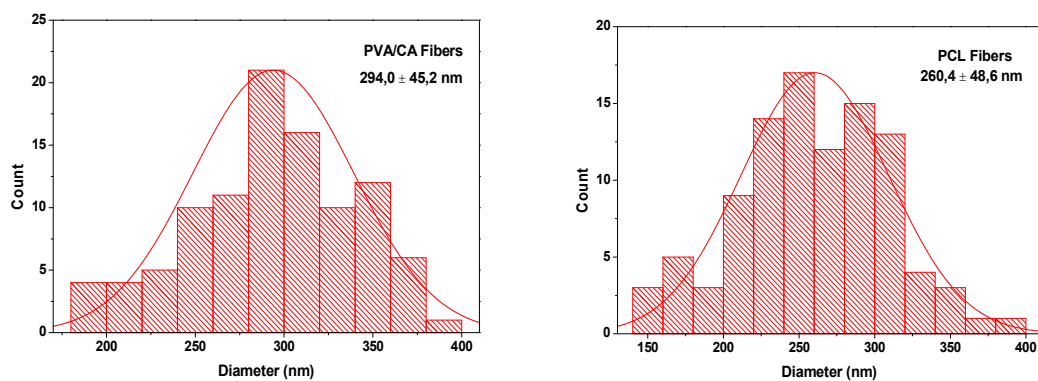


Figure 2: Histograms of fiber diameter distribution obtained by *ImageJ* software from the PVA/CA and PCL with ionic liquid C₁₆MimCl samples, respectively.



Microscopy Techniques to the Characterization of Biocompatible Materials and Tissues

Bárbara S. Caldas^{1*}, Giovanna Picoli Libel¹, Cátia S. Nunes¹, Manuela R. Panice¹, Marília Cestari¹, Débora B. Scariot², Danielle Lazarin-Bidóia², Celso Vataru Nakamura², Sami Halila³, Redouane Borsali³, Edvani Curti Muniz⁴, Eduardo Radovanovic¹.

¹ Chemistry Department, Univ. Estadual de Maringá – UEM, Av. Colombo, 5790 – Zona 7, 87020-900 Maringá, PR, Brazil

² Laboratory of Technological Innovation on the Development of Drugs and Cosmetics, Health Basic Sciences Department, UEM, Av. Colombo, 5790 – Zona 7, 87020-900 Maringá, PR, Brazil.

³ Univ. Grenoble Alpes, CNRS, CERMAV, BP53, 38041 Grenoble Cedex 9, France

⁴ Chemistry Department, Universidade Federal do Piauí – UFPI, Campus Petrônio Portella, Bairro Ininga, 64049-550 Teresina, Brazil
*barbarasthefanicaldas@gmail.com

Developing smart materials capable to help professionals to overcome the current biomedical misfortunes is a challenge to the researchers. Knowing that microscopy is of a great importance to the biological, physical, mechanical and another several sciences, authors would like to highlight that a sort of these techniques are employed to determinate structural aspects of biocompatible and sometimes biodegradable polymeric materials with applicability on cancer therapies^{1,2}, tissue compatibility and regeneration^{3,4}, and to eliminate microbial organisms⁵. Materials developed in our research group as follow, nanoparticles (NP) made by polyisoprene-*b*-maltoheptaose (PI-*b*-MH) block-copolymers (BCP) and polyelectrolyte complexes (PEC) (physical hydrogels) made by chitosan (CT) with chondroitin sulfate (CS) following two methods (M1 and M2), were charged with curcumin (CUR), a natural active principle, and applied to kill cancer cells of many sorts. Nanofibers (NF) made by silk fibroin (SF) with chondroitin sulfate, associated with silver sulfadiazine and made by polycaprolactone and ionic liquids, serve respectively to wound healing applications, specifically to burn injuries and to antibacterial surfaces covering. These materials are prepared by specific methodologies as **a**) nanoprecipitation: where BCPs form self-assembled structures as NP, by the addition of a selective solvent into de media and migration of the incompatible blocks by evaporation of the good solvent, **b**) electrolytic interaction: where electrostatic forces hold polyelectrolytes, positively and negatively charged, together forming physically-crosslinked structures and **c**) electrospinning: where a magnetic field applied between a needle connected to a pump and a metallic collector, lead a polymeric solution to form thin fibers. Several characterization techniques including transmission (TEM), atomic force (AFM), scanning (SEM) and optical (OM) microscopies besides *in vitro* and *in vivo* assays guarantee the success in design and application of the materials.

REFERENCES

[1] Caldas, B. S.; Nunes, C. S.; Panice, M. R.; Scariot, D. B.; Nakamura, C. V.; Muniz, E. C. ;*International Journal of Biological Macromolecules* **2021**, *180*, 88.

- [2] Caldas, B. S.; Lazarin-Bidóia, D.; Nakamura, C. V.; Halila, S.; Borsali, R.; Muniz, E. C. ;*Journal of Molecular Liquids* **2020**, *309*, 113022.
- [3] Cestari, M.; Muller, V.; Rodrigues, J. H. da S.; Nakamura, C. V.; Rubira, A. F.; Muniz, E. C. ;*Biomacromolecules* **2014**, *15*, 1762.
- [4] Mavis, B.; Demirtaş, T. T.; Gümüşderelioğlu, M.; Gündüz, G.; Çolak, Ü. ;*Acta Biomaterialia* **2009**, *5*, 3098.
- [5] Souza, P. R.; Vilsinski, B. H.; de Oliveira, A. C.; Berton, S. B. R.; Nunes, C. S.; Kipper, M. J.; Schrekker, H. S.; Martins, A. F.; Muniz, E. C. ;*Journal of Molecular Liquids* **2021**, *330*, 115548.

AKNOWLEDGEMENTS

Authors acknowledge Capes, CNPq (Brazil) and CNRS (France) by the sponsorship.

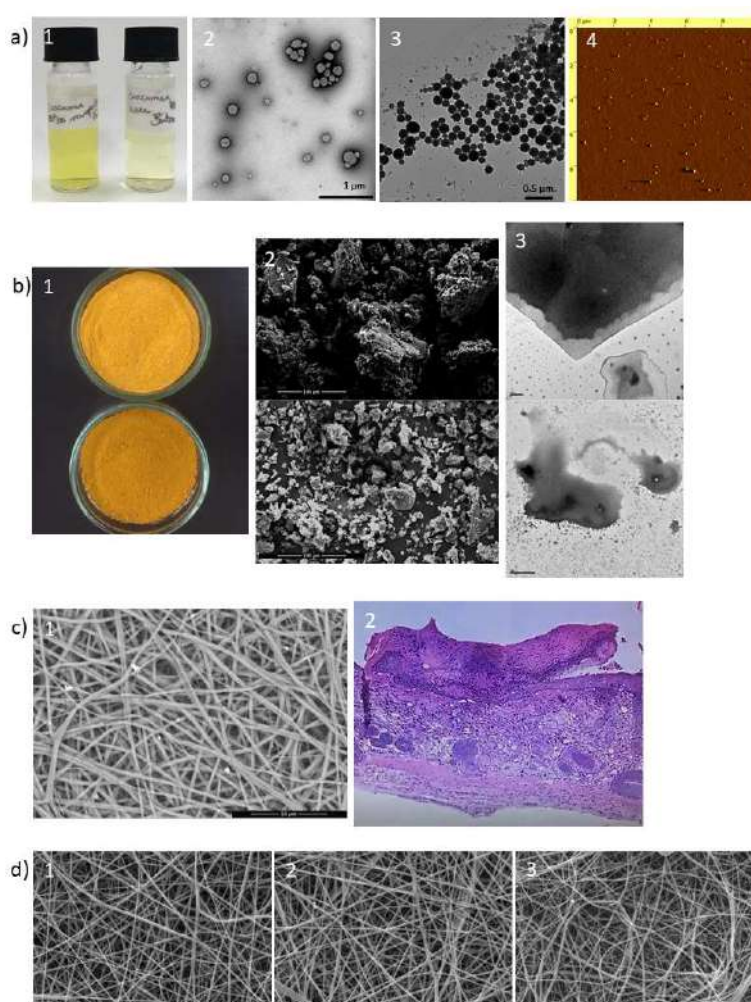


Figure 1. Images from **a.1**) PI-*b*-MH + CUR nanoparticles (left) and water + CUR (right); TEM images from NP+CUR negatively coloured with **a.2**) uranyl acetate, size bar: 1 μm and **a.3**) osmium tetroxide, size bar: 0,5 μm and **a.4**) AFM from NP; **b.1**) PEC made by method 1 (up) and method 2 (down), SEM from **b.2**) PEC+CUR M1 (up) and PEC+CUR M2 (down), size bars: 100 μm and TEM from **b.3**) PEC+CUR M1 (up) and PEC+CUR M2 (down), size bars: 2 μm ; **c.1**) SEM from SF+CS NF, size bar: 10 μm and **c.2**) OM



from animal tissue after treatment with NF; SEM from PCL NF under conditions **d.1)** 1, **d.2)** 2 and **d.3)** 3, size bars: 10 μm .



Characterization of graphene-based materials deposited on interdigitated electrodes for ammonia gas sensor applications

Eric Schwartz^{1*}, Suzana Bottega Peripolli¹, José Brant de Campos¹, Fernando Massa Fernandes², Hirschel Valiente Rouco¹

¹Rio de Janeiro State University, Mechanical Engineering Department, Rio de Janeiro, Brazil.

²Rio de Janeiro State University, Electronic Engineering Department, Rio de Janeiro, Brazil

[*ericschwartzeng@gmail.com](mailto:ericschwartzeng@gmail.com)

Ammonia gas is widely used as a component in various industrial sectors, such as the production of pharmaceuticals, plastics, chemicals, fertilizers, textiles, among others. Due to its caustic nature a prolonged exposure and continues to high concentrations can cause serious damage to the respiratory system, the nervous system, eyes, human skin and in extreme cases death. Thus, precise sensing and control of its concentration are necessary to ensure safety in environments with the presence of ammonia [2]. The most used ammonia gas sensors use as material oxides-metal as WO_3 , SnO_2 and TiO_2 and have as characteristics ultra sensitivity, response and rapid recovery. However, exposure at high temperatures (100 – 450 °C) has a high energy consumption, low lifetime and high manufacturing cost [1]. As a way to reduce the operating temperature and increase the life time graphene has been used as an alternative to metal oxides because it requires a lower energy consumption for sensor operation [3]. Although graphene is chemically inert, reduced graphene oxide (RGO) has oxygenated functional groups that allow the chemical functionalization of the material for gas sensing applications such as ammonia [2]. The structure of the graphene-based ammonia sensor will be investigated by images of Scanning Electron Microscopy and Kelvin Atomic Force Microscopy (KPFM) to characterize the conductivity of the sample since it is expected that the vacancies and oxygenated functional groups present in the RGO improve the adsorption of ammonia, as demonstrated in the literature [1,2]. This work aims the study of the characterization of electrodes with interdigitated patterns that will be used in the manufacture of an ammonia sensor based on graphene with reproducibility, sensitivity and selectivity that works at room temperature. The characterizations presented in the work are of a silicon substrate with copper layers with PMMA polymer and pristine graphene on the electrodes, according to the illustrative diagram in Figure 1. The image in Figure 2 shows an optical microscopy with the presence of graphene (pristine monolayer graphene), deposited on the interdigitated layers and the morphology of the substrate surface is presented in the scanning electron microscopy (SEM) images in Figure 3(a), where it is possible to observe the organization of copper tracks, shown in Figure 3 (b), obtained in a JEOL-JSM-7100FT equipment at NANOFAB/UERJ. Cross-sectional observation of the material was performed to investigate the interaction of copper trails with the layers that make up the sample, according to the image in Figure 4, where it is possible to observe the dimensions of the layers and their organization after the deposit.

The authors would like to acknowledge the financial support offered by agencies CNPq, Capes Scholarship System (88887.597050/2021-00) and the NANOFAB for making this work possible.

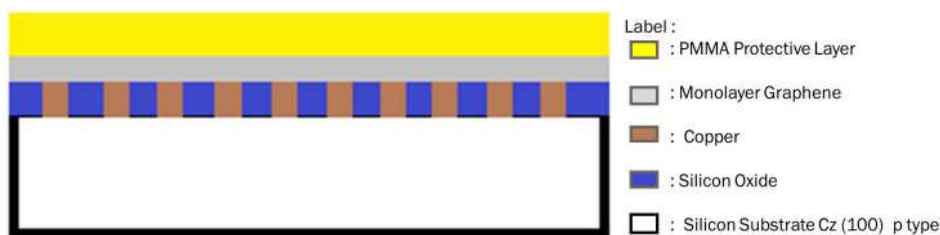


Figure 1. Schematic view of the arrangement of the polymer and graphene layer and copper trails on the electrodes.

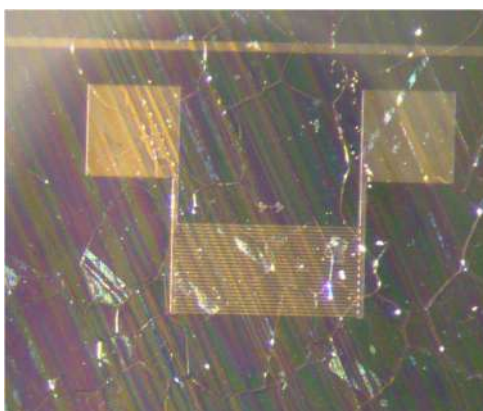


Figure 2. Optical microscopy image of the interdigitated pattern coated with monolayer graphene

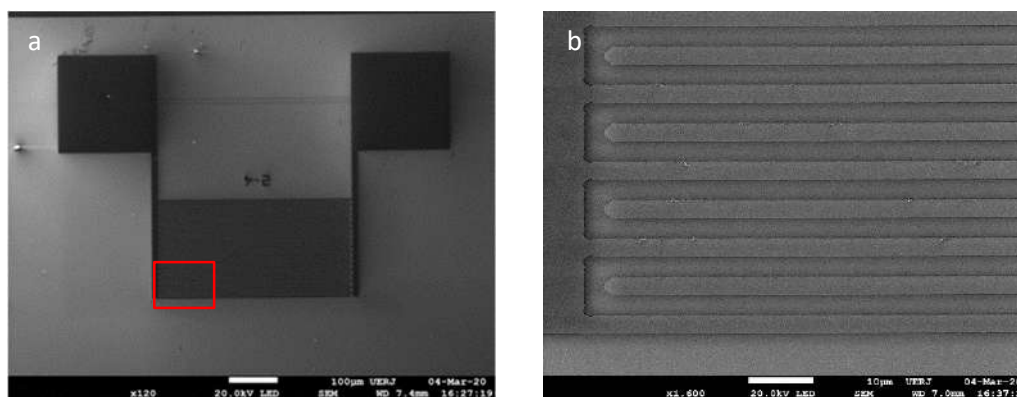


Figure 3. Scanning electron microscopy image with surface view of the electrode pattern (a), and the detail of the trails in the inner region of the electrode magnified (red region) (b).

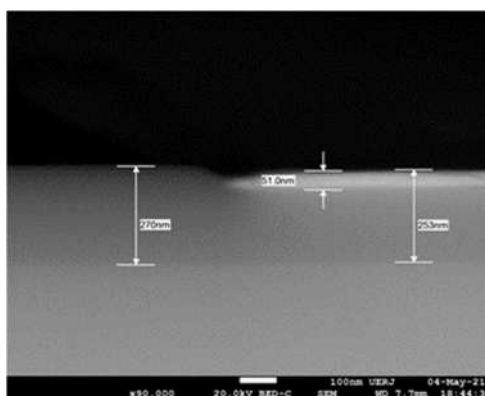


Figure 4. Scanning electron microscopy image with a view of the cross-section of the copper trails of the electrodes and dimensions of the layers that make up the sample.



REFERENCES

- [1] Xiaohui Tang, Jean-Pierre Raskin, Nadzeya Kryvutsa, Sophie Hermans, Oleksandr Slobodian, Alexei N. Nazarov, Marc Debliquy, *B: Chemical*, Volume 305, 2020, 127423, ISSN 0925-4005, <https://doi.org/10.1016/j.snb.2019.127423>.
- [2] Raj Kumar, Ruma Ghosh, *Research*, Volume 28, 2020, 100336, ISSN 2214-1804, <https://doi.org/10.1016/j.sbsr.2020.100336>.
- [3] Dongwook Kwak, Yu Lei, Radenka Maric, , *Talanta*, Volume 204, 2019, Pages 713-730, ISSN 0039-140, <https://doi.org/10.1016/j.talanta.2019.06.034>.



In-Situ X-Ray MicroCT Imaging of The Microstructural Changes in Carbonate Coquina Under Oedometric Loading Conditions

SILVA JUNIOR, Francisco José Rodrigues da^{1*}, VELLOSO, Raquel Q.² and PACIORNIK, S.¹, ZHEMCHUZHNIKOV, Alexandr², DE PINHO MAURÍCIO, Marcos Henrique¹

¹ Dept. of Chemical and Materials Engineering (DEQM), PUC-Rio, Rio de Janeiro, Brazil

² Dept. of Civil Engineering (CIV), PUC-Rio, Rio de Janeiro, Brazil

*Corresponding author, engphb@gmail.com

Carbonate coquinas are a kind of sedimentary rock, mainly composed of shells and fragments. These rocks have different texture characteristics related to sedimentation and diagenesis, which affect the pore system and thus the permeability. To preview the quality of a reservoir, it is necessary to understand how the different coquinas are distributed and how they relate to petrophysics [1]. During the well drilling, there is a change in the state of the stress in its surroundings, causing deformation in the rock that can induce a significant loss of porosity and permeability [2, 3]. In this work, we study the influence of mechanical damage on coquina's properties using x-ray microtomography (microCT) coupled to a cell developed for in situ stress application under edometric loading (uniaxial deformation). A carbonate coquina sample of 8 mm in diameter and 12 mm in height was scanned under 4 conditions: without load, after application of 10 MPa, 20 MPa, and after unloading. The cell allowed the load variations to be performed without removing the sample from the tomograph, allowing a quantitative comparison between the 3D images in the 4 conditions. Data such as total porosity, absolute permeability, pore and capillaries diameter, and connectivity of the pores were obtained. Image processing steps illustrated in Fig. 1 were fundamental for the calculation of the coquinas' porosity. Thus, porosity values of $P_{atm} = 43,6\%$; $P_{10MPa} = 21,6\%$; $P_{20MPa} = 16,8\%$; $P_{depressurization} = 17,6\%$ were obtained. Pore Network Modelling (PNM) (Fig. 2) was used to calculate permeability showing that values decrease after loading and increase after depressurization. In addition, in Fig. 3, PNM analysis shows that coquinas properties such as pore and capillaries diameter, and connectivity decrease after loading.

REFERENCES

- [1] Chinelatto, G.F., Belila, A.M.P., Basso, M., Souza, J.P.P., Vidal, A.C., 2020. A taphofacies interpretation of shell concentrations and their relationship with petrophysics: A case study of Barremian-Aptian coquinas in the Itapema Formation, Santos Basin-Brazil. *Marine and Petroleum Geology* 116, 104317. <https://doi.org/10.1016/j.marpetgeo.2020.104317>
- [2] Saenger, E.H., Lebedev, M., Uribe, D., Osorno, M., Vialle, S., Duda, M., Iglauer, S., Steeb, H., 2016. Analysis of high-resolution X-ray computed tomography images of Bentheim sandstone under elevated confining pressures. *Geophys. Prospect.* <https://doi.org/10.1111/1365-2478.12400>
- [3] Schindler, M., Prasad, M., 2016. Micro X-ray CT imaging of sediments under confining pressure, in: SEG Technical Program Expanded Abstracts 2016. <https://doi.org/10.1190/segam2016-13966227.1>
- [4] This research was supported by Petrobras, CNPq, CAPES and FAPERJ.

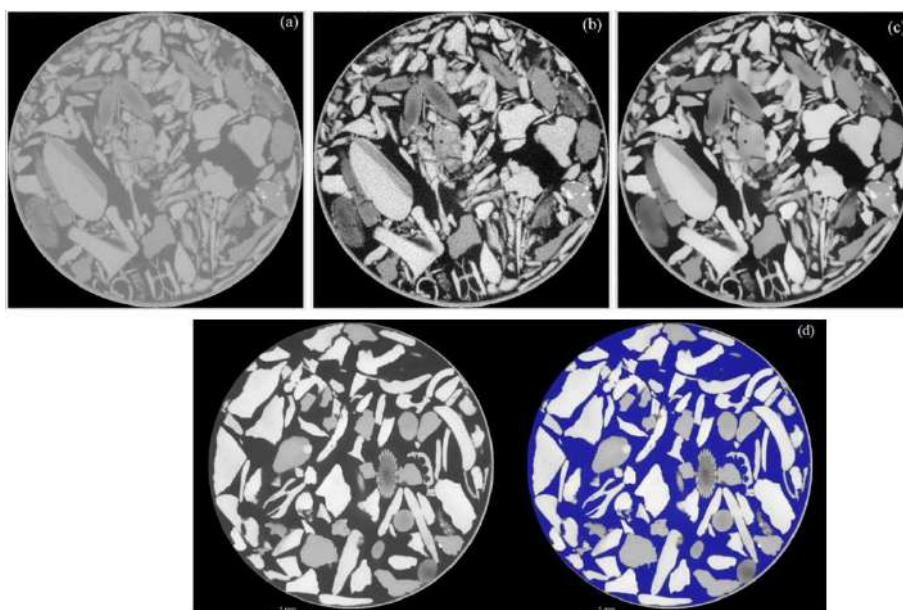


Fig. 1 - Pre-processing and segmentation steps: (a) untreated image; (b) brightness and contrast correction; (c) noise correction with the NLM filter; (d) pore segmentation.

```

air = op.phases.Air(network=pn)
phys = op.physics.Standard(network=pn, phase=air, geometry=geo)
sf_x = op.algorithms.StokesFlow(network=pn, phase=air)
Pin = 101325
Pout = 0.0
sf_x.set_value_BC(pores=pn.pores('left'), values=101325)
sf_x.set_value_BC(pores=pn.pores('right'), values=0.0)
sf_x.run()

fig = op.topotools.plot_coordinates(pn, color=sf_x['pore.pressure'],
                                   size_by=pn['pore.diameter'],
                                   markersize=50)

# Simulação Permeabilidade absoluta
pi=math.pi
Q = sf_x.rate(pores=pn.pores('left'), mode='group')
A = (pi*(im.shape[1]*im.shape[1])/4) * resolution**2
L = im.shape[2] * resolution
mu = air['pore.viscosity'].max()
delta_P = 101325 - 0
K = Q * L * mu / (A * delta_P)
print('The value of K is:', K/0.98e-12, 'D')

```

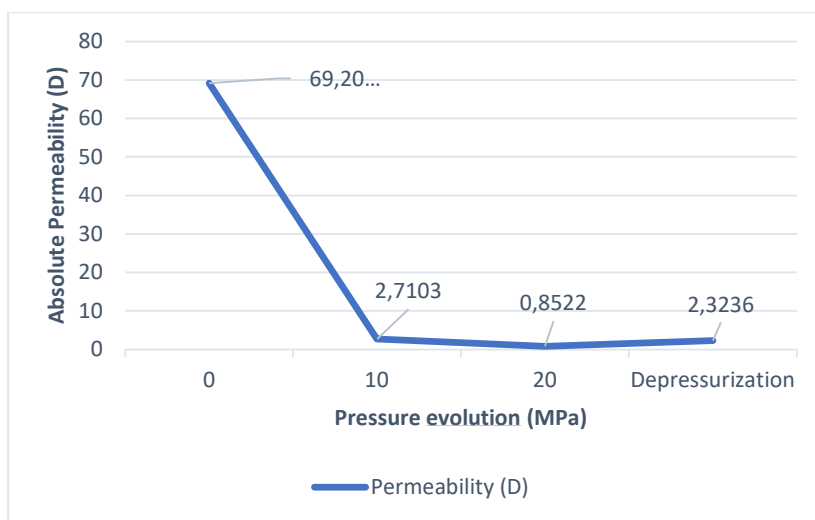
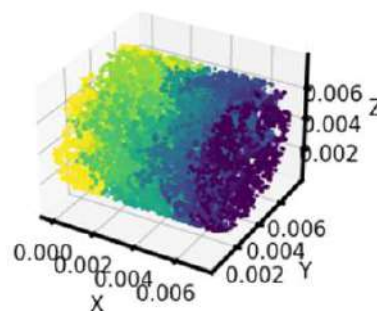


Fig. 2 - Absolute permeability values for P_{atm} , P_{10MPa} , P_{20MPa} , $P_{depressurization}$, respectively.

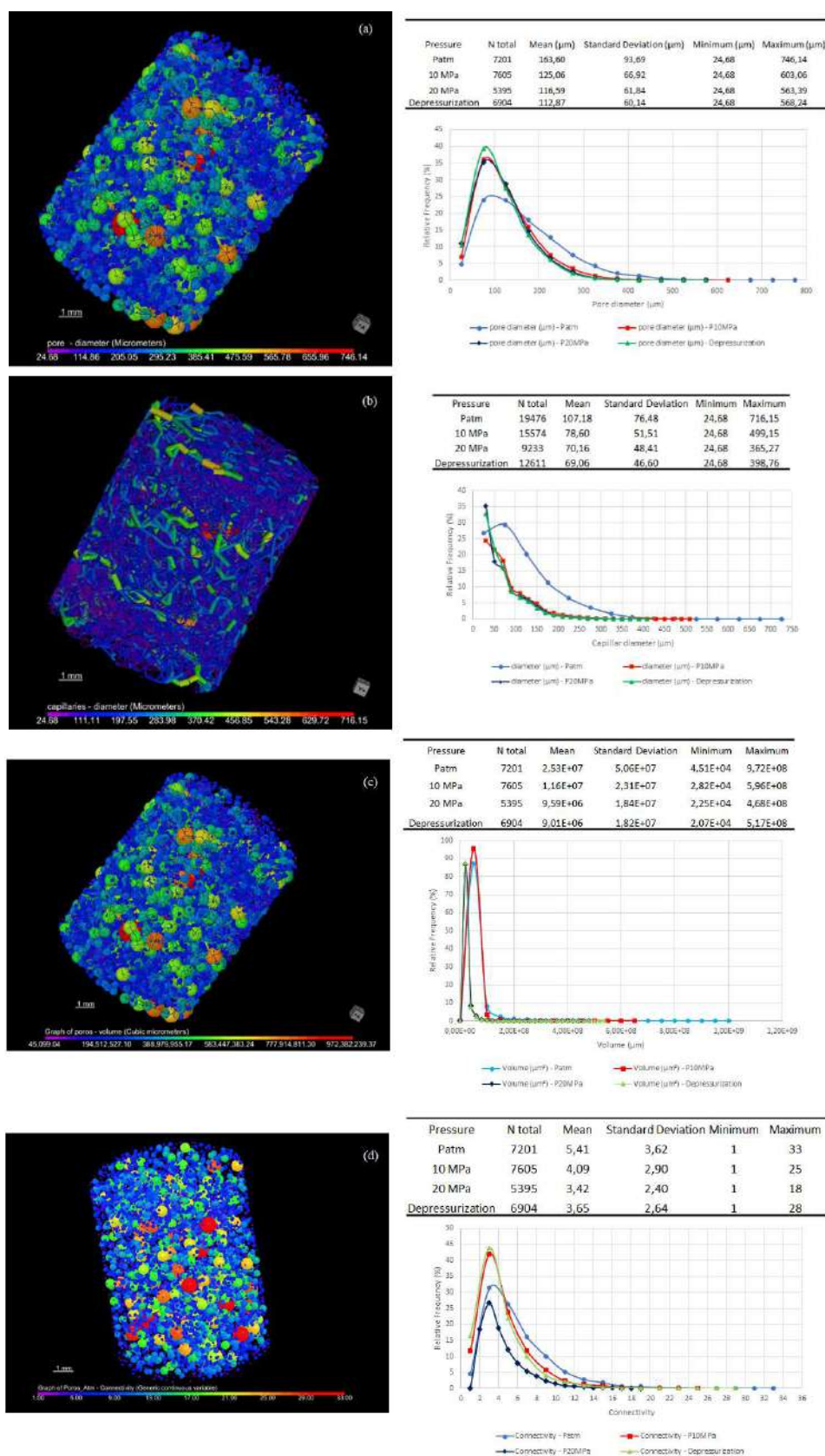


Fig. 3 – Properties for P_{atm} , P_{10MPa} , P_{20MPa} , $P_{depressurization}$ conditions respectively: (a) Pore diameter measurements; (b) Capillaries diameter measurements; (c) pore volume measurements; (d) connectivity measurements.



Controlling the Morphology Of ZnO Microstructured Films Grown On Copper.

Ígor Silveira^{1*}, Jonder Moraes² and Maria do Carmo M. Alves^{1*}

¹ UFRGS, Departamento de Química Inorgânica/Instituto de Química, Porto Alegre, Brazil, * maria@iq.ufrgs.br, igorsilveira5454@gmail.com .

² UFRGS, Instituto de Física, Porto Alegre, Brazil.

The development of micro and nanostructured materials has been shown to be crucial for the design and their direct application in microelectronics, chemical and biological devices. Several potential use are foreseen in photovoltaic cells, batteries, capacitors, hydrogen storage devices, light emitting devices, catalysts, among others. For instance, zinc oxide (ZnO) is a promising technological material that has been constantly investigated due to the numerous micro and nano morphologies that it may be tailored and hence, enabling to achieve improved properties, such as a greater capacity for ions and molecules adsorption, tunable light emission, etc [1-2]. Additives introduced during ZnO wet synthesis process allows to manufacture exceptional shapes. The basic strategy underneath is via the control the growth orientation and rate based on the difference in surface energy of certain crystalline planes, which in turn determines the final physical and chemical properties of ZnO. In the present study we have produced ZnO films grown on the surface of a copper substrate, and verified the influence of different synthesis conditions on the final morphological aspects. By varying the concentration of the chemical components on the chemical set up it was possible to grow ZnO in a columnar morphology, as observed by the use of SEM (Scanning Electron Microscopy). Particularly we verified the morphology dependence with the reaction time (Figure 1). The average columns tip width was evaluated yielding the value of $0.280 \pm 0.006 \mu\text{m}$. Additionally, x-ray Photoelectron spectroscopy (XPS) allowed to characterize the surface chemical composition of the ZnO films. The fitting of the O 1s indicated the presence of three chemical components at the ZnO surface, corresponding to O-Zn, O-Ovacancies and O-H bonds. The Zn 2p spectrum was deconvoluted considering only one component related to Zn-O bonds. A systematic study that leads to the different ZnO morphologies will be presented.

[1] A. Sulciute et al., J. Phys. Chem. C 125 (2) (2021) 1472.

[2] C. Lausecker et al., Inorg. Chem. 60 (3) (2021) 1612.

ACKNOWLEDGEMENTS

The authors thank the Centro de Microscopia e Microanálise (CMM-UFRGS). This research was supported by CNPq, CAPES, INCT-INES and FAPERGS (Brazil).

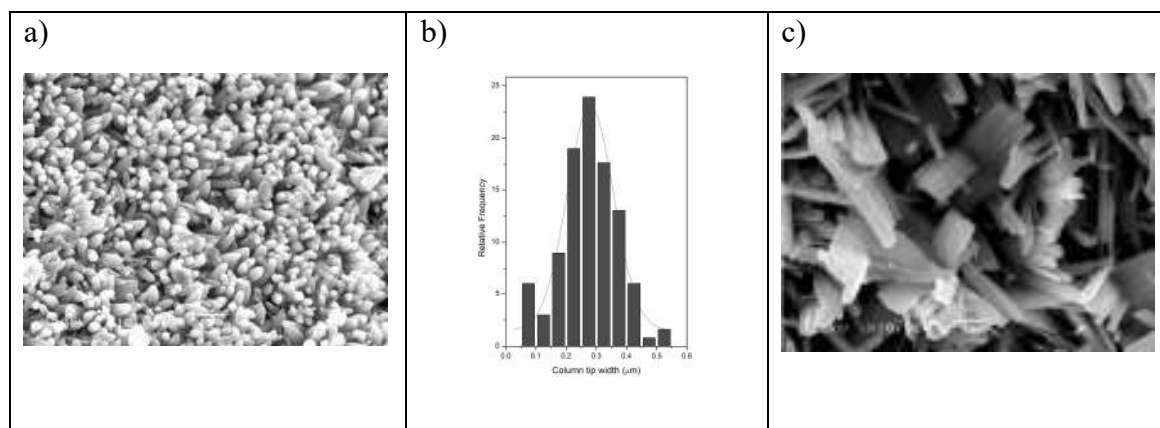


Figure 1 – SEM images acquired for a synthesis conducted during a) 5h along with b) the corresponding histogram. c) Morphology after 6h of synthesis. (The images were taken at the CMM-UFRGS, 20 kV, 10000 X amplification, 1 cm corresponds to 1 μm).

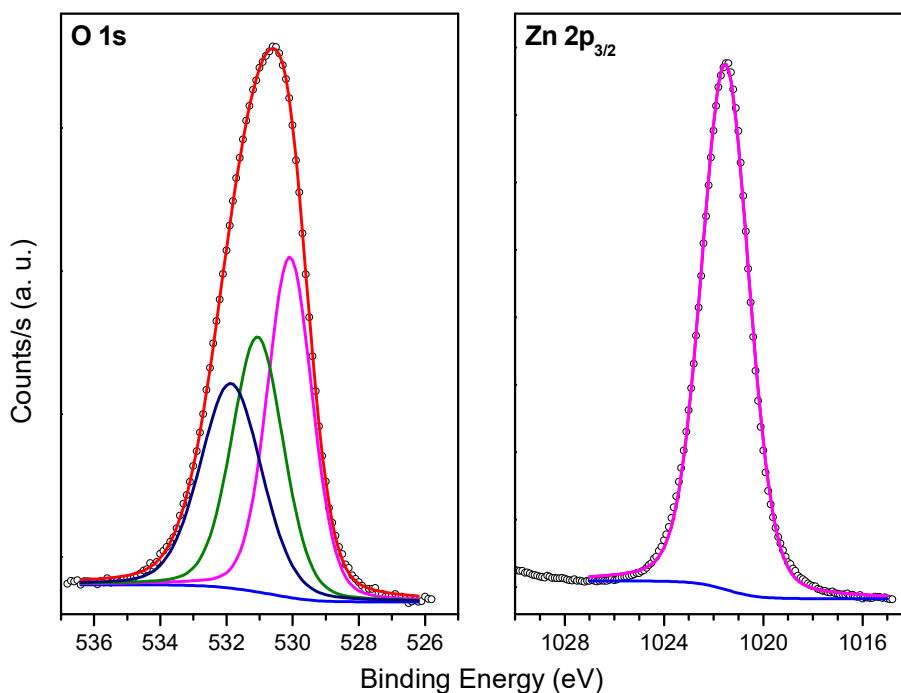


Figure 2 – O 1s and Zn 2p XPS spectra for the ZnO film obtained by forced hydrolysis of zinc ions and grown in aqueous solution during 5h.



Analysis of the Formation of Concrete Porosity with Addition of Recycled Aggregate Through the Study by X-Ray Microtomography

Isabel Christina de Almeida Ferreira^{1*}, Sidnei Paciornik¹ and Flávio A. Silva²

¹. Department of Chemical and Materials Engineering, Catholic University of Rio de Janeiro (DEQM-PUC-Rio), Rio de Janeiro, Brazil.

². Department of Civil and Environmental Engineering Engineering, Catholic University of Rio de Janeiro (DEQM-PUC-Rio), Rio de Janeiro, Brazil.

*isabel.ferreira@aluno.puc-rio.br

According to the Brazilian Association for Recycling Construction and Demolition Waste, civil construction is responsible for approximately 290,556 tons of RCD (construction waste) deposited daily in landfills throughout Brazil, many of them unregulated [1]. In several studies, it can be noted that, unlike conventional concretes, which have only one interfacial transition zone (ITZ) between the cement paste and the aggregate, RCD concretes have two interface zones: one between the new paste of cement and the RCD aggregate, and the second, between the RCD and the old cement mass. This characteristic can be directly linked to the quality of concrete with RCD, since the porosity can increase in this interface zone. The nature of concrete is fragile, as it breaks under static loads with a reasonably small shape [2]. The use of destructive testing is disclosed to analyze the effects of porosity formation in concrete. These tests show, for example, an impact on the strength of the material studied. However, transformed data such as the formation of porous channels, the volume of porosity and characteristics of the cementitious mass-aggregate interface zone end up being lost. From the data mentioned above, it would be possible to understand which material is more efficient in reusing CDW. MicroCT is an ideal technique in this regard, as it is non-destructive and allows monitoring the same specimen at different stages of stress / deformation [3]. The samples were cast with conventional concrete and concrete with the addition of RCD. All specimens were subjected to the curing process. MicroCT images were acquired with a resolution of approximately 28 μm and submitted to digital processing with FIJI / ImageJ and Dragonfly software. **Figure 13** presents a pre-processed and segmented image. It is possible to visualize the pores in 2D (Figure 1a) and 3D (Figure 1b). **Figure 14** shows the pore size distribution of one of the samples. In addition to the pore volume, measurements of sphericity, aspect ratio and formation of porous channels were performed. To obtain more information on the formation of porous channels, the Porous Network Modeling (PNM) technique was used, as shown in **Figure 15**. From these results, it is possible to visualize the connection between the pores and understand the behavior of the structure. of the materials used. The greater the connection between the channels, the more the concrete element becomes fragile.

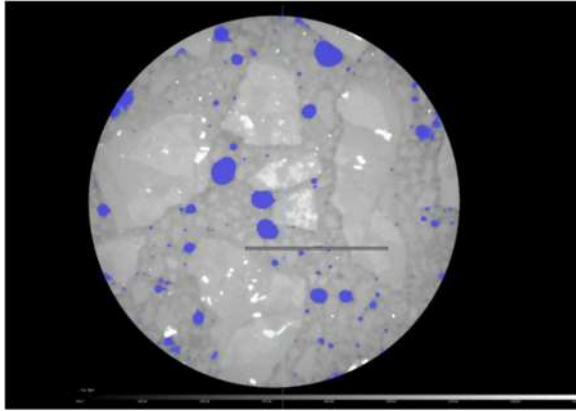
- [1] E. Varela, L. Torres, “Manual de Aplicação do Agregado Reciclado”, ABRECON, 2019.
- [2] A. Hosan, F. Shaikh, P. Sarker et al., “Nano- and micro-scale characterization of interfacial transition zone (ITZ) of high-volume slag and slag-fly ash blended concretes containing nano SiO₂ and nano CaCO₃”, Construction and Building Materials, vol 269, 2021.
- [3] M. Zhang, “Pore-scale modelling of relative permeability of cementitious materials using X-ray computed microtomography images”, Cement and Concrete Research, vol 95, pp. 18-29, 2017.



[4] The authors acknowledge the financial support by CAPES, CNPq and FAPERJ.

FIGURAS

a)



b)

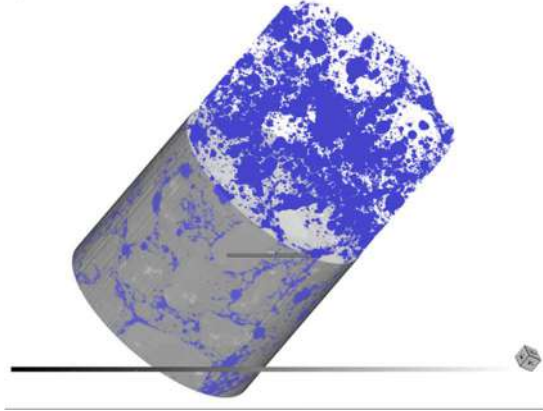


Figure 13: Slice 802/2993 - Image obtained in Dragonfly software of pores in concrete with addition of recycled aggregate – a. 2D b. 3D

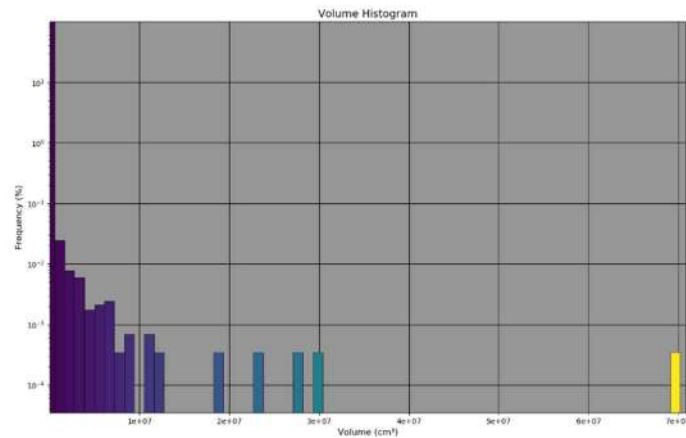


Figure 14: Pore volume distribution of concrete with recycled aggregates

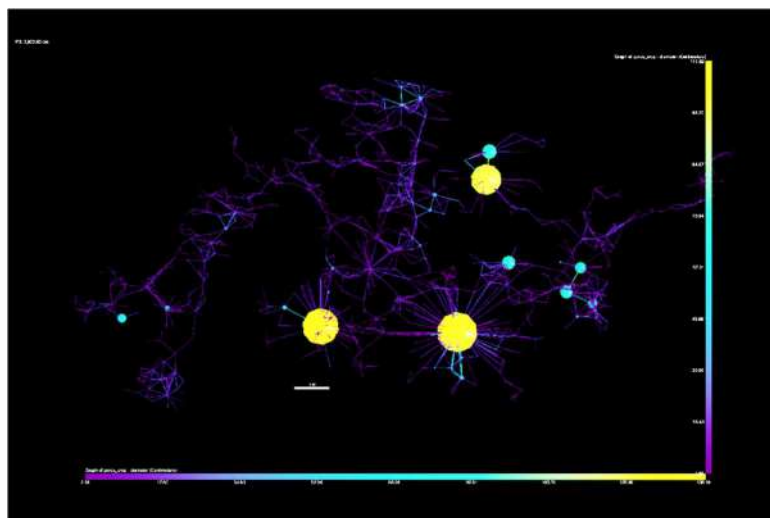


Figure 15: PNM image channels and pores of concrete with addition of recycled aggregates. The color scale represents the diameter values of channels and pores (in purple the channels with the smallest diameter and in yellow the pores with the largest diameter).



Synthesis and Crystal Growth of Dolomite under Hydrothermal Conditions

Hannah Larissa Siqueira Matos Pimentel^{1,3*}, Flávia Gomes de Souza³, Cecília Maria Alves de Oliveira^{1,3}, Jesiel Freitas Carvalho^{2,3}.

¹Instituto de Química, Universidade Federal de Goiás, Goiânia, Goiás, Brasil.

²Instituto de Física, Universidade Federal de Goiás, Goiânia, Goiás, Brasil.

³Centro Regional para o Desenvolvimento Tecnológico e Inovação (CRTI), Universidade Federal de Goiás (UFG), Goiânia, Goiás, Brasil.

*hannahlarissa@ufg.br

Dolomite, $[\text{CaMg}(\text{CO}_3)_2]$, is a very common carbonate mineral found in numerous geological environments, mainly as a diagenetic mineral replacing pre-existing carbonate rocks [1, 2]. However, the physicochemical of the dolomitization process are still discussed and many studies are carried out intending its reproduction in laboratory [3]. In this study, dolomites were obtained by hydrothermal synthesis at 220°C for 15 days, through reaction of CaCO_3 with MgCO_3 and Na_2CO_3 solutions (1:1:2). Calcium and magnesium carbonates were dissolved at pH 2 under room temperature and pressure, and then the pH was adjusted to 10 (experiment 1) and 7 (experiment 2), and the carbonate source (Na_2CO_3) was added to both solutions. In the experiment 1 (DOL 1), a precipitate was formed just after the addition of sodium carbonate; in the experiment 2 (DOL 2) no precipitate was observed at environment conditions. The solutions were enclosed in two autoclaves and heated at 220°C for 15 days. After this time, the autoclaves were cooled to room temperature and the precipitated solids were dried and analyzed by X-ray diffraction (XRD) and scanning electron microscopy (SEM). The XRD patterns of DOL 1 and DOL 2, see Figure 1, demonstrated the formation of dolomite in both experiments, accompanied by other minor phases like magnesite, calcite, brucite and halite. The obtained crystals present different morphologies for each experiment, as illustrated in Figure 2. These results indicate that pH has high influence in the process of nucleation and growth of dolomite crystals under hydrothermal conditions. The morphology in DOL 1 suggests the occurrence of a high nucleation rate leading to the formation of spherulites with 10-50 μm formed by small and intergrown rhombohedrons with 1-5 μm . In the DOL 2 experiment, larger and well-defined rhombohedral crystals with micrometric dimensions were grown. In this second case the nucleation rate was smaller, making possible the growth of larger crystals. This study provides important insight concerning the effect of pH on the dolomite crystal growth under hydrothermal conditions, and additional studies are in progress.

[1] C.J.R. Braithwaite, Earth and Environmental Science Transactions of the Royal Society of Edinburgh, 8 (Issue 2) (1991) 99.

[2] J.M. Gregg et al., Sedimentology, 62 (2015) 1749.

[3] S.E. Kaczmarek, B.P. Thornton, Chemical Geology, 468 (2017) 32.

The authors would like to thank FINEP, CNPq, FAPEG and Petrobras for funding and to CRTI for access to the analytical facilities.

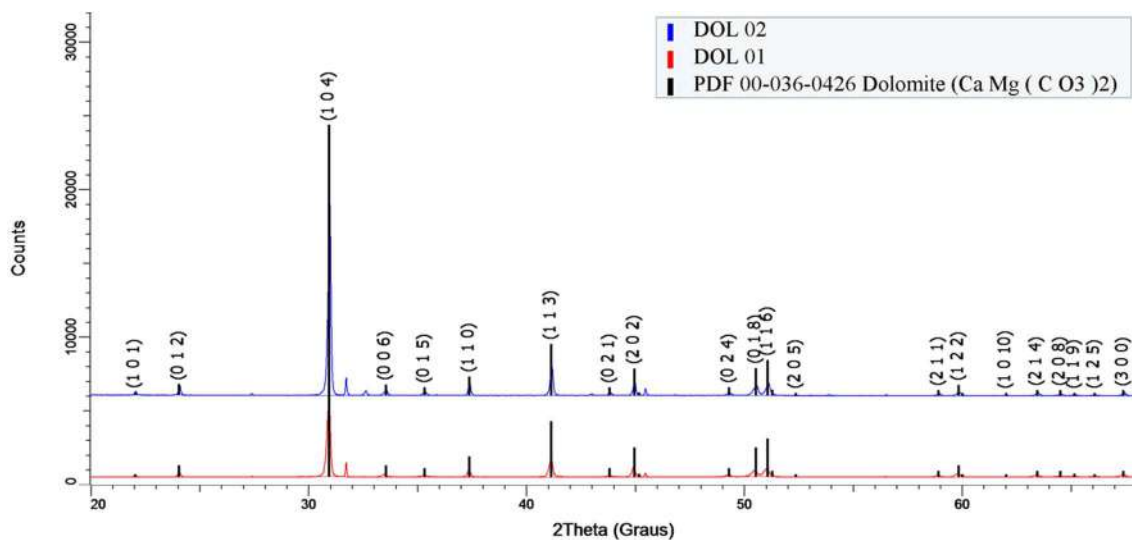


Figure 1. X-ray diffraction patterns of DOL 1 and DOL 2 microcrystals.

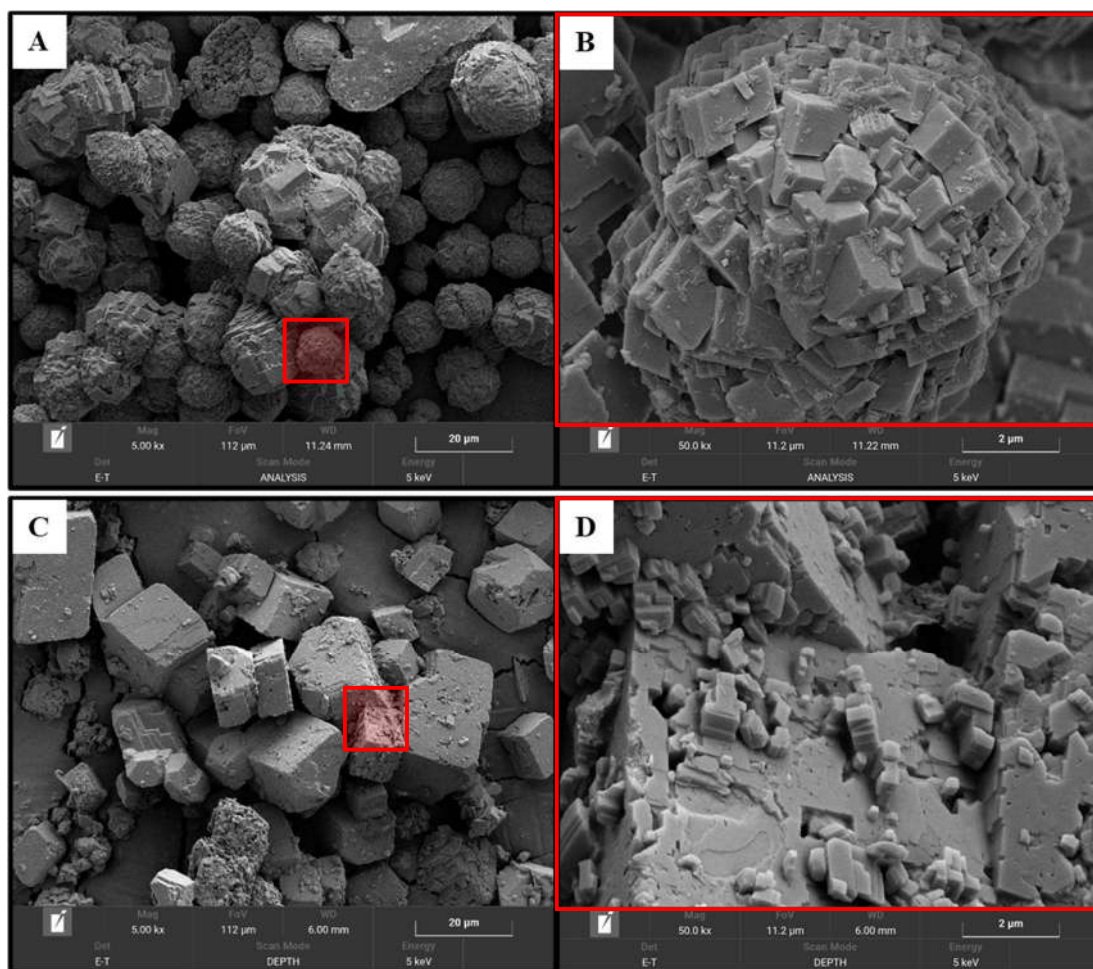


Figure 2. SEM images revealing the morphologies of DOL 1 (A and B), and DOL 2 (C and D) microcrystals.



Microwave Irradiation Treatment for Recycling Titanium Alloys to be Applied to Reinforcement of Weld Metal

Alicia Ramos Modesto¹, Leonardo Shiguelo Moreira Wagatuma¹, Rafael Borgheri dos Santos¹ and Juno Gallego^{1*}

¹ Department of Mechanical Engineering, São Paulo State University – UNESP, Ilha Solteira, Brazil.

* juno.gallego@unesp.br

Titanium and its alloys are materials characterized by excellent physical and chemical properties, which make their application in different areas from medicine to aerospace advantageous. The processing of these materials by machining generates significant residue quantities in the form of chips. The high cost of titanium and its alloys stimulates the reuse of these residues, transforming them into new consumables or products. The aim of this work is to recycle the chips of the ASTM F67 (pure Ti) and F136 (Ti-6Al-4V) titanium alloys for the production of fine powders to be used as welding additives, using microwave irradiation. Processing of metallic residues begins with their chemical cleaning to remove organic contaminants, as described in a previous work [1]. A mixture containing 5 g of titanium residues and 30 g of powdered charcoal was placed in a ceramic container which was used to promote fragility of the chips during microwave irradiation treatment. For this purpose a common microwave oven was applied, with nominal power of 1000 W. Working as susceptor the charcoal absorbs microwaves, promoting the formation of gases and intense heating of the metallic charge, Fig.1. The charge was irradiated for 10 minutes, followed by air cooling. The powdered charcoal was separated from the metallic chips by sieving, followed by mechanical milling at 120 RPM with alumina balls during 4 hours. Fine metallic particles were separated using 140 and 325 mesh sieves, being that particles collected after last sieve are smaller than 45 μm and were characterized by X-ray Fluorescence (XRF) and X-ray Diffraction (XRD). XRF analysis was performed on a Shimadzu EDX-720 fluorescence spectrometer, being applied a Siemens DL5005 X-ray Diffractometer for XRD characterization. The XRD diffractometer was equipped with a copper tube working at 40 kV/40mA and a graphite monochromator, 2θ sweep between 30 to 100 degrees, 0.02 degree step for 1.5 s. The diffraction analysis was performed using the PROFEX software, version 4.3.1 [2], using CIF cards extracted from ICSD. XRF results confirmed the presence of Ti (80.9% wt), Al (12.7% wt) and V (3.1% wt) in addition to other elements, Fig.2. XRD analysis, Fig.3, has identified several phases such as Ti(α) (ICSD 44390), Ti_{10.83}N_{0.17} (ICSD 108614), Ti₂O (ICSD 24081) e Ti₂(V,Al) (ICSD 185875) with mass fractions of 31.6%, 34.1%, 33.3% and 1.3% respectively. This Ti-rich powder presents potential application as welding additive, contributing to the formation of titanium carbide (TiC) that becomes more wear resistant weld metal.

REFERENCES

- [1] J. G. Fagundes et al. J. Phys.: Conf. Ser. 1386 (2019) 012046.
- [2] N. Doebelin and R. Kleeberg. J. Appl. Cryst. 48 (2015) 1573-1580.

ACKNOWLEDGMENTS

This research was supported by CNPq and CAPES (Brazil). The authors also thank to the LCE/DEMa/UFSCar.

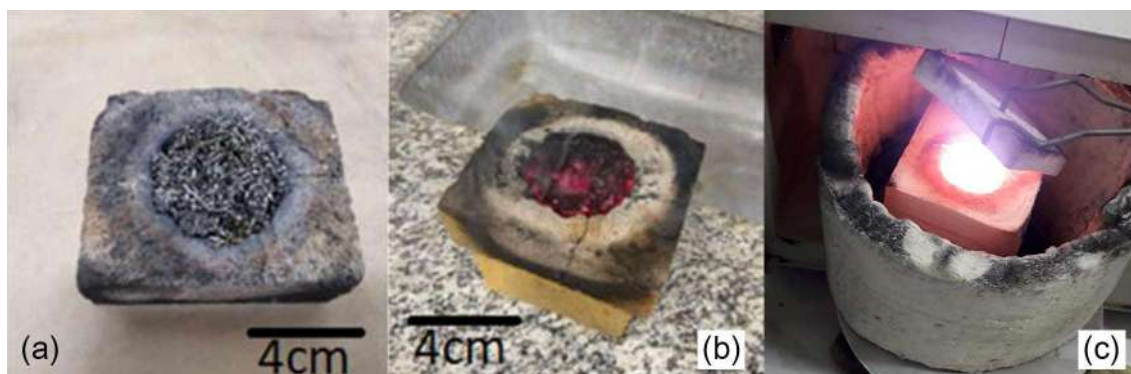


Fig.1: Chips before (a) and after (b) microwave irradiation treatment. Metallic charge after 10 minutes of irradiation (c), when titanium residues were at a high temperature.

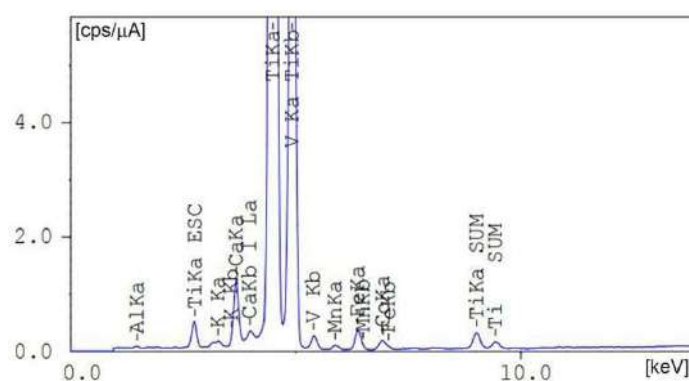


Fig.2: XRF spectrum of the powder obtained after microwave irradiation.

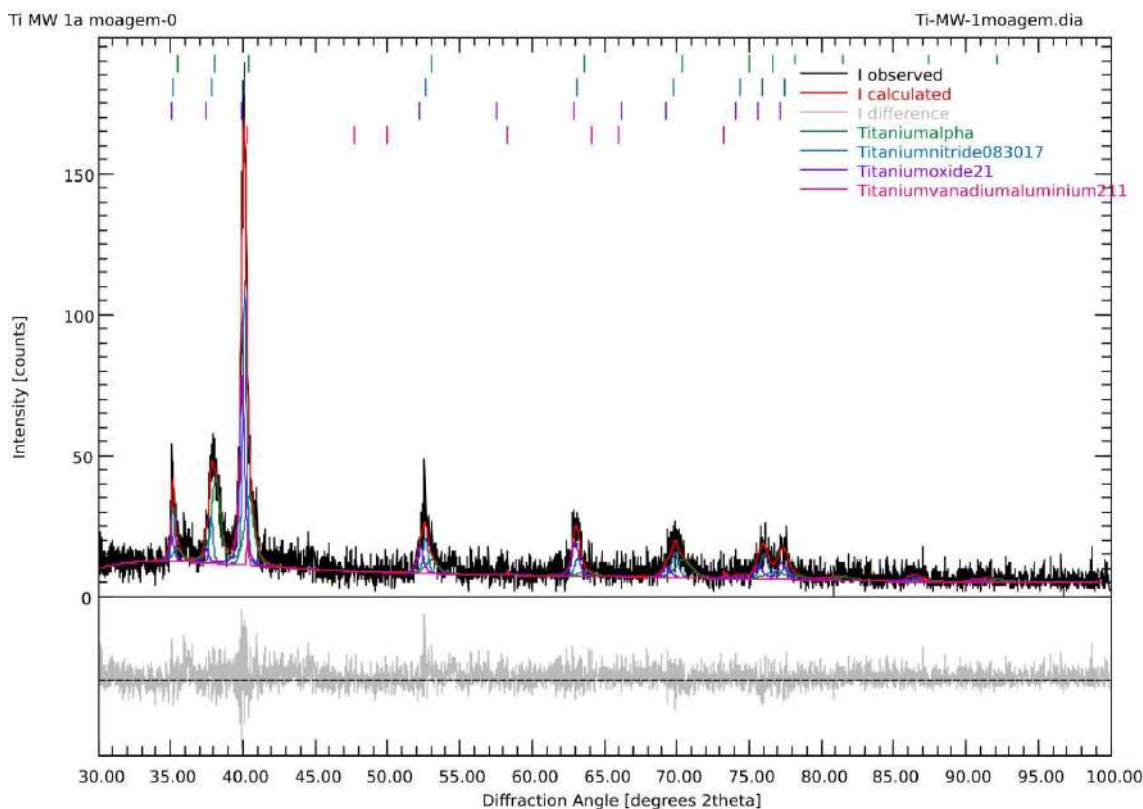


Fig.3: X-ray diffraction pattern of the powder obtained after microwave irradiation.



Microstructure of Nd:YAG Laser Welding TiC Reinforced Formed by Addition of Recycled Titanium

Rafael Borgheri dos Santos¹, João Gustavo Souza Lago¹, Alicia Ramos Modesto¹ and Juno Gallego^{1*}

¹ Department of Mechanical Engineering, São Paulo State University – UNESP, Ilha Solteira, Brazil.

* juno.gallego@unesp.br

The production of dental implants involves the machining of titanium alloys, such as ASTM F67 (pure Ti) and F136 (Ti-6Al-4V), resulting in larger quantities of metallic residues as machining chips. Such materials are quite expensive, justifying efforts to reuse them by recycling. The objective of this work is to characterize the microstructure and the formation of TiC in the weld metal produced by Laser Nd-YAG welding (LBW). During LBW titanium-rich powder, made with microwave irradiation processing on recycled ASTM F67 and F136 machining chips, was used and whose processing is described in earlier work [1]. A mixture containing 10 g of powdered chips, 2 g of graphite and 1 g of sodium silicate was used to form a paste with water, applied 0.25 mm thick layer on a piece of ASTM A36 steel. LBW was carried out by United Winners machine, model UW 150A, using the following parameters: frequency 9 Hz, pulse duration 5-9 ms, pulse energy 6-12 J, peak power 1, 2-1.6 kW and welding speed 1 mm/s. Pure argon was shielding gas. Metallographic samples were prepared in the traditional way. Weld geometry was analyzed by stereomicroscope, Fig.1. The weld metal microstructures were analyzed by SEM, EDS and XRD. The image contrast by atomic number, achieved with backscattered electrons (BSE), has facilitated the identification of the titanium carbides formed in the ferritic matrix during SEM observation. In the analyzed samples a large number of fine particles with globular morphology were observed. The microstructure composed of the largest amount of carbides was observed in the weld metal obtained with pulse duration of 5 ms, pulse energy of 9 J and peak power of 1.6 kW, Fig.2. The average particle size was estimated at 400 nm by the ImageJ software, ranging from 200 to 650 nm. The rounded morphology and small size of the TiC particles were associated with LBW rapid thermal cycle, which did not allow the carbides to grow. Electron Dispersive Energy Spectroscopy (EDS) analysis confirmed that the particles were really complex carbides. The particle showed in Fig.3 contained 45.6% Ti, 1.0% V, 2.2% Fe and 51.2% C (atomic %), suggesting that precipitate has stoichiometry close to TiC-type. The XRD analysis was performed using PROFEX [2] software, Fig.3, confirmed the presence of ferrite Fe(α) (ICSD 52258) and TiC_{0.59} (ICSD 95560) with mass fractions of 66.9% and 19.8% respectively. Other titanium-rich phases have also been identified, such as oxides and intermetallic compounds. The obtained complex microstructure in the weld metal, composed mainly of ferrite and carbides, has potential application as hardfacing for wear-resistant surfaces.

REFERENCES

- [1] G.I. PONTIN et al. Anais do I Congresso Brasileiro Interdisciplinar em Ciência e Tecnologia. Diamantina: Even3, 2020. v. 1. p. 1-5.
- [2] N. Doebelin and R. Kleeberg. J. Appl. Cryst. 48 (2015) 1573-1580.

ACKNOWLEDGMENTS

This research was supported by CNPq and CAPES (Brazil). The authors also thank to the LCE/DEMa/UFSCar.

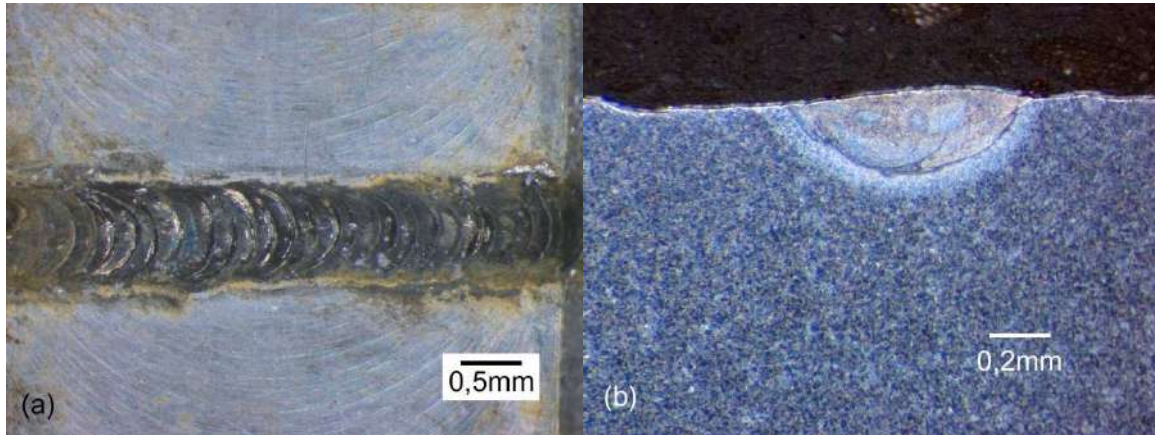


Fig.1: Typical Laser Nd:YAG weld metal. (a) Top view. (b) Transverse section. Pulse energy: 9.6 J, Peak power: 1.6 kW.

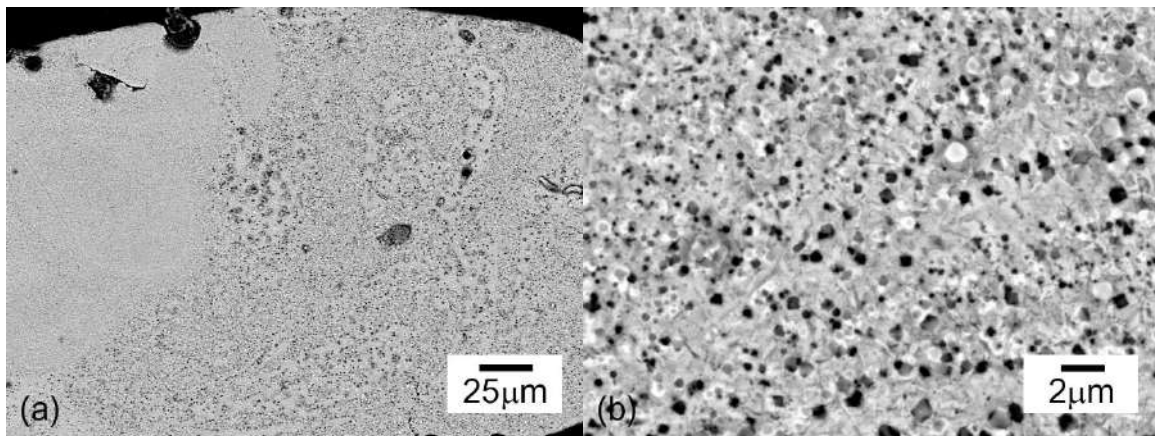


Fig.2: SEM micrographs showing LBW weld metal obtained with 9 J pulse energy and 1.6 kW peak power. BSE contrast. (a) panoramic view. (b) fine titanium carbides in ferrite.

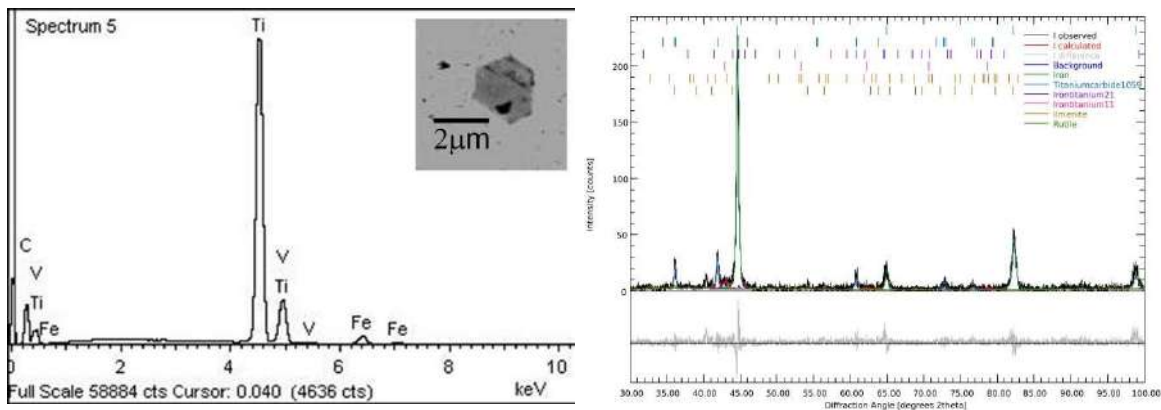


Fig.3: Typical EDS spectrum in TiC particles (a). X-ray diffraction pattern extracted from weld metal (b) of Fig.2, analyzed by the PROFEX software [2].



Comparing quantitative EDS and WDS using microanalytical standards

Karla Balzuweit^{1,2*}, Márcio de Almeida Flores² Luis A.R. Garcia², Breno Barbosa Moreira², Ramon Aranda²

¹ Departamento de Física, ICEx, Universidade Federal de Minas Gerais, Belo Horizonte, Brasil.

² Centro de Microscopia da Universidade Federal de Minas Gerais, Belo Horizonte, Brasil.

*karla@fisica.ufmg.br

Microanalysis has been an increasing need as analytical characterization, performed in several types of equipment by the most diverse areas, from traditionally metallurgy, geology and chemistry into forensic science, environmental sciences, cultural heritage, and many others. In electron microscopy, historically microprobe analysis (EPMA) has been used for quantitative analysis. Scanning Electron Microscopes (SEM) were always more a visualization tool where low current, of the order of pA are key for high resolution imaging, but unfit for reliable quantification. However, the last decades have seen an astonishing evolution of the electron microscopes: at the same time, they are much more versatile, more stable, easier to use, with higher resolution and magnification, more sensitive detectors and a much better signal to noise relation. The stability of the current SEM's plus the Silicon Drift Detectors Electron Dispersive X-ray Spectrometer (SDD-EDS) is slowly turning them into both visualization and real analytical tools as there is a growing need for better, faster and higher magnification quantitative analytical data combined with imaging, on heterogeneous samples.

The present work compares several microanalytical standards in order to assess the use of EDS-SDD as a reliable analytical tool as long as good practices are followed.

A Jeol 8900 microprobe with 4 WDS spectrometers, a Quanta200FEG SEM with a Bruker SDD-EDS and a Quanta3D FEG dual SEM-FIB with a Bruker SDD-EDS were used to analyze microanalytical standards. Care about good practices on sample preparation, correct alignment of the microscopes, spectrometer calibration, enough count rate, use of matrix correction routines (ZAF) and calibration standards were fundamental to guarantee the reliability of the results.

Figure 1 shows results of a platinum palladium sulfide. The lines represent the EPMA data and the points with the error bars the SDD-EDS SEM data, showing a very reasonable agreement even for overlapping peaks as for platinum and palladium. However, samples as monazites where rare earth elements overlap heavily is still a problem for SDD-EDS quantification, as can be seen in figure 3.

Summarizing, quantitative results for several types of materials performed with SDD-EDS SEM are in quite good agreement with WDS-EPMA analysis considering a precision of about 10 times less. However, some samples with many overlapping peaks as monazites are still a challenge for quantification.



Acknowledgments: all measurements were performed at Centro de Microscopia da UFMG, and we acknowledge our funding agencies FINEP, FAPEMIG and CNPq.

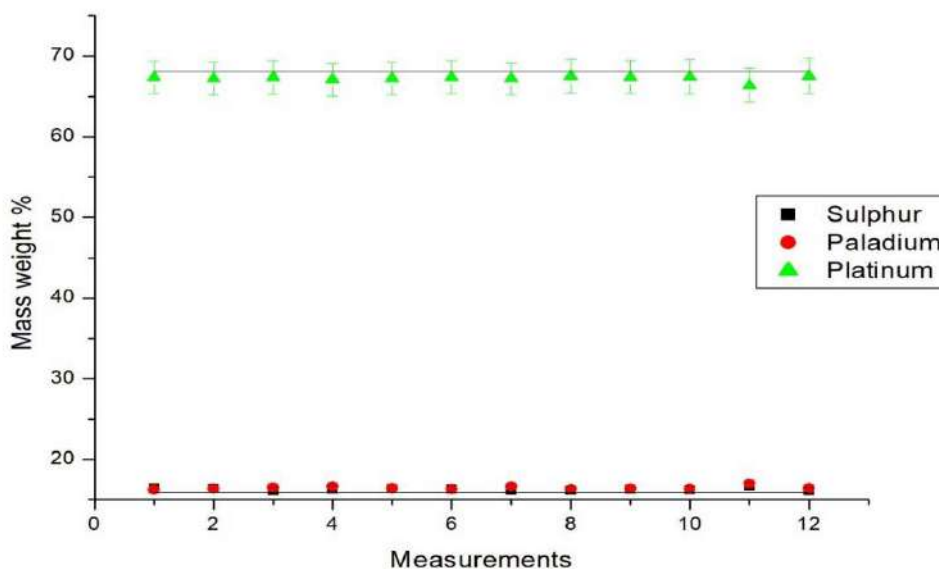


Figure 1. Comparative schema of EDS and WDS mass weight % of a Palladium Paltinum Sulfide standard. Dots are EDS measurements with respective error bars, lines are WDS data, which error bars are of the order 10 times smaller.

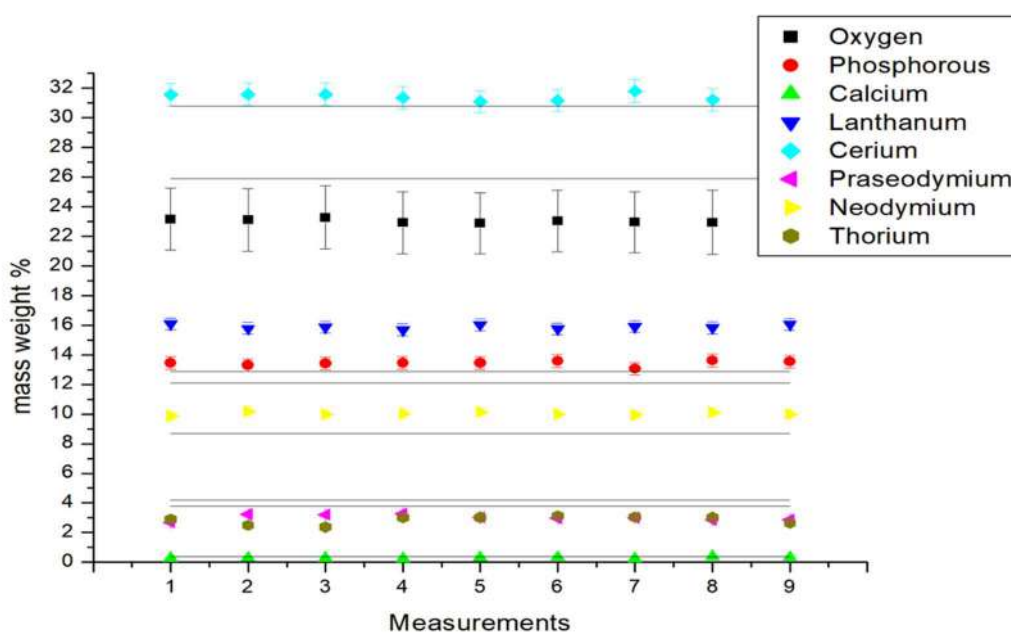


Figure 2. Comparative schema of EDS and WDS mass weight % of a Monazite standard. Dots are EDS measurements with respective error bars, lines are WDS data, which error bars are of the order 10 times smaller.



Effects Of Aluminum Intake On Trabecular Bone – A Preliminar Study In Neonatal Rats.

Mara Rubia Marques^{1*}, Anderson Camargo Moreira², Iara Frangiotti Mantovani², Celso Peres Fernandes², Fernanda Cristina Alcântara dos Santos¹.

¹ Embriology and Cell Biology Department, Biological Sciences Institute, Histology, Federal University of Goiás, Goiânia, Goiás, Brazil.

² Laboratory of Porous Media and Thermophysical Properties (LMPT) - Department of Mechanical Engineering, Federal University of Santa Catarina, Florianópolis, Santa Catarina, Brazil.

*mara_rubia_marques@ufg.br

The human being is constantly exposed to Aluminum (Al) by the air, food and beverages, drinking water, pharmaceuticals and agrochemicals [1]. Despite being abundant in the environment its active role on biological process is unknown and some interactions with biological organisms gives it toxicity. Among many disorders, Al has been associated with osteomalacia and osteodegenerative diseases [2]. According to the Joint FAO/WHO Expert Committee on Food Additives (JECFA) the Al intake should be below 2mg/kg/week [3]; however, the average consumption of six months old children fed with formulas varies between 37 to 106 mg/day [4]. Breast milk and infant formulas are fonts of Al contamination and they contributes to increase the systemic aluminum body burden in neonates [4]. In addition, vaccines and immunizations against allergens may also elevate the Al concentration in the body [5]. A strong relationship between chronic exposure to Al and bone disorders is well established in adults [6], however, evidences showing the effects of Al short period exposure during the neonatal phase is lacking. Therefore, this study evaluated endochondral ossification in the tibia of neonatal rodents submitted to Al intake in order to understand the effects of this metal on bone structure during the neonatal period. Four newborn *wistar* rats were divided into control and Al groups (n=2 animals each group). From the 1st to 15st day of live rats received, via gavage, AlCl₃ solution (10 mg/kg/day in 0.9% saline solution- 2,02 mg/Al/kg/day 1/35 DI50). The control group receive the saline solution only. Animals were euthanized in the 16st day and right tibias were dissected, kept in alcohol and analyzed by X-ray microtomography (microCT) (XRM-Versa 500). The images were filtered via denoising tools application and binarized with Avizo, the characterization was carried out with ImageJ-BoneJ plugin [7]. Volumes of interest (VOI) were determined into the subchondral bone for the analysis. The parameters evaluated were bone volume/Tissue volume (Bv/Tv), trabecular thickness (Tb.Th), trabecular number (Tb.N), trabecular separation (Tb.Sp) and connectivity density (Conn.D). The preliminary results showed that except for Tb.Th and Tb.Sp, all the other parameters decreased in the Al group (Table 1 and Figure 1), suggesting that Al intake impairs endochondral ossification during the neonatal phase. It is necessary to expand the sample size in order to confirm these data.

REFERENCES

- [1] P.M. SCHMIDT. Dissertação (Mestrado em bioquímica) - Universidade Federal do Pampa, Araguaiana, Mato Grosso (2015).
- [2] H.A. WIER; R.J. KUHN. Ann Pharmacother, v.46, (2012), 137.
- [3] G. Crisponi, D. Fanni, C. Gerosa, S. Nemolato, V.M. Nurchi, M. Crespo-Alonso, J.I. Lachowicz, G. Faa. Biomol. Concepts. 4 (2013).
- [4] D. Fanni, R. Ambu, C. Gerosa, S. Nemolato, N. Iacovidou, P. Van Eyken, V. Fanos, M. Zaffanello, G. Faa. World J. Pediatr. (2014), 10.
- [5] L.S. Keith, D.E. Jones, C.-H.S.J. Chou, Vaccine, (2002), 20.
- [6] B.L.PAN, S.S. LOKE. PLoS One, v.10, n.13 (2018).

[7] DOUBE M., KŁOSOWSKI M.M, ARGANDA-CARRERAS I., CORDELIÉRES F., DOUGHERTY R.P., JACKSON J., SCHMID B., HUTCHINSON J.R., SHEFELBINE S.J. BONEJ: Bone 47 (2010), 1076.

Table 1. Bone parameters.

Parameter	Group	
	Control	Al
Bv/Tv	21.06 (%)	20.99 (%)
Tb.Th	10.44 (µm)	10.12 (µm)
Tb.N	20.8 (1/mm)	20.1 (1/mm)
Tb.Sp	27.68 (µm)	31.25 (µm)
Conn.D	31949 (1/mm ³)	22034 (1/mm ³)

Bv/Tv = bone volume/Tissue volume; Tb.Th = trabecular thickness; Tb.N = trabecular number; Tb.Sp = trabecular separation; Conn.D = connectivity density.

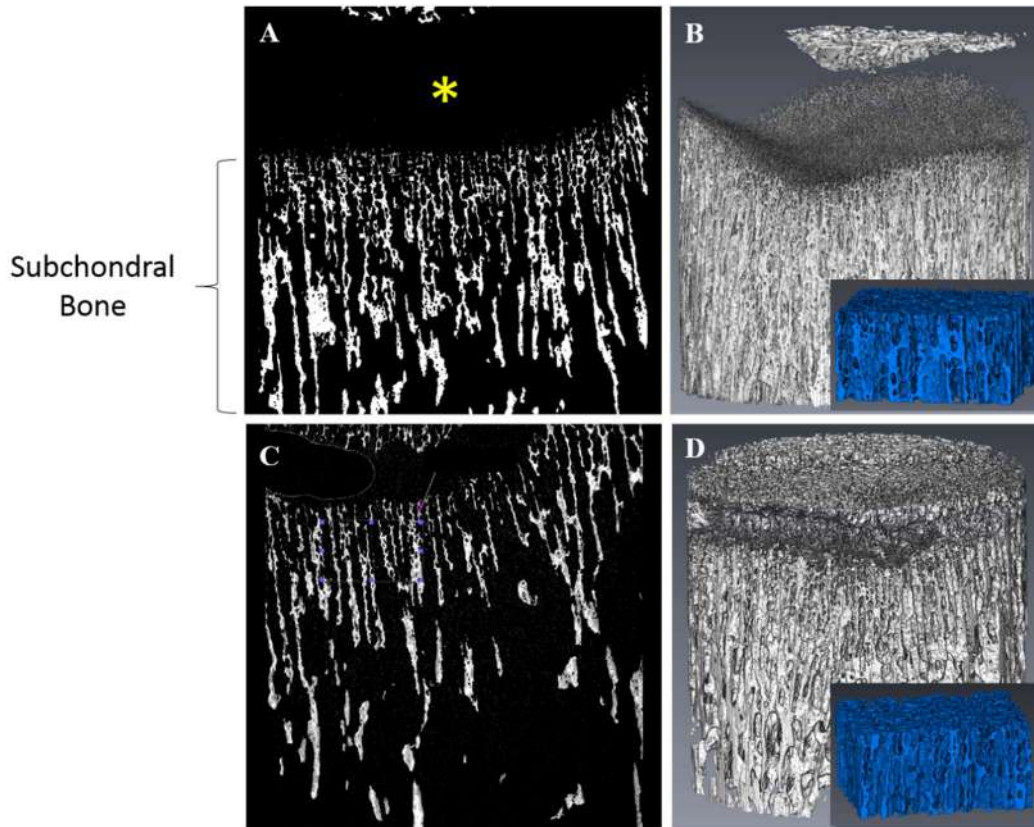


Figure 1. Microarchitecture of the subchondral bone. Control group bone microarchitecture in 2D (A) and 3D (B) reconstruction. Al group bone microarchitecture in 2D (C) and 3D (D) reconstruction. * Region of epiphyseal cartilage. Blue insert: higher magnification of the VOI. Voxel size: 2.096 µm. Volume VOI: 0.102 mm³.



Aging Stability Of The Structure Of Mn-based M41S Family Silicas.

Marcus Andrei Ullmann^{1*}, Daniela Bianchini¹

¹ Universidade Federal de Pelotas (UFPEL), Centro de Ciências Químicas, Físicas e de Alimentos, Campus Capão do Leão, RS, Brazil.

*mullmann.iqg@ufpel.edu.br

M41S family materials, such as MCM-41, are vastly studied for applications in environmental waste removal technologies [1] and photocatalysis devices [2]. Molecular sieves functionalized with manganese were employed as catalysts in oxidation processes [3]. Despite the wide usage of these silica sieves, their experimental conditions for the synthesis demands attention [4]. After a long aging time (2 years) of synthesized Mn-SiO₂ silicas with different manganese amounts added to the inorganic precursor during sol-gel process (Stöber method) that was observed modifications on MCM-41 structure. As far as we know, the aging event over M41S family silicas with Mn are unreported at literature. Profiles were analysed using Modelling II tool, available in the Irena evaluation routine as implemented in the Igor Pro software package (WaveMetrics, Portland, USA); this tool allows to combine a simplified version of unified levels and diffraction peaks [5]. The addition of manganese to the structure tends to contribute to the formation of lumps and plates, which corroborate the hypothesis of co-precipitation of manganese oxides in the basic reaction medium during synthesis (Figure 1). Comparing SAXS patterns of raw synthesized Mn-SiO₂ (X %) systems, where X % is the Mn/SiO₂ content, (Figure 2a) and patterns of the same system after aging (Figure 2b), it is possible to see an increasing in 2nd population of Guinier area (around 0.6 nm⁻¹) and a high decreasing in 1st diffraction peak intensity (100 plane). After aging time, the diffraction peaks related to the planes (110) and (200) respectively at $q \sim 4.1 \text{ nm}^{-1}$ and $q \sim 4.8 \text{ nm}^{-1}$ vanish, as shown in Figure 2c. This behavior indicates that the MCM-41 porous systems collapsed over the time. SAXS parameters indicates that Mn-SiO₂ (0.0 %) and Mn-SiO₂ (0.3 %) pores crack through aging time, therefore, generate a high asymmetric particles, it means, reduction of power-law exponent and particles radii (R_p). However, MCM-41 porous system coalesced through time at silica devices with more than 1.0 wt.-% of Mn amount, and thus generate a densification with increasing of power-law exponent and particles radii (R_p) (Figure 3). It suggests that Mn amounts at the regular structured systems modifies or drives the form that silica aged.

REFERÊNCIAS

- [1] Y. Liu, *et al.*, J. Hazard. Mater. 408 (2021) 124911.
- [2] E. Amdeha, *et al.*, Ceram. Int. (2021).
- [3] T. Qi, *et al.*, Chem. Eng. Sci. 241 (2021) 116691.
- [4] B.B. Cazula, *et al.*, Mater. Chem. Phys. 266 (2021) 124553.
- [5] J. Ilavsky, P.R., J. Appl. Crystallogr. 42 (2009) 347-353.

AGRADECIMENTOS

The authors thank LNLS, project D11A-SAXS1-11586, for SAXS analyses; MCT/CNPq/MEC/CAPES-Ação transversal n° 06/2011-Casadinho/Procad-Processo n° 552197/2011-4 for the partial support to the project and CAPES for the scholarship.

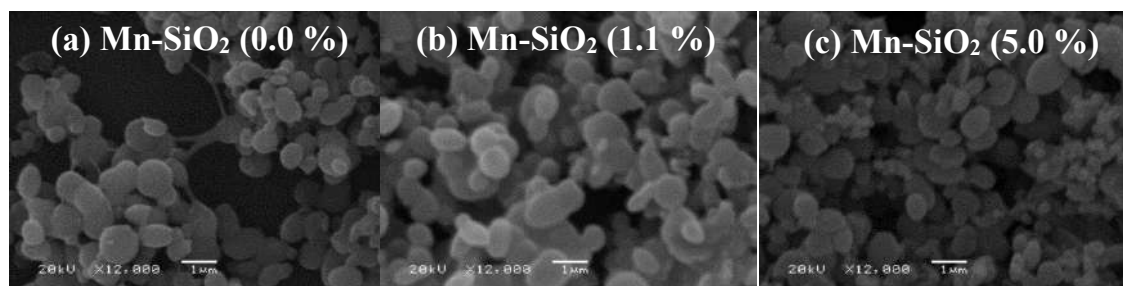


Figure 1. Raw systems with x12,000 of magnification and 1 μm resolution.

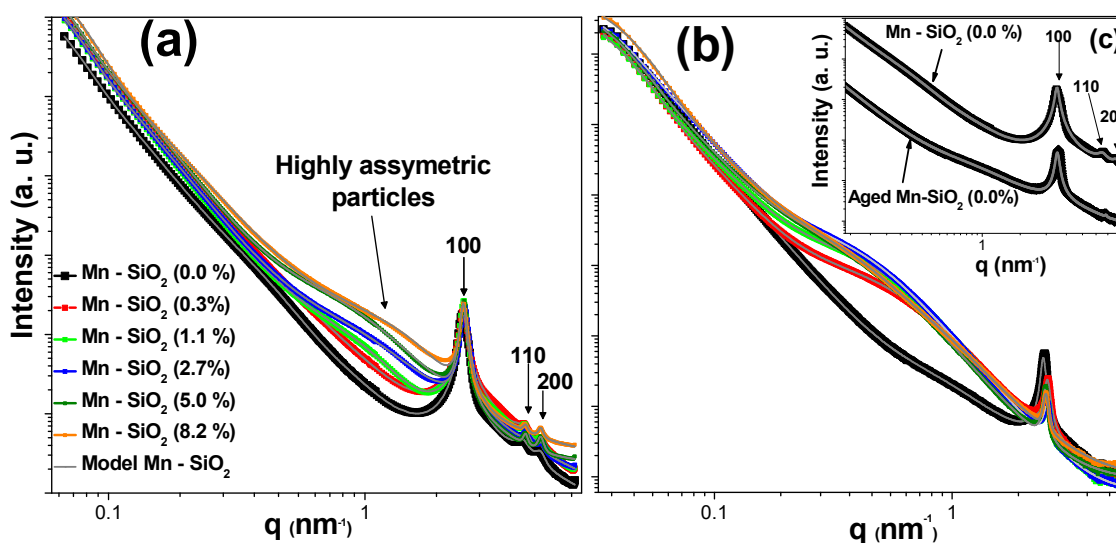


Figure 2. SAXS patterns of Mn-SiO₂ (X %) systems. (a) Patterns of raw synthesized systems. (b) Patterns of the systems after aging time. (c) Comparison of Patterns of Mn-SiO₂ (0.0 %) system: raw and aged.

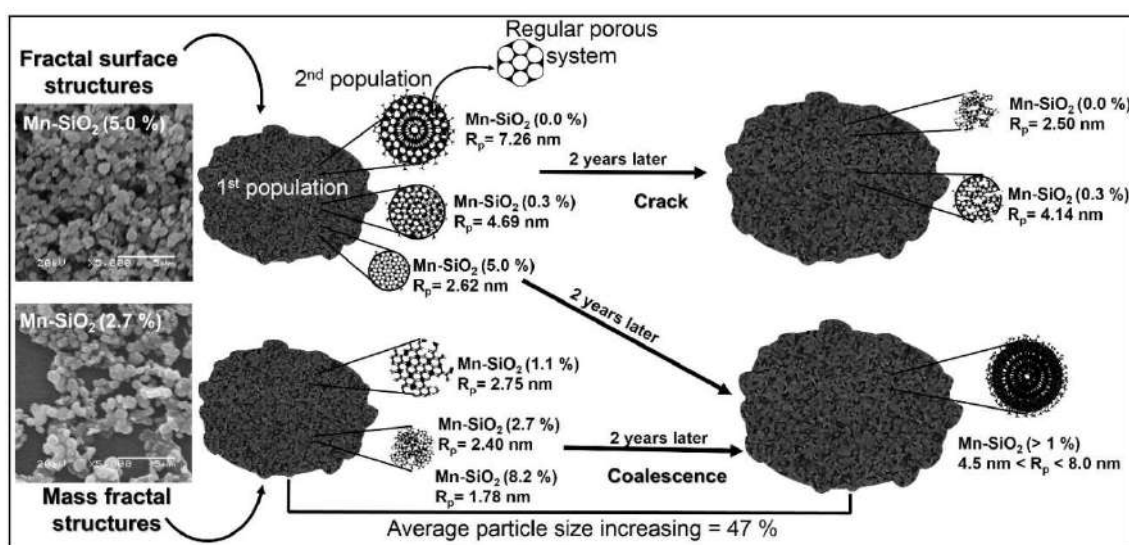


Figure 3. Model of how the hierarchical particles that form the Mn-SiO₂ system evolve by an aging time against its manganese content.



Advancing Life Science SEM-EDS analysis with the XFlash® FlatQUAD

Patzschke, M. and Menzies, A.H.
Bruker Nano GmbH, Berlin; Germany

SEM-EDS is often challenging when it comes to life science samples and elemental analysis. This is particularly difficult when standard sample preparation methods, like carbon-coating or polishing, are not possible. Then topographically complex samples often lead to data shadow effects and charging occurs for uncoated samples. In addition, low beam currents often have to be applied so that the sample is not damaged, and this subsequently leads to low count rates and potentially long analytical times.

To overcome such analytical challenges, the XFlash FlatQUAD (Figure 1) has been developed. This detector is inserted between the pole-piece and the sample and is ideally suited for the analysis of topographically complex and beam sensitive samples. Shadowing effects are minimized as there are four separate X-ray detector segments that cover a large solid angle of 1.1sr. This allows sufficient data to be collected at low beam currents, such as the pA range, where a sample can be investigated without carbon coating under high vacuum. Compared to low vacuum analysis, this results in higher spatial resolution of the SEM images and X-ray element mappings. Furthermore, high-speed mapping is possible due to the ultra-high-count rates that are acquired. In addition, when using normal beam currents, a complete thin section (40 x 25 mm) can be mapped in few minutes of acquisition time.

Different life science examples were analysed at low beam currents to avoid charging and beam damage on the sample, as well as enable ultra-high-speed data acquisition. Here we will present examples from this life science study, samples from a sea urchin, a bacterium, a microbial mat of diatoms, a wasp and geological thin sections were investigated with this unique SDD detector.

The EDS map (Figure 2) shows a sea urchin (*Paracentrotus lividus*) collected in the Aegean Sea near Athens, Greece. The bumps visible on the two top images are the sockets where the urchins' long spines are attached. They are being held in place by muscles and collagen so that they can be moved if the urchin wants to hide in a crevasse and they can be held rigid in a defensive mode, e.g. when stepped on. The two bottom images showing individual salt (green) and sand (red) grains. The skeleton of the sea urchin is produced by biomineralization, consisting of high-magnesium calcite. The architecture of the skeleton reveals a sponge-like lightweight structure, which can bare extremely high weights.

It is possible to classify hypermaps as per their mineralogy as well. Figure 3 shows an example of this where the elemental information is able to be defined on a pixel-by-pixel

basis to yield a mineralogical definition. Once this is established it is possible to investigate the data set in a variety of ways, such as by mineralogy, mineral grain size or element department.

Thus, the XFlash FlatQUAD is able to expand the capabilities of a standard SEM, enhancing the ability to analyse complicated samples due to topographic effects or low beam currents, as well as significantly improving analytical times due to an extremely high X-ray count throughput.



Figure 1. The XFlash® FlatQUAD detector which is positioned directly between sample and pole piece which yields a solid angle of 1.1sr.

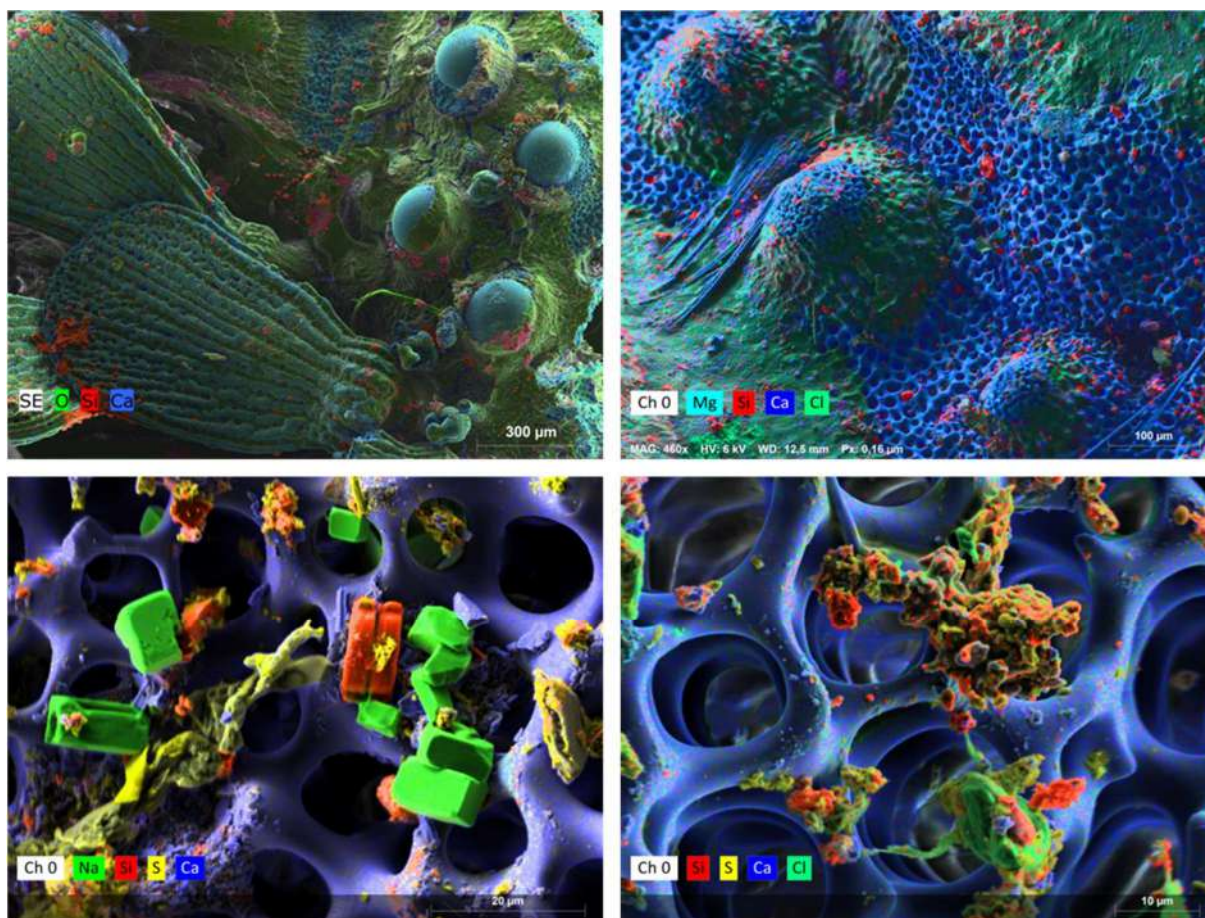


Figure 2. Sea urchin (*Paracentrotus lividus*). The bumps on the two top images are the sockets where the urchins long spines are attached. The skeleton of the sea urchin is produced by biomineralization,



consisting of high-magnesium calcite. The architecture of the skeleton reveals a sponge-like lightweight structure, which can bare extremely high weights.

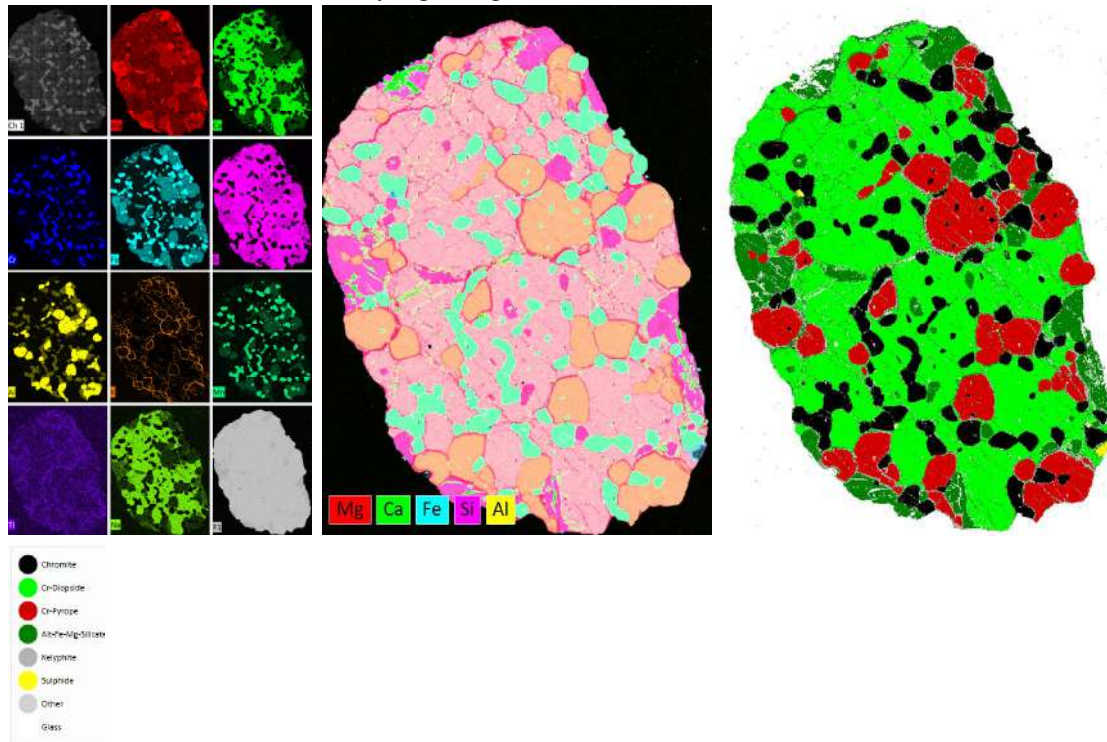


Figure 3. Large area map of a mantle peridotite sample (20 x 15 mm) showing (from left to right): (i) various individual elemental distributions; (ii) combined elemental maps of Mg, Ca, Fe, Si, Al which highlight the different minerals in the samples; and (iii) mineralogy classified using AMICS (Automated Mineralogy) software.



Study of Morphological and Chemical Changes on FCC Equilibrium Catalysts by Scanning Electron Microscopy

Paulo Sergio S. Carvalho^{1*}, Beatriz R. Canabarro¹, Anderson F. Pereira¹, Manoel Jorge R. Marim¹, Marco Antonio S. de Abreu², Edisson Morgado Junior², Paula Mendes Jardim¹

¹ Federal University of Rio de Janeiro, COPPE/UFRJ, Rio de Janeiro, Brazil.

² Leopoldo Américo Miguez de Mello Research and Development Center, CENPES/Petrobrás, Rio de Janeiro, Brazil.

[*carvalhops@poli.ufrj.br](mailto:carvalhops@poli.ufrj.br)

Fluid Catalytic Cracking (FCC) is a key refining process that converts crude oil into more valuable products for the market, like gasoline. The process employs the use of particulate catalysts that are brought into contact with vaporized gasoil feed, promoting cracking reactions. The continuous conversion/regeneration cycles induce structural changes in the catalyst, leading to a decrease in average catalyst activity. Deposition of metals such as Iron (Fe), Nickel (Ni), and Vanadium (V) on catalysts also lead to irreversible damage. Due to the decrease in average catalyst activity over time, a continuous replacement of a spent catalyst fraction by a fresh catalyst is essential to maintain the overall catalyst activity constant. The spent catalyst fraction purged from the unit is called equilibrium catalyst (ecat) and is composed of particles of different ages and levels of contamination [1-3]. The metals deposition profile onto FCC catalyst particles is specific to each element. Nickel and Iron are known to deposit mainly on the outer portion of the catalyst particle. Vanadium is known to have great mobility, therefore penetrating deeper into the particle as well as migrating between them [3-4]. In this study, ecat particles supplied by CENPES were separated by density and further analyzed by x-ray fluorescence spectrometry (XRF), Nitrogen Physisorption, and Field Emission Scanning Electron Microscopy (FE-SEM) coupled with X-ray Energy Dispersive Spectrometry (XEDS). For the microscopy analysis the separated fractions were embedded in epoxy and cut for the observation of the particles cross-section. For the density separation procedure of the chosen ecat, it was used the sink/float method with diiodomethane and acetone, and resulted in four fractions of the original ecat, designated by F1 (heaviest), F2, F3, and F4 (lightest). Since the oldest catalysts are exposed to higher levels of metal contamination over time (hence, presenting higher density), the density separation of the ecat fraction can be used as a means of classification of the catalysts by age as well (with F1 being the oldest and F4 the newest groups). Figure 1 shows FE-SEM backscattered electron images of F1 (Figure 1-(A) and (C)) and F4 (Figure 1-(B) and (D)) samples. It can be noticed that the lightest fraction (F4) presented higher porosity compared to the oldest one (F1). The changes in porosity during catalyst particle lifetime are related to hydrothermal deactivation associated with metal deposition [4]. Besides, it was observed that the heaviest particles (F1) showed an increase in circularity compared to their counterparts, which could be attributed to the higher abrasion undergone by these particles during FCC cycles. Figure 2 shows the XEDS mappings of the elements of interest for samples F1 (Figure 2(A)) and F4 (Figure 2(B)). For the oldest fraction (F1), these preliminary analyses suggest the existence of two types of particles (one more enriched in Si and the



other in Al), while, for the F4 fraction, Si and Al were more equally distributed amongst the particles. Further analyses are being performed to verify the statistic relevance of these results. The XEDS mappings also revealed a higher level of Vanadium and Nickel present on the heaviest fraction (F1). Finally, the results presented show that electron microscopy can bring valuable information on the understanding of morphological and chemical changes on FCC catalysts over operational time.

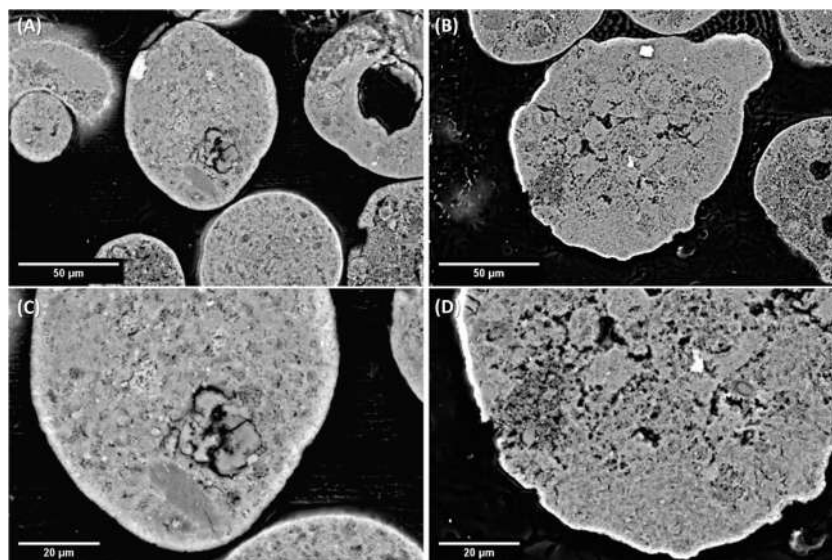


Figure 1 – FE-SEM backscattered electrons images of particles cross-sections of F1 (A, C) and F4 (B, D) samples, in two different magnifications.

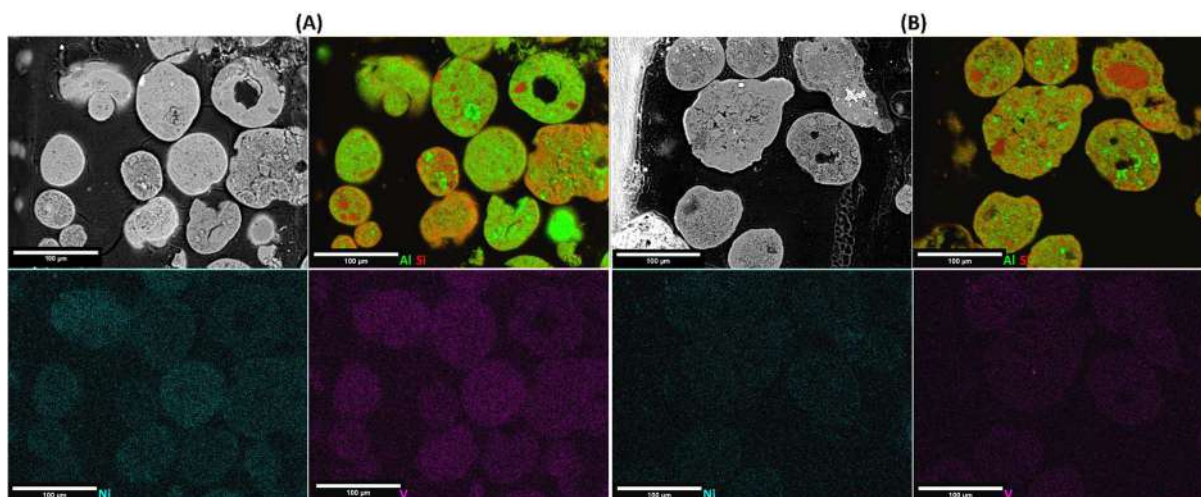


Figure 2 – BSE Images and XEDS Elemental Mappings of Al (green), Si (red), Ni (cyan) and V (magenta) for F1 (A) and F4 (B).



Heat Treatment post SLM from the Mixed Ni and Ti Powders

Eduardo Hoisler Sallet¹, Rodolfo da Silva Teixeira¹, Rebeca Vieira de Oliveira¹, Patrícia Freitas Rodrigues², Talita Gama de Sousa¹, Naiara Vieira Le Sénéchal¹, Ygor Pereira de Lima¹, Danilo Abílio Correa Gonçalves¹, Edilainea Alves Oliveira Melo¹, Paulo Inforçatti Neto³, Jorge Vicente Lopes da Silva³, Luiz Paulo Mendonça Brandão¹, Andersan dos Santos Paula^{1,*}

¹Seção de Engenharia de Materiais, Instituto Militar de Engenharia (IME), Praça General Tibúrcio 80, Urca, Rio de Janeiro/RJ, Brazil

²Department of Mechanical Engineering, University of Coimbra, CEMMPRE, R. Luís Reis Santos, Coimbra, Portugal

³Centro de Tecnologia da Informação Renato Archer, Rodovia Dom Pedro I (SP- 65), Km 143,6 - Chácaras Campos dos Amarais, Campinas/SP, Brazil

*andersan@ime.eb.br

NiTi shape memory alloys (SMA) have attracted much interest due their functional properties such as shape memory effect (SME) and superelasticity (SE), which it desirable to use in many applications in different fields, for instance aerospace and automotive industry and biomedical engineering [1]. Usually, these kinds of alloys are made by casting, which could possibility of contamination during melting and affect the functional properties. Therefore, this study amid to evaluate the effects of heat treatment in specimen of Ni-Ti manufactured through selective laser melting (SLM), a common additive manufacturing (AM) process [2,3]. For this, starting from individual powders of Ni (particle size $\approx 2.1 \mu\text{m}$), and the Ti HDH from grade 1 (particle size $\approx 100.0 \mu\text{m}$), the cylindrical specimens (10 mm height and 7 mm diameter) were manufactured through SLM in argon-controlled atmosphere using fixed processing parameters. After that, the specimens were subjected to heat treatment at 950 °C for 4 and 6 h, under argon-controlled atmosphere. Through Scanning Electron Microscopy (SEM) from secondary electrons detector (SE) analyses, it was identified the presence of coarse porous, probably associated there was not complete coalescence of the powder, as shown in Figure 1 [2]. Based on the SEM from backscattered electrons detector (BSE) analyses, the heat treatment of 4 h has not been enough to promoted homogenization, as observed in Figure 2 (a), can be considered similar to the condition just processed in SLM. It was detected the presence of Ti island, Figure 2 (b), and the intermetallic of Ni-Ti system, Figure 2 (c). Increasing the temperature from 4 to 6 h, there has been an improve in the homogenization on microstructure (Figure 3 (a)). However, there has been detected second phases, as shown in Figure (c,e,f) [4].

References

- [1] K. Otsuka, X. Ren, Prog. Mater. Sci. 50 (2005) 511-678.
- [2] R. V. Oliveira, *et al.*, K. Mater. Eng. Perform. (2021).
- [3] E. Faber, Mater. Today Proc. 30 (2019) 761-767.
- [4] This research was supported by CAPES/Pró-Defesa IV (Process 88887.285953 /2018-00) and CNPq (PQ-2 - Process 307798/ 2015-1) (Brazil)

Acknowledgments

The authors would like to thank the Brazilian institutions/companies: Brats, IPT (São Paulo), INT and Tecnow. The authors acknowledge the funding of the European Program: IRSES



- Marie Curie PIRSES GA-2013-6125855, FEDER funds through the program COMPETE
- and by national funds through FCT – Portugal, under the project UIDB/00285/2020.

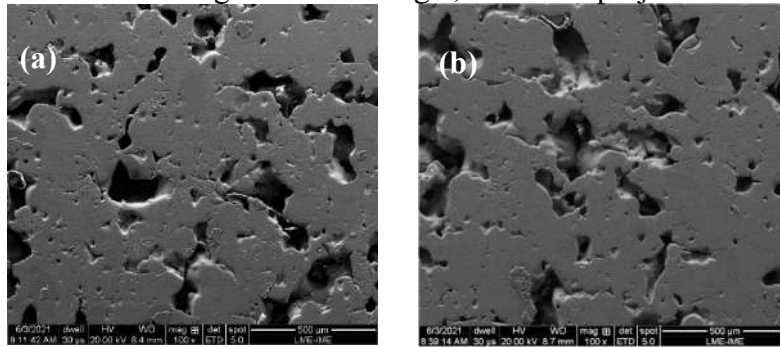


Figure 1: SEM/SE micrographs of the cross sections of the cylinders at (a) 4h and (b) 6 h, after SLM with 0.11 mm hatch spacing (h), 0.03 mm layer thickness (t) and 95 W laser power (P) and 1350 mm/s scanning speed (v), resulting in 21,32 J/mm³ energy density.

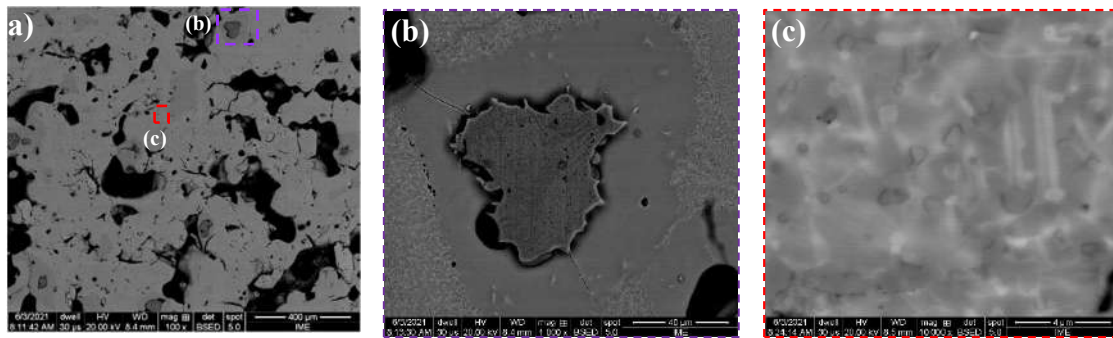


Figure 2: SEM/BSE micrographs of the cross sections of the cylinders after heat treatment of 4 h.

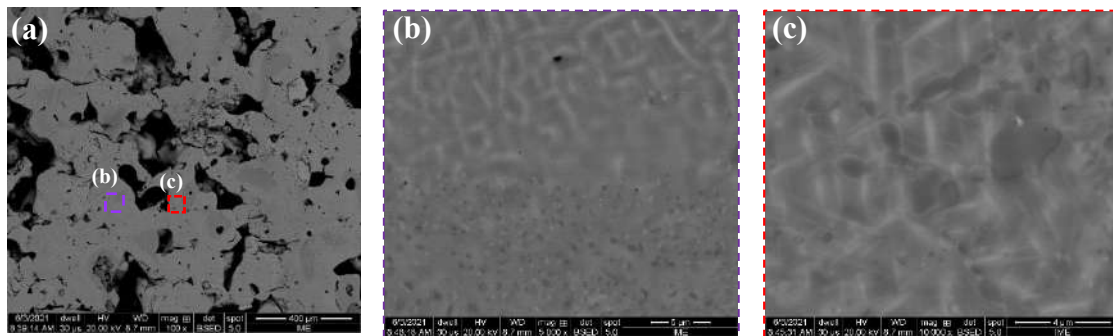


Figure 3: SEM/BSE micrographs of the cross sections of the cylinders after heat treatment of 6 h.



Yttrium Effect on δ Precipitation In The Hot Forged Nickel-Alloy 718

Rosa Maria Sales da Silveira^{1*}, Alessandra Vieira Guimarães¹, Leonardo Sales Araujo¹
Loïc Malet² and Luiz Henrique de Almeida¹

¹ Department of Metallurgical and Materials Engineering – Alberto Luiz Coimbra Institute for Graduate Studies and Engineering Research-Federal University of Rio de Janeiro (COPPE-UFRJ), Rio de Janeiro, RJ, Brazil.

² Université Libre de Bruxelles, Chemical and Materials Department, C. P. 194/03, Brussels, Belgium

*rosasilveira@coppe.ufrj.br

The use of the yttrium as alloying element of superalloys has been studied due to its many beneficial effects, when correctly added during manufacturing [1–3]. Previous study showed that Y considerably increases the ductility of the nickel-alloy 718 [4]. Different Y-rich phases are formed, mainly the intermetallic Ni_{17}Y_2 in addition to sulfides and oxides [4]. The quantity, size and morphology of the precipitated δ phase plays an important role in controlling the properties of alloy 718 [5]. For this reason, the aim of this work is to study the influence of Y addition on δ phase precipitation in the alloy 718.

The alloys were casted in a vacuum induction furnace, homogenized and then hot forged into round bars. Two different Y contents were added to the alloy 718 as shown in Table 1. The alloys were submitted to solution annealing heat treatment at 945 °C for 1h, followed by water quenching, favoring δ phase precipitation.

The alloys microstructures were characterized by scanning electron microscopy in backscattered electron mode (Tescan Vega 3, 20 kV), by energy-dispersive X-ray spectrometry and EBSD analysis. The sample metallographic preparation consisted on conventionnal grinding down to 1 μm and colloidal silica for 1 hour. Yttrium particles were identified by EBSD analysis as Ni_{17}Y_2 mainly located at grain boundaries as shown on Figure 1. A small fraction of Y-oxides and Y-sulphides were detected by EDS, as presented on Figure 2. SEM images of Figure 3 exhibited that a low Y content apparently contributed to inhibit the δ precipitation, while a high Y content produced an intense precipitation of Y-rich particles on grain boundaries that seemed to favor the δ precipitation. Additionally, Figure 3(c) shows that δ precipitation also occurs associated to the Ni_{17}Y_2 , meaning that the Y-rich phases may contribute for increasing the volumetric fraction of δ .

References

- [1] K. Di Xu et al, Rare Met. 33 (2014) 111–126.
- [2] F.C. Nunes et al, Mater. Charact. 58 (2007) 132–142.
- [3] P.J. Zhou et al, Scr. Mater. 57 (2007) 643–646.
- [4] A.V. Guimarães et al, Mater. Sci. Eng. A 776 (2020).
- [5] M. Anderson et al, Mater. Sci. Eng. A 679 (2017) 48–55.

The authors would like to thank CNPq (Brazil) for the financial support and Villares Metals. S.A. for supplying the alloys for this research



Table 1 – Chemical composition of reference alloy A, low-Y content alloy B and High-Y content alloy C (%wt.)

Alloy	Ni	Cr	Fe	Mo	Nb	Al	Ti	C	S	O	N	Y
A	52.7	17.81	19.71	2.90	5.10	0.518	0.972	0.026	0.0040	0.0042	0.0110	0.000
B	52.5	17.80	20.05	2.90	4.99	0.519	0.980	0.023	0.0016	0.0020	0.0055	0.052
C	51.4	17.62	20.69	2.91	5.01	0.549	0.966	0.024	0.0010	0.0012	0.0060	0.613

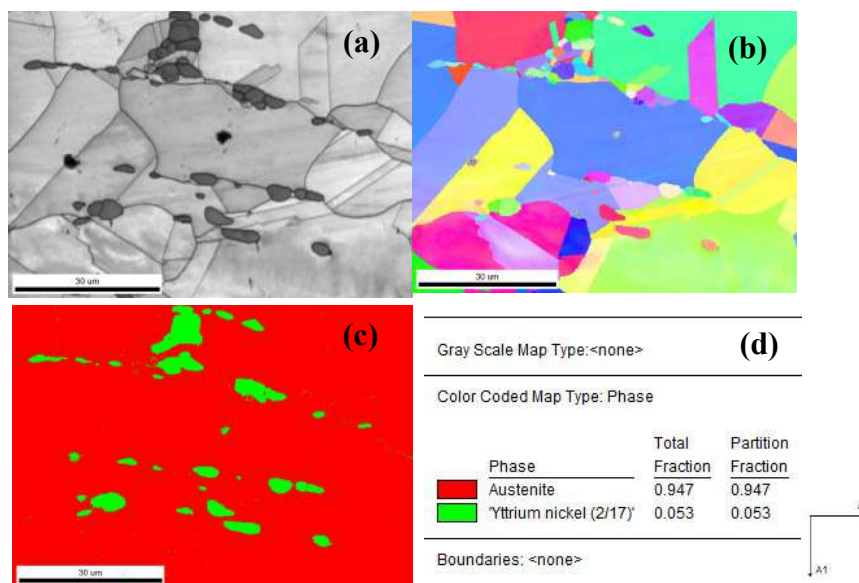


Figure 16 - $Ni_{17}Y_2$ identification by EBSD analysis.

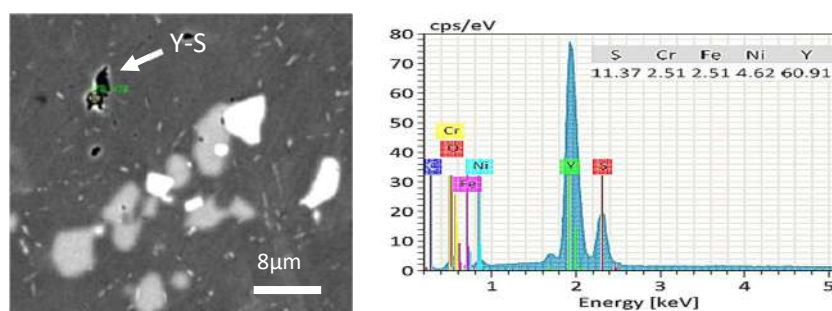


Figure 17 - EDS characterization of a Y-S particle.

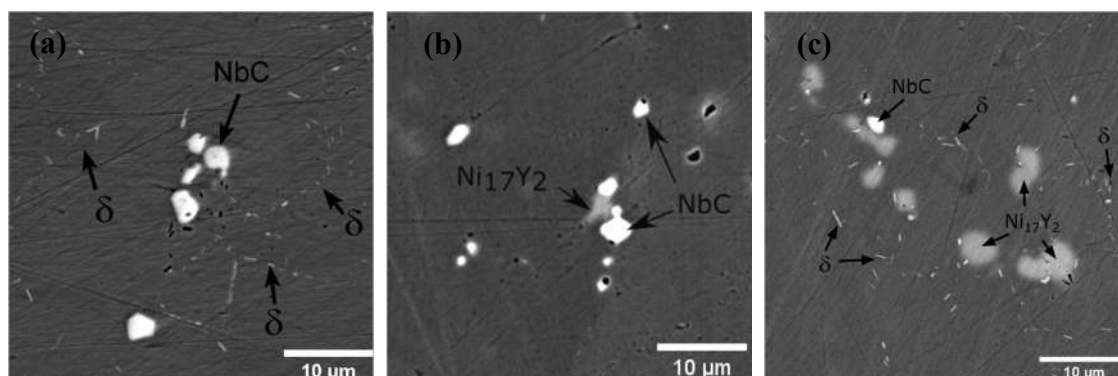




Figure 18 - Microstructure of reference alloy (a), low-Y content alloy (b) and high-Y content alloy (c).



HMDSO thin films and their potential application as flame retardant coatings for fabrics

Soraya Nassar Sakalem^{1*} and Renata Antoun Simão²

¹ Universidade Federal do Rio de Janeiro, PENT/COPPE, Rio de Janeiro, Brazil.

² Universidade Federal do Rio de Janeiro, PEMM/COPPE, Rio de Janeiro, Brazil.

*snsakalem@coppe.ufrj.br

Fires can lead to immeasurable damage, such as the loss of material goods, records and memories. To minimize the damage caused by fires, researchers are looking for flame retardant materials. The most common flame retardant materials can be harmful to health and the environment, once they have formaldehyde, phosphorous or brominated additives in their composition [1]. With the advent of nanotechnology, new health safe and ecofriendly materials with flame retardant characteristics started to be studied. As an example of flame retardants nanomaterials, the use of silicon nanoparticles and also clay in cotton fabrics can be mentioned [2,3]. Given this context, this work aimed to modify the surface of fabrics, make them flame retardant, through the deposition of silicon nanoparticles, using plasma treatment of HMDO (hexamethyldisiloxane) and HMDSO combined with CO₂ (carbon dioxide) [4]. To evaluate the characteristics of these films, they were deposited on aluminum plates due to their inert characteristics. Images of atomic force microscopy and scanning electron microscopy were used evaluate the morphology of the deposited films and energy dispersive spectroscopy were used to analyze their chemical composition. Both AFM (**Figure 19**) and SEM (**Figure 20**) images suggests the formation of granules with nanometric dimensions, and with the inclusion of CO₂ in the deposition process, these granules become even smaller. Regarding the chemical composition, the EDS (**Figure 21**) results suggests the presence of carbon, oxygen and silicon in the samples, which was expected, given the chemical nature of the precursors. Furthermore, it is observed that the inclusion of CO₂ in the chamber during deposition increases the silicon concentration in the film. These results indicates that those films can act as a physical barrier to protect the fabric from fire due to the presence of silicon in the protective layer, and we observed that when even more silicon there is, more efficient the coating is for flame retardants purpose (**Figure 22**).

REFERENCES

- [1] A. R. Horrocks, Rev. Prog. Color. Relat. Top., 16 (1986) 62
- [2] S. Lu e I. Hamerton, Prog. Polym. Sci., 27 (2002) 1661
- [3] S. Liang et al., Prog. Org. Coatings, 76 (2013) 1642
- [4] M. D. F. Albuquerque et al., Thin Solid Films, 564 (2014) 73

ACKNOWLEDGMENTS

The authors thank the support from FAPERJ Brazilian funding agency.

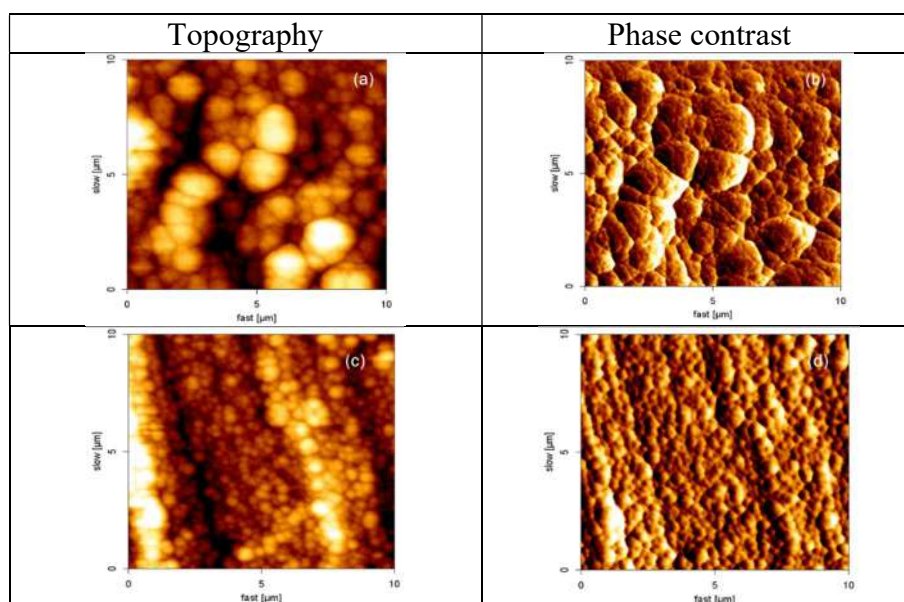


Figure 19. AFM topography images for HMDSO films (a) and HMDSO combined with CO₂ films (c). Phase contrast images obtained for HMDSO films (b) and HMDSO combined with CO₂ films (d).

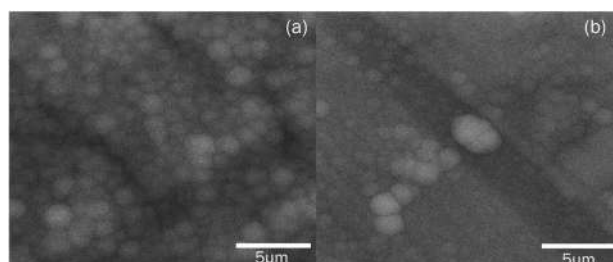


Figure 20. MEV images for HMDSO films (a) and HMDSO combined with CO₂ films (b)

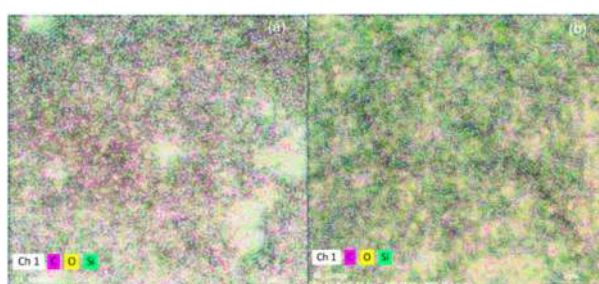


Figure 21. EDS for HMDSO films (a) and HMDSO combined with CO₂ films (b)

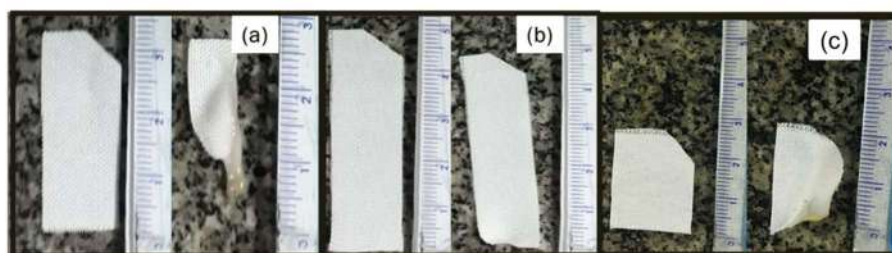


Figure 22. Visual tests of flame resistance of untreated fabrics (a), treated with HMDSO combined with CO₂ (b) and treated with HMDSO (c)



Effect of Cold Rolling on the Microstructure and Young's Modulus of a New β -metastable Ti-24Nb-4Mo-6Zr alloy

Aline Raquel Vieira Nunes^{1*}, Sinara Borborema², Leonardo Sales Araújo¹,
Luiz Henrique de Almeida¹

¹ Federal University of Rio de Janeiro, UFRJ, Rio de Janeiro – RJ, Brazil

² Rio de Janeiro State University – FAT/UERJ, Resende – RJ, Brazil

*e-mail: alineraquel@coppe.ufrj.br

The effect of cold rolling deformation on the microstructure and on Young's modulus (YM) of a new β metastable Ti-24Nb-4Mo-6Zr alloy were studied. The ingots were produced by arc melting under high purity argon atmosphere, homogenized at 1000 °C for 24 h and then quenching. The ingot was cold rolled with reductions of 30%, 70% and 90%. The microstructural evolution was characterized by optical microscopy (OM), electron backscattered diffraction (EBSD) and X-ray diffraction (XRD). Figure 1 presents the XRD patterns of the alloy homogenized (HM) and cold rolled (CR). Single β phase were identified in HM and 30% CR conditions. After 70% and 90%, the orthorhombic α'' phase was clearly identified indicating the stress-induced martensitic phase transformation (β to α'') occurred during cold rolling. Figure 2 shows the microstructure of the homogenized sample presents single-phase equiaxial β grains. After cold rolling with 70% reduction, the microstructure shows elongated grains with visible deformation bands. After cold rolling with 90% reduction, the microstructure exhibits fibrous stripe owing to the severe cold deformation. Twinning and stress-induced α'' martensitic transformation are typical deformation mechanisms in Ti- β alloys. There are two possible twinning systems in Ti- β alloys and they can be distinguished by EBSD by the misorientations identification [1,2]. EBSD orientation map shows the occurrence of numerous β primary and secondary twins after 30% deformation (Fig. 3). Primary twins have a CSL boundary $\Sigma 11$ (in red) which corresponds to a $\{332\}\langle 113\rangle$ twinning system. Secondary twins have a CSL boundary $\Sigma 3$ (in green) which corresponds to a $\{112\}\langle 111\rangle$ twinning system. Figure 2 (c) confirms that the point-to-point misorientation angle across the β -Matrix (M) and β -twin 1 (T1) is 50° corresponding to $\{332\}\langle 113\rangle$ twinning system. The point-to-point misorientation angle across the β -twin (T2) and β -twin 1 (T1) is 60° corresponding to $\{112\}\langle 111\rangle$ twinning system. These 2 systems are the twinning systems already mentioned in the literature for β -Ti alloys [2]. The Young's modulus (YM) of metastable Ti- β alloys presents a complex relationship with the processed microstructure. Homogenized single β microstructure exhibited the lowest YM, 56 GPa. With 30% and 70% CR these properties increased to 70 and 72 GPa respectively. Finally, with 90% of deformation YM reduced it to 64 GPa. For all studied conditions, the YM values were close to that of human bone, showing the correctness of proposed chemical composition for this new alloy.

[1] A.R.V. Nunes et al., *Microsc. Microanal.* 25 (2019) 2634–2635.

[2] F. Sun et al., *Acta Mater.* 61 (2013) 6406–6417.

The authors gratefully acknowledge to CNPq, FAPERJ and CAPES.

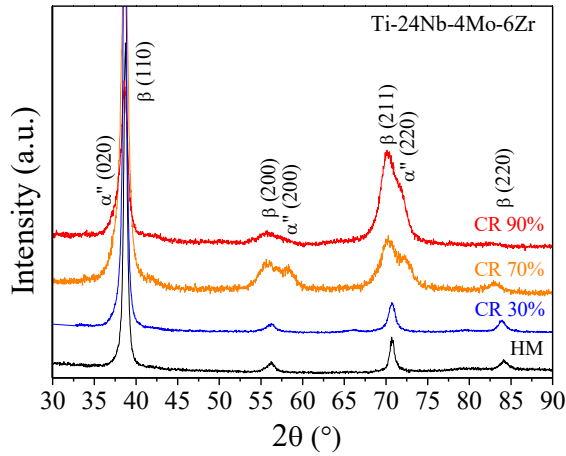


Figure 1: XRD patterns of the homogenized (HM) and cold rolled samples (30%, 70% and 90%). Alloy Ti-24Nb-4Mo-6Zr.

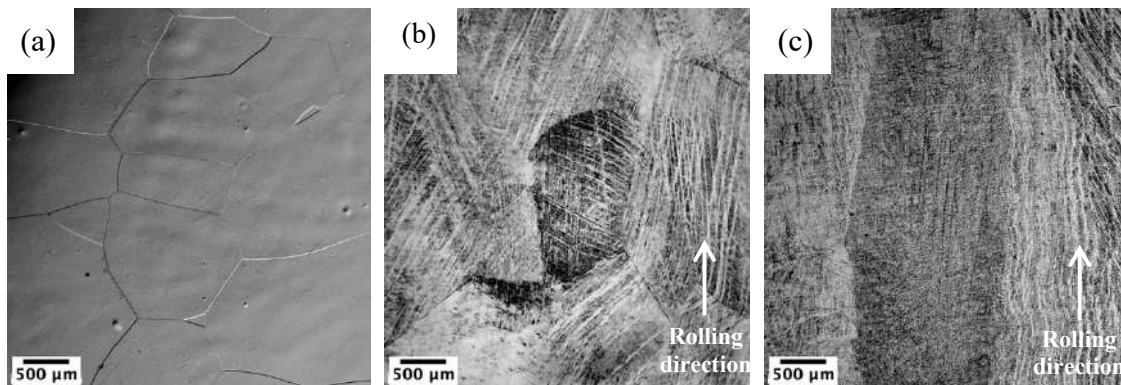
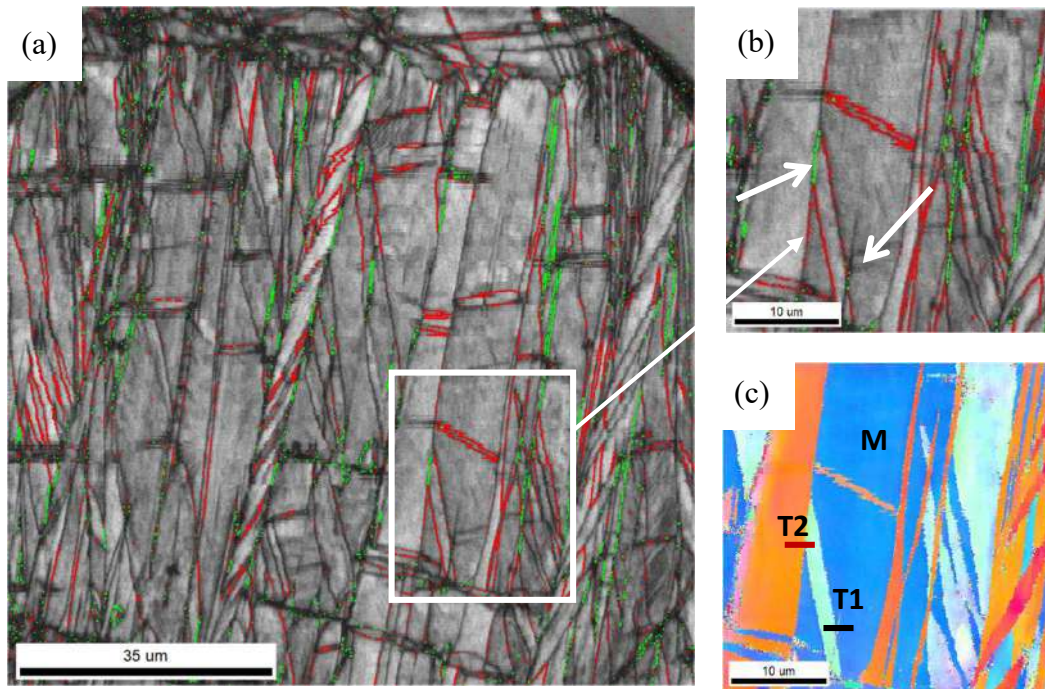


Figure 2: OM images of the Ti-24Nb-4Mo-6Zr alloy (a) homogenized, (b) 70% cold rolled, (c) 90% cold rolled.



Boundaries: CSL							
	Sigma	Tolerance	Fraction	Volume	MDF Value	Number	Length
	11	4.52	0.096	0.0075	12.75	15961	1.38226 mm
	3	8.66	0.043	0.0176	2.45	7184	622.152 microns

Figure 3: Microstructural characterization of Ti-24Nb-4Mo-6Zr alloy after 30% deformation; EBSD β orientation map with CSL boundaries ($\Sigma 3$ in green, $\Sigma 11$ in red).



Nanostructured $\text{Pr}_{1-x}\text{Sr}_x\text{MnO}_3$ films synthesized by pulsed laser deposition under 1 torr: impact of thermal treatment on morphology, crystallinity and magnetization

N. R. Checca¹, W. S. Torres², F. Garcia¹, A. Mello¹, A. L. Rossi¹ and D. Rocco²

¹ Brazilian Center for Physics Research, R. Dr. Xavier Sigaud 150, 22290-180, Rio de Janeiro-RJ, Brazil.

² Institute of Physics, Federal University Fluminense, Brazil.
nomifsc@gmail.com

Manganites with perovskite structure in nanometer scale are studied intensively due to the effects of defects on the surface cause topological disturbances, resulting in changes on physical properties in compared with their bulk counterparts; opening new approaches for potential applications [1]. In this work, we produced nanostructured $\text{Pr}_{1-x}\text{Sr}_x\text{MnO}_3$ films by pulsed laser deposition starting of a $\text{Pr}_{0.5}\text{Sr}_{0.5}\text{MnO}_3$ target homemade with crystalline orthorhombic (*Pnma*) phase. The films were deposited using the laser beam Green with fluence of 25.50 mJ/cm^2 under high argon gas pressure (1 Torr) on silicon substrates for 120 min at room temperature (PSMO_1). The films were heat treated at 600°C (PSMO_2), 750°C (PSMO_3) and 900°C (PSMO_4) for 1 hour in air for the purpose of studying the impact of heat treatment on the crystallinity and morphology and its effect on the magnetic properties. The crystallinity of the films was studied by X-ray diffraction (XRD) and selected area electron diffraction (SAED). The orthorhombic phase was found as the main phase in films treated with high temperatures. Scanning electron microscopy (SEM) revealed a porous morphology of "trees like" vertically elongated grains formed by the vertical stacking of nanoparticles (NPs). Transmission electron microscopy (TEM) revealed the evolution of NPs morphology and size with temperature starting from spherical shaped particles with $\langle D \rangle = 16.6 \text{ nm}$ to faceted shaped particles with $\langle D \rangle = 82.2 \text{ nm}$. The strontium concentration (x) in stoichiometry $\text{Pr}_{1-x}\text{Sr}_x\text{MnO}_3$ samples was determined by X-ray energy dispersive spectroscopy (EDS) and found around of $x = 0.35 - 0.40$. The magnetic properties revealed by the MxT measures exhibit high ferromagnetic transition temperatures ($\sim 300 \text{ K}$). This work encourages the production of nanostructured manganite films by PLD for different applications due to its interesting "trees-like" morphology composed of faceted NPs and high ferromagnetic transition temperature.

REFERENCES

[1] V. Andrade et al., Journal of Solid State Chemistry. 219 (2014) 87.

ACKNOWLEDGMENT

This research was supported by FAPERJ, CNPq and LABNANO/CBPF (Brazil).

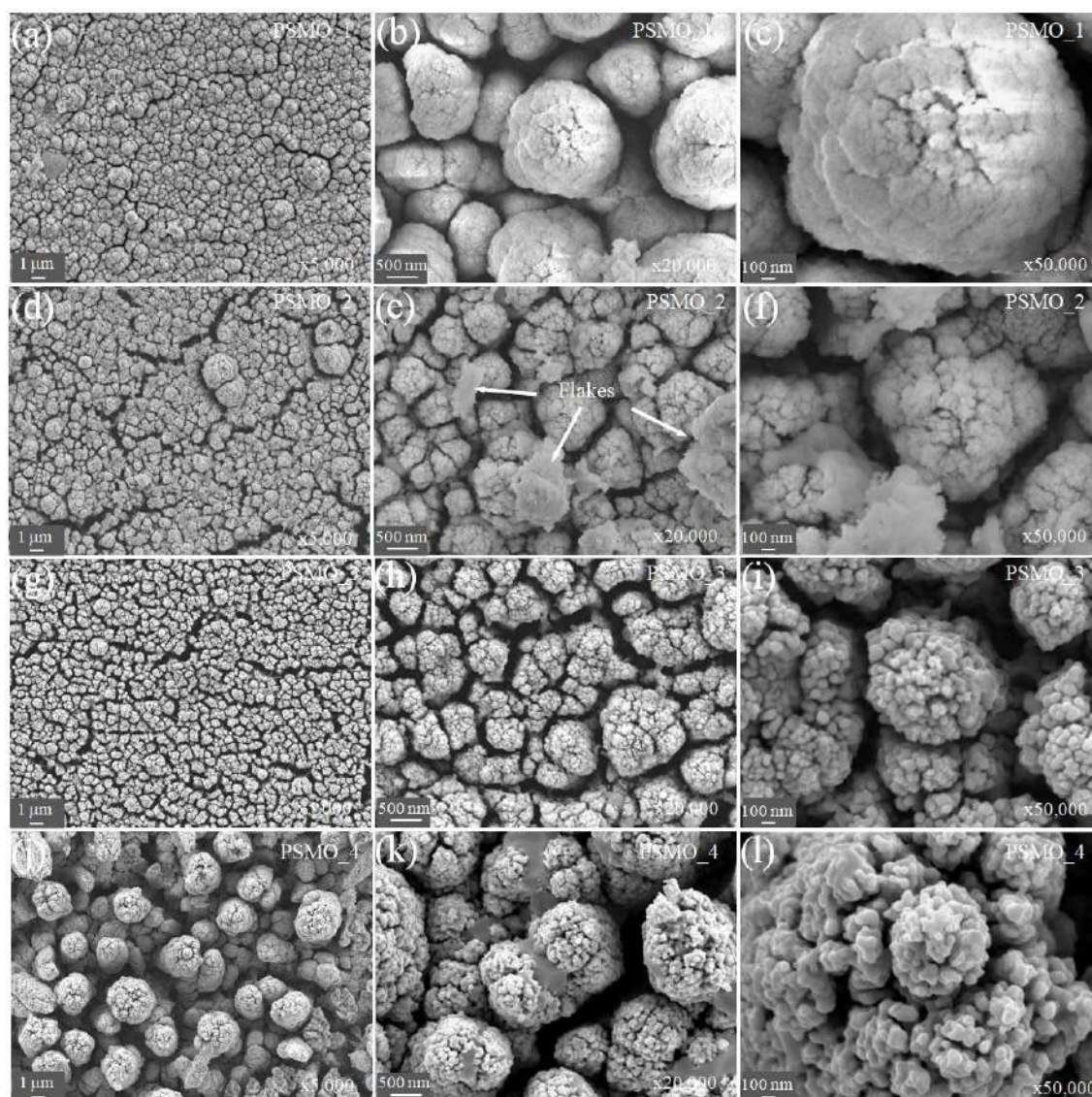


Fig.1 Top view of PSMO_1, PSMO_2, PSMO_3 and PSMO_4 films showing the evolution with the heat treatment.

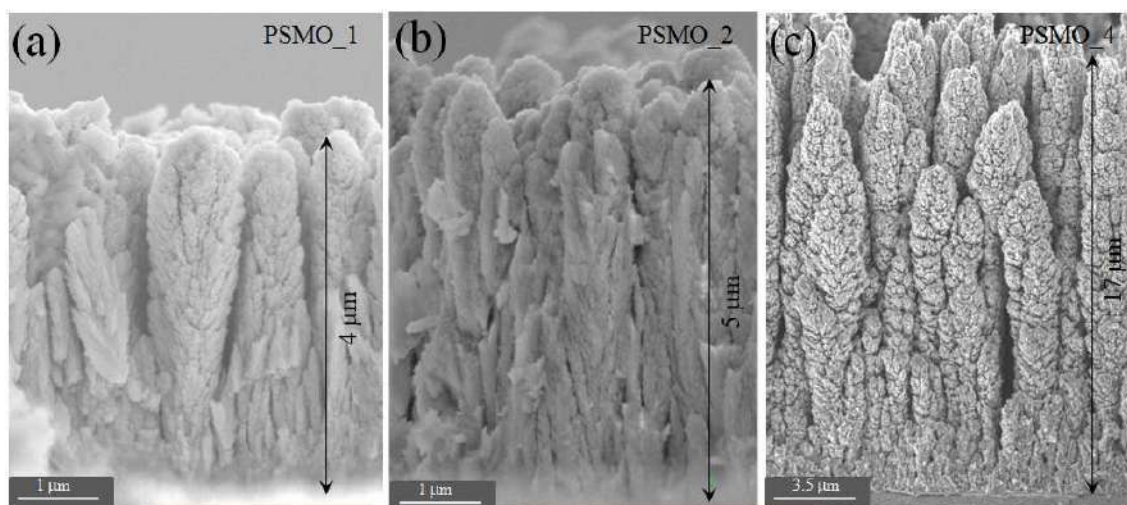


Fig. 2 SEM images from the cross-section of films: (a) PSMO_1, (b) PSMO_2 and (b) PSMO_4.

E.C. GONÇALVES
EDITOR CIENTÍFICO